

Cumhuriyet Science Journal
Faculty of Science Cumhuriyet University 58140
Sivas-TURKEY
Phone: +90(346)2191010-1522
Fax: +90(346)2191186
e-mail: csj@cumhuriyet.edu.tr
http://dergipark.gov.tr/csj

Cumhuriyet Science Journal Vol: 42 No: 1 Year: 2021



Sivas Cumhuriyet University

ISSN : 2587-2680
e-ISSN : 2587-246X

Cumhuriyet
Science
Journal



Volume: 42

Number: 1

Year: 2021



ISSN: 2587-2680
e-ISSN: 2587-246X
Period: Quarterly
Founded: 2002
Publisher: Sivas Cumhuriyet
University

Cumhuriyet Science Journal (CSJ)

Journal Previous Name: Cumhuriyet Üniversitesi Fen-Edebiyat Fakültesi Fen Bilimleri Dergisi

Old ISSN: 1300-1949

Owner on behalf of the Sivas Cumhuriyet University, Faculty of Science

Prof. Dr. İdris Zorlutuna (Sivas Cumhuriyet University)

Editor in Chief

Prof. Dr. İdris ZORLUTUNA (Sivas Cumhuriyet University)

Managing Editor

Assoc. Prof. Dr. Adil ELİK (Sivas Cumhuriyet University)

Editors

Prof. Dr. Baki KESKİN

bkeskin@cumhuriyet.edu.tr

Subjects: Mathematics and Statistics

Institution: Sivas Cumhuriyet University

Assoc. Prof. Dr. Adil ELİK

elik@cumhuriyet.edu.tr

Subjects: Chemistry and Chemical Engineering,
Environmental Sciences, Basic Sciences (General)

Institution: Sivas Cumhuriyet University

Prof. Dr. Nilüfer TOPSAKAL

ntopsakal@cumhuriyet.edu.tr

Subjects: Applied Mathematics

Institution: Sivas Cumhuriyet University

Prof. Dr. Serkan AKKOYUN

sakkoyun@cumhuriyet.edu.tr

Subjects: Physics and Physical Engineering

Institution: Sivas Cumhuriyet University

Prof. Dr. Hülya KURŞUN

hkursun@cumhuriyet.edu.tr

Subjects: Earth Sciences

Institution: Sivas Cumhuriyet University

Prof. Dr. Halil İbrahim ULUSOY

hiulusoy@cumhuriyet.edu.tr

Subjects: Chemistry, Analytical Chemistry, Drug Analysis, Pharmacy

Institution: Sivas Cumhuriyet University

Assoc. Prof. Dr. Nail ALTUNAY

naltunay@cumhuriyet.edu.tr

Subjects: Bioanalytical Chemistry, Chemometric Analysis

Institution: Sivas Cumhuriyet University

Section Editors

Prof. Dr. Natalia BONDARENKO

bondarenkonp@info.sgu.ru

Subjects: Applied Mathematics and Physics

Institution: Samara University

Prof. Dr. Muhammet BEKÇİ

mbekci@cumhuriyet.edu.tr

Subjects: Statistics

Institution: Sivas Cumhuriyet University

Prof. Dr. Marcello LOCATELLI

marcello.locatelli@unich.it

Subjects: Analytical Chemistry

Institution: University "G. d'Annunzio" of Chieti-Pescara

Prof. Dr. Konstantin P. KATIN

kpkatin@yandex.ru

Subjects: Theoretical Chemistry, Computational design of nanostructures, nanodevices and nanotechnologies

Institution: National Research Nuclear University

Assoc. Prof. Dr. Duran KARAKAŞ

dkarakas@cumhuriyet.edu.tr

Subjects: Inorganic Chemistry, Theoretical Chemistry

Institution: Sivas Cumhuriyet University

Assoc. Prof. Dr. Yaşar ÇAKMAK

ycakmak@cumhuriyet.edu.tr

Subjects: Applied Mathematics

Institution: Sivas Cumhuriyet University

Assoc. Prof. Dr. Sevgi DURNA DAŞTAN

sdurna@cumhuriyet.edu.tr

Subjects: Molecular Biology

Institution: Sivas Cumhuriyet University

Assist. Prof. Dr. Didem ALTUN

didemaltun@cumhuriyet.edu.tr

Subjects: Engineering sciences

Institution: Sivas Cumhuriyet University

Abstracted&Indexing

ULAKBİM TR-Dizin

Index Copernicus (ICI Journals Master List)

Clarivate Analytics Zoological Record

Crossref

Directory of Open Access Journals (DOAJ)

WorldCat

Akademik Dizin

Arastirmax Bilimsel Yayın İndeksi

Bielefeld Academic Search Engine (BASE)

Directory of Research Journal Indexing (DRJI)

Google Scholar

Research Gate

Idealonline

Editorial Board

Prof. Dr. Sezai ELAGÖZ (ASELSAN)
Prof. Dr. Mustafa SOYLAK (Erciyes University)
Prof. Dr. Chuan Fu Yang (Nanjing University of Science and Technology)
Prof. Dr. Münevver SÖKMEN (KGTU)
Prof. Dr. Hüseyin MERDAN (TOBB ETU)
Prof. Dr. Mehmet AKKURT (Erciyes University)
Prof. Dr. Mustafa KAVUTÇU (Gazi University)
Prof. Dr. Francois VOS (The University of Queensland)
Prof. Dr. Abuzar KABIR (International Forensic Research Institute)
Prof. Dr. Mustafa TÜZEN (GOP University)
Prof. Dr. Songül KAYA MERDAN (METU)
Prof. Dr. Jose Javier Valiente-Dobon (INFN-LNL, Padova University)
Prof. Dr. Yeşim SAĞ AÇIKEL (Hacettepe University)
Prof. Dr. Mehmet ŞİMŞİR (Sivas Cumhuriyet University)
Prof. Dr. Atalay SÖKMEN (KGTU)
Prof. Dr. Ricardo I. JELDRES (Universidad de Antofagasta)
Prof. Dr. Mustafa YILDIRIM (Sivas Cumhuriyet University)
Prof. Dr. Ali DELİCEOĞLU (Erciyes University)
Prof. Dr. Tuncay BAYRAM (Karadeniz Technical University)
Prof. Dr. Gökhan KOÇAK (Erciyes University)
Prof. Dr. Nadjet Laouet (Freres Mentouri Constantine-1 University)
Assoc. Prof. Dr. Savaş KAYA (Sivas Cumhuriyet University)

Layout Editors:

Assist. Prof. Dr. Merve Esra TÜRKAY
Lecturer Aykut HASBEK

Copyeditors:

Research Assistant Özgür İNCE
Research Assistant Doğa Can SERTBAŞ
Research Assistant Dr. Hacı Ahmet KARADAŞ

Proofreader:

Assist. Prof. Dr. Yener ÜNAL
Lecturer Aykut HASBEK

Publication Type. Peer Reviewed Journal

Cite Type: Cumhuriyet Sci. J.

Contact Information

Faculty of Science Cumhuriyet University
58140 Sivas- TURKEY
Phone: +90(346)2191010-1522
Fax: +90(346)2191186
e-mail: csj@cumhuriyet.edu.tr
<http://dergipark.gov.tr/csj>

CONTENTS

PAGES

Ahmet Kemal FİLİZ, Sebahattin KARABULUT

The effect of penicillin-induced epileptiform activity on proinflammatory cytokines levels in the rat brain..... 1-6

Sinem DEMİR, Mehmet ATAŞ

*Comparison of *tul4*, *fopA*, 16S rRNA and RD1 gene regions of Francisella tularensis strains isolated from Sivas, Turkey* 7-12

Emre ASLAN

Hydrogen evolution by ternary metal selenide at biomembrane-like soft interfaces..... 13-21

Asuman UÇAR, Mükerrerem FINDIK, Nuriye KOÇAK, Alper ÇOLAK, Onur ŞAHİN

Hydrothermal synthesis and crystal structures of a novel Keggin-type polyoxometalate based on 1,10-phenanthroline. 22-29

Meliha ÇETİN KORUKÇU

N-Alkoxy carbonyl / carbamoylmethyl substituted 1H-imidazol-2-yliden-Pd (II) complexes as highly efficient catalysts for Suzuki-Miyaura cross-coupling reaction..... 30-37

Savaş KAYA, Robson Fernandes De FARIAS

Electron affinities for highly charged groups 15 and 16 anions..... 38-44

Zinet ZAIM, Duran KARAKAŞ

Computational study on the structural, electronic, molecular and thermochemical properties of hypothetical [Tp(CO)2Mo≡C-Ph]2+ and [L(CO)2Mo≡C-Ph]+ carbyne complexes..... 45-59

Özlem KAPLAN, Nazan GÖKŞEN

Biosynthesis of silver nanoparticles from Teucroside and investigation of its antibacterial activity..... 60-67

Ayşegül ŞENOCAK, Hüseyin AKBAŞ

Palladium complexes of NO type Schiff bases: synthesis, characterization and antioxidant activities..... 68-74

Sıla Övgü KORKUT UYSAL, Yeşim ÇİÇEK

Numerical solution of the brusselator model by time splitting method..... 75-87

Asif YOKUŞ, Hülya DURUR

(G'/G, I/G)-expansion method for analytical solutions of Jimbo-Miwa equation..... 88-98

Özgün GÜRMEAN ALANSAL, Ummahan EGE ARSLAN

Crossed modules bifibred over k-Algebras..... 99-114

Emin AYGUN, Betül ERDAL

Radicals of soft intersectional ideals in semigroups..... 115-122

Sevda YILDIZ

Statistical relative uniform convergence of a double sequence of functions at a point and applications to approximation theory..... 123-131

Emrah YILMAZ, Sertaç GÖKTAŞ

On the solution of a Sturm-Liouville problem by using Laplace transform on time scales..... 132-140

Sefa Anıl SEZER, İbrahim ÇANAK

On the Euler method of summability and concerning Tauberian theorems..... 141-144

Nuray YAVUZKANAT

Geant4 investigation of the alpha-beta-gamma detector system used in medical imaging, environmental and nuclear site monitoring..... 145-151

Aykut Evren YAVUZ

Determination of order parameter and birefringence depending on temperature of nematic calamitic mesophase formed by TTAB + water binary system using polarized microscopy..... 152-155

Canel EKE, Mavra ISHFAQ <i>A study on the activity concentrations of natural radionuclides and annual effective dose values in some tobacco samples.....</i>	156-163
Adnan ÖZDEMİR <i>Investigation of the thermoluminescence properties Ti⁴⁺ doped MgO synthesized solid-state assisted solution combustion synthesis method.....</i>	164-169
Yasemin GÜNDOĞDU, Mehmet TAŞER, Hamdi Şükür KILIÇ <i>Systematic discrimination of heptane isomers with femtosecond laser linear time of flight mass spectrometry.....</i>	170-176
Yeşim ŞAHİN, Mahmut BOYUKATA <i>Description of even-even Ti isotopes within IBM-1 model.....</i>	177-183
İsmail ALTUNTAS <i>XRD and photoluminescence measurements of GaN grown on dome shaped patterned sapphire with different NH₃ flow rates.....</i>	184-190
Hasan Hüseyin GÜL, Hülya BAYRAK <i>Proposed nonparametric tests for the ordered alternative in a completely randomized and randomized block mixed design.....</i>	191-200
Mehmet YILMAZ, Muhammet BEKÇİ <i>Construction of a bivariate copula by Rüschendorf's method.....</i>	201-208
Aydın DEMİR <i>The fundamental frequencies of longitudinally vibrating rods carrying tip mass and transversally vibrating beams carrying tip mass by using several methods.....</i>	209-217
Fethullah GÖÇER <i>Improving sustainable supplier evaluation by an integrated MCDM method under pythagorean fuzzy environment.....</i>	218-235



The effect of penicillin-induced epileptiform activity on proinflammatory cytokines levels in the rat brain

Ahmet Kemal FİLİZ¹ , Sebahattin KARABULUT^{2,*} 

¹Sivas Cumhuriyet University, School of Medicine, Department of Physiology, Sivas/ TURKEY

²Sivas Cumhuriyet University, Vocational School of Health Services, Department of Medical Services and Techniques, Sivas/ TURKEY

Abstract

Emerging evidence indicates a pathogenic role of protracted neuroinflammation in the various neurodegenerative diseases, including epilepsy. Neuroinflammation may contribute to neuronal hyperexcitability underlying seizure formation. The current research aims to examine the changes in the levels of proinflammatory cytokines such as interleukin-1 β (IL-1 β) and tumor necrosis factor- α (TNF- α) in the penicillin epilepsy model. In the present study, 12 male Wistar albino rats were randomly divided into two groups as sham and penicillin epilepsy model. Seizures were induced with the intracortical (i.c.) single microinjection 500 IU of penicillin-G into neocortex. Rats were decapitated after observing the cortical epileptic activity and brains were removed by craniotomy. Proinflammatory cytokines (TNF- α and IL-1 β) were measured by using ELISA methods in the cortical and hippocampal brain regions. Penicillin significantly up-regulated the expression of IL-1 β and TNF- α in the rat cortex, but did not affect the hippocampal cytokines levels. This study is indicative of the neuroinflammatory potential of cortical penicillin administration.

Article info

History:

Received: 28.07.2020

Accepted: 06.03.2021

Keywords:

Neuroinflammation,
Cytokine,
Penicillin epilepsy
model,
Rat.

1. Introduction

Epilepsy is a neurological disease that is characterized by recurrent unprovoked seizures and the associated comorbidities, including cognitive, psychiatric, and social consequences [1]. Patients with epilepsy are generally suffer from behavior such as loss of awareness, jerking, and déjà vu caused by the suddenly synchronous and excessive discharges in the brain. Unfortunately, 30% of all cases of epilepsy patients are unresponsive to pharmacotherapy, most of them are not convenient for surgery and have to continue to suffer from recurring seizures and debilitating side effects of antiepileptic drugs [2]. Furthermore, the available antiepileptic drugs have been developed for antiictogenesis (prevention of seizures) and not for antiepileptogenesis (prevention of epilepsy or disease-modifying). Hence, this calls for more research to investigate new and effective therapies for the treatment of epilepsy, by primarily understanding the basis for the initiation and progression of seizures. This need including therapies that target epileptogenesis as well as ictogenesis.

Epileptogenesis, by which a normal brain becomes epileptic, is a dynamic process that increasingly alters

neuronal excitability. The evidence to date suggests that seizures can be derived from cortical or limbic lesions, including focal cortical dysplasia and hippocampal sclerosis. Moreover, the hippocampal formation is more vulnerable to epileptic activity in comparison to the cerebral cortex [3]. Hippocampal sclerosis caused by status epilepticus is characterized by pathological structural and functional changes that can affect epileptogenesis such as neuronal damage, gliosis and mossy fiber sprouting. There is strong evidence that inflammatory processes within the brain might constitute an essential mechanism in the etiopathogenesis of epileptogenesis [4]. Also, it is well-accepted that brain inflammation takes part to be an integral part of the diseased hyperexcitable brain tissue from which spontaneous seizures arise. Several lines of evidence from animal and human studies suggest that epileptic seizures can induce the production of proinflammatory cytokines such as interleukin-1 β (IL-1 β) and tumor necrosis factor- α (TNF- α) in the brain, which in turn may affect the epileptogenesis and the course of epilepsies [4-5]. Therefore, the increase in knowledge about the role of the inflammatory aspects of seizure may encourage the use of anti-inflammatory agents for developing disease-modifying therapy.

*Corresponding author. e-mail address: : sbkarabulut@cumhuriyet.edu.tr

Animal models have played a crucial role in epilepsy research, including a better understanding of the disease and the discovery of new antiepileptic drugs. These experimental models of epilepsy have been instrumental in the understanding of the association of inflammation with epileptogenesis, and to resolve the role of inflammation and associated pathways in the formation of a seizure in the brain as well. Findings from the studies performed in rodent epilepsy models suggested the role of inflammation as either the cause or the consequence of epilepsy contributing to its etiopathogenesis [6]. The penicillin-epilepsy model has been commonly used in experimental animal studies to research the neuronal basis of epilepsy. Seizures are induced in a generalized fashion by the intracortical, intracerebroventricular, or intraperitoneal administration of penicillin, a GABA receptor antagonist, on the experimental animals [7-9]. There is no study in the literature on the roles of proinflammatory cytokines in the penicillin rat model of epilepsy. For that reason, this study was planned to assess whether penicillin-induced seizures affect the proinflammatory cytokines such as IL-1 β and TNF- α in the cortex and hippocampus.

2. Materials and Methods

2.1. Animals

This study was performed using twelve adult male Wistar rats (230-250 g in weight) were obtained from

the Cumhuriyet University Animal Laboratory. All animal care and experimental procedures were performed in accordance with the guidelines of the Local Ethics Committee for the welfare of experimental animals and were approved (approval code 65202830-050.04.04-422). Animals were maintained in an air-conditioned room with controlled temperature (22 ± 2 °C) under a 12-h light/dark cycle with lights on at 07:00 am.

2.2. Drugs

Penicillin G (İ.E. Ulagay, Turkey) was dissolved in physiological saline. All other general agents were used in the studies were of analytical grade.

2.3. Experimental protocol

Adult male Wistar rats (weighing 230-250 g) were used in the experiments. The rats were fully anesthetized with Ketamine at a dose of 90 mg/kg administered intraperitoneally (i.p.). After the onset of anesthesia, rats were placed in a stereotaxic frame and the heads of rats were shaved. The head skin was incised by using a surgical blade at midline rostra-caudal level of the scalp and the periosteum was removed by scraping. With reference to bregma point with the stereotaxic tool, a total of 3 holes having 2 mm diameters each were opened using a micro drill.

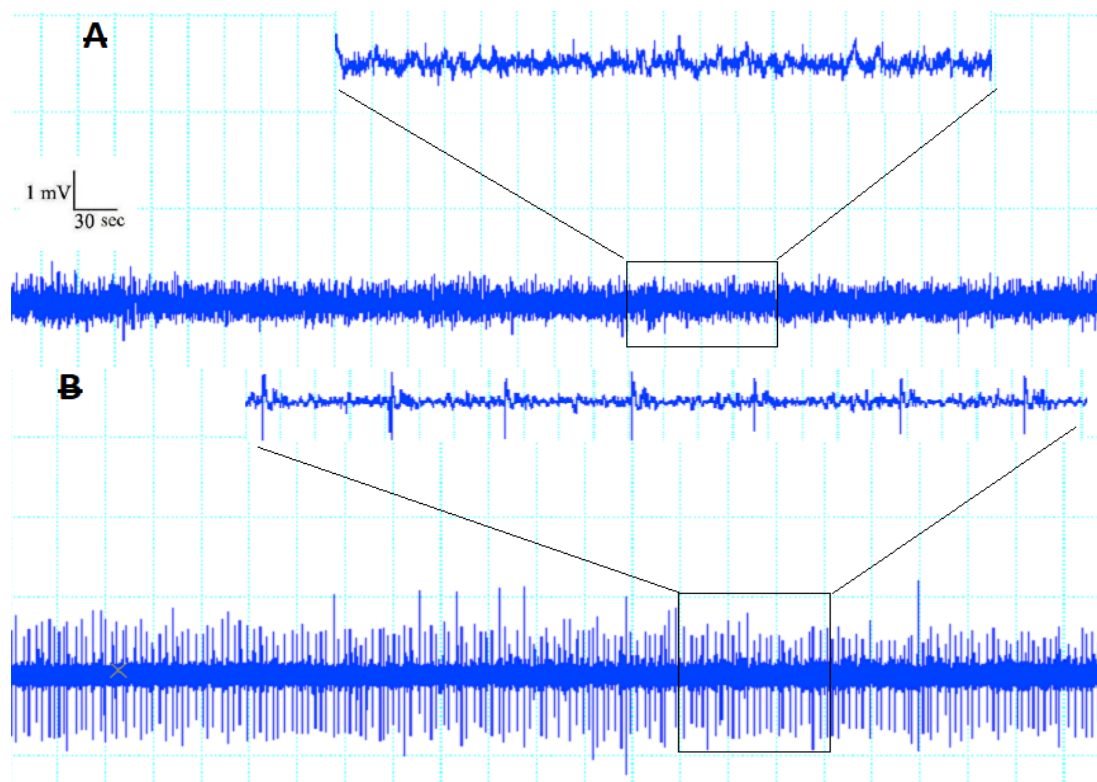


Figure 1. Representative illustration of ECoG recordings for Sham (A) and Penicillin groups (B).

500 IU penicillin-G was injected into the neocortex (by a Hamilton microsyringe with an infusion rate of 0.5 $\mu\text{L}/\text{min}$), with the guidance of Paxinos and Watson stereotaxic atlas, which is located at coordinates of 1.1 mm anteroposterior, 1.5 mm lateral to bregma, and 3.2 mm vertical from the dura [10]. Saline was given i.c. to the sham group instead of penicillin-G. The recording electrodes were located on the cortex to record cortical electrical activity during electrocorticography (ECoG). The first electrode was placed in a position 3 mm lateral to sagittal suture and 4 mm anterior to bregma, while the second one was mounted in a position 3 mm lateral to sagittal suture and 4 mm posterior to bregma. A third electrode was used as a reference and implanted in the skin [7]. The ECoG activity was monitored online using a PowerLab 4/25 (AD Instruments, Australia) data acquisition system (Figure 1). After observing the epileptic activity of penicillin injection, all rats were decapitated and their brains were removed surgically for biochemical assessment.

2.4. Biochemical analysis

The rat's brains were excised after killed, and the cortex and hippocampus were dissected. Then these tissue samples were homogenized in ice-cold Phosphate-Buffered Saline (PBS) solution (pH 7.4) using a mechanical homogenizer (Analytic Jena speed mill plus, Jena, Germany). The homogenates were centrifuged at $12,000 \times g$ for 10 min at 4°C . Then, the supernatants were collected for determination of total protein levels in samples by a Bradford protein assay kit. (Merck, Germany) [11]. The levels of cortical and hippocampal TNF- α and IL-1 β were determined by using rat ELISA commercial kits (Shanghai Sunred Biological Technology, Shanghai, China). In brief, the standard solution and tissue samples were incubated for 60 min at 37°C after they were added to the plate. Following the washing phase, after addition of staining solutions, the tissue samples were incubated for 15 min at 37°C . Then, following the application of stop solution, the wells were read at 450 nm without delay.

2.5. Statistical analysis

The data are expressed as mean \pm standard error of mean (SEM). The differences between the mean values for each group of the levels of TNF- α and IL-1 β were analyzed using the independent samples t-test. A p-value of less than 5% was accepted as statistically significant.

3. Results and Discussion

Increasing evidence from patient studies and experimental models implicate the presence of neuroinflammation in epilepsy [12]. Proinflammatory cytokines, such as IL-1 β and TNF- α , contribute to hyperexcitability and can cause spontaneous seizures [13,14]. These results of which signify the great value of cytokines in the development of new therapeutic strategies against epilepsy. It has been proposed that drugs that block specific inflammatory processes may have therapeutic potential for epilepsy is associated with proinflammatory signals in the brain. Therefore, in the current study, the levels of IL-1 β and TNF- α were investigated in the hippocampus and cortex after penicillin-treatment. We found that the levels of IL-1 β and TNF- α increased in the cortex after i.c. penicillin administration, but did not change in the hippocampus.

IL-1 β belongs to the IL-1 family of proinflammatory cytokines and acts as an amplifier of immune reactions [15]. It is secreted by activated microglia and astrocytes within nearly two hours of central nervous system insult, such as status epilepticus [16]. In the present study, the level of IL-1 β in the cortex was significantly up-regulated by penicillin administration (Figure 2A, $p < 0.001$). The regulation of the level of IL-1 β in several epileptic animal models is well-known, but there are few studies on the involvement of this cytokine in penicillin model epilepsy. In an early pharmacological study, it has been reported that penicillin-induced electrocorticographic and motor seizures are weakened by using nonsteroidal antiinflammatory drugs in rats [17]. Zhu et al. reported that penicillin leads to the release of inflammatory factors (IL-1 β and TNF- α) and activates the MAPK signaling pathway, ultimately cause epilepsy in primary astrocyte cell culture [18]. This is coherent with the results of the present study where we demonstrate that penicillin cause an increase in the level of cortical IL-1 β . However, unlike the cortical IL-1 β , no significant difference between the groups was found in hippocampal IL-1 β levels (Figure 2B, $p > 0.05$). In penicillin model epilepsy, the seizures start from the cortex and then spread to limbic structures such as the hippocampus. In addition, as in our study, there may not be enough time to obtain an inflammatory response in an acute seizure model. Supporting this possibility, in a recent study, Taskiran et al. compared inflammatory markers in the brain in PTZ-induced acute seizure and chronic epilepsy model and reported more significant results in the chronic PTZ model compared to acute seizure model [19].

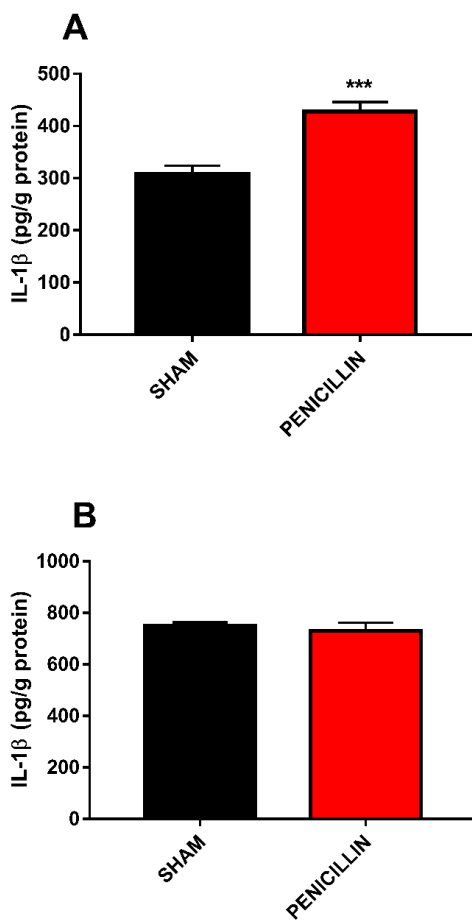


Figure 2. Effects of intracortical penicillin administration on the level of IL-1 β in the cortex (A) and hippocampus (B) in rat. Data expressed as mean \pm SEM. n=6. ***p<0.001 compared with Sham group.

Similar to IL-1 β , pro-inflammatory cytokine TNF- α is also released from activated glial cells [20]. Although TNF- α is rapidly induced after seizures in rodent epilepsy models, its role in epilepsy remains controversial. TNF- α plays a bidirectional role in epilepsy. Balosso et al. showed that transgenic mice with astrocytic overexpression of TNF- α display reduced susceptibility to seizures [21]. Conversely, Shandra et al. reported that i.p. injection of TNF- α elongated the duration of epileptic discharges in amygdala-kindled animals [22]. These apparent contradictions can be reconciled by considering either the activation of its different receptors in the brain or the differences in TNF- α concentrations. According to this, lower concentrations of TNF- α were proconvulsive, whereas higher concentrations of TNF- α have an anticonvulsive effect. In our study, we found that penicillin caused a significant increase in the level of proinflammatory cytokine TNF- α in the rat cortex (Figure 3A, p<0.01).

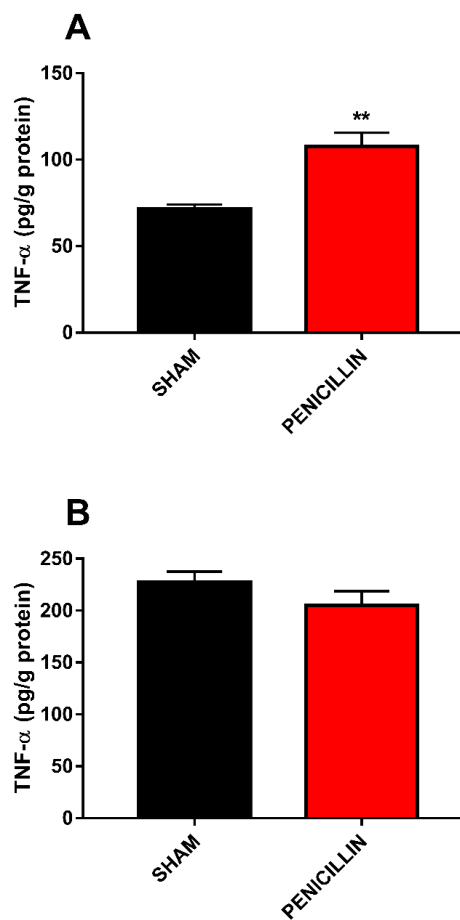


Figure 3. Effects of intracortical penicillin administration on the level of TNF- α in the cortex (A) and hippocampus (B) in rat. Data expressed as mean \pm SEM. n=6. **p<0.01 compared with Sham group.

This finding implies that TNF- α contributes to penicillin-induced epileptic seizures. In animal models, seizures can increase the concentration of TNF- α in the brain while its mechanism remains obscure. Moreover, due to the lack of clinical studies, the role of TNF- α in epilepsy has not yet been elucidated in humans [3]. However, detected no differences across the two groups after penicillin administration in hippocampal TNF- α levels (Figure 3B, p>0.05). As noted above, this result can be attributed to the area of the brain where penicillin was injected and/or the use of an acute seizure model.

In conclusion, we firstly demonstrated that i.c. penicillin administration upregulated proinflammatory cytokines such as IL-1 β and TNF- α in the rat cortex. To the best of our knowledge, the presence of proinflammatory cytokines in the penicillin model of epilepsy remains to be elucidated. Clarifying changes in the specific brain region of other proinflammatory

cytokines involved in epilepsy will be important for future targeted treatments for this disease.

Acknowledgment

The authors thank the institution for using the facilities of the Sivas Cumhuriyet University.

Conflicts of interest

The authors state that did not have conflict of interests.

References

- [1] Fisher R.S., Acevedo C., Arzimanoglou A., Bogacz A., Cross J. H., Elger C.E., Engel J., Forsgren L., French J.A., Glynn M., Hesdorffer D.C., Lee B.I., Mathern G.W., Moshé S.L., Perucca E., Scheffer I.E., Tomson T., Watanabe M., Wiebe S., ILAE official report: A Practical Clinical Definition of Epilepsy, *Epilepsia*, 55(4) (2014) 475-482.
- [2] Chen Z., Brodie M.J., Liew D., Kwan P., Treatment Outcomes in Patients with Newly Diagnosed Epilepsy Treated with Established and New Antiepileptic Drugs: A 30-Year Longitudinal Cohort Study, *JAMA Neurol.*, 75(3) (2018) 279-286.
- [3] Li Z.H., Li L.L., Jin M.F., Chen X.Q., Sun Q., Ni H., Dysregulation of zinc/lipid metabolism-associated genes in the rat hippocampus and cerebral cortex in early adulthood following recurrent neonatal seizures, *Mol. Med. Rep.*, 16(4) (2017) 4701-4709.
- [4] Vezzani A., French J., Bartfai T., Baram T.Z., The role of inflammation in epilepsy, *Nat Rev Neurol.*, 7(1) (2011) 31-40.
- [5] Li G., Bauer S., Nowak M., Norwood B., Tackenberg, B., Rosenow F., Knake S., Oertel W.H., Hamer H.M., Cytokines and Epilepsy. *Seizure*, 20(3) (2011) 249-256.
- [6] Rawat C., Kukal S., Dahiya U.R., Kukreti R., Cyclooxygenase-2 (COX-2) inhibitors: future therapeutic strategies for epilepsy management, *J Neuroinflammation*, 16(1) (2019) 1-15.
- [7] Sumbul O., Aygun H., The effect of vitamin D3 and paricalcitol on penicillin-induced epileptiform activity in rats., *Epilepsy Res.*, 159 (2020) 106262.
- [8] Marangoz A.H., Kocacan S.E., Him A., Kuruoglu E., Cokluk C., Marangoz C., Proconvulsant Effect of Papaverine on Penicillin-Induced Epileptiform Activity in Rats., *Turk Neurosurg.*, 28(3) (2018) 479-482.
- [9] Bo G.P., Mainardi P., Benassi E., Besio G., Faverio A., Scotto P.A., Loeb C., Parenteral penicillin model of epilepsy in the rat: a reappraisal, *Methods Find Exp. Clin. Pharmacol.*, 8(8) (1986) 491-496.
- [10] Paxinos G., Watson C., The Rat Brain in Stereotaxic Coordinates, 6th ed., Amsterdam: Elsevier Academic Press, (2007).
- [11] Kruger N.J., The Bradford method for protein quantitation, *Methods Mol. Biol.*, 32 (1994) 9-15.
- [12] Webster K.M., Sun M., Crack P., O'Brien T.J., Shultz S.R., Semple B.D., Inflammation in epileptogenesis after traumatic brain injury, *J. Neuroinflammation*, 14(1) (2017) 10.
- [13] Robel S., Buckingham S.C., Boni J.L., Campbell S.L., Danbolt N.C., Riedemann T., Sutor B., Sontheimer H., Reactive astrogliosis causes the development of spontaneous seizures, *J Neurosci.*, 35(8) (2015) 3330-3345.
- [14] Eyo U.B., Murugan M., Wu L.J., Microglia-neuron communication in epilepsy, *Glia*, 65 (2017) 5–18.
- [15] Dinarello C.A., Biologic basis for interleukin-1 in disease, *Blood*, 87(6) (1996) 2095–2147.
- [16] De Simoni M.G., Perego C., Ravizza T., Moneta D., Conti M., Marchesi F., De Luigi A., Garattini S., Vezzani A., Inflammatory cytokines and related genes are induced in the rat hippocampus by limbic status epilepticus, *Eur. J. Neurosci.*, 12(7) (2000) 2623-2633.
- [17] Wallenstein M.C., Attenuation of penicillin models of epilepsy by nonsteroidal anti-inflammatory drugs, *Exp Neurol.*, 98(1) (1987) 152-160.
- [18] Zhu X., Chen Y., Du Y., Wan Q., Xu Y., Wu J., Astragaloside IV attenuates penicillin-induced epilepsy via inhibiting activation of the MAPK signaling pathway, *Mol. Med. Rep.*, 17(1) (2018) 643-647.
- [19] Taşkıran AŞ., Taştumur Y., The comparison of inflammatory markers in pentylene-tetrazole-induced acute epileptic seizure model and chronic epilepsy model in rats., *Cumhuriyet Sci. J.*, 41(3) (2020) 635-641.

- [20] Devinsky O., Vezzani A., O'Brien T.J., Jette N., Scheffer I.E., de Curtis M., Perucca P., *Epilepsy, Nat. Rev. Dis. Primers*, 4 (2018) 18024.
- [21] Balosso S., Ravizza T., Perego C., Peschon J., Campbell I.L., De Simoni M.G., Vezzani A., Tumor necrosis factor-alpha inhibits seizures in mice via p75 receptors, *Ann. Neurol.*, 57(6) (2005) 804-812.
- [22] Shandra A.A., Godlevsky L.S., Vastyanov R.S., Oleinik A.A., Konovalenko V.L., Rapoport E.N., Korobka N.N., The role of TNF-alpha in amygdala kindled rats, *Neurosci Res.*, 42(2) (2002) 147-153.



Comparison of *tul4*, *fopA*, 16S rRNA and RD1 gene regions of *Francisella tularensis* strains isolated from Sivas, Turkey

Sinem DEMİR , Mehmet ATAŞ *

Sivas Cumhuriyet University, Faculty of Pharmacy, Department of Pharmaceutical Microbiology, Sivas / TURKEY

Abstract

Tularemia is a zoonotic disease that can infect animals and people. It is known that tularemia outbreaks in Turkey is water-borne and causative agent *F. tularensis* subsp. *holarctica*. Eight *F. tularensis* were isolated from the water samples in tularemia outbreaks observed in Sivas during 2011-2013. In this study; *tul4*, *fopA*, RD1 and 16S rRNA gene regions of eight *F. tularensis* isolates were amplified by PCR method and investigated by sequencing method. Sequence analysis of the gene regions were compared with each other and the samples found in GenBank. All samples were found to be similar in terms of the partial sequence of the *tul4* and *fopA* gene region. In terms of 16S rRNA gene region, Belkent2012 and Belkent2013 isolates and Çiçekoğlu and Döllük isolates were detected similar among themselves. Bahçeici and Karaören isolates were found similar at RD1 gene regions. In the sequence comparison of GenBank in terms of examined gene regions, 94-100% similarity was determined with *F. tularensis* subsp. *holarctica* LVS and *F. tularensis* subsp. *holarctica* PHIT-FT049. As a result of our study; the *tul4* and *fopA* gene regions of eight *F. tularensis* subsp. *holarctica* isolates were found to have identical and different base sequence origins in 16S rRNA and RD1 gene regions in tularemia outbreaks in Sivas. In order to reveal the phylogeography of *F. tularensis* in Turkey, it is necessary to produce new isolates from epidemic regions and to investigate them with advanced molecular techniques.

Article info

History:

Received: 18.12.2020

Accepted: 08.03.2021

Keywords:

Tularemia,
Holarctica,
16S rRNA,
tul4,
fopA.

1. Introduction

Francisella tularensis, a gram-negative intracellular bacterium, causes tularemia in humans and animals. *F. tularensis* is transmitted to humans mainly by arthropod bites, direct contact with infected animals, infected animal tissues, contaminated water, food and inhalation of infected aerosols [1, 2]. *F. tularensis* is composed of 4 recognized subspecies: subsp. *tularensis* (type A), subsp. *holarctica* (type B), subsp. *novicida*, and subsp. *mediasiatica*. Only *F. tularensis* subsp. *tularensis* and subsp. *holarctica* are considered clinically significant in humans [3].

F. tularensis subsp. *tularensis* (Type A) is one of the most infectious pathogens known and isolated from North America. It is transmitted to humans and animals by arthropods such as ticks, deer flies, or infected aerosols. *F. tularensis* subsp. *holarctica* (Type B) is found throughout the Northern Hemisphere, but has recently been detected in Australia [4, 5]. Type B tularemia cases caused by *F. tularensis* subsp. *holarctica* are associated with aquatic environments such as rivers, lakes, streams, and muskrat and beavers

living in these environments. It has also been isolated from rabbits and other animals [1, 2]. *F. tularensis* subsp. *mediasiatica* have been reported only in a few Central Asian countries, and its virulence is similar to subsp. *holarctica*. The subspecies *novicida* causes infections in immunocompromised individuals [6].

Tularemia was first reported in Turkey in 1936 and then was sporadically reported for several decades [7]. Between 1988 and 2018, 28 tularemia outbreaks linked to consumption of contaminated water has been reported in Turkey [6]. Ulceroglandular, glandular, oculoglandular, oropharyngeal, typhoidal and pneumonic types may be observed based on the entrance route to the body and location of the bacteria. Although the clinical presentation may vary, oropharyngeal tularemia is the most commonly seen clinical form in Turkey [8].

The first tularemia outbreak in Sivas, a central Anatolian city, was observed in 2009. *F. tularensis* was produced by culture method in water samples taken from the epidemic regions, and as a result of molecular studies, the agent was identified as *F. tularensis* subsp. *holarctica* [9, 10]. At the same time, in 2011 and 2012

*Corresponding author. e-mail address: : atasmehmet@gmail.com

years at Sivas province, *F. tularensis* was produced by culture method in water samples and it was confirmed that the agent was *F. tularensis* subsp. *holarctica* by PCR method [11].

In this study, it was aimed to investigate the phylogenetic relationship (regarding to *tul4*, *fopA*, *RD1* and *16S rRNA* gene regions) between *F. tularensis* subsp. *holarctica* strains isolated from Sivas, in Turkey and also other countries.

2. Materials and Methods

2.1. Bacterial strains and DNA isolation

In this study, a total of eight *F. tularensis* isolates were used. The isolates were obtained by culture method

from water samples of regions where tularemia cases were observed in Sivas (Central Anatolia, Turkey) during 2011-2013. The isolates were confirmed to be *F. tularensis* subsp. *holarctica* by PCR using *Tul4* and *RD1* specific primers [11] (Table 1). The isolates stored in glycerol broth (16%) at -20 °C were revived in Glucose Cysteine Blood Agar (GCBA) medium under a 5% CO₂ environment. DNA isolation was performed from the isolates produced in the medium using the GeneJet Genomic DNA Purification Kit (Thermo Scientific, Waltham, Massachusetts, USA) according to the manufacturer's instructions.

Table 1. The names of the isolates used in the study and the regions where they were isolated

No	Isolate Name	Region of Isolation
1	Çiçekoğlu	Sivas-Gemerek-Çiçekoğlu village
2	Bahçeçi	Sivas-Gürün-Bahçeçi village
3	Karaören	Sivas-Gürün-Karaören village
4	Hüyük	Sivas-Şarkışla-Hüyük village
5	Maksutlu	Sivas-Şarkışla-Maksutlu village
6	Döllük	Sivas-Şarkışla-Döllük village
7	Belkent2012	Sivas-Şarkışla- Belkent fountain (2012)
8	Belkent2013	Sivas- Şarkışla- Belkent fountain(2013)

2.2. Target gene regions and PCR

The *tul4*, *fopA*, *16S rRNA* and *RD1* target gene region of the isolates used in the study were amplified by PCR method (Table 2). After confirmation of the isolates as *F. tularensis* by PCR with *tul4* primers, another conventional PCR assay targeting the region of differentiation 1 (*RD1*) was performed in order to determine subspecies identification [12, 13]. *F. tularensis* subsp. *holarctica* LVS strain (NCTC 10857)

was used as a positive control in the PCR study. Each PCR reaction was performed in a 50 µl volume; 1X PCR buffer, 1,25 U Taq DNA polymerase (GeneAll, Korea), 0,2 mM dNTP (GeneDireX, Inc., Miaoli County, Taiwan), 0,2 µM primer ve 5 µl DNA sample. GeneAmp® PCR System 9700 (Perkin-Elmer Applied Biosystems, Norwalk, Conn.) thermal cycler was used in the study. The PCR products were electrophoresed and the results were visualized with the aid of gel imaging system.

Table 2. Details of the PCR Amplification Reactions

Target of PCR	Primers	Sequence (5' - 3')	PCR Program	Fragment Size (bp)
<i>tul4</i>	TUL4-435 TUL4-863	GCTGTATCATCATTTAATAAACTGCTG TTGGGAAGCTTGTATCATGGCACT	1 cycle: 94°C 4 min; 40 cycles: 94°C 40 s, 64°C 30s, 72°C 45 s; 1 cycle: 72°C 5 min	410
<i>fopA</i>	FNA7L FNB1L	CTTGAGTCTTATGTTTCGGCATGTGAATAG CCAACTAATTGGTTGTACTGTACAGCGAAG	1 cycle: 94°C 4 min; 40 cycles: 94°C 40 s, 64°C 30s, 72°C 45 s; 1 cycle: 72°C 5 min	401
<i>RD1</i>	F R	TTTATATAGGTAATGTTTTACCTGTACCA GCCGAGTTTGATGCTGAAAA	1 cycle: 95°C 3 min; 30 cycles: 95°C 30 s, 58°C 1 min, 72°C 1 min; 1 cycle: 72°C 5 min	900/1100 ^a 1500 ^b ve 1400 ^c
<i>16S rRNA</i>	F11 F5	TACCAGTTGGAAACGACTGT CCTTTTTGAGTTTCGCTCC	1 cycle: 94°C 3 min; 40 cycles: 94°C 30 s, 55°C 1 min, 72°C 35 s; 1 cycle: 72°C 5 min	1100

Note. ^asubspecies *holarctica*. ^bsubspecies *tularensis*. ^csubspecies *mediasiatica*

2.3. Sequencing of PCR products and phylogenetic analysis

Sequence analysis of the amplification products of the four gene regions (tul4, fopA, 16S rRNA and RD1) of *F. tularensis* isolates was performed by a commercial company (MG Bioinformatic, Turkey). The amplified product was purified using the QIAquick Extraction Kit (Qiagen GmbH). Purified DNA was sequenced using the BigDye Terminator V3.1 CycleSequencing Kit (Applied Biosystems, Foster City, CA). Automated fluorescence sequencing was performed with an Applied Biosystems™ 3730xl DNA Analyzer device. Nucleotide sequences were evaluated using the program BLAST (National Center for Biotechnology Information, www.blast.ncbi.nlm.nih.gov/Blast). The gene sequences of the isolates were compared using Molecular Evolutionary Genetic Analysis (MEGA) software version 10.0.5. The phylogenetic tree was produced according to the neighbor-joining method after Kimura 2-parameter correction in the MEGA using bootstrap analyses with 1000 replicates [14]. The partial sequences of 16S rRNA gene was deposited in the GenBank under the accession numbers MK249699-706.

3. Results and Discussion

Tularemia is a highly infectious zoonotic disease caused by the bacterium *F. tularensis* that affects humans and other animals. The disease was first defined by George McCoy and Chapin in Tulare County, California in 1911 [6]. In Turkey, tularemia has been known since the 1930's. The first published tularemia epidemic in Turkey had been reported in 1936 from Thrace region (Lüleburgaz town), and the second was in 1945 again in the same location. In recent years, tularemia outbreaks were reported from various regions of Turkey [8, 15]. It is known that tularemia outbreaks in Turkey are caused by contaminated water and food, and are mostly seen in oropharyngeal form and the factor is *F. tularensis* subsp. *holarctica* [6, 8].

In this study, *F. tularensis* strains isolated from water samples taken from tularemia outbreak regions in Sivas province were used. The tul4 gene region encoding the 17 kDa outer membrane proteins of *F. tularensis*, the fopA gene region encoding the 43 kDa outer membrane protein, the 16S rRNA gene amplified for the identification of *F. tularensis* and the RD1 target gene region was amplified by classical PCR method and sequence analysis was performed. The PCR test targeting the *tul4* gene which is common in *F. tularensis* species was found positive in all

isolates investigated in this study (Figure 1). For the determination of the subspecies of *Francisella tularensis* strains, the region of difference 1 (RD1) subspecies-specific PCR test was employed (Figure 1). All study isolates (n=8) yielded RD1 fragments of 900-1000 bp that corresponds to the RD1 size of *F. tularensis* subsp. *holarctica*. All isolates were identified as *F. tularensis* subsp. *holarctica* in agreement with earlier study by Ataş [11]. In the PCR study of the fopA gene region of *F. tularensis* bacteria, a band of approximately 400 bp was observed in all isolates. Similarly, using the 16S rRNA specific primer, we detected that the amplification products of all isolates approximately 1100 bp (Figure 1).

As a result of the sequencing analysis of the tul4 and fopA gene regions of the *F. tularensis* subsp. *holarctica* isolates, no difference was found and the tul4 and fopA gene regions of all samples were found to be identical. According to BLAST analysis, our samples were found to be 100% similar to the *F. tularensis* subsp. *holarctica* LVS (accession number CP009694) and *F. tularensis* subsp. *holarctica* PHIT-FT049 (accession number CP007148) samples in terms of tul4 gene region. *F. tularensis* subsp. *holarctica* PHIT-FT049 (accession number CP007148) was isolated from water sample in Turkey and was identified biovar *japonica* [16]. In terms of fopA gene region, it was determined that it was 100% similar to *F. tularensis* subsp. *holarctica* LVS (accession number CP009694) and 99.45% with *F. tularensis* subsp. *holarctica* PHIT-FT049 (accession number CP007148).

It is possible to distinguish *F. tularensis* subspecies from each other by PCR directed to the RD1 gene region. As a result of PCR directed to this gene region, *F. tularensis* subsp. *tularensis* in the 1500 bp region, subsp. *holarctica* in the 900/1100 bp region, subsp. *mediasiatica* gives bands in the region of 1400 bp [12]. In our study, as a result of the PCR made for the RD1 gene region, a band was observed in the region slightly less than 1000 bp (Figure 1). With this study for determination of subspecies, it was determined that the samples belong to the subspecies *holarctica*. As a result of the sequence analysis of the RD1 gene region of the *F. tularensis* isolates, the sequenced 835 bp was compared and it was found that the Bahçeici and Karaören isolates were the same in terms of this gene region. Both of Bahçeici and Karaören samples have been isolated from tularemia outbreaks in Gürün district. In terms of RD1 gene region, the other six samples were found to be different from Bahçeici and Karaören isolates and from each other in terms of base distribution.

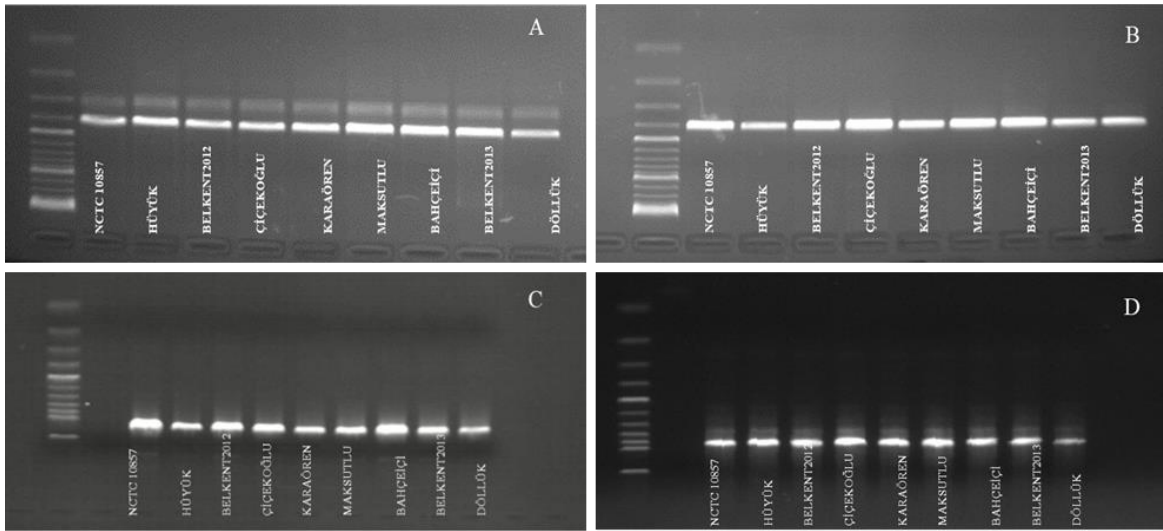


Figure 1. The amplification results of the isolates. *F. tularensis* subsp. *holarctica* LVS strain (NCTC 10857) was used as a positive control. A 100 bp-ladder (Promega) was used as a marker. A) tul4 (410 bp) B) fopA (401 bp) C) 16S rRNA (1100 bp) D) RD1 (900-1000 bp).

In comparison with GenBank, our samples were found to be 99.75% similar to *F. tularensis* subsp. *holarctica* PHIT-FT049 (accession number CP007148) and 94.64 to 95.10% with *F. tularensis* subsp. *holarctica* LVS (accession number CP009694) in terms of RD1 gene region.

According to the 16S rRNA gene region sequence analysis results, the base sequences of Belkent 2012 and 2013 isolates, Çiçekoğlu and Döllük isolates were determined to be identical. Belkent2012 and Belkent2013 strains were isolated from water samples taken from Belkent fountain of Şarkışla district 2012 and 2013 years, respectively. The other four isolates (Bahçeici, Karaören, Hüyük and Maksutlu) were found to have different base sequences in terms of 16S rRNA

gene region. Our samples were found to be 97.74 - 98.49% similar to *F. tularensis* subsp. *holarctica* LVS (accession number CP009694) and 97.56 - 98.31% to *F. tularensis* subsp. *holarctica* PHIT-FT049 (accession number CP007148) in terms of 16S rRNA gene region (Figure 2). In a study conducted in Spain, 42 *F. tularensis* subsp. *holarctica* isolates were found to be similar in terms of 16S rRNA gene region. The sequence detected in this study shared 99% similarity to those of strains from another Spanish outbreak of tularemia [17]. As a result of three gene-based phylogenetic analysis (tul4, fopA and 16S rRNA gene regions) of 10 *F. tularensis* subsp. *holarctica* strains isolated from China, the correlation not found between the genotype and the geographical area from which the bacteria were isolated [13].



Figure 2. Phylogenetic tree (Neighbor-joining, Kimura 2-parameters) based on 16S rRNA gene sequences comparing the *F. tularensis* subsp. *holarctica* strains of Sivas with other known GenBank records. Bootstrap percentage values from 1,000 replicates are located at nodes of the tree. Sequence alignments and tree generation were conducted in MEGA10.

During the tularemia epidemic in Sivas province between 2009 and 2010, *F. tularensis* DNA in lymph node samples of two patients was found positive by PCR method and it was stated that the outbreaks were waterborne. In this epidemic, 75.9% of the disease was observed in the oropharyngeal form [9]. The first cases of tularemia were observed in Tokat, which is adjacent to Sivas province, in 2005 and the disease is reported to be waterborne [18]. Two cases of tick-borne tularemia have been reported from Yozgat, another neighboring city of Sivas [19]. However, the presence of *F. tularensis* could not be detected by PCR method in 2054 ticks collected from vegetation in Sivas province (unpublished data). In a study conducted in Kayseri province, which is approximately 200 km away from Sivas, 1477 tick samples and 6203 mosquito samples were examined for the presence of *F. tularensis*. Francisella-like endosymbionts (FLEs) and *F. tularensis* were not detected in any genomic DNA pools constructed from ixodid ticks and mosquitos [20]. The first *F. tularensis* isolation from Sivas region with culture method was carried out in 2009. Şimşek et al. isolated *F. tularensis* from water samples taken from Sivas, Çorum and Samsun regions by culture method, and it was found that these samples were 100% similar to *F. tularensis* subsp. *holarctica* LVS in the 16S rRNA sequence analysis [10]. *F. tularensis* subsp. *holarctica* strains isolated from water samples in the outbreaks observed in Sivas and Çorum were found similar with the Whole Genome Sequencing method [21]. In a study conducted in our country, Gürcan et al. isolated two *F. tularensis* subsp. *holarctica* strain from lymph node aspirates of patients in Yazıkara and Nuhören villages in Gerede, Bolu. This strains were found similar to strains isolated from Bulgaria as a result of MLVA analysis [22].

F. tularensis subsp. *holarctica* has three biovars, biovar I, biovar II and biovar japonica. Biovars are divided according to erythromycin resistance, glucose and glycerol fermentation properties [23]. In Turkey, 250 *F. tularensis* subsp. *holarctica* strains were investigated and 249 strains were typed as biovar II and one strain as biovar japonica [16]. Çelebi et al. examined 776 samples isolated from various sources and in their study they typed 764 samples as *F. tularensis* subsp. *holarctica* and 12 samples as *F. tularensis* subsp. *holarctica* biovar japonica [24]. Kılıç et al. studied 40 samples with the "single nucleotide polymorphisms (SNP)" method and found that the samples were *F. tularensis* subsp. *holarctica*. In this study, the canSNP method was used and *F. tularensis* subsp. *holarctica* isolates are divided into 3 main

groups and also subgroups [7]. As a result of our study, it was determined that *F. tularensis* isolates obtained from water samples in Sivas region belong to *holarctica* subspecies, were similar in terms of tul4 and fopA gene regions, and showed polymorphism in terms of 16S rRNA and RD1 gene regions. A limitation of this study is that relatively few strains were used. In the future, it is planned to isolate new strains from possible epidemic areas in our region and to conduct more comprehensive studies.

Acknowledgment

This work was supported by the Scientific Research Project Fund of Sivas Cumhuriyet University (CÜBAP) under the project number ECZ-054. This study consists of the master's thesis of Sinem Demir, who graduated from the Pharmaceutical Microbiology master program in 2018. The authors would like to thank the Sivas Cumhuriyet University, Faculty of Medicine Research Center (CÜTFAM) for its technical support. We would like to thank Dr. Bekir Çelebi (Public Health Institution of Turkey, National Tularemia Reference Laboratory, Ankara, Turkey) for the *F. tularensis* subsp. *holarctica* LVS strain (NCTC 10857).

Conflicts of interest

The authors state that did not have conflict of interests.

References

- [1] Ellis J., Oyston P.C., Green M., Titball R.W., Tularemia, *Clin. Microbiol. Rev.*, 15(4) (2002) 631-646.
- [2] WHO, WHO Guidelines on Tularemia, France : World Health Organization, (2007) WHO/CDS/EPR/2007.7.
- [3] Fey P.D., Dempsey M.M., Olson M.E., Chrustowski M.S., Engle J.L., Jay J.J., Dobson M.E., Kalasinsky K.S., Shea A.A., Iwen P.C., Wickert R.C., Francesconi S.C., Crawford R.M., Hinrichs S.H., Molecular analysis of Francisella tularensis subspecies tularensis and holarctica, *Am. J. Clin. Pathol.*, 128(6) (2007) 926-935.
- [4] Sjöstedt A., Tularemia: history, epidemiology, pathogen physiology and clinical manifestations, *Ann. N. Y. Acad. Sci.*, 1105 (2007) 1-29.
- [5] Jackson J., McGregor A., Cooley L., Ng J., Brown M., Ong C.W., Darcy C., Sintchenko V., Francisella tularensis subspecies holarctica, Tasmania, Australia 2011, *Emerg. Infect. Dis.*,

- 18(9) (2012) 1484-1486.
- [6] Hennebique A., Boisset S., Maurin M., Tularemia as a waterborne disease: a review, *Emerg. Microbes Infect.*, 8(1) (2019) 1027-1042.
- [7] Kiliç S., Birdsell D.N., Karagöz A., Çelebi B., Bakkaloglu Z., Arıkan M., Sahl J.W., Mitchell C., Rivera A., Maltinsky S., Keim P., Üstek D., Durmaz R., Wagner D.M., Water as source of Francisella tularensis infection in humans, Turkey, *Emerg. Infect. Dis.*, 21(12) (2015) 2213–2216.
- [8] Kılıç S., A General Overview of Francisella tularensis and the Epidemiology of Tularemia in Turkey, *Flora.*, 15(2) (2010) 37-58.
- [9] Engin A., Altuntaş E.E., Cankorkmaz L., Kaya A., Elaldı N., Şimşek H., Dökmetaş İ., Bakır M., The first Tularemia outbreak detected in Sivas province: Evaluation of 29 Cases., *Klimik Journal.*, 24(1) (2011) 17-23.
- [10] Şimşek H., Taner M., Karadenizli A., Ertek M., Vahaboğlu H., Identification of Francisella tularensis by both culture and real-time TaqMan PCR methods from environmental water specimens in outbreak areas where tularemia cases were not previously reported, *Eur. J. Clin. Microbiol. Infect. Dis.*, 31(9) (2012) 2353-2357.
- [11] Ataş M., Investigation of Francisella tularensis in Acanthamoeba Species Isolated from Various Water Samples, PD thesis, Cumhuriyet University, Health Sciences Institute, (2012).
- [12] Broekhuijsen M., Larsson P., Johansson A., Byström M., Eriksson U., Larsson E., Prior R.G., Sjöstedt A., Titbal R.W., Forsman M., Genome-wide DNA microarray analysis of Francisella tularensis strains demonstrates extensive genetic conservation within the species but identifies regions that are unique to the highly virulent F. tularensis subsp. Tularensis, *J. Clin. Microbiol.*, 41(7) (2003) 2924-2931.
- [13] Wang Y., Hai R., Zhang Z., Xia L., Cai H., Liang Y., Shen X., Yu D., Genetic relationship between Francisella tularensis strains from China and from other countries, *Biomed. Environ. Sci.*, 24(3) (2011) 310-314.
- [14] Kumar S., Stecher G., Li M., Niyaz C., Tamura K., MEGA X: molecular evolutionary genetics analysis across computing platforms, *Mol. Biol. Evol.*, 35(6) (2018) 1547-1549.
- [15] Gürcan S., Francisella tularensis and Tularemi in Turkey, *Mikrobiyol. Bul.*, 41(4) (2007) 621-636.
- [16] Kiliç S., Çelebi B., Acar B., Ataş M., In vitro susceptibility of isolates of Francisella tularensis from Turkey, *Scand. J. Infect. Dis.*, 45(5) (2013) 337–341.
- [17] García Del Blanco N., Dobson M.E., Vela A.I., De La Puente V.A., Gutiérrez C.B., Hadfield T.L., Kuhnert P., Frey J., Domínguez L., Rodríguez Ferri E.F., Genotyping of Francisella tularensis strains by pulsed-field gel electrophoresis, amplified fragment length polymorphism fingerprinting, and 16S rRNA gene sequencing, *J. Clin. Microbiol.*, 40(8) (2002) 2964-2972.
- [18] Barut S., Cetin I., A tularemia outbreak in an extended family in Tokat Province, Turkey: observing the attack rate of tularemia, *Int. J. Infect. Dis.*, 13(6) (2009) 745-748.
- [19] Yeşilyurt M., Kiliç S., Çağaşar Ö., Çelebi B., Gül S., Two Tick-borne Tularemia Cases in Yozgat Province, *Mikrobiyol. Bul.*, 45(4) (2011) 746-754.
- [20] Duzlu O., Yildirim A., İnci A., Gumussoy K.S., Ciloglu A., Onder Z., Molecular investigation of Francisella-like endosymbiont in ticks and Francisella tularensis in ixodid ticks and mosquitoes in Turkey, *Vector Borne Zoonotic Dis.*, 16(1) (2016) 26-32.
- [21] Karadenizli A., Forsman M., Şimşek H., Taner M., Öhrman C., Myrtenäs K., Lärkeryd A., Johansson A., Özdemir L., Sjödin A., Genomic analyses of Francisella tularensis strains confirm disease transmission from drinking water sources, Turkey, 2008, 2009 and 2012, *Euro. Surveill.*, 20(21) (2015) 21136.
- [22] Gurcan S., Karabay O., Karadenizli A., Karagol C., Kantardjiev T., Ivanov I.N., Characteristics of the Turkish isolates of Francisella tularensis, *Jpn. J. Infect. Dis.*, 61(3) (2008) 223-225.
- [23] Olsufjev N.G., Meshcheryakova I.S., Subspecific taxonomy of Francisella tularensis McCoy and Chapin 1912, *Int. J. Syst. Bacteriol.*, 33(4) (1983) 872-874.
- [24] Çelebi B., Bakkaloglu Z., Ünaldı Ö., Karagöz A., Kılıç S., Durmaz, R., Determination of Isolated Francisella tularensis Subspecies in Turkey with Molecular Methods, *Mikrobiyol. Bul.*, 54(1) (2020) 1-10.

Hydrogen evolution by ternary metal selenide at biomembrane-like soft interfaces

Emre ASLAN^{1,*} 

¹ Selcuk University, Department of Biochemistry, Konya / TURKEY

Abstract

Two phase reactions are the analogy of biomembranes, which are polarized by Galvani potential difference at interface between two immiscible electrolyte solutions. Energy conversion reactions such as oxygen reduction reaction or hydrogen evolution reaction have been great drawn attention at soft interfaces due to the similarity of natural biochemical reactions. In this study, copper-based ternary metal selenide (copper tungsten selenide, Cu_2WSe_4) was first reported in the literature for hydrogen evolution reaction catalysis at the water/1,2-dichloroethane interface. The synthesized Cu_2WSe_4 catalyst is characterized by morphological and structural techniques. Catalytic activity of Cu_2WSe_4 at liquid-liquid interfaces by lipophilic dexamethylferrocene as the sacrificial electron donor agent. This catalytic activity was tracked by four-electrode voltammetry at the water/1,2-dichloroethane interface and biphasic reactions monitored by gas chromatography. The rates of the hydrogen evolution reaction catalyzed by the Cu_2WSe_4 were found to be approximately 160-fold than the rate for the reaction performed in the absence of a catalyst.

Article info

History:

Received: 21.07.2020

Accepted: 16.01.2021

Keywords:

Hydrogen evolution, liquid/liquid interfaces, electrochemistry.

1. Introduction

Hydrogen is seen as a future energy carrier by virtue of the fact that it is renewable, does not evolve the "greenhouse gas" CO_2 in combustion and is easily converted to electricity by fuel cells. Nowadays hydrogen is generally produced by using fossil fuels, which release greenhouse gases and other climate-changing emissions. Hydrogen production from water is biggest candidate to control of climate change due to the not releasing greenhouse gases. Catalysts need to use to produce hydrogen because of positive Gibbs free energy of water splitting into hydrogen and oxygen gases [1]. Most common and efficient catalyst, platinum (Pt), is used as catalysts in the hydrogen evolution reaction (HER). However, Pt is scarce and expensive and there is more study to find as an alternative to Pt with more abundant and cheaper than noble metal catalysts. Well-known noble metal-free MoS_2 , WS_2 , MoSe_2 and WSe_2 are drawn attention as an alternative to Pt in hydrogen evolution reaction (HER) [2-5]. Molybdenum selenide and tungsten selenide displayed high electrocatalytic HER performance because of having the large amount of active edge sites [6]. 3D dendritic [7,8], graphene-like nanosheet [9], thin film [10] and monolayer nanosheet [11] shapes of WSe_x have been investigated in the electrocatalytic

HER as the electrocatalyst. In addition, tungsten selenide photoelectrode has been studied by coating noble metal catalysts such as Ru and Pt, which are displayed $> 7\%$ solar-to-hydrogen conversion efficiency on photoelectrochemical HER in a broad pH range [12]. Copper incorporated molybdenum and tungsten sulfides have aroused interest in photocatalytic and electrocatalytic HER due to their advanced physical properties, novel chemical and unique structures [13]. Although, Cu_2WS_4 is used in the electrochemical hydrogen evolution [14], there is no report HER by using Cu_2WSe_4 in the literature up to now.

The analogy with biomembranes of an interface between two immiscible electrolyte solutions (ITIES) has been drawn a great deal of attention. Herein, liquid/liquid interfaces (LLI) are used as a model system for the catalytic hydrogen evolution. Electrochemistry at LLI has found applications in important areas such as chemical sensing, drug release, phase-transfer catalysis and energy-conversion systems by mimicking of the biological membranes [15]. LLI afford a unique platform to investigate hydrogen evolution reactions at which protons in the aqueous phase react with electron donors in the organic phase in the absence or presence of different catalysts by proton-coupled electron-transfer (PCET) reaction

*Corresponding author. e-mail address: emreaslan89@gmail.com

[16]. Herein, water/organic interfaces can be polarized either application of an external potential by a potentiostat or chemically by dissolving a common ion in both phases. Some metallocenes such as cobaltocene, osmocene, decamethyl-osmocene, decamethylruthenocene and decamethylferrocene (DMFc) were used at LLI for the catalytic HER as organic electron donor [17-22]. DMFc is most common electron donor for HER catalysis at the water/1,2-dichloroethane (DCE) interface [22]. Metallic nanoparticles [23, 24], metal oxides [25], metal carbide and metal boride [26], binary metal sulfides [27-29], ternary metal sulfides [30], amorphous ternary metal chalcogenides [31-33], quaternary metal sulfides [34] and also its nanocomposites [35-39] supported on mesoporous carbon, graphene or carbon nanotube is used as the catalyst for HER by DMFc at water/DCE interface. However, there is no study reported for the metal selenide HER catalysts at LLI.

Herein, it is firstly reported that hydrogen evolution reaction catalysis by using copper tungsten selenide (Cu_2WSe_4) at the biomembrane-like water/DCE interface by the organic reducing agent DMFc. The catalytic HER activity of Cu_2WSe_4 catalyst at LLI is investigated by four-electrode voltammetry and biphasic reactions using electrochemical and chromatographic techniques, respectively. The HER rate was relatively increased in the presence of the Cu_2WSe_4 catalysts with 4.8 μmol hydrogen measured after only 30 min of biphasic reactions (the maximum stoichiometric amount of hydrogen is 5 μmol). In addition, HER kinetic is calculated and Cu_2WSe_4 catalyst is enhanced the reaction rate about 160-times when compared to non-catalyzed reaction.

2. Materials and Methods

2.1. Synthesis of Cu_2WSe_4 nanostructures

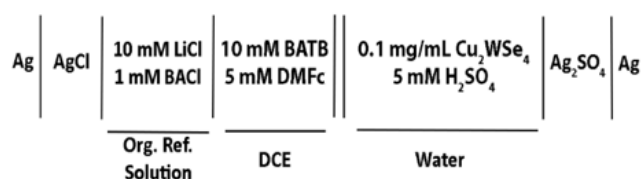
Cu_2WSe_4 have been synthesized by using hot-injection method according to reported literature [40,41]. Herein, stoichiometric amount of copper (II) chloride dihydrate (134.45 mg) and tungsten (IV) chloride (162.825 mg) were mixed with oleylamine (OLA) (12 mL) in a two-neck flask and evacuated at room temperature for 30 min under Ar flow. Then, another solution was prepared, which is included with 64 mg Se powder dissolved in 2 mL OLA, under magnetic stirring, until the OLA was dissolved (reddish-black). Afterwards, the first solution was heated to 300°C and the OLA-Se solution was rapidly injected about to 180 °C; then the temperature mixture solution was kept for 30 minutes by stirring. The reaction was finished by stopped of the heating mantle and allowed to cool

down to room temperature effortlessly. The product was washed two times with toluene-ethanol mixtures.

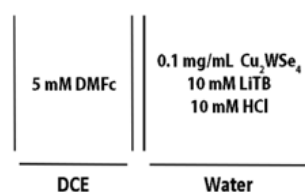
2.2. Hydrogen evolution experiments at liquid/liquid interfaces

Hydrogen evolution reaction at liquid/liquid interfaces (LLI) have been tracked by electrochemical polarization and chemical polarization. Electrochemical and chemical polarization were provided according to Scheme 1 a and b, respectively. BACl, BATB, DMFc and LiTB are the abbreviations of bis (triphenylphosphoranylidene) ammonium chloride, bis (triphenylphosphoranylidene) ammonium tetrakis (pentafluorophenyl) borate, ecamethylferrocene and lithium tetrakis (pentafluorophenyl) borate, respectively, in the Scheme 1. Organic supporting electrolyte BATB was prepared by metathesis as reported previously [42]. Electrochemical polarization was carried out by using four-electrode voltammetry in the presence of H_2SO_4 and BATB in the aqueous and organic phases, respectively, as the supporting electrolyte by using a CHI 760 D potentiostat with a four-electrode cell (geometric area is 1.53 cm^2) under oxygen free conditions. Galvani potential difference across the water/DCE interface determined by standard ion transfer potential of the tetraethylammonium cation (TEA^+) as 0.019 V [37]. Biphasic reactions were figured out by using DMFc and LiTB as the electron donor and proton transfer catalyst, respectively, under oxygen free conditions in the 10 mL volume glass flasks by magnetic stirring in the absence and presence of Cu_2WSe_4 catalyst. The evolved hydrogen amount was measured by gas chromatography (Shimadzu GC2010Plus), which calculated with calibration curve by using standard samples of H_2 in N_2 .

(a)



(b)



Scheme 1. (a) Electrochemical and (b) biphasic polarization of the water/DCE interface

3. Results and Discussion

3.1. Characterization of Cu_2WSe_4

Morphological and structural characterizations of Cu_2WSe_4 catalysts were carried out by using scanning electron microscopy (SEM), transmission electron microscopy (TEM), elemental mapping, X-ray diffraction (XRD) and energy dispersive x-ray (EDX) spectroscopy techniques. SEM image of Cu_2WSe_4 shows uniform dispersity of particles (Figure 1a). Morphology and particle shape of Cu_2WSe_4 were investigated by TEM technique as shown in Figure 1b-c. According to TEM images, Cu_2WSe_4 catalyst displayed square and rectangular sheet-like shapes with approximately 50 nm of edge sizes [41]. Selected area electron diffraction (SAED) pattern shows that Cu_2WSe_4 has a single crystalline and well crystallized [40,43]. In addition, elemental composition and distribution were examined by SEM-EDX techniques with area mapping (Figure 1d). Moreover, crystalline formation and phase purity of Cu_2WSe_4 catalyst were investigated by using XRD technique. As shown in Figure 1e, XRD pattern displayed a pure tetragonal P42m symmetry with primitive phase of Cu_2WSe_4 ($P\text{-Cu}_2\text{WSe}_4$, PDF no: 01-081-1159), which corresponding crystal structure is seen in the inset of Figure 1e [44]. The crystalline structure, which is obtained by XRD, is also in the harmony with SAED pattern. Furthermore, chemical composition of Cu_2WSe_4 was determined by EDX (Figure 1f) and it is very close to the ideal stoichiometry (2:1:4). The undefined peaks approximately 0, 1, 2 and 4 keV based on the used surfactant OLA and gold coating for the EDX analysis along with imaging of SEM.

3.2. Catalytic hydrogen evolution at liquid/liquid interfaces

Catalytic hydrogen evolution reaction (HER) activity of Cu_2WSe_4 at the water/DCE interface was investigated by using four-electrode voltammetry and biphasic reactions for the first time. Electrochemical polarization of water/DCE interface was figured out by using four-electrode cell as shown in Scheme 1a under anaerobic condition. First of all, potential window has been determined by transfer potential of SO_4^{2-} and H^+ at the negative and positive potentials, respectively (Figure 2, black solid line). Then, while organic electron donor DMFc added to organic phase, current density is increased and onset potential is shifted to negative potentials at the positive potentials (Figure 2, orange solid line). The return peak observed in the back

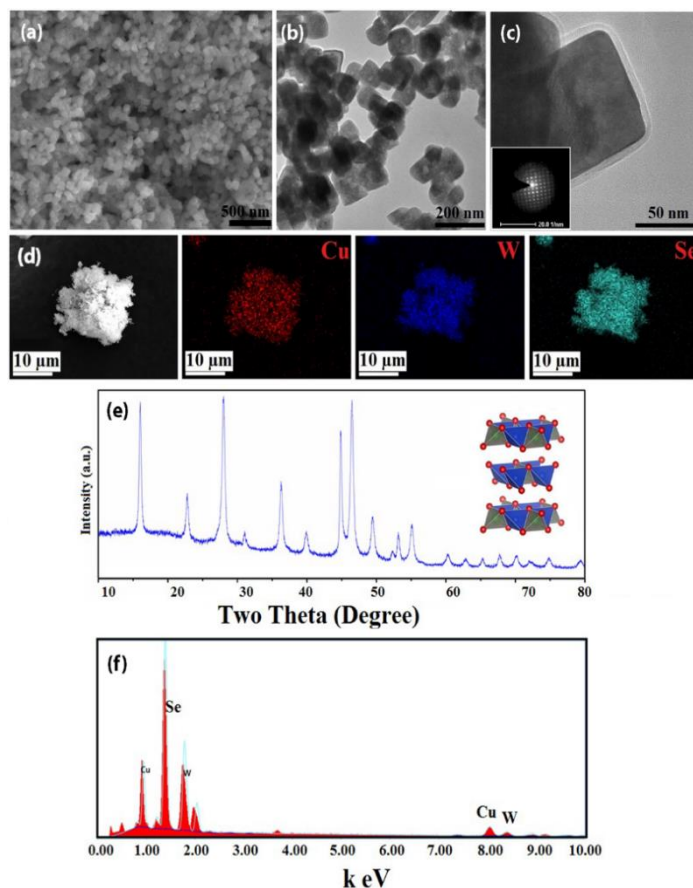


Figure 1. (a) Scanning electron microscope (SEM), (b-c) transmission electron microscope images (TEM, HR-TEM and SAED pattern) and (d) elemental mapping, (e) X-Ray diffraction (XRD) patterns with corresponding crystal structure (inset) and (f) energy dispersive X-ray (EDX) spectrum of the Cu_2WSe_4

scan can be attributed to the backward transfer of protons from DCE to the water phase. Herein, the proton, which is in the form of DMFcH^+ , was either consumed at a very slow rate or unconsumed in the organic phase because of the deficiency of chemical reactions to produce H_2 and DMFc^+ . In the presence of both Cu_2WSe_4 and DMFc added to the aqueous and organic phases, respectively, both onset potential is more shifted to negative and current density is more increased irreversibly with no back peak when compared to using only DMFc in the organic phase (Figure 2, green solid line) because protons adsorbed on the surface of Cu_2WSe_4 catalyst undergo rapid electron transfer with DMFc, which the protons are consumed fully [28]. No eligible current response was observed by using only Cu_2WSe_4 in the aqueous phase without DMFc (Figure 2, black dashed line) when

compared to the blank cell. In addition, the catalytic activity can be pursued by magnitude of reversible DMFc⁺ transfer peak, which is seen about -0.27 V. Herein, DMFc⁺ transfer peak is increased by using Cu₂WSe₄ and DMFc in the aqueous and organic

phases, respectively, when compared using only DMFc in the organic phase. These results proofed the catalytic activity of Cu₂WSe₄ by using organic electron donor DMFc.

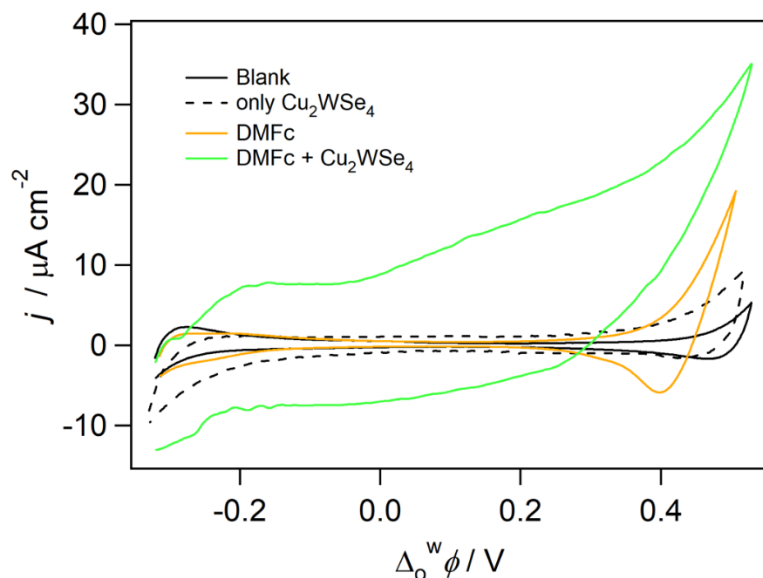
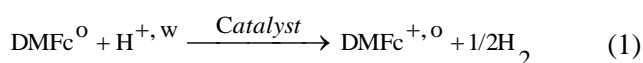


Figure 2. Cyclic voltammograms of four-electrode voltammetry by using only supporting electrolytes BATB and H₂SO₄ in the organic and aqueous phases, respectively (black solid line), in the presence of only Cu₂WSe₄ in the aqueous phase (black dashed line), in the presence of only DMFc in the organic phase (orange solid line), and in the presence of both DMFc and Cu₂WSe₄ in the organic and aqueous phases, respectively (green solid line).

The catalytic activity of Cu₂WSe₄ catalyst is also investigated by two phase system to supply Galvani potential difference without any external bias, which is named as “two-phase reaction” or “shake-flask” experiments. The chemical polarization of water/DCE interface is supplied by distribution of a common ion tetrakis-(pentafluorophenyl)borate anion (TB⁻), which is fixed Galvani potential difference to 0.58 V in order to transfer of proton from aqueous to organic phase [22]. The protons can be reduced in the organic phase by organic sacrificial agent DMFc into H₂ gas, according to their redox potentials in DCE as 0.04 V and 0.55 V vs SHE for DMFc and H⁺, respectively [22]. The reaction between DMFc and H⁺ is written as:



where o and w denote the organic and aqueous phases, respectively. According to these values, aqueous H⁺ can be reduced by DMFc with higher Galvani potential difference than 0.55 V [22]. Catalytic hydrogen evolution experiments were carried out according to Scheme 1b in the absence and presence of Cu₂WSe₄. Gas chromatograms and reaction cells are given in the Figure 3a and 3b, respectively, after 30 min of shaking in the absence and presence Cu₂WSe₄. Herein, hydrogen evolution rate is increased in the presence of Cu₂WSe₄ when compared to non-catalyzed reaction. In addition, color of organic phase in is changed rapidly from yellow to green the presence of Cu₂WSe₄ because of changing DMFc (absorption wavelength = 425 nm) into DMFc⁺ (absorption wavelength = 779 nm) [27], which is indirectly related to hydrogen evolution rate according to Equation (1).

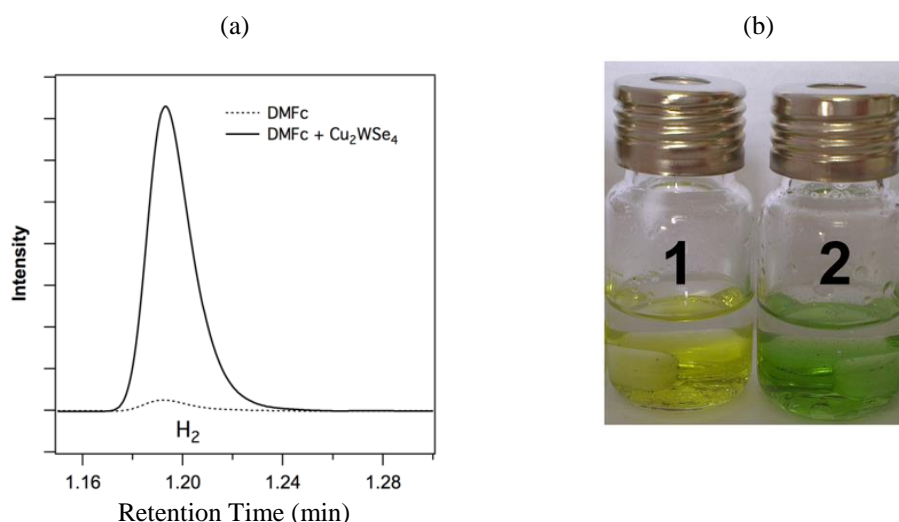


Figure 3. (a) Gas chromatograms of the headspace with (solid black line) or without (dashed black line) Cu_2WSe_4 catalyst after 30 min of biphasic reactions by using headspace cells (b) in the absence (flask 1) and presence (flask 2) of Cu_2WSe_4 catalyst.

Herein, kinetic experiments have been carried out by using Cu_2WSe_4 catalyst. Firstly, non-catalytic reaction was carried out in the absence of catalyst according to Scheme 1b. Accordingly, HER rate is very low and reached $0.8 \mu\text{mol}$ after 24 hours [27]. However, the amount of hydrogen was reached $4.8 \mu\text{mol}$ after 30 min in the presence of Cu_2WSe_4 (Figure 4a). These results pointed out approximately 96% efficiency according to Equation (1), which is limited by initial concentration of DMFc. In the absence of Cu_2WSe_4 , the amount of H_2 is only $0.061 \mu\text{mol}$ after 30 min. These results displayed that Cu_2WSe_4 catalyzed well to HER by DMFc at water/DCE interface.

The HER rate catalyzed by Cu_2WSe_4 is assumed as 1st order kinetics according to DMFc concentration as displayed in Equation (2) [36].

$$v = k[\text{DMFc}] \quad (2)$$

Reaction kinetic are explained by integrated rate law as shown in Equation (3) [36].

$$kt = \ln \frac{[\text{DMFc}]_0}{[\text{DMFc}]_0 - [\text{DMFc}^+] } \quad (3)$$

Herein, rate constants (k, min^{-1}) were calculated from slopes of straight lines in the absence and presence of Cu_2WSe_4 (Figure 4b). k was found out to be 0.00042 min^{-1} without any catalyst. However, k was increased to the 0.0662 min^{-1} in the presence of Cu_2WSe_4 . For the rate constant ratios in the presence and absence of Cu_2WSe_4 , increasing of catalytic activity was turned out to be about 160-fold by using Cu_2WSe_4 catalyst.

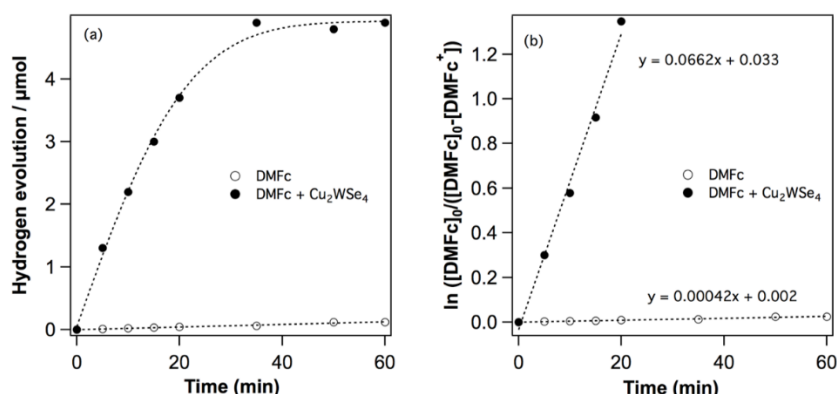


Figure 4. (a) Time dependent hydrogen evolution amount in the absence and presence of Cu_2WSe_4 catalyst. (b) Rate constant (k) determination: plots of the integrated rate law versus time (min) for the HER, indicating 1st order kinetics. The slopes of the straight lines illustrate the rate constants (k, min^{-1}) for a 1st order reaction.

The catalytic activity of Cu_2WSe_4 can be compared with the similar structure of Cu_2WS_4 , which is reported by our group in 2016 [30], at the water/DCE interface by DMFc for hydrogen evolution. Herein, catalytic activity of Cu_2WSe_4 is found out lower than that of Cu_2WS_4 (Table 1). These differences can be explained by the atomic radii of sulfur and selenium. Catalytic activities of selenium based catalysts are lower than sulfur based catalysts because they may be prone to high recombination rates [13]. In addition, higher radius of selenium than sulfur might be supplied to keep the more electrons on the surface in stable and it is not prone to react in the ternary metal chalcogenides [13]. Moreover, the catalytic activity differences

between Cu_2WSe_4 and Cu_2WS_4 is able to related band gap and energy band levels of catalysts. Band gaps and energy band levels of Cu_2WX_4 catalysts were calculated by our previous published paper for the determination of differences photocatalytic activities for HER (Table 1) [41]. According to conduction band levels of Cu_2WX_4 catalyst, having close conduction band level, which is -0.16 V vs. NHE for Cu_2WS_4 to H^+/H_2 (0 V vs. NHE) is more apt to react. Herein, the lower catalytic activity of Cu_2WSe_4 than Cu_2WS_4 could be based on the conduction band level of Cu_2WSe_4 , which is far from H^+/H_2 . Eventually, in this study catalytic activity differences of catalysts are able to explain with two factor proof.

Table 1. Catalytic parameters and band gap structure differences of Cu_2WS_4 and Cu_2WSe_4 .

Catalyst	Cu_2WS_4	Cu_2WSe_4
Hydrogen evolution in 5 min (μmol)	2.9	1.3
Reaching time for maximum theoretical stoichiometric amount of hydrogen (min)	10	35
Reaction increment by factor	1005	160
Optical band gap (eV)	1.80	1.65
Electrochemical band gap (eV)	1.66	1.80
$E_{\text{Valance Band}}$ (V vs. NHE)	1.50	1.24
$E_{\text{Conduction Band}}$ (V vs. NHE)	-0.16	-0.56

The mechanism of hydrogen evolution can be explained by proton coupled electron transfer (PCET). Hydrogen evolution is based on assisted proton transfer (APT) from aqueous to organic phases by electron donor DMFc in the absence of catalysts [22]. However, HER is actualized by adsorbed protons on catalyst while in the presence of catalyst. Herein, HER is figured out by adsorbed protons on the active surface on the Cu_2WSe_4 catalyst with giving electrons from DMFc as displayed in Figure 5.

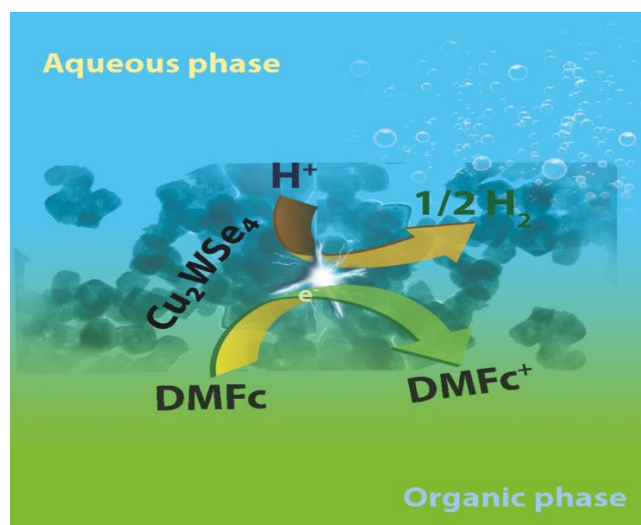


Figure 5. The proposed mechanism of hydrogen evolution by using Cu_2WSe_4 catalyst at the water/DCE interface.

4. Conclusions

The catalytic activity of square / rectangular sheet-like shapes of copper-based ternary metal selenide (Cu_2WSe_4) catalyst are investigated at the polarized water/1,2 dichloroethane (DCE) interface for the reduction of aqueous protons to molecular hydrogen by the organic electron donor DMFc for the first time. Catalytic HER activity is improved by Cu_2WSe_4 sheet-like structures at the biphasic water/DCE system using DMFc electron donor in the organic phase when compared to non-catalyzed reaction. In addition, the catalytic activity differences between Cu_2WS_4 and Cu_2WSe_4 are compared according to atomic radius and energy band structure of catalysts. The main advantages of this work are that catalytic activities of ternary metal chalcogenides can be explained by molecular and electronic structures of catalyst. These results open new perspectives for the exploration for the observing different selenide-based catalyst on the HER at the soft interfaces. First time reported catalytic activity of Cu_2WSe_4 paves the way that ternary metal selenide-based materials will be used in the different energy conversion reactions such as solar cell, batteries, supercapacitors, and so on.

Acknowledgment

The author would like to thank you to Selcuk University Scientific Research Projects (Grant number: 19401163) for financial supports, as well as Assoc. Prof. Dr. Faruk Özel and Prof. Dr. Imren Hatay Patir for the valuable guidance and contributions on the use of laboratory equipment.

Conflicts of interest

The authors state that there is no conflict of interests.

References

- [1] Chen X., Shen S., Guo L., Mao S.S., Semiconductor-based Photocatalytic Hydrogen Generation, *Chemical Reviews*, 110(11) (2010) 6503-6570.
- [2] Jaramillo T.F., Jørgensen K.P., Bonde J., Nielsen J.H., Horch S., Chorkendorff I., Identification of Active Edge Sites for Electrochemical H₂ Evolution from MoS₂ Nanocatalysts, *Science*, 317(5834) (2007) 100-102.
- [3] Merki D., Hu X., Recent developments of molybdenum and tungsten sulfides as hydrogen evolution catalysts, *Energy & Environmental Science*, 4(10) (2011) 3878-3888.
- [4] Morales-Guio C.G., Hu X., Amorphous Molybdenum Sulfides as Hydrogen Evolution Catalysts, *Accounts of Chemical Research*, 47(8) (2014) 2671-2681.
- [5] Voiry D., Yamaguchi H., Li J., Silva R., Alves D.C.B., Fujita T., Chen M., Asefa T., Shenoy V.B., Eda G., Chhowalla M., Enhanced catalytic activity in strained chemically exfoliated WS₂ nanosheets for hydrogen evolution, *Nature Materials*, 12 (2013) 850-855.
- [6] Wang H., Kong D., Johannes P., Cha J.J., Zheng G., Yan H., Liu N., Cui Y., MoSe₂ and WSe₂ Nanofilms with Vertically Aligned Molecular Layers on Curved and Rough Surfaces, *Nano Letters*, 13(7) (2013) 3426-3433.
- [7] Zou M., Zhang J., Zhu H., Du M., Wang Q., M. Zhang M., Zhang X., A 3D dendritic WSe₂ catalyst grown on carbon nanofiber mats for efficient hydrogen evolution, *Journal of Materials Chemistry A*, 3(23) (2015) 12149-12153.
- [8] Liu Z., Zhao H., Li N., Zhang Y., Zhang X., Du Y., Assembled 3D electrocatalysts for efficient hydrogen evolution: WSe₂ layers anchored on graphene sheets, *Inorganic Chemistry Frontiers*, 3(2) (2016) 313-319.
- [9] Wang X., Chen Y., Zheng B., Qi F., He J., Li Q., Li P., Zhang W., Graphene-like WSe₂ nanosheets for efficient and stable hydrogen evolution, *Journal of Alloys and Compounds*, 691 (2017) 698-704.
- [10] Velazquez J.M., Saadi F.H., Pieterick A.P., Spurgeon J.M., Soriaga M.P., Brunshwig B.S., Lewis N.S., Synthesis and hydrogen-evolution activity of tungsten selenide thin films deposited on tungsten foils, *Journal of Electroanalytical Chemistry*, 716 (2014) 45-48.
- [11] Sun Y., Zhang X., Mao B., Cao M., Controllable selenium vacancy engineering in basal planes of mechanically exfoliated WSe₂ monolayer nanosheets for efficient electrocatalytic hydrogen evolution, *Chemical Communications*, 52(99) (2016) 14266-14269.
- [12] McKone J.R., Pieterick A.P., Gray H.B., Lewis N.S., Hydrogen Evolution from Pt/Ru-Coated p-Type WSe₂ Photocathodes, *Journal of the American Chemical Society*, 135(1) (2013) 223-231.
- [13] Gao T., Zhang Q., Li L., Zhou X., Li L., Li H., Zhai T., 2D Ternary Chalcogenides, *Advanced Optical Materials*, 6(14) (2018) 1-16.
- [14] Wu Q., Ma Y., Peng R., Huang B., Dai Y., Single-Layer Cu₂WS₄ with Promising Electrocatalytic Activity toward Hydrogen Evolution Reaction, *ACS Applied Materials & Interfaces*, 11(49) (2019) 45818-45824.
- [15] Reymond F., Fermín D., Lee H.J., Girault H.H., Electrochemistry at liquid/liquid interfaces: methodology and potential applications, *Electrochimica Acta*, 45(15) (2000) 2647-2662.
- [16] Girault H.H., Hard Science at Soft Interfaces, in *Developments in Electrochemistry*, John Wiley & Sons Ltd., 2014; 295-308.
- [17] Koelle U., Infelta P.P., Graetzel M., Kinetics and mechanism of the reduction of protons to hydrogen by cobaltocene, *Inorganic Chemistry*, 27(5) (1988) 879-883.
- [18] Ge P.Y., Todorova T.K., Patir I.H., Olaya A.J., Vruble H., Mendez M., Hu X.L., Corminboeuf C., Girault H.H., Biphasic water splitting by osmocene, *Proceedings of the National Academy of Sciences of the United States of America*, 109(29) (2012) 11558-11563.

- [19] Ge P.Y., Olaya A.J., Scanlon M.D., Patir I.H., Vrubel H., Girault H.H., Photoinduced Biphasic Hydrogen Evolution: Decamethylsiloxane as a Light-Driven Electron Donor, *Chemphyschem*, 14(10) (2013) 2308-2316.
- [20] Rivier L., Stockmann T.J., Méndez M.A., Scanlon M.D., Peljo P., Opallo M., H.H. Girault, Decamethylruthenocene Hydride and Hydrogen Formation at Liquid|Liquid Interfaces, *The Journal of Physical Chemistry C*, 119(46) (2015) 25761-25769.
- [21] Rivier L., Peljo P., Vannay L.A.C., Gschwend G.C., Méndez M.A., Corminboeuf C., Scanlon M.D., H.H. Girault, Photoproduction of Hydrogen by Decamethylruthenocene Combined with Electrochemical Recycling, *Angewandte Chemie International Edition*, 56(9) (2017) 2324-2327.
- [22] Hatay I., Su B., Li F., Partovi-Nia R., Vrubel H., Hu X., Ersoz M., H.H. Girault, Hydrogen evolution at liquid-liquid interfaces, *Angewandte Chemie International Edition*, 48(28) (2009) 5139-5142.
- [23] Nieminen J.J., Hatay I., Ge P., Mendez M.A., Murtomaki L., Girault H.H., Hydrogen evolution catalyzed by electrodeposited nanoparticles at the liquid/liquid interface, *Chem Commun*, 47(19) (2011) 5548-5550.
- [24] Aslan E., Patir I.H., Ersoz M., Cu nanoparticles electrodeposited at liquid-liquid interfaces: a highly efficient catalyst for the hydrogen evolution reaction, *Chemistry - A European Journal*, 21(12) (2015) 4585-4589.
- [25] Yanalak G., Aljabour A., Aslan E., Ozel F., Patir I.H., Kus M., Ersoz M., NiO and Co₃O₄ nanofiber catalysts for the hydrogen evolution reaction at liquid/liquid interfaces, *Electrochimica Acta*, 291 (2018) 311-318.
- [26] Scanlon M.D., Bian X., Vrubel H., Amstutz V., Schenk K., Hu X., Liu B., Girault H.H., Low-cost industrially available molybdenum boride and carbide as "platinum-like" catalysts for the hydrogen evolution reaction in biphasic liquid systems, *Phys. Chem. Chem. Phys.*, 15(8) (2013) 2847-2857.
- [27] Hatay I., Ge P.Y., Vrubel H., Hu X., Girault H.H., Hydrogen evolution at polarised liquid/liquid interfaces catalyzed by molybdenum disulfide, *Energy & Environmental Science*, 4(10) (2011) 4246-4251.
- [28] Aslan E., Hatay Patir I., Ersoz M., Catalytic Hydrogen Evolution by Tungsten Disulfide at Liquid-Liquid Interfaces, *Chem.Cat.Chem.*, 6(10) (2014) 2832-2835.
- [29] Hirunpinyopas W., Rodgers A.N.J., Worrall S.D., Bissett M.A., Dryfe R.A.W., Hydrogen Evolution at Liquid|Liquid Interfaces Catalyzed by 2D Materials, *Chem. Nano Mat.*, 3(6) (2017) 428-435.
- [30] Ozel F., Aslan E., Sarilmaz A., and Hatay Patir I., Hydrogen Evolution Catalyzed by Cu₂WS₄ at Liquid-Liquid Interfaces, *ACS Applied Materials & Interfaces*, 8(39) (2016) 25881-25887.
- [31] Aslan E., Sarilmaz A., Ozel F., Hatay Patir I., Girault H.H., Catalytic Hydrogen Evolution by Molybdenum-based Ternary Metal Sulfide Nanoparticles, *ACS Applied Nano Materials*, 2(11) (2019) 7204-7213.
- [32] Aslan E., Sarilmaz A., Ozel F., Hatay Patir I., Girault H.H., 1D Amorphous Tungsten-Based Ternary Refractory Metal Sulfides for Catalytic Hydrogen Evolution at Soft Interfaces, *Chem. Nano Mat.*, 5(12) (2019) 1461-1466.
- [33] Aslan E., Sarilmaz A., Yanalak G., Ozel S.S., Ozel F., Hatay Patir I., Transition metal-incorporated tungsten-based ternary refractory metal selenides (MWSe_x; M = Fe, Co, Ni and Mn) as hydrogen evolution catalysts at soft interfaces, *Materials Today Energy*, 18 (2020) 1-8.
- [34] Ozel F., Yar A., Aslan E., Arkan E., Aljabour A., Can M., Hatay Patir I., Kus M., Ersoz M., Earth-Abundant Cu₂CoSnS₄ Nanofibers for Highly Efficient H₂ Evolution at Soft Interfaces, *Chem. Nano Mat.*, 1(7) (2015) 477-481.
- [35] Ge P., Scanlon M.D., Peljo P., Bian X., Vrubel H., O'Neill A., Coleman J.N., Cantoni M., Hu X., Kontturi K., Liu B., Girault H.H., Hydrogen evolution across nano-Schottky junctions at carbon supported MoS₂ catalysts in biphasic liquid systems, *Chemical Communications*, 48(52) (2012) 6484-6486.
- [36] Bian X., Scanlon M.D., Wang S., Liao L., Tang Y., Liu B., Girault H.H., Floating conductive catalytic nano-rafts at soft interfaces for hydrogen evolution, *Chemical Science*, 4(9) (2013) 3432-3441.
- [37] Aslan E., Akin I., Hatay Patir I., Highly Active Cobalt Sulfide/Carbon Nanotube Catalyst for Hydrogen Evolution at Soft Interfaces, *Chemistry - A European Journal*, 22(15) (2016) 5342-5349.
- [38] Aslan E., Akin I., Hatay Patir I., Enhanced Hydrogen Evolution Catalysis Based on Cu

- Nanoparticles Deposited on Carbon Nanotubes at the Liquid/Liquid Interface, *Chem. Cat. Chem.*, 8(4) (2016) 719-723.
- [39] Akin I., Aslan E., Hatay Patir I., Enhanced Hydrogen Evolution Catalysis at the Liquid/Liquid Interface by Ni_xS_y and Ni_xS_y /Carbon Nanotube Catalysts, *European Journal of Inorganic Chemistry*, 2017(33) (2017) 3961-3966.
- [40] Sarilmaz A., Can M., Ozel F., Ternary copper tungsten selenide nanosheets synthesized by a facile hot-injection method, *Journal of Alloys and Compounds*, 699 (2017) 479-483.
- [41] Genc E., Coskun H., Yanalak G., Aslan E., Ozel F., Hatay Patir I., Dye-sensitized photocatalytic hydrogen evolution by using copper-based ternary refractory metal chalcogenides, *International Journal of Hydrogen Energy*, 45(32) (2020) 15915-15923.
- [42] Su B., Hatay I., Trojáněk A., Samec Z., Khoury T., Gros C.P., Barbe J.M., Daina A., Carrupt P.A., Girault H.H., Molecular Electrocatalysis for Oxygen Reduction by Cobalt Porphyrins Adsorbed at Liquid/Liquid Interfaces, *Journal of the American Chemical Society*, 132(8) (2010) 2655-2662.
- [43] Yıldırım M., Sarilmaz A., Özel F., Investigation of optical and device parameters of colloidal copper tungsten selenide ternary nanosheets, *Journal of Materials Science: Materials in Electronics*, 29(1) (2018) 762-770.
- [44] Crossland C.J., Hickey P.J., Evans J.S.O., The synthesis and characterisation of Cu_2MX_4 (M = W or Mo; X = S, Se or S/Se) materials prepared by a solvothermal method, *Journal of Materials Chemistry*, 15(34) (2005) 3452-3458.



Hydrothermal synthesis and crystal structures of a novel Keggin-type polyoxometalate based on 1,10-phenanthroline

Asuman UÇAR^{1,*} , Mükerrerem FINDIK² , Nuriye KOÇAK³ , Alper Tolga ÇOLAK⁴
Onur ŞAHİN⁵

¹Ağrı İbrahim Çeçen University, Education Faculty, Department of Science Education, Ağrı / TURKEY

²Necmettin Erbakan University, A.K. Education Faculty, Department of Chemistry Education, Research Laboratory, Konya / TURKEY

³Necmettin Erbakan University, A.K. Education Faculty, Department of Science Education, Konya / TURKEY

⁴Kütahya Dumlupınar University, Faculty of Arts and Science, Department of Chemistry, Kütahya / TURKEY

⁵Sinop University, Faculty of Health Sciences, Department of Occupat Health & Safety, Sinop / TURKEY

Abstract

Herein a novel inorganic-organic hybrid Keggin-type heteropolymolybdate $[\text{Ni}_2\text{Na}(\text{C}_{12}\text{H}_8\text{N}_2)_4(\text{BMo}_{12}\text{O}_{40})(\text{H}_2\text{O})_2]$ (**1**) has been synthesized under hydrothermal conditions in aqueous solution. The crystal structure was fully characterized by powder X-ray diffraction (XRD), elemental analysis, Fourier-transform infrared spectrum (FT-IR), Thermogravimetric analysis (TGA) and Scanning Electron Microscopy (SEM) analysis. Single crystal X-ray structural analysis demonstrates that the complex consists of a Keggin anion $[\text{BMo}_{12}\text{O}_{40}]^{5-}$ polyanion, four 1,10-phenanthroline ($\text{C}_{12}\text{H}_8\text{N}_2$) ligands, two Ni(II) ions, two Na(I) ions and two aqua ligands. The experimental powder X-ray diffraction (XRD) result of the crystal is consistent with the calculated data. The SEM image shows that the compound crystals have a cubic structure.

Article info

History:

Received: 18.10.2020

Accepted: 21.01.2021

Keywords:

Polyoxometalates,
Coordination complexes,
Oxoclusters,
Hydrothermal synthesis,
Keggin.

1. Introduction

Polyoxometalates (POMs) are ametal-oxygen cluster compounds consisting of higher oxidation states of oxo-anions of early transition metals (W^{VI} , Mo^{VI} , V^{V} and Nb^{V}) [1-2]. Polyoxometalates are used as inorganic compound because of their various shapes, large size and rich electronic and magnetic properties [3]. The POM has been extensively studied because of the terminal and active bridging oxygen atoms, tunable composition, the high charge density, and diversity of shape and size [4]. Keggin-type POMs can be used as POM-based inorganic-organic hybrid compounds because of their simple synthesis procedure, thermal stability, large electron density and abundant surfaces [5-7]. POMs have been taken part in many fields such as sensitive devices, medicine, catalysis, nanotechnology, energy storage, photochemistry, materials science, nuclear waste treatment and magnetism due to their excellent topological and electronic versatility [8-18]. In previous studies, polyoxomolybdates have been

synthesized such as $[\text{XMo}_{12}\text{O}_{40}]^n$ ($\text{X} = \text{As}, \text{P}, \text{Si}, \text{Ge}, \text{Ni}, \text{Co}$) [19-22]. The $[\text{BMo}_{12}\text{O}_{40}]^{5-}$ framework, which is a boron-containing Keggin type polyoxomolybdate anion, was synthesized for the first time by our research group [23]. POMs are widely used as a catalysts for water oxidation [24] and transformation of CO_2 into desirable chemical products [25]. Alamdari et al. synthesized Mo132-MimAM for the oxidation of sulfides and Hasannia et al. synthesized LDH-PWFe for the oxidation of alcohols [26-27]. These studies by researchers have shown that POMs have great potential in catalysis studies and paved the way for new studies. In the present study, a new organic-inorganic hybrid based on 1,10-phenanthroline ($\text{C}_{12}\text{H}_8\text{N}_2$) ligands and Keggin anion $[\text{BMo}_{12}\text{O}_{40}]^{5-}$ was synthesized to support new catalysis studies, which is the main purpose of our study. It is also thought that the POM synthesized by our group will serve as a new model for the design of transition metal-substituted POM architectures. Because of the high catalytic properties of hybrid POMs, it offers a great variety of catalytic applications with different fields of study, such as redox reactions,

*Corresponding author. e-mail address: asucar340@gmail.com

<http://dergipark.gov.tr/csj> ©2021 Faculty of Science, Sivas Cumhuriyet University

energy, environmental, biomedical and green chemistry. Herein, the crystal $[\text{Ni}_2\text{Na}(\text{C}_{12}\text{H}_8\text{N}_2)_4(\text{BMo}_{12}\text{O}_{40})(\text{H}_2\text{O})_2]$ (1) was hydrothermally synthesized for the first time and characterized in detail using single crystal X-ray structural analysis, XRD, elemental analysis, FT-IR, TGA and SEM techniques both structurally and morphologically.

2. Materials and Methods

2.1. Reagents and apparatus

All reagents were obtained from commercial resources and used without further purification. Nickel(II)chloride hexahydrate ($\text{NiCl}_2 \cdot 6\text{H}_2\text{O}$) and hydrochloric acid (HCl) were supplied by Merck. Sodium tungstate dehydrate ($\text{Na}_2\text{MoO}_4 \cdot 2\text{H}_2\text{O}$), boric acid (H_3BO_3) and 1,10-phenanthroline were supplied by Sigma-Aldrich. Perkin-Elmer 2400 CHN (PerkinElmer Inc, USA) elemental analyzer was used for elemental analysis (C, N and H) of sample. The FT-IR spectrum was recorded at room temperature on a Perkin Elmer model 100 ATR-FTIR spectrometer (PerkinElmer Inc, USA). Thermogravimetric analysis (TGA) was carried out with a Setaram thermal gravimetric analyzer (Simultaneous Thermal Analysis, Setaram Instrumentation, France) at a heating rate of $1^\circ\text{C}/\text{min}$ under N_2 atmosphere ($25\text{--}1000^\circ\text{C}$). SEM image was investigated on a Hitachi – SU 1510 at accelerating voltage of 20 kV and magnification of 10.00 kX. Powder XRD measurements were taken using Bruker D.8 Advance (Germany) X-ray diffractometer.

2.2. Preparation of $[\text{Ni}_2\text{Na}(\text{C}_{12}\text{H}_8\text{N}_2)_4(\text{BMo}_{12}\text{O}_{40})(\text{H}_2\text{O})_2]$ (1)

The compound as synthesized according to our previous article [25].

A mixture of H_3BO_3 (0.186 g, 3.0 mmol), $\text{Na}_2\text{MoO}_4 \cdot 2\text{H}_2\text{O}$ (1.46 g, 6.00 mmol), $\text{NiCl}_2 \cdot 2\text{H}_2\text{O}$ (0.392 g, 1.65 mmol), 1,10-phenanthroline (0.3 g, 1.5 mmol) and H_2O (20 ml) was stirred for an hour. The pH of the mixture was adjusted to 2 with 6 M HCl. The mixture was allowed to react in a Teflon-lined stainless steel reactor for 7 days at 185°C . After 7 days of reaction, the product was cooled down to room temperature by 10 degrees per hour and green crystals were obtained (yield 83 %) (Figure 1).

Anal. Calcd. For $\text{C}_{48}\text{H}_{36}\text{BMo}_{12}\text{N}_8\text{NaNi}_2\text{O}_{42}$ (2699.35g/mol): C, 21.34%; H, 1.33%; N, 4.15%. Found: C, 21.52%; H, 1.46%; N, 4.33%. FT-IR (cm^{-1}): 3578, 3062, 1628, 1517, 1429, 1037, 984, 940, 896.

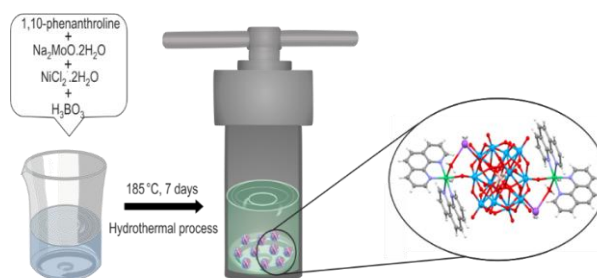


Figure 1. Synthetic routes for the compound.

2.3. X-Ray diffraction analysis

The hydrogen atoms bound to carbon atoms were treated as riding atoms with distances of 0.93 \AA . Other H atoms were refined freely. In order to avoid ADP and NPD problems, the EADP command was used to refine the non-H atoms. With SHELXS-2013 [28], the structure of compound 1 was solved by direct methods and refined using full-matrix least-squares methods with SHELXL-2013 program [29] within WinGX [30]. The structural data of compound 1 was collected on Bruker APEX2 (APEX2, Bruker AXS Inc. Madison Wisconsin USA 2013). MERCURY program was used for molecular graphics. Details of data collection and crystal structure determinations are shown in Table 1. Crystallographic data of the structure has been deposited in the Cambridge Crystallographic Data Center with CCDC number 1844844.

3. Results and Discussion

3.1. Structural analysis

The molecular structure unit of compound 1 with the atom labeling is shown in Figure 2. The unsymmetrical unit of compound 1 has been proved to consist of one Na(I) ion, one Ni(II) ion, a half of $[\text{BMo}_{12}\text{O}_{40}]^{5-}$ polyanion, two phenanthroline ligands and one aqua ligand. The B1 atom is located on the inversion center ($1/2, 1/2, 1/2$). The polyanion $[\text{BMo}_{12}\text{O}_{40}]^{5-}$ anion with a Keggin-type structure has a structure with a central BO_4 [B-O bond distances range of $1.60(2)\text{--}1.62(3) \text{ \AA}$] surrounded by the $\text{Mo}_{12}\text{O}_{36}$ group with tetrahedron coordination geometry. The oxygen atoms of BO_4 group are disordered over two positions. According to different coordination environments, the Mo–O bonds can be categorized into three groups: Mo–O (terminal oxygen atom) with lengths range between $1.652(11)\text{--}1.683(11) \text{ \AA}$, Mo–O (bridging oxygen atoms) with lengths range between $1.788(16)\text{--}2.039(17) \text{ \AA}$ and Mo–O (central oxygen atom) with lengths range between $2.34(3)\text{--}2.449(19) \text{ \AA}$. The Ni(II) ion is coordinated by four nitrogen atoms [Ni–N lengths range between $2.064(13)\text{--}2.093(13) \text{ \AA}$] from

phenanthroline ligands, one oxygen atom [Ni1-O21=2.115(11) Å] from [BMo₁₂O₄₀]⁵⁻ polyanion and one oxygen atom [Ni1-O23=2.068(12) Å] from aqua ligand, thence indicating a distorted octahedral geometry. At the same time, the Ni1 atom and [BMo₁₂O₄₀]⁵⁻ polyanion are bridged by Na1 atom, thus produce [Ni₂Na(C₁₂H₈N₂)₄(BMo₁₂O₄₀)(H₂O)₂] cluster. Selected bond lengths for NiBWO (Å) are shown in Table 2. The [Ni₂Na(C₁₂H₈N₂)₄(BMo₁₂O₄₀)(H₂O)₂] clusters are combined by O-H...O hydrogen bonds, creating 1D supramolecular network running parallel to the [001] direction (Figure 3). Similarly, adjacent

[Ni₂Na(C₁₂H₈N₂)₄(BMo₁₂O₄₀)(H₂O)₂] clusters are combined by C-H...O hydrogen bonds, generating 1D supramolecular network running parallel to the [010] direction (Figure 4). The combination of O-H...O and C-H...O hydrogen bonds (Table 3) is generating 2D supramolecular network.

The most important step of the experimental studies using UV-Vis spectrophotometry is the selection of the measurement wavelength. Because all the experimental measurements were performed at the selected wavelength. If the correct wavelength is not selected, all experimental results are affected.

Table 1. Crystal data and structure refinement parameters for compound 1

Empirical formula	C ₄₈ H ₃₆ BMo ₁₂ N ₈ NaNi ₂ O ₄₂
Formula weight	2699.35
Crystal system	Triclinic
Space group	P-1
<i>a</i> (Å)	10.789 (3)
<i>b</i> (Å)	13.295 (4)
<i>c</i> (Å)	13.622 (3)
<i>α</i> (°)	69.268 (7)
<i>β</i> (°)	71.433 (6)
<i>γ</i> (°)	77.446 (7)
<i>V</i> (Å ³)	1720.3 (7)
<i>Z</i>	1
Diffractometer	BRUKER D8-QUEST
Temperature (K)	296
<i>F</i> (000)	1292
<i>θ</i> range (°)	3.2-28.4
Measured refls.	77058
Independent refls.	6739
Parameters	454
<i>R</i> _{int}	0.030
<i>S</i>	1.08
<i>R</i> ₁ / <i>wR</i> ₂	0.113/0.225

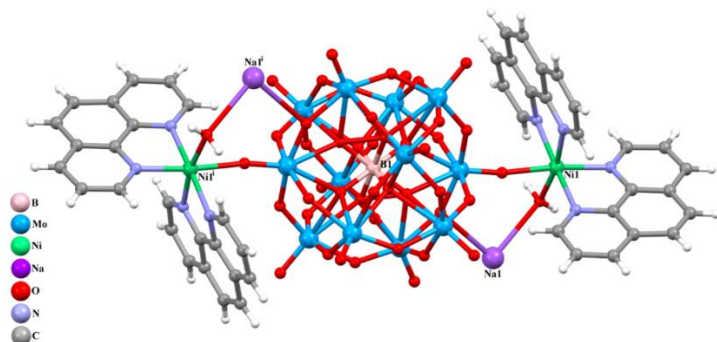
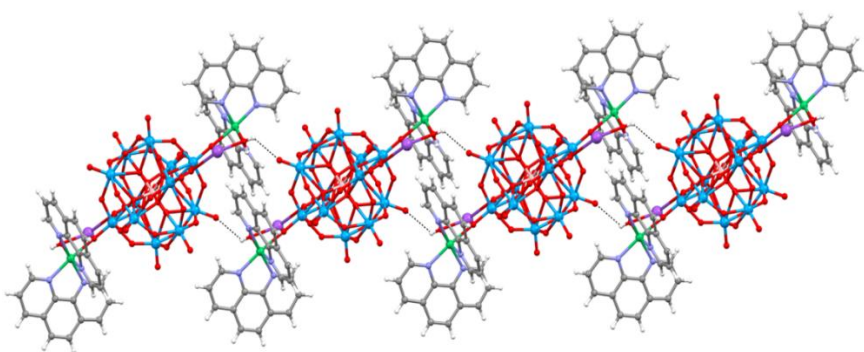
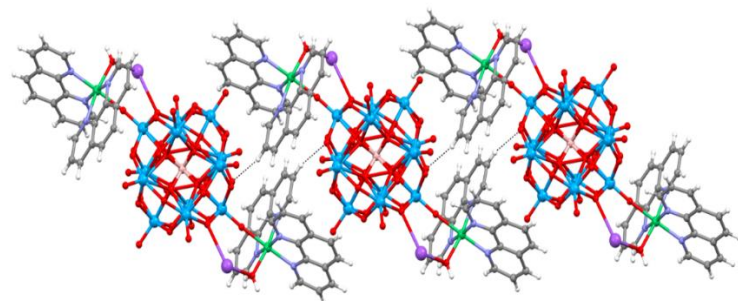
Table 2. Selected bond distances for compound 1 (Å)

B1-O1	1.60(2)	B1-O2	1.62(3)	B1-O3	1.61(3)
B1-O4	1.60(3)	Mo1-O21	1.683(11)	Mo1-O9	1.798(17)
Mo1-O18 ⁱ	1.841(16)	Mo1-O8	1.982(16)	Mo1-O15 ⁱ	2.001(16)
Mo1-O2	2.34(3)	Mo1-O1	2.382(19)	Mo2-O20	1.661(12)
Mo2-O8	1.809(17)	Mo2-O19	1.825(16)	Mo2-O7	1.989(17)
Mo2-O10	2.003(16)	Mo2-O2	2.43(3)	Mo2-O3	2.43(3)
Mo3-O17	1.663(12)	Mo3-O7	1.799(16)	Mo3-O6	1.799(16)
Mo3-O18	2.009(16)	Mo3-O13 ⁱ	2.010(16)	Mo3-O3	2.38(3)
Mo3-O1 ⁱ	2.407(19)	Mo4-O16	1.658(12)	Mo4-O5	1.788(16)
Mo4-O15	1.805(16)	Mo4-O6	1.996(16)	Mo4-O12	2.023(16)
Mo4-O4 ⁱ	2.41(3)	Mo4-O1 ⁱ	2.449(19)	Mo5-O14	1.658(11)
Mo5-O13	1.813(17)	Mo5-O11	1.815(16)	Mo5-O19 ⁱ	1.991(16)
Mo5-O5	1.992(17)	Mo5-O3 ⁱ	2.38(3)	Mo5-O4 ⁱ	2.40(3)
Mo6-O22	1.652(11)	Mo6-O12	1.794(16)	Mo6-O10	1.810(16)
Mo6-O11	1.986(16)	Mo6-O9	2.039(17)	Mo6-O4 ⁱ	2.41(3)
Mo6-O2	2.43(3)	N1-Ni1	2.084(13)	N2-Ni1	2.093(13)
N3-Ni1	2.064(13)	N4-Ni1	2.074(13)	Ni1-O23	2.068(12)
Ni1-O21	2.115(11)	Na1-O23	2.74(2)	Na1-O18 ⁱ	2.98(2)

Symmetry code: (i) -x+1, -y+1, -z+1.

Table 3. Hydrogen-bond parameters for compound 1 (Å, °)

D-H···A	D-H	H···A	D···A	D-H···A
C9—H9···O8 ⁱⁱⁱ	0.93	2.60	3.49 (2)	162
C13—H13···O14 ^{iv}	0.93	2.48	3.14 (2)	128
O23—H23A···O22 ^{iv}	0.83 (2)	2.36 (6)	2.877 (16)	121
O23—H23B···N1	0.83 (2)	2.58 (8)	3.010 (18)	114

Symmetry codes: (iii) $-x+1, -y+2, -z+1$; (iv) $-x+1, -y+1, -z+2$.**Figure 2.** The molecular view of the compound indicating the atom numbering scheme.**Figure 3.** The molecular view of the compound, demonstrating the formation of a chain through [001] created by O-H···O hydrogen bonds.**Figure 4.** The molecular view of the compound, demonstrating the formation of a chain through [010] created by C-H···O hydrogen bond.

3.2. X-ray diffraction

The calculated pattern from single-crystal structures and experimental XRD patterns of the compound is shown in Figure 5. The experimental data is consistent with the calculated patterns, indicating the phase purity of the compound. The preferred orientation of the powder sample may cause differences in intensity. Powder X-ray diffraction results of the structure are similar to other related studies [16,31].

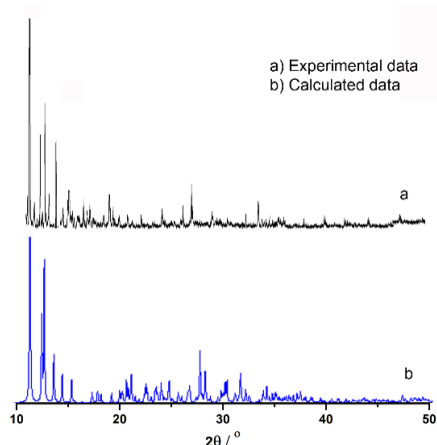


Figure 5. XRD spectra of the compound 1.

3.3. FT-IR spectrum

The crystal contains the identical Keggin POM $[\text{BMo}_{12}\text{O}_{40}]^{5-}$ and as can be seen in Figure 6, the FT-IR spectrum shows the specific vibrations of Keggin type POMs [32]. Characteristics bands of the Keggin unit appeared at 1037, 984, 940 and 896 cm^{-1} can be respectively assigned to B–O, terminal Mo–O, inter-octahedral Mo–O–Mo, and intra-octahedral Mo–O–Mo vibrations [6,33,34]. The band seen at 3578 cm^{-1} can be attributed to the coordinated water [35]. The absorption bands at 3062, 1628, 1517 and 1429 cm^{-1} are assigned to aromatic $\nu(\text{C-H})$, azomethine $\nu(\text{C=N})$, $\nu(\text{C=C})$ and $\nu(\text{C-N})$ stretching, respectively [36-39].

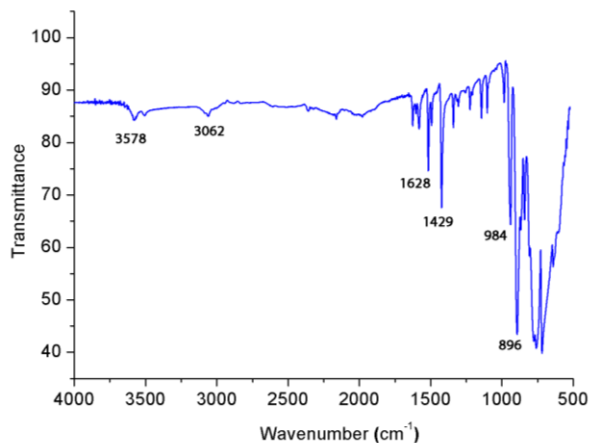


Figure 6. FT-IR spectrum of the compound 1.

3.4. Thermogravimetric analysis

The thermal behaviors of the crystal were investigated with the thermal analysis methods. As shown in Figure 7, the water removal causes the slight weight loss below 478 °C [40]. The weight loss in the range of 478-690 °C is attributed to the decomposition of the two 1,10-phenanthroline ligands (calc. 26.7%; found 27.1%) [41].

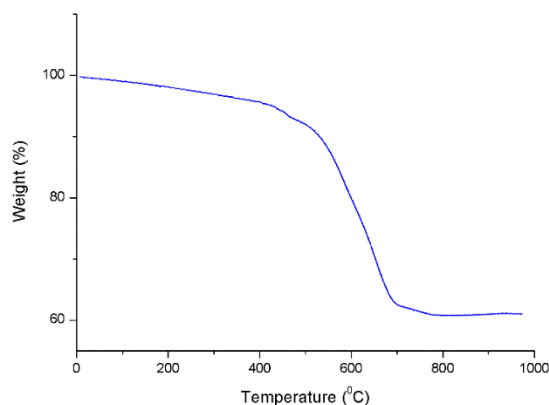


Figure 7. TG curve of the crystal

3.5. SEM analysis

SEM is used to examine the three important factors surfactant morphology (surface structural properties based on shape and size), surface crystallography (ie, surface formation of atoms) and surface composition (in terms of surface composition, compounds and elements). So, the surface property of the compound 1 was checked by using SEM (Figure 8). According to the SEM image, each crystal has a cubic structure.

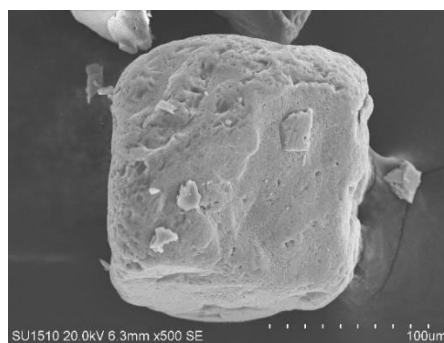


Figure 8. The SEM images of the compound 1.

4. Conclusion

In summary, we have prepared a novel Keggin-type inorganic-organic hybrid compound by using metal Ni(II) ion and 1,10-phenanthroline ($\text{C}_{12}\text{H}_8\text{N}_2$) ligand based on boron atom as the central atom. TGA, FT-IR and XRD methods were used for the structure analysis

of the compound. These analyzes support the results from the single crystal X-ray structural analysis. The content of the structure is determined as a half of $[\text{BMo}_{12}\text{O}_{40}]^{5-}$ polyanion, two phenanthroline ligands and one aqua ligand according to by single crystal X-ray diffraction. It is thought that a new POM synthesis with the simple synthesis process used in this study will contribute to the development of new inorganic-organic POM materials.

Acknowledgment

This study was supported by the Necmettin Erbakan University Research Foundation (151210002) and for the use of the Bruker D8 QUEST diffractometer, the authors are grateful to Scientific and Technological Research Application and Research Center, Sinop University, Turkey.

Conflicts of interest

The authors state that there is no conflict of interests.

References

- [1] Gupta R., Parbhakar S., Khan I., Behera J.N., Hussain F., Early lanthanoid substituted organic-inorganic hybrids of silico- and germano-tungstates: Syntheses, crystal structures and solid-state properties, *Indian Journal of Chemistry*, 57A (2018) 52-58.
- [2] Rezvani M.A., Khandan S., Synthesis and characterization of new sandwich-type polyoxometalate/nanoceramic anocomposite, $\text{Fe}_2\text{W}_{18}\text{Fe}_4@\text{FeTiO}_3$, as a highly efficient heterogeneous nanocatalyst for desulfurization of fuel, *Solid State Sciences*, 98 (2019) 106036-106044.
- [3] Han Z.G., Li S., Wu J.J., Zhai X.L., Hydrothermal synthesis and structural characterization of two new polytungstate-based hybrids, *Journal of Coordination Chemistry*, 64 (2011) 1525–1532.
- [4] Mirzaei M., Eshtiagh-Hosseini H., Hassanpoor A., Different behavior of PDA as a preorganized ligand versus PCA ligand in constructing two inorganic-organic hybrid materials based on Keggin-type polyoxometalate, *Inorganica Chimica Acta.*, 484 (2019) 332–337.
- [5] Yang D.D., Mu B., Lv L., Huang R.D., The assembly of POM-induced inorganic–organic hybrids based on copper ion sand mixed ligands, *Journal of Coordination Chemistry*, 68 (2015) 752–765.
- [6] Arichi J., Pereira M.M., Esteves P.M., Louis B., Synthesis of Keggin-type polyoxometalate crystals, *Solid State Sciences*, 12 (2010) 1866–1869.
- [7] Lü Y., Xiao N., Hao X.R., Cui X.B., Xu J.Q., A series of organic–inorganic hybrid compounds formed by $[\text{P}_2\text{W}_{18}\text{O}_{62}]^{6-}$ and several types of transition metal complexes, *Dalton Transactions*, 46 (2017) 14393-14405.
- [8] Wang X., Li T., Tian A., Xu N., Zhang R., Introduction of secondary pyridyl-1H-tetrazole derivatives into Keggin–Ag–(1,10-phenanthroline) system for tuning dimensionalities and architectures: assembly and properties, *Journal of Coordination Chemistry*, 69 (2016) 2532–2544.
- [9] Dianat S., Bordbar A.K., Tangestaninejad S., Zarkesh-Esfahani S.H., Habibi P., Kajani A.A., ctDNA interaction of Co-containing Keggin polyoxomolybdate and in vitro antitumor activity of free and its nano-encapsulated derivatives, *Journal of The Iranian Chemical Society*, 13 (2016) 1895-1904.
- [10] Ucar A., Findik M., Gubbuk I.H., Kocak N., Bingol H., Catalytic degradation of organic dye using reduced grapheneoxide–polyoxometalate nanocomposite, *Materials Chemistry and Physics*, 196 (2017) 21-28.
- [11] Bicho R.C., Soares A.M.V.M., Nogueira H.I.S., Amorim M.J.B., Effects of europium polyoxometalate encapsulated in silica nanoparticles (nanocarriers) in soil invertebrates, *Journal of Nanoparticle Research*, 18 (2016) 360-366.
- [12] Xia S.L.F., Li X., Cheng F., Sun C., Liu J.J., Guo H., An inorganic–organic hybrid supramolecular framework as a high-performance anode for lithium-ion batterie, *Dalton Transactions*, 47 (2018) 5166-5170.

- [13] Ishizuka T., Ohkawa S., Ochiai H., Hashimoto M., Ohkubo K., Kotani H., Sadakane M., Fukuzumi S., Kojima T., A supramolecular photocatalyst composed of a polyoxometalate and a photosensitizing water-soluble porphyrindiacid for the oxidation of organic substrates in water, *Green Chemistry*, 20 (2018) 1975-1980.
- [14] Zhao P., Zhang Y., Li D., Cui H., Zhang L., Mesoporous polyoxometalate-based ionic hybrid as a highly effective heterogeneous catalyst for direct hydroxylation of benzene to phenol, *Chinese Journal of Catalysis*, 39 (2018) 334-341.
- [15] Dubal D.P., Chodankar N.R., Vinu A., Kim D.H., Gomez-Romero P., Asymmetric Supercapacitors Based on Reduced Graphene Oxide with Different Polyoxometalates as Positive and Negative Electrodes, *Chemsuschem*, 10 (2017) 2742-2750.
- [16] Zhang T.T., Hu Y.Y., Zhang X., Cui X.B., New compounds of polyoxometalates and cadmium mixed-organic-ligand complexes, *Journal of Solid State Chemistry*, 283 (2020) 121168-121177.
- [17] Wang J., Niu Y., Zhang M., Ma P., Zhang C., Niu J., Wang J., Organo phosphonate-Functionalized Lanthano polyoxomolybdate: Synthesis, Characterization, Magnetism, Luminescence, and Catalysis of H₂O₂-Based Thioether Oxidation, *Inorganic Chemistry*, 57 (2018) 1796-1805.
- [18] Rafieea E., Pami N., Zinatizadeh A.A., Eavani S., A new polyoxometalate-TiO₂ nanocomposite for efficient visible photodegradation of dye from waste water, liquorice and yeast extract: Photoelectrochemical, electrochemical and physical investigations, *Journal of Photochemistry & Photobiology A: Chemistry*, 386 (2020) 112145-112156.
- [19] An D., Chen Z., Zheng J., Chen S., Wang L. and Su W., Polyoxometalate functionalized tris(2,2-bipyridyl)dichlororuthenium(II) as the probe for electrochemiluminescence sensing of histamine, *Food Chemistry*, 194 (2016) 966-971.
- [20] Yu X.Y., Cui X.B., Lu J., Luo Y.H., Zhang H., Gao W.P., Five inorganic-organic hybrids based on Keggin polyanion [SiMo₁₂O₄₀]⁴⁻: From 0D to 2D network, *Journal of Solid State Chemistry*, 209 (2014) 97-104.
- [21] Li S., Ma P., Niu H., Zhao J., Niu J., {[Cu(phen)₃Cl₄]₂[GeMo₁₂O₄₀]}: Synthesis, crystal structure and magnetic property of a new trinuclear copper complex based on germanomolybdate, *Inorganic Chemistry Communications*, 13 (2010) 805-808.
- [22] Igarashi T., Zhang Z., Haioka T., Iseki N., Hiyoshi N., Sakaguchi N., Kato C., Nishihara S., Inoue K., Yamamoto A., Yoshida H., Tsunoji N., Ueda W., Sano T., Sadakane M., Synthesis of ε-Keggin-Type Cobaltomolybdate-Based 3D Framework Material and Characterization Using Atomic-Scale HAADF-STEM and XANES, *Inorganic Chemistry*, 56 (2017) 2042-2049.
- [23] Findik M., Ucar A., Colak A.T., Sahin O., Bingol H., Sayin U., Kocak N., Self-assembly of a new building block of {BMo₁₂O₄₀} with excellent catalytic activity for methylene blue, *Polyhedron*, 160 (2019) 229-237.
- [24] Gang Z., Bond A.M., Zhao C., Recent trends in the use of polyoxometalate-based material for efficient water oxidation, *Science China Chemistry*, 54 (2011) 1877-1887.
- [25] Song Y., Tsunashima R., Recent advances on polyoxometalate-based molecular and composite materials, *Chemical Society Reviews*, 41 (2012) 7384-7402.
- [26] Alamdari R.F., Zekri N., Moghadam A.J., Farsani M.R., Green oxidation of sulfides to sulfoxides and sulfones with H₂O₂ catalyzed by ionic liquid compounds based on Keplerate polyoxometalates, *Catalysis Communications*, 98 (2017) 71-75.
- [27] Hasannia S., Yadollahi B., Zn-Al LDH nanostructures pillared by Fe substituted Keggin type polyoxometalate: Synthesis, characterization and catalytic effect in green oxidation of alcohols, *Polyhedron*, 99 (2015) 260-265.

- [28] Sheldrick G.M., A short history of SHELX, *Acta Crystallographica Section A*, A64 (2008) 112–122.
- [29] Sheldrick G.M., Crystal structure refinement with SHELXL, *Acta Crystallographica Section C*; C71 (2015) 3–8.
- [30] Farrugia L.J., WinGX and ORTEP for Windows: an update, *J. Appl. Cryst.*, 45 (2012) 849–854.
- [31] Wang T., Peng J., Liu H., Zhu D., Tian A., Wang L., Open framework complex constructed from polyoxometalate and dinuclear Cu–phenanthroline, *Journal of Molecular Structure*, 892 (2008) 268–271.
- [32] Hu Y.Y., Zhang T.T., Zhang X., Zhao D.C., Cui X.B., Huo Q.S., Xu J.Q., New organic–inorganic hybrid compounds constructed from polyoxometalates and transition metal mixed-organic-ligand complexes, *Dalton Transactions*, 45 (2016) 2562–2573.
- [33] Chen Y., Zhou B., Zhao J., Li Y., Su Z., Zhao Z., Two novel hybrid compounds based on $[MW_{12}O_{40}]^{5-}$ (M=B, Al) heteropolyanions and copper coordination polymer with bpp ligands, *Inorganica Chimica Acta*, 363 (2010) 3897–3903.
- [34] Olgun A., Çolak A.T., Gübbük I.H., Şahin O., Kanar E., A new Keggin-type polyoxometalate catalyst for degradation of aqueous organic contaminants, *Journal of Molecular Structure*, 1134 (2017) 78–84.
- [35] Chen Y., Gu X., Peng J., Shi Z., Wang E., Hydrothermal synthesis and crystal structure of organic–inorganic hybrid vanadate: $[Zn(phen)(H_2O)V_2O_6]$ (phen=1,10-phenanthroline), *Journal of Molecular Structure*, 692 (2004) 243–247.
- [36] Sundararajan M.L., Jeyakumar T., Anandakumaran J., Selvan B.K., Synthesis of metal complexes involving Schiff base ligand with methylenedioxy moiety: Spectral, thermal, XRD and antimicrobial studies, *Spectrochimica Acta Part A: Molecular and Biomolecular Spectroscopy*, 131 (2014) 82–93.
- [37] Iftikhar B., Javed K., Khan M.S.U., Akhter Z., Mirza B., Mckee V., Synthesis, characterization and biological assay of Salicylaldehyde Schiff base Cu(II) complexes and their precursors, *Journal of Molecular Structure*, 1155 (2018) 337–348.
- [38] Wang X., Jia G., Yu Y., Gao Y., Zhang W., Wang H., Cao Z., Liu J., A New Homogeneous Electrocatalyst For Electrochemical Carbonylation Of Methanol To Dimethyl Carbonate, *Química Nova*, 38 (2015) 298–302.
- [39] Küçük I., Vural S., Kılıvcım N., Adıgüzel I., Köytepe S., Seçkin T., Hydrothermal Synthesis of Polyoxometalate Containing Cobalt Ion and Its Polyurethane Composites for Dielectric Material Applications, *Polymer-Plastics Technology And Materials*, 59 (2020) 1822–1841.
- [40] Ge W., Long Z., Cai X., Wang Q., Zhou Y., Xu Y., Wang J., A new polyoxometalate-based Mo/V coordinated crystalline hybrid and its catalytic activity in aerobic hydroxylation of benzene, *RSC Advance*, 4 (2014) 45816–45822.
- [41] Zhang B.S., Wu C.S., Qiu J.P., Li Y.X., Liu Z.X., α -Keggin tungstogermanate-supported transition metal complexes: hydrothermal synthesis, characterization, and magnetism of $Cu_2(phen)_4(GeW_{12}O_{40})$ and $[Ni_2(bpy)_4(H_2O)_2(GeW_{12}O_{40})]_2 \cdot H_2O$, *Journal of Coordination Chemistry*, 67 (2014) 787–796.



***N*-Alkoxy carbonyl / carbamoylmethyl substituted 1*H*-imidazol-2-yliden-Pd (II) complexes as highly efficient catalysts for Suzuki-Miyaura cross-coupling reaction**

Meliha ÇETİN KORUKÇU *

Bursa Uludağ University, Faculty of Arts and Science, Department of Chemistry, 16059 Bursa / TURKEY

Abstract

N-Alkoxy carbonyl / carbamoylmethyl substituted 1*H*-imidazol-2-yliden-Pd (II) complexes (Cat-1-5) were used for the first time as catalysts in the Suzuki-Miyaura reaction between aryl bromides and arylboronic acids. All complexes screened were found to be excellent catalysts in the selected coupling between 4-bromobenzaldehyde and phenylboronic acid at room temperature. Cat-3 was shown to be the most efficient one and used for the optimisation of the reaction conditions and determining the substrate scope. The application of the optimised method provided a series of biaryls (3a-1) in excellent isolated yields. With these promising results the catalysts could be applied successfully to some other classic cross-coupling reactions such as Sonogashira, Stille and Buchwald-Hartwig.

Article info

History:

Received: 10.10.2020
Accepted: 27.01.2021

Keywords:

N-Heterocyclic,
Carbenes,
Pd(II)-N-Heterocyclic
Carbene complexes,
Suzuki coupling.

1. Introduction

Suzuki-Miyaura cross-coupling reaction is one of the most powerful reactions used to form C-C bonds in organic chemistry. It is a mild and facile route to prepare biaryls from the reaction of an aryl halide (vinylhalide or sulfonate) with an arylboronic acid (or ester) by using catalytic amounts of Pd compounds [1]. It is most frequently used in the formation of biaryls (one of the major skeletons in organic chemistry) which take place in many pharmaceuticals, agrochemicals and biologically active natural compounds [2]. Biaryls have also been used recently in the area of material chemistry for the preparation of functional molecules such as organic light emitting diodes (OLEDs) [3], molecular wires, liquid crystals, conducting polymers etc [4].

Since the palladium complexes involving tertiary phosphine ligands used in Suzuki-Miyaura coupling are toxic, often air, oxygen and water sensitive and require high temperature [5], the use of less toxic catalysts and more environmentally friendly conditions like aqueous organic solvents (as DMF-H₂O, toluene-H₂O etc.) and working at room temperature have become the determining factors of the reaction [6].

N-heterocyclic carbenes, the imidazol-2-ylidenes, are convenient ligands [7] that have been used in Suzuki-Miyaura reaction in the last decades [8]. Their

palladium complexes, in particular, have been used successfully not only in Suzuki-Miyaura but also in many other coupling reactions such as Heck-Mizoroki, Negishi, Sonogashira, Hiyama, Buchwald-Hartwig etc [9]. Apart from that, they have various properties and interesting areas of usage [10].

In one of our previous works we reported the preparation of a new type of bidentate N-heterocyclic carbene enolates (NHCE) and their palladium complexes via transmetalation of silver complexes [11]. First we treated 1,4-diaryl and 1,2,4-triarylimidazoline N-oxides with dimethyl acetylenedicarboxylate (DMAD) to get isoxazolines. Rearrangement of these isoxazolines under reflux in toluene provided the 1,4-diaryl or 1,2,4-triarylimidazoles and corresponding 3*H*-imidazol-1-ium ylides. The reaction of ylides (with no substituent at C-2) with silver nitrate and triethylamine at room conditions provided C-2 metallated N-heterocyclic carbene ylides (Ag(NHCY)(Et₃N)). The treatment of these precursors with equimolar amounts of Pd(CH₃CN)₂Cl₂ in CH₂Cl₂ provided mono Pd(II)-NHCE complexes that are in equilibrium with their bis-Pd(II)-NHCE analogues [12]. All the new complexes were fully characterized with IR, NMR, elemental analysis and thermogravimetric analysis (TGA). In the same study, we also tried these newly prepared Pd complexes in a model Heck-Mizoroki and in a model Suzuki-Miyaura reactions and showed that they were

*Corresponding author. e-mail address: melihacetin@uludag.edu.tr

pretty good as catalysts. We also used the Hammett type correlations in order to reveal the substituent effect on the aryl halides, catalysts, styrenes and arylboronic acids.

In a different study, we reported the synthesis and characterisations of another group of Pd (II)-NHC complexes starting from appropriate imidazolium salts [13]. All the new complexes were characterized with spectral methods and elemental analysis and their thermal behaviours were investigated in detail. We also screened the new complexes for their catalytic activities in Heck-Mizoroki coupling and revealed the catalysts to be highly efficient.

As a continuation of our last research, in this study catalysts 1-5 are used in Suzuki-Miyaura cross-coupling for the first time, with very low catalyst loadings, in an aqueous solvent, at room temperature, in very short time with extremely high yields and easy isolation method.

2. Materials and Methods

2.1. Apparatus

An Electrothermal Digital melting point apparatus was used for determining the melting points of the compounds. ^1H and ^{13}C NMR experiments were performed on an Agilent 400 MHz spectrometer. The preparative TLC was performed with silica gel 60 HF254 (90% < 45 μm). All of the reagents and solvents used in this work were provided commercially and used without any further purifications.

2.2. Synthesis of the biphenyls (3)

General procedure: Aryl bromide (0.2 mmol) and arylboronic acid (0.3 mmol) are stirred in *N,N*-dimethylformamide-water (1:1, v/v, 0.6 mL) with Cs_2CO_3 (0.4 mmol, 0.132 g) and cat-3 (0.0002 mmol, 0.12 mg) in screwed vials at room conditions. The reactions are monitored with thin layer chromatography (ethyl acetate-petroleum ether (EA-PE, 1:3)). Once the reaction is completed 2 mL of water is added and aqueous mixture is extracted with CHCl_3 (3 X 2 mL). After combining the organic extracts they are washed with 3 mL of water and dried over anhydrous Na_2SO_4 . The solvent is evaporated under vacuum. The pure biphenyls are isolated from preparative TLC (EA-PE / 1:3 as eluent system) and crystallized from diethyl ether-petroleum ether (1:2). The identity of the products was proved comparing with the physical and spectral characteristics of the original samples. ^1H and ^{13}C NMR data of the biphenyls are given in Table 1.

3. Results and Discussion

3.1. Preparation of the catalysts

The catalysts used in this study were prepared according to our reported work mentioned above [13]. The reactions of appropriate imidazolium salts with Ag_2O (or with AgNO_3 and Et_3N) in CH_2Cl_2 at room temperature provides Ag-metallated complexes. Treatment of these Ag-complexes with $\text{Pd}(\text{CH}_3\text{CN})_2\text{Cl}_2$ in CH_2Cl_2 provides catalysts 1-5 at room temperature in high yields. The NMR, IR and elemental analysis data of the compounds are matching with those in the literature. Structures of the catalysts are given in Figure 1.

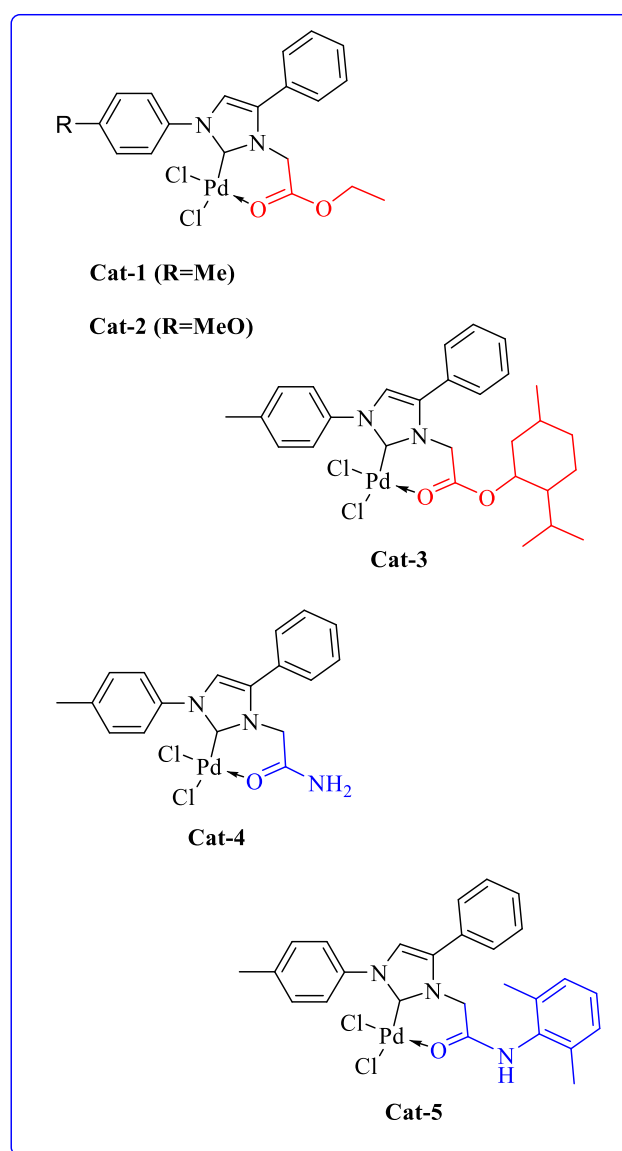


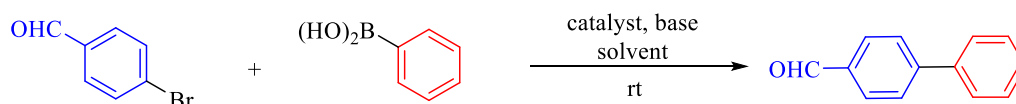
Figure 1. Structures of the catalysts (1-5) used in this study.

Table 1. The ^1H and ^{13}C NMR data of the biphenyls.

Biphenyl (3)	^1H NMR (400 MHz, CDCl_3) (δ)	^{13}C NMR (100 MHz, CDCl_3) (δ)
a	7.35 (t, $J = 7.6$ Hz, 2H), 7.44 (t, $J = 7.6$ Hz, 4H), 7.60 (d, $J = 6.8$ Hz, 4H)	127.0, 127.2, 128.8, 141.1
b	2.39 (s, 3H), 7.25-7.27 (m, 2H), 7.31 (t, $J = 7.2$ Hz, 1H), 7.43 (t, $J = 8.0$ Hz, 2H), 7.48 (d, $J = 8.0$ Hz, 2H), 7.58 (d, $J = 8.0$ Hz, 2H)	21.2, 126.8, 126.9, 128.8, 128.9, 129.4, 137.1, 138.2, 141.0
c	3.86 (s, 3H), 6.97 (d, $J = 9.2$ Hz, 2H), 7.31 (t, $J = 7.2$ Hz, 1H), 7.43 (t, $J = 8.0$ Hz, 2H), 7.51-7.55 (m, 4H)	55.2, 114.3, 126.7, 126.8, 128.1, 128.6, 133.9, 140.8, 159.1
d	7.43-7.52 (m, 3H), 7.65 (d, $J = 9.6$ Hz, 2H), 7.74 (d, $J = 8.0$ Hz, 2H), 7.94 (d, $J = 8.0$ Hz, 2H), 10.05 (s, 1H)	127.43, 127.8, 128.4, 129.0, 130.2, 135.1, 139.8, 147.3, 191.9
e	7.39 (t, $J = 7.2$ Hz, 1H), 7.46 (t, $J = 7.2$ Hz, 2H), 7.60-7.64 (m, 3H), 7.85 (dd, $J = 9.6$; 1.6 Hz, 2H), 8.09 (m, 1H), 10.08 (s, 1H)	127.1, 128.1, 128.3, 128.6, 129.0, 129.4, 133.2, 136.8, 139.8, 142.0, 192.4.
f	2.43 (s, 3H), 7.22-7.25 (m, 1H), 7.36 (t, $J = 8.0$ Hz, 1H), 7.44-7.46 (m, 2H), 7.72-7.75 (m, 2H), 7.92-7.94 (m, 2H), 10.06 (s, 1H)	23.6, 126.6, 129.7, 130.2, 131.2, 131.5, 132.5, 137.2, 140.8, 141.9, 149.4, 194.2
g	3.86 (s, 3H), 7.03 (t, $J = 5.8$ Hz, 2H), 7.59 (t, $J = 5.8$ Hz, 2H), 7.70 (d, $J = 8.0$ Hz, 2H), 7.92 (d, $J = 8.0$ Hz, 2H), 10.04 (s, 1H)	55.3, 114.4, 127.1, 128.6, 130.2, 132.1, 134.5, 146.9, 160.2, 192.0
h	7.79 (d, $J = 8.2$ Hz, 4H), 8.01 (d, $J = 8.2$ Hz, 4H), 10.08 (s, 2H).	127.9, 130.3, 136.0, 145.4, 191.8
i	7.44-7.46 (m, 2H), 7.55-7.57 (m, 2H), 7.72-7.74 (m, 2H), 7.96-7.98 (m, 2H), 10.05 (s, 1H)	127.5, 128.7, 129.1, 130.5, 134.6, 135.5, 138.2, 146.0, 191.7.
j	7.50 (d, $J = 8.0$ Hz, 2H), 7.61 (d, $J = 8.0$ Hz, 2H), 7.72 (d, $J = 8.0$ Hz, 2H), 7.96 (d, $J = 8.0$ Hz, 2H), 10.06 (s, 1H).	122.9, 127.6, 128.9, 130.3, 132.2, 135.5, 138.7, 145.7, 192.0.
k	3.84 (s, 3H), 2.36 (s, 3H), 6.93-6.97 (m, 2H), 7.23 (d, $J = 6.8$ Hz, 2H), 7.44 (d, $J = 8.0$ Hz, 2H), 7.47-7.50 (m, 2H)	21.0, 55.7, 115.2, 126.6, 128.0, 129.4, 130.5, 130.9, 138.1, 159.0.
l	3.85 (s, 6H), 6.97 (d, $J = 7.2$ Hz, 4H), 7.49 (d, $J = 7.6$ Hz, 4H)	55.7, 114.2, 128.8, 133.5, 158.9

3.2. Optimisation of the Suzuki-Miyaura reaction conditions

The optimisation studies started with determination of the best catalyst in the series Cat-1-5 where 4-bromobenzaldehyde and phenylboronic acid were stirred in screw cap vials in dioxane with Cs_2CO_3 and 1 mol % catalyst loading at room conditions (Table 2,



Scheme 1. Suzuki-Miyaura reaction between 4-bromobenzaldehyde and phenylboronic acid.

The reactions were performed with Cs_2CO_3 , K_2CO_3 , Na_2CO_3 , NaHCO_3 and NaOAc as a base and 1 mol % cat-3. There was no conversion with K_2CO_3 , for the

entries 1-5, Scheme 1). The reactions were monitored by TLC. According to TLC images, the initial conversion rates of Cat-2 and Cat-3 were almost the same but at the end Cat-3 was superior to all others. The other catalysts provided nearly the same yields. Thereby the Cat-3 was selected as lead catalyst and the optimisation studies went on by searching for the best base in dioxane.

reactions performed with Cs_2CO_3 , Na_2CO_3 , NaHCO_3 and NaOAc the isolated yields were 44, 16, 17 and 22 % respectively (Table 2, entries 6-10).

Table 2. Optimisation studies of the Suzuki-Miyaura coupling between 4-bromobenzaldehyde and phenylboronic acid.

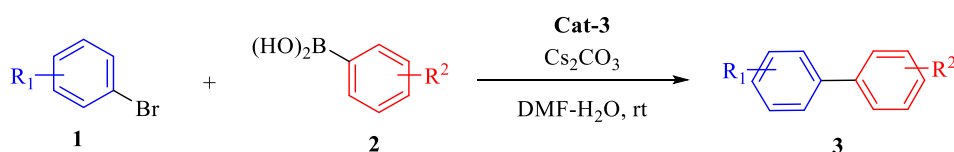
Entry	Cat	Cat (mol %)	Base	Solvent	React Time (h)	Yield ¹ (%)
1	1	1	Cs ₂ CO ₃	1,4-Dioxane	24	33
2	2	1	Cs ₂ CO ₃	1,4-Dioxane	24	35
3	3	1	Cs ₂ CO ₃	1,4-Dioxane	24	45 ⁵
4	4	1	Cs ₂ CO ₃	1,4-Dioxane	24	34
5	5	1	Cs ₂ CO ₃	1,4-Dioxane	24	35
6	3	1	Cs ₂ CO ₃	1,4-Dioxane	24	44 ⁵
7	3	1	Na ₂ CO ₃	1,4-Dioxane	24	16
8	3	1	K ₂ CO ₃	1,4-Dioxane	24	nr ²
9	3	1	NaHCO ₃ ³	1,4-Dioxane	24	17
10	3	1	NaOAc ³	1,4-Dioxane	24	22
11	3	1	Cs ₂ CO ₃	1,4-Dioxane	24	47 ⁵
12	3	1	Cs ₂ CO ₃	Formamide	24	nr
13	3	1	Cs ₂ CO ₃	DMF-H ₂ O ⁴	5 min	95 ⁶
14	3	1	Cs ₂ CO ₃	DMF	2.5	94
15	3	1	Cs ₂ CO ₃	DMAc	24	16
16	3	1	Cs ₂ CO ₃	NMP	24	19
17	3	1	Cs ₂ CO ₃	H ₂ O	24	90
18	3	0.1	Cs ₂ CO ₃	DMF-H ₂ O	5 min	96 ⁶
19	3	0.01	Cs ₂ CO ₃	DMF-H ₂ O	2	97 ⁶
20	3	0.001	Cs ₂ CO ₃	DMF-H ₂ O	48	18
21	3	0.0001	Cs ₂ CO ₃	DMF-H ₂ O	48	10

¹ Isolated yields. ² No reaction. ³ 4 eqs of base were used. ⁴ The ratio of the solvents is 1:1 (v/v). ⁵ The isolated yields from three different experiments. ⁶ The reactions occur with quantitative conversion, the yields are isolated yields. (Abbreviations: DMF: *N,N*-Dimethylformamide, DMAc: *N,N*-Dimethylacetamide, NMP: *N*-Methyl-2-pyrrolidone)

Due to its higher performance, Cs₂CO₃ was used in the experiments to investigate the best solvent and the reactions were performed with 1 mol % catalyst loading in seven different solvents.

There was no conversion in formamide. The reaction in DMF-H₂O (1:1) occurred very fast (the reaction finished within 5 minutes). The reactions in DMF and H₂O also occurred with pretty good results in 2.5 and

24 hours respectively (Table 2, entries 11-17). After determination of the lead catalyst, solvent and the base, concentration studies were performed with different mol % concentrations (0.1, 0.01, 0.001 and 0.0001) of the catalyst. The isolated yields of the reactions were 96, 97, 18 and 10 % and the TONs are 0.96x10³, 0.97x10⁴, 1.8x10⁴ and 10⁵ respectively (Table 2, entries 18-21).

**Scheme 2.** Suzuki-Miyaura cross-coupling reaction of aryl bromides with phenylboronic acids catalysed with Cat-3.

After all, the reactions of substrate scope were carried on in DMF-H₂O (1:1) with Cs₂CO₃ and 0.1% mole of Cat-3 (Scheme 2). The reaction of bromobenzene, 4-bromotoluene, 4-bromoanisole, 4-bromobenzaldehyde with phenylboronic acid occurred very fast so that it was not possible to observe any substituent effect of aryl bromides. Only the reaction with 3-bromobenzaldehyde and phenylboronic acid was a little bit slower compared to the others. It might be from the meta substitution of formyl group (Table

3, entries 1-5). Then 4-bromobenzaldehyde was chosen as aryl bromide and the reactions performed with different arylboronic acids. All reactions occurred with quantitative conversions and excellent isolated yields (Table 3, entries 6-10). The reaction was also run with different matching. 4-Bromotoluene and 4-bromoanisole were treated with 4-methoxyphenylboronic acid and the corresponding biphenyls obtained with pretty good yields (Table 3, entries 11-12)

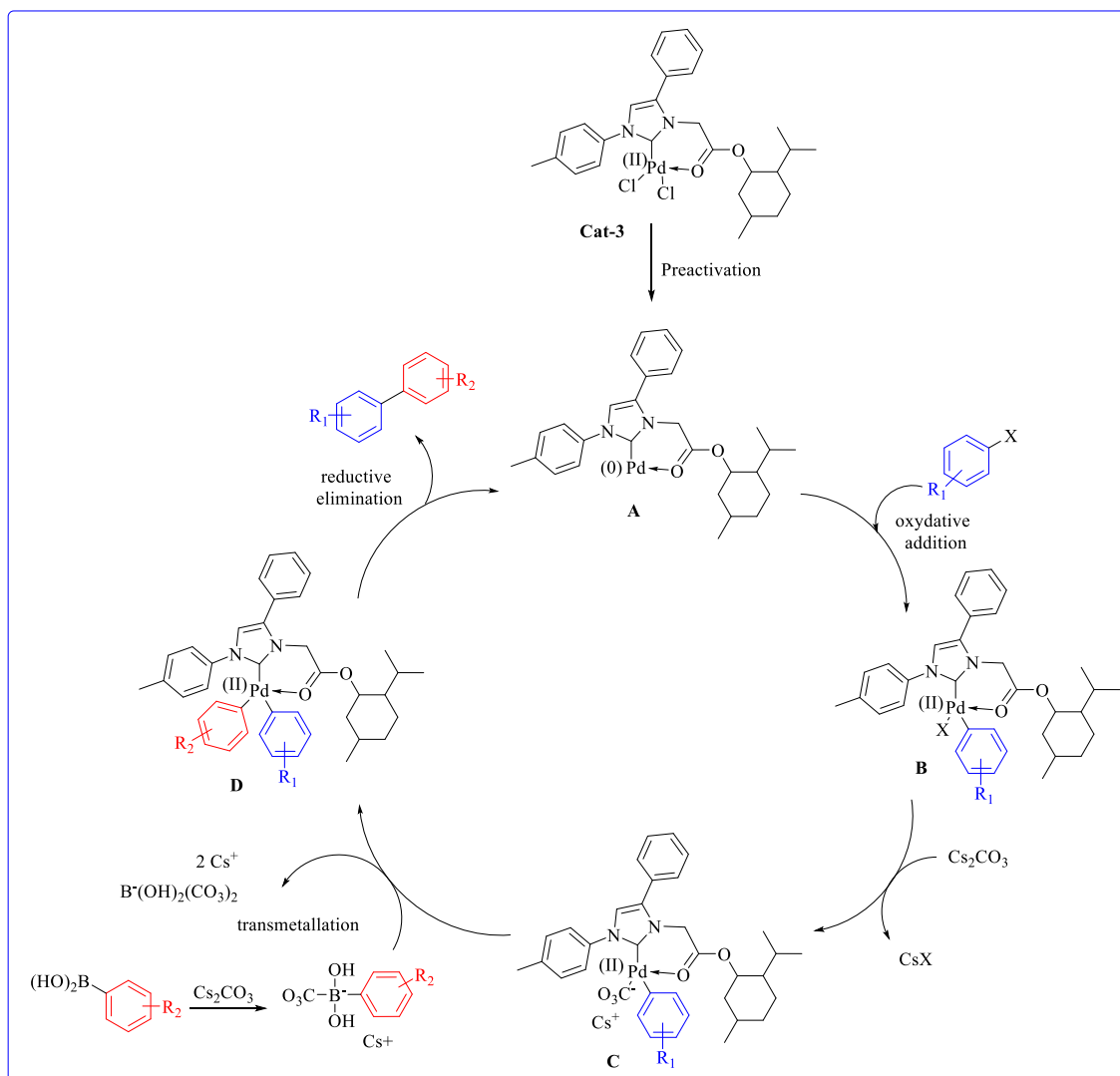
Table 3. Substrate scope of the Suzuki-Miyaura cross-coupling reaction catalysed with Cat-3.

Biphenyl (3)	R ₁	R ₂	React. Time (min)	Yield ¹ (%)	Mp. (°C)	Lit. Mp. (°C)	Ref.
a	H	H	5	98	69-70	69-70	[12]
b	4-Me	H	5	98	40-41	41-42	[11]
c	4-MeO	H	5	97	86-87	85-86	[12]
d	4-CHO	H	5	98	61-62	59-60	[12]
e	3-CHO	H	30	95	53-54	53-54	[12]
f	4-CHO	3-Me	10	96	56-57	57-58	[12]
g	4-CHO	4-MeO	10	98	103-104	103-104	[12]
h	4-CHO	4-CHO	30	97	147-148	148-150	[12]
i	4-CHO	4-Cl	10	98	115-116	114-115	[12]
j	4-CHO	4-Br	10	96	142-143	135-140	[14]
k	4- Me	4-MeO	10	95	110-112	111-112	[15]
l	4- MeO	4-MeO	10	95	177-178	178-180	[15]

¹Isolated yields from quantitative conversions. General conditions of the reaction: 1 (0.2 mmol) and 2 (0.3 mmol) were stirred in DMF:H₂O (1:1, v/v, 0.6 mL) with Cs₂CO₃ (0.4 mmol) and Cat-3 (0.1 % mmol) in screwed vials at room temperatures.

With the courage from the results of aryl bromides the reactions were tried with aryl chlorides which are known to be less prone to this reaction. For that purpose 4-methoxyphenylboronic acid was chosen as arylboronic acid and a series of reactions were run with 4-chlorotoluene, 4-chloroanisole, 4-chlorobenzaldehyde, 4-chlorobenzonitrile and chlorobenzene in the same conditions. Unfortunately the desired biphenyls could not be obtained instead only self-coupling product of the 4-methoxyphenylboronic acid was observed. Increasing the catalyst amount and the reaction temperature did not change the result.

The mechanism of the Suzuki-Miyaura coupling is a well-known mechanism which includes palladium (0) and palladium (II) species. The probable mechanism for Suzuki-Miyaura reaction catalysed with Cat-3 is depicted in Scheme 3. When palladium (II) complexes are used, the mechanism starts with preactivation step to get palladium (0) complex A and goes on by the oxidative addition step to form organopalladium species B. The reaction of base with organopalladium species B gives intermediate C. Then the transmetalation step occurs and another organopalladium species D forms. After the reductive elimination step the desired product 3 and the starting palladium (0) compound A are emerged.

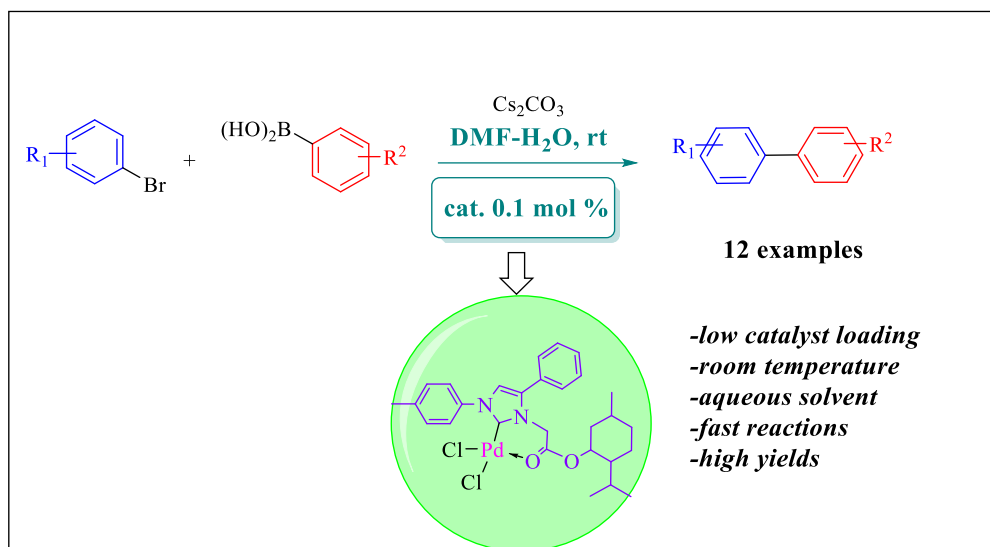


Scheme 3. Probable mechanism for Suzuki-Miyaura reaction catalysed with Cat-3.

4. Conclusion

The catalysts Cat-1-5 were screened in Suzuki-Miyaura cross-coupling reaction for the first time. The reactions occurred very fast with excellent yields in DMF-H₂O with Cs₂CO₃ and 0.1% mole of catalyst at

room temperature (Scheme 4). With these promising results it is reasonably foreseeable that these catalysts could be applied successfully to some other classic cross-coupling reactions such as Sonogashira, Stille and Buchwald-Hartwig. Relevant studies are in progress.



Scheme 4. Suzuki-Miyaura reaction catalysed with Cat-3.

Acknowledgment

The author would like to acknowledge Prof. Dr. Necdet COŞKUN for his technical and editorial assistance.

Conflicts of interest

The author states that she did not have conflict of interests.

References

- [1] Blakemore D.C., Suzuki-Miyaura Coupling. In: Blakemore D.C., Doyle P.M., Fobian Y.M., (Eds). *Synthetic Methods in Drug Discovery Volume 1*. Cambridge: RSC, (2016); 1-69.
- [2] Koshvandi T. K. A., Heravi M. M., Momeni T., Current Applications of Suzuki-Miyaura Coupling Reaction in The Total Synthesis of Natural Products: An update, *Appl. Organomet. Chem.*, 32(3) (2018) 1–59.
- [3] Dhangar G., Serrano J. L., Schulzke C., Gunturu K. C., Kapdi A. R., Palladacycle-Catalyzed Triple Suzuki Coupling Strategy for the Synthesis of Anthracene-Based OLED Emitters, *ACS Omega*, 2(7) (2017) 3144–3156.
- [4] García-López J. A., Greaney M. F., Synthesis of biaryls using aryne intermediates, *Chem. Soc. Rev.*, 45(24) (2016) 6766–6798.
- [5] Beletskaya I. P., Alonso F., Tyurin V., The Suzuki-Miyaura reaction after the Nobel prize, *Coord. Chem. Rev.*, 385(2019) 137–173.
- [6] Hooshmand S. E., Heidari B., Sedghi R., Varma R. S., Recent advances in the Suzuki-Miyaura cross-coupling reaction using efficient catalysts in eco-friendly media, *Green Chem.*, 21(3) (2019) 381–405.
- [7] Froese R. D. J., Lombardi C., Pompeo M., Rucker R. P., Organ M. G., Designing Pd-N-Heterocyclic Carbene Complexes for High Reactivity and Selectivity for Cross-Coupling Applications, *Acc. Chem. Res.*, 50(9) (2017) 2244–2253.
- [8] Charra V., de Frémont P., Braunstein P., Multidentate N-heterocyclic carbene complexes of the 3d metals: Synthesis, structure, reactivity and catalysis, *Coord. Chem. Rev.*, 341 (2017) 53–176.
- [9] Korch K. M., Watson D. A., Cross-Coupling of Heteroatomic Electrophiles, *Chem. Rev.*, 119(13) (2019) 8192–8228.
- [10] Peris E., Smart N-Heterocyclic Carbene Ligands in Catalysis, *Chem. Rev.*, 118(19) (2018) 9988–10031.
- [11] Coşkun N., Çetin M., Thermal rearrangements of tetrahydroimidazo[1,5-b]isoxazole-2,3-dicarboxylates. Synthesis of 3H-imidazol-1-ium ylides and their silver derivatives, *Tetrahedron*, 66(11) (2010) 2053–2060.
- [12] Syntheses of metal heterocyclic carbene enolates as coupling reactions catalysts. Available at: <https://patents.google.com/patent/WO2017099693A1/it>.
- [13] Çetin Korukçu M., Coşkun N., Synthesis and catalytic activities of 1-alkoxycarbonyl- and 1-carbamoylmethyl-5-phenyl-3-aryl-3H-imidazol-1-yliden-Pd(II) complexes, *J. Organomet. Chem.*, 832(2017) 47–56.

- [14] Simoni D., Giannini G., Roberti M., Rondanin R., Baruchello R., Rossi M., Grisolia G., Invidiata F. P., Aiello S., Marino S., Cavallini S., Siniscalchi A., Gebbia N., Crosta L., Grimaudo S., Abbadessa V., Cristina A. D., Tolomeo M., Studies on the apoptotic activity of natural and synthetic retinoids: Discovery of a new class of synthetic terphenyls that potently support cell growth and inhibit apoptosis in neuronal and HL-60 cells, *J. Med. Chem.*, 48(13) (2005) 4293–4299.
- [15] Du Z., Zhou W., Wang F., Wang J.X., In situ generation of palladium nanoparticles: Ligand-free palladium catalyzed ultrafast Suzuki-Miyaura cross-coupling reaction in aqueous phase at room temperature, *Tetrahedron*, 67(26) (2011) 4914–4918.



Electron affinities for highly charged groups 15 and 16 anions

Savaş KAYA^{1,*} , Robson Fernandes De FARIAS²

¹ Sivas Cumhuriyet University, Health Services Vocational School, Department of Pharmacy, 58140, Sivas/TURKEY

² Universidade Federal do Rio Grande do Norte, Cx. Postal 1664, 59078-970, Natal, RN, BRAZIL

Abstract

Electron affinity, electronegativity, and electrophilicity are chemical concepts that have been related to electron accepting power of chemical species. In the literature, although there are many theoretical approaches proposed to calculate the electronegativity and electrophilicity of atoms, ions, and molecules, just a few approaches suggested are related to the prediction of sequential electron affinities of atoms. In the present work, the electron affinities for highly charged groups 15 and 16 anions are calculated by the semi-empirical (PM6) method. The obtained values are compared with those from literature. So far, the authors are concerned, the third and fourth electron affinities for S, P, As and Sb are calculated for the first time. It is well-known that in the calculation of the lattice energy of any inorganic ionic crystal via Born-Haber thermochemical cycle, many parameters regarding any crystal the atoms forming the crystal are considered. One of these parameters is electron affinity. It should be noted that our electron affinity values calculated are in good agreement with both experimental data, other theoretical approaches, and the data obtained in the light of the Born- Haber cycle.

Article info

History:

Received: 22.05.2020

Accepted: 07.02.2021

Keywords:

Electron affinity, Born-Haber thermochemical cycle, groups 15 and 16 anions, PM6 Method.

1. Introduction

As is known, atoms are the simplest chemical systems; electron affinity of an atom A is equal to the difference of ground state total energies (E_{tot}) of A and its negative ion A⁻, and can be given as: [1]. In the Conceptual Density Functional Theory [2], chemical concepts such as hardness, electronegativity, chemical potential, and softness have been associated with ionization energy and electron affinity values of chemical species via the following equations. For that reason, the methodologies proposed for the accurate prediction of electron affinities of atoms, ions, and molecules are quite noteworthy for theoretical chemists.

$$\chi = -\mu = (IE + EA) / 2 \quad (1)$$

$$\eta = IE - EA \quad (2)$$

Electron affinity is a quantity that can be physically observed and can be experimentally determined although the same is not the case for electronegativity and electrophilicity. Atomic electronegativities have been defined by chemists and physicists from different perspectives. For instance, some researchers noted the electron affinity as the energy required to remove an electron from the negative ion of an A atom, some authors reported this quantity as the energy released

when atom A receives an electron. It can be said that both definitions are widely used in the literature [3].

Computational chemistry tools are widely used in the prediction of atomic and molecular properties like electron affinity, ionization energy, proton affinity vs. Pople and co-workers [4] investigated the performances of B-LYP functional with the help of basis sets such as 6-31G(d), 6-311G (3df,2p) in the prediction of the mentioned properties. Proft and Geerlings [5] calculated electron affinity, ionization energy, electronegativity, and hardness values of some atoms in the light of Dunning's correlation consistent basis sets and analyzed the performances of B3LYP and B3PW91 exchange-correlation functionals.

Chemical hardness is reported as the resistance against electron cloud polarization of chemical species (atoms, ions, and molecules) [6]. This concept has been widely considered in the understanding of the logic of many chemical events. According to Hard and Soft acid-base principle [7] that is an approach introduced based on the chemical hardness concept, "Hard acids prefer to coordinate to hard bases and soft acids prefer to coordinate to soft bases." Another principle about the concept is the Maximum Hardness Principle [8] states that soft molecules are more reactive compared to hard ones. HSAB Principle has been successful in explaining the geochemistry in nature of the elements.

*Corresponding author. e-mail address: savaskaya@cumhuriyet.edu.tr
<http://dergipark.gov.tr/csj> ©2021 Faculty of Science, Sivas Cumhuriyet University

For instance, hard acids like Fe³⁺ and Al³⁺ are found as oxides and fluorides in nature while soft acids such as Hg²⁺ and Cd²⁺ prefer to bond to the sulphide ion (S²⁻). Some double-charged negative ions like N²⁻, S²⁻, Se²⁻ and O²⁻ exist in the structure of inorganic ionic solids. In the light of this information, Baughan [9] calculated electron affinities of some negative ions situated in the structure of crystals. Considering Electronegativity Equalization Process in a molecule, Orsky and Whitehead [10] defined the chemical hardness for acid and a base as:

$$\eta_A = 1/4(IE_{A^+} - EA_{A^0})$$

$$\eta_B = 1/4(IE_{B^0} - EA_{B^-}) \quad (3)$$

It is apparent from the equation given above that to calculate the chemical hardness of a base via the Orsky-Whitehead definition, we need to sequential electron affinity values of atoms or ions. For that reason, the methodologies developed for the calculation of electron affinities of negative ions are quite remarkable for chemists and physicists.

Laszlo von Szentpaly known with his studies regarding chemical reactivity of chemical species imparted a useful equation to science to calculate the second electron affinities of atoms [11]. The equation is given as follows.

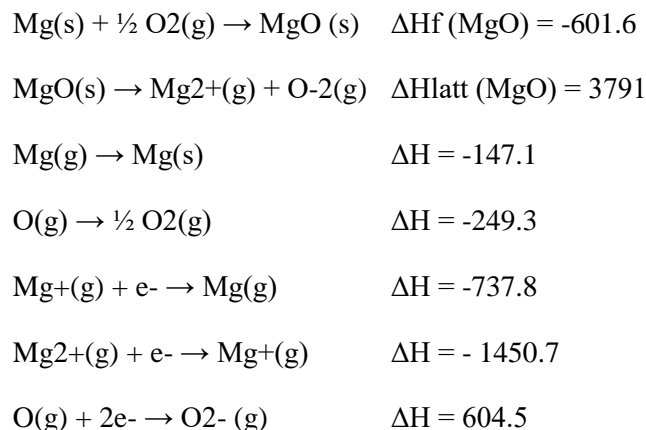
$$EA_{2,cal} = EA_1 - (7/6)\eta^0 \quad (4)$$

Where in, IE₂, IE₁, and η^0 are second electron affinity, first electron affinity, and chemical hardness value of the neutral form of chemical species. It should be noted that this methodology proposed by Szentpaly is very useful in the calculation of second electron affinities.

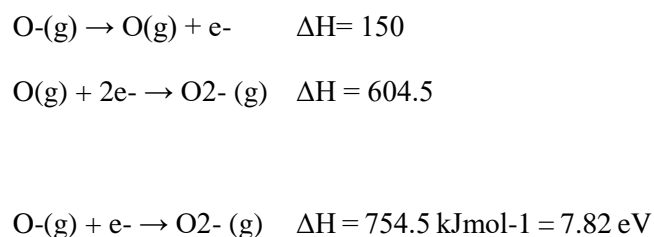
2. Materials and Methods

The employed reference data were taken from the literature [12,13]. All computations were performed using Spartan [14]. Thermochemical calculations were performed by semi-empirical (PM6) method. The SE-PM6 approach was chosen to take into account its minor computation time consuming and its reliability for inorganic species, as verified for PtF₆ [15]. To verify the reliability of the employed theoretical approach, besides the anions (P-3, S-3), etc., investigated here for the first time, the electron affinities for the neutral atoms (first electron affinity) and the respective monoanionic (second electron affinities) were also calculated and the results compared with reference values.

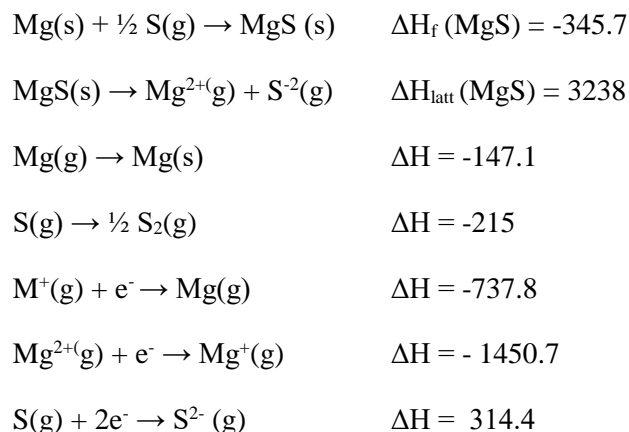
Also, in order to verify such reliability, the second electron affinity for oxygen was calculated through a Born-Haber cycle:



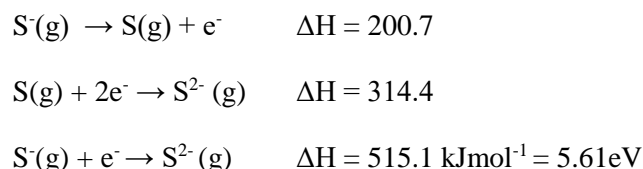
With the help of the obtained result above, the following statements can be written.



The same procedure was repeated for sulphur



With the help of the obtained result above for sulphur, the following statements can be written.



3. Results and Discussion

The obtained results are summarized in Table 1. When available, reference values are provided. As can be verified by Table 1 data, the values to the electron affinity for O⁻ (that is, the second electron affinity for oxygen, forming O²⁻) obtained by the Born-Haber cycle and the SE-PM6 method are in exceptional agreement, testifying the reliability of the chose theoretical approach. For sulphur, the agreement between the calculated (SE-PM6) and Born-Haber cycle values are not so good. However, it is necessary to remember that the SE calculated value is for a modelled gas phase specie, whereas the Born-Haber cycle employs values for condensed phase species. Furthermore, since sulphur is more polarizable than oxygen, the superimposition of orbitals (condensed phase compounds) must be taken into account.

In Table 2 are summarized the electron affinity values calculated in the presented work and previous ones, from literature. Guo and Whitehead [16] have calculated second electron affinities for atoms from helium to krypton using the self-interaction corrected generalized exchange local-spin-density functional theory with the correlation energy functional. The dependence of the second electron affinities of the elements O, S, and Se on the Watson sphere radius was considered. As can be seen in Table 2, there is a really good agreement between those values calculated for the second electron affinity for oxygen, especially taking into account the significant differences between the employed theoretical approaches (present work and Ref. 4). Nevertheless, we think that the value calculated here is most reliable, taking into account, for example, the exceptional agreement between our value and those obtained through a Born-Haber cycle for the second electron affinity to oxygen.

On the other hand, the agreement observed for oxygen is not verified for sulphur and selenium. Indeed, as can be verified, the agreement between the values calculated in the previous work and those obtained by Guo and Whitehead decreases down the group, that is, for the heavier and more polarizable elements (S and Se) the agreement is poor, whereas is good for the lighter (and less polarizable) element (oxygen). Based on the results obtained for oxygen, we believe that our values are more reliable. As can be verified, the second electron affinity decreases down the group: 7.81, 4.20, and 3.87 eV for O, S, and Se, respectively. Such results are compatible with the fact that the heavier and more polarizable elements require a minor amount of energy to “accept” a second “extra” electron in their electro sphere.

Table 1. Electron affinities (EA) for several species as calculated by SE-PM6 method.

Species	EA/eV _{ref.value}	EA/eV _{calc.}
O	-1.46 ^a	-0.88
O ⁻	7.82 ^b	7.81
S	-2.08 ^a	-2.67
S ⁻	5.61 ^b	4.20
S ⁻²	–	17.25
S ⁻³	–	49.74
Se	-2.02 ^a	-2.21
Se ⁻	–	3.87
Te	-1.97 ^a	-1.55/-1.67 ^c
Te ⁻	–	4.97/6.31 ^c
N	(not stable) ^a	0.23
N ⁻	–	9.81
N ⁻²	–	19.39
P	-0.75 ^a	-0.14
P ⁻	–	7.14
P ⁻²	–	14.41
P ⁻³	–	205.58
As	-0.80 ^a	-0.40
As ⁻	–	8.85
As ⁻²	–	17.28
As ⁻³	–	113.07
Sb	-1.05 ^a	1.34
Sb ⁻	–	10.30
Sb ⁻²	–	19.20
Sb ⁻³	–	190.59

^a CRC Handbook, 2016; ^bThrough a Born-Haber cycle; Calc.= through SE-PM6 method; ^cWith a relativistic correction (multiplied by γ).

Table 2. Electron affinities (EA) for several species as calculated by SE-PM6 method (present work) and those previously obtained by another theoretical approach.

Species	EA/eV _{calc.}	EA/eV _{Ref. 5}
O	-0.88	
O ⁻	7.81	8.22/8.89 ^a
S	-2.67	
S ⁻	4.20	5.83/6.49 ^a
S ⁻²	17.25	
S ⁻³	49.74	
Se	2.21	
Se ⁻	3.87	5.53/6.19 ^a
Te	-1.55/-1.67 ^c	
Te ⁻	4.97/6.31 ^c	
N	0.23	
N ⁻	8.81	8.68/9.51 ^a
N ⁻²	19.39	
P		
P ⁻	7.14	6.56/7.37 ^a
P ⁻²	14.41	
P ⁻³	205.58	
As	—	
As ⁻	8.58	6.35/7.14 ^a
As ⁻²	17.28	
As ⁻³	113.07	
Sb	1.34	
Sb ⁻	10.30	
Sb ⁻²	19.20	
Sb ⁻³	190.59	—

Calc.= present work; ^aWith and without VWN (Vosko, Wilk and Nusair) correlation energy functional.

In Figure 1, the calculated second electron affinities for oxygen, sulphur, and selenium are plotted as a function of their polarizabilities: 0.802, 2.90, and 3.77 for O, S, and Se, respectively. The obtained curve ($r= 0.9773$) provides the equation:

$$EA = -1.40p + 8.78 \quad (5)$$

where EA is the second electron affinity and p is the polarizability (in units of 10^{-24} cm^3).

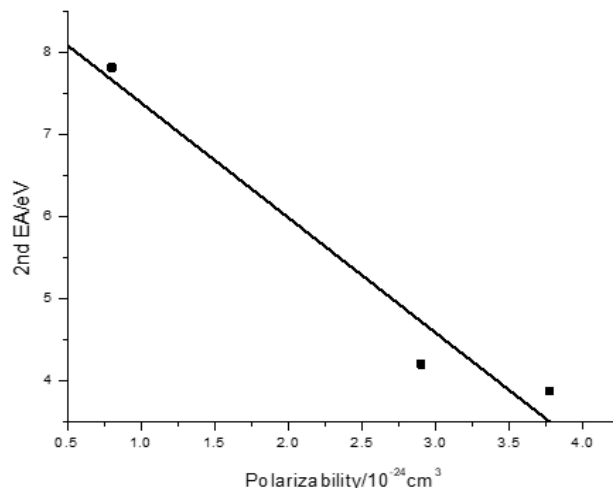


Figure 1. Second electron affinity (eV) as a function of the polarizability (10^{-24} cm^3) for O, S, and Se.

To tellurium ($Z = 52$) it is necessary to remember that relativistic contributions matter [17]. That is, the higher relativistic contraction/effects must be taken into account.

The relativistic and non-relativistic equations can be related by using $\gamma = 1/[1-(v^2/c^2)]$, where v is the velocity of the considered body (in our case, an electron). The velocity of the 1s electron is $\approx Z/137$, where Z is the atomic number. Hence, $\gamma = 1/[1-((Z/137)^2/c^2)]^{1/2}$. For tellurium $\gamma= 1.08$ and to polonium, $\gamma= 1.27$. The relativistic corrected values are also shown in Tables 1 and 2. About the correlation between the second electron affinity and the polarizability, an important observation must be done: the polarizability reference values [1] for O, S, and Se have an estimated accuracy of 2%, whereas for tellurium (5.5) such estimated accuracy is high as 25%, making a possible correlation unreliable.

As can be verified, the second electrons affinities to N and P calculated in the present work agree very well with those values calculated by Guo and Whitehead. As mentioned to oxygen, the verified agreement is really good, especially taking into account the significant differences between the employed theoretical approaches. As verified for group 16 anions, the agreement between SE-PM6 results and Whitehead data decreases as the polarizability increases down the group.

In Figure 2, the calculated second electron affinities for phosphorus, arsenic, and antimony are plotted as a function of their polarizabilities: 3.63, 4.32, and 6.6 for P, As and Sb, respectively [1]. The obtained curve ($r= 0.9692$) provides the equation:

$$EA = 0.987p + 3.889 \quad (6)$$

where EA is the second electron affinity and p is the polarizability (in units of 10^{-24} cm^3).

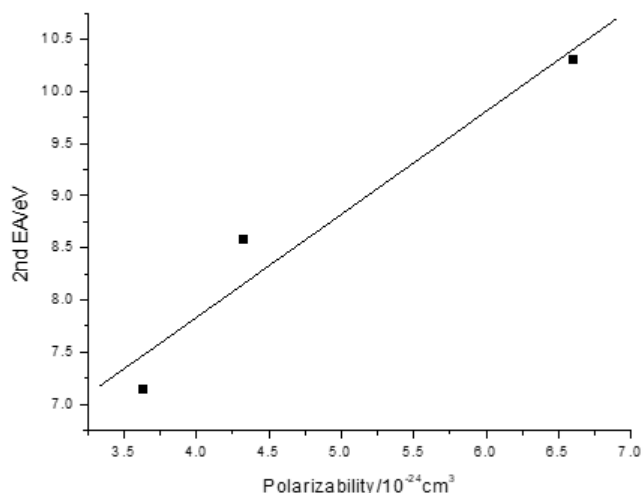


Figure 2. Second electron affinity (eV) as a function of the polarizability (10^{-24} cm^3) for P, As, and Sb.

Nitrogen (the lightest and harder, less polarizable element of the group) deviate from linearity, as predictable. Chattaraj and Duley [18] also investigated the electron affinities for a series of anions, including some studied in the present work, as N^- and O^- . All the calculations were done at the HF/6-311+G(d), B3LYP/6-311+G(d), and MP2/6-311+G(d) levels of theory. However, we have chosen do not to use such values for comparison since they are (a series of sometimes very different values for the same specie) highly dependent on the chose theoretical approach. For example, to gas phase N^- , they had obtained values from -3.28 eV (B3LYP/6-11+G(d) level of theory) to -6.80 eV (Hartree-Fock).

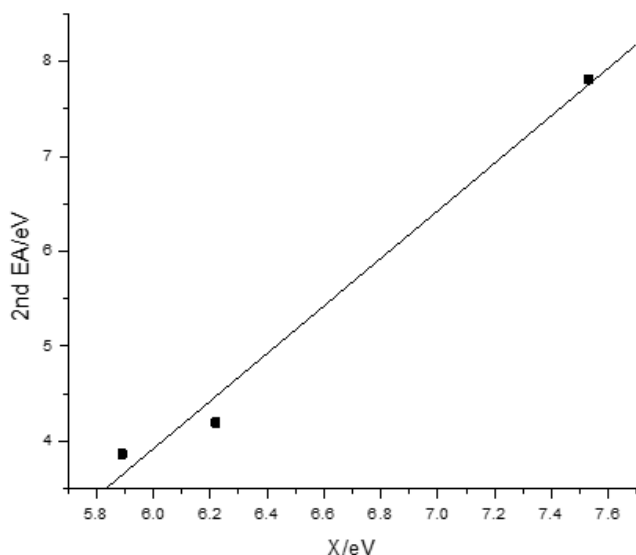


Figure 3. Calculated second electron affinity (eV) as a function of the experimental Mulliken electronegativities (eV) for O, S, and Se.

Hence, although some of their calculated values agree well with those obtained in the present work (e.g. 7.24 eV for O^- , by B3LYP method), we do not consider such values as really conclusive and useful (reliable) for comparison. If the calculated electron affinity values for O^- , S^- and Se^- (that is, the second electron affinities for O, S, and Se) are plotted as a function of the experimental values for Mulliken electronegativities [19,20] for those elements (7.53, 6.22 and 5.89, respectively), the curve shown in Figure 3 ($r= 0.9933$) is obtained. Providing the equation:

$$EA = 2.503\chi - 11.092 \quad (7)$$

where EA is the second electron affinity and χ is the Mulliken electronegativity (eV).

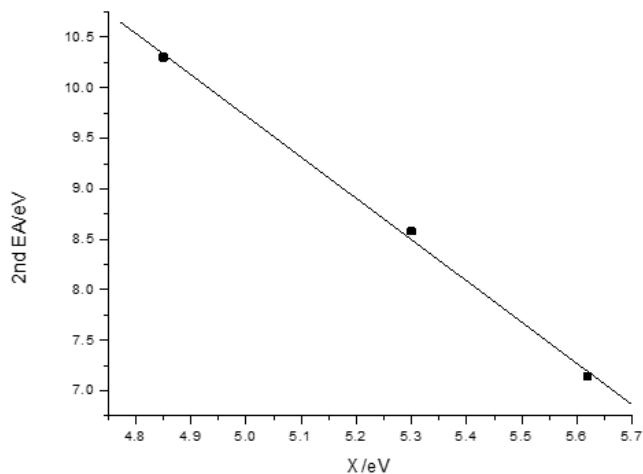


Figure 4. Calculated second electron affinity (eV) as a function of the experimental Mulliken electronegativities (eV) for P, As, and Sb.

If the calculated electron affinity values for P^- , As^- and Sb^- (that is, the second electron affinities for P, As and Sd) are plotted as a function of the experimental values for Mulliken electronegativities for those elements (5.62, 5.30 and 4.85, respectively), the curve shown in Figure 4 ($r= 0.9989$) is obtained. Providing the equation:

$$EA = -4.086\chi + 30.150 \quad (8)$$

where EA is the second electron affinity and χ is the Mulliken electronegativity (eV).

Of course, analogous relationships can be obtained employing the third and fourth electron affinities.

To S, S^- , S^{2-} , and S^{3-} , if the calculated SE-PM6 electron affinities are plotted as a function of the nuclear

effective charges (Z_{eff} , using Slater rules: 5.45, 5.10, 4.75 and 0.8, respectively), the curve shown in Figure 5 ($r = 0.9727$) is obtained, providing the equation:

$$EA = -10.43Z_{\text{eff}} + 59.11 \quad (9)$$

Of course, analogous curves and equations can be obtained to P, As and Sb.

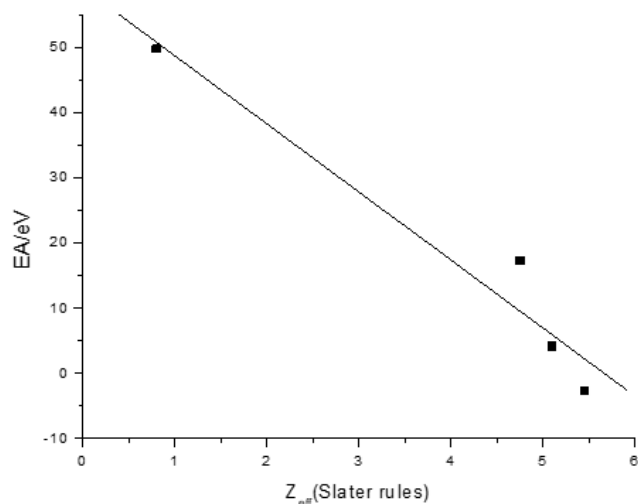


Figure 5. Calculated (SE-PM6) electron affinities for S, S⁻, S⁻², and S⁻³ as a function of nuclear effective charges (Slater rules).

Conflict of interest

The authors declare that they have no known competing financial interests or personal relationships that could have appeared to influence the work reported in this paper.

References

- [1] Manaa M. R., Determination of adiabatic ionization potentials and electron affinities of energetic molecules with the Gaussian-4 method, *Chem. Phys. Lett.*, 678 (2017) 102-106.
- [2] Islam N., Kaya S. (Eds), *Conceptual Density Functional Theory and Its Application in the Chemical Domain*, 1st ed. Apple Academic Press, (2018).
- [3] Kebarle P., Chowdhury S., Electron affinities and electron-transfer reactions, *Chem. Rev.*, 87(3) (1987) 513-534.
- [4] Gill P. M., Johnson B. G., Pople J. A., Frisch, M. J., The performance of the Becke—Lee—Yang—Parr (B—LYP) density functional theory with various basis sets, *Chem. Phys. Lett.*, 197(4-5) (1992) 499-505.
- [5] Proft F.D., Geerlings P., Calculation of ionization energies, electron affinities, electronegativities, and hardnesses using density functional methods, *J. Chem. Phys.*, 106(8) (1997) 3270-3279.
- [6] Kaya S., Kaya C., A new equation for calculation of chemical hardness of groups and molecules, *Mol. Phys.*, 113(11) (2015) 1311-1319.
- [7] Kokalj A., On the HSAB based estimate of charge transfer between adsorbates and metal surfaces, *Chem. Phys.*, 393 (2012) 1-12.
- [8] Kaya S., Kaya C., A simple method for the calculation of lattice energies of inorganic ionic crystals based on the chemical hardness, *Inorg. Chem.*, 54(17) (2015) 8207-8213.
- [9] Baughan E.C., The repulsion energies in ionic compounds. Part 2. —Lattice energies of some metallic nitrides., *Transactions of the Faraday Society*, 55 (1959) 2025-2029.
- [10] Orsky A.R., Whitehead M.A., Electronegativity in density functional theory: diatomic bond energies and hardness parameters, *Can. J. Chem.*, 65(8) (1987) 1970-1979.
- [11] Von Szentpaly L., Universal method to calculate the stability, electronegativity, and hardness of dianions, *J. Phys. Chem. A.*, 114(40) (2010) 10891-10896.
- [12] CRC Handbook of Chemistry and Physics, 96th ed., Taylor and Francis, Boca Raton, CRC Press, (2016).
- [13] Kaya C., Kaya S., Banerjee P., A novel lattice energy calculation technique for simple inorganic crystals, *Physica B: Condensed Matter*, 504 (2017) 127-32.
- [14] Wavefunction Inc. Irvine California, Available at <https://www.wavefun.com/spartan-latest-version>. Retrieved 2021.
- [15] Farias R.F., Computational gaseous phase formation enthalpy and electron affinity for platinum hexafluoride: it is gaseous PtF₆ diamagnetic due to a relativistic effect?, *Inorg. Chem.*, 55(23) (2016) 12126-12127.
- [16] Guo Y., Whitehead M. A., Calculation of the second electron affinities of atoms, *Can. J. Chem.*, 68(9) (1990) 1585-1589.
- [17] Leszczynski J., *Relativistic Methods for Chemists*, New York: Springer, (2010).

- [18] Chattaraj P.K., Duley S., Electron affinity, electronegativity, and electrophilicity of atoms and ions, *J. Chem. Eng. Data*, 55(5) (2010) 1882-1886.
- [19] Parr R.G., Pearson R.G., Absolute hardness: companion parameter to absolute electronegativity, *J. Am. Chem. Soc.*, 105 (26) (1983) 7512-7516.
- [20] Pearson R.G., Chemical Hardness, Weinheim: Wiley-VCH Verlag GmbH, (1997).

Computational study on the structural, electronic, molecular and thermochemical properties of hypothetical $[\text{Tp}(\text{CO})_2\text{Mo}\equiv\text{C-Ph}]_2^+$ and $[\text{L}(\text{CO})_2\text{Mo}\equiv\text{C-Ph}]^+$ carbyne complexes

Zinet ZAİM , Duran KARAKAŞ * 

Sivas Cumhuriyet University, Science Faculty, Chemistry Department, 58140 SİVAS, TURKEY

Abstract

The structural, electronic, molecular and thermochemical properties of hypothetical $[\text{Tp}(\text{CO})_2\text{Mo}\equiv\text{C-Ph}]_2^+$ (1) [Tp = hydridotris(pyrazolyl) borate] and $[\text{L}(\text{CO})_2\text{Mo}\equiv\text{C-Ph}]^+$ (2) [L=hydrido 2-phenoxybis(pyrazolyl) borate] carbyne complexes were investigated by quantum chemical calculations. The carbyne complexes were optimized at B3LYP/LANL2DZ/6-31G(d) level. Structural parameters, vibration spectra, electronic spectra and NMR spectra were computationally obtained. Environment geometry of the molybdenum atom was predicted to be distorted octahedral. Mulliken atomic charges, molecular electrostatic potential maps, molecular orbital energy diagrams and frontier orbital contour diagrams were calculated and interpreted to estimate the electronic properties of the complexes. In order to predict the molecular properties of complexes, some electronic structure descriptors were calculated and discussed. The thermal stability of the complexes was investigated. Thermochemical parameters of the complexes were found to increase with increasing temperature. Metal-carbyne bond dissociation energies of complex (1) and complex (2) were calculated as 955 and 912 K, respectively.

Article info

History:

Received: 16.11.2020

Accepted: 12.02.2021

Keywords:

Carbyne complex,
Computational
research,
Spectroscopic analysis,
Molecular properties,
Thermochemical
stability.

1. Introduction

$\text{L}_n\text{M}\equiv\text{C-R}$ type organometallic compounds are known as alkylidyne or carbyne complexes. The ligands in the C-R general formula (R = H, alkyl, aryl, SiMe_3 , NEt_2 , PMe_3 , SPh, Cl) are called alkylidyne or carbyne ligands [1] and L ligands are ancillary ligands. Such compounds are used in the synthesis of alkynes and nitriles and act as catalysts in organic reactions [2,3]. Carbyne complexes catalyze alkyne metathesis reactions and form new alkyne compounds. Ancillary ligands have important roles on the catalytic activities of the carbyne complexes and the steric and electronic properties of ancillary ligands are generally considered as important factors to improve the catalytic activity [4-7].

In carbyne complexes, the metal-carbon bond can be considered as a combination of a σ bond and two π bonds. As seen in Fig. 1, sp hybrid orbital on the carbon atom of the carbyne ligand contains a lone electron pair. This lone electron pair is transferred to a suitable orbital on the metal atom and an M-C σ bond is formed. In addition, carbyne carbon has two empty p orbitals. Electrons are transferred from metal to empty p orbitals

of the carbyne ligand and two π bonds are formed [8]. As understood from this description, the carbyne ligand is both a σ donor and π receptor. Schematic representation of overlapping orbitals in the formation of σ and π bonds in carbyne complexes is given in Figure 1.

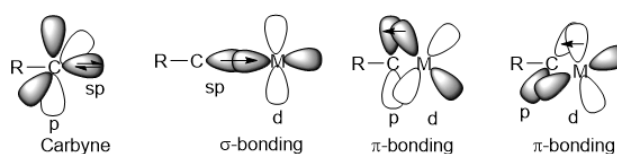


Figure 1. Orbital overlaps in the formation of σ and π bonds in carbyne complexes

Various methods have been used in the synthesis of carbyne complexes. One of them is the Fischer method. The first carbyne complex was synthesized by Fischer and Schubert in 1975 by this method [1]. In this method, when the carbene complex is reacted with Lewis acids of the type BX_3 (X = Cl, Br, I), Lewis acid first attacks the oxygen atom bound to the carbene carbon and the methoxy group is attached to the Lewis acid of the type BX_3 . For the first time, $[(\text{CO})_4\text{ClCr}\equiv\text{C-Ph}]$ carbyne complex was synthesized from the

*Corresponding author. e-mail address: dkarakas@cumhuriyet.edu.tr

reactions of carbene complexes with Lewis acids [9]. The structure of the complex was examined by X-ray crystallography. The other method used in synthesizing the carbyne complexes is the Mayr procedure [10]. In this method, the carbene complexes are reacted with oxalyl chloride in a solvent of dichloromethane at low temperatures to form a halide-containing carbyne intermediate. Carbyne complex is prepared by adding a strong multi-dental ligand on this intermediate at low temperatures. Stone and colleagues used the Mayr procedure to prepare $\text{Cp}(\text{CO})_2\text{M}\equiv\text{C-R/Ar}$ and $\text{Tp}(\text{CO})_2\text{W}\equiv\text{C-Tol}$ type carbyne complexes. Where Cp =cyclopentadienyl, Tp =hydridotris(pyrazolyl)borate and Tol =p-tolyl [9,11,12]. In addition, new Fischer type tungsten carbyne complexes such as $\text{L}(\text{CO})_2\text{W}\equiv\text{C-R/Ar}$ were synthesized by A. Sarkar at al. using the Mayr method [13]. Here L is a tridentate and -1 charged ligand. In this study, it was found that the synthesized complexes were thermally stable and did not decompose in long term storage at room temperature.

Although extensive studies have been conducted on other organometallic compounds such as metal carbonyls and carbene complexes, research on carbyne complexes is limited due to the thermal instability of the carbyne complexes. The development of quantum chemical calculation methods and advancement in computer technology made it easier to predict the structural, electronic and molecular characteristic of complexes. In this work, the structural, electronic, molecular and thermochemical properties of hypothetical $[\text{Tp}(\text{CO})_2\text{Mo}\equiv\text{C-Ph}]^{2+}$ (**1**) and $[\text{L}(\text{CO})_2\text{Mo}\equiv\text{C-Ph}]^+$ (**2**) alkylidyne complexes were investigated by quantum chemical calculations. Where Tp is hydrido tris(pyrazolyl)borate] and L is hydrido 2-phenoxy bis(pyrazolyl)borate. In order to determine the structure of hypothetical complexes, molecular structure parameters, IR, UV-VIS and NMR spectra were computed. Electronic properties were determined by calculating molecular orbital energy diagrams, molecular electrostatic potential maps and electronic charges of atoms. Various molecular structure identifying were calculated to estimate the molecular properties. Thermochemical parameters, total energy (E), enthalpy (H), heat capacity (C_v) and entropy (S) values of the complexes were calculated at 200, 298.15 and 400 K temperatures to predict the complex stability. Correlations were generated which allowed the calculation of thermochemical parameters of complexes at various temperatures.

2. Materials and Methods

Quantum chemical calculations were made on hypothetical $[\text{Tp}(\text{CO})_2\text{Mo}\equiv\text{C-Ph}]^{2+}$ and $[\text{L}(\text{CO})_2\text{Mo}\equiv\text{C-Ph}]^+$ carbyne complexes. GaussView 5.0.8 program [14] was used for drawing complex structures, preparation of account input files and visualization of the calculation results, Gaussian 09 AS64L-G09 RevD.01 program [15] for the calculations, and ChemDraw Professional 17.0 program for editing the visualized results and saving them as word files. Optimized structure calculations were performed with B3LYP hybrid functional based on density functional theory (DFT) method [16,17]. In the calculations, LANL2DZ/6-31G(d) mixed base set was used [18,19]. The central molybdenum atomic orbitals were represented by the LANL2DZ base set containing the internal potential, the remaining atomic orbitals in the complex were represented by the 6-31G(d) base set. The base set 6-31G(d) is the polarized base set that adds d functions to non-hydrogen atoms. Spin multiplicity of the complexes was taken as singlet and closed shell calculations were made. No negative frequency was calculated as a result of the optimization. This result indicates that the calculated structures are in the ground state.

For the structural analysis, some bond length, bond angles, IR spectrum, UV-VIS spectrum, NMR spectrum of the complexes were calculated. Molecular structural parameters and IR spectrum were obtained from gas phase optimizations. The electronic spectra of the carbyne complexes were calculated at the TD/B3LYP/LANL2DZ/6-31G(d) level and the electronic transitions of the bands in the spectra were investigated. $^1\text{H-NMR}$ and $^{13}\text{C-NMR}$ spectra were computed at GIAO/B3LYP/LANL2DZ/6-31G(d) levels and chemical shift values were found according to TMS standard. In order to predict the electronic properties of complexes, Mulliken charges of atoms, electrophilic and nucleophilic regions of complexes and contour diagrams of frontier orbitals were obtained. In order to predict the molecular properties of the complexes, HOMO and LUMO energies were taken from the molecular orbital energy diagrams and some molecular structure descriptors such as ionization energy (I), electron affinity (A), LUMO-HOMO energy gap (ΔE), hardness (η), softness (σ), Mulliken electronegativity (χ), chemical potential (CP), electrophilicity index (ω), static dipole moment (μ) and average linear polarizability (α) were calculated by using eq. (1)-(10) [19,20].

$$I = -E_{HOMO} \quad (1)$$

$$A = -E_{LUMO} \quad (2)$$

$$\Delta E = E_{LUMO} - E_{HOMO} \quad (3)$$

$$\eta = \frac{E_{LUMO} - E_{HOMO}}{2} \quad (4)$$

$$\sigma = \frac{I}{\eta} \quad (5)$$

$$\chi = -\frac{E_{HOMO} + E_{LUMO}}{2} \quad (6)$$

$$\mu_{cp} = -\chi \quad (7)$$

$$\omega = \frac{\mu_{cp}^2}{2\eta} \quad (8)$$

$$\mu = \sqrt{(\mu_x^2 + \mu_y^2 + \mu_z^2)} \quad (9)$$

$$\alpha = \frac{I}{3} (\alpha_{xx} + \alpha_{yy} + \alpha_{zz}) \quad (10)$$

Thermochemical parameters which are total energy (E), enthalpy (H), heat capacity (C_v) and entropy (S) were calculated at 200, 298.15 and 400 K temperatures. The temperature dependence of complexes stability was investigated computationally.

3. Results and Discussions

3.1. Structural characterization

Optimized structures of $[\text{Tp}(\text{CO})_2\text{Mo}\equiv\text{C-Ph}]^{2+}$ and $[\text{L}(\text{CO})_2\text{Mo}\equiv\text{C-Ph}]^+$ carbyne complexes were computed at B3LYP/LANL2DZ/6-31G(d) level in the gas phase under standard conditions (1.00 atm and 298.15 K) and given in Fig. 2 together with atomic labels. Some structure parameters which are obtained from the optimized structures are given in Table 1 and Table 2.

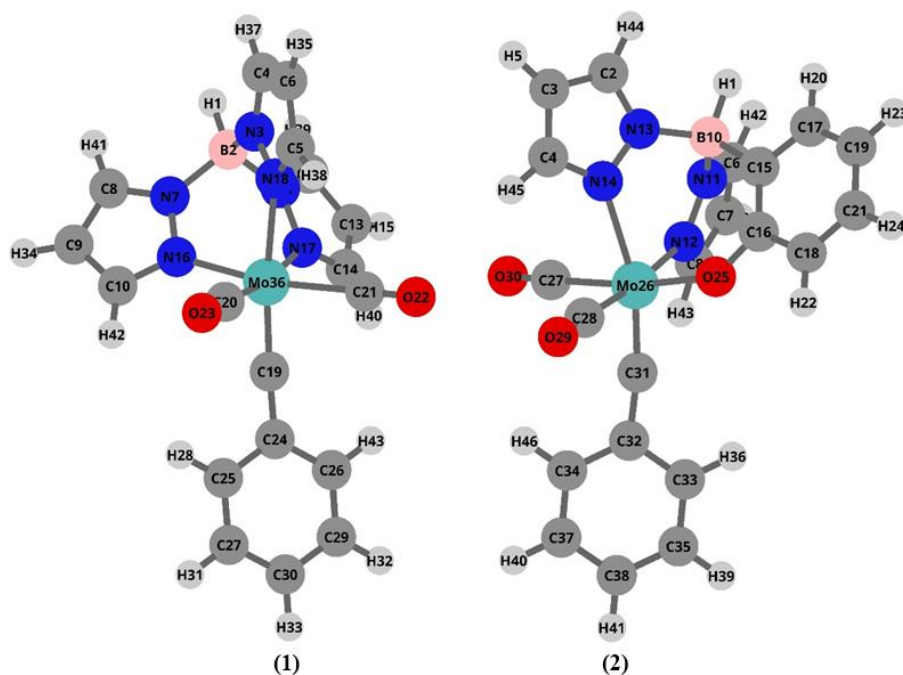


Figure 2. Molecular structure of the $[\text{Tp}(\text{CO})_2\text{Mo}\equiv\text{C-Ph}]^{2+}$ (1) and $[\text{L}(\text{CO})_2\text{Mo}\equiv\text{C-Ph}]^+$ (2) complexes.

Table 1. Bond lengths (Å) and bond angles (°) of complex (1)

Bond	length (Å)	Bond	Angles (°)
Mo36-N16	2.077	N16-Mo36-N17	87.1
Mo36-N17	2.077	N16-Mo36-N18	87.6
Mo36-N18	2.287	N16-Mo36-C19	104.2
Mo36-C19	1.853	N16-Mo36-C20	89.4
Mo36-C20	2.198	N16-Mo36-C21	170.7
Mo36-C21	2.198	N17-Mo36-N18	87.6
C19-C24	1.398	N17-Mo36-C19	104.2
C20-O23	1.133	N17-Mo36-C20	170.7
N3-N18	1.369	N17-Mo36-C21	89.3
N7-N16	1.378	N18-Mo36-C19	163.5
N11-N17	1.378	N18-Mo36-C20	83.6
N3-C4	1.352	N18-Mo36-C21	83.6
N7-C8	1.337	C19-Mo36-C20	85.0
N11-C12	1.337	C19-Mo36-C21	85.0
N16-C10	1.370	C20-Mo36-C21	92.9
N17-C14	1.370	H1-B2-N3	111.6
N18-C5	1.347	H1-B2-N7	109.8
B2-N3	1.532	H1-B2-N11	109.8
B2-N7	1.567	N3-B2-N7	109.3
B2-N11	1.567	N3-B2-N11	109.3
B2-H1	1.192	N7-B2-N11	106.8
C4-C6	1.388	C24-C19-Mo36	172.9

Table 2. Bond lengths (Å) and bond angles (°) of complex (2)

Bond	length (Å)	Bond	Angles (°)
Mo26-N12	2.145	N12-Mo26-N14	88.6
Mo26-N14	2.321	N12-M26-O25	89.3
Mo26-O25	1.975	N12-Mo26-C27	84.1
Mo26-C27	2.146	N12-Mo26-C28	173.6
Mo26-C28	2.134	N12-Mo26-C31	102.7
Mo26-C31	1.827	N14-Mo26-O25	90.5
C31-C32	1.420	N14-Mo26-C27	83.6
C27-O30	1.139	N14-Mo26-C28	85.0
C28-O29	1.140	N14-Mo26-C31	164.1
N11-N12	1.371	O25-Mo26-C27	171.3
N13-N14	1.362	O25-Mo26-C28	90.2
O25-C16	1.314	O25-Mo26-C31	100.6
C15-C16	1.442	C27-Mo26-C28	95.6
C16-C18	1.430	C27-Mo26-C31	86.5
N11-C6	1.342	C28-Mo26-C31	83.7
N12-C8	1.354	H1-B10-N11	105.7
N13-C2	1.348	H1-B10-N13	107.0
N14-C4	1.346	H1-B10-C15	109.5
B10-N11	1.572	N11-B10-N13	109.5
B10-N13	1.552	N11-B10-C15	112.6
B10-C15	1.630	N13-B10-C15	112.1
B10-H1	1.202	C32-C31-Mo26	171.0

As can be seen from Table 1 and Table 2, Mo36-N18 for the complex (1) and Mo26-N14 bonds for the complex (2) are longer from the other Mo-N bonds. The lengths of Mo36-N18 and Mo26-N14 bonds are 2.287 and 2.321 Å, respectively. These bonds contain the carbyne ligand in the trans position. The Mo-C(carbyne) lengths are 1.853 and 1.827 Å in the complex (1) and complex (2), respectively. This result indicates that Mo-C(carbyne) binding is stronger and carbyne carbon makes stronger back bonding. This result is consistent with that of many other carbyne complexes. In many other carbyne complexes, the length of M-C(carbyne) is given between 1.765-1.878 Å [21]. The stronger Mo-C(carbyne) bond caused weakening and elongation of the bonds in the trans position. The other bond lengths calculated for the complexes are consistent with the expected values and bond degrees.

C24-C19-Mo36 bond angle is calculated as 172.9° for complex (1) and C32-C31-Mo26 bond angle is obtained as 171.0° for complex (2). These M-C-R bond angles are consistent with similar carbyne complexes [21]. It is seen from these results that the carbyne carbon environmental geometry is near linear in the complex (1) and (2). As seen from the bond angles, the cis angles are about 90 degrees and the trans angles are about 180 degrees around the central metal atom. Therefore, central molybdenum environmental geometry is distorted octahedral. However, the angles N16-Mo36-C19 and N17-Mo36-C19 have deviated considerably from 90 degrees due to the steric and chelate effect. Boron atom environmental geometry in Tp ligand is distorted tetrahedral. The boron environment angles in the Tp ligand are expected to be 109.5 degrees. The calculated angles in boron environment are almost 109.5 degrees. Similar bonding angles have been obtained experimentally in similar carbyne complexes [13].

3.2. IR spectrum and labeling of peaks

IR spectrums of complex (1) and complex (2) were calculated at B3LYP/LANL2DZ/6-31G(d) level. The calculated IR spectrums are given in Fig. 3 with peak numbers.

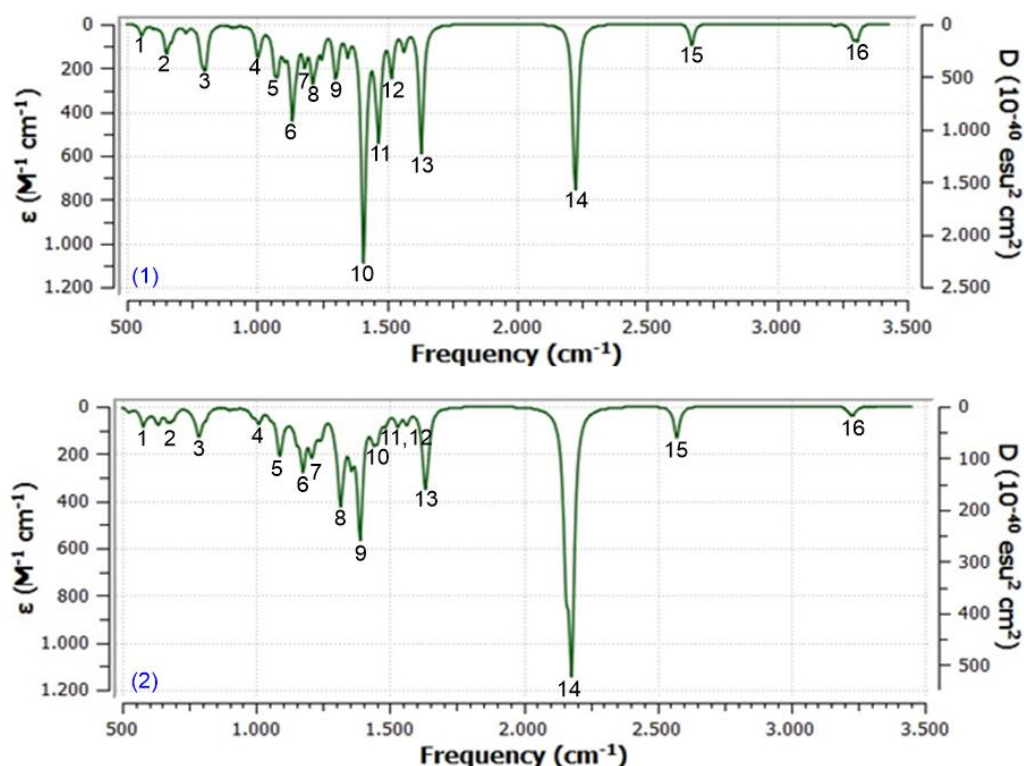


Figure 3. Calculated IR spectrum of complex (1) and complex (2).

Peak number, vibration mode number, frequencies and assignment of peaks given in Fig. 3 are given in Table 3 and Table 4. The frequencies in the tables are harmonic frequencies. No scale factor was found in the

literature for the calculation level. Peak assignments were performed with vibrational energy distribution analysis (VEDA) program [22].

Table 3. Assignment of the peaks observed in the IR spectrum of the complex (1)

Peak No	Mod No	Frequency (cm ⁻¹)	Assignment
1	34	556.6	B (C-C-Mo), T (C-C-C-C)
2	41	651.6	S (Mo-C), B (C-C-C),
3	51	803.5	T (H-C-C-N), T (H-C-C-C)
4	65	1000.7	B (C-C-C)
5	71	1068.0	B (C-N-N)
6	77	1135.8	S (C-N)
7	81	1183.5	S (N-N)
8	84	1213.7	B (H-C-C)
9	88	1300.8	S (C-N)
10	93	1409.5	S (C-C)
11	98	1467.9	S (C-C), B (C-N-N)
12	101	1517.4	S (C-C), B (H-C-C)
13	106	1631.7	S (C-C)
14	108	2226.5	S (C-O)
15	109	2672.1	S (B-H)
16	120	3295.1	S (C-H)

B: Bending, T: Torsion, S: Stretching

Table 4. Assignment of the peaks observed in the IR spectrum of the complex (2)

Peak No	Mod No	Frequency (cm ⁻¹)	Assignment
1	38	577.9	B (C-C-C), T (C-N-N-C)
2	43	635.1	B (O-C-C), B (C-C-C)
3	45	667.6	S (Mo-C), B (C-C-C)
4	70	1008.4	B (C-C-C)
5	77	1086.9	S (C-C), B (N-N-C), B (H-C-C)
6	85	1175.8	S (C-C), S (C-B), B (H-C-C), B (H-B-C)
7	88	1206.3	S (N-C), S (N-N)
8	94	1315.4	S (C-O) phenoxy
9	100	1388.9	S (C-C)
10	103	1454.3	B (H-C-C)
11	108	1529.5	S (C-C), B (H-C-C)
12	110	1563.7	S (C-C), B (H-C-C)
13	113	1631.7	S (C-C), B (H-C-C)
14	116	2179.8	S (C-O)
15	117	2572.6	S (B-H)
16	125	3230.6	S (C-H)

B: Bending, T: Torsion, S: Stretching

As shown in Table 3 and Table 4, bending, torsion and Mo-C(carbyne) stretching vibrations are observed in the 500-1000 cm⁻¹ region. Bending and torsion vibrations have no important function in determining the structure. However, the peak of Mo-C(carbyne) stretching vibrations was calculated in this region. The frequencies of 651.6 cm⁻¹ for complex (1) and 667.6 cm⁻¹ for complex (2) belong to the Mo-C(carbyne) bond stretching vibration. It is known that the vibration frequencies ($\bar{\nu}$) are directly proportional to the square root of the bond force constant (k) and inversely proportional to the square root of reduced masses (μ) of the connected atoms according to the Eq. 11.

$$\bar{\nu} = \frac{1}{2\pi c} \sqrt{\frac{k}{\mu}} \quad (11)$$

For Mo-C bonds, in general, the Mo-C stretching frequencies are expected to be small since the force constant is small and the reduced mass is large. Therefore, Mo-C stretching vibrations are observed at low frequency.

Numerous peaks emerged in the region of 1000-1650 cm⁻¹. This is the region where single and double bond stretching vibrations are observed. In this region, peaks of C-C, C=C, N-N, C-N, C=N, B-N, C-O(phenoxy) bond stretching vibrations and some bending vibrations were calculated.

Peaks of C-O stretching for both complexes are very prominent. The peaks 14 for the complex (1) and (2) belong to C-O stretching vibrations. For both complexes, these frequencies are in the carbonyl stretching region. Another prominent peak in the IR spectrum of complexes is related to B-H stretching. B-H stretching frequencies were calculated at 2672.1 cm⁻¹ in the complex (1) and 2572.6 cm⁻¹ in the complex (2). C-H, N-H, O-H vibrations are observed around 3000 cm⁻¹. Although these bonds are single bonds, they are observed at high frequency because the reduced mass is small. The smaller the reduced mass according to eq. (11), the greater the frequency of the vibration.

3.3. UV-VIS spectrum and main band assignment

UV-VIS spectrums of the complexes were calculated at TD-B3LYP/LANL2DZ/6-31G(d) level in gas phase and given in Fig. 4. The bands in the UV-VIS spectrum of the molecules arise from allowed electronic transitions. The allowed electronic transitions have a molar absorption coefficient greater than 1000 L/mol.cm. Electronic transitions with large molar absorption coefficients are shown in Fig. 4 with band number.

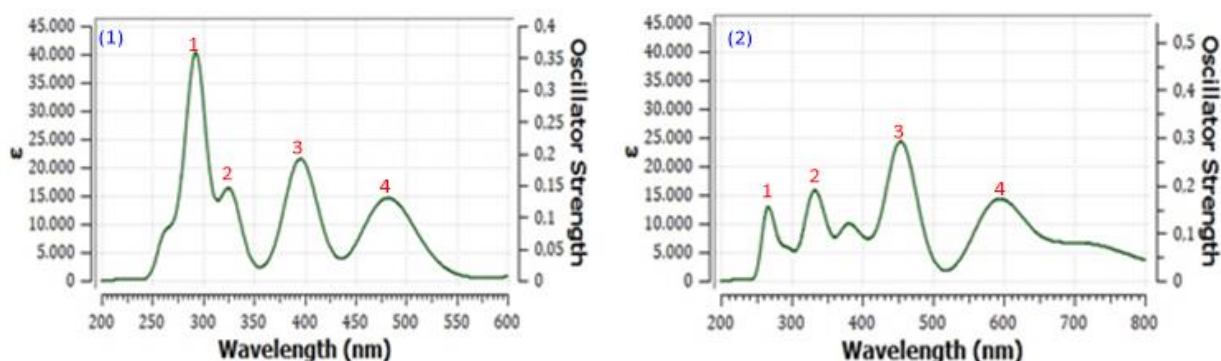


Figure 4. Calculated UV-VIS spectrums of the complex (1) and (2)

As shown in Fig. 4, there are four bands in the UV-VIS spectrum of the both complexes. Main band is shown with number 1 for complex (1) and number 3 for complex (2). Here, the electronic transitions forming the main bands will be analyzed. Table 5 shows the

wavelengths of the main bands, the electronic transitions forming the main bands and the wave function coefficients of the electronic transitions for each excitation.

Table 5. Wavelengths of the main bands in the UV-VIS spectra of the studied complexes, electronic transitions forming the main bands and wave function coefficients

Complex	Wavelength (nm)	Transitions	Wave function coefficient
(1)	294.1	HOMO-13 → LUMO	0.199
		HOMO-4 → LUMO+2	0.145
		HOMO-2 → LUMO+2	0.576
		HOMO-1 → LUMO+1	0.238
(2)	454.9	HOMO-9 → LUMO	0.163
		HOMO-8 → LUMO	0.621
		HOMO-6 → LUMO	-0.124
		HOMO-1 → LUMO	0.173
		HOMO → LUMO	0.117

When the wave function coefficients of the electronic transitions which form the main band (294.1 nm) of complex (1) are examined, it is seen that the wave function coefficient of HOMO-2 → LUMO+2 electronic transition is the highest. This finding indicates that the highest contribution to the formation of the main band of complex (1) is due to the electronic transition of HOMO-2 → LUMO+2. Likewise, it can be said that the main band (454.9 nm) of complex (2) is mainly caused by HOMO-8 → LUMO transition. The characters of these orbitals can be determined from wave function coefficients or contour diagrams. The contour diagrams of HOMO-2, LUMO+2 for complex (1) and HOMO-8 and LUMO for complex (2) are given in Figure 5.

For complex (1), it can be said that HOMO-2 is a π molecular orbital consisting of the overlap of

molybdenum d orbital and carbyne carbon p orbital in two regions. LUMO+2 is a π^* antibonding molecular orbital formed by the difference between molybdenum d orbital and carbyne carbon p orbital.

The HOMO-2 → LUMO+2 transition is then a $\pi \rightarrow \pi^*$ transition. HOMO-8 of complex (2) represents π molecular orbital formed by the overlap of the p orbitals of the carbon atoms in the pyrazole ring. LUMO indicates π^* orbitals consisting of central molybdenum d orbitals and phenoxy oxygen p orbitals [23]. Therefore, this electronic transition can be considered as a ligand-to-metal charge transfer transition (LMCT). The same results are obtained when the molecular orbital coefficients are examined.

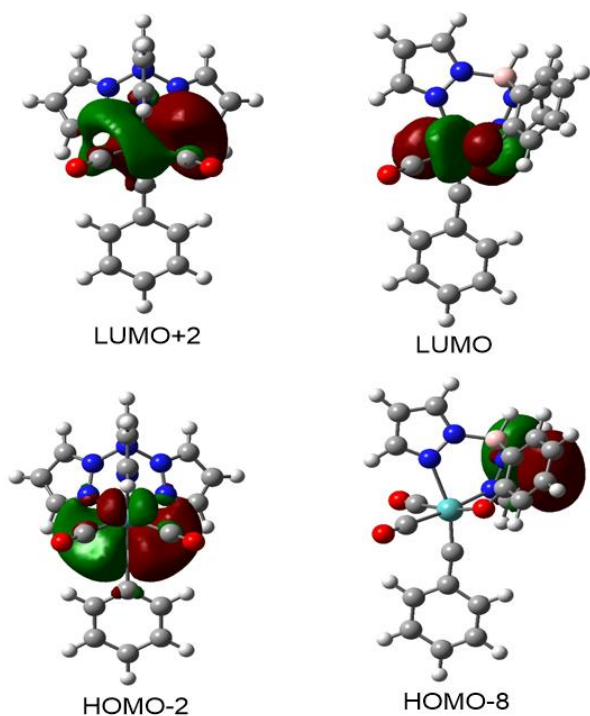


Figure 5. Contour diagrams of HOMO-2, LUMO+2 for complex (1) and HOMO-8 and LUMO for complex (2)

3.4. $^1\text{H-NMR}$ and $^{13}\text{C-NMR}$ spectrums and assignment of peaks

$^1\text{H-NMR}$ and $^{13}\text{C-NMR}$ spectrums of the complexes were computed with Gauge-Independent Atomic Orbital (GIAO) method at the level of B3LYP/LANL2DZ/6-31G(d). Tetramethyl silane (TMS) was taken as reference to determine chemical shifts. Chemical shift of carbon and hydrogen atoms for TMS in the same level were calculated as 193.0 and 32.4 ppm, respectively. $^1\text{H-NMR}$ and $^{13}\text{C-NMR}$ spectrums of the complexes are given in Fig. 6 and Fig. 7. ^1H and $^{13}\text{C-NMR}$ chemical shift values are given in Table 6.

As can be seen from Figure 6, Figure 7 and Table 6, there are seven peaks in the $^1\text{H-NMR}$ spectrums of both complexes. Some protons have the same chemical shift value. This result indicates that some hydrogens are equivalent. The chemical shift value of hydrogen bound to the boron atom was calculated as 4.65 ppm for complex (1) and 4.47 ppm for complex (2). The chemical shift values of the hydrogens bonded carbon atoms vary between 5.9-8.4 ppm. This can be explained by the fact that the hybridization types of boron and carbon atoms are different [24]. Carbon atoms have sp^2 hybridization and boron atom sp^3 hybridization. S-characters of the hybrid orbitals in the

boron atom are about 25%, whereas the s-characters of the hybrid orbitals in the carbon atom are about 33%.

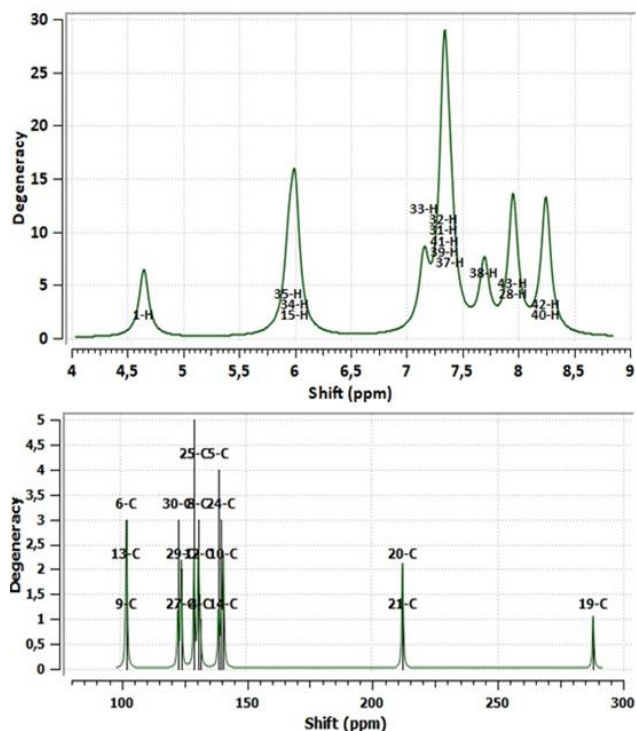


Figure 6. $^1\text{H-NMR}$ and $^{13}\text{C-NMR}$ spectra for $[\text{Tp}(\text{CO})_2\text{Mo}\equiv\text{C-Ph}]^{2+}$ complex calculated at B3LYP/LANL2DZ/6-31G(d) level by GIAO method

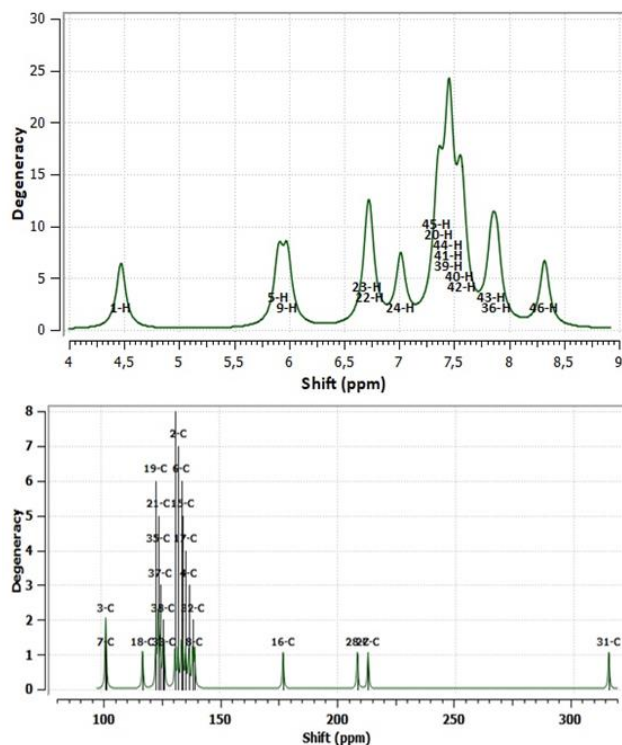


Figure 7. $^1\text{H-NMR}$ and $^{13}\text{C-NMR}$ spectra for $[\text{L}(\text{CO})_2\text{Mo}\equiv\text{C-Ph}]^+$ complex calculated at B3LYP/LANL2DZ/6-31G(d) level by GIAO method

Table 6. ^1H and ^{13}C -NMR chemical shift values (ppm) of the studied complexes

Complex (1)		Complex (2)	
^1H -NMR assignment	$\delta(\text{ppm})$	^1H -NMR assignment	$\delta(\text{ppm})$
1H	4.65	1H	4.47
15H,34H,35H	5.95-6.00	5H,9H	5.91-5.98
33H	7.16	22H,23H	6.71-6.74
31H,32H,37H,39H,41H	7.34-7.39	24H	7.02
38H	7.70	20H,39H,40H,41H,42H,44H,45H	7.35-7.58
28H,43H	7.95	36H,43H	7.84-7.89
40H,42H	8.25	46H	8.32
^{13}C -NMR assignment	$\delta(\text{ppm})$	^{13}C -NMR assignment	$\delta(\text{ppm})$
6C,9C,13C	102.7	3C,7C	102.2
27C,29C,30C	123.1-124.4	18C	117.8
25C,26C	129.6	19C,21C,33C,35C,37C,38C	123.4-126.9
4C,8C,12C	131.2-131.9	2C,4C,6C,8C,15C,17C,32C,34C,	131.5-139.8
5C,10C,14C,24C	139.3-141.2	16C	177.2
20C,21C	212.4	28C	208.6
19C	288.1	27C	213.1
		31C	314.9

As the s-character of the hybrid orbitals decreases, the nuclei are more shielded by electrons. Highly shielded nuclei are observed at low chemical shift value. Therefore, the chemical shift of the hydrogen bound to the boron atom is lower. The slightly different chemical shift values of the hydrogens bound to carbon atoms are related to the distance of the carbon atoms to the electronegative atom. The chemical shift values of the hydrogens attached to carbons close to the electronegative atom such as nitrogen and oxygen are slightly higher. Because the nuclei of the carbons adjacent to the atom with high electronegativity are less shielded. The less shielded core is observed at high ppm.

When the ^{13}C -NMR spectra and chemical shift values of the complexes are examined, it is seen that the chemical shift of the carbyne carbon is higher than the others. 19C = 288.1 ppm for complex (1) and 31C = 314.9 ppm for complex (2). In general, the chemical shift of carbon atoms with $\text{M}\equiv\text{C}$ binding is reported to be between 235-401 ppm [25]. The chemical shift values calculated in this study are consistent with these results. The calculated carbonyl carbon chemical shift values are also around 210 ppm. Experimentally, ^{13}C -chemical shift values for M-CO bonded carbonyl compounds are generally in the range of 177-275 ppm [25]. The values calculated in this study are in agreement with this range. 16C chemical shift (177.2 ppm) in complex (2) is also different. This value belongs to the carbon to which the phenoxy group

oxygen is attached. The high electronegativity of oxygen leads to a reduction in electron density on 16C and less shielding of the nucleus. The less shielded core has a high chemical shift value. As can be seen from Table 6, the chemical shift of other carbons is between 100-140 ppm. These values vary according to the chemical environment of carbon atoms. Carbons with electronegative atoms around have a higher chemical shift value.

3.5. Charge distribution

In order to estimate the electronic structures of the complexes, charges of some atoms, electrostatic potential maps of the complexes, molecular orbital energy diagrams and frontier orbital contour diagrams were calculated. The charges of the atoms in the complexes were calculated according to Mulliken method. Mulliken charges of some atoms are given in Table 7.

Table 7. Mulliken charges of some atoms in the complexes

Complex (1)		Complex (2)	
Atom	Charge	Atom	Charge
2B	0.484	10B	0.344
16N	-0.417	12N	-0.385
17N	-0.417	14N	-0.318
18N	-0.339	25O	-0.556
19C	-0.161	26Mo	0.843
20C	0.298	27C	0.280
21C	0.298	28C	0.254
36Mo	0.946	31C	-0.184

It was considered that central molybdenum is +3 charged, hydridotris(pyrazolyl)borate (Tp) ligand is -1 charged and hydrido-2-phenoxybis(pyrazolyl)borate (L) is -2 charged in the computational design. In this case, the total charge of complex (1) is +2 and the total charge of complex (2) is +1. As shown in Table 7, positive formal charges were calculated for boron atoms (2B, 10B) in the Tp and L ligands, carbonyl carbon (20C, 21C, 27C, 28C) and central molybdenum atoms. Negative formal charges were obtained for donor nitrogen atoms (16N, 17N, 18N, 12N, 14N) phenoxy group oxygen atom (25O) and carbyne carbons (19C, 31C). It is seen that central molybdenum atom reduces the positive charge in complex formation. The molybdenum atom, which was considered to be +3 charged in the isolated state, had a charge of +0.946 in complex (1) and +0.843 in complex (2). This result indicates that molybdenum receives electrons from the ligands in complex formation. In the complexes, the formal charges of carbyne carbons appear to be very close to zero. This is suitable for metal-carbyne back bonding. Carbyne carbon gives electrons in sp hybrid orbitals to metal and positively charged. However, the low-energy p orbitals receive electrons from the metal and negatively charged. The similar $\text{Cl}(\text{CO})_4\text{Cr}\equiv\text{C-Ph}$ complex were studied by Dao *at al.* Electronic charges were obtained from X-ray and neutron diffraction methods. It is seen that there is a partial negative charge on the carbyne carbon atom [26].

3.6. Molecular electrostatic potential (MEP) maps

MEP maps were calculated to determine the regions of the complexes suitable for nucleophilic and electrophilic attacks. The colors in these maps range from red to blue. In the MEP maps, the red zone electron density is the highest and the blue zone electron density is the lowest. Thus, the molecule can attack the nucleophiles from the red region and the electrophiles from the blue region. MEP maps of carbyne complex ions were calculated at B3LYP/LANL2DZ/6-31G(d) level and given in Figure 8.

As shown in Fig. 8, the MEP map of complex (1) is darker-blue. The darker-blue indicates that the electron density is low and the electrophilicity of the complex is high. According to this assessment, complex (1) is more electrophilic than complex (2). This is also consistent with the charges of the complexes. Since both complexes are positively charged, there are no red regions with high electron density in the MEP maps.

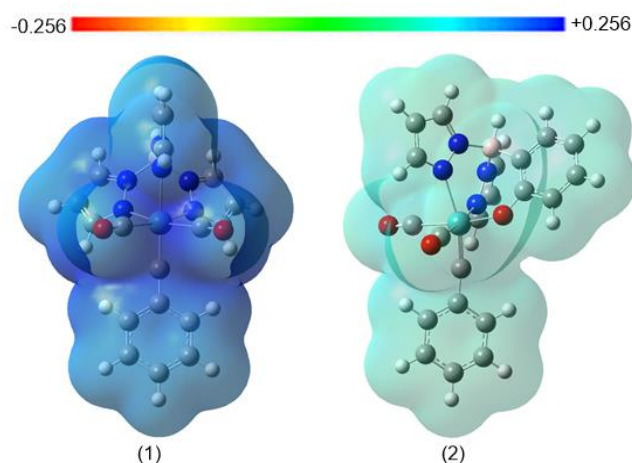


Figure 8. MEP maps of complex (1) and complex (2)

3.7 Molecular orbital energy diagrams and frontier orbital contour diagrams

The diagrams obtained by ordering the molecular orbitals according to their increasing energy are called molecular orbital energy diagram (MOED). The energies of the highest occupied molecular orbital (E_{HOMO}) and the lowest unoccupied molecular orbital (E_{LUMO}) and contour diagrams of frontier orbitals are generally used to estimate the electronic properties. Molecular orbital energy diagrams of the complexes between HOMO-4 and LUMO+4 and contour diagrams of HOMO, LUMO are given in Figure 9.

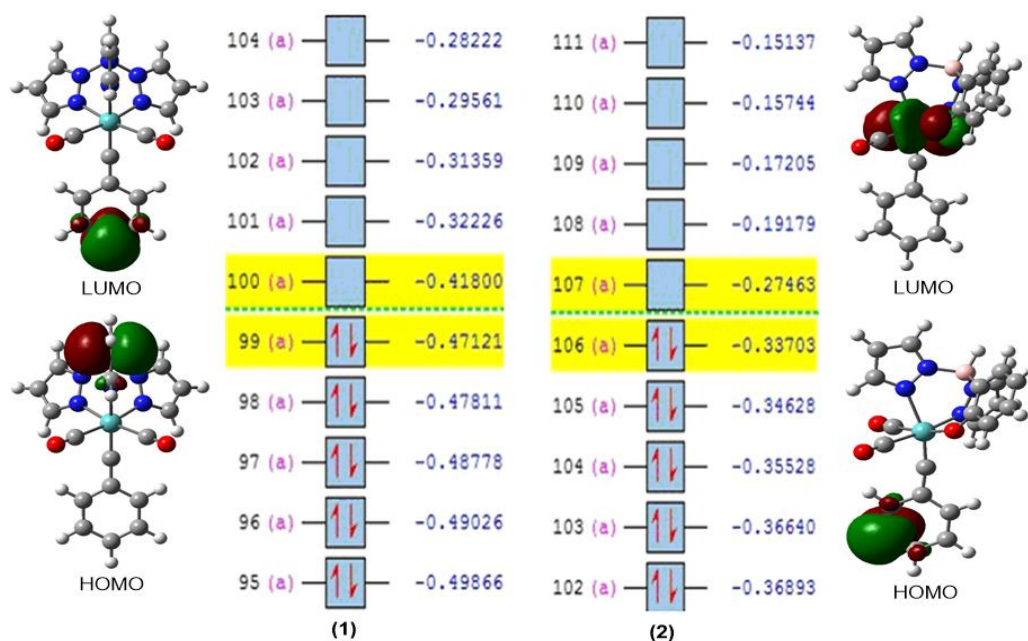


Figure 9. Contour diagrams of the frontier orbitals and MOED for complexes (1) and (2).

Table 8. Some molecular properties calculated for B3LYP/LANL2DZ/6-31G(d) level for complex (1) and complex (2)

Descriptor	(Unit)	Complex (1)	Complex (2)
E_{HOMO}	eV	-12.8188	-9.1686
E_{LUMO}	eV	-11.3713	-7.4710
I	eV	12.8188	9.1686
A	eV	11.3713	7.4710
ΔE	eV	1.4475	1.6975
η	eV	0.7238	0.8488
σ	eV^{-1}	1.3817	1.1782
χ	eV	12.0950	8.3198
CP	eV	-12.0950	-8.3198
ω	eV	101.0616	40.7763
μ	D	3.5757	1.9049
α	\AA^3	345.6023	390.1813

As can be seen from the molecular orbital energy diagram of the complexes, $E_{\text{HOMO}} = -0.4712$ and $E_{\text{LUMO}} = -0.4180$ for complex (1), $E_{\text{HOMO}} = -0.3370$ and $E_{\text{LUMO}} = -0.2746$ for complex (2). Here the energies are in the Hartree unit. 1 Hartree = 27.2116 eV. For complex (1), HOMO is concentrated on the boron atom, LUMO is concentrated on the phenyl ring. On the other hand, for complex (2), HOMO is concentrated on the phenyl ring and LUMO is concentrated on the central molybdenum atom. HOMO is the orbital where the first electron will be removed and LUMO is the first electron to enter.

3.8. Some electronic structure descriptors

Some molecular structure descriptors such as ionization energy (I), electron affinity (A), LUMO-HOMO energy gap (ΔE), chemical hardness (η),

chemical softness (σ), Mulliken electronegativity (χ), chemical potential (CP), electrophilicity index (ω), static dipole moment (μ) and average linear polarizability (α) were calculated for predicting the molecular properties of the complexes. HOMO and LUMO energies were taken from the molecular orbital energy diagrams (MOED). The electronic structure descriptors calculated from eq. (1)-(10) are given in Table 8.

As seen from eq. (1) and eq. (2), HOMO and LUMO energies is connected with ionization energy (I) and electron affinity (A) according to the Koopmans theorem [27]. It is seen from Table 8 that the HOMO energy of complex (1) is lower than that of complex (2). The lower ionization energy of complex (1) is higher than that of complex (2) since the low HOMO energy will cause higher ionization energy. LUMO energy is also associated with electron affinity. Again, the LUMO energy of complex (1) is low and the electron affinity of complex (1) is higher than that of complex (2).

It is seen from the equation (3) - (7) that the energy gap is associated with hardness, softness, electronegativity and chemical potential. The species with a large energy gap are harder and the smaller ones are softer. Since the ΔE value of complex (1) is higher than that of complex (2), complex (1) is harder than complex (2) [28].

Mulliken electronegativity is defined as the arithmetic mean of ionization energy (I) and electron affinity (A).

The higher the I and A values, the higher the χ value and the lower the CP. As shown in Table 8, since the I and A values of complex (1) are higher than those of complex (2), χ value is higher and CP value is lower.

The higher the electrophilicity index, the higher the electrophilicity. An electrophile interacts more strongly with a nucleophile and there is more electron flow in this interaction. This electron flux reduces the energy more. As shown in Table 8, the ω value of complex (1) is higher than that of complex (2). Therefore, complex (1) is more electrophile. This result is consistent with the results obtained from MEP maps.

Dipole moment is a measure of the polarity of compounds. Molecules with a dipole moment greater than zero are called polar molecules. In this sense, the complexes studied are both polar. Polarizability can be defined as the softness of the electron cloud of the molecule. According to the data in Table 8, the polarizability (α) of complex (2) is higher than complex (1). It is stated that substances whose polarizability (α) and hyperpolarizability (β) are

higher than those of urea can be used in production of nonlinear optical materials [29]. The polarizabilities of both complexes are higher than that of urea ($\alpha=5.0708 \text{ \AA}^3$, $\beta=5.30 \times 10^{-28} \text{ cm}^5/\text{esu}$ for urea). Complexes can be used to make nonlinear optical materials according to their polarizability values.

3.9. Thermochemistry of the complexes

It has already been stated that due to the thermal instability of most alkylidene complexes, it has been studied in a limited manner [13]. In this paper, thermal stability of the hypothetical complex (1) and complex (2) were investigated computationally. Complex (1) and complex (2) were optimized in the gas phase at a pressure of 1.00 atm and temperatures of 200, 298.15 and 400 K at the level of B3LYP/LANL2DZ/6-31G(d). Imaginary frequency was not obtained as a result of the optimization. This finding indicates that the complexes are in the ground state with minimum energy. Thermochemical parameters which are total energy (E), enthalpy (H), heat capacity (C_v) and entropy (S) obtained at 200, 298.15 and 400 K temperatures for the complexes are given in Table 9.

Table 9. Thermochemical parameters at various temperatures for complex (1) and complex (2)

Complex	Thermochemical parameters	Temperature (K)		
		200	298.15	400
Complex (1)	E ^a	-1265.4433	-1265.4307	-1265.4132
	H ^a	-1265.4426	-1265.4297	-1265.4119
	C _v ^b	67.354	94.164	120.152
	S ^b	143.455	176.124	208.105
Complex (2)	E ^a	-1346.3984	-1346.3850	-1346.3664
	H ^a	-1346.3978	-1346.3841	-1346.3652
	C _v ^b	70.935	100.218	128.270
	S ^b	148.319	182.908	216.924

^a Hartree, ^b cal/molK

As shown in Table 9, thermochemical parameters of complexes increase as the temperature increases. This result indicates that the stability of the complexes

decreases with increasing temperature. The following equations were obtained for the relationship between thermochemical parameters and temperature.

For complex (1)

$$E = 2.13158 \times 10^{-7} T^2 + 2.24551 \times 10^{-5} T - 1.26546 \times 10^3 \quad R^2 = 0.999$$

$$H = 2.13172 \times 10^{-7} T^2 + 2.56169 \times 10^{-5} T - 1.26546 \times 10^3 \quad R^2 = 0.999$$

$$C_v = -8.99689 \times 10^{-5} T^2 + 3.17971 T + 7.35848 \quad R^2 = 1.000$$

$$S = -9.422335 \times 10^{-5} T^2 + 3.79790 \times 10^{-1} T + 7.12663 \times 10^1 \quad R^2 = 1.000$$

For complex (2)

$$E = 2.31241 \times 10^{-7} T^2 + 2.11903 \times 10^{-5} T - 1.34641 \times 10^3 \quad R^2 = 1.000$$

$$H = 2.31255 \times 10^{-7} T^2 + 2.43522 \times 10^{-5} T - 1.34641 \times 10^3 \quad R^2 = 1.000$$

$$C_v = -1.14624 \times 10^{-4} T^2 + 3.55449 \times 10^{-1} T + 4.43007 \quad R^2 = 1.000$$

$$S = -9.21412 \times 10^{-5} T^2 + 3.98310 \times 10^{-1} T + 7.23427 \times 10^1 \quad R^2 = 1.000$$

As shown in these equations, R^2 values are almost equal to one. Thermochemical parameters can then be calculated for a given temperature using these equations. At the same time, the temperature required to break a metal-carbyne triple bond can be calculated. The bond dissociation energy of $M \equiv CH$ triple bond is given as 523, 477, 607, 423 and 418 kJ/mol for La, V, Nb, Fe and Co, respectively [21]. When these values are averaged, the average bond dissociation energies of $M \equiv C$ triple bonds are found to be 490 kJ/mol. Carbyne

complexes are reported to be stable at room temperature. Thus, when the energy at 298.15 K of the carbyne complex is increased about 490 kJ/mol, the metal-carbyne triple bond can be broken. Since 1 Hartree is equal to $4.3597482 \times 10^{-18}$ Joule [30], 490 kJ/mol is equal to 0.186631 Hartree. When 0.186631 Hartree is added to total energies of complex (1) and complex (2) at 298.15 K and replaced in the total energy equation, the following equations are obtained.

$$\text{For complex (1)} \quad 2.13158 \times 10^{-7} T^2 + 2.24551 \times 10^{-5} T - 2.159721 \times 10^{-1} = 0$$

$$\text{For complex (2)} \quad 2.31241 \times 10^{-7} T^2 + 2.11903 \times 10^{-5} T - 2.115860 \times 10^{-1} = 0$$

When these equations are solved for temperature, the $M \equiv C$ bond dissociation temperatures of complex (1) and complex (2) are found to be 955 and 912 K. These results show that the hypothetical carbyne complexes designed can be stable at high temperatures. In addition, the bond dissociation energy of complex (1) is higher than that of complex (2).

4. Conclusion

Structural, electronic, molecular and thermochemical properties of hypothetical $[Tp(CO)_2Mo \equiv C-Ph]^{2+}$ (1) and $[L(CO)_2Mo \equiv C-Ph]^+$ (2) carbyne complexes were investigated by B3LYP/ LANL2DZ/6-31G(d) level. Bond lengths, bond angles, IR, UV-Vis and 1H -NMR, ^{13}C -NMR spectrums were calculated to predict the complex structures. Charges of some atoms, MEP maps, molecular orbital energy diagrams and frontier orbital contour diagrams were calculated to estimate the electronic structures of the complexes. Some molecular structure descriptors were calculated for predicting the molecular properties. In order to predict the thermochemical stability of the complexes, total energy (E), enthalpy (H), heat capacity (C_v) and

entropy (S) were calculated at 200, 298.15 and 400 K temperatures. It is found that hypothetical carbyne complexes designed in this study can be stable at high temperatures.

Acknowledgments

The authors are grateful for their support to the Sivas Cumhuriyet University, Scientific Research Unit (Project No: F-580).

Conflict of interest

The authors state that there is no conflict of interests.

References

- [1] Fischer E. O., Kreis G., Kreiter C. G., Müller J., Huttner G., Lorenz H., trans-Halogeno [alkyl(aryl)carbyne] tetracarbonyl Complexes of Chromium, Molybdenum and Tungsten, A New Class of Compounds Having a Transition Metal-Carbon Triple Bond, *Angewandte Chemie International Edition in English*, 12(7) (1973) 564-565.
- [2] Wu X., Daniliuc C.G., Hrib C.G., Tamm M., Phosphoraneiminato tungsten alkylidyne complexes as highly efficient alkyne metathesis catalysts, *Journal of Organometallic Chemistry*, 696(25) (2011) 4147-4151.
- [3] Lysenko S., Daniliuc C. G., Jones P. G., Tamm M., Tungsten alkylidyne complexes with ancillary imidazolin-2-iminato and imidazolidin-2-iminato ligands and their use in catalytic alkyne metathesis, *Journal of Organometallic Chemistry*, 744 (2013) 7-14.
- [4] Fey N., Orpen A. G., Harvey J. N., Building ligand knowledge bases for organometallic chemistry: Computational description of phosphorus (III)-donor ligands and the metal-phosphorus bond, *Coordination Chemistry Reviews*, 253(5-6) (2009) 704-722.
- [5] Snelders D. J., Van Koten G., Klein Gebbink R. J., Steric, electronic, and secondary effects on the coordination chemistry of ionic phosphine ligands and the catalytic behavior of their metal complexes, *Chemistry—A European Journal*, 17(1) (2011) 42-57.
- [6] Díez-González S., Nolan S. P., Stereo electronic parameters associated with N-heterocyclic carbene (NHC) ligands: a quest for understanding, *Coordination Chemistry Reviews*, 251(5-6) (2007) 874-883.
- [7] Peris E., Smart N-heterocyclic carbene ligands in catalysis, *Chemical Reviews*, 118(19) (2017) 9988-10031.
- [8] Kim H. P., Angelici R. J., Transition metal complexes with terminal carbyne ligands, *In Advances In Organometallic Chemistry*, 27 (1987) 51-111.
- [9] Hart I. J., Hill A. F., Stone F. G. A., Synthesis of alkynylmethylidyne molybdenum and-tungsten complexes and their reactions with octacarbonyldicobalt and hexacarbonylbis (g-cyclopentadienyl) dimolybdenum, *J. Chem. Soc. Dalton Trans*, (1989) 2261-2267.
- [10] McDermott G. A., Dorries A. M., Mayr A., Synthesis of carbyne complexes of chromium, molybdenum, and tungsten by formal oxide abstraction from acyl ligands, *Organometallics*, 6(5) (1987) 925-931.
- [11] Dossett S. J., Hill A. F., Jeffery J. C., Marken F., Sherwood P., Stone F. G. A., Chemistry of polynuclear metal complexes with bridging carbene or carbyne ligands. Part 79. Synthesis and reactions of the alkylidyne metal complexes $[M(\text{triple bond, length half m-dash}CR)(CO)_2(\eta\text{-}C_5H_5)]$ ($R=C_6H_3$, Me 2-2, 6, $M=Cr$, Mo , or W ; $R=C_6H_4Me$ -2, C_6H_4OMe -2, or C_6H_4NMe 2-4, $M=MO$); crystal structure of the compound $[MoFe(\mu\text{-}CC_6H_3\text{ Me}2\text{-}2,6)(CO)_5(\eta\text{-}C_5H_5)]$, *Journal of the Chemical Society Dalton Transactions*, (9) (1988) 2453-2465.
- [12] Fernández J.R., Stone F.G.A., Chemistry of polynuclear metal complexes with bridging carbene or carbyne ligands. Part 83. Molybdenum and tungsten complexes containing the alkylidyne group $C\{\eta^6\text{-}C_6H_4(OMe\text{-}2)Cr(CO)_3\}$, *Journal of the Chemical Society Dalton Transactions*, (12) (1988) 3035-3040.
- [13] Hazra D., Sinha-Mahapatra D. K., Puranik V. G., Sarkar A., Synthesis and structure of novel, air-stable carbyne complexes of tungsten, *Journal of Organometallic Chemistry*, 671(1-2) (2003) 52-57.
- [14] Dennington R. D., Keith T. A., Millam C. M., GaussView 5.0 Wallingford. In CT, (2009).
- [15] Frisch M. J., Trucks G. W., Schlegel H. B., Scuseria G. E., Robb M. A., Cheeseman, J. R., Nakatsuji H., Gaussian 09, (Revision A. 1, Inc., Wallingford CT) (2009).
- [16] Becke A. D., Density - functional thermochemistry. I. The effect of the exchange-only gradient correction, *The Journal of Chemical physics*, 96(3) (1992) 2155-2160.
- [17] Lee C., Yang W., Parr R. G., Development of the Colle-Salvetti correlation-energy formula into a functional of the electron density, *Physical Review B*, 37(2) (1988) 785.
- [18] Karakaş D., Kariper S.E., Theoretical investigation on the vibrational and electronic spectra of three isomeric forms of dicobalt octacarbonyl, *Journal of Molecular Structure*, 1062 (2014) 77-81.

- [19] Gövdeli N., Karakaş D., Quantum chemical studies on hypothetical Fischer type $\text{Mo}(\text{CO})_5[\text{C}(\text{OEt})\text{Me}]$ and $\text{Mo}(\text{CO})_5[\text{C}(\text{OMe})\text{Et}]$ carbene complexes, *Journal of Molecular Structure*, 1163 (2018) 94-102.
- [20] Erkan S., Karakaş D., Computational investigation of structural, nonlinear optical and anti-tumor properties of dinuclear metal carbonyls bridged by pyridyl ligands with alkyne unit, *Journal of Molecular Structure*, 1199 (2020) 127054.
- [21] Mayr A., Hoffmeister H., Recent advances in the chemistry of metal-carbon triple bonds, *In Advances In Organometallic Chemistry*, 32 (1991) 227-324.
- [22] Jamróz M. H., Vibrational energy distribution analysis (VEDA): scopes and limitations, *Spectrochimica Acta Part A: Molecular and Biomolecular Spectroscopy*, 114 (2013) 220-230.
- [23] Majumdar D., Das S., Thomas R., Ullah Z., Sreejith S.S., Das D., Shukla P., Bankura K., Mishra D., Syntheses, X-ray crystal structures of two new Zn(II)-dicyanamide complexes derived from H₂vanen-type compartmental ligands: Investigation of thermal, photoluminescence, in vitro cytotoxic effect and DFT-TDDFT studies, *Inorganica Chimica Acta*, 492 (2019) 221-234
- [24] Bowser J. R., Inorganic Chemistry, Brooks, Cole Publishing Company, (1993) 721-725
- [25] Miessler G. L., Tarr D. A., Inorganic Chemistry, 2nd ed., New Jersey, Prentice Hall, (2003) 472-474.
- [26] Spasojevic-de Bire A., Dao N. Q., Fischer E. O., Hansen N.K., trans-Chlorotetracarbonyl (phenylmethylidyne) chromium: experimental electron deformation density, *Inorganic Chemistry*, 32(23) (1993) 5354-5361.
- [27] Pearson R. G., Absolute electronegativity and hardness: application to inorganic chemistry, *Inorganic Chemistry*, 27(4) (1988) 734-740.
- [28] Majumdar D., Agrawal Y., Thomas Y., Ullah Z., Santra M. K., Das S., Pal T.K., Bankura K., Mishra D., Syntheses, characterizations, crystal structures, DFT/TD-DFT, luminescence behaviors and cytotoxic effect of bicompartamental Zn (II)-dicyanamide Schiff base coordination polymers: An approach to apoptosis, autophagy and necrosis type classical cell death, *Applied Organometallic Chemistry*, 34(1) (2020) 5269.
- [29] Kose M., Hepokur C., Karakas D., McKee V., Kurtoglu M., Structural, computational and cytotoxic studies of square planar copper (II) complexes derived from dicyandiamide, *Polyhedron*, 117 (2016) 652-660.
- [30] Cohen E. R., Taylor B. N., The 1986 adjustment of the fundamental physical constants, *Reviews of Modern Physics*, 59(4) (1987) 1121.



Biosynthesis of silver nanoparticles from *Teucroside* and investigation of its antibacterial activity

Özlem KAPLAN¹, * , Nazan GÖKŞEN TOSUN²

¹Istanbul University, Department of Molecular Biology and Genetics, Faculty of Science, Istanbul, TURKEY

²Tokat Gaziosmanpaşa University, Graduate School of Natural and Applied Science, Department of Biomaterials and Tissue Engineering, Tokat, TURKEY

Abstract

Teucroside, 9'-decarboxyrosmarinic acid 4'-O- α -rhamnosyl-(1'' \rightarrow 6''')-O- β -galactosyl-(1'' \rightarrow 4''')-O- α -rhamnoside is a natural phenolic compound. It has been isolated and identified from the genus *Teucrium*. *Teucrium* genus is widely used in traditional medicine for its antioxidant, diuretic, antiulcer, antitumor, anti-inflammatory, antispasmodic and antibacterial properties. Since silver nanoparticles have superior physicochemical properties, they have an important role in biology and medicine. In this study, the biosynthesis of silver nanoparticles was carried out using *Teucroside* and AgNO₃. The effect of five independent variables (pH, AgNO₃ concentration, *Teucroside* volume/total volume, microwave power and time) on nanoparticle formation was evaluated using a central composite design (CCD) based response surface methodology (RSM). Nanoparticle formation was demonstrated by UV-Vis spectroscopy and FTIR analysis. The particle size and zeta potential of silver nanoparticles were determined by dynamic light scattering method (DLS). The results showed that 5 mM AgNO₃, *Teucroside* volume/total volume:0.3, 475 watt, 60 sec. and pH:7.5 were optimal reaction parameters. The antibacterial activity of biosynthesized silver nanoparticles was tested against common pathogens such as *Enterococcus faecalis*, *Pseudomonas aeruginosa*, *Staphylococcus aureus*, and *Klebsiella pneumonia*. Obtained results demonstrated that biosynthesized silver nanoparticles from *Teucroside* have great potential as a new antibacterial agent.

Article info

History:

Received:12.10.2020

Accepted:27.02.2021

Keywords:

Teucroside,
silver nanoparticle,
antibacterial activity.

1. Introduction

Silver nanoparticles (AgNPs) are very important metallic nanomaterials used in various applications due to their unique optical, electrical and biological properties [1]. The antimicrobial properties of AgNPs have made them widely used in medicine and agriculture [2, 3]. Because of the superior properties of AgNPs such as high antimicrobial activity even at low concentrations, their use reduces the environmental risk associated with excessive antibiotic or pesticide use [4-8]. Bacterial infection and resistance to antibiotics pose a serious threat to human health [9]. AgNPs exhibit adjustable structural properties and broad antibacterial spectrum advantages against antibiotic resistant bacteria. Thus, AgNPs are considered promising antibacterial agents [10]. Flavonoids, aromatic compounds, sugars, polyphenols found in plant extracts are functional groups involved in the biosynthesis of AgNPs [11, 12].

The *Teucrium* genus belongs to the *Lamiaceae* family and has about 300 species widespread all over the world [13]. Due to its pharmacological effects, various species of this genus are used widely in traditional medicine for their antioxidant, diuretic, antiulcer, antitumor, anti-inflammatory, antispasmodic and antibacterial properties [14]. Therefore, interest in *Teucrium* species has increased in recent years. One of the most studied species in the genus is *Teucrium chamaedrys* (germander). Phytochemical constituents of this species comprise flavonoids, diterpenoids and glycosides [13, 15]. Phenylethanoid glycosides are the main phenolic compounds in *Teucrium* species. Recently reports have shown the wide range of biological and pharmacological properties of these components. *Teucroside* (9'-decarboxyrosmarinic acid 4'-O- α -rhamnosyl-(1'' \rightarrow 6''')-O- β -galactosyl-(1'' \rightarrow 4''')-O- α -rhamnoside) is L-lyxose containing phenylethanoid glycoside found in *Teucrium* genus [13-16]. In this study, it is aimed to synthesize AgNPs in a fast, simple, environmentally friendly and low cost

*Corresponding author. e-mail address: ozlem.kaplan@istanbul.edu.tr

<http://dergipark.gov.tr/csj> ©2021 Faculty of Science, Sivas Cumhuriyet University

using *Teucroside*. The effects of experimental conditions on the biosynthesis of silver nanoparticles were investigated with response surface methodology, the most widely used statistical technique for process optimization [17, 18]. There are studies in the literature regarding the application of response surface methodology in the biosynthesis of AgNPs [19, 20]. The response surface methodology is a useful method for complete, rapid optimization of conditions and the correct design of the synthesis process. Also, antibacterial activity of the synthesized AgNPs was tested against common pathogens such as *Pseudomonas aeruginosa*, *Klebsiella pneumonia*, *Staphylococcus aureus* and *Enterococcus faecalis*.

2. Materials and Methods

2.1. Biosynthesis of silver nanoparticles and characterization

2.1.1. Extraction and identification of *Teucroside*

Teucroside was extracted, isolated and identified with methods which were explained in previous study by Dr. Elmastaş and his team [13].

2.1.2. Experimental design and optimization

Response surface methodology (RSM) based on a central composite design (CCD) was used to evaluate five independent variables (pH, AgNO₃ concentration, *Teucroside*/AgNO₃ ratio, microwave power and time) for the nanoparticle formation. Design Expert 12 software was used for regression and graphic analysis of the data. The experimental design consisted of 46 experiments for five independent variables. The absorbance data obtained from the UV-spectrum were used as optimization criteria. The experimental design along with the response was shown in Table 1.

Table 1. The central composite experimental design for *Teucroside*&AgNPs synthesis

Run	Factor 1 A:AgNO ₃ Conc. (mM)	Factor 2 B:Extract Vol./Total Vol.	Factor 3 C:Time(sec)	Factor 4 D:Power (Watt)	Factor 5 E:pH	Response % Yield
1	3	0.1	35	475	3	0
2	5	0.3	60	475	7.5	49.99
3	3	0.1	60	475	7.5	59.58
4	3	0.3	35	150	12	55.12
5	5	0.3	35	475	12	72.33
6	3	0.5	60	475	7.5	37.02
7	3	0.1	35	800	7.5	75.11
8	3	0.5	35	475	3	0
9	1	0.3	60	475	7.5	42.35
10	3	0.3	35	800	3	0
11	3	0.3	10	475	12	65.99
12	3	0.3	10	150	7.5	37.45
13	3	0.3	60	475	12	70.03
14	3	0.3	35	475	7.5	46.52
15	3	0.5	10	475	7.5	43.27
16	3	0.1	10	475	7.5	55.21
17	3	0.3	35	150	3	0
18	1	0.3	10	475	7.5	45.24
19	5	0.3	10	475	7.5	43.88
20	3	0.3	35	475	7.5	46.54
21	1	0.3	35	475	12	59.29
22	5	0.3	35	475	3	0
23	3	0.3	35	475	7.5	46.58
24	3	0.3	35	800	12	100
25	3	0.5	35	150	7.5	33.37
26	3	0.3	60	150	7.5	60.18
27	1	0.5	35	475	7.5	45.12
28	5	0.3	35	800	7.5	75.12
29	1	0.3	35	800	7.5	60.11
30	3	0.3	35	475	7.5	46.49
31	1	0.3	35	150	7.5	46.55
32	5	0.1	35	475	7.5	65.12
33	5	0.5	35	475	7.5	40.49
34	1	0.1	35	475	7.5	50.05
35	3	0.1	35	150	7.5	45.13
36	3	0.3	10	800	7.5	80.15
37	3	0.3	35	475	7.5	46.38
38	3	0.3	10	475	3	0
39	5	0.3	35	150	7.5	35.62
40	3	0.5	35	475	12	50.12
41	3	0.3	60	800	7.5	50.23
42	3	0.1	35	475	12	85.23
43	3	0.3	60	475	3	0
44	1	0.3	35	475	3	0
45	3	0.3	35	475	7.5	46.50
46	3	0.5	35	800	7.5	61.06

2.1.3. Synthesis and characterization of *Teucroside*&AgNPs

Teucroside aqueous solution (5% w/v) was prepared. The biosynthesis of AgNPs was carried out using different pH, AgNO₃ concentration, *Teucroside*/AgNO₃ ratio, microwave power and time. The mixture was centrifuged at 20.000 g for 10 minutes and AgNPs were precipitated. The AgNPs were washed with distilled water and they were dried overnight at 37°C. Biosynthesis of AgNPs were confirmed by UV-Vis spectroscopy and FTIR analysis. The particle size and zeta potential analysis of synthesized AgNPs were determined by dynamic light scattering method using HORIBA SZ-100 Nanoparticle Analyzer.

2.2. Antibacterial activity of *Teucroside*&AgNPs

Antibacterial activity was studied with two gram negatives bacterium (*Pseudomonas aeruginosa* (ATCC 27853) and *Klebsiella pneumonia* (ATCC 15380)) and two gram positive bacterium (*Enterococcus faecalis* (ATCC 29212) and *Staphylococcus aureus* (ATCC 25923)). The antimicrobial activity of AgNPs was analyzed by the minimum inhibitory concentration (MIC). Cultures were grown in exponential phase in nutrient broth at 37°C for 16 h. The various AgNPs concentrations (250 µg/ml–3.9 µg/ml) and *Teucroside* (250 µg/ml–3.9 µg/ml) were used for antimicrobial tests. The intensity of bacteria was standardized to equal a 0.5 McFarland

standard (approximately 5x10⁷ organisms ml⁻¹) for each concentration. The bacteria were then inoculated 96 well-plates and were incubated at 37°C for 24 h. After 24 h, the optical density of each well was recorded at 600 nm using a microplate reader [21]. The experiments were repeated three times, and the mean values were used.

3. Results and Discussion

3.1. Experimental design and optimization of biosynthesis of *Teucroside*&AgNPs

Design Expert 12 software was used to optimize the synthesis procedure of AgNPs. The experimental design consisted of 46 experiments for five independent variables (pH, AgNO₃ concentration, *Teucroside*/AgNO₃ ratio, microwave power and time). The absorbance data obtained from the UV-spectrum were used as optimization criteria. The acquired data coincided with the quadratic polynomial model and various statistical parameters were used to fit the analysis. After data modeling which is demonstrating the existence of interaction and curvature effect was performed, polynomial equation was generated for response factor. The data obtained overlap the empirical model with correlation coefficient (r²) values of 0.9898. The model diagnostic graphs for response are shown in Figure 1, showing that the data is parallel to the selected model.

$$\begin{aligned} \%Yield = & 46,504 + 2,07969 * A + -7,79367 * B + -0,126277 * C + 11,5005 * D + 34,5181 \\ & * E + -4,87543 * AB + 2,33788 * AC + 6,63818 * AD + 3,17526 * AE \\ & + -2,65788 * BC + -0,543163 * BD + -8,75 * BE + -13,25 * CD + 1,00232 \\ & * CE + 10 * DE + 0,305598 * A^2 + 1,61369 * B^2 + 1,11769 * C^2 + 6,85954 \\ & * D^2 + -14,46 * E^2 \end{aligned}$$

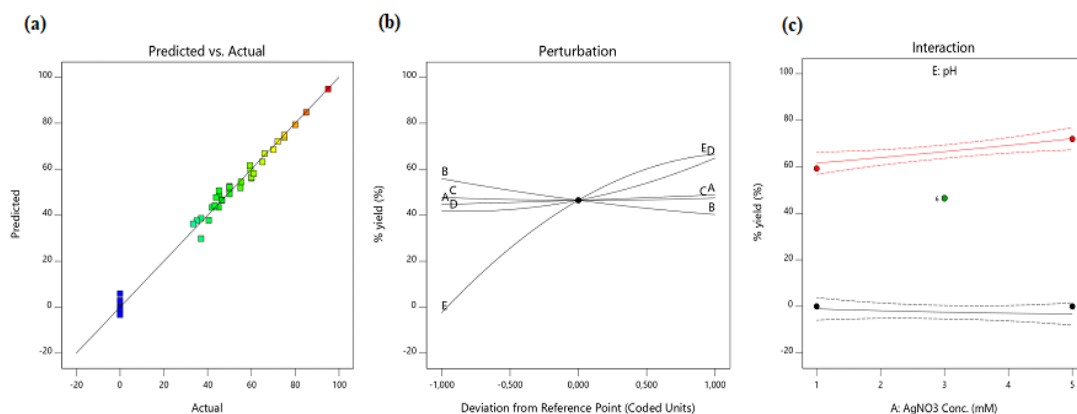


Figure 1. The graphs showing (a) predicted vs. actual plot, (b) perturbation chart, (c) interaction plot for response values

Response surface analysis was obtained using 3D response surface plots which elucidated the existence of interactions among the factors and their impacts on the response factor. 3D response surface plots of particle formation (% Yield) of synthesized AgNPs as a function of pH, AgNO₃ concentration, *Teucroside*/AgNO₃ ratio, microwave power and time are shown in Figure 2. It is seen that the effect of pH on the yield of nanoparticle formation is quite high (Figure 2 d, g, i, j). Nanoparticle formation is very low at acidic pH in all parameters. In all experiments where pH is above 7, it is seen that the increase in AgNO₃

concentration, *Teucroside*/AgNO₃ ratio, microwave power and time parameters increases the particle formation efficiency. The dependence of the nanoparticle formation rate on the pH of the solution has also been reported in the literature. According to these studies, nucleation of silver nanoparticles occurs in alkaline conditions, while nanoparticle aggregation is performed in acidic conditions. When examined in terms of nanoparticle efficiency, there was no nanoparticle formation in the acidic range, but it caused a gradual increase in nanoparticle production with the increase in pH [18, 22, 23].

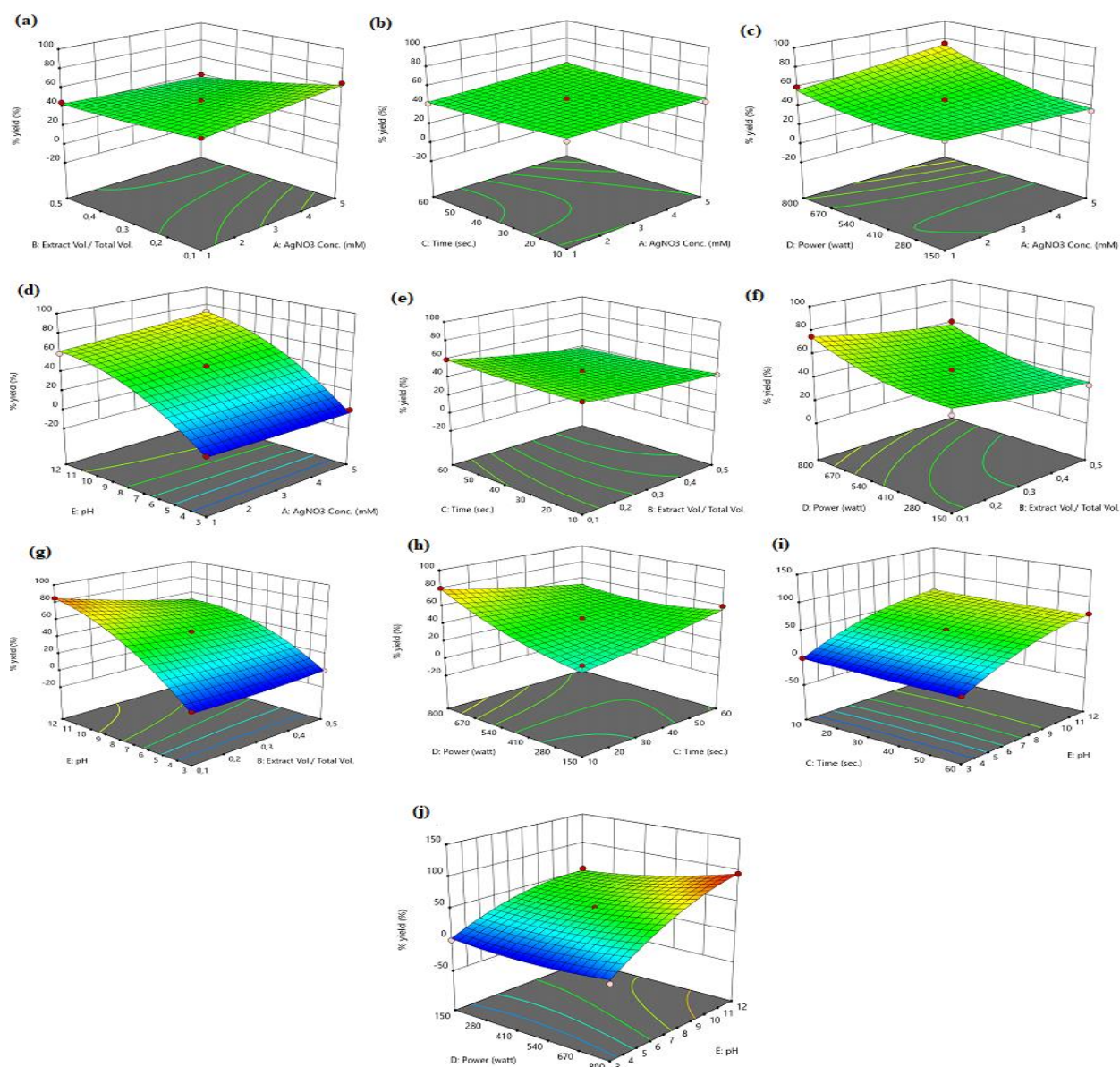


Figure 2. 3D response surface plots of particle formation (% Yield) of synthesized silver nanoparticles as a function of pH, AgNO₃ concentration, *Teucroside*/AgNO₃ ratio, microwave power and time. (a) AgNO₃ concentration and Extract vol./Total vol. (b). AgNO₃ concentration and time (c). AgNO₃ concentration and power (d) AgNO₃ concentration and pH (e) Extract vol./Total vol. and time (f) Extract vol./Total vol. and power (g) Extract vol./Total vol. and pH (h) Time and power (i) pH and time (j) pH and power.

The AgNPs were optimized and then their values were evaluated to identify with numerical optimization. It was seen that the desirability function value was close to 1 and the goal for the response variable was achieved. As the optimized silver nanoparticles

synthesis setting, the overlay plot showed the yellow color area as the optimized area along with the flagged point displaying 5 mM AgNO₃, *Teucroside* volume/total volume:0.3, 475 watt, 60 sec. and pH:7.5 were optimal reaction parameters in Figure 3.

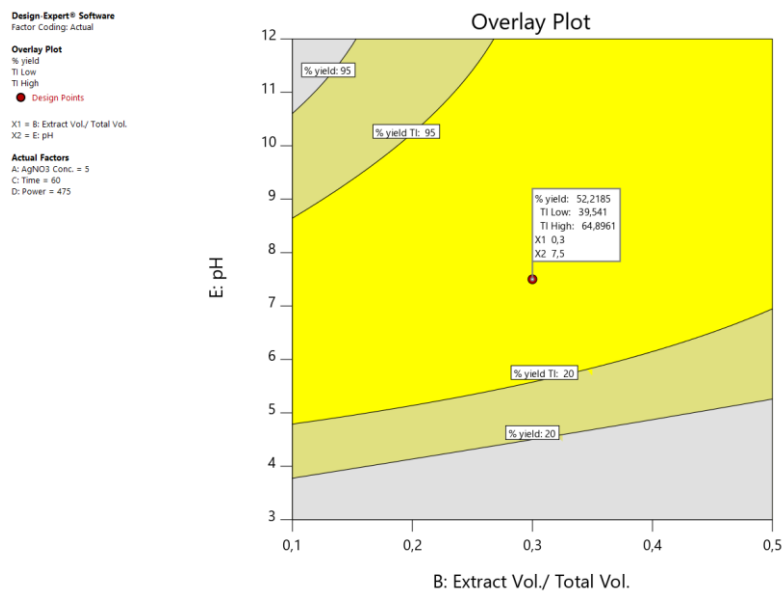


Figure 3. The graphs showing yellow color area as the optimized area and flagged point as the selected *Teucroside*&AgNPs

3.2. Characterization of *Teucroside*&AgNPs

The obtained AgNPs as a result of optimization were characterized by UV-VIS spectrophotometry and the result was shown in Figure 4. The spectrum indicating the peak was observed at 421 nm and this result was fitting with brownish color of the nanoparticles.

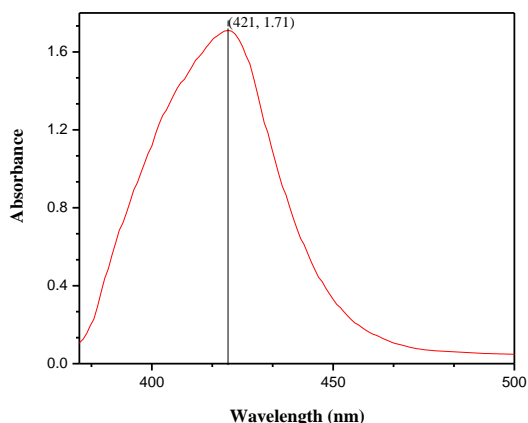


Figure 4. UV-Visible spectra of *Teucroside*&AgNPs

FTIR spectrum of the was shown in Figure 5. The significant absorption bands for silver nanoparticles were observed at 2901.38, 1630.52 and 1399.1. The optimized silver nanoparticles were exhibited a wide absorption band of –OH groups at 3268.75. The absorption bands at 2901.38 and 2986.23 were associated with C–H stretching of aliphatic –CH, –CH₂ groups. The absorption peaks at 1630.52 and 1399.1 were assigned to the asymmetrical and symmetrical –COO stretching of carboxylate compounds in *Teucroside*.

The size of the prepared silver nanoparticle was determined using dynamic light scattering as shown in Figure 6. The average size of the synthesized AgNPs was 165.9±3.1 nm. The nanoparticles showed homogeneous distribution (polydispersity index: 0.508±0.028). Also, the zeta potential value of the synthesized AgNPs was found to be -31.5±0.7 mV. A negative charge on the surface of the produced nanoparticles indicates that they have high stability.

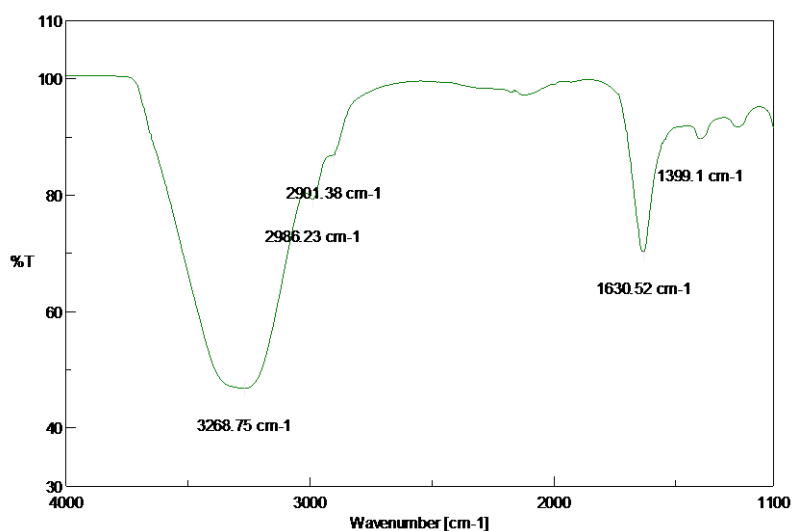


Figure 5. FTIR spectra of *Teucroside&AgNPs*

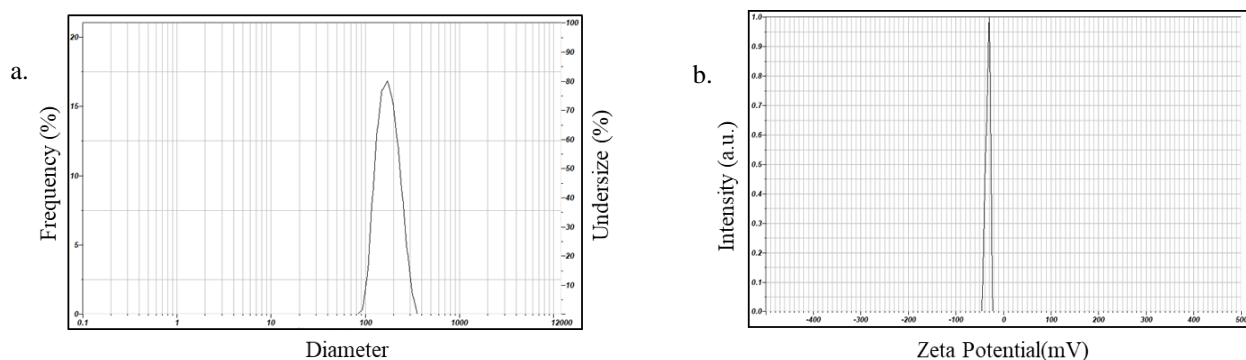


Figure 6. Dynamic light scattering (DLS) and zeta potential of *Teucroside&AgNPs* a. DLS of *Teucroside&AgNPs* and b. Zeta potential of *Teucroside&AgNPs*

3.3. Antibacterial activity of *Teucroside&AgNPs*

Growth inhibition curves of pathogenic microorganisms treated with *Teucroside* extract and *Teucroside&AgNPs* were shown in Figure 7. Our results show that the produced AgNPs have significant antimicrobial activity against different bacterial

strains. *Teucroside* concentration of 250 µg/ml inhibited just % 15 of the *K. pneumoniae* strain, % 2 of *S. aureus* strain and *P. aeruginosa* strain and there was no influence on *E. faecalis* strain (Figure 7a). However, the optimized *Teucroside&AgNPs* at concentration of 125 µg/ml completely inhibited all of the bacteria strains (Figure 7b).

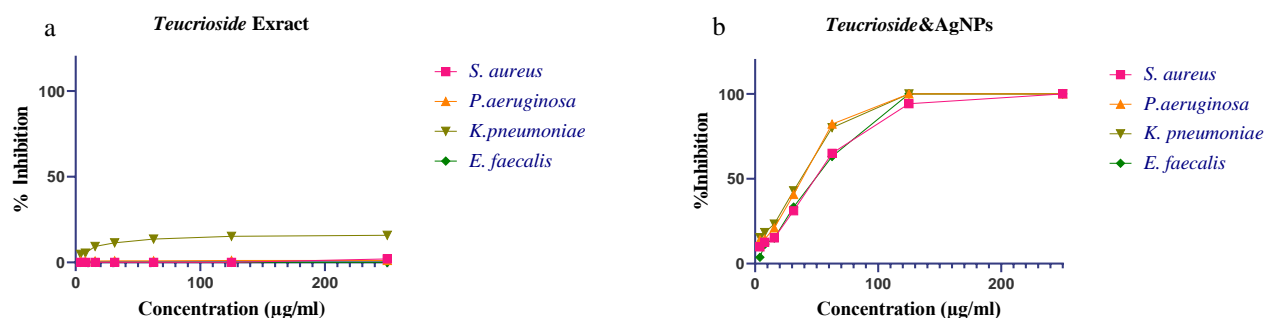


Figure 7. Growth inhibition curves of pathogenic microorganisms exposed to *Teucroside* extract and *Teucroside&AgNPs* a. Growth inhibition curves of pathogenic microorganisms exposed to *Teucroside* extract b. Growth inhibition curves of pathogenic microorganisms exposed to *Teucroside&AgNPs*

Minimum inhibitory concentrations (MIC) of the produced AgNPs were given in Figure 8. When the MIC values are examined, it is seen that *Teucroside*&AgNPs are effective on gram negative bacteria (*Pseudomonas aeruginosa* and *Klebsiella pneumonia*) than gram positive bacteria (*Enterococcus faecalis* and *Staphylococcus aureus*) at relatively lower concentrations. The more effective antimicrobial activity of silver nanoparticles against gram negative bacteria is likely due to their shape and size [24].

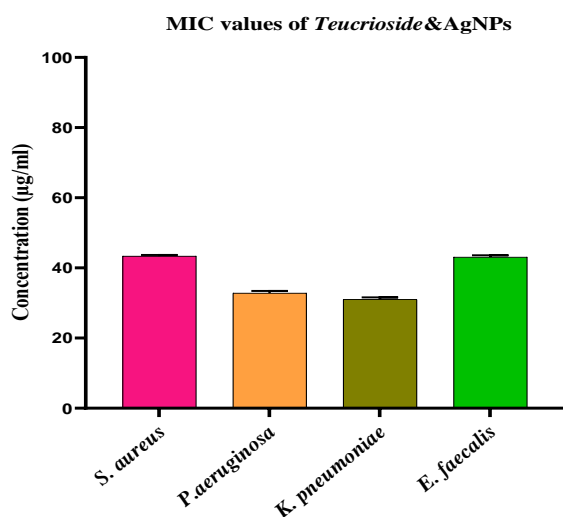


Figure 8. MIC value of *Teucroside*&AgNPs

MIC values of *Teucroside*&AgNPs were determined as 42.91 ± 6.85 µg/ml, 32.03 ± 8.36 µg/ml, 30.14 ± 8.848 µg/ml and 42.30 ± 6.75 µg/ml, respectively on *S. aureus*, *P. aeruginosa*, *K. pneumonia* and *E. faecalis*. There are numerous studies on the antimicrobial effects of synthesized silver nanoparticles from various biological materials. The obtained MIC values in our study are acceptable when compared to the previously stated concentrations of 10-100 µg/ml [2, 5, 6, 8, 25]. The results clearly demonstrated that *Teucroside*&AgNPs have strong antibacterial potential.

4. Conclusions

Silver nanoparticles have attractive physicochemical properties and are often used in biology and medicine because of these properties. Silver nanoparticles play an important role in the development of new antibacterial against pathogenic microorganisms. In this study, *Teucroside*&AgNPs were synthesized by *Teucroside* using as a biological reduction agent. The synthesized silver nanoparticles were systematically optimized by Design Expert 12.0 software. The experimental design consisted of 46 experiments for five independent variables (pH, AgNO₃ concentration, *Teucroside*/AgNO₃ ratio, microwave power and time). It was observed that the pH value was highly effective in the yield of nanoparticle formation. Also, an

increase in nanoparticle formation efficiency was observed with increasing AgNO₃ concentration, *Teucroside*/AgNO₃ ratio, microwave power and time. The optimum conditions were determined as 5 mM AgNO₃, *Teucroside* volume/total volume:0.3, 475 watt, 60 sec. and pH:7.5. The mean size and zeta potential of the synthesized AgNPs were 165.9 ± 3.1 nm and -31.5 ± 0.7 mV, respectively. The antibacterial activity of *Teucroside*&AgNPs and *Teucroside* were showed against gram positive and gram negative bacteria strains. Obtained results demonstrated *Teucroside*&AgNPs exhibit potential as a new antibacterial agent.

Acknowledgment

We would like to thank Prof. Dr. Mahfuz Elmastaş and his team for giving us the *Teucroside*.

Conflicts of interest

The authors declare that they have no conflict of interest.

References

- [1] Zhang X. F., Liu Z. G., Shen W., Gurunathan S., Silver Nanoparticles: Synthesis, Characterization, Properties, Applications, and Therapeutic Approaches., *Int J. Mol. Sci.*, 17 (2016) 1534-1568.
- [2] Das G., Patra J. K., Shin H. S., Biosynthesis and potential effect of fern mediated biocompatible silver nanoparticles by cytotoxicity, antidiabetic, antioxidant and antibacterial, studies, *Mater. Sci. Eng. C. Mater. Biol. Appl.*, 114 (2020) 111011.
- [3] Panacek A., Smekalova M., Vecerova R., Bogdanova K., Roderova M., Kolar M., Kilianova M., Hradilova S., Froning J. P., Havrdova M., Pucek R., Zboril R., Kvitek L., Silver nanoparticles strongly enhance and restore bactericidal activity of inactive antibiotics against multiresistant Enterobacteriaceae, *Colloids Surf B Biointerfaces*, 142 (2016) 392-399.
- [4] Wang Y., Li Z., Yang D., Qiu X., Xie Y., Zhang X., Microwave-mediated fabrication of silver nanoparticles incorporated lignin-based composites with enhanced antibacterial activity via electrostatic capture effect, *J. Colloid Interface Sci.*, 583 (2020) 80-88.
- [5] Elgamouz A., Idriss H., Nassab C., Bihi A., Bajou K., Hasan K., Abu Haija M., Patole S.P., Green Synthesis, Characterization, Antimicrobial, Anti-Cancer, and Optimization of Colorimetric Sensing of Hydrogen Peroxide of Algae Extract Capped Silver Nanoparticles, *Nanomaterials (Basel)*, 10 (2020).

- [6] Dube P., Meyer S., Madiehe A., Meyer M., Antibacterial activity of biogenic silver and gold nanoparticles synthesized from *Salvia africana-lutea* and *Sutherlandia frutescens*, *Nanotechnology*, 31 (2020) 505-607.
- [7] Alqahtani M. A., Al Othman M. R., Mohammed A. E., Bio fabrication of silver nanoparticles with antibacterial and cytotoxic abilities using lichens, *Sci. Rep.*, 10 (2020) 16781.
- [8] Garibo D., Borbon-Nunez H. A., de Leon J. N. D., Garcia Mendoza E., Estrada I., Toledano-Magana Y., Tiznado H., Ovalle-Marroquin M., Soto-Ramos A. G., Blanco A., Rodriguez J. A., Romo O. A., Chavez-Almazan L. A., Susarrey-Arce, A., Green synthesis of silver nanoparticles using *Lysiloma acapulcensis* exhibit high-antimicrobial activity, *Sci. Rep.*, 10 (2020) 12805.
- [9] Willyard C., The drug-resistant bacteria that pose the greatest health threats, *Nature*, 543 (2017) 15.
- [10] Xiu Z. M., Zhang Q. B., Puppala H. L., Colvin V. L., Alvarez P. J. Negligible particle-specific antibacterial activity of silver nanoparticles, *Nano Lett.*, 12 (2012) 4271-4275.
- [11] Dzul-Erosa M. S., Cauich-Diaz M. M., Razo-Lazcano T. A., Avila-Rodriguez M., Reyes-Aguilera J. A., Gonzalez-Munoz M. P., Aqueous leaf extracts of *Cnidioscolus chayamansa* (Mayan *chaya*) cultivated in Yucatan Mexico. Part II: Uses for the phytomediated synthesis of silver nanoparticles, *Mater. Sci. Eng. C. Mater. Biol. Appl.*, 91 (2018) 838-852.
- [12] Amooaghaie R., Saeri M. R., Azizi M., Synthesis, characterization and biocompatibility of silver nanoparticles synthesized from *Nigella sativa* leaf extract in comparison with chemical silver nanoparticles, *Ecotoxicol Environ. Saf.*, 120 (2015) 400-408.
- [13] Elmastas M., Erenler R., Isnac B., Aksit H., Sen O., Genc N., Demirtas I., Isolation and identification of a new neo-clerodane diterpenoid from *Teucrium chamaedrys* L., *Nat. Prod. Res.*, 30 (2016) 299-304.
- [14] Antognoni F., Iannello C., Mandrone M., Scognamiglio M., Fiorentino A., Giovannini P. P., Poli F., Elicited *Teucrium chamaedrys* cell cultures produce high amounts of teucroside, but not the hepatotoxic neo-clerodane diterpenoids, *Phytochemistry*, 81 (2012) 50-59.
- [15] Bedir E., Lata, H., Schaneberg B., Khan I. A., Moraes R. M., Micropropagation of *Hydrastis canadensis*: Goldenseal a North American endangered species, *Planta Med.*, 69 (2003) 86-88.
- [16] Erden Tayhan S., Bilgin S., Elmastaş M., Evaluation of the Wound Healing Potential of Teucroside, *Int. J. Chem. Technol.*, 2(1) (2018) 16-19.
- [17] Hormozi-Nezhad M. R., Robatjazi H., Jalali-Heravi M., Thorough tuning of the aspect ratio of gold nanorods using response surface methodology, *Anal Chim Acta*, 779 (2013) 14-21.
- [18] Nikaen G., Yousefinejad S., Rahmdel S., Samari F., Mahdavinia S., Central Composite Design for Optimizing the Biosynthesis of Silver Nanoparticles using *Plantago major* Extract and Investigating Antibacterial, Antifungal and Antioxidant Activity, *Sci. Rep.*, 10 (2020) 9642.
- [19] Hashemi S. H., Kaykhaii M., Jamali Keikha A., Sajjadi Z., Mirmoghaddam M., Application of response surface methodology for silver nanoparticle stir bar sorptive extraction of heavy metals from drinking water samples: a Box-Behnken design, *Analyst*, 144 (2019) 3525-3532.
- [20] Sivagnanam S. P., Getachew A. T., Choi J. H., Green Synthesis of Silver Nanoparticles from Deoiled Brown Algal Extract via Box-Behnken Based Design and Their Antimicrobial and Sensing Properties, *Green Process Synth.*, (2017) 147-160.
- [21] Wiegand I., Hilpert K., Hancock R. E., Agar and broth dilution methods to determine the minimal inhibitory concentration (MIC) of antimicrobial substances, *Nat Protoc.*, 3 (2008) 163-175.
- [22] Bhutto A. A., Kalay S., Sherazi S. T. H., Culha M., Quantitative structure-activity relationship between antioxidant capacity of phenolic compounds and the plasmonic properties of silver nanoparticles, *Talanta*, 189 (2018) 174-181.
- [23] Parthiban E., Manivannan N., Ramanibai R., Mathivanan N., Green synthesis of silver-nanoparticles from *Annona reticulata* leaves aqueous extract and its mosquito larvicidal and anti-microbial activity on human pathogens, *Biotechnol Rep.*, 21 (2019) 297-301.,
- [24] Manosalva N., Tortella G., Cristina Diez M., Schalchli H., Seabra A. B., Duran N., Rubilar O., Green synthesis of silver nanoparticles: effect of synthesis reaction parameters on antimicrobial activity, *World J. Microbiol. Biotechnol.*, 35 (2019) 88.
- [25] Mousavi S. M., Hashemi S. A., Ghasemi Y., Atapour A., Amani A. M., Savar Dashtaki A., Babapoor A., Arjmand O., Green synthesis of silver nanoparticles toward bio and medical applications: review study, *Artif Cells Nanomed. Biotechnol.*, 46 (2018) 855-872.



Palladium complexes of NO type Schiff bases: synthesis, characterization and antioxidant activities

Ayşegül ŞENOCAK * , Hüseyin AKBAŞ 

Tokat Gaziosmanpaşa University, Department of Chemistry, Tokat / TURKEY

Abstract

The reaction of o-aminophenol with para hydroxy and methoxy substituted benzaldehydes yielded two Schiff bases. These Schiff bases functioning precursors were turned into palladium complexes by treating palladium acetate. The structural formulas based on spectral methods (elemental analysis, FT-IR spectroscopy, NMR spectroscopy and QTOF-LC/MS spectroscopy) were suggested for obtained both complexes. According to the structural characterization methods, one of the complexes had also an acetate co-ligand along with the hydroxy substituted Schiff base ligand. In the other complex, the palladium central ion was proposed to be coordinated with two methoxy substituted Schiff bases. Besides, DPPH scavenging activities of the all synthesized compounds were determined and compared to well-known antioxidant standards. According to the results, antioxidant activities of the palladium complexes was mild but lower than parent Schiff bases.

Article info

History:

Received: 11.11.2020

Accepted: 17.03.2021

Keywords:

Schiff base,
o-aminophenol,
DPPH scavenging
activity,
palladium complex,
spectroscopic methods.

1. Introduction

Schiff bases are frequently studied compound group ever since Hugo Schiff reported preparation of the first example in 1864. Schiff bases, so called imines or azomethines, are of great importance due to their wide application areas varying from polymer, dye, pharmaceutical and food industry to agrochemical and sensor applications [1–13]. The structural stability and versatility in addition to easy synthesis of imine compounds induced gaining wide currency of this substance class. Among its various features, bioactivity of Schiff bases especially comes to the forefront in consequence of interactions and hydrogen bonds between the azomethine group and certain sites in the cell structure beside structural factors like solubility, dipole moment and cell permeability [14]. Also, electrons in sp^2 hybrid orbitals of azomethine nitrogen play a crucial role in biological applications [15].

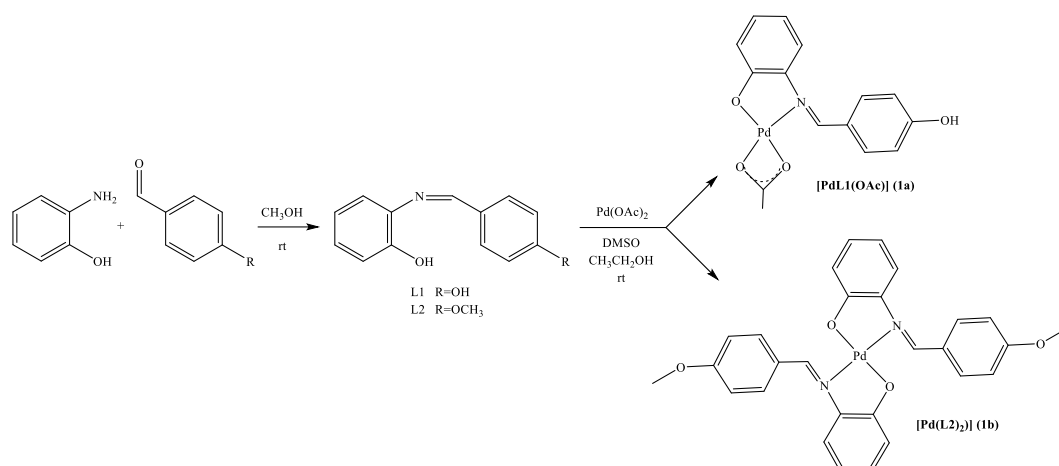
Schiff bases can effectively coordinate metal ions, especially if they contain electron donor groups such as -OH, -NH, -SH in positions proper for coordination in conjunction with azomethine group. Various transition metal ions like nickel(II), copper(II), zinc(II), palladium(II) etc. can be used to synthesize

complex structures with Schiff bases and resulted complexes have wide industrial and biological coverage. Among biological applications of Schiff base complexes, antibacterial, antioxidant, antifungal and anticancer activities can be mentioned [16–22].

Recently, researchers have been working extensively on natural-source or synthetic antioxidants to reduce the effect of oxidative stress on living cells. These antioxidant materials have protected the living cells by acting as free radical scavengers and metal chelators. There are many palladium Schiff base complexes synthesized for this purpose in the literature. It was stated that these complexes generally exhibited average antioxidant activity and antioxidant property of the complexes were greater than Schiff bases [23–26].

In this research, two new palladium complexes of NO type Schiff bases were prepared and proposed two different complex structures based on the results of spectroscopic methods (FT-IR, NMR, QTOF-LC/MS, elemental analysis) and previous studies [27,28]. DPPH scavenging activities of the synthesized compounds were determined. The compounds were compared to the standard antioxidants (Butylated hydroxyanisole (BHA), Butylated hydroxytoluene (BHT), Trolox and α -Tocopherol).

*Corresponding author. e-mail address: : aysegul.senocak@gop.edu.tr



Scheme 1. Reaction scheme for Schiff bases and palladium complexes along with proposed complex structures

2. Materials and Methods

2.1. Apparatus

All chemicals were used as received from commercial sources. The FT-IR spectra were measured by using a Jasco FT-IR 4700 spectrometer in the range of 400-4000 cm^{-1} . Elemental analyses were recorded on a Elementar Vario Micro Cube elemental analyzer. ^1H - and ^{13}C -NMR spectra of all imine compounds were saved using AC Bruker 400 MHz NMR spectrometer in CDCl_3 at ambient temperature. Mass spectra were obtained by using Agilent 6530 Accurate-Mass QTOF-LC/MS Spectrometer.

2.2. Synthesis of the Schiff bases

The synthesis of the Schiff bases was carried out according to the literature methods with slight modifications [29]. Methanol solutions of *o*-hydroxyaniline and benzaldehyde derivatives in equivalent amounts were mixed at room temperature. Reaction completion was followed by TLC method. When starting materials were all consumed, ethanol was evaporated and the product was extracted with chloroform for three times. The final product was dried with Na_2SO_4 , filtered and obtained as oily compounds. The structural characterization results were in harmony with the previous study [29].

2.3. Synthesis of the Palladium complexes (1a and 1b)

Schiff bases (1 mmol) and palladium acetate (1eq) solved in ethanol (20 mL) and DMSO (10 mL) was mixed in a round-bottom flask at room temperature. Red-brown precipitate was observed immediately. Reaction mixture was stirred for 48 hours at room temperature. After all of the Schiff base was consumed, the reaction mixture was filtered and obtained precipitate was washed with ethanol and diethyl ether.

[PdL1(OAc)] (1a): Yield 64%. FT-IR (cm^{-1}): 3568-3088 (O-H), 3055,3004 ($\text{C-H}_{\text{arom.}}$), 2927,2890 ($\text{C-H}_{\text{aliph.}}$), 1580 (C=O), 1538 (azomethine, C=N), 1296 (C-O); $^1\text{H-NMR}$ (DMSO- d_6 , δ , ppm): 2.08 (3H, s, CH_3 -acetate), 6.38-6.27 (4H, m, CH), 6.86-6.80 (2H, m, CH), 7.11 (1H, d, $^3J_{\text{H}}$ 8.21 Hz, CH), 7.21 (1H, d, $^3J_{\text{H}}$ 7.99 Hz, CH), 8.19 (1H, s, CH), 10.05 (1H, s, OH). $^{13}\text{C-NMR}$ (DMSO- d_6 , δ , ppm): 21.53, 112.06, 113.88, 116.82, 120.62, 122.26, 130.61, 131.68, 136.40, 145.08, 159.71, 161.20, 161.67, 171.30, 172.48. Anal. calcd. for $\text{C}_{15}\text{H}_{13}\text{NO}_4\text{Pd}$ (377.69 g/mol): C, 47.70; H, 3.47; N, 3.71. Found: C, 47.85; H, 3.63; N, 3.96%.

[Pd(L2) $_2$] (1b): Yield 58%. FT-IR (cm^{-1}): 3053 ($\text{C-H}_{\text{arom.}}$), 2995,2934,2833 ($\text{C-H}_{\text{aliph.}}$), 1537 (azomethine, C=N); $^1\text{H-NMR}$ (DMSO- d_6 , δ , ppm): 3.74 (6H, s, CH_3), 6.29-6.35 (6H, m, CH), 6.59-6.56 (2H, m, CH), 6.91-6.85 (4H, m, CH), 7.24-7.22 (4H, m, CH), 8.25 (2H, s, CH). $^{13}\text{C-NMR}$ (DMSO- d_6 , δ , ppm): 55.56 (2C), 109.72 (2C), 114.00 (2C), 117.09 (2C), 120.78 (2C), 121.10 (2C), 131.01 (2C), 131.33 (2C), 136.22 (2C), 146.90 (2C), 160.68 (2C), 160.93 (2C), 161.06 (2C), 171.61 (2C). Anal. calcd. for $\text{C}_{28}\text{H}_{24}\text{N}_2\text{O}_4\text{Pd}$ (558.93 g/mol): C, 60.17; H, 4.33; N, 5.01. Found: C, 59.93; H, 4.50; N, 5.22%.

2.4. Antioxidant activity

2.4.1. Preparation of samples and antioxidant standards

The antioxidant activities of the prepared phenolic Schiff bases and palladium complexes were determined by using some in vitro tests with intend to create the structure-activity connection. For this aim, all samples and well known antioxidant standards (BHA, BHT, trolox and α -tocoferol) were prepared as 1000 ppm stock solutions and diluted to specific concentrations before use.

2.4.2. DPPH scavenging activity

DPPH scavenging activities of the phenolic compounds were determined by decolorizing of purple-colored ethanol solution of 1,1-diphenyl-1-picrylhydrazyl (DPPH) as a result of treatment with test compounds [30]. The aliquots in four different concentrations (10-100 ppm) were prepared from the test compounds and the standards. 1 mL DPPH solution in 1 mM concentration was added to each aliquot prepared in 3 mL ethanol. The absorbance at 517 nm was measured against ethanol after 30 min of incubation in dark at room temperature. The inhibition activities were calculated by the following:

$$\%Inhibition = \left(1 - \frac{A_{sample}}{A_{control}}\right) \times 100 \quad (1)$$

3. Results and Discussion

Two new palladium Schiff base complexes were prepared by interacting o-aminophenol Schiff bases

with palladium acetate. The Schiff bases and the complexes were stable at room conditions. While the Schiff bases had high solubility in common alcohols (ethanol, methanol,...etc.) and organic solvents (CHCl₃, CH₂Cl₂,...etc.), the palladium complexes were soluble in DMSO, but had low solubility in common alcohols. The possible structural formulas for the complexes were proposed in accordance with elemental analysis, FT-IR, NMR (¹H- and ¹³C-) and QTOF-LC/MS data. According to the characterization methods, it is proposed that acetate ion behaved as a co-ligand to complete the coordination sphere in 1a while two Schiff base ligands formed the coordination environment in 1b.

3.1. FT-IR spectral studies

Figure 1 includes the FT-IR spectra of 1a and starting Schiff base L1, comparatively. The majority of the main groups belonging to the Schiff base were also observed in the spectra of the resulting palladium complexes with shifts in their positions.

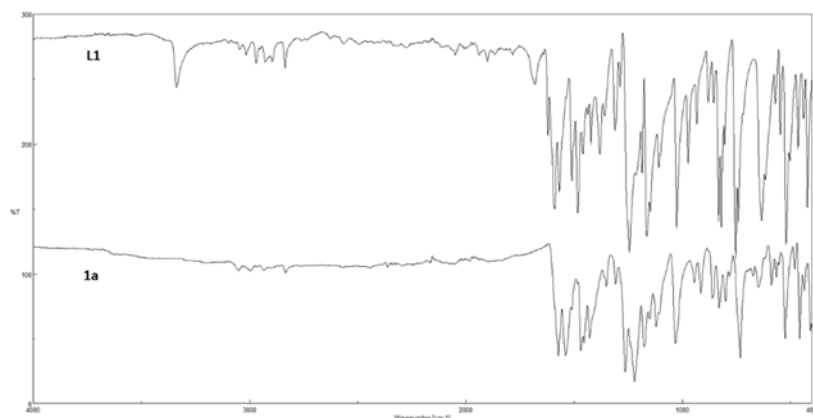


Figure 1. The FT-IR spectra of **1a** and **L1**.

All the Schiff bases and their palladium complexes exhibited similar spectra with little differences. In the spectrum of 1a, the sharp O-H stretching band around 3300 cm⁻¹ disappeared because of deprotonation of the hydroxyl group as a result of coordination. νC=N stretches of two palladium complexes between 1550-1650 cm⁻¹ shifted to lower wave numbers in harmony with the literature [32]. The involvement of the acetate group as co-ligand to the complex structure ended up with birth of two new bands in the spectra of the complex 1a: νC=O (1580 cm⁻¹) and νC-O (1296 cm⁻¹). Remaining characteristic groups like aliphatic and aromatic C-H groups, ether groups etc. were observed with expected shifts in the spectra of the synthesized compounds.

3.2. ¹H- and ¹³C-NMR spectral studies

NMR spectra of the palladium complex **1a** and starting Schiff base ligand L1 recorded in DMSO-d₆ at room temperature were shown in Figure 2. Full NMR data belonging to ¹H- and ¹³C-NMR were shown in the experimental section.

When the NMR spectra of 1a and L1 were compared, the formation of a new singlet at 2.08 ppm has drawn attention because of the participation of the acetate ligand to the coordination environment. Because only one of the two hydroxyl groups belonging to L1 ligand was deprotonated, a singlet pointing out the hydroxyl group was observed around 10 ppm in the spectrum of the complex 1a.

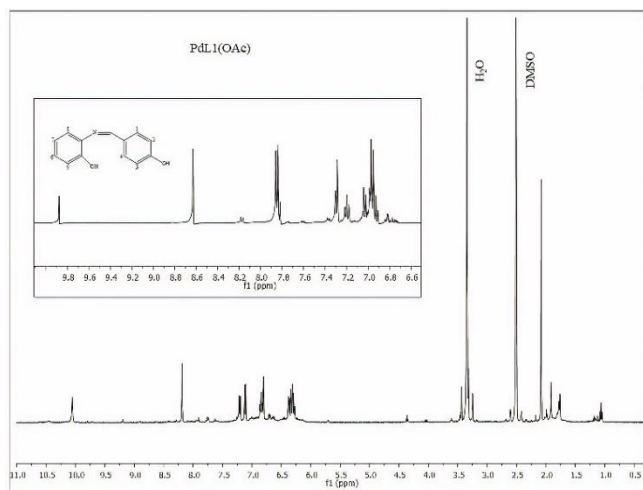


Figure 2. NMR spectra of **1a** and **L1** (inside window).

While the singlet at 8.19 ppm was designated to the azomethine proton, aromatic protons 1 and 2 appeared at 7.21 and 7.11 ppm as multiplets. Besides, the multiplet between 6.86 and 6.80 ppm was attributed to aromatic protons 6 and 7. When it comes to remaining aromatic protons, they overlapped in the range of 6.38 to 6.27 ppm. ^{13}C -NMR spectrum was verified the expected structure for **1a**, too. Imin carbon atom was observed at 171.31 ppm while methyl and carbonyl carbon peaks indicating the existence of acetate ligand appeared at 21.53 and 172.48 ppm. Other carbons appeared in the area expected for aromatic carbons.

Figure 3 demonstrates the NMR spectra of the complex **1b** and Schiff base **L2** measured in DMSO- d_6 at ambient temperature. Full NMR data belonging to ^1H - and ^{13}C -NMR were shown in the experimental section. Two singlet peaks at 3.74 ppm and 8.25 ppm in the spectrum were induced by methoxy and imin protons, respectively.

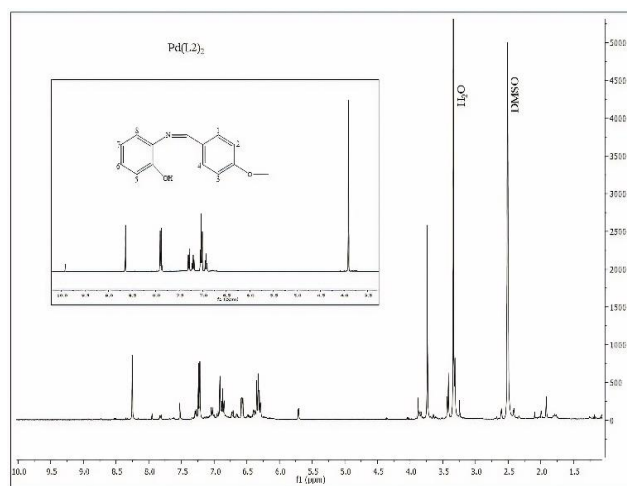


Figure 3. NMR spectra of **1b** and **L2** (inside window).

Aromatic ring protons were observed similar ways and range with complex **1a**, as expected. While the resonances belonging to aromatic protons 3 and 4 appeared at 7.24-7.22 ppm interval, the multiplet in the range of 6.91 to 6.85 ppm pointed out 6 and 7. ^{13}C -NMR spectrum was verified the structure, too. Imin carbon and methoxy carbon were observed at 171.61 and 55.56 ppm, respectively. Other carbons appeared in the area expected for aromatic carbons.

3.3. Mass spectral studies

QTOF-LC/MS spectra of the palladium complexes were consistent with proposed formulas. In the spectra of the both complexes, a signal corresponding to $[\text{Pd}(\text{PhNH}_2\text{OH})(\text{DMSO})]$ fragment at 294 was observed because of the usage of DMSO as solvent in the QTOF-LC/MS spectra (Figure 4). Also, the peak appeared at 228 in the spectrum of **1b** was attributed to the Schiff base **L2**. While the molecule ion peak was found at 558 for **1b**, **1a** had a molecular ion peak at 360 in response to $[\text{PdL1}(\text{OAc})\text{-OH}]$ fragment.

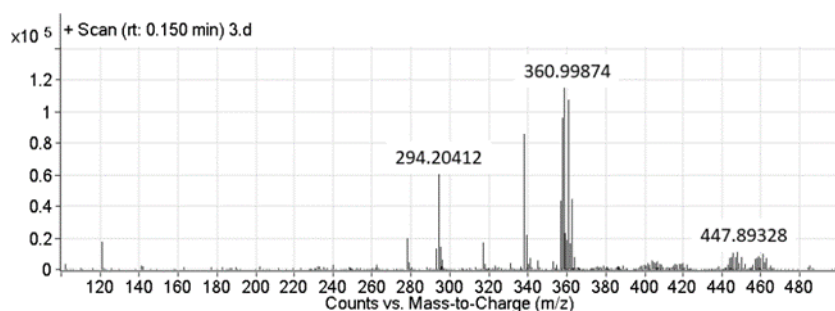


Figure 4. QTOF-LC/MS spectra of **1a**.

3.4. Antioxidant activity studies

Antioxidant activities of the synthesized compounds were expressed by the IC_{50} value which is the concentration that can scavenge %50 of a free radical.

Calculated IC_{50} values of the compounds were compared with well-known positive controls BHA, BHT and α -Tocopherol and tabulated in Table 1.

Table 1. IC50 values of the test compounds for DPPH scavenging assay

Test compounds	IC50
L1	19.21
Complex 1a	57.77
L2	10.48
Complex 1b	80.20
BHA	5.42
BHT	5.97
Trolox	13.66
α -tocopherol	4.39

The antioxidant capacities of the Schiff bases and their palladium complexes were examined by DPPH scavenging assay. DPPH scavenging activity has a great importance because the compounds exhibiting DPPH scavenging activity are the anticancer and the anti-inflammatory agents as well [33]. For this reason, these type compounds have been attracting attention as potential anticancer drugs. According to the results of DPPH assay, L1 and L2 exhibited great scavenging activity towards DPPH (for L2 even greater than Trolox standard). When it comes to complexes 1a and 1b, it appeared that the complexation had a negative effect on DPPH scavenging activities of Schiff bases L1 and L2. Nevertheless, 1a and 1b had mild activity to scavenge DPPH. This finding is also in accordance with a previous study revealing the close relationship between redox and antioxidant properties of the metal complexes [34].

4. Conclusions

In conclusion, two Schiff bases derived from o-aminophenol were converted to palladium complexes by reacting palladium acetate in this study. The combined evaluation of the structural characterization methods (FT-IR, ^1H - and ^{13}C -NMR, elemental analysis, QTOF-LC/MS) revealed two different formulas for synthesized palladium complexes. An acetate ligand was coordinated to palladium ion in combination with Schiff base ligand L1 in complex 1a. When it comes to 1b, coordination sphere was composed of two Schiff base ligand L2. Antioxidant capacities of the prepared complexes were determined by DPPH scavenging assay. The results exhibited good antioxidant activity for the Schiff base ligands L1 and L2 compared to well-known antioxidant standards BHA, BHT, Trolox and Alpha-tocopherol. The scavenger capacities of the prepared palladium complexes were mild.

Conflicts of interest

The authors state that did not have conflict of interests

References

- [1] Baran T., Menten A., Polymeric material prepared from Schiff base based on o carboxymethyl chitosan and its Cu(II) and Pd(II) complexes, *J. Mol. Struct.*, 1115 (2016) 220-227.
- [2] Nair B.P., Gangadharan D., Mohan N., Sumathi B., Nair P.D., Hybrid scaffold bearing polymer-siloxane Schiff base linkage for bone tissue engineering, *Mater. Sci. Eng. C.*, 52 (2015) 333-342.
- [3] Erdem E., Yildirim Sari E., Kilincarslan R., Kabay N., Synthesis and characterization of azo-linked Schiff bases and their nickel(II), copper(II), and zinc(II) complexes, *Trans. Met. Chem.*, 34 (2009) 167-174.
- [4] Ispir E., The synthesis, characterization, electrochemical character, catalytic and antimicrobial activity of novel, azo-containing Schiff bases and their metal complexes, *Dyes Pigments*, 82 (2009) 13-19.
- [5] Fakhari A.R., Khorrami A.R., Naeimi H., Synthesis and analytical application of a novel tetradentate N2O2 Schiff base as a chromogenic reagent for determination of nickel in some natural food samples, *Talanta*, 66 (2005) 813-817.
- [6] Laddha P.R., Biyani K.R., Synthesis and Biological Evaluation of Novel Schiff Bases of Aryloxy Moiety, *J. Drug Deliv.*, 9 (2005) 44-49.
- [7] Dewangan D., Nakhate K.T., Verma V.S., Nagori K., Tripathi D.K., Synthesis, Characterization, and Screening for Analgesic and Anti-Inflammatory Activities of Schiff Bases of 1,3,4-Oxadiazoles Linked With Quinazolin-4-One, *J. Heterocycl. Chem.*, 54 (2017) 3187-3194.
- [8] Amorim C.R., Pavani T.F.A., Lopes A.F.S., Duque M.D., Mengarda A.C.A., Silva M.P., de Moraes J., Rando D.G.G., Schiff bases of 4-Phenyl-2-Aminothiazoles as hits to new antischistosomes: Synthesis, in vitro, in vivo and in silico studies, *Eur. J. Pharm. Sci.*, 150 (2020) 105-371.
- [9] Kumar B.D., Rawat D.S., Synthesis and antioxidant activity of thymol and carvacrol based Schiff bases, *Bioorg. Med. Chem. Lett.*, 23 (2013) 641-645.

- [10] Albayrak Kastas C., Kastas G., Guder A., Gur M., Muglu H., Buyukgungor O., Investigation of two o-hydroxy Schiff bases in terms of prototropy and radical scavenging activity, *J. Molec. Struct.*, 1130 (2017) 623-632.
- [11] Fernandes S.A., Tavares E.C., Teixeira R.R., da Silva C.M., Montanari R.M., de Fatima A., Anconi C.P.A., de Almeida W.B., dos Santos H.F., Silva A.A., Inclusion complexes of Schiff bases as phyto-growth inhibitors, *J. Incl. Phenom. Macro*, 75 (2013) 197-204.
- [12] Gupta V.K., Singh A.K., Ganjali M.R., Norouzi P., Mergu N., Comparative study of colorimetric sensors based on newly synthesized Schiff bases Sensor, *Actuat. B-Chem.*, 182 (2013) 642-651.
- [13] Berhanu A.L., Gaurav Mohiuddin I., Malik A.K., Aulakh J.S., Kumar V., Kim K.-H., A review of the applications of Schiff bases as optical chemical sensors, *Trend. Anal. Chem.*, 116 (2019) 74-91.
- [14] Deivanayagam P., Bhoopathy P., Thanikaikarasan S., Synthesis, characterization, antimicrobial, analgesic and CNS studies of Schiff base Cu(II) complex derived from 4-chloro-phenylene Diamine, *Int. J. Adv. Chem.*, 2 (2014) 166-170.
- [15] Yu Z., Kuroda-Sowa T., Kume H., Okubo T., Maekawa M., Munakata M., Effects of Metal Doping on the Spin-Crossover Properties of an Iron(II) Complex with Extended pi-Conjugated Schiff-Base Ligand Having an N4O2 Donor Set, *B. Chem. Soc. Jpn.*, 82 (2009) 333-337.
- [16] Fathi A.M., Mandour H.S., Anouar H., Characteristics of multidentate Schiff base ligand and its complexes using cyclic voltammetry, fluorescence, antimicrobial behavior and DFT-calculations, *J. Molec. Struct.*, 1224 (2021) 129263-129271.
- [17] El-Sherif A.A., Eldebss T.M.A., Synthesis, spectral characterization, solution equilibria, in vitro antibacterial and cytotoxic activities of Cu(II), Ni(II), Mn(II), Co(II) and Zn(II) complexes with Schiff base derived from 5-bromosalicylaldehyde and 2-aminomethylthiophene, *Spectrochim. Acta*, 79A (2011) 1803-1814.
- [18] Abu-Dief A.M., Nassr L.A.E., Tailoring, physicochemical characterization, antibacterial and DNA binding mode studies of Cu(II) Schiff bases amino acid bioactive agents incorporating 5-bromo-2-hydroxybenzaldehyde, *J. Iran. Chem. Soc.*, 12 (2015) 943-955.
- [19] Elsayed S.A., El-Gharabawy H.M., Butler I.S., Atlam F.M., Novel metal complexes of 3-acetylcoumarin-2-hydrazinobenzothiazole Schiff base: Design, structural characterizations, DNA binding, DFT calculations, molecular docking and biological studies, *Appl. Organomet. Chem.*, 34 (2020) 5643-5661.
- [20] Szady-Chełmieniecka A., Rzuchowska A., Markowska-Szczupak A., Schilf W., Rozwadowski Z., New "one-pot" Pd(II) and Zn(II) complexes of Schiff bases, derivatives of 1-amino-1-deoxy-D-sorbitol: Spectroscopic studies and biological and catalytic activities, *Appl. Organomet. Chem.*, 34 (2020) 5485-5492.
- [21] Mbugua S.N., Sibuyi N.R.S., Njenga L.W., Odhiambo R.A., Wandiga S.O., Meyer M., Lalancette R.A., Onani, M.O., New Palladium(II) and Platinum(II) Complexes Based on Pyrrole Schiff Bases: Synthesis, Characterization, X-ray Structure, and Anticancer Activity, *ACS Omega* 5, (2020) 14942-14954.
- [22] Satheeshkumar R., Wu J., Chandrasekaran R., Revathi K., Sparkes H.A., Wang W.L., Synthesis of 2-aminobenzophenone-based Schiff base Pd(II) complexes: Investigation on crystal structure, biological behavior of DNA/protein-binding, molecular docking, and in vitro anticancer activities, *Appl. Organomet. Chem.*, 34 (2020) e5856-5870.
- [23] Jirjees V.Y., Suleman V.T., Ahmed S.D., Al-Hamdani A.A.S., Determination Of Antioxidant Activity For Metal Ions Complexes, *J. Univ. Duhok*, 32 (2020) 41-50.
- [24] Said M.A., Al-Unizi A., Al-Mamary M., Alzahrani S., Lentz D., Easy coordinate geometry indexes, τ_4 and τ_5 and HSA study for unsymmetrical Pd(II), Fe(II), Zn(II), Mn(II), Cu(II) and VO(IV) complexes of a tetradentate ligand: Synthesis, characterization, properties, and antioxidant activities, *Inorg. Chim. Acta*, 505 (2020) 119434-119446.
- [25] Aly S.A., Fathalla S.K., Preparation, characterization of some transition metal complexes of hydrazone derivatives and their antibacterial and antioxidant activities, *Arab. J. Chem.*, 13 (2020) 3735-3750.
- [26] Bingöl M., Turan N., Schiff base and metal(II) complexes containing thiophene-3-carboxylate: Synthesis, characterization and antioxidant

- activities, *J. Molec. Struct.*, 1205 (2020) 127542-127550.
- [27] Robinson S.D., Uttley M.F., Complexes of the Platinum Metals. Part 11.1 Carboxylato(triphenylphosphine) Derivatives of Ruthenium, Osmium, Rhodium, and Iridium, *J. Chem. Soc., Dalton Trans.*, 1912 (1973) 1912-1920.
- [28] Faghih Z., Neshat A., Wojtczak A., Faghih Z., Mohammadi Z., Varestan S., Palladium (II) Complexes Based on Schiff Base Ligands Derived from Ortho-vanillin; Synthesis, Characterization and Cytotoxic Studies, *Inorg. Chim. Acta.*, 471 (2018) 404-412.
- [29] Lu J., Li C., Chai Y.F., Yang D.Y., Sun C.R., The antioxidant effect of imine resveratrol analogues, *Bioorg. & Med. Chem. Lett.*, 22 (2012) 5744-5747.
- [30] Blois M.S., Antioxidant Determinations by the Use of a Stable Free Radical, *Nature*, 26 (1958) 1199-1200.
- [31] Dinis T.C.P., Madeira V.M.C., Almeida L.M., Action of Phenolic Derivatives (Acetaminophen, Salicylate and 5-Aminosalicylate) as Inhibitors of Membrane Lipid Peroxidation and as Peroxyl Radical Scavengers, *Arch. Biochem. Biophys.*, 315 (1994) 161-169.
- [32] Ravoof T.B.S.A., Crouse K.A., Tahir M.I.M., Cowley A.R., Ali M.A., Synthesis, characterization and bioactivity of mixed-ligand Cu(II) complexes containing Schiff bases derived from S-benzylthiocarbamate and saccharinate ligand and the X-ray crystal structure of the copper-saccharinate complex containing S-benzyl-b-N-(acetylpyrid-2-yl)methylenedithiocarbamate, *Polyhedron*, 26 (2007) 1159-1165.
- [33] Kontogiorgis C., Hadjipavlou-Litina D., Biological evaluation of several coumarin derivatives designed as possible anti-inflammatory/antioxidant agents, *J. Enzyme Inhib. Med. Chem.*, 18 (2003) 63-69.
- [34] Tyurin V.Y., Moiseeva A.A., Shpakovsky D.B., Milaeva E.R., The electrochemical approach to antioxidant activity assay of metal complexes with dipicolylamine ligand, containing 2,6-di-tert-butylphenol groups, based on electrochemical DPPH-test, *J. Electroanal. Chem.*, 756 (2015) 212-221.



Numerical solution of the brusselator model by time splitting method

Sıla Övgü KORKUT^{1,*} , Yeşim ÇİÇEK¹ 

¹Izmir Katip Celebi University, Department of Engineering Sciences, IZMIR/TURKEY

Abstract

One of the significant models in chemical reactions with oscillations is the Brusselator model. This model essentially describes a nonlinear reaction-diffusion equation. Brusselator system arises in applications of many physical and chemical models. In this study, the Brusselator model is solved numerically with the help of a time-splitting method. Consistency and stability of the method are proved with the help of auxiliary lemmas. Additionally, the positivity preservation of the method is analyzed. The accuracy of the presented method is also tested on numerical examples and all theoretical results are supported by the tables and figures.

Article info

History:

Received:27.02.2020

Accepted:16.12.2020

Keywords:

Local error analysis,
Brusselator model,
Splitting method,
Non-linear partial
differential equation,
Reaction-Diffusion
equation

1. Introduction

Reaction-diffusion models have great importance in the study of chemical and biological systems. One of the main important reaction-diffusion equations is known as the Brusselator system, which is used to describe the mechanism of chemical reaction-diffusion with non-linear oscillations [1-4]. In 1952 Turing [5] showed the importance of oscillations in biochemical systems that leads to the theory of morphogenesis. The Brusselator system occurs in a large number of physical problems such as the formation of ozone by atomic oxygen through a triple collision and enzymatic reactions. In 1968 Prigogine and Lefever proposed the system and the name was coined by Tyson in [6]. In the middle of the last century, Belousov and Zhabotinsky discovered chemical systems exhibiting oscillations.

The non-linear two-dimensional reaction-diffusion Brusselator system is given by [7]

$$\frac{\partial u}{\partial t} = \alpha \Delta u + B + u^2 v - (A + 1)u \quad (1)$$

$$\frac{\partial v}{\partial t} = \alpha \Delta v + Au - u^2 v, \quad (2)$$

for $u(x, y, t)$ and $v(x, y, t)$ in the two-dimensional region, $\Omega = [a, b]^2$, with initial condition

$$(u(x, y, 0), v(x, y, 0)) = (p(x, y), q(x, y)),$$

and Dirichlet boundary condition

$$(u(x, y, t), v(x, y, t)) = (M(x, y, t), N(x, y, t)) \quad \text{for } (x, y) \in \partial\Omega, \quad t > 0$$

or subject to Neumann's boundary conditions on the boundary $\partial\Omega$. Here $u(x, y, t)$ and $v(x, y, t)$ represent dimensionless concentrations of two reactants, A and B are constants concentrations of two reactants, α is diffusion coefficient, Δ is Laplace operator, and $p(x, y)$, and $q(x, y)$ are suitably prescribed functions.

The numerical solution of the reaction-diffusion Brusselator system has been an important area of research. There is limited literature on the numerical solution of the Brusselator system. A decomposition method is applied for

*Corresponding author. email address: silaovgu@gmail.com.

the numerical solution of the reaction-diffusion Brusselator system in [8]. Twizell et al. [9] developed a second-order (in space and time) finite difference method for a diffusion-free Brusselator system. The modified Adomain decomposition method is applied by Wazwaz in [10]. Ang, in [7] presented the dual-reciprocity boundary element method for the numerical solution of the reaction-diffusion Brusselator system. In [11] the authors proposed a modified cubic B-spline differential quadrature method to show computational modeling of a two-dimensional Brusselator system for Neumann's boundary conditions. A polynomial based differential quadrature method is employed for numerical solutions of two-dimensional nonlinear reaction-diffusion Brusselator system in [12]. A meshless method has been suggested in [13] to obtain a numerical solution of the mentioned system. Another meshfree method based on the radial basis functions has been presented in [14]. Furthermore, more recently, a finite element approach has been applied to several chemical reaction-diffusion equations including the Brusselator system in [15-16] by Yadav and Jiware. Also, a meshfree algorithm based on radial basis multiquadric functions and differential quadrature (DQ) technique has been developed to approximate the numerical solution of the Brusselator system in [17]. Bhatt and Chowdhury have presented a comparative study of performances of meshfree (radial basis functions) and mesh-based (finite difference) schemes in terms of their accuracy and computational efficiency for solving multi-dimensional Brusselator system in [18]. Moreover, several chemical systems including a two-dimensional Brusselator model have been studied in [19]. All mentioned researches take into account space discretization. Even though the authors in [19] suggest a kind of splitting method, they utilize the method as dimensional splitting to get one-dimensional problems. Unlike their study, we focus on a kind of splitting method for separating the operators concerning their linearity structure. Our purpose is not underestimating that study but considering the problem from a different angle.

The main aim of the present study is that the Lie-Trotter splitting method which is a well-known first-order time splitting method is applied for the numerical solution of Equation 1-2. The essential idea of the splitting methods is that instead of the sum, the operators are considered separately. This means that the original problem is split into sub-problems and the numerical solution of the original problem is obtained from a combination of numerical solutions of these sub-problems. The reader interested in the splitting methods can see [20-23] and the references therein. One of the important advantages of these methods is that the operators with different structures can be solved by different methods. Moreover, employing the splitting idea, some operators can be solved exactly which can increase the reliability of the solution. This is one of our purposes. The other purpose is to preserve some physical behavior such as positivity, stability, and preserving the dynamics of the system.

The paper is organized as follows: Section 2 is devoted to introducing the idea of the time splitting for Equation 1-2. All theoretical results such as consistency and stability are presented in this section. For consistency and stability analyses, the auxiliary lemmas are utilized. Furthermore, the preservation of the positivity of the proposed method has been shown in the current section. In section 3, we apply the proposed scheme to different types of problems related to the reaction-diffusion Brusselator system in both one- and two- dimensional cases. The obtained numerical solutions are tested in both compatibility and accuracy. The theoretical claims are supported by simulations and tables. Finally, Section 4 concludes the study.

2. Materials and Methods

In this section, we introduce the Lie-Trotter splitting method (LSM) for the Brusselator model given in Equation 1-2. For this purpose, we first set up the equations given in Equation 1-2 with the appropriate system form.

$$u_t = \alpha \Delta u + f(u, v) \quad (3)$$

$$v_t = \alpha \Delta v + g(u, v) \quad (4)$$

where $f(u, v) = B + u^2v - (A + 1)u$ and $g(u, v) = Au - u^2$ are scalar functions and the operator Δ corresponds to the spatial derivatives. Equation 3-4 turn into system form as follows:

$$\begin{bmatrix} u_t \\ v_t \end{bmatrix} = \alpha \begin{bmatrix} \Delta & \mathbf{0} \\ \mathbf{0} & \Delta \end{bmatrix} \begin{bmatrix} u \\ v \end{bmatrix} + \begin{bmatrix} f(u, v) \\ g(u, v) \end{bmatrix} \quad (5)$$

Throughout the section, we denote $(u, v)^T$ by the variable Y for the sake of simplicity of the notations. Thus, Equation 5 can be expressed as follows:

$$Y_t = \alpha DY + F(Y), \quad Y(t): \mathbb{D}(D) \cap \mathbb{D}(F(Y)) \rightarrow X \tag{6}$$

where $\mathbb{D}(D): C^2(\Omega)$, and $\mathbb{D}(F(Y)): C^1(\Omega \times [0, t_{end}])$ and X is a Banach space. As mentioned previously, the essential idea of the time splitting methods is that instead of the sum, the operators are considered separately. To do this, the original problem is divided into sub-problems and they are solved efficiently by an appropriate numerical method. The connections of these sub-problems are via the initial conditions. That is,

$$Y_{t,1} = \alpha DY_1, \quad Y_1(t_n) = Y(t_n) \quad \forall t \in [t_n, t_{n+1}], \tag{7}$$

$$Y_{t,2} = F(Y_2), \quad Y_2(t_n) = Y_1(t_{n+1}) \quad \forall t \in [t_n, t_{n+1}], \tag{8}$$

where Y_1 and Y_2 denote the sub-problems and t_n denotes the present time whereas t_{n+1} does the future. Moreover, matrix D stands for the matrix consisting of spatial derivative operators. Such splitting leads to two initial value problems which will be solved sequentially. Due to the linearity of Equation 7, the exact solution of this part is already known. However, an efficient solver will be used to obtain a solution of Equation 8, numerically, which will be stored as the approximated one, i. e. $Y(t_{n+1}) = Y_2(t_{n+1})$. By the nonlinearity of Equation 8, a predictor-corrector method is the correct choice to obtain the approximate solution. In the current study, we utilize Heun's method to obtain the approximate solution for the non-linear part. For the sake of simplicity of notations, Heun's method can be expressed on the non-linear part as follows:

$$Y_2(t_{n+1}) = Y_2(t_n) + \frac{\Delta t}{2} \left(F(Y_2(t_n)) + F(Y_2(t_n) + \Delta t F(Y_2(t_n))) \right), \forall t \in [t_n, t_{n+1}] \tag{9}$$

The convergence of the composite of numerical flows should be validated by appropriate analysis. The upcoming subsections present the preservation of positivity and the issue of convergence with the concepts of consistency and stability.

2.1. Positivity preservation of the LSM

Since the solution of the Brusselator system given in Equation 1-2 describes the concentrations of two reactants, the solution is positive naturally. Thus, the approximate solution must satisfy the positivity for each time step. To guarantee the positivity of the LSM we only impose the following assumption:

Assumption 1. Let $Y(x, y, 0) = Y_0 \geq 0$. Assume that

$$F_i(Y^i) \geq 0, \quad \forall Y^i \geq 0, \quad i = 1, 2$$

where F corresponds to the nonlinear part of the Brusselator system, and F_i and Y^i denote the i th components of the F and Y , respectively.

Due to this condition, vector field F pushes the trajectories back to the positive domain whenever the solutions approach the boundary. Moreover, the condition on the nonlinear field is enough to say the LSM preserves the positivity of the solution. Our general reference on positivity preservation is the book given in [24].

Theorem 1. Let Assumption 1 hold for Equation 1-2. The LSM preserves the positivity of the solutions over all the time.

Proof. To prove the positivity we shall first write the approximate solution on $[0, \Delta t]$:

$$\tilde{Y}(\Delta t) = e^{D\Delta t} Y(t_0) + \frac{\Delta t}{2} \left(F(Y_2(t_0)) + F(Y_2(t_0) + \Delta t F(Y_2(t_0))) \right) \tag{10}$$

where $Y_2(t_0) = Y_1(\Delta t) = e^{D\Delta t} Y_1(t_0)$. One can be easily seen that the solution obtained by Equation 7 gives a positive solution when the initial condition is positive, i. e. $Y(t_0) \geq 0$. This provides the positivity of the second term with the help of Assumption 1, which concludes the positivity of $\tilde{Y}(\Delta t) = \tilde{Y}(t_1)$. The solution is stored as

the initial condition for the next interval $[\Delta t, 2\Delta t]$. Inductively, since the scheme preserves the positivity at each one step we guarantee the positivity of the approximate solution $\tilde{Y}(t_{k+1})$ for all $Y(t_k) \geq 0$.

In [25] the author proposed a finite difference scheme preserving the positivity of the reaction-diffusion equation which requires the differentiability of the field. It is crucial to emphasize that the LSM does not need to have any condition on the derivative of the field.

2.2. Local error analysis

The present section aims to analyze the consistency of the method. One can be seen in Table 1 that the eigenvalues of the discretization matrix to approximate to the Laplace operator are negative. Thus, the solutions of Equation 7 remain bounded over all the time. With the help of these results, Remark 1 is given.

Table 1. Several examples of eigenvalues of D for different domains

Domain	$\max_{\Omega} eig(D)$	$\min_{\Omega} eig(D)$
$\Omega = [0,1] \times [0,1]$	-19.7291	-1.2780e+4
$\Omega = [0,10] \times [0,10]$	-0.1973	-127.8027
$\Omega = [0,30] \times [0,30]$	-0.0219	-88.8670

Remark 1. Due to the $\max_{\Omega} eig(D) \leq 0$, where $eig(D)$ represents the eigenvalues of D , the solution of the linear part of the Brusselator system is bounded by the initial condition as follows:

$$\|e^{\alpha Dt} Y_0\|_X \leq \gamma \|Y_0\|_X \tag{11}$$

where the constant $\gamma \in [0, 1]$ provided that $\alpha \geq 0$.

Moreover, the nonlinear part of the Brusselator system, which is given in Equation 1-2, is bounded, under the well-posedness of the solutions.

Lemma 1. Let the field $F(Y): C^1(\Omega \times [0, t_{end}]) \rightarrow X$ be a nonlinear operator. Suppose that there exists $M, N \in \mathbb{R}^+$ such that

$$\|F(Y)\|_X \leq M \|Y_0\|_X \tag{12}$$

$$\|\partial F(Y)\|_X \leq N \|Y_0\|_X \tag{13}$$

$$\text{where } \partial F = \frac{\partial(f,g)}{\partial(u,v)} = \begin{bmatrix} 2uv - (A + 1) & u^2 \\ A - 2uv & -u^2 \end{bmatrix}.$$

Theorem 2 presents the local error analysis of the LSM. To do this, the method is considered on $[0, \Delta t]$.

Theorem 2. Let Remark 1 and Lemma 1 be fulfilled. LSM is the first-order accuracy with error bound

$$\|Y(\Delta t) - \tilde{Y}(\Delta t)\|_X \leq C \Delta t^2 + \sigma(\Delta t^3) \tag{14}$$

where C depends on M and $\|Y_0\|_X$.

Proof: To obtain the local error bound of the numerical scheme we employ the standard technique. That is, $\|Y(\Delta t) - \tilde{Y}(\Delta t)\|_X$ will be calculated.

On one hand, by Picard-Lindelöf theorem the exact solution of Equation 6 is expressed as follows:

$$Y(\Delta t) = e^{D\Delta t} Y_0 + \int_0^{\Delta t} e^{D(\Delta t-s)} F(Y(s)) ds \tag{15}$$

On the other hand, the numerical solution is defined by

$$\tilde{Y}(\Delta t) = e^{D\Delta t}Y_0 + \frac{\Delta t}{2} \left(F(e^{D\Delta t}Y_0) + F(e^{D\Delta t}Y_0 + \Delta t F(e^{D\Delta t}Y_0)) \right) \quad (16)$$

For the convenience of calculations we restate the exact solution as follows:

$$Y(\Delta t) = e^{D\Delta t}Y_0 + \int_0^{\Delta t} e^{D(\Delta t-s)} F(e^{Ds}Y_0 + \int_0^s e^{D(s-\tau)} F(Y(\tau)) d\tau) ds \quad (17)$$

With the help of the Taylor's Expansion Equation 16 and Equation 17 can be rewritten as follows:

$$Y(\Delta t) = e^{D\Delta t}Y_0 + \int_0^{\Delta t} e^{D(\Delta t-s)} F(e^{Ds}Y_0) ds + \int_0^{\Delta t} e^{D(\Delta t-s)} \left(\int_0^s e^{D(s-\tau)} F(Y(\tau)) d\tau \partial F(e^{Ds}Y_0) + \sigma(s^2) \right) ds \quad (18)$$

and

$$\tilde{Y}(\Delta t) = e^{D\Delta t}Y_0 + \frac{\Delta t}{2} \left(F(e^{D\Delta t}Y_0) + F(e^{D\Delta t}Y_0 + \Delta t F(e^{D\Delta t}Y_0)) \partial F(e^{D\Delta t}Y_0) + \sigma(\Delta t^2) \right) \quad (19)$$

Subtracting Equation 19 from Equation 18 the residual term is achieved. By virtue of Lemma 1 and Remark 1, the local error bound is attained as follows:

$$\|Y(\Delta t) - \tilde{Y}(\Delta t)\|_X \leq C\Delta t^2 + \sigma(\Delta t^3) \quad (20)$$

where C depends on M, N , and $\|Y_0\|_X$.

2.3. Stability analysis

Theorem 3. Let Remark 1 and Lemma 1 be satisfied. The LSM is unconditionally stable.

Proof: To prove the stability of the method we first start with finding a bound of one-step approximate solution given as follows:

$$\tilde{Y}_1 = e^{D\Delta t}Y_0 + \frac{\Delta t}{2} \left(F(e^{D\Delta t}Y_0) + F(e^{D\Delta t}Y_0 + \Delta t F(e^{D\Delta t}Y_0)) \right), \quad (21)$$

where $\tilde{Y}_1 = Y_2(\Delta t)$ in Equation 7-8. Taking the norm of both sides and utilizing from Remark 1 yield

$$\|\tilde{Y}_1\|_X = \left\| e^{D\Delta t}Y_0 + \frac{\Delta t}{2} \left(F(e^{D\Delta t}Y_0) + F(e^{D\Delta t}Y_0 + \Delta t F(e^{D\Delta t}Y_0)) \right) \right\|_X \quad (22)$$

$$\|\tilde{Y}_1\|_X \leq \gamma \|Y_0\|_X + \Delta t \left(1 + \frac{\Delta t}{2} \right) M\gamma \|Y_0\|_X \quad (23)$$

Equation 23 represents the boundedness of a one-step solution by the initial condition as $\Delta t \rightarrow 0$. If the process is repeated inductively, one can obtain

$$\|\tilde{Y}_n\|_X \leq \gamma^n \left(1 + M\Delta t + M\frac{\Delta t^2}{2} \right)^n \|Y_0\|_X \quad (24)$$

where the coefficient of $\|Y_0\|_X$ denotes the amplification factor of LSM. As it can be easily seen in Equation 24, the terms consisting of Δt are negligible when n increases. This leads to

$$\|\tilde{Y}_n\|_X \leq \gamma^n \|Y_0\|_X \quad (25)$$

which concludes the proof. This also guarantees that the LSM is unconditionally stable.

3. Results and Discussion

The current section is dedicated to confirming the theoretical results obtained in the previous section. In this context, it is crucial to state the Brusselator system from both physical and chemical aspects. A chemical process is related to converting reactants into products. One of the most important points for closed systems such as Brusselator is that one can generate an oscillating chemical reaction model using the Belousov-Zhabotinsky reaction which is corresponding to our considered problems. For a more detailed discussion on the Brusselator system and its dynamics we refer the reader to the dissertation about that system, see [26]. An oscillating chemical reaction as the pendulum passes through its equilibrium point while oscillates. The mean of the equilibrium is the equilibrium concentration for all the components. Thus, from a point of mathematical view, as well as its convergence properties it is expected that a numerical scheme to obtain a solution should preserve its dynamics. That is, by the nature of chemical reactions all solutions should be positive. Additionally, due to entropy, the reactants should reach their equilibrium as time increases.

Under the lights of the information above, we consider some test problems both one- and two- dimensional cases to check the accuracy and efficiency of the LSM.

3.1. Example 1

To check the efficiency of the method we first start with a one-dimensional Brusselator system, which is

$$\begin{aligned} \frac{\partial u}{\partial t} &= \alpha \frac{\partial^2 u}{\partial x^2} + B + u^2 v - (A + 1)u \\ \frac{\partial v}{\partial t} &= \alpha \frac{\partial^2 v}{\partial x^2} + Au - u^2 v, \end{aligned}$$

subject to

$$\begin{aligned} u(0, t) = u(1, t) = B; \quad v(0, t) = v(1, t) = A/B \\ u(x, 0) = B + x(1 - x); \quad v(x, 0) = A/B + x^2(1 - x) \end{aligned}$$

By taking parameters given as in [27] we have obtained the approximated solutions which are illustrated in Figure 1.

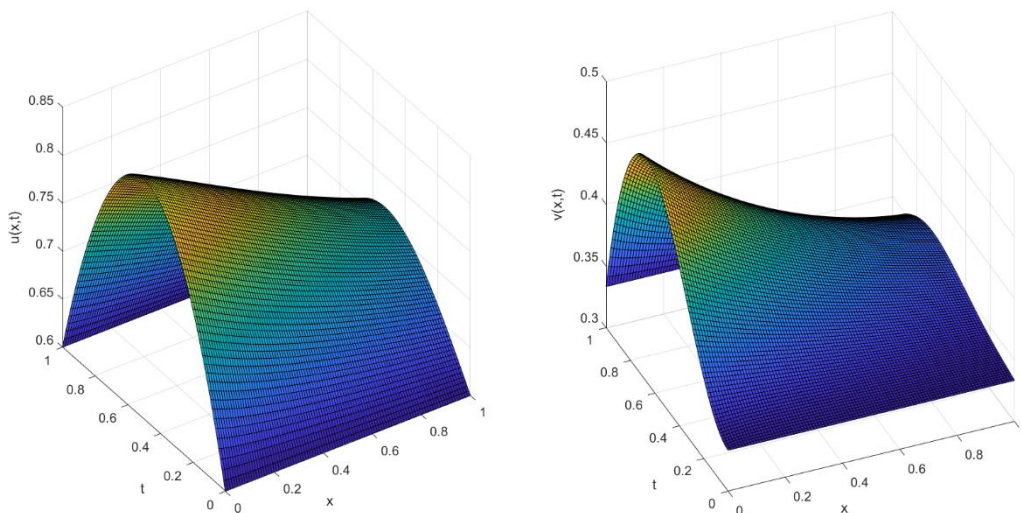


Figure 1. The physical behavior of the approximated solutions for $u(x, t)$ and $v(x, t)$. The numerical solutions are obtained by taking $B = 0.6$, $A = 0.2$, $\alpha = \frac{1}{40}$, where $x \in [0,1]$ and $t \in [0,1]$.

It is important to say Table 2 emphasizes that the LSM remains stable and preserves the positivity of the solutions for both $u(x, t)$ and $v(x, t)$ for different final times.

Table 2. Maximum and Minimum values of numerical solutions for the parameters $B = 0.6, A = 0.2, \alpha = \frac{1}{40}$,

t_{end}	$\max_{\substack{x \in [0,1] \\ t \in [0, t_{end}]}} u(x, t)$	$\min_{\substack{x \in [0,1] \\ t \in [0, t_{end}]}} u(x, t)$	$\max_{\substack{x \in [0,1] \\ t \in [0, t_{end}]}} v(x, t)$	$\min_{\substack{x \in [0,1] \\ t \in [0, t_{end}]}} v(x, t)$
1	0.8500	0.60	0.4812	0.3301
10	0.8500	0.60	0.4812	0.3301
20	0.8500	0.5998	0.4812	0.3302

Furthermore, the theoretical results which are given in [9] state that the limit cycles do not exist for the Brusselator model when $1 - A + B^2 < 0$. Figure 2.a illustrates such a case. However, limit cycles occur for the case of $1 - A + B^2 \geq 0$ and Figure 2.b presents that case. To validate if the proposed method is compatible with the specified system the parameters have been taken from [9].

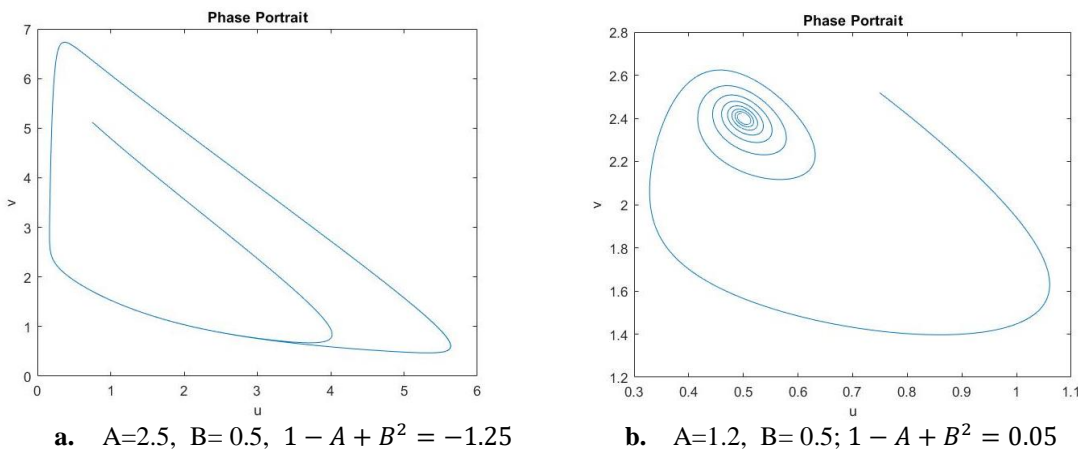


Figure 2. The limit cycles of the diffusion-free Brusselator system for different choices of parameters.

Figure 2 is evidence that the proposed method preserves the limit cycles which is the physical dynamics of the Brusselator system. The obtained results are consistent with the results that of [9].

3.2. Example 2

As our second test problem, we consider a benchmark problem in the literature. The corresponding equation is the two-dimensional Brusselator system given in Equation 1-2 with parameters $\alpha = 0.25, A = 1$ and $B = 0$ in the region $\Omega = [0,1]^2$. By the particular choices of parameters, the exact equations of Equation 1-2 are

$$u(x, y, t) = e^{-x-y-0.5t},$$

$$v(x, y, t) = e^{x+y+0.5t}.$$

All necessary conditions are extracted from the exact solution. Table 3 lists the numerical solution generated by LSM by comparing it with those in [7] and [14] for the case of $M=10$ (denotes the notation for the spatial discretization for their studies).

Table 3. Comparison of the results of LSM with the other methods in the literature and exact solution.

t_{end}	$u(0.4,0.6, t_{end})$				$v(0.4,0.6, t_{end})$			
	LSM	[7]	[14]	Exact	LSM	[7]	[14]	Exact
0.3	0.31667	0.3168	0.3174	0.31665	3.15834	3.1530	3.1580	3.15804
0.6	0.27257	0.2724	0.2732	0.27255	3.66956	3.6600	3.6680	3.66911
0.9	0.23459	0.2345	0.2351	0.23457	4.26365	4.2500	4.2620	4.26311
1.2	0.20192	0.2016	0.2024	0.20191	4.95342	4.9390	4.9520	4.95278
1.5	0.17379	0.1739	0.1742	0.17377	5.75535	5.7350	5.7540	5.75460
1.8	0.14958	0.1489	0.1499	0.14957	6.68676	6.6700	6.6850	6.68589

The given table verifies that the proposed method, LSM, in very good agreement with the exact solution for both u and v . Moreover, it can be easily seen that the LSM is better over time.

Furthermore, Figure 3 and Figure 4 depict the comparison of the physical behaviors of the numerical solutions computed by the LSM and the exact solution. The exhibited figures, Figure 3-4, are obtained by taking $\Delta t = 0.01$ over $[0, 4]$ where the spatial domain, $\Omega = [0,1] \times [0,1]$, is divided into 10 equal intervals.

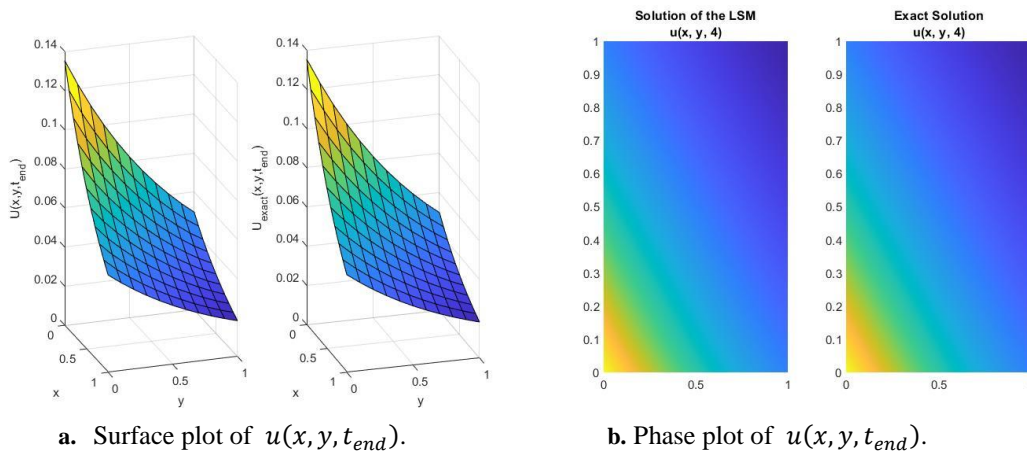


Figure 3. The physical behavior of the solutions of $u(x, y, t)$. The parameters are taken as $A = 1, B = 0, \alpha = 0.25$ for Equation 1-2.

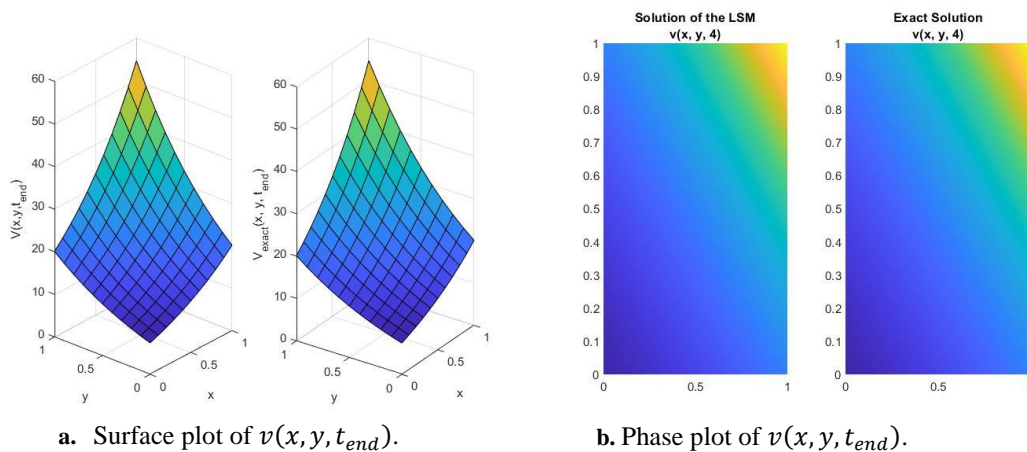


Figure 4. The physical behavior of the solutions of $v(x, y, t)$. The parameters are taken as $A = 1, B = 0, \alpha = 0.25$ for Equation 1-2.

Table 3 and Figure 3-4 are evidence of the validity, compatibility and accuracy of the proposed method for Equation 1-2.

3.3. Example 3

As our final test problem, we consider the two-dimensional Brusselator system which is given in Equation 1-2 for $\alpha = 0.002$, $A = \frac{1}{2}$ and $B = 1$ in the region $\Omega = [0,1]^2$ with the initial and Neumann's boundary conditions are given as follows:

$$u(x, y, 0) = \frac{1}{2}x^2 - \frac{1}{3}x^3 \text{ and } v(x, y, 0) = \frac{1}{2}y^2 - \frac{1}{3}y^3,$$

$$\begin{aligned} \frac{\partial u(x, y, 0)}{\partial x} \Big|_{x=0} &= \frac{\partial u(x, y, 0)}{\partial x} \Big|_{x=1} = \frac{\partial u(x, y, 0)}{\partial y} \Big|_{y=0} = \frac{\partial u(x, y, 0)}{\partial y} \Big|_{y=1} = 0, \\ \frac{\partial v(x, y, 0)}{\partial x} \Big|_{x=0} &= \frac{\partial v(x, y, 0)}{\partial x} \Big|_{x=1} = \frac{\partial v(x, y, 0)}{\partial y} \Big|_{y=0} = \frac{\partial v(x, y, 0)}{\partial y} \Big|_{y=1} = 0, \end{aligned}$$

All parameters for this example are taken from the study of [13]. We have checked the convergence of the method to the equilibria point for the two-dimensional Brusselator system. Table 4 guarantees that the numerical solutions converge to their equilibrium points as t increases.

Table 4. The values of $u(x, y, t)$ and $v(x, y, t)$ at the specified x, y and t .

	(0.2,0.2, t_{end})		(0.4,0.6, t_{end})		(0.5,0.5, t_{end})		(0.8,0.9, t_{end})	
t_{end}	u	v	u	v	u	v	u	v
1	0.5303	0.1632	0.5602	0.2538	0.5511	0.2278	0.5832	0.3148
2	0.7020	0.3676	0.7312	0.4283	0.7224	0.4113	0.7536	0.4664
3	0.8167	0.4930	0.8474	0.5202	0.8382	0.5129	0.8696	0.5348
4	0.9097	0.5356	0.9342	0.5396	0.9271	0.5389	0.9506	0.5398
5	0.9715	0.5307	0.9849	0.5261	0.9812	0.5275	0.9930	0.5223
6	0.9997	0.5146	1.0041	0.5103	1.0029	0.5115	1.0064	0.5005
7	1.0063	0.5038	1.0065	0.5017	1.0065	0.5023	1.0064	0.5005
8	1.0047	0.4996	1.0039	0.4990	1.0042	0.4992	1.0033	0.4987
9	1.0021	0.4989	1.0015	0.4989	1.0016	0.4989	1.0011	0.4989
10	1.0005	0.4993	1.0002	0.4994	1.0003	0.4993	1.0001	0.4995
↓	↓	↓	↓	↓	↓	↓	↓	↓
∞	1	0.5	1	0.5	1	0.5	1	0.5

The values of Table 4 have been obtained by dividing the spatial domain into 20 equally divided intervals whereas the number of intervals varies for the time domain. That is, $N_x = N_y = 20$ and $\Delta t = 0.01$. The relative errors and the rate of convergence of the LSM method are presented in Table 5 and Table 6. To do this, the relative errors are defined by the following equations,

$$\|e_u\|_R = \frac{\|u(\Delta t) - u(\Delta t/2)\|_\infty}{\|u(\Delta t/2)\|_\infty}, \text{ and } \|e_v\|_R = \frac{\|v(\Delta t) - v(\Delta t/2)\|_\infty}{\|v(\Delta t/2)\|_\infty},$$

Table 5. Relative errors and orders at $t_{end} = 1$ with different time step Δt .

$t_{end} = 1$	Relative Error		Order	
Δt	$\ e_u\ _R$	$\ e_v\ _R$	u	v
0.1	9.1737×10^{-4}	3.8232×10^{-4}	2.0934	2.0969
0.05	2.1495×10^{-4}	8.9365×10^{-5}	2.0422	2.0164
0.025	5.2187×10^{-5}	2.2087×10^{-5}	2.0140	1.9490
0.0125	1.2920×10^{-5}	5.7205×10^{-6}	1.9933	1.8669
0.00625	3.2449×10^{-6}	1.5683×10^{-6}	1.9701	1.7510

and

Table 6. Relative errors and orders at $t_{end} = 10$ with different time step Δt .

$t_{end} = 10$	Relative Error		Order		
	Δt	$\ e_u\ _R$	$\ e_v\ _R$	u	v
	0.1	$5.4600x10^{-6}$	$5.8788x10^{-6}$	1.9864	2.1264
	0.05	$1.3779x10^{-6}$	$1.3463x10^{-6}$	2.0056	2.0652
	0.025	$3.4314x10^{-7}$	$3.2171x10^{-7}$	2.0197	2.0355
	0.0125	$8.4618x10^{-8}$	$7.8472x10^{-8}$	2.0428	2.0235
	0.00625	$2.0536x10^{-8}$	$1.9300x10^{-8}$	2.0903	2.0234

To see the validity of the solutions over time, computations are carried out for a different final time, $t = 1$ and $t = 10$ in Table 5 and Table 6, respectively. For both tables, we take $N_x = N_y = 20$. Even though the proposed method is a first-order method, the results of Table 5 and Table 6 are evidence that the method has second-order accuracy. It is crucial to say that this situation is mainly because of the usage of the exact solution on the diffusion part. Moreover, Table 5 and Table 6 guarantee that the method remains stable which also confirms the theoretical results.

In addition, Table 7 exhibits the comparison of the relative errors obtained by the Meshless Local Petrov-Galerkin (MLPG) method which is studied in [13], and the proposed method, LSM. Although it is a first-order method, it is seen from Table 7 that the LSM achieves good results for a different choice of Δt . It is important to note that this study deals with the time splitting algorithms whereas the compared study has mainly focused on the space discretization technique.

Table 7. Comparison of the relative errors at $t_{end} = 4$ with different time step Δt produced by LSM with the results of [13].

$t_{end} = 4$	LSM		MLPG [13]		
	Δt	$\ e_u\ _R$	$\ e_v\ _R$	$\ e_u\ _R$	$\ e_v\ _R$
	0.1	$5.4604x10^{-5}$	$1.4324x10^{-4}$	$1.7883x10^{-6}$	$6.0686x10^{-7}$
	0.05	$1.7669x10^{-5}$	$4.3478x10^{-5}$	$1.7565x10^{-6}$	$5.5350x10^{-7}$
	0.01	$5.2534x10^{-7}$	$1.1857x10^{-6}$	$1.7331x10^{-6}$	$5.2272x10^{-7}$
	0.005	$1.4540x10^{-7}$	$2.8553x10^{-7}$	$1.7301x10^{-6}$	$5.1900x10^{-7}$
	0.001	$2.2007x10^{-9}$	$1.1446x10^{-8}$	$1.7278x10^{-6}$	$5.1605x10^{-7}$

Furthermore, the exhibited figure, Figure 5, illustrates the numerical solution of u and v for the two-dimensional Brusselator system for the parameters $\alpha = 0.002$, $A = \frac{1}{2}$ and $B = 1$ on $t \in [0,3]$. To show the compatibility of the solution, the proposed method has been compared by a well-known Crank-Nicolson method without applying any splitting process. It can be easily seen that values of u and v approach the values 1 and 0.5 respectively.

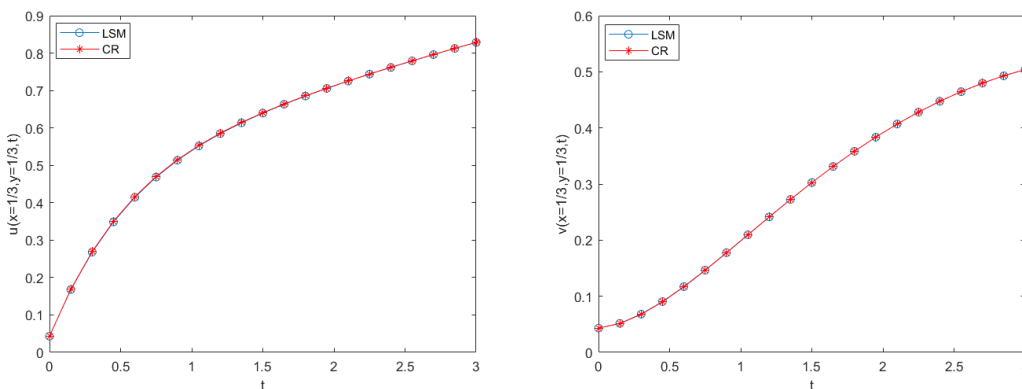


Figure 5. Graphs of $u\left(\frac{1}{3}, \frac{1}{3}, t\right)$ and $v\left(\frac{1}{3}, \frac{1}{3}, t\right)$ against time t for Example 3.

The graphs of the numerical solutions obtained for u and v at $t = 10$ with $N_x = N_y = 20$ and $\Delta t = 0.01$ are presented in Figure 6. Initial profiles of u and v are given in Figure 7.

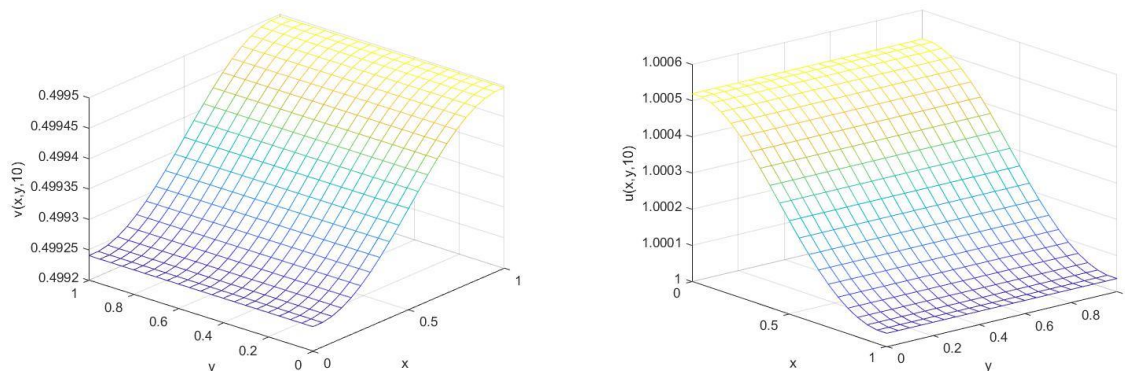


Figure 6. The solutions of u and v at $t = 10$.

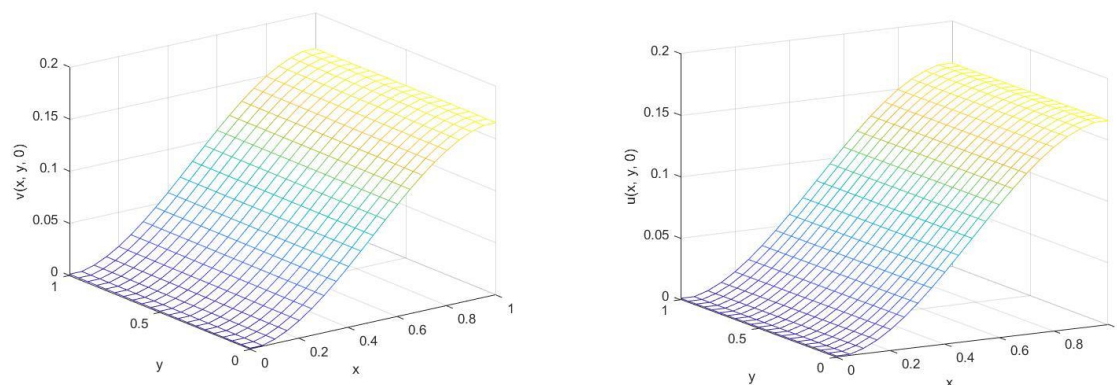


Figure 7. Initial concentration profiles of reactants u and v .

Figure 6 and Figure 7 present that the concentrations tend to approach their equilibrium points. From a mathematical point of view, the proposed method preserves the physical behavior of the initial profiles.

4. Conclusion and Comment

A kind of operator splitting method, the LSM, has been applied to solve the nonlinear reaction-diffusion Brusselator system. The system has been divided into two equations which are solved iteratively. The main contribution of this process is solving the diffusion part exactly which leads to getting high accuracy. Second-order Heun's method has been used for the nonlinear part. By the concepts of stability and consistency analyses, the convergence of the proposed method has been discussed. Additionally, it is shown that the method preserves the positivity of the solutions which plays a key role in chemical reaction-diffusion systems theoretically. In addition to these theoretical results, the current study has been also enriched computationally by applying the proposed method on several Brusselator systems. After generating an accuracy table the convergence rate of the method has been shown. It is important to emphasize that by virtue of the exact solution on the linear part the method performed as a second-order method even though it is a first-order method theoretically. Moreover, one can be seen on the tables and simulations the system reaches its equilibrium point for both one- and two-dimensional versions. All these results are evidence that the method is a very compatible and accurate method both physically and mathematically for the specified system.

Acknowledgment

The authors would like to thank the reviewers and the Editor-in-Chief for their contribution to the progress of the study through constructive, valuable, and insightful comments to this study.

Conflicts of interest

The authors state that there is no conflict of interests.

References

- [1] Lefever R., Nicolis G., Chemical instabilities and sustained oscillations, *Journal of Theoretical Biology*, 30 (1971) 267-284.
- [2] Nicolis G., Prigogine I., Self-Organization in Non-Equilibrium Systems: From Dissipative Structures to Order through Fluctuations, Wiley/Interscience, New York, London, Sydney, Toronto (1977).
- [3] Prigogine I., Lefever R., Symmetries breaking instabilities in dissipative systems II. *The Journal of Chemical Physics*, 48 (1968) 1695-1700.
- [4] Tyson J. J., Some further studies of nonlinear oscillations in chemical systems, *The Journal of Chemical Physics*, 58 (1973) 3919-3930.
- [5] Turing A., The chemical basis of morphogenesis. *Philosophical Transactions of the Royal Society of London Series B, Biological Sciences*, 237 (1952) 37-72.
- [6] Tyson J. J., The Belousov-Zhabotinskii Reaction (Lecture Notes in Biomathematics), 10, Springer-Verlag, Heidelberg, 1976.
- [7] Ang W-T., The two-dimensional reaction-diffusion Brusselator system: a dual-reciprocity boundary element solution, *Engineering Analysis with Boundary Elements*, 27 (2003) 897-903.
- [8] Adomian G., The diffusion-Brusselator equation, *Computers & Mathematics with Applications*, 29 (5) (1995) 1-3.
- [9] Twizell E. H., Gumel A.B., Cao Q., A second-order scheme for the “Brusselator” reaction-diffusion system, *Journal of Mathematical Chemistry*, 26 (1999) 297-316.
- [10] Wazwaz A.-M., The decomposition method applied to systems of partial differential equations and to the reaction-diffusion Brusselator model, *Applied Mathematics and Computation*, 110 (2000) 251-264.
- [11] Jiwari R., Yuan J., A computational modeling of two dimensional reaction-diffusion Brusselator system arising in chemical processes, *Journal of Mathematical Chemistry*, 52 (2014) 1535-1551.
- [12] Mittal R.C., Jiwari R., Numerical solution of two-dimensional reaction-diffusion Brusselator system, *Applied Mathematics and Computation*, 217 (2011) 5404-5415.
- [13] Shirzadi A., Sladek V., Sladek J., A Meshless Simulations for 2D Nonlinear Reaction-diffusion Brusselator System, *Computer Modeling in Engineering and Sciences*, 95 (2013) 259-282.
- [14] Siraj-ul-Islam Ali A., Haq S., A computational modeling of the behavior of the two-dimensional reaction-diffusion Brusselator system, *Applied Mathematical Modelling*, 34 (2010) 3896-3909.
- [15] Yadav O. P., Jiwari R., A finite element approach for analysis and computational modelling of coupled reaction diffusion models, *Numerical Methods for Partial Differential Equations*, 35 (2019) 830-850.
- [16] Yadav O. P., Jiwari R., A finite element approach to capture Turing patterns of autocatalytic Brusselator model, *Journal of Mathematical Chemistry*, 57 (2019) 769-789.
- [17] Kumar S., Jiwari R., Mittal R.C., Numerical simulation for computational modelling of reaction-diffusion Brusselator model arising in chemical processes, *Journal of Mathematical Chemistry*, 57 (2019) 149-179.
- [18] Bhatt H., Chowdhury A., Comparative analysis of numerical methods for the multidimensional Brusselator system, *Open Journal of Mathematical Sciences*, 3 (2019) 262-272.

- [19] Asante-Asamani E. O., Wade B. A., A Dimensional Splitting of ETD Schemes for Reaction-Diffusion Systems, *Communications in Computational Physics*, 19 (2016) 1343-1356.
- [20] McLachlan R., Quispel G., Splitting methods, *Acta Numerica*, 11 (2002) 341-434.
- [21] Hosseini R., Tatari M., Some splitting methods for hyperbolic PDEs, *Applied Numerical Mathematics*, 146 (2019) 361-378.
- [22] Zurnacı F., Gücüyenen-Kaymak N., Seydaoğlu M., Tanoğlu G., Convergence analysis and numerical solution of the Benjamin-Bona-Mahony equation by Lie-Trotter splitting, *Turkish Journal of Mathematics*, 42 (2018) 1471-1483.
- [23] Seydaoğlu M., An accurate approximation algorithm for Burgers' equation in the presence of small viscosity, *Journal of Computational and Applied Mathematics*, 344 (2018) 473-481.
- [24] Hundsdorfer W., Verwer J., Numerical Solution of Time-Dependent Advection-Diffusion-Reaction Equations. 1st ed. Springer, Berlin, Heidelberg, (2003) 116-121.
- [25] Mickens R.E., Nonstandard finite difference schemes for reaction-diffusion equation, *Numerical Methods for Partial Differential Equations*, 15 (1999) 201-214.
- [26] Singh R., Brusselator as a Reaction-Diffusion, Master Dissertation, Homi Bhabha National Institute, The Institute of Mathematical Sciences, (2008).
- [27] Manaa S. A., Saeed R. K., Easif F. H., Numerical Solution of Brusselator Model by Finite Difference Method, *Journal of Applied Sciences Research*, 6 (11) (2010) 1632-1646.



$(G'/G, 1/G)$ -expansion method for analytical solutions of Jimbo-Miwa equation

Asif YOKUŞ¹ , Hülya DURUR^{2,*}

¹Firat University, Faculty of Science, Department of Actuary, Elazığ/TURKEY

²Ardahan University, Faculty of Engineering, Department of Computer Engineering, Ardahan/TURKEY

Abstract

The main goal of this study is obtaining analytical solutions for (3+1)-dimensional Jimbo-Miwa Equation which the second equation in the well-known KP hierarchy of integrable systems. For the (3+1DJM) equation, hyperbolic, trigonometric, complex trigonometric and rational traveling wave solutions have been constructed by applying the $(G'/G, 1/G)$ -expansion method. Then, real and imaginary graphics are presented by giving special values to the constants in the solutions obtained. These graphics are a special solution of the (3+1DJM) equation and represent a stationary wave of the equation. The $(G'/G, 1/G)$ -expansion method is an effective and powerful method for solving nonlinear evolution equations (NLEEs). Ready computer package program is used to obtain the solutions and graphics presented in this study.

Article info

History:

Received:15.02.2020

Accepted:23.12.2020

Keywords:

(3+1)-dimensional Jimbo-Miwa equation, Exact solution, $(G'/G, 1/G)$ -expansion method, Traveling wave solution.

1. Introduction

Non-linear science phenomena take an important place in applied mathematics and mathematical physics. The appearance of the solitary wave in nature is quite common particularly in plasmas, condensed matter physics, optical fibers, solid-state physics, chemical kinematics, electrical circuits, etc. Solutions of nonlinear evolutionary equations are the cornerstone of many physical phenomena. For example; such as signaling, ocean waves, shallow water waves, heat dissipation. In wave theory, these physical events are mathematized with traveling wave solutions. Therefore, the traveling wave solution is an indispensable instrument of both mathematics and physics. Last year, NLEEs are applied in many areas of science. Various methods have been used to obtain solutions for different types of NLEEs. Some of these are the extended trial equation method [1], the new extended direct algebraic method [2], (G'/G) -expansion method [3], $(G'/G, 1/G)$ -expansion method [4], Clarkson–Kruskal (CK) direct method [5], improved $\tan \phi(\xi)/2$ -expansion method [6], Sumudu transform method [7], new expansion method [8], extended sinh-Gordon equation expansion method [9], the modified Kudryashov method [10], $(1/G')$ -expansion method [11-15], collocation method [16,17], first integral method [18],

F-expansion method [19], the modified exponential function method [20], Difference scheme method [21] and so on [22-29].

In this article, the authors attained the exact solutions of the (3+1DJM) equation. Consider the form of the (3+1DJM) equation [30],

$$u_{xxxy} + 3u_y u_{xx} + 3u_x u_{xy} + 2u_{yt} - 3u_{xz} = 0. \quad (1)$$

Jimbo-Miwa equation was examined first by Jimbo and Miwa [31] and later by several authors. Some of these are as follows: Wazwaz has been attained multiple soliton solutions of two extended (3+1DJM) equation using the simplified Hirota's method [32], Zhang has been obtained different type solutions of (3+1DJM) equation using Hirota bilinear form [33], Ma and Lee have been attained (3+1DJM) equation using Bäcklund transformation [34], Sun and Chen have been attained lump solutions, the lump–kink of (3+1DJM) equation via bilinear forms [35], Yang and Ma have been obtained Lump-type solutions of the (3+1DJM) equation by applying Hirota bilinear form [36], Liu and Jiang have been attained new exact solutions of the (3+1DJM) equation with the help of extended homogeneous balance method [37], Öziş and Aslan have been attained analytical and explicit generalized solitary solutions of the (3+1DJM) equation using the Exp-function method [38], Tang

*Corresponding author. email address: hulyadurur@ardahan.edu.tr

and Liang have been obtained variable separation solutions of the (3+1DJM) equation [39], Ma has been attained four classes of lump-type solutions for the (3+1DJM) equation using Hirota bilinear form [40].

2. (G'/G, 1/G)-Expansion Method

Consider the general form of NLEEs containing two or more arguments to be analyzed is written as follows [23]:

$$T\left(u, \frac{\partial u}{\partial t}, \frac{\partial u}{\partial x}, \frac{\partial u}{\partial y}, \frac{\partial^2 u}{\partial x^2}, \dots\right) = 0. \tag{2}$$

Let $u = u(x, y, z, t) = U(\xi) = U$, $\xi = \alpha x + \beta y + \gamma z - ct$ and transmutation Eq. (1) can be converted into following nODE for $U(\xi)$:

$$L(U, U', U'', UU', \dots) = 0, \tag{3}$$

where prime refers to derivatives related to ξ . Complexity can be reduced by integrating Eq. (3). By the nature of this method, $G(\xi) = G$ is solution function of the second-order ODE as

$$G''(\xi) + \lambda G(\xi) = \mu. \tag{4}$$

It as $\phi = \phi(\xi) = G'/G$ and $\psi = \psi(\xi) = 1/G$ supply operational esthetic. We may write derivatives of the functions described

$$\phi' = -\phi^2 + \mu\psi - \lambda, \psi' = -\phi\psi, \tag{5}$$

We can offer the behavior of solution function Eq. (4) according to the state of λ taking into account the equations given by the Eq. (5).

i) If $\lambda < 0$,

$$G(\xi) = c_1 \sinh(\sqrt{-\lambda}\xi + c_2 \cosh\sqrt{-\lambda}\xi) + \frac{\mu}{\lambda}, \tag{6}$$

whereas c_1 and c_2 are real numbers. Considering Eq. (6);

$$\psi^2 = \frac{-\lambda}{\lambda^2\sigma + \mu^2}(\phi^2 - 2\mu\psi + \lambda), \sigma = c_1^2 - c_2^2, \tag{7}$$

Eq. (7) is obtained.

ii) If $\lambda > 0$,

$$G(\xi) = c_1 \sin(\sqrt{\lambda}\xi + c_2 \cos\sqrt{\lambda}\xi) + \frac{\mu}{\lambda}, \tag{8}$$

whereas c_1 and c_2 are real numbers. Considering Eq. (8),

$$\psi^2 = \frac{\lambda}{\lambda^2\sigma - \mu^2}(\phi^2 - 2\mu\psi + \lambda), \sigma = c_1^2 + c_2^2, \tag{9}$$

Eq. (9) is written.

iii) If $\lambda = 0$,

$$G(\xi) = \frac{\mu}{2}\xi^2 + c_1\xi + c_2, \tag{10}$$

here c_1 and c_2 are real numbers. Considering Eq. (10),

$$\psi^2 = \frac{1}{c_1^2 - 2\mu c_2}(\phi^2 - 2\mu\psi). \tag{11}$$

Eq. (11) is written.

For ψ and ϕ polynomials, solution of Eq. (3) is

$$u(\xi) = \sum_{i=0}^n a_i \phi^i + \sum_{i=1}^n b_i \phi^{i-1} \psi. \tag{12}$$

Here, a_i and b_i are real numbers be identified. n is a positive equilibrium term which may be attained by comparing the maximum order derivative with the maximum order nonlinear term in Eq. (8). Whether Eq. (12)

is written in Eq. (3) along with equations (5), (7), (9), or (11) is written. Each coefficient of $\phi^i \psi^j$ ($i = 0, 1, \dots, n$) ($j = 1, \dots, n$) terms of the attained polynomial functions are equals zero and there is a system of algebraic equations for $a_i, b_i, c_1, c_2, \alpha, \beta, c$, and λ , ($i = 0, 1, \dots, n$). The necessary coefficients are obtained by solving an algebraic equation with the help of computer package programs. Obtained coefficients are put into Eq. (12) and $U(\xi)$ solution function of the ODE given as (3) is attained and if $\xi = \alpha x + \beta y + \gamma z - ct$ transmutation is employed, we will attain exact solution $u(x, y, z, t)$ of Eq. (2).

3. Solutions of the (3+1DJM) Equation

We consider Eq. (1) and using transformation $u = u(x, y, z, t) = U(\xi) = U$, $\xi = \alpha x + \beta y + \gamma z - ct$, where β, γ, α and c are constants, once obtained (ODE) after integration, we get

$$\alpha^3 \beta U'''' + 3\beta \alpha^2 (U')^2 - (2\beta c + 3\alpha \gamma) U' = 0, \tag{13}$$

where the integration constant is zero. In Eq. (13), we get term $n = 1$ from the definition of balancing term and the following situation is obtained in Eq. (5),

$$U(\xi) = a_0 + a_1 \phi[\xi] + b_1 \psi[\xi]. \tag{14}$$

Replacing Eq. (14) into Eq. (13) and the coefficients of Eq. (1) are equal to zero, we may establish the following algebraic equation systems

$$\begin{aligned} Const: & 2c\beta\lambda a_1 + 3\alpha\gamma\lambda a_1 - 2\alpha^3\beta\lambda^2 a_1 + \frac{3\alpha^3\beta\lambda^2\mu^2 a_1}{\mu^2 + \lambda^2\sigma} + 3\alpha^2\beta\lambda^2 a_1^2 - \frac{3\alpha^2\beta\lambda^2\mu^2 a_1^2}{\mu^2 + \lambda^2\sigma} = 0, \\ \phi[\xi]: & -\frac{6\alpha^3\beta\lambda^2\mu b_1}{\mu^2 + \lambda^2\sigma} + \frac{6\alpha^2\beta\lambda^2\mu a_1 b_1}{\mu^2 + \lambda^2\sigma} = 0, \\ \phi[\xi]^2: & 2c\beta a_1 + 3\alpha\gamma a_1 - 8\alpha^3\beta\lambda a_1 + \frac{3\alpha^3\beta\lambda\mu^2 a_1}{\mu^2 + \lambda^2\sigma} + 6\alpha^2\beta\lambda a_1^2 - \frac{3\alpha^2\beta\lambda\mu^2 a_1^2}{\mu^2 + \lambda^2\sigma} - \frac{3\alpha^2\beta\lambda^2 b_1^2}{\mu^2 + \lambda^2\sigma} = 0, \\ \phi[\xi]^3: & -\frac{6\alpha^3\beta\lambda\mu b_1}{\mu^2 + \lambda^2\sigma} + \frac{6\alpha^2\beta\lambda\mu a_1 b_1}{\mu^2 + \lambda^2\sigma} = 0, \\ \psi[\xi]: & -2c\beta\mu a_1 - 3\alpha\gamma\mu a_1 + 5\alpha^3\beta\lambda\mu a_1 - \frac{6\alpha^3\beta\lambda\mu^3 a_1}{\mu^2 + \lambda^2\sigma} - 6\alpha^2\beta\lambda\mu a_1^2 + \frac{6\alpha^2\beta\lambda\mu^3 a_1^2}{\mu^2 + \lambda^2\sigma} = 0, \\ \phi[\xi]\psi[\xi]: & 2c\beta b_1 + 3\alpha\gamma b_1 - 5\alpha^3\beta\lambda b_1 + \frac{12\alpha^3\beta\lambda\mu^2 b_1}{\mu^2 + \lambda^2\sigma} + 6\alpha^2\beta\lambda a_1 b_1 - \frac{12\alpha^2\beta\lambda\mu^2 a_1 b_1}{\mu^2 + \lambda^2\sigma} = 0, \\ \phi[\xi]^2\psi[\xi]: & 12\alpha^3\beta\mu a_1 - 6\alpha^2\beta\mu a_1^2 + \frac{6\alpha^2\beta\lambda\mu b_1^2}{\mu^2 + \lambda^2\sigma} = 0, \end{aligned} \tag{15}$$

the aim with ready computer package program, reaching the solutions of system (15) and we obtained the following stations.

If $\lambda < 0$,

Case 1.

$$a_1 = \alpha, \quad b_1 = i\alpha\sqrt{\lambda}\sqrt{\sigma}, \quad c = \frac{-3\alpha\gamma - \alpha^3\beta\lambda}{2\beta}, \quad \mu = 0, \quad \xi = \alpha x + \beta y + \gamma z - ct, \tag{16}$$

replacing values Eq. (16) into Eq. (14) and attain the following hyperbolic exact solutions for Eq. (1):

$$u_1(x, y, z, t) = \frac{2\alpha(c_2\sqrt{-\lambda}\text{Cosh}[\sqrt{-\lambda}\xi] + c_1\sqrt{-\lambda}\text{Sinh}[\sqrt{-\lambda}\xi])}{c_1\text{Cosh}[\sqrt{-\lambda}\xi] + c_2\text{Sinh}[\sqrt{-\lambda}\xi]} + a_0. \tag{17}$$

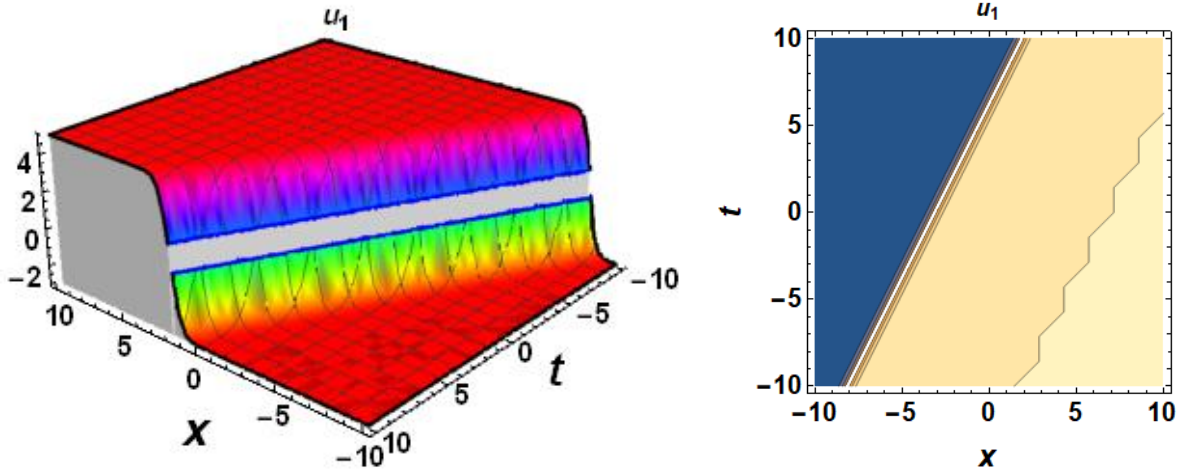


Figure 1. Graphs of $u_1(x, y, z, t) = u_1$ for $\lambda = -4, \beta = 1, \gamma = 5, \delta_1 = 4, \delta_2 = -1, a_0 = 1, \alpha = 2, c_1 = 1, c_2 = 2, y = 1, z = 1$.

Case 2.

$$a_1 = 2\alpha, b_1 = 0, c = \frac{-3\alpha\gamma - 4\alpha^3\beta\lambda}{2\beta}, \mu = 0, \xi = \alpha x + \beta y + \gamma z - ct, \tag{18}$$

replacing values Eq. (18) into Eq. (14) and attain the following hyperbolic exact solution for Eq. (1):

$$u_2(x, y, z, t) = \frac{2\alpha(c_2\sqrt{-\lambda}\text{Cosh}[\sqrt{-\lambda}\xi] + c_1\sqrt{-\lambda}\text{Sinh}[\sqrt{-\lambda}\xi])}{c_1\text{Cosh}[\sqrt{-\lambda}\xi] + c_2\text{Sinh}[\sqrt{-\lambda}\xi]} + a_0. \tag{19}$$

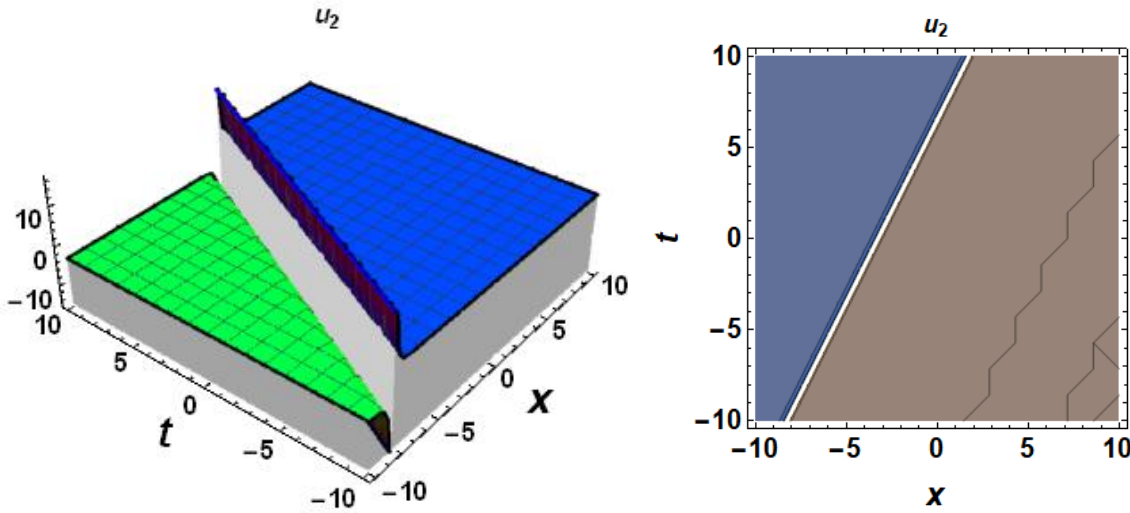


Figure 2. Graphs of $u_2(x, y, z, t) = u_2$ for $\lambda = -1, \beta = 1, a_0 = 1, \gamma = 5, \alpha = 2, c_1 = 1, c_2 = 2, y = 1, z = 1$.

ii) If $\lambda > 0$,

Case 3.

$$a_1 = 2\alpha, b_1 = 0, c = \frac{-3\alpha\gamma - 4\alpha^3\beta\lambda}{2\beta}, \mu = 0, \xi = \alpha x + \beta y + \gamma z - ct, \tag{20}$$

replacing values Eq. (20) into Eq. (14) and attain the following trigonometric exact solution for Eq. (1):

$$u_3(x, y, z, t) = \frac{2\alpha(c_2\sqrt{\lambda}\cos[\sqrt{\lambda}\xi] - c_1\sqrt{\lambda}\sin[\sqrt{\lambda}\xi])}{c_1\cos[\sqrt{\lambda}\xi] + c_2\sin[\sqrt{\lambda}\xi]} + a_0. \tag{21}$$

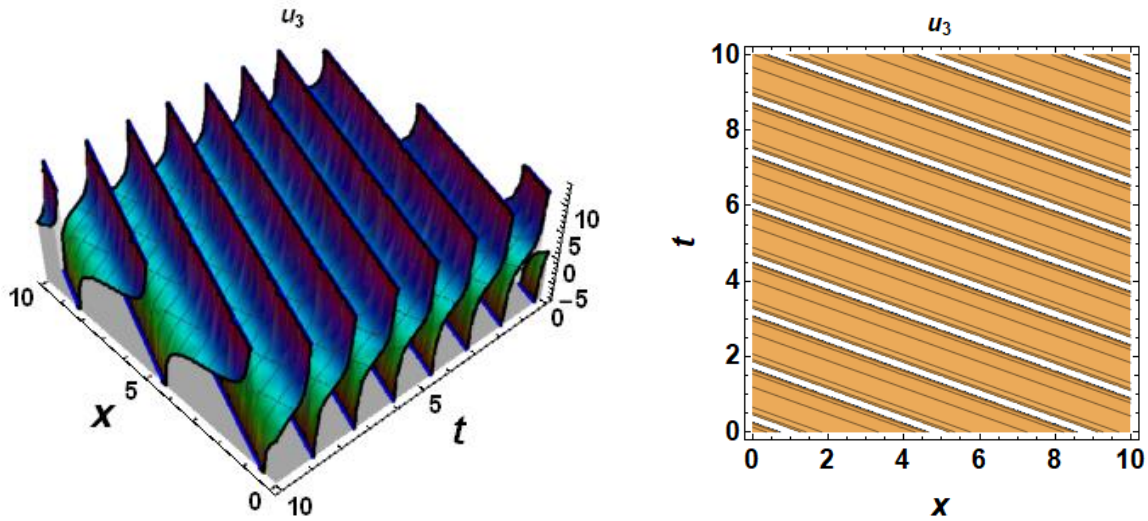


Figure 3. Graphs of $u_3(x, y, z, t) = u_3$ for $\lambda = 1, \beta = 1, a_0 = 3, \gamma = 1, \alpha = 0.8, c_1 = -1, c_2 = 1, y = 0, z = 0$.

Case 4.

$$a_1 = \alpha, b_1 = -\frac{\alpha\sqrt{-\mu^2 + \lambda^2\sigma}}{\sqrt{\lambda}}, \beta = -\frac{3\alpha\gamma}{2c + \alpha^3\lambda}, \xi = \alpha x + \beta y + \gamma z - ct, \tag{22}$$

replacing values Eq. (22) into Eq. (14) and attain the following trigonometric exact solution for Eq. (1):

$$u_4(x, y, z, t) = -\frac{\alpha\sqrt{(c_1^2 + c_2^2)\lambda^2 - \mu^2}}{\sqrt{\lambda}\left(\frac{\mu}{\lambda} + c_1\cos\left[\sqrt{\lambda}\left(-ct + \alpha x + \gamma z - \frac{3y\alpha\gamma}{2c + \alpha^3\lambda}\right)\right] + c_2\sin\left[\sqrt{\lambda}\left(-ct + \alpha x + \gamma z - \frac{3y\alpha\gamma}{2c + \alpha^3\lambda}\right)\right]\right)} + \frac{\alpha(c_2\sqrt{\lambda}\cos\left[\sqrt{\lambda}\left(-ct + \alpha x + \gamma z - \frac{3y\alpha\gamma}{2c + \alpha^3\lambda}\right)\right] - c_1\sqrt{\lambda}\sin\left[\sqrt{\lambda}\left(-ct + \alpha x + \gamma z - \frac{3y\alpha\gamma}{2c + \alpha^3\lambda}\right)\right])}{\frac{\mu}{\lambda} + c_1\cos\left[\sqrt{\lambda}\left(-ct + \alpha x + \gamma z - \frac{3y\alpha\gamma}{2c + \alpha^3\lambda}\right)\right] + c_2\sin\left[\sqrt{\lambda}\left(-ct + \alpha x + \gamma z - \frac{3y\alpha\gamma}{2c + \alpha^3\lambda}\right)\right]} + a_0. \tag{23}$$

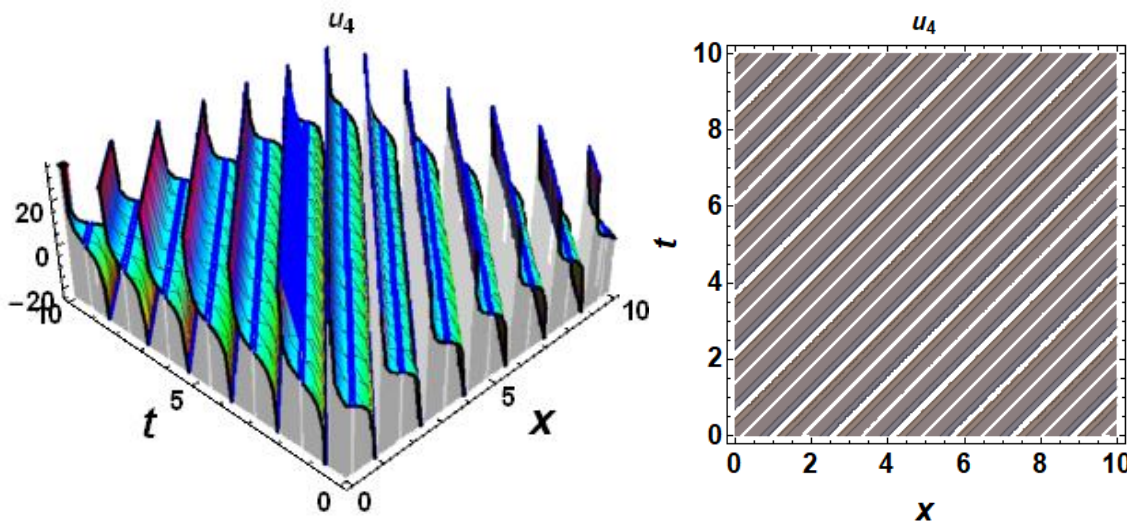


Figure 4. Graphs of $u_4(x, y, z, t) = u_4$ for $\lambda = 16, c = 1, a_0 = 5, \gamma = 1, \alpha = 1, \mu = 1, c_1 = -1, c_2 = 1, y = 0, z = 0$.

Case 5.

$$a_1 = \alpha, b_1 = \alpha\sqrt{\lambda}\sqrt{\sigma}, c = \frac{-3\alpha\gamma - \alpha^3\beta\lambda}{2\beta}, \mu = 0, \xi = \alpha x + \beta y + \gamma z - ct, \tag{24}$$

replacing values Eq. (24) into Eq. (14) and attain the following trigonometric exact solution for Eq. (1):

$$u_5(x, y, z, t) = \frac{\sqrt{c_1^2+c_2^2}\alpha\sqrt{\lambda}}{c_1\text{Cos}[\sqrt{\lambda}\xi]+c_2\text{Sin}[\sqrt{\lambda}\xi]} + \frac{\alpha(c_2\sqrt{\lambda}\text{Cos}[\sqrt{\lambda}\xi]-c_1\sqrt{\lambda}\text{Sin}[\sqrt{\lambda}\xi])}{c_1\text{Cos}[\sqrt{\lambda}\xi]+c_2\text{Sin}[\sqrt{\lambda}\xi]} + a_0. \tag{25}$$

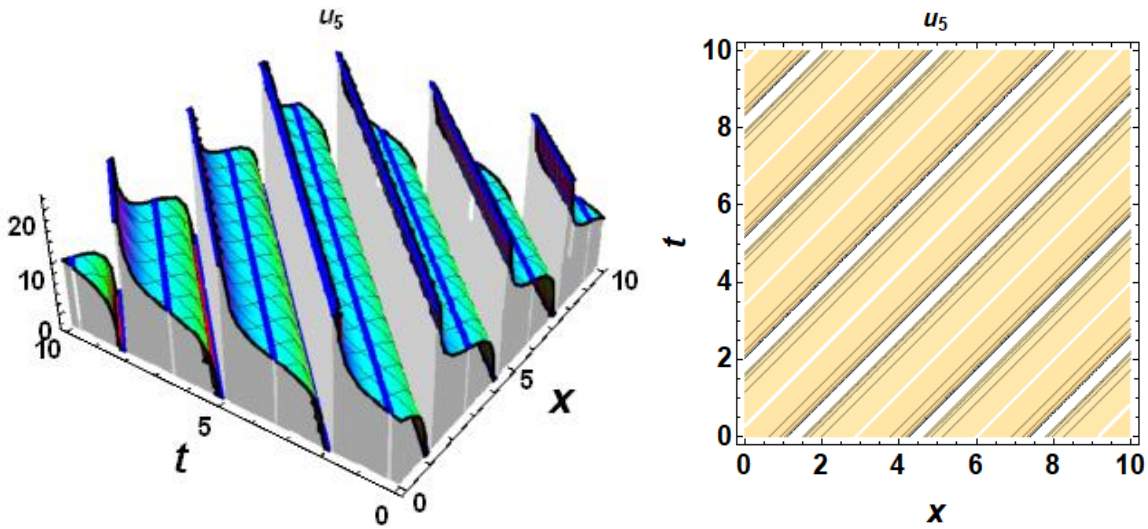


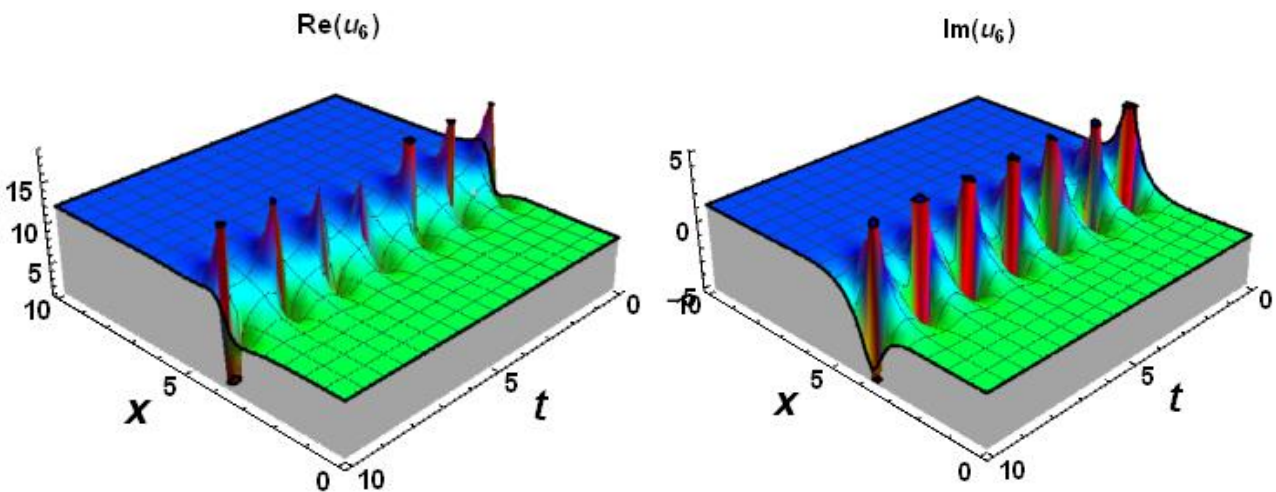
Figure 5. Graphs of $u_5(x, y, z, t) = u_5$ for $\lambda = 4$, $\beta = 10$, $\gamma = 1$, $\alpha = 1$, $a_0 = 10$, $c_1 = 1, c_2 = -2$, $y = 1$, $z = 1$, $c = 1$.

Case 6.

$$a_1 = \alpha, b_1 = \alpha\sqrt{\lambda}\sqrt{\sigma}, \mu = 0, \beta = -\frac{3\alpha\gamma}{2c+\alpha^3\lambda}, \xi = \alpha x + \beta y + \gamma z - ct, \tag{26}$$

replacing values Eq. (26) into Eq. (14) and attain the following complex trigonometric exact solution for Eq. (1):

$$u_6(x, y, z, t) = \frac{\sqrt{c_1^2+c_2^2}\alpha\sqrt{\lambda}}{c_1\text{Cos}[\sqrt{\lambda}(-ct+x\alpha+z\gamma-\frac{3y\alpha\gamma}{2c+\alpha^3\lambda})]+c_2\text{Sin}[\sqrt{\lambda}(-ct+x\alpha+z\gamma-\frac{3y\alpha\gamma}{2c+\alpha^3\lambda})]} + \frac{\alpha(c_2\sqrt{\lambda}\text{Cos}[\sqrt{\lambda}(-ct+x\alpha+z\gamma-\frac{3y\alpha\gamma}{2c+\alpha^3\lambda})]-c_1\sqrt{\lambda}\text{Sin}[\sqrt{\lambda}(-ct+x\alpha+z\gamma-\frac{3y\alpha\gamma}{2c+\alpha^3\lambda})])}{c_1\text{Cos}[\sqrt{\lambda}(-ct+x\alpha+z\gamma-\frac{3y\alpha\gamma}{2c+\alpha^3\lambda})]+c_2\text{Sin}[\sqrt{\lambda}(-ct+x\alpha+z\gamma-\frac{3y\alpha\gamma}{2c+\alpha^3\lambda})]} + a_0. \tag{27}$$



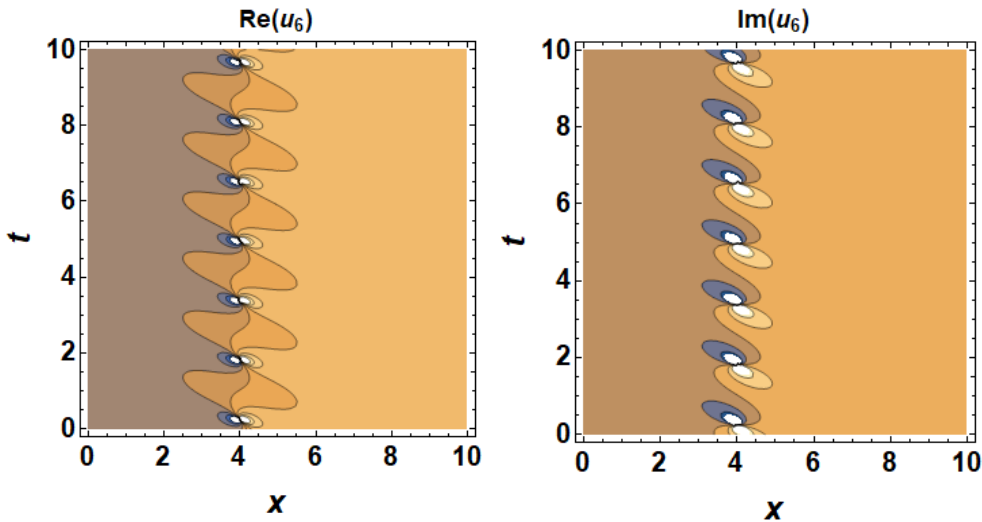


Figure 6. Real and imaginary graphs of $u_6(x, y, z, t) = u_6$ for $\lambda = 4$, $c = 1$, $a_0 = 10$, $\gamma = 8$, $c_1 = 2$, $c_2 = 10$, $y = 1$, $z = 1$.

iii) If $\lambda = 0$,

Case 7.

$$a_1 = \alpha, b_1 = -\sqrt{c_2^2 \alpha^2 - 2 c_1 \alpha^2 \mu}, c = -\frac{3\alpha\gamma}{2\beta}, \xi = \alpha x + \beta y + \gamma z - ct, \tag{28}$$

replacing values Eq. (28) into Eq. (14) and attain the following rational exact solution for Eq. (1):

$$u_7(x, y, z, t) = -\frac{\sqrt{c_2^2 \alpha^2 - 2 c_1 \alpha^2 \mu}}{c_1 + c_2 \left(x\alpha + y\beta + z\gamma + \frac{3t\alpha\gamma}{2\beta} \right) + \frac{1}{2} \left(x\alpha + y\beta + z\gamma + \frac{3t\alpha\gamma}{2\beta} \right)^2 \mu} + \frac{\alpha \left(c_2 + \left(x\alpha + y\beta + z\gamma + \frac{3t\alpha\gamma}{2\beta} \right) \mu \right)}{c_1 + c_2 \left(x\alpha + y\beta + z\gamma + \frac{3t\alpha\gamma}{2\beta} \right) + \frac{1}{2} \left(x\alpha + y\beta + z\gamma + \frac{3t\alpha\gamma}{2\beta} \right)^2 \mu} + a_0. \tag{29}$$

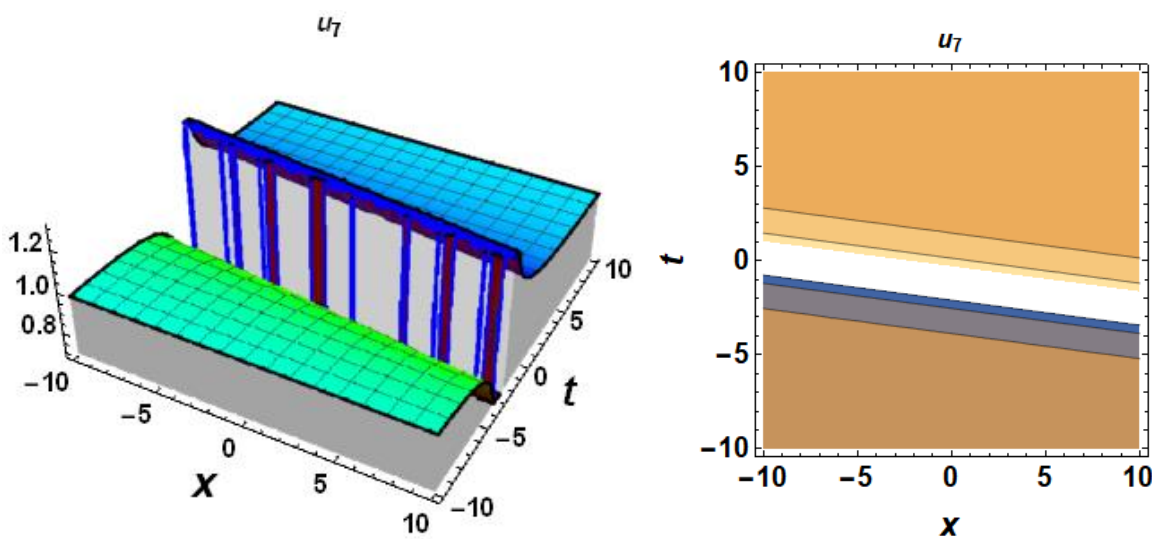


Figure 7. Graphs of $u_7(x, y, z, t) = u_7$ for $\mu = 2$, $\beta = 1$, $a_0 = 10$, $\gamma = 5$, $\alpha = 2$, $c_1 = 3$, $c_2 = 2$, $y = 1$, $z = 1$.

Case 8.

$$a_1 = 2\alpha, \quad b_1 = 0, \quad c = -\frac{3\alpha\gamma}{2\beta}, \quad \mu = 0, \quad \xi = \alpha x + \beta y + \gamma z - ct, \tag{30}$$

replacing values Eq. (30) into Eq. (14) and attain the following rational exact solution for Eq. (1):

$$u_8(x, y, z, t) = \frac{2 c_2 \alpha}{c_1 + c_2(x\alpha + y\beta + z\gamma + \frac{3t\alpha\gamma}{2\beta})} + a_0. \tag{31}$$

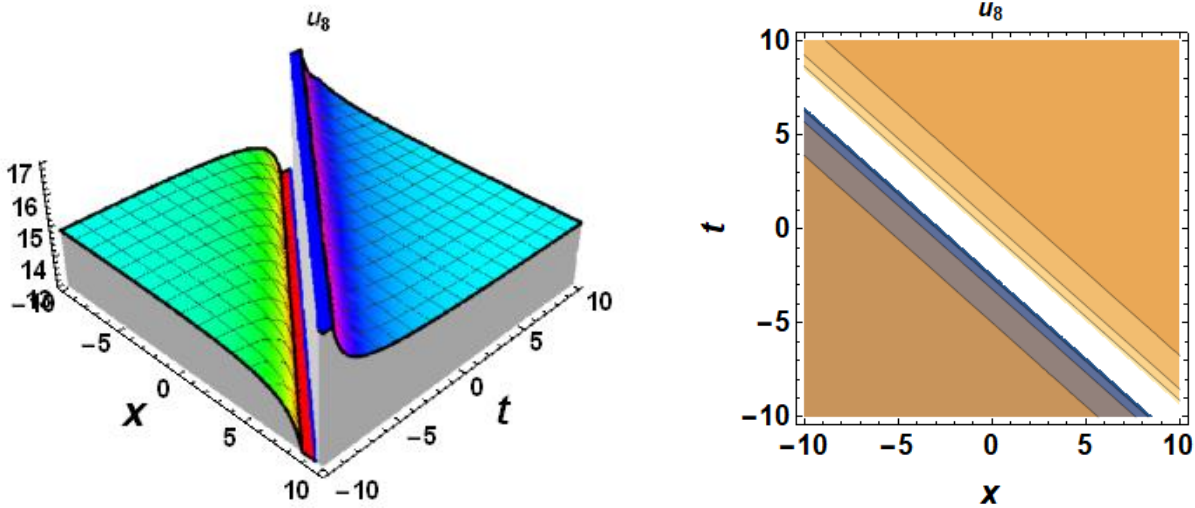


Figure 8. Graphs of $u_8(x, y, z, t) = u_8$ for $\beta = 4, a_0 = 15, \gamma = 3, a_0 = 5, \alpha = 5, c_1 = 1, c_2 = 1, y = 1, z = 1$.

Case 9.

$$a_1 = 2\alpha, \quad b_1 = 0, \quad \mu = 0, \quad \beta = -\frac{3\alpha\gamma}{2c}, \quad \xi = \alpha x + \beta y + \gamma z - ct, \tag{32}$$

replacing values Eq. (32) into Eq. (14) and attain the following rational exact solution for Eq. (1):

$$u_9(x, y, z, t) = \frac{2 c_2 \alpha}{c_1 + c_2(-ct + x\alpha + z\gamma - \frac{3y\alpha\gamma}{2c})} + a_0. \tag{33}$$

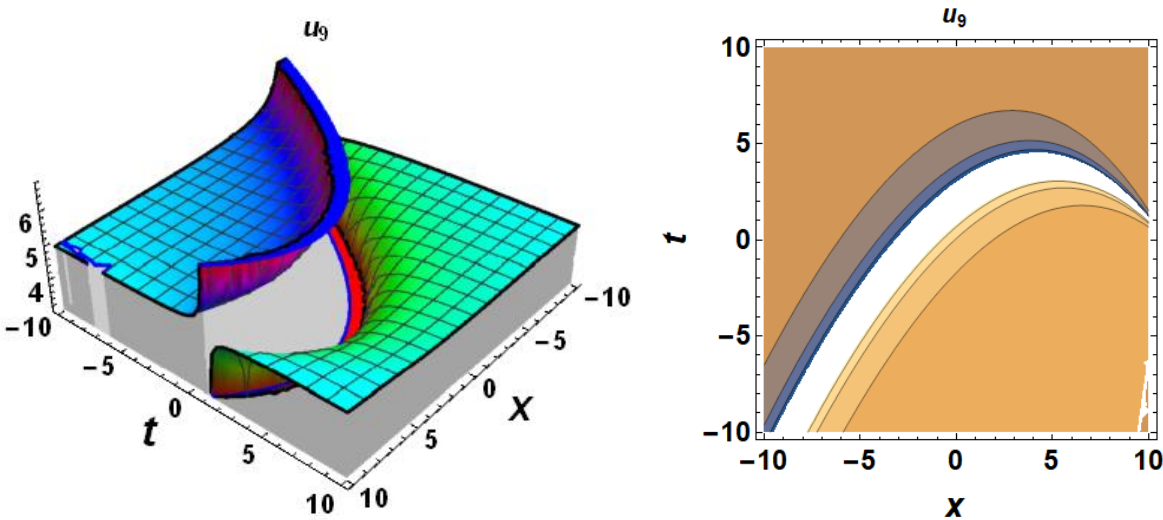


Figure 9. Graphs of $u_9(x, y, z, t) = u_9$ for $c = 1, \beta = 1, a_0 = 5, \gamma = 4, \alpha = 7, c_1 = 5, c_2 = 3, z = 1.5, y = 2$.

4. Conclusion

The $(G'/G, 1/G)$ -expansion method was used to establish hyperbolic, trigonometric, complex trigonometric, and rational traveling wave solutions for the (3+1DJM) equation. For the solutions found, real and imaginary graphics are presented for different values given to the constants. This equation has been presented by many authors by applying different methods, traveling wave solutions. The $(G'/G, 1/G)$ -expansion method was applied to the (3+1DJM) equation for the first time and the solutions produced by this method are of different types. The traveling wave solutions produced by the $(G'/G, 1/G)$ -expansion method are trigonometric, complex trigonometric, hyperbolic and rational type solutions. There is a singular point within these solutions. Therefore, constants in solutions presented in shock wave theory and asymptotic behavior analysis will be much more valuable when the physical meaning is loaded. In this study, the applied method is effective, powerful, and will be used in future works to establish new exact solutions of many other NLEEs. Also, the ready computer package program is used for graphics and computations in this letter.

Acknowledgment

We would like to thank Fırat University and Ardahan University for their support to our study.

Conflict of Interest Statement

The authors declare that they have no known competing financial interests or personal relationships that could have appeared to influence the work reported in this paper.

Author Contribution Statement: All authors have contributed equally to the manuscript.

References

- [1] Ekici M., Mirzazadeh M., Sonmezoglu A., Ullah M. Z., Zhou Q., Triki H., Biswas A., Optical solitons with anti-cubic nonlinearity by extended trial equation method, *Optik*, 136 (2017) 368-373.
- [2] Rezazadeh H., Tariq H., Eslami M., Mirzazadeh M., Zhou Q., New exact solutions of nonlinear conformable time-fractional Phi-4 equation, *Chinese Journal of Physics*, 56 (6) (2018) 2805-2816.
- [3] Durur H., Different types analytic solutions of the (1+1)-dimensional resonant nonlinear Schrödinger's equation using (G'/G) -expansion method, *Modern Physics Letters B*, 34(03) (2020) 2050036.
- [4] Yokus A., Kuzu B., Demiroğlu U., Investigation of solitary wave solutions for the (3+1)-dimensional Zakharov - Kuznetsov equation. *International Journal of Modern Physics B*, 33(29) (2019) 1950350.
- [5] Su-Ping Q., Li-Xin T., Modification of the Clarkson–Kruskal Direct Method for a Coupled System, *Chinese Physics Letters*, 24 (10) (2007) 2720.
- [6] Manafian J., Lakestani, M., Abundant soliton solutions for the Kundu–Eckhaus equation via $\tan(\phi(\xi))$ -expansion method, *Optik*, 127 (14) (2016) 5543-5551.
- [7] Yavuz M., Özdemir N., An Integral Transform Solution for Fractional Advection-Diffusion Problem, *Mathematical Studies and Applications*, 442 (2018) 4-6 October.
- [8] Duran S., Kaya D., Applications of a new expansion method for finding wave solutions of nonlinear differential equations, *World Applied Sciences Journal*, 18 (11) (2012) 1582-1592.
- [9] Cattani C., Sulaiman T. A., Baskonus H. M., Bulut H., On the soliton solutions to the Nizhnik-Novikov-Veselov and the Drinfel'd-Sokolov systems, *Optical and Quantum Electronics*, 50 (3) (2018) 138.
- [10] Kumar D., Seadawy A. R., Joardar A. K., Modified Kudryashov method via new exact solutions for some conformable fractional differential equations arising in mathematical biology, *Chinese journal of physics*, 56 (1) (2018) 75-85.
- [11] Yokuş A., Durur H., Complex hyperbolic traveling wave solutions of Kuramoto-Sivashinsky equation using $(1/G')$ expansion method for nonlinear dynamic theory, *Journal of Balıkesir University Institute of Science and Technology*, 21 (2) (2019) 590-599.

- [12] Yokus A., Durur H., Ahmad H., Thounthong, P., Zhang Y. F., Construction of exact traveling wave solutions of the Bogoyavlenskii equation by $(G'/G, 1/G)$ -expansion and $(1/G')$ -expansion techniques, *Results in Physics*, 19 (2020) 103409.
- [13] Yokus A., Durur H., Ahmad H., Hyperbolic type solutions for the couple Boiti-Leon-Pempinelli system, *Facta Universitatis, Series: Mathematics and Informatics*, 35 (2) (2020) 523-531.
- [14] Durur H., Yokuş A., Analytical solutions of Kolmogorov–Petrovskii–Piskunov equation, *Journal of Balikesir University Institute of Science and Technology*, 22 (2) (2020) 628-636.
- [15] Yokus A., Durur H., Ahmad H., Yao S. W., Construction of Different Types Analytic Solutions for the Zhiber-Shabat Equation, *Mathematics*, 8 (6) (2020) 908.
- [16] Aziz I., Şarler, B., The numerical solution of second-order boundary-value problems by collocation method with the Haar wavelets, *Mathematical and Computer Modelling*, 52 (9-10) (2010) 1577-1590.
- [17] Aziz I., Asif M., Haar wavelet collocation method for three-dimensional elliptic partial differential equations, *Computers & Mathematics with Applications*, 73 (9) (2017) 2023-2034.
- [18] Darvishi M., Arbabi S., Najafi M., Wazwaz, A., Traveling wave solutions of a (2+1)-dimensional Zakharov-like equation by the first integral method and the tanh method, *Optik*, 127 (16) (2016) 6312-6321.
- [19] Gao W., Silambarasan R., Baskonus H. M., Anand R. V. and Rezaadeh H., Periodic waves of the non-dissipative double dispersive micro strain wave in the micro structured solids, *Physica A: Statistical Mechanics and its Applications*, 545 (2020).
- [20] Duran S., Askin M., Sulaiman T. A., New soliton properties to the ill-posed Boussinesq equation arising in nonlinear physical science, *An International Journal of Optimization and Control: Theories & Applications (IJOCTA)*, 7 (3) (2017) 240-247.
- [21] Faraj B., Modanli M., Using Difference Scheme Method for the Numerical Solution of Telegraph Partial Differential Equation, (2017).
- [22] Çelik N., Seadawy A. R., Özkan Y. S., Yaşar E., A model of solitary waves in a nonlinear elastic circular rod: Abundant different type exact solutions and conservation laws, *Chaos, Solitons & Fractals*, 143 (2021) 110486.
- [23] Duran S., Solitary Wave Solutions of the Coupled Konno-Oono Equation by using the Functional Variable Method and the Two Variables $(G'/G, 1/G)$ -Expansion Method, *Adıyaman University Journal of Science*, 10 (2) (2020) 585-594.
- [24] Yavuz M., Sulaiman T. A., Yusuf A., Abdeljawad T., The Schrödinger-KdV equation of fractional order with Mittag-Leffler nonsingular kernel. *Alexandria Engineering Journal*, 60(2) (2021) 2715-2724.
- [25] Evirgen F., Uçar S., Özdemir N., Hammouch Z., System response of an alcoholism model under the effect of immigration via non-singular kernel derivative, *Discrete and Continuous Dynamical Systems-S*, (2018) 10.
- [26] Kaya D., Bulut H., Inc, M., Numerical Study of a Klein-Gordon Equation by The Adomian's Decomposition Method, *Hadronic Journal*, 28 (3) (2005) 311.
- [27] Duran S., Exact Solutions for Time-Fractional Ramani and Jimbo-Miwa Equations by Direct Algebraic Method, *Advanced Science, Engineering and Medicine*, 12 (7) (2020) 982-988.
- [28] Yokuş A., Durur H., Abro K. A., Kaya D., Role of Gilson–Pickering equation for the different types of soliton solutions: a nonlinear analysis, *The European Physical Journal Plus*, 135 (8) (2020) 1-19.
- [29] Duran S., Kaya D., New Wave Solutions for Nonlinear Differential Equations using an Extended Bernoulli Equation as a New Expansion Method, In ITM Web of Conferences, Kıbrıs-Girne, (2018), (22) 01035 1-5.
- [30] Siddique I., Rizvi, S. T. R., Batool, F., New exact travelling wave solutions of nonlinear evolution equations, *International Journal of Nonlinear Science*, 9 (1) (2010) 12-18.

- [31] Jimbo M., Miwa T., Solitons and infinite dimensional Lie algebras, Publications of the Research Institute for Mathematical Sciences, 19 (3) (1983) 943-1001.
- [32] Wazwaz A. M., Multiple-soliton solutions for extended (3+1)-dimensional Jimbo–Miwa equations, *Applied Mathematics Letters*, 64 (2017) 21-26.
- [33] Zhang S., New periodic wave solutions of a (3+1)-dimensional Jimbo–Miwa equation. *SN Applied Sciences*, 1 (3) (2019) 201.
- [34] Ma W. X., Lee J. H., A transformed rational function method and exact solutions to the 3+1 dimensional Jimbo–Miwa equation, *Chaos, Solitons & Fractals*, 42 (3) (2009) 1356-1363.
- [35] Sun H. Q., Chen, A. H., Lump and lump–kink solutions of the (3+1)-dimensional Jimbo–Miwa and two extended Jimbo–Miwa equations, *Applied Mathematics Letters*, 68 (2017) 55-61.
- [36] Yang J. Y., Ma W. X., Abundant lump-type solutions of the Jimbo–Miwa equation in (3+1)-dimensions, *Computers & Mathematics with Applications*, 73 (2) (2017) 220-225.
- [37] Liu X. Q., Jiang S., New solutions of the 3+1 dimensional Jimbo–Miwa equation. *Applied mathematics and computation*, 158 (1) (2004) 177-184.
- [38] Öziş T., Aslan İ., Exact and explicit solutions to the (3+ 1)-dimensional Jimbo–Miwa equation via the Exp-function method, *Physics Letters A*, 372 (47) (2008) 7011-7015.
- [39] Tang X. Y., Liang Z. F., Variable separation solutions for the (3+1)-dimensional Jimbo–Miwa equation, *Physics Letters A*, 351 (6) (2006) 398-402.
- [40] Ma W. X., Lump-type solutions to the (3+1)-dimensional Jimbo–Miwa equation, *International Journal of Nonlinear Sciences and Numerical Simulation*, 17 (7-8) (2016) 355-359.



Crossed modules bifibred over k -Algebras

Özgül GÜRMEŒ ALANSAL^{1,*} , Ummahan EGE ARSLAN²

¹Kütahya Dumlupınar University, Department of Mathematics, Kütahya, TURKEY

²Eskişehir Osmangazi University, Department of Mathematics and Computer Science, Eskişehir/ TURKEY

Abstract

In this paper we examine on a pair of adjoint functors (ϕ^*, ϕ_*) for a subcategory of the category of crossed modules over commutative algebras where $\phi_*: XMod/P \rightarrow XMod/Q$, induced, and $\phi^*: XMod/Q \rightarrow XMod/P$, pullback (co-induced), which enables us to move from crossed Q -modules to crossed P -modules by an algebra morphism $\phi: P \rightarrow Q$. We show that this adjoint functor pair (ϕ^*, ϕ_*) makes $p: XMod \rightarrow k-Alg$ into a bi-fibred category over $k-Alg$, the category of commutative algebras, where p is given by $p(C, R, \partial) = R$. Also, we give some examples and results on induced crossed modules in the case when ϕ is an epimorphism or the inclusion of an ideal.

Article info

History:

Received: 27.04.2020

Accepted: 13.01.2021

Keywords:

Induced crossed modules,

Base change functors,

Fibred and co-fibred

categories.

1. Introduction

The concept of fibration of categories concerns to give a general background to constructions similar to the pullback by a morphism. It seems to be a very useful notion for dealing with hierarchical structures. A functor which forgets the top level of structure is often usefully seen as a fibration or co-fibration of categories. In this work we give the main result that the forgetful functor $p: XMod \rightarrow k-Alg$ which sends $(C, R, \partial) \rightarrow R$ (base algebra) is (co)fibred. We see that the notion of (co)induced crossed modules plays a critical role in this result. Induced and co-induced crossed module constructions correspond the notion of “change of base” in the module theory. The idea is similar to the one above. That is if $\phi: S \rightarrow R$ is a ring homomorphism, then there is a functor ϕ^* from Mod/R to Mod/S where S acts on an R -module via ϕ . This functor has a left adjoint ϕ_* giving the well known induced module via the tensor product. Analogously induced and co-induced crossed modules give a pair of adjoint functors (ϕ^*, ϕ_*) for a subcategory of the category of crossed modules over commutative algebras where $\phi^*: XMod/Q \rightarrow XMod/P$ and $\phi_*: XMod/P \rightarrow XMod/Q$. Porter, [1], and Nizar, [2], have just mentioned that this adjoint functor pair (ϕ^*, ϕ_*) makes $p: XMod \rightarrow k-Alg$ into a fibred and co-fibred category over $k-Alg$ for commutative and associative algebras, respectively. But nonetheless we prove this result with details using related definition and proposition. In particular, we give some examples

and results on crossed modules induced by a morphism of commutative algebras $\phi: S \rightarrow R$ in the case when ϕ is an epimorphism or the inclusion of an ideal. In the applications to commutative algebras, the induced crossed modules play an important role since the free crossed modules which are related to Koszul complexes given by Porter [3] are a special case of induced crossed modules. In [3], any finitely generated free crossed module $C \rightarrow R$ of commutative algebras was shown to have $C \cong R^n/d(\Lambda^2 R^n)$, i.e. the 2^{nd} Koszul complex term module the 2-boundaries where $d: \Lambda^2 R^n \rightarrow R^n$ is the Koszul differential. So, we think that the induced crossed modules of commutative algebras give useful information on Koszul-like constructions.

Analogous result has appeared in [4,5,6] for the group and groupoid theoretical case and in [7] it is showed that braided regular crossed module of groupoids bi-fibred over regular groupoids. Also, fibrations of 2-crossed modules of groups is given in [8].

Conventions: Throughout this paper k is a fixed commutative ring, R is a k -algebra with identity. All k -algebras will be assumed commutative and associative, but they will not be required to have unit elements unless stated otherwise.

2. Crossed Modules of Commutative Algebras

The general concept of a crossed module originates in the work [9] of Whitehead in algebraic topology.

*Corresponding author. e-mail address: ozgun.gurmen@dpu.edu.tr

A *crossed module* of algebras, (C, R, ∂) , consists of an R -algebra C and a k -algebra R with an action of R on C , $(r, c) \rightarrow r \cdot c$ for $c \in C, r \in R$, and an R -algebra morphism $\partial : C \rightarrow R$ satisfying the following condition for all $c, c' \in C$,

$$\partial(c) \cdot c' = cc'.$$

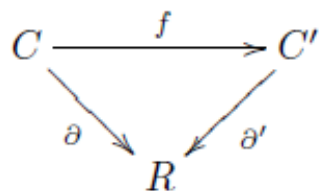
This condition is called the *Peiffer identity*. We call R , the base algebra and C , the top algebra. When we wish to emphasise the base algebra R , we call (C, R, ∂) , a crossed R -module.

A *morphism of crossed modules* from (C, R, ∂) to (C', R', ∂') is a pair (f, ϕ) of k -algebra morphisms $f : C \rightarrow C'$,

$$\phi : R \rightarrow R'$$

$$(i) \partial' f = \phi \partial \text{ and } (ii) f(r \cdot c) = \phi(r) \cdot f(c)$$

for all $c \in C, r \in R$. Thus, one can obtain the category $XMod$ of crossed modules of algebras. In the case of a morphism (f, ϕ) between crossed modules with the same base R , say, where ϕ is the identity on R ,



then we say that f is a morphism of crossed R -modules. This gives a subcategory $XMod/R$ of $XMod$.

Examples of crossed modules

1. Any ideal, I , in R gives an inclusion map $i : I \hookrightarrow R$, which is a crossed module then we will say (I, R, i) is an ideal pair. In this case, of course, R acts on I by multiplication and the inclusion homomorphism i makes (I, R, i) into a crossed module, an “inclusion crossed modules”. Conversely,

Lemma 1. If (C, R, ∂) is a crossed module, $\partial(C)$ is an ideal of R .

2. Any R -module M can be considered as an R -algebra with zero multiplication and hence the zero morphism $0 : M \rightarrow R$ is a crossed module. Again conversely,

Lemma 2. If (C, R, ∂) is a crossed module, $Ker \partial$ is an ideal in C and inherits a natural R -module structure from R -action on C . Moreover, $\partial(C)$ acts trivially on $Ker \partial$, hence $Ker \partial$ has a natural $R/\partial(C)$ -module structure. As these two examples suggest, general crossed modules lie between the two extremes of ideal and modules. Both aspects are important.

3. In the category of algebras, the appropriate replacement for automorphism groups is the bi-multiplication algebra $Bim(R)$ defined by Mac Lane [10]. (see also [11,12]). Let R be an associative (not necessarily unitary or commutative) k -algebra. $Bim(R)$ consists of pairs (γ, δ) of R -linear mappings from R to R such that

$$\begin{aligned} \gamma(rr') &= \gamma(r) \cdot r' \delta(rr') \\ &= r \cdot \delta(r') \text{ and} \\ r \cdot \gamma(r') &= \delta(r) \cdot r'. \end{aligned}$$

If R is a commutative algebra and $Ann(R) = 0$ or $R^2 = R$, then, since

$$\begin{aligned} x \cdot \delta(r) &= \delta(r) \cdot x \\ &= r \cdot \gamma(x) \\ &= \gamma(x) \cdot r \\ &= \gamma(xr) \\ &= \gamma(rx) \\ &= \gamma(r) \cdot x \\ &= x \cdot \gamma(r) \end{aligned}$$

for every $x \in R$, we get $\gamma = \delta$. Thus, $Bim(R)$ may be identified with the k -algebra $M(R)$ of multipliers of R . Recall that a multiplier of R is a linear mapping $\lambda : R \rightarrow R$ such that for all $r, r' \in R$

$$\lambda(rr') = \lambda(r) r'.$$

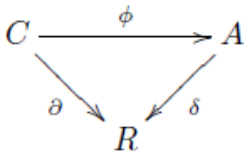
Also, $M(R)$ is commutative as

$$\begin{aligned} \lambda' \lambda(xr) &= \lambda' (\lambda(x)r) \\ &= \lambda(x) \lambda'(r) \\ &= \lambda'(r) \lambda(x) \\ &= \lambda \lambda'(rx) \\ &= \lambda \lambda'(xr) \end{aligned}$$

for any $x \in R$. Thus, $M(R)$ is the set of all multipliers λ such that $\lambda\gamma = \gamma\lambda$ for every multiplier γ . So automorphism crossed module corresponds to the multiplication crossed module $(R, M(R), \mu)$ where $\mu : R \rightarrow M(R)$ is defined by $\mu(r) = \lambda_r$ with $\lambda_r(r') = rr'$ for all $r, r' \in R$ and the action is given by $\lambda \cdot r = \lambda(r)$ (See [13] for details).

2.1. Free crossed modules

Let (C, R, ∂) be a crossed module, Y be a set, and $v : Y \rightarrow C$ be a function, then (C, R, ∂) is said to be a free crossed module with basis v or alternatively, on the function $\partial v : Y \rightarrow R$ if for any crossed R -module (A, R, δ) and a function $w : Y \rightarrow A$ such that $\delta w = \partial v$, there is a unique morphism $\phi : (C, R, \partial) \rightarrow (A, R, \delta)$ such that the diagram



is commutative.

For our purpose, an important standard construction of free crossed R-modules is as follows:

Suppose given $f : Y \rightarrow R$. Let $E = R^+[Y]$, the positively graded part of the polynomial ring on Y . f induces a morphism of R-algebras, $\theta : E \rightarrow R$ defined on generators by $\theta(y) = f(y)$. We define an ideal P in E (sometimes called by analogy with the group theoretical case, the Peiffer ideal relative to f) generated by the elements

$$\{pq - \theta(p)q : p, q \in E\}$$

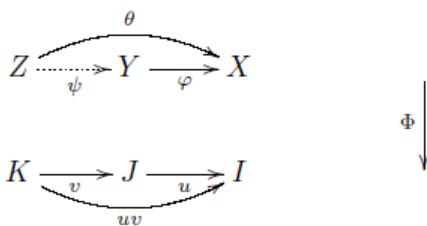
clearly $\theta(P) = 0$, so putting $C = E/P$, one obtains an induced morphism $\delta : C \rightarrow R$ which is the required free crossed R-module on f (cf. [3]). This construction will be seen later as a special case of an induced crossed module.

3. Fibrations and Co-fibrations Categories

We recall the definitions of fibration and co-fibration of categories which are also known as Grothendieck fibrations and co-fibrations.

Definition 3. Let $\Phi : X \rightarrow B$ be a functor. A morphism $\varphi : Y \rightarrow X$ in X over $u := \Phi(\varphi)$ is called cartesian if and only if for all $v : K \rightarrow J$ in B and $\theta : Z \rightarrow X$ with $\Phi(\theta) = uv$ there is a unique morphism $\psi : Z \rightarrow Y$ with $\Phi(\psi) = v$ and $\theta = \varphi\psi$.

This is illustrated by the following diagram:



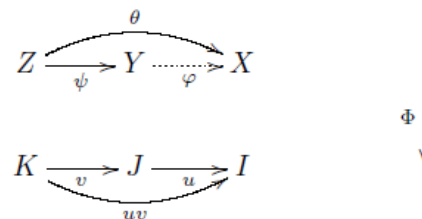
It is straightforward to check that cartesian morphisms are closed under composition, and that φ is an isomorphism if and only if φ is a cartesian morphism over an isomorphism.

A morphism $\alpha : Z \rightarrow Y$ is called vertical (with respect to Φ) if and only if $\Phi(\alpha)$ is an identity morphism in B . In particular, for $I \in B$ we write X/I , called the fibre over I , for the subcategory of X consisting of those morphisms α with $\Phi(\alpha) = id_I$.

Definition 4. The functor $\Phi : X \rightarrow B$ is a fibration or category fibred over B if and only if for all $u : J \rightarrow I$ in B and $X \in X/I$ there is a cartesian morphism $\varphi : Y \rightarrow X$ over u : such a φ is called a cartesian lifting of X along u .

In other words, in a category fibred over B , $\Phi : X \rightarrow B$, we can pull back objects of X along any arrow of B .

Definition 5. Let $\Phi : X \rightarrow B$ be a functor. A morphism $\varphi : Z \rightarrow Y$ in X over $v := \Phi(\varphi)$ is called cocartesian if and only if for all $u : J \rightarrow I$ in B and $\theta : Z \rightarrow X$ with $\Phi(\theta) = uv$ there is a unique morphism $\psi : Y \rightarrow X$ with $\Phi(\psi) = u$ and $\theta = \varphi\psi$. This is illustrated by the following diagram:



It is straightforward to check that co-cartesian morphisms are closed under composition, and that ψ is an isomorphism if and only if ψ is a co-cartesian morphism over an isomorphism.

Definition 6. The functor $\Phi : X \rightarrow B$ is a co-fibration or category co-fibred over B if and only if for all $v : K \rightarrow J$ in B and $Z \in X/K$ there is a cocartesian morphism $\psi : Z \rightarrow Z'$ over v : such a ψ is called a cocartesian lifting of Z along v .

Proposition 7. Let $\Phi : X \rightarrow B$ be a fibration of categories. Then $\psi : Z \rightarrow Y$ in X over $v : K \rightarrow J$ in B is cocartesian if only if for all $\theta' : Z \rightarrow X'$ over v there is a unique morphism $\psi' : Y \rightarrow X'$ in X/J with $\theta' = \psi'\psi$.

Taking this background into account, we get following results. These results are given in [6] in the case of crossed modules of groupoids.

Proposition 8. The forgetful functor $p: XMod \rightarrow k - Alg$ which sends $(C, R, \partial) \mapsto R$ (base algebra), is fibred.

Proof. Let (C, R, ∂) be a crossed R-module and let $\phi: S \rightarrow R$ be a morphism of k-algebras. Then

$\phi^*(C) = \{(c, s) \mid \phi(s) = \partial(c), s \in S, c \in C\}$ has the S-algebra structure by

$$s \cdot (c, s') = (\phi(s) \cdot c, ss')$$

for $(c, s') \in \phi^*(C)$, $s \in S$ and $\partial^*: \phi^*(C) \rightarrow S, \partial^*((c, s)) = s$ is a crossed S-module. It is immediate that ∂^* is a S-algebra morphism, while the Peiffer identity condition is proved as follows:

$$\begin{aligned} \partial^*(c, s) \cdot (c', s') &= s \cdot (c', s') \\ &= (\phi(s) \cdot c', ss') \\ &= (\partial(c) \cdot c', ss') \\ &= (cc', ss') \\ &= (c, s)(c', s') \end{aligned}$$

for $(c, s), (c', s') \in \phi^*(C)$. Also,
 $(\phi^C, \phi): (\phi^*(C), S, \partial^*) \rightarrow (C, R, \partial)$

is a morphism of crossed modules where $(\phi^C(c, s) = c, s)$, since

$$\begin{aligned} \phi^C(s'(c, s)) &= \phi^C(\phi(s')c, s's) \\ &= \phi(s') \cdot c \\ &= \phi(s') \cdot \phi^C(c, s) \end{aligned}$$

and clearly $\partial\phi^C = \phi\partial^*$.

Then for $g: T \rightarrow S$ in $k\text{-Alg}$ and $(f, \phi g): (B, T, \partial') \rightarrow (C, R, \partial)$ in $X\text{Mod}$ with $p((f, \phi g)) = \phi g$, there is a unique morphism of crossed modules $(f^*, g): (B, T, \partial') \rightarrow (\phi^*(C), S, \partial^*)$ given by $f^*(b) = (f(b), g\partial'(b))$ for all $b \in B$ such that $p((f^*, g)) = g$ and $(f, \phi g) = (\phi^C, \phi) = (f^*, g)$.

Existence of

$$\begin{aligned} (f^*, g): \partial^*(f^*(b)) &= \partial^*(f(b), g\partial'(b)) = g\partial'(b) \\ f^*(t \cdot b) &= (f(t \cdot b), g\partial'(t \cdot b)) \\ &= ((\phi g)(t) f(b), g(t)g\partial'(b)) \\ &= g(t) \cdot (f(b), g\partial'(b)) \\ &= g(b). \end{aligned}$$

Uniqueness of (f^*, g) : Suppose that $(f^{*'}, g')$: $(B, T, \partial') \rightarrow (\phi^*(C), S, \partial^*)$ is a crossed module morphism with

$$p((f^{*'}, g')) = g \text{ and } (f, \phi g) = (\phi^C, \phi)(f^{*'}, g').$$

It is clear that $g' = g$. $f^{*'}$ is defined as

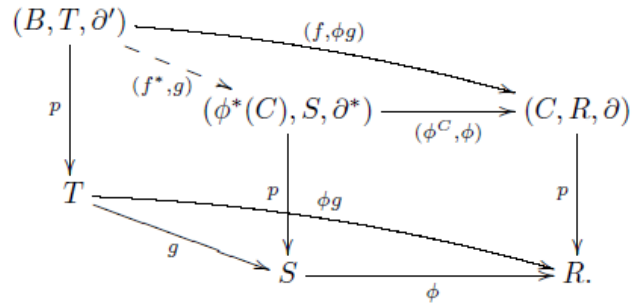
$(f^{*'}(b) = (c', s'))$ for some $c' \in C, s' \in S$. Then we have $f^{*'} = f^*$ as follows

$$\begin{aligned} (f^{*'}(b)) &= (c', s') \\ &= (\phi^C(c', s'), \partial^*(c', s')) \\ &= (\phi^C(f^{*'}(b), \partial^*(f^{*'}(b))) \\ &= (f(b), g'\partial'(b)) \\ &= (f(b), g\partial'(b)) \\ &= f^*(b) \end{aligned}$$

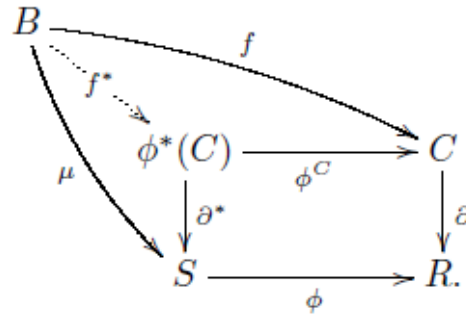
for all $b \in B$.

Thus, we get a cartesian morphism $(\phi^C, \phi): (\phi^*(C), S, \partial^*) \rightarrow (C, R, \partial)$, for $\phi: S \rightarrow R$ in $k\text{-Alg}$ and (C, R, ∂) in $X\text{Mod}/R$, as required.

This is illustrated by the following diagram:



We note that $(\phi^*(C), S, \partial^*)$ is usually called “pullback crossed module” and it can be given by a pullback diagram:



We will give some examples of pullback crossed modules of commutative algebras, some of them is given in [2] for non-commutative algebra case.

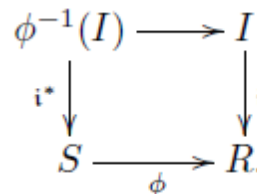
Examples of pullback crossed modules

1. Given crossed module $i: I \hookrightarrow R$ where i is an inclusion of an ideal. The pullback crossed module is $(\phi^*(I), S, i^*) \cong (\phi^{-1}(I), S, i^*)$

where,

$$\begin{aligned} \phi^*(I) &= \{(i, s) \mid \phi(s) = i(i), s \in S, i \in I\} \\ &\cong \{s \in S \mid \phi(s) = i \in I\} = \phi^{-1}(I) \\ &\trianglelefteq S \end{aligned}$$

The pullback diagram is



Particularly if $I = \{0\}$, then

$$\phi^*(\{0\}) \cong \text{Ker } \phi$$

and so $(\text{Ker } \phi, S, i^*)$ is a pullback crossed module. Kernels are thus particular cases of pullbacks.

Also, if ϕ is onto and $I = R$, then $\phi^*(R) \cong S$

2. Given a crossed module $0 : M \rightarrow R, 0(m) = 0$, where M is any R -module, so it is also an R -algebra with zero multiplication.

Then $\phi^*(M, R, 0) = \phi^*(M), S, 0^*$ where

$$\phi^*(M) = \{(m, s) \in M \times S \mid \phi(s) = 0(m) = 0\} \cong M \times \text{Ker}\phi$$

The corresponding pullback diagram is

$$\begin{array}{ccc} M \times \text{Ker}\phi & \longrightarrow & M \\ \downarrow 0^* & & \downarrow 0 \\ S & \xrightarrow{\phi} & R. \end{array}$$

So, if ϕ is injective, then $M \cong \phi^*(M)$. If $M = \{0\}$, then $\phi^*(M) \cong \text{Ker}\phi$.

A pullback crossed module $(\phi^*(C), S, \partial^*)$ for $\phi : S \rightarrow R$ in $k\text{-Alg}$ gives a functor

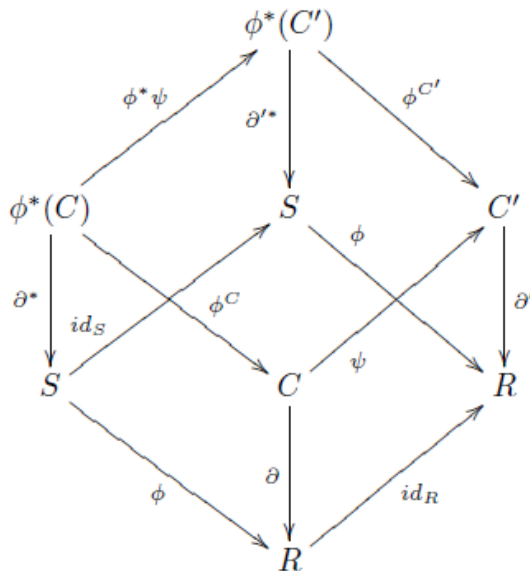
$$\phi^* : \text{XMod}/R \rightarrow \text{XMod}/S$$

which has appeared in the work of Porter [1] as “restriction along $\phi : S \rightarrow R$ ”.

Proposition 9. For each morphism $(\psi, id_R) : (C, R, \partial) \rightarrow (C', R', \partial')$ in XMod/R , the morphism

$(\phi^*\psi, id_S) : \phi^*(C), S, \partial^* \rightarrow \phi^*(C'), S, \partial'^*$ in XMod/S is the unique morphism satisfying the equality $(\psi, id_R)(\phi^C, \phi) = (\phi^{C'}, \phi)(\phi^*\psi, id_S)$.

Proof. Since $\phi^{C'}((\phi^*\psi)(c, s)) = \phi^{C'}(\psi(c), s) = \psi(c) = \psi\phi^C(c, s)$ for $(c, s) \in \phi^*(C)$ and $id_R\phi = \phi id_S$, we get the equation as required.



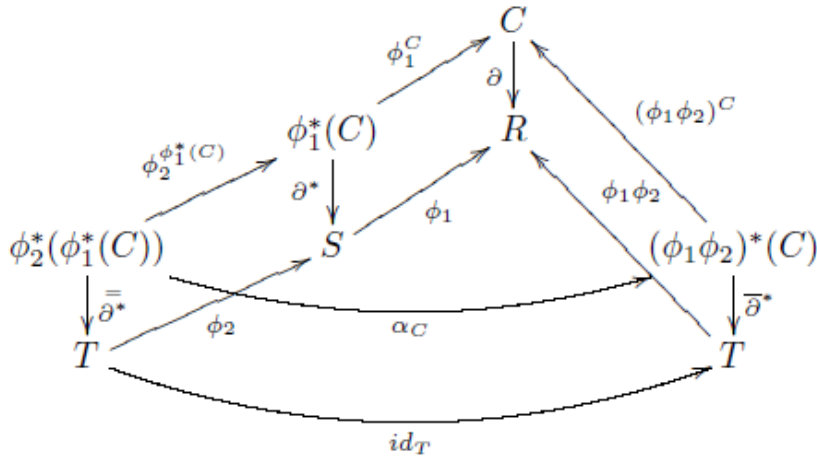
Proposition 10. If $\phi_1 : S \rightarrow R, \phi_2 : T \rightarrow S$ are two morphisms of k -algebras, then $(\phi_1\phi_2)^*$ and $\phi_2^*\phi_1^*$ are naturally isomorphic.

Proof. Given any crossed R -module (C, R, ∂) , we define $\alpha_C : \phi_2^*\phi_1^*(C) \rightarrow (\phi_1\phi_2)^*(C)$ as $\alpha_C((c, \phi_2(t)), t) = (c, t)$ for all $((c, \phi_2(t)), t) \in \phi_2^*\phi_1^*(C)$. Clearly α_C is well defined and a k -algebra morphism. Also, since

$$\begin{aligned} \alpha_C(t' \cdot (c, \phi_2(t)), t) &= \alpha_C(\phi_2(t')) \cdot ((c, \phi_2(t)), t't) \\ &= \alpha_C((\phi_1(\phi_2(t'))) \cdot c, \phi_2(t')\phi_2(t), t't) \\ &= \alpha_C((\phi_1(\phi_2(t'))) \cdot c, \phi_2(t't), t't) \\ &= (\phi_1(\phi_2(t'))) \cdot c, t't) \\ &= t' \cdot (c, t) \\ &= t' \cdot \alpha_C((c, \phi_2(t)), t) \end{aligned}$$

and

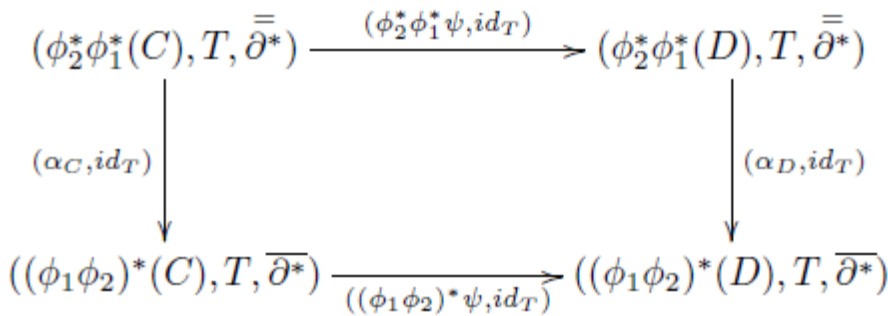
$\bar{\partial}^*\alpha_C((c, \phi_2(t)), t) = \bar{\partial}^*(c, t) = t = id_T\bar{\partial}^*((c, \phi_2(t)), t)$, (α_C, id_R) is a crossed module morphism. It is clear that (α_C, id_T) is an isomorphism.



In addition, for each crossed R -module morphism $(\psi, id_R): (C, R, \partial) \rightarrow (D, R, \varphi)$ and $((c, \phi_2(t)), t) \in \phi_2^* \phi_1^*(C)$, we get

$$\begin{aligned} ((\phi_1 \phi_2)^* \psi) \alpha_C((c, \phi_2(t)), t) &= ((\phi_1 \phi_2)^* \psi)(c, t) \\ &= (\psi(c), t) = \alpha_D((\psi(c), \phi_2(t)), t) \\ &= \alpha_D(\phi_2^* \phi_1^* \psi)((c, \phi_2(t)), t) \end{aligned}$$

i.e., the diagram



is commutative and this completes the proof.

Proposition 11. If $p : XMod \rightarrow k\text{-Alg}$ is fibred, $\phi: S \rightarrow R$ in $k\text{-Alg}$, and a reindexing functor

$$\begin{aligned} \phi^*: XMod/R \rightarrow XMod/S \text{ is chosen, then there is a bijection} \\ XMod_\phi((B, S, \mu), (C, R, \partial)) \cong XMod/S((B, S, \mu), \phi^*(C), S, \partial^*) \end{aligned}$$

natural in $(B, S, \mu) \in XMod/S$, $(C, R, \partial) \in XMod/R$ where $XMod_\phi((B, S, \mu), (C, R, \partial))$ consists of those morphisms $\alpha \in XMod((B, S, \mu), (C, R, \partial))$ with $p(\alpha) = \phi$.

Proof. Define

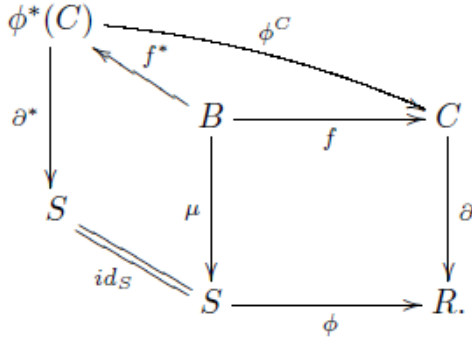
$$F: XMod_\phi((B, S, \mu), (C, R, \partial)) \rightarrow XMod/S((B, S, \mu), \phi^*(C), S, \partial^*)$$

as $F(f, \phi) = (f^*, id_S)$ such that $f^*(b) = (f(b), \mu(b))$. Assume that for $(f, \phi), (g, \phi) \in XMod_\phi((B, S, \mu), (C, R, \partial))$, $F(f, \phi) = F(g, \phi)$. Then we get $(f^*, id_S) = (g^*, id_S)$ and so

$(f(b), \mu(b)) = (g(b), \mu(b))$ i.e., $f = g$. Thus, F is one to one. Suppose that $(f^*, id_S) \in XMod/S((B, S, \mu), \phi^*(C), S, \partial^*)$. Then there is $(\phi^C f^*, \phi) \in XMod_\phi((B, S, \mu), (C, R, \partial))$ where $\phi^C(c, s) = c$ such that $F(\phi^C f^*, \phi) = (f^*, id_S)$.

It is clear from $F(\varphi^C f^*, \varphi) = ((\varphi^C (f^*)^*, id_S)$ and

$$\begin{aligned} (\varphi^C f^*)^*(b) &= ((\varphi^C f^*)(b), \mu(b)) \\ &= (\varphi^C(f(b), \mu(b)), \mu(b)) \\ &= (f(b), \mu(b)) \\ &= f^*(b) \end{aligned}$$



So, F is a bijection.

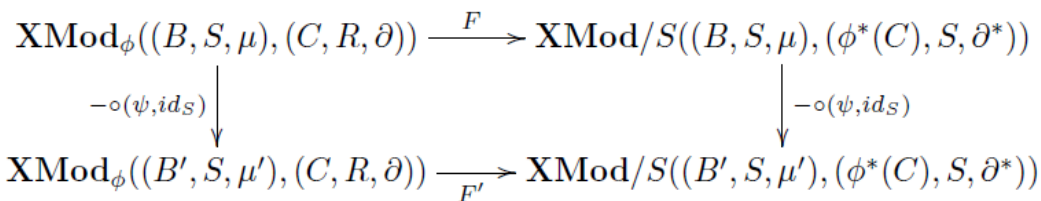
Moreover, since for crossed module morphism $(\psi, id_S): (B', S, \mu) \rightarrow (B, S, \mu')$, $b' \in B'$

$$\begin{aligned} (f^*\psi)(b') &= (f(\psi(b')), \mu(\psi(b'))) \\ &= ((f\psi)(b'), (\mu\psi)(b')) \\ &= (f\psi^*)(b') \end{aligned}$$

and

$$\begin{aligned} (- \circ (\psi, id_S))F(f, \phi) &= (- \circ (\psi, id_S))(f^*, id_S) \\ &= (f^*\psi, id_S) \\ &= ((f\psi)^*, id_S) \\ &= F'(f\psi, \phi) \\ &= (F'(- \circ (\psi, id_S)))(f, \phi), \end{aligned}$$

we get following commutative diagram



Thus, F is natural in (B, S, μ) . Furthermore, for $(\psi, id_R): (C, R, \partial') \rightarrow (C', R, \partial')$ we have

$$\begin{aligned} (\psi f)^*(b) &= ((\psi f)(b), \mu(b)) = (\psi(f(b)), \mu(b)) \\ &= (\phi^*\psi)(f(b), \mu(b)) \\ &= (\phi^*\psi)f^*(b) \end{aligned}$$

for $b \in B$, and

$$\begin{aligned}
 ((\phi^*\psi, id_S) \circ -)F(f, \phi) &= (\phi^*\psi, id_S)(f^*, id_S) \\
 &= ((\phi^*\psi)f^*, id_S) \\
 &= ((\psi f)^*, id_S) \\
 &= F''(\psi f, \phi) \\
 &= (F''((\psi, id_R) \circ -))(f, \phi).
 \end{aligned}$$

which means the diagram

$$\begin{array}{ccc}
 \mathbf{XMod}_\phi((B, S, \mu), (C, R, \partial)) & \xrightarrow{F} & \mathbf{XMod}/S((B, S, \mu), (\phi^*(C), S, \partial^*)) \\
 (\psi, id_R) \circ - \downarrow & & \downarrow (\phi^*\psi, id_S) \circ - \\
 \mathbf{XMod}_\phi((B, S, \mu), (C', R, \partial')) & \xrightarrow{F''} & \mathbf{XMod}/S((B, S, \mu), (\phi^*(C'), S, \partial'^*)).
 \end{array}$$

is commutative and F is natural in (C, R, ∂) .

We now give the dual of Proposition [8].

Proposition 12. The forgetful functor $p: \mathbf{XMod} \rightarrow k\text{-Alg}$ is co-fibred.

Proof. Given a k -algebra morphism $\phi: S \rightarrow R$ and a crossed module $\partial: D \rightarrow S$, and let the set $F(D \times R)$ be a free algebra generated by the elements of $D \times R$. Let P be the ideal generated by all the relations of the three following types:

$$\begin{aligned}
 (d_1, r) + (d_2, r) &= (d_1 + d_2, r) \\
 (s \cdot d, r) &= (d, \phi(s)r) \\
 (d_1, r_1)(d_2, r_2) &= (d_2, r_1(\phi\partial d_1)r_2)
 \end{aligned}$$

for any $d, d_1, d_2 \in D$, and $r \in R, s \in S$. We define

$$\phi_*(D) = F(D \times R)/P.$$

This is an R -algebra with

$$r' \cdot (d \otimes r) = d \otimes r'r$$

for $d \in D, r, r' \in R$ and $\partial_*: \phi_*(D) \rightarrow R, \partial_*(d \otimes r) = \phi\partial(d)r$ is an R -algebra morphism and since

$$\begin{aligned}
 \partial_*(d \otimes r) \cdot (d_1 \otimes r_1) &= ((\phi\partial d)r) \cdot (d_1 \otimes r_1) \\
 &= (d_1 \otimes \phi(\partial d)rr_1) \\
 &= (\partial d \cdot d_1 \otimes rr_1) \\
 &= (dd_1 \otimes rr_1) \\
 &= (d \otimes r)(d_1 \otimes r_1),
 \end{aligned}$$

for $d \otimes r, d_1 \otimes r_1 \in D \otimes_S R$, ∂_* is a crossed R -module. Also, since R has a unit, if $\phi': D \rightarrow \phi_*(D)$ is defined by $\phi'(d) = (d \otimes 1)$, then

$$\begin{aligned}
 \phi'(s \cdot d) &= (s \cdot d \otimes 1) \\
 &= (d \otimes \phi(s)) \\
 &= \phi(s) \cdot (d \otimes 1) \\
 &= \phi(s) \cdot \phi'(d)
 \end{aligned}$$

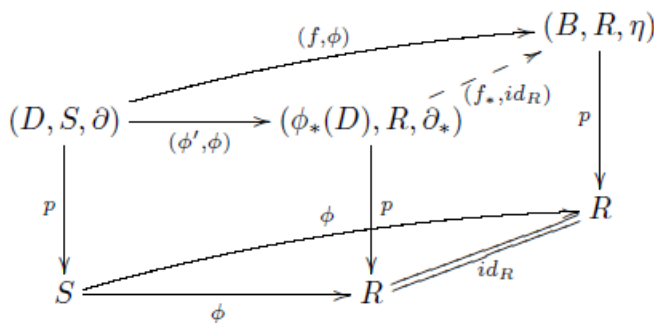
for $d \in D$, $s \in S$, and clearly $\partial_* \phi' = \phi \partial$, so $(\phi', \phi): (D, S, \partial) \rightarrow (\phi_*(D), R, \partial_*)$ is a crossed module morphism. Then for $(f, \phi): (D, S, \partial) \rightarrow (B, R, \eta)$ over $\phi: S \rightarrow R$ there is a unique morphism $(f_*, id_R): (\phi_*(D), R, \partial_*) \rightarrow (B, R, \eta)$ given by $f_*(d \otimes r) = r \cdot f(d)$ for all $d \otimes r \in \phi_*(D)$ in $XMod/R$ with $(f, \phi) = (f_*, id_R)(\phi', \phi)$.

Existence of (f_*, id_R) :

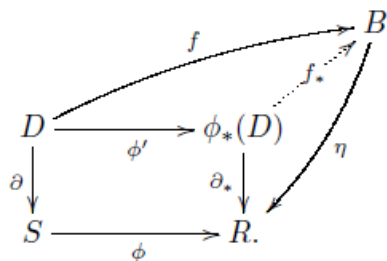
$$\begin{aligned} f_*(r' \cdot (d \otimes r)) &= f_*(d \otimes r'r) \\ &= r'r \cdot f(d) \\ &= r' \cdot (r \cdot f(d)) \\ &= r' \cdot f_*(d \otimes r) \\ &= id_R(r') \cdot f_*(d \otimes r) \end{aligned}$$

and

$$\begin{aligned} (\eta f_*)(d \otimes r) &= \eta(f_*(d \otimes r)) \\ &= \eta(r \cdot f(d)) \\ &= r\eta(f(d)) \\ &= r\phi(\partial(d)) \\ &= \partial_*(d \otimes r) \\ &= id_R \partial_*(d \otimes r) \end{aligned}$$



We have seen that the above result is described in terms of the crossed module $\partial_*: \phi_*(D) \rightarrow R$ induced from the crossed module $\partial: D \rightarrow S$ by a morphism $\theta: S \rightarrow R$. It is called “induced crossed module” and it can be given by the following diagram:



We will give the following examples of induced crossed modules of commutative algebras.

for each $d \otimes r \in \phi_*(D), r' \in R$ so (f_*, id_R) is a crossed R -module morphism also $f_* \phi' = f$.

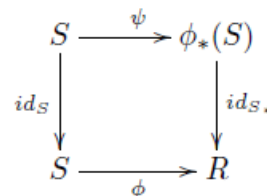
Uniqueness of (f_*, id_R) : Suppose that $(f'_*, id_R): (\phi_*(D), R, \partial_*) \rightarrow (B, R, \eta)$ is a crossed module morphism with $p(f'_*, id_R) = id_R$ and $(f, \phi) = (f'_*, id_R)(\phi', \phi)$. Then we get

$$\begin{aligned} f_*(d \otimes r) &= r \cdot f(d) \\ &= r \cdot f'_* \phi'(d) \\ &= r \cdot f'_*(d \otimes 1) \\ &= f'_*(r \cdot (d \otimes 1)) \\ &= f'_*(d \otimes r), \end{aligned}$$

so $f'_* = f_*$. Thus, we have a cocartesian morphism (ϕ', ϕ) in $XMod$ over $\phi: S \rightarrow R$ in $k-Alg$ by Proposition [7]. That is, we obtain the following commutative diagram:

Examples of induced crossed modules

Let $D = S$ and $id_S: S \rightarrow S$ be identity crossed S -modules. The induced crossed module diagram is



where $\phi_*(S) = S \otimes_S R$.

(Remark: S has not unit, otherwise $S \otimes_S R \cong R$). When we take $S = k^+[X]$ the positively graded part of the polynomial algebra over k on the set of generators

X , we have the induced crossed module $\partial_*: k^+[X] \otimes_{k^+[X]} R \rightarrow R$ which is the free R -module on $f: X \rightarrow R$. Thus, the free crossed modules is the special case of the induced crossed modules.

with $\theta(p, r) = \partial_*(p \otimes r) = \phi(p)r$ for all $p \in k^+[X]$, $r \in R$, where P is an ideal generated by all the relations given in the proof of Proposition 12. From

Considering the free crossed module construction given in the first section, we have a diagram

$$\begin{array}{ccc} k^+[X] \times R & \xrightarrow{\theta} & R \\ \downarrow & \searrow \theta_* & \\ (k^+[X] \times R) / P = k^+[X] \otimes_{k^+[X]} R & & \end{array}$$

$$\begin{aligned} \theta((p_1, r) + (p_2, r) - (p_1 + p_2, r)) &= \theta(p_1, r) + \theta(p_2, r) - \theta(p_1 + p_2, r) \\ &= \phi(p_1)r + \phi(p_2)r - (\phi(p_1) + \phi(p_2))r \\ &= 0 \end{aligned}$$

$$\begin{aligned} \theta((p \cdot q, r) - (q, \phi(p)r)) &= \theta(pq, r) - \theta(q, \phi(p)r) \\ &= \phi(pq)r + \phi(q)\phi(p)r \\ &= 0 \end{aligned}$$

$$\begin{aligned} \theta((p_1, r_1)(p_2, r_2) - (p_2, r_1\phi\partial(p_1)r_2)) &= \theta(p_1, r_1)\theta(p_2, r_2) - \theta(p_2, r_1\phi\partial(p_1)r_2) \\ &= \phi(p_1)r_1\phi(p_2)r_2 - \phi(p_2)r_1\phi\partial(p_1)r_2 \\ &= 0, \end{aligned}$$

we get $\theta(P) = 0$, and have the pushout diagram

$$\begin{array}{ccccc} X & \longrightarrow & k^+[X] & \xrightarrow{\phi'} & \phi_*(k^+[X]) & \longrightarrow & A \\ \parallel \text{id} & & \downarrow \partial & & \downarrow \partial_* & \nearrow \delta & \\ X & \xrightarrow{i} & k^+[X] & \xrightarrow{\phi} & R & & \end{array}$$

where $\phi_*(k^+[X]) = k^+[X] \otimes_{k^+[X]} R$. Also, by considering the connection between free crossed module $\partial: k^+[X] \otimes_{k^+[X]} R \rightarrow R$ and the usual Koszul differential $d: \Lambda^2 R^n \rightarrow R^n$, we get

$$k^+[X] \otimes_{k^+[X]} R \cong R^n / d(\Lambda^2 R^n).$$

(see [1,3] and [14] for details.)

2. Let D be S -module and $0 = \partial: D \rightarrow S$ be zero morphism. The pushout diagram is

$$\begin{array}{ccc}
 D & \xrightarrow{\psi} & \phi_*(D) \\
 \partial=0 \downarrow & & \downarrow \partial_* \\
 S & \xrightarrow{\phi} & R
 \end{array}$$

where

$$\begin{aligned}
 \partial_*(d \otimes r) &= \phi(\partial(d))r \\
 &= \phi(0)r \\
 &= 0r = 0
 \end{aligned}$$

so $\partial_* = 0$ and $P = 0$. Thus,

$$\phi_*(D) = F(D \times R)$$

Then, the induced crossed modules are free S -module on $D \times R$.

3. Given crossed module $i = \partial: I \hookrightarrow S$ where i inclusion of an ideal. Using any surjective homomorphism $\phi: S \rightarrow S/I$ the induced diagram is

$$\begin{array}{ccc}
 I & \xrightarrow{\psi} & \phi_*(I) \\
 i=\partial \downarrow & & \downarrow \partial_* \\
 S & \xrightarrow{\phi} & S/I
 \end{array}$$

Thus, we get $\phi_*(I) = I \otimes (S/I) \cong I/I^2$ which is an S/I -module. So ϕ_* does not preserve ideals.

Thus, we get a direct deduction from these discussions as follows.

Corollary 15. The category $XMod$ is bifibred over $k-Alg$, by the forgetful functor $p: XMod \rightarrow k-Alg$.

Proof. For any k -algebra morphism $\phi: S \rightarrow R$, there is an adjoint functor pair (ϕ^*, ϕ_*) as we mentioned above. That is, there is a bijection

$$\theta: XMod/R((\phi_*(D), R, \partial_*), (B, R, \eta)) \rightarrow XMod/S((D, S, \partial), \phi^*(B), S, \eta^*)$$

which is natural in $(D, S, \partial) \in XMod/S, (B, R, \eta) \in XMod/R$. It is clear that $\theta(f_*) = f^*$ and $\theta^{-1}(f^*) = f_*$.

Last two examples appear in [2] for associative algebras.

It is not difficult to see that the induced crossed module construction gives a functor

$$\phi_*: XMod/S \rightarrow XMod/R$$

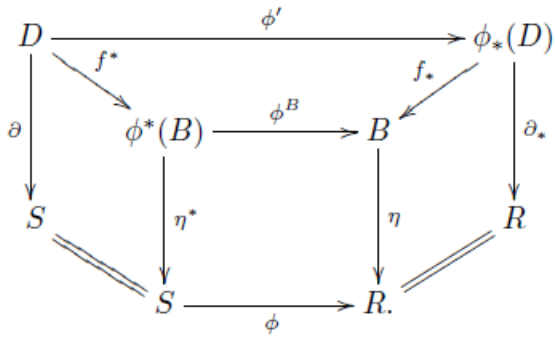
called “extension along a morphism” by Porter [1].

Proposition 13. If $\phi_1: S \rightarrow R, \phi_2: T \rightarrow S$ are two morphisms of k -algebras, then $(\phi_1\phi_2)_*$ and $\phi_{2*}\phi_{1*}$ are naturally isomorphic.

Proposition 14. Suppose $p: XMod \rightarrow k-Alg, \phi: S \rightarrow R$ in $k-Alg$, and a reindexing functor $\phi_*: XMod/S \rightarrow XMod/R$ is chosen. Then there is a bijection

$$\begin{aligned}
 XMod_\phi((D, S, \partial), (B, R, \eta)) \\
 \simeq XMod/R((\phi_*(D), R, \partial_*), (B, R, \eta))
 \end{aligned}$$

natural in $(D, S, \partial) \in XMod/S, (B, R, \eta) \in XMod/R$ where $XMod_\phi((D, S, \partial), (B, R, \eta))$ consists of those morphisms $\alpha \in XMod((D, S, \partial), (B, R, \eta))$ with $p(\alpha) = \phi$.



Properties of induced crossed module

$\phi_*(D)$ induced crossed R -module can be expressed more simply for the case when $\phi: S \rightarrow R$ is an epimorphism of k -algebras.

Epimorphism case:

Proposition 16. Let $\partial: D \rightarrow S$ be a crossed S -module and $\phi: S \rightarrow R$ epimorphism with $\text{Ker}\phi = K$. Then

$$\phi_*(D) \cong D/KD$$

where KD is an ideal of D generated by $\{k \cdot d \mid d \in D, k \in K\}$.

Proof. Because S acts on D/KD , K acts trivially on D/KD and ϕ is an epimorphism, $R \cong S/K$ acts on D/KD . As follows

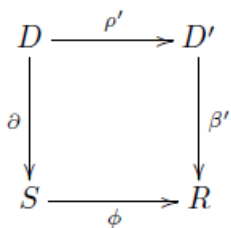
$$(s + K) \cdot (d + KD) = s \cdot d + KD$$

$\beta: D/KD \rightarrow R$ given by $\beta(d + KD) = \partial(d) + K$ is a crossed R -module. Indeed,

$$\begin{aligned} \beta(d + KD) \cdot (d' + KD) &= (\partial d + K) \cdot (d' + KD) \\ &= \partial(d) \cdot d' + KD \\ &= dd' + KD \\ &= (d + KD)(d' + KD) \end{aligned}$$

$(\rho, \phi): (D, S, \partial) \rightarrow (D/KD, R, \beta)$ is a crossed module morphism where $\rho: D \rightarrow D/KD, \rho(d) = d + KD$ since $\rho(s \cdot d) = \phi(s) \cdot \rho(d)$.

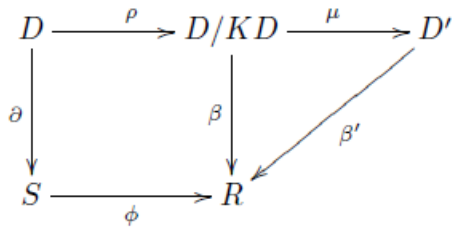
Suppose that the following diagram of crossed module is commutative.



Since $\rho'(s \cdot d) = \phi(s) \cdot \rho'(d)$ for any $d \in D, s \in S$, we have

$$\rho'(k \cdot d) = \phi(k) \cdot \rho'(d) = 0 \cdot \rho'(d) = 0$$

so $\rho'(KD) = 0$. Then, there is a unique morphism $\mu: (D/KD) \rightarrow D'$ given by $\mu(d + KD) = \rho'(d)$ such that $\mu\rho = \rho'$ and μ is well defined, because of $\rho'(KD) = 0$. Finally, the diagram



commutes, since for all $d \in D$

$$\begin{aligned}
 \beta(d + KD) &= \beta\rho(d) \\
 &= \phi\partial(d) \\
 &= \beta'\rho'(d) \\
 &= \beta'\mu(d + KD)
 \end{aligned}$$

and

$$\begin{aligned}
 \mu(r \cdot (d + KD)) &= \mu((s \cdot d) + KD) = \mu(\rho(s \cdot d)) = \rho'(s \cdot d) \\
 &= \phi(s) \cdot \rho'(d) = r \cdot \mu\rho(d) = r \cdot \mu(d + KD)
 \end{aligned}$$

so μ preserves the actions.

The above proposition is given in [2] and [15] for noncommutative and Lie algebras, respectively.

When $\phi: S \rightarrow R$ is the inclusion of an ideal, we can give the following result:

Monomorphism case:

In this subsection, we consider the crossed modules induced by a morphism $\phi: S \rightarrow R$ of k -algebras, where k is a field, the particular case when S is an ideal of R . It is found the Lie algebra version of that in [15].

If $d \in D$, then the class of d in D/D^2 is written as $[d]$. Then the augmentation ideal of $I(R/S)$ of a quotient algebra R/S has the basis $\{\bar{e}_{i_1}\bar{e}_{i_2}\dots\bar{e}_{i_p}, i_1 \leq i_2 \leq \dots i_p, i_j \in I\}_{(i) \neq \emptyset}$, where \bar{e}_{i_j} is the projection of the basic element $e_{i_j} \in I(R)$ on R/S .

Theorem 17. Let $D \subseteq S$ be ideals of R so that R acts on S and D by multiplication. Let $\partial: D \rightarrow S$, $\phi: S \rightarrow R$ be the inclusions and let \mathcal{D} denote the crossed module (D, S, ∂) with the multiplication action. Then the induced crossed R -module $\phi_*(\mathcal{D})$ is isomorphic as a crossed R -module to

$$\begin{aligned}
 \zeta: D \times (D/D^2 \otimes I(R/S)) &\rightarrow R \\
 (d, [t] \otimes \bar{x}) &\mapsto d.
 \end{aligned}$$

The action is given by

$$r \cdot (d, [t] \otimes \bar{x}) = (r \cdot d, [d] \otimes \bar{r} + [t] \otimes \bar{r}x - [x \cdot t] \otimes \bar{r})$$

for, $t \in D$; $\bar{x} \in I(R/S)$ where \bar{r}, \bar{x} denote the image of r, x in R/S , respectively.

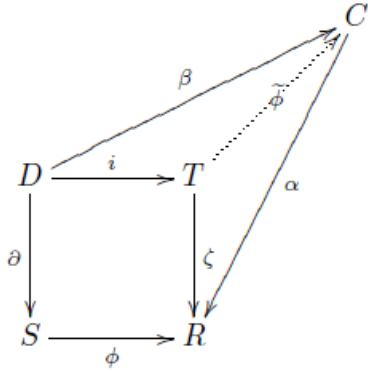
Proof. First, we will show that

$$\mathcal{T} = (\zeta: T = (D \times (D/D^2 \otimes I(R/S))) \rightarrow R), \zeta(d, [t] \otimes \bar{x}) = d$$

is a crossed module with the given action:

$$\begin{aligned}
 \zeta(d', [t'] \otimes \bar{x}') \cdot (d, [t] \otimes \bar{x}) &= d' \cdot (d, [t] \otimes \bar{x}) \\
 &= (d' \cdot d, [d] \otimes \bar{d}' + [t] \otimes \bar{d}'x - [x \cdot t] \otimes \bar{d}') \\
 &= (d'd, 0) \\
 &= (d'd, [t't] \otimes \bar{x}'\bar{x})
 \end{aligned}$$

Consider $i: D \rightarrow D \times (D/D^2 \otimes I(R/S))$, $i(d) = (d, 0)$. We have the following diagram:



Clearly we have a morphism of crossed modules $(i, \phi): \mathcal{D} \rightarrow \mathcal{T}$. We just verify that when a morphism of crossed module $(\beta, \phi): (D, S, \partial) \rightarrow (C, R, \alpha)$ is given, there is a unique morphism $\tilde{\phi}: T = D \times (D/D^2 \otimes I(R/S)) \rightarrow C$ such that $\tilde{\phi}i = \beta$ and $\alpha\tilde{\phi} = \zeta$. Since $\tilde{\phi}$ has to be a homomorphism and preserve the action, we have

$$\begin{aligned} \tilde{\phi}(d, [t] \otimes \bar{e}_{(i)}) &= \tilde{\phi}\left((d, 0) + (0, [t] \otimes \bar{e}_{(i)})\right) \\ &= \tilde{\phi}\left((d, 0) + (e_{(i)} \cdot t, [t] \otimes \bar{e}_{(i)}) + (-e_{(i)} \cdot t, 0)\right) \\ &= \tilde{\phi}\left((d, 0) + (e_{(i)} \cdot (t, 0) + (-e_{(i)} \cdot t, 0))\right) \\ &= \tilde{\phi}\left((d, 0)\right) + \tilde{\phi}\left(e_{(i)} \cdot (t, 0) + (-e_{(i)} \cdot t, 0)\right) \\ &= \tilde{\phi}\left((d, 0)\right) + \tilde{\phi}\left(e_{(i)} \cdot (t, 0)\right) + \tilde{\phi}\left(-e_{(i)} \cdot t, 0\right) \\ &= \tilde{\phi}i(d) + e_{(i)} \cdot \tilde{\phi}i(t) - \tilde{\phi}i(e_{(i)} \cdot t) \\ &= \beta(d) + e_{(i)} \cdot \beta(t) - \beta(e_{(i)} \cdot t) \end{aligned}$$

for any $d \in D$, $([t] \otimes \bar{e}_{(i)}) \in D/D^2 \otimes I(R/S)$. This proves uniqueness of any such a $\tilde{\phi}$. We now prove that this formula gives a well-defined morphism.

It is immediate from the formula that $\tilde{\phi}: D \times (D/D^2 \otimes I(R/S)) \rightarrow C$ must be defined by $\tilde{\phi}(d, u) = \beta(d) + \gamma(u)$ where $\gamma: D/D^2 \otimes I(R/S) \rightarrow C$, $\gamma([d] \otimes \bar{e}_{(i)}) = \gamma_{e_{(i)}}(d)$ and $\gamma_r: D \rightarrow C$, $\gamma_r(d) = r \cdot \beta(d) - \beta(r \cdot d)$.

Since

$$\begin{aligned} \alpha\gamma_r(d) &= \alpha(r \cdot \beta(d) - \beta(r \cdot d)) \\ &= \alpha(r \cdot \beta(d)) - \alpha(\beta(r \cdot d)) \\ &= r\alpha(\beta(d)) - \phi\partial(r \cdot d) \\ &= r\phi\partial(d) - \phi(r\partial(d)) \\ &= r\partial(d) - r\partial(d) = 0 \end{aligned}$$

for $d \in D$, $\gamma_r(D)$ is contained in the annihilator $\text{Ann}(C)$ of C . Also, we get

$$\begin{aligned} \gamma_r(dd') &= r \cdot \beta(dd') - \beta(r \cdot (dd')) \\ &= r \cdot (\beta(d)\beta(d')) - \beta(r \cdot d)\beta(d') \\ &= r \cdot \beta(d)\beta(d') - \beta(r \cdot d)\beta(d') \\ &= \gamma_r(d)\beta(d') \\ &= 0 \\ &= \gamma_r(d)\gamma_r(d') \end{aligned}$$

for $d, d' \in D$. Consequently γ_r is a homomorphism of commutative algebras that factors through D/D^2 .

The function $\tilde{\phi}$ is clearly a well-defined morphism of commutative algebras:

$$\begin{aligned} \tilde{\phi}((d, u)(d', u')) &= \tilde{\phi}(dd', uu') \\ &= \beta(dd') + \gamma(uu') \\ &= \beta(d)\beta(d') + \gamma(u)\gamma(u') \\ &= \beta(d)\beta(d') + \beta(d)\gamma(u') + \gamma(u)\beta(d') + \gamma(u)\gamma(u') \\ &= (\beta(d) + \gamma(u))(\beta(d') + \gamma(u')) \\ &= \tilde{\phi}(d, u)\tilde{\phi}(d', u') \end{aligned}$$

Further, $\tilde{\phi}i = \beta$ and $\alpha\tilde{\phi} = \zeta$, as $\alpha\gamma$ is trivial:

$$\begin{aligned} \alpha\gamma([t] \otimes \bar{e}_{(i)}) &= \alpha(e_{(i)} \cdot \beta(t) - \beta(e_{(i)} \cdot t)) \\ &= e_{(i)} \cdot \alpha(\beta(t)) - \alpha(\beta(e_{(i)} \cdot t)) \\ &= e_{(i)} \cdot \phi\partial(t) - \phi\partial(e_{(i)} \cdot t) \\ &= e_{(i)} \cdot \partial(t) - \partial(e_{(i)} \cdot t) \\ &= 0. \end{aligned}$$

Finally, we prove that $\tilde{\phi}$ preserves the action. Let $d, t \in D, r \in R$ and $\bar{e}_{(i)}$ be an element in the basis of $I(R/S)$, then we have

$$\begin{aligned} \tilde{\phi}(r \cdot (d, [t] \otimes \bar{e}_{(i)})) &= \tilde{\phi}(r \cdot d, [d] \otimes \bar{r} + [t] \otimes \bar{r}e_{(i)} - [e_{(i)} \cdot t] \otimes \bar{r}) \\ &= \beta(r \cdot d) + \gamma([d] \otimes \bar{r} + [t] \otimes \bar{r}e_{(i)} - [e_{(i)} \cdot t] \otimes \bar{r}) \\ &= \beta(r \cdot d) + \gamma_r(d) + \gamma_{re_{(i)}}(t) - \gamma_r(e_{(i)} \cdot t) \\ &= \beta(r \cdot d) + r \cdot \beta(d) - \beta(r \cdot d) + re_{(i)} \cdot \beta(t) - \beta(re_{(i)} \cdot t) \\ &\quad - r \cdot \beta(e_{(i)} \cdot t) + \beta(r \cdot (e_{(i)} \cdot t)) \\ &= \beta(r \cdot d) + re_{(i)} \cdot \beta(t) - r \cdot \beta(e_{(i)} \cdot t) \\ &= r \cdot (\beta(d) + e_{(i)} \cdot \beta(t) - \beta(e_{(i)} \cdot t)) \\ &= r \cdot (\beta(d) + \gamma_{e_{(i)}}(t)) \\ &= r \cdot \tilde{\phi}(d, [t] \otimes \bar{e}_{(i)}). \end{aligned}$$

Conflicts of interest

The author states that she did not have a conflict of interest.

References

- [1] Porter T., Some Categorical Results in the Theory of Crossed Modules in Commutative Algebras., *J. Algebra*, 109 (1987) 415-429.
- [2] Shammu N. M., Algebraic and Categorical Structure of Categories of Crossed Modules of Algebras., Ph.D. Thesis, U.C.N.W, (1992).
- [3] Porter T., Homology of Commutative Algebras and an Invariant of Simis and Vasconceles., *J. Algebra*, 99(1986) 458-465.
- [4] Brown R., Higgins P. J., On the Connection between the Second Relative Homotopy Groups of Some Related Spaces, *Proc. London Math. Soc.*, 36(3) (1978) 193-212.
- [5] Brown R., Higgins P. J., Sivera R., Nonabelian Algebraic Topology, *European Mathematical Society Tracts in Mathematics*, 15 (2011).
- [6] Brown R., Sivera R., Algebraic Colimit Calculations in Homotopy Theory using Fibred and Cofibred Categories, *Theory*

- and Applications of Categories*, 22 (2009) 221-251.
- [7] Odabaş A, Ulualan E, Braided Regular Crossed Modeles Bifibered over Regular Groupoids, *Turkish Journal of Mathematics*, 41 (2017) 1385-1403.
- [8] Arslan Ege U., Akça İ.İ., Irmak Onarlı G., Avcıoğlu O., Fibrations of 2-crossed modules, *Mathematical Methods in the Applied Sciences*, 42(16) (2019) 5293-5304.
- [9] Whitehead J. H. C., Combinatorial Homotopy I and II., *Bull. Amer. Math. Soc.*, 55 (1949) 231-245 and 453-496.
- [10] Mac Lane S., Extension and Obstructions for Rings., *Illinois Journal of Mathematics*, 121 (1958), 316-345.
- [11] Dedecker P., Lue, A. S. T., A Non-abelian Two dimensional Cohomology for Associative Algebras., *Bull. Amer. Soc.*, 72 (1966) 1044-1050.
- [12] Lue A. S. T., Non-abelian Cohomology of Associative Algebras., *Quart. J. Math. Oxford Ser.*, 2 (1968) 159-180.
- [13] Arvasi Z., Ege U., Annihilators, Multipliers and Crossed Modules, *Applied Categorical Structures*, 11 (2003) 487-506.
- [14] Arvasi Z., Porter T., Simplicial and Crossed Resolutions of Commutative Algebras, *Journal of Algebras*, 181 (1996) 426-448.
- [15] Casas J. M., Ladra M., Colimits in the Crossed Modules Category in Lie Algebras. *Georgian Mathematical Journal*, 7(3) (2000) 461-474.



Radicals of soft intersectional ideals in semigroups

Emin AYGÜN¹ , Betül ERDAL^{1,*}

¹ Erciyes University, Department of Mathematics, Kayseri/ TURKEY

Abstract

In this paper, we introduce IS-radical, IS-quasi radical, IS-interior radical and IS-nil radical in semigroups. We obtain radical structures that will contribute to the theoretical studies of soft sets. We consider the ideal structures of intersectional soft sets in semigroups and we define IS-radical, IS-quasi radical, IS-interior radical and IS-nil radical. We use two different methods to define the soft radicals and give the results. In our study, we also give several examples and propositions to see differences among these structures.

Article info

History:
Received:17.05.2020
Accepted:25.01.2021

Keywords:
Soft radical,
IS-radical,
IS-quasi radical,
IS-interior radical,
IS-nil radical.

1. Introduction

Since the modelling of uncertain data in many fields was very complex, it was difficult to successfully deal with them by classical methods. With the emergence of soft set theory in 1999, overcoming uncertain problems have been a major field of study for mathematicians. A lot of work has been done on soft set theory in applied and theoretical fields and it is continuing with an increasing speed. Molodtsov [1] proposed soft set theory for modelling vagueness and uncertainty. Soft set theory has provided various solutions to the information systems and decision-making methods in the literature [2- 8]. At the same time, the new algebraic operations in soft set theory was described by various researchers. In addition, by defining the soft group [9] in 2007, the soft set theory has experienced rapid growth in algebraic structures [10-16]. In 2014, Song et al. [17] introduced the notions of int-soft semigroups, int-soft ideal and int-soft quasi ideals. And in [18-19], Sezgin et al. made new approach to the classical semigroup theory via soft sets and defined soft intersection semigroups, soft intersection ideal, soft intersection quasi ideal and soft intersection interior ideal. Using these notions, we have produced radicals of intersectional soft ideals. We have used two different methods to define the soft radicals. Firstly, we have examined whether a soft set is a radical of own sub-soft set. Secondly, we have defined a radical of intersectional soft ideal. Also, we have gave several examples and propositions to see differences among these structures.

2. Materials and methods

Let \mathcal{S} be a semigroup and \mathcal{J} be nonempty ideal of semigroup \mathcal{S} . $\sqrt{\mathcal{J}} = \{x: x^n \in \mathcal{J}, \forall x \in \mathcal{S}, \exists n \in \mathbb{N}\}$ is called radical of \mathcal{J} . Let \mathcal{S}^1 be a monoid and $\mathcal{J} = \{e\}$ be the identity-ideal of \mathcal{S}^1 . $\sqrt{\mathcal{J}} = \{s: s^n = e, \forall s \in \mathcal{S}^1, \exists n \in \mathbb{N}\}$ is called nil radical of \mathcal{J} [20]. Avoiding the details, other definitions of semigroups are not given in this study. The reader can refer to Howie [21].

2.1. Definition A pair (Φ, Γ) is called a soft set over \mathcal{U} , where Φ is a mapping $\Phi: \Gamma \rightarrow \mathcal{P}(\mathcal{U})$ [1]. In other words, a soft set over \mathcal{U} is a parameterized family of subsets of the universe \mathcal{U} . For $e \in \Gamma$, $\Phi(e)$ is considered as the set of e-elements of the soft set (Φ, Γ) or as the set of e-approximate elements of the soft set.

2.2. Definition Let \mathcal{A} be a non-empty subset of \mathcal{S} over \mathcal{U} . Then $(\chi_{\mathcal{A}}, \mathcal{S})$ is called the characteristic soft set over \mathcal{U} , defined as follows:

$$\chi_{\mathcal{A}}: \mathcal{S} \rightarrow \mathcal{P}(\mathcal{U}), a \rightarrow \begin{cases} \mathcal{U}, & a \in \mathcal{A} \\ \emptyset, & \text{otherwise} \end{cases} \text{ for all } a \in \mathcal{S} \text{ [17].}$$

*Corresponding author. email address: b-rdal@hotmail.com
<http://dergipark.gov.tr/csj> ©2021 Faculty of Science, Sivas Cumhuriyet University

2.3. Definition Let (ω, \mathcal{S}) and (φ, \mathcal{S}) be soft sets over \mathcal{U} . Then $(\omega \tilde{\circ} \varphi, \mathcal{S})$ is called intersectional soft product of (ω, \mathcal{S}) and (φ, \mathcal{S}) , defined as follows:

$$(\omega \tilde{\circ} \varphi, \mathcal{S})(a) = \begin{cases} \bigcup_{a=bc} \{\omega f(b) \cap \varphi(c)\}, & \exists b, c \in \mathcal{S} \text{ için } a = bc \\ \emptyset, & \text{otherwise} \end{cases} \quad \text{for all } a \in \mathcal{S} \text{ [17].}$$

2.4. Definition Let \mathcal{S} be a semigroup and (φ, \mathcal{S}) be a soft set over \mathcal{U} . Then,

2.4.1. (φ, \mathcal{S}) is called an intersectional soft semigroup of \mathcal{S} if it satisfies:

$$\varphi(xy) \supseteq \varphi(x) \cap \varphi(y) \text{ for all } x, y \in \mathcal{S} \text{ [17].}$$

2.4.2. (φ, \mathcal{S}) is called an intersectional soft ideal of \mathcal{S} if it satisfies:

$$\varphi(xy) \supseteq \varphi(x) \text{ and } \varphi(xy) \supseteq \varphi(y) \text{ for all } x, y \in \mathcal{S} \text{ [17].}$$

2.4.3. (φ, \mathcal{S}) is called an intersectional soft quasi-ideal of \mathcal{S} if it satisfies:

$$(\varphi \tilde{\circ} \chi_{\mathcal{S}}, \mathcal{S}) \tilde{\cap} (\chi_{\mathcal{S}} \tilde{\circ} \varphi, \mathcal{S}) \subseteq (\varphi, \mathcal{S}) \text{ [17].}$$

2.4.4. (φ, \mathcal{S}) is called an intersectional soft interior-ideal of \mathcal{S} if it satisfies:

$$\varphi(xsy) \supseteq \varphi(s) \text{ for all } x, y, s \in \mathcal{S} \text{ [19].}$$

3. Results

In this section, we examine whether a soft set is a radical of own sub-soft set. And also, we define radicals of intersectional soft ideals (ideal/quasi ideal/interior ideal). Next, we produce nil radicals of these int-ideals.

In what follows, \mathcal{S} regarded as a semigroup and \mathcal{A} regarded as a non-empty subset of \mathcal{S} . We briefly show intersectional-soft as IS to avoiding repetition.

3.1. Definition Let (φ, \mathcal{A}) be an IS- ideal over \mathcal{U} . A non-null soft set (φ, \mathcal{S}) is called IS-radical of (φ, \mathcal{A}) if it satisfies:

$$\varphi(s^n x) \supseteq \varphi(x) \text{ and } \varphi(xs^n) \supseteq \varphi(x) \text{ for all } x \in \mathcal{A}, s \notin \mathcal{A}, s \in \mathcal{S} \text{ and } \exists n \in \mathbb{N}.$$

3.2. Example Let $\mathcal{U} = \{u_1, u_2, u_3, u_4, u_5\}$ and $\mathcal{S} = \{0, x, 1, 2, y\}$. Then, $(\mathcal{S}, *)$ is semigroup for the following Cayley table:

*	0	x	1	2	y
0	0	0	0	0	0
x	0	0	0	x	1
1	0	x	1	0	0
2	0	0	0	2	y
y	2	2	y	0	0

Let (φ, \mathcal{S}) be soft set over \mathcal{U} defined as follows:

$$\varphi: \mathcal{S} \rightarrow \mathcal{P}(\mathcal{U}), (\varphi, \mathcal{S}) = \{(0, \{u_1, u_2, u_3, u_4\}), (x, \{u_1, u_3\}), (1, \{u_2, u_3, u_4\}), (2, \mathcal{U}), (y, \mathcal{U})\}.$$

Let $\mathcal{A} = \{0, x, 1\}$ be the subset of \mathcal{S} , then (φ, \mathcal{A}) is an IS- ideal over \mathcal{U} . There exists $n \in \mathbb{N}$ such that $2^n = 2$ and $y^n = 0$.

$$\begin{aligned} \varphi(2.0) &\supseteq \varphi(0) \text{ and } \varphi(0.2) \supseteq \varphi(0). \\ \varphi(2.x) &\supseteq \varphi(x) \text{ and } \varphi(x.2) \supseteq \varphi(x). \end{aligned}$$

$\varphi(2.1) \supseteq \varphi(1)$ and $\varphi(1.2) \supseteq \varphi(1)$.
 $\varphi(0.0) \supseteq \varphi(0)$.
 $\varphi(0.x) \supseteq \varphi(x)$ and $\varphi(x.0) \supseteq \varphi(x)$.
 $\varphi(0.1) \supseteq \varphi(1)$ and $\varphi(1.0) \supseteq \varphi(1)$.

For all $x \in \mathcal{A}$, $\varphi(s^n x) \supseteq \varphi(x)$ and $\varphi(xs^n) \supseteq \varphi(x)$. Therefore, (φ, \mathcal{S}) is IS-radical of (φ, \mathcal{A}) .

3.3. Proposition If (φ, \mathcal{S}) be an IS- ideal over \mathcal{U} , then (φ, \mathcal{S}) is IS-radical of (φ, \mathcal{A}) for a subset \mathcal{A} of \mathcal{S} .

Proof. Let (φ, \mathcal{S}) be an IS- ideal over \mathcal{U} . It is clear that $\varphi(s^n x) \supseteq \varphi(x)$ and $\varphi(xs^n) \supseteq \varphi(x)$ for $n = 1$ by Definition 3.1. Thus, (φ, \mathcal{S}) is IS-radical of (φ, \mathcal{A}) for a subset \mathcal{A} of \mathcal{S} .

3.4. Example Let $\mathcal{U} = \{i_1, i_2, i_3, i_4, i_5\}$ and $\mathcal{S} = \{r, s, t, k\}$. Then, $(\mathcal{S}, *)$ is a semigroup for the following Cayley table:

*	r	s	t	k
r	r	r	r	r
s	r	r	r	r
t	r	r	s	r
k	r	r	s	s

Let (μ, \mathcal{S}) be soft set over \mathcal{U} defined as follows:

$$\mu: \mathcal{S} \rightarrow \mathcal{P}(\mathcal{U}), \quad \dot{x} \rightarrow \begin{cases} \{i_1, i_2, i_3, i_4\} & \text{if } \dot{x} = r, \\ \{i_2, i_3\} & \text{if } \dot{x} = s, \\ \{i_1, i_4\} & \text{if } \dot{x} = t, \\ \{i_1, i_2, i_5\} & \text{if } \dot{x} = k, \end{cases}$$

Consider the subset $\mathcal{A} = \{r, s, t\}$ of \mathcal{S} . Then, (μ, \mathcal{A}) is an IS- ideal over \mathcal{U} . For $n = 2, k^2 = s$.

$\mu(r.s) \supseteq \mu(r)$ and $\mu(s.r) \supseteq \mu(r)$,
 $\mu(s.s) \supseteq \mu(s)$,
 $\mu(t.s) \supseteq \mu(t)$ and $\mu(r.t) \supseteq \mu(t)$.

Hence, (μ, \mathcal{S}) is IS-radical of (μ, \mathcal{A}) . Since $\mu(r.k) \not\supseteq \mu(k)$ and $\mu(k.r) \not\supseteq \mu(k)$, (μ, \mathcal{S}) is not IS-ideal over \mathcal{U} .

3.5. Definition Let (ϕ, \mathcal{A}) be an IS-ideal of \mathcal{S} . Then, the $(\sqrt{\phi}, \mathcal{S})$ is called an IS-radical of (ϕ, \mathcal{A}) , defined by

$$\sqrt{\phi}(s) = \begin{cases} \bigcap \phi(s^n); & s \notin \mathcal{A}, s^n \in \mathcal{A}, \exists n \in \mathbb{N} \\ \emptyset; & s \notin \mathcal{A}, s^n \notin \mathcal{A}, \forall n \in \mathbb{N} \\ \phi(s); & s \in \mathcal{A} \end{cases},$$

where $\sqrt{\phi}: \mathcal{S} \rightarrow \mathcal{P}(\mathcal{S})$. The IS-radical $(\sqrt{\phi}, \mathcal{S})$ can be denoted by $\sqrt{(\phi, \mathcal{A})}$.

3.6. Example Let consider the IS- ideal (φ, \mathcal{A}) in Example 3.2.

By Definition 3.5, $(0, \{u_1, u_2, u_3, u_4\}), (x, \{u_1, u_3\})$ and $(1, \{u_2, u_3, u_4\}) \in (\sqrt{\varphi}, \mathcal{S})$. For all $n \in \mathbb{N}, 2^n = 2$ and $y^n = 0$, So $(2, \emptyset)$ and $(y, \{u_1, u_2, u_3, u_4\}) \in (\sqrt{\varphi}, \mathcal{S})$. Hence,

$$(\sqrt{\varphi}, \mathcal{S}) = \{(0, \{u_1, u_2, u_3, u_4\}), (x, \{u_1, u_3\}), (1, \{u_2, u_3, u_4\}), (2, \emptyset), (y, \{u_1, u_2, u_3, u_4\})\}.$$

One can see that the IS-radical $(\sqrt{\varphi}, \mathcal{S})$ is not IS-ideal. Since, $\sqrt{\varphi}(xy) = \sqrt{\varphi}(1) \not\supseteq \sqrt{\varphi}(x)$.

3.7. Remark The radical of an IS-ideal may not be an IS-ideal over \mathcal{U} .

3.8. Definition Let (ϕ, \mathcal{A}) be an IS-quasi ideal over \mathcal{U} . A nonempty soft set (ϕ, \mathcal{S}) is called IS-quasi radical of (ϕ, \mathcal{A}) if it satisfies:

$$\phi(xs^n) \cap \phi(s^n x) \subseteq \phi(x) \text{ for all } x \in \mathcal{A}, s \in \mathcal{S}, s \notin \mathcal{A}, \exists n \in \mathbb{N}.$$

3.9. Example Consider the semigroup $\mathcal{S} = \{1, a, b, c\}$. Then, $(\mathcal{S}, *)$ is semigroup for the following Cayley table:

*	1	a	b	c
1	1	1	1	1
a	1	1	1	1
b	1	1	1	a
c	1	1	a	b

Let (ψ, \mathcal{S}) be soft set over \mathbb{Z}_4 defined as follows:

$$\psi: \mathcal{S} \rightarrow \mathcal{P}(\mathbb{Z}_4), \quad x \rightarrow \begin{cases} \{\bar{0}\} & , x = 1 \text{ ise,} \\ \{\bar{0}, \bar{1}, \bar{2}\} & , x = a \text{ ise,} \\ \{\bar{0}, \bar{2}, \bar{3}\} & , x = b \text{ ise,} \\ \mathbb{Z}_4 & , x = c \text{ ise,} \end{cases}$$

Consider $\mathcal{A} = \{a, b\}$ subset of \mathcal{S} . Since $\psi(a) \supseteq \psi(b.c) \cap \psi(c.b)$ and $\psi(b) \supseteq \psi(c.c) \cap \psi(c.c)$, (ψ, \mathcal{A}) is an IS-quasi ideal over \mathbb{Z}_4 .

For all $n \in \mathbb{N}$, $1^n = 1$ and $c^4 = 1$. One can easily see that

$$\begin{aligned} \psi(a.1) \cap \psi(1.a) &\subseteq \psi(a); \{\bar{0}\} \cap \{\bar{0}\} \subseteq \{\bar{0}, \bar{1}, \bar{2}\}, \\ \psi(b.1) \cap \psi(1.b) &\subseteq \psi(b); \{\bar{0}\} \cap \{\bar{0}\} \subseteq \{\bar{0}, \bar{2}, \bar{3}\}. \end{aligned}$$

Therefore, (ψ, \mathcal{S}) is IS-quasi radical of (ψ, \mathcal{A}) .

3.10. Proposition If (φ, \mathcal{S}) be an IS-quasi ideal over \mathcal{U} , then (φ, \mathcal{S}) is IS-quasi radical of (φ, \mathcal{A}) for a subset \mathcal{A} of \mathcal{S} .

Proof. Let (φ, \mathcal{S}) be an IS-quasi ideal over \mathcal{U} . It is clear that $\phi(xs^n) \cap \phi(s^n x) \subseteq \phi(x)$ for $n = 1$ by Definition 3.8. Thus, (φ, \mathcal{S}) is IS-quasi radical of (φ, \mathcal{A}) for a subset \mathcal{A} of \mathcal{S} .

3.11. Example Consider the semigroup $\mathcal{S} = \{0, 1, 2, 3\}$. Then, $(\mathcal{S}, *)$ is semigroup for the following Cayley table:

*	0	1	2	3
0	0	0	0	0
1	0	1	1	1
2	0	1	2	3
3	0	1	1	1

Let β be non-empty subset of \mathcal{U} and (σ, \mathcal{S}) be soft set over \mathcal{U} defined as follows:

$$\sigma: \mathcal{S} \rightarrow \mathcal{P}(\mathcal{U}), \quad x \rightarrow \begin{cases} \beta, & x = 3 \\ \emptyset, & x = 0, 1, 2 \end{cases}$$

Consider $\mathcal{A} = \{0, 2, 3\}$ subset of \mathcal{S} , (σ, \mathcal{A}) is an IS-quasi ideal over \mathcal{U} . Since $1^n = 1$ for all $n \in \mathbb{N}$,

$$\begin{aligned} \sigma(0) &\supseteq \sigma(0.1) \cap \sigma(1.0); \sigma(0) \supseteq \sigma(0) \cap \sigma(0) = \sigma(0), \\ \sigma(2) &\supseteq \sigma(2.1) \cap \alpha(1.2); \sigma(2) \supseteq \sigma(1) \cap \sigma(1) = \sigma(1), \\ \sigma(3) &\supseteq \sigma(3.1) \cap \sigma(1.3); \sigma(3) \supseteq \sigma(1) \cap \sigma(1) = \sigma(1). \end{aligned}$$

Therefore, (σ, \mathcal{S}) is IS-quasi radical of (σ, \mathcal{A}) , Since $\sigma(1) \not\subseteq \sigma(3.3)$, (σ, \mathcal{S}) is not IS-quasi ideal over \mathcal{U} .

3.12. Definition Let (ϕ, \mathcal{A}) be an IS-quasi ideal of \mathcal{S} . Then, the $(\sqrt{\phi}, \mathcal{S})$ is called an IS-quasi radical of (ϕ, \mathcal{A}) , defined by

$$\sqrt{\phi}(s) = \begin{cases} \cap \phi(s^n); & s \notin \mathcal{A}, s^n \in \mathcal{A}, \exists n \in \mathbb{N} \\ \emptyset; & s \notin \mathcal{A}, s^n \notin \mathcal{A}, \forall n \in \mathbb{N} \\ \phi(s); & s \in \mathcal{A} \end{cases},$$

where $\sqrt{\phi}: \mathcal{S} \rightarrow \mathcal{P}(\mathcal{S})$. The IS-quasi radical $(\sqrt{\phi}, \mathcal{S})$ can be denoted by $\sqrt{(\phi, \mathcal{A})}$.

3.13. Example Consider the IS-quasi ideal (ψ, \mathcal{A}) in Example 3.9. Since $c^2 = b, c^3 = a$ and $1^n = 1$ for all $n \in \mathbb{N}$, $(1, \emptyset)$ and $(c, \{\bar{0}, \bar{1}, \bar{2}\} \cap \{\bar{0}, \bar{2}, \bar{3}\}) \in (\sqrt{\psi}, \mathcal{S})$. Hence,

$$(\sqrt{\psi}, \mathcal{S}) = \{(1, \emptyset), (a, \{\bar{0}, \bar{1}, \bar{2}\}), (b, \{\bar{0}, \bar{2}, \bar{3}\}), (c, \{\bar{0}, \bar{2}\})\}.$$

One can see that the IS-quasi radical $(\sqrt{\psi}, \mathcal{S})$ is not IS-quasi ideal.

3.14. Remark The radical of an IS-quasi ideal may not be an IS-quasi ideal over \mathcal{U} .

3.15. Theorem Every IS-quasi radical is an IS-bi radical over \mathcal{S} .

Proof. Let $(\sqrt{\psi}, \mathcal{S})$ be an IS-quasi radical over a semigroup \mathcal{S} . Then, $\sqrt{\psi}(x)$ is a quasi ideal over \mathcal{S} for all $x \in \mathcal{S}$. Since every quasi-ideal is a bi-ideal of \mathcal{S} , $(\sqrt{\psi}, \mathcal{S})$ is an IS-bi radical over \mathcal{S} .

3.16. Definition Let (ϕ, \mathcal{A}) be an IS-interior ideal over \mathcal{U} . A non-null soft set (ϕ, \mathcal{S}) is called IS-interior radical of (ϕ, \mathcal{A}) if it satisfies:

$$\phi(xs^n y) \supseteq \phi(s) \text{ for all } x, y \in \mathcal{A}, s \in \mathcal{S}, s \notin \mathcal{A}, \exists n \in \mathbb{N}.$$

3.17. Example Let $\mathcal{U} = \{i_1, i_2, i_3, i_4, i_5, i_6\}$ and $\mathcal{S} = \{a, b, c, d\}$. Then, $(\mathcal{S}, *)$ is semigroup for the following Cayley table:

*	a	b	c	d
a	a	a	a	a
b	a	b	b	b
c	a	b	c	d
d	a	b	b	b

Let (μ, \mathcal{S}) be soft set over \mathcal{U} defined as follows:

$$\mu: \mathcal{S} \rightarrow \mathcal{P}(\mathcal{U}) \quad \dot{x} \rightarrow \begin{cases} \mathcal{U} & \text{if } \dot{x} = a, \\ \{i_1, i_2, i_5\} & \text{if } \dot{x} = b, \\ \{i_4, i_5, i_6\} & \text{if } \dot{x} = c, \\ \{i_5\} & \text{if } \dot{x} = d, \end{cases}$$

Consider the subset $\mathcal{A} = \{a, b, c\}$ of \mathcal{S} . Then, (μ, \mathcal{A}) is an IS- interior ideal over \mathcal{U} . Since $d^2 = b$ and $\mu(x.b.y) \supseteq \mu(d)$ for all $x, y \in \mathcal{A}$, (μ, \mathcal{S}) is IS-interior radical of (μ, \mathcal{A}) .

3.18. Proposition If (μ, \mathcal{S}) be an IS-interior ideal over \mathcal{U} , then (μ, \mathcal{S}) is IS-interior radical of (μ, \mathcal{A}) for a subset \mathcal{A} of \mathcal{S} .

Proof. Let (μ, \mathcal{S}) be an IS-interior ideal over \mathcal{U} . It is clear that $\mu(xs^n y) \supseteq \mu(s)$ for $n = 1$ by Definition 3.16. Thus, (μ, \mathcal{S}) is IS-interior radical of (μ, \mathcal{A}) for a subset \mathcal{A} of \mathcal{S} .

3.19. Example Consider the IS-interior radical (μ, \mathcal{S}) in Example 3.17. Since $\mu(b.c.d) \not\subseteq \mu(c)$, the subset (μ, \mathcal{S}) is not an IS- interior ideal over \mathcal{U} .

3.20. Definition Let (ϕ, \mathcal{A}) be an IS-interior ideal of \mathcal{S} . Then, the $(\sqrt{\phi}, \mathcal{S})$ is called an IS-interior radical of (ϕ, \mathcal{A}) , defined by

$$\sqrt{\phi}(s) = \begin{cases} \cap \phi(s^n); & s \notin \mathcal{A}, s^n \in \mathcal{A}, \exists n \in \mathbb{N} \\ \emptyset; & s \notin \mathcal{A}, s^n \notin \mathcal{A}, \forall n \in \mathbb{N} \\ \phi(s); & s \in \mathcal{A} \end{cases},$$

where $\sqrt{\phi}: \mathcal{S} \rightarrow \mathcal{P}(\mathcal{S})$. The IS-interior radical $(\sqrt{\phi}, \mathcal{S})$ can be denoted by $\sqrt{(\phi, \mathcal{A})}$.

3.21. Example Consider the IS-interior ideal (μ, \mathcal{A}) in Example 3.17. Since $d^n = b$ for all $n \in \mathbb{N}$, $(d, \{i_1, i_2, i_3\}) \in (\sqrt{\mu}, \mathcal{S})$. Therefore,

$$(\sqrt{\mu}, \mathcal{S}) = \{(a, \mathcal{U}), (b, \{i_1, i_2, i_3\}), (c, \{i_4, i_5, i_6\}), (d, \{i_1, i_2, i_3\})\}.$$

One can see that the IS-interior radical $(\sqrt{\mu}, \mathcal{S})$ is not IS-interior ideal.

3.22. Remark The radical of an IS-interior ideal may not be an IS-interior ideal over \mathcal{U} .

3.23. Theorem Let (ϕ, \mathcal{A}) be an IS-ideal (quasi/interior) of semigroup \mathcal{S} . Then, there exists an IS-ideal (quasi/interior) (ϕ, \mathcal{B}) such that

$$(\phi, \mathcal{A}) = \sqrt{(\phi, \mathcal{B})} \Leftrightarrow (\phi, \mathcal{A}) = \sqrt{(\phi, \mathcal{A})}.$$

Proof. Suppose that there exists a soft ideal (ϕ, \mathcal{A}) such that $(\phi, \mathcal{A}) = \sqrt{(\phi, \mathcal{B})}$.

If for all $s \notin \mathcal{A}$ there exists $n \in \mathbb{N}$ such that $s^n \in \mathcal{A}$, then we have

$$\begin{aligned} s^n \in \mathcal{B} &\Leftrightarrow (s, \cap \phi(s^n)) \in \sqrt{(\phi, \mathcal{B})} \\ &\Leftrightarrow (s, \cap \phi(s^n)) \in (\phi, \mathcal{A}) \\ &\Leftrightarrow (s, \cap \phi(s^n)) \in \sqrt{(\phi, \mathcal{A})} \\ &\Leftrightarrow (\phi, \mathcal{A}) = \sqrt{(\phi, \mathcal{A})} \end{aligned} \tag{1}$$

Similarly, if for all $s \notin \mathcal{A}$ there exists $n \in \mathbb{N}$ such that $s^n \notin \mathcal{A}$, then we have

$$\begin{aligned} s^n \notin \mathcal{B} &\Leftrightarrow (s, \emptyset) \in \sqrt{(\phi, \mathcal{B})} \\ &\Leftrightarrow (s, \emptyset) \in (\phi, \mathcal{A}) \\ &\Leftrightarrow (s, \emptyset) \in \sqrt{(\phi, \mathcal{A})} \\ &\Leftrightarrow (\phi, \mathcal{A}) = \sqrt{(\phi, \mathcal{A})} \end{aligned} \tag{2}$$

Similarly, for all $s \in \mathcal{A}$, we have

$$\begin{aligned} s \in \mathcal{B} &\Leftrightarrow (s, \phi(s)) \in \sqrt{(\phi, \mathcal{B})} \\ &\Leftrightarrow (s, \phi(s)) \in (\phi, \mathcal{A}) \\ &\Leftrightarrow (s, \phi(s)) \in \sqrt{(\phi, \mathcal{A})} \\ &\Leftrightarrow (\phi, \mathcal{A}) = \sqrt{(\phi, \mathcal{A})}. \end{aligned} \tag{3}$$

From (1), (2), (3), we have $(\phi, \mathcal{A}) = \sqrt{(\phi, \mathcal{B})} \Leftrightarrow (\phi, \mathcal{A}) = \sqrt{(\phi, \mathcal{A})}$.

In what follows, \mathcal{S}^1 regarded as a monoid and \mathcal{A} regarded as be the non-empty subset of \mathcal{S}^1 which is consisting identity element.

3.24. Definition Let (ϕ, \mathcal{A}) be an IS-ideal (quasi/interior) of \mathcal{S}^1 over \mathcal{U} . A non-null soft set (ϕ, \mathcal{S}^1) is called IS-nil radical of (ϕ, \mathcal{A}) if it satisfies:

$$\phi(s) \subseteq \phi(e) \text{ for all } s \in \mathcal{S}^1, s^n \in \mathcal{A}, \exists n \in \mathbb{N}.$$

3.25. Example Let $\mathcal{S}^1 = (\mathbb{Z}_6, .)$ be a monoid and $\mathcal{A} = \{\bar{1}\}$ be the subset of \mathcal{S}^1 .

Consider the function $\phi: \mathcal{S}^1 \rightarrow \mathcal{P}(\mathbb{Z}_6)$ over $\mathcal{U} = \{i_1, i_2, i_3, i_4, i_5, i_6\}$ defined by $\phi(\bar{0}) = \{i_1, i_2\}$, $\phi(\bar{1}) = \mathcal{U}$, $\phi(\bar{2}) = \{i_2, i_3\}$, $\phi(\bar{3}) = \mathcal{U}$, $\phi(\bar{4}) = \{i_4, i_5, i_6\}$ and $\phi(\bar{5}) = \{i_1, i_2, i_3, i_4\}$.

Since, there exists some $n \in \mathbb{N}$ such that $\bar{0}^n, \bar{2}^n, \bar{3}^n, \bar{4}^n \notin \mathcal{A}$, but $\bar{5}^n \in \mathcal{A}$. Hence, (ϕ, \mathcal{S}^1) is IS-nil radical of (ϕ, \mathcal{A}) .

3.26. Definition Let (ϕ, \mathcal{A}) be an IS-ideal (quasi/interior) of \mathcal{S}^1 over \mathcal{U} . A non-null soft set $(\sqrt{\phi}, \mathcal{S}^1)$ is called IS-nil radical of (ϕ, \mathcal{A}) defined by

$$\sqrt{\phi}(s) = \begin{cases} \phi(e), & s^n = e \\ \emptyset, & s^n \neq e \end{cases}$$

where $\sqrt{\phi}: \mathcal{S} \rightarrow \mathcal{P}(\mathcal{U})$ for all $s \in \mathcal{S}^1$ and some $n \in \mathbb{N}$.

3.27. Example Consider the IS- ideal (quasi/interior) (ϕ, \mathcal{A}) in Example 3.25. Hence, we have

$$(\sqrt{\phi}, \mathcal{S}^1) = \{(\bar{0}, \emptyset), (\bar{1}, \mathcal{U}), (\bar{2}, \emptyset), (\bar{3}, \emptyset), (\bar{4}, \emptyset), (\bar{5}, \mathcal{U})\}.$$

4. Discussion

In this study, it is aimed to construct a new algebraic structure on soft set theory which has paved the way for many studies. Throughout this paper, IS-radical, IS-quasi radical, IS-interior radical and IS-nil radical in semigroups were obtained. We have used two different methods to define the soft radicals. We have gave several examples and propositions. Important results were specifically mentioned in the article. Based on these results, some further works can be developed on the properties of the soft radicals for ideals in regular semigroups.

Conflicts of interest

The authors state that did not have conflict of interests

References

- [1] Molodtsov D., Soft Set Theory First Results, *Comput. Math. Appl.*, 37 (1999) 19–31.
- [2] Maji P.K., Biswas R., Roy, R., An Application of Soft Sets in A Decision-Making Problem, *Comput. Math. Appl.*, 44 (2002) 1077–1083.
- [3] Maji P.K., Biswas R., Roy R., Soft Set Theory, *Comput. Math. Appl.*, 45 (2003) 555–562.
- [4] Feng F., Li Y., Fotea V.L., Application of Level Soft Sets in Decision Making Based on Interval-Valued Fuzzy Soft Sets, *Comput. Math. Appl.*, 60 (2010) 1756-1767.
- [5] Feng F., Li Y., Cagman N. Generalized Uni-Int Decision Making Schemes Based on Choice Value Soft Sets, *Eur. J. Oper. Res.*, 220 (2012) 162–170.
- [6] Cagman N., Enginoglu S., Soft Set Theory and Uni-Int Decision Making, *Eur. J. Oper. Res.*, 207 (2010) 848–855.
- [7] Aygun E., Soft Matrix Product and Soft Cryptosystem, *Filomat*, 32:19 (2018) 6519–6530.

- [8] Aygun E., Kamacı H., Some Generalized Operations in Soft Set Theory and Their Role in Similarity and Decision Making, *J. Intell. Fuzzy Syst.*, 36 (2019) 6537–6547.
- [9] Aktas H., Cagman N., Soft Sets and Soft Groups, *Inform. Sci.*, 177 (2007) 2726-2735.
- [10] Feng F., Jun Y.B., Zhao X.Z. Soft Semirings, *Comput. Math. Appl.*, 56 (2008) 2621–2628.
- [11] Acar U., Koyuncu F., Tanay B., Soft Sets and Soft Rings, *Comput. Math. Appl.*, 59 (2010) 3458-3463.
- [12] Ali M.I., Shabir M., Shum K.P., On Soft Ideals over Semigroups. *Southeast Asian Bull. Math.*, 34 (2010) 595-610.
- [13] Atagun A.O., Sezgin A., Soft Substructures of Rings, fields and modules, *Comput. Math. Appl* 61 (3) (2011) 592-601.
- [14] Sezgin A., Atagun A.O., Aygun E., A Note on Soft Near-Rings and Idealistic Soft Near-Rings, *Filomat* 25 (1) (2011) 53- 68.
- [15] Sezgin A., Atagun A.O. Soft Groups and Normalistic Soft Groups, *Comput. Math. Appl*, 62 (2) (2011) 1457-1467.
- [16] Atagun A.O., Aygun E., Groups of Soft Sets., *J. Intell. Fuzzy Syst.*, 30 (2016) 729-733.
- [17] Song S.Z., Kim H.S., Jun Y.B., Ideal Theory in Semigroups Based on Intersectional Soft Sets, *Sci. World J.*, (2014) 136424.
- [18] Sezgin A., Cagman N., Atagun A.O., Ali M.I., Turkmen E., Soft Intersection Semigroups, Ideals and Bi-Ideals: a New Application on Semigroup Theory I. *Filomat*, 29(5) (2015) 917-946.
- [19] Sezgin A., Cagman N., Atagun A.O., Soft Intersection Interior Ideals, Quasi-ideals and Generalized Bi-Ideals: A New Approach to Semigroup Theory II., *J. Multi. Valued Log.S*, 3.1-2(2014) 161-207.
- [20] Atiyah M., Macdonald I.G. Introduction to Commutative Algebra, Addison Wesley, (1994).
- [21] Howie J.M., An Introduction to Semigroup Theory, Academic Press, (1976).



Statistical relative uniform convergence of a double sequence of functions at a point and applications to approximation theory

Sevda YILDIZ *

Sinop University, Department of Mathematics, Sinop/ TURKEY

Abstract

In the present paper, we introduce a new kind of convergence, called the statistical relative uniform convergence, for a double sequence of functions at a point, where the relative uniform convergence of the set of the neighborhoods of the given point is considered. By the use of the statistical relative uniform convergence, we investigate a Korovkin type approximation theorem which makes the proposed method stronger than the ones studied before. After that, we give an example using this new type of convergence. We also study the rate of convergence of the proposed convergence.

Article info

History:

Received: 25.11.2020

Accepted: 03.03.2021

Keywords:

Double sequence,
Korovkin theorem,
Rate of convergence,
Statistical relative
uniform convergence.

1. Introduction

It is well-known that the first definition of statistical convergence was given by Fast [1] and Steinhaus [2], independently. It is more general than the ordinary convergence. The statistical convergence in approximation theory was first used by Gadjiev and Orhan [3] to prove the Korovkin-type approximation theorem [4]. The studies and related results can be found in [5-8].

Moore [9] was the first who introduced the notion of relative uniform convergence of a sequence of functions. Later on, Chittenden [10] gave a detailed definition of this convergence (which is equivalent to Moore's definition). Recently, Demirci and Orhan [11] defined a new type of statistical convergence by using this convergence and they presented its applications to Korovkin type approximation. For more details on these types of convergences and their applications, we refer to [12-17].

Another interesting type of convergence is the uniform convergence of a sequence of functions at a point [18]. More recently, Demirci et al. [19] extended this type of convergence to relative uniform convergence of a sequence of functions at a point where the set of the neighborhoods of the point at which relative uniform convergence is considered (see, e.g., [20, 21]).

Our focus of the present work is to generalize the concept of statistical convergence using relative uniform convergence at a point. For this purpose, we first define the concept of statistical relative uniform convergence of double sequences of functions at a point and we give some examples, showing that our results are strict generalization of the corresponding classical ones. We also establish some important approximation results.

2. Preliminaries

The idea of uniform convergence of a sequence of functions at a point was defined by J. Klippert and G. Williams in [18]. This type of convergence is a stronger method than the well known uniform convergence. Recently, Demirci et al. [19] gave the notion of relative uniform convergence of a sequence of functions at a point and they proved the Korovkin type approximation theorems. Now we recall these interesting types of convergences:

Definition 2.1 [18] Suppose that (f_j) is a sequence of real functions defined on $G \subset \mathbb{R}$. Let $u_0 \in G$. We say that (f_j) converges uniformly at the point u_0 to $f: G \rightarrow \mathbb{R}$ provided that for every $\varepsilon > 0$, there exist $\delta > 0$ and $J \in \mathbb{N}$ such that for every $j \geq J$, if $|u - u_0| < \delta$, then $|f_j(u) - f(u)| < \varepsilon$.

*Corresponding author. email address: sevdaorhan@sinop.edu.tr

Definition 2.2 [19] Let (f_j) be a sequence of real functions defined on G and $u_0 \in G$. We say that (f_j) converges relatively uniformly at the point u_0 to $f: G \rightarrow \mathbb{R}$ with respect to the scale function $\sigma(u)$, $|\sigma(u)| \neq 0$, if for every $\varepsilon > 0$, there exist $\delta > 0$ and $J \in \mathbb{N}$ such that for every $j \geq J$, if $|u - u_0| < \delta$, then

$$|f_j(u) - f(u)| < \varepsilon |\sigma(u)|.$$

More recently, Dirik et al. [21] introduced the uniform convergence of a sequence of functions at a point for double sequences. Before this definition, we first give the following:

A double sequence $u = (u_{ij})$ is said to be convergent in Pringsheim's sense iff for every $\varepsilon > 0$, there exists $J = J(\varepsilon) \in \mathbb{N}$ such that $|u_{ij} - L| < \varepsilon$ whenever $i, j > J$. Then, L is called the Pringsheim limit of u and is denoted by $P - \lim_{i,j \rightarrow \infty} u_{ij} = L$ (see [22]). In this case, we say that u is " P -convergent to L ". Also, if there exists a positive number I such that $|u_{ij}| \leq I$ for all $(i, j) \in \mathbb{N}^2 = \mathbb{N} \times \mathbb{N}$, then u is said to be bounded. It is important to say that a convergent double sequence need not be bounded but it is necessary to be bounded for a convergent single sequence.

Definition 2.3 [21] Suppose that (f_{ij}) is a double sequence of real functions defined on $G^2 \subset \mathbb{R}^2$. Let $(u_0, v_0) \in G^2$. We say that (f_{ij}) converges uniformly at the point (u_0, v_0) to $f: G^2 \rightarrow \mathbb{R}$ iff for every $\varepsilon > 0$, there are $\delta > 0$ and $J \in \mathbb{N}$ such that for every $i, j \geq J$, if $\sqrt{(u - u_0)^2 + (v - v_0)^2} \leq \delta$ (or $|u - u_0| \leq \delta$ and $|v - v_0| \leq \delta$), then

$$|f_{ij}(u, v) - f(u, v)| < \varepsilon.$$

Example 2.1 Define $g_{ij}: [0,1]^2 \rightarrow \mathbb{R}$ by

$$g_{ij}(u, v) = \begin{cases} u^2 + v^2, & j \text{ is a square,} \\ 0, & \text{otherwise.} \end{cases}$$

We claim that (g_{ij}) converges uniformly to $g = 0$ at $(u_0, v_0) = (0,0)$. Indeed, let $\varepsilon > 0$ be given and choose $\delta = \sqrt{\frac{\varepsilon}{2}}$ and $J = 1$. Let $i, j \geq J$ and $u, v \in [0,1]$ with $|u| \leq \delta$, $|v| \leq \delta$. Then,

$$|g_{ij}(u, v) - g(u, v)| = |g_{ij}(u, v)| \leq u^2 + v^2 \leq 2\delta^2 = \varepsilon.$$

However, (g_{ij}) does not converge uniformly to $g = 0$ on $[0,1]^2$.

3. Statistical Relative Uniform Convergence At a Point

The statistical convergence for single sequences was given in 1951 and this concept was extended to the double sequences by Moricz [23] in 2004 as follows:

Let $A \subseteq \mathbb{N}^2$ be a two-dimensional subset of positive integers, then A_{ij} denotes the set $\{(m, n) \in A: m \leq i, n \leq j\}$ and $|A_{ij}|$ denotes the cardinality of A_{ij} . The double natural density of A is given by

$$\delta_2(A) := P - \lim_{i,j \rightarrow \infty} \frac{1}{ij} |A_{ij}|,$$

if it exists. The number sequence $u = (u_{ij})$ is said to be statistically convergent to L provided that for every $\varepsilon > 0$, the set

$$A = A_{mn}(\varepsilon) := \{i \leq m, j \leq n: |u_{ij} - L| \geq \varepsilon\}$$

has natural density zero; in that case, we write $st_2 - \lim_{i,j \rightarrow \infty} u_{ij} = L$ (see [23]).

Now, we can give the following definition which is our new type of convergence:

Definition 3.1 Let $G^2 \subset \mathbb{R}^2$ and suppose that (f_{ij}) is a double sequence of real functions defined on G^2 . Let $(u_0, v_0) \in G^2$. We say that (f_{ij}) converges statistically relatively uniformly at the point (u_0, v_0) to $f: G^2 \rightarrow \mathbb{R}$ with respect to the scale function σ iff for each $\varepsilon > 0$ there are $\eta > 0$ and $A \subseteq \mathbb{N}^2$ with $\delta_2(A) = 0$ such that for every $\varepsilon > 0$ and $(i, j) \in \mathbb{N}^2 \setminus A$, if $\sqrt{(u - u_0)^2 + (v - v_0)^2} \leq \eta$ (or $|u - u_0| \leq \eta$ and $|v - v_0| \leq \eta$), then

$$|f_{ij}(u, v) - f(u, v)| < \varepsilon |\sigma(u, v)|.$$

Now we give the following remark that gives the relations between types of convergences.

Remark 3.1 It can be immediately seen that if (f_{ij}) is statistically relatively uniformly convergent to a function f on G^2 , then (f_{ij}) converges statistically relatively uniformly at each point in G^2 . Also, observe that the statistical uniform convergence of a double sequence of functions at a point is the special case of statistical relative uniform convergence of a double sequence of functions at a point in which the scale function is a non-zero constant. If $\sigma(u, v)$ is bounded, then the statistical relative uniform convergence at a point implies the statistical uniform convergence at a point. However, the statistical relative uniform convergence at a point does not imply the statistical uniform convergence at a point, when $\sigma(u, v)$ is unbounded.

Now, we give the following example to show the effectiveness of newly proposed method:

Example 3.1 Define $h_{ij}: [0,1]^2 \rightarrow \mathbb{R}$ by

$$h_{ij}(u, v) = \begin{cases} i^2 j u^2 v, & i = k^2 \text{ and } j = l^2, \\ \frac{2i^2 j u^2 v}{5+i^2 j u^2 v}, & \text{otherwise.} \end{cases} \tag{1}$$

$k, l = 1, 2, \dots$. We claim that (h_{ij}) converges statistically relatively uniformly to $h = 0$ at $(u_0, v_0) = (0,0)$ to the scale function

$$\sigma(u, v) = \begin{cases} \frac{1}{uv}, & (u, v) \in]0,1]^2, \\ 1, & u = 0 \text{ or } v = 0. \end{cases} \tag{2}$$

Indeed, let $\varepsilon > 0$ be given and choose $\eta = \sqrt{\frac{\varepsilon}{2}}$ and $A = \{(i, j): i = k^2 \text{ and } j = l^2, k, l = 1, 2, \dots\}$. Then $\delta_2(A) = 0$. Let $(i, j) \in \mathbb{N}^2 \setminus A$ and $(u, v) \in [0,1]^2$ with $|u| \leq \eta$ and $|v| \leq \eta$. Then,

$$\left| \frac{h_{ij}(u, v)}{\sigma(u, v)} \right| \leq \left| \frac{2i^2 j u^3 v^2}{5+i^2 j u^2 v} \right| \leq 2|u||v| < 2\eta^2 = \varepsilon.$$

However, (h_{ij}) does not converge statistically uniformly at $(0,0)$. Indeed, for $\varepsilon = \frac{1}{5}$, $(u, v) = (\frac{1}{i}, \frac{1}{j}) \in]0,1]^2$ with $\frac{1}{i} < \eta$, $\frac{1}{j} < \eta$ and $(i, j) \in \mathbb{N}^2 \setminus A$, we get

$$\frac{2i^2 j u^2 v}{5+i^2 j u^2 v} = \frac{1}{3} > \frac{1}{5}.$$

Also, it is neither uniformly nor relatively uniformly convergent to $h = 0$.

4. Korovkin Type Approximation

In this section, we apply the notion of statistical relative uniform convergence of double sequences of functions at a point to prove a Korovkin type approximation theorem. Suppose that $C(G^2)$ is the space of all functions f continuous on G^2 . We know that $C(G^2)$ is a Banach space with norm $\|f\| = \sup_{(u,v) \in G^2} |f(u, v)|$.

We denote the value of $L_{ij}(f)$ at a point $(u, v) \in G^2$ by $L_{ij}(f(s, t); u, v)$ or briefly, $L_{ij}(f; u, v)$ and we use the test functions

$$e_0(u, v) = 1, e_1(u, v) = u, e_2(u, v) = v \text{ and } e_3(u, v) = u^2 + v^2.$$

Theorem 4.1 [7] Suppose that (L_{ij}) is a double sequence of positive linear operators acting from $C(G^2)$ into itself. Then, for all $f \in C(G^2)$,

$$st_2 - \lim_{i,j \rightarrow \infty} \|L_{ij}(f) - f\| = 0 \text{ iff}$$

$$st_2 - \lim_{i,j \rightarrow \infty} \|L_{ij}(e_r) - e_r\| = 0, (r = 0,1,2,3).$$

Now, we give the following main theorem.

Theorem 4.2 Let (L_{ij}) be a double sequence of positive linear operators acting from $C(G^2)$ into itself. Then $(L_{ij}(e_r))$ ($r = 0,1,2,3$) converges statistically relatively uniformly at (u_0, v_0) to e_r with respect to the scale function σ_r iff for each $f \in C(G^2)$, $(L_{ij}(f))$ converges statistically relatively uniformly at (u_0, v_0) to f with respect to the scale function σ where $\sigma(u, v) = \max\{|\sigma_r(u, v)|: r = 0,1,2,3\}$, $|\sigma_r(u, v)| > 0$ and $|\sigma_r(u, v)|$ is possibly unbounded, $r = 0,1,2,3$.

Proof We begin the proof of the "if" part. Our hypothesis is that $(L_{ij}(f))$ converges statistically relatively uniformly at (u_0, v_0) to f for each $f \in C(G^2)$ with respect to the scale function σ , which means that $\forall f \in C(G^2)$, $\forall \varepsilon > 0$, $\exists \eta > 0$ and $A \subseteq \mathbb{N}^2$ with $\delta_2(A) = 0$ such that $|L_{ij}(f; u, v) - f(u, v)| \leq \varepsilon |\sigma(u, v)|$, $\forall (i, j) \in \mathbb{N}^2 \setminus A$ and $\sqrt{(u - u_0)^2 + (v - v_0)^2} \leq \eta$. Since $e_r \in C(G^2)$, $r = 0,1,2,3$, if we choose $\varepsilon = \frac{\varepsilon^* |\sigma_r(u, v)|}{\sigma(u, v)}$, then we get $\forall \varepsilon^* > 0$, $\exists \eta > 0$ and $A \subseteq \mathbb{N}^2$ such that $|L_{ij}(e_r; u, v) - e_r(u, v)| \leq \varepsilon^* |\sigma_r(u, v)|$, $r = 0,1,2,3$, $\forall (i, j) \in \mathbb{N}^2 \setminus A$ and $\sqrt{(u - u_0)^2 + (v - v_0)^2} \leq \eta$. Now, we turn to the "only if" part. Let $f \in C(G^2)$ and $(u, v) \in G^2$ be fixed. Let $E = \max\{|u|, |u|^2\}$, $F = \max\{|v|, |v|^2\}$ and $H = \max\{E, F\}$. Also, by the continuity of f on G^2 , we can write $|f(u, v)| \leq M$. Hence,

$$|f(s, t) - f(u, v)| \leq |f(s, t)| + |f(u, v)| \leq 2M.$$

Moreover, since f is uniformly continuous on G^2 , we write that for every $\varepsilon > 0$, there exists a number $\delta > 0$ such that $|f(s, t) - f(u, v)| < \varepsilon$ holds for all $(s, t) \in G^2$ satisfying $\sqrt{(s - u)^2 + (t - v)^2} < \delta$. Hence, we get

$$|f(s, t) - f(u, v)| < \frac{\varepsilon}{4} + \frac{2M}{\delta^2} \{(s - u)^2 + (t - v)^2\}. \tag{3}$$

This means

$$-\frac{\varepsilon}{4} - \frac{2M}{\delta^2} \{(s - u)^2 + (t - v)^2\} < f(s, t) - f(u, v) < \frac{\varepsilon}{4} + \frac{2M}{\delta^2} \{(s - u)^2 + (t - v)^2\}.$$

Without loss of generality, ε can be chosen such that $0 < \varepsilon \leq 1$. By the hypothesis, for every $r = 0,1,2,3$ there are $\eta_r > 0$ and $A_r \subseteq \mathbb{N}^2$ with $\delta_2(A_r) = 0$ such that

$$|L_{ij}(e_r; u, v) - e_r(u, v)| \leq \min \left\{ \frac{\varepsilon}{4}, \frac{\varepsilon}{4M}, \frac{\varepsilon \delta^2}{56M}, \frac{\varepsilon \delta^2}{56MH} \right\} |\sigma_r(u, v)|$$

whenever $(i, j) \in \mathbb{N}^2 \setminus A_r$, $|u - u_0| \leq \eta_r$ and $|v - v_0| \leq \eta_r$. Then, we get

$$|L_{ij}(e_r; u, v) - e_r(u, v)| \leq \min \left\{ \frac{\varepsilon}{4}, \frac{\varepsilon}{4M}, \frac{\varepsilon\delta^2}{56M}, \frac{\varepsilon\delta^2}{56MH} \right\} \sigma(u, v)$$

whenever $(i, j) \in \mathbb{N}^2 \setminus A$, $|u - u_0| \leq \eta$ and $|v - v_0| \leq \eta$ where

$$A = \cup_{r=0}^3 A_r \text{ with } \delta_2(A) = 0 \text{ and } \eta = \min\{\eta_r: r = 0,1,2,3\}.$$

We write

$$\begin{aligned} &L_{ij}((. - u)^2 + (. - v)^2; u, v) \\ &\leq |L_{ij}(e_3; u, v) - e_3(u, v)| + 2|u| |L_{ij}(e_1; u, v) - e_1(u, v)| + 2|v| |L_{ij}(e_2; u, v) - e_2(u, v)| \\ &\quad + |u^2 + v^2| |L_{ij}(e_0; u, v) - e_0(u, v)| \\ &\leq \frac{\varepsilon\delta^2}{8M} \sigma(u, v) \end{aligned}$$

for $(i, j) \in \mathbb{N}^2 \setminus A$ and $(u, v) \in G^2$ with $|u - u_0| \leq \eta$ and $|v - v_0| \leq \eta$. Using the linearity and the positivity of the operators L_{ij} and (3), we have

$$\begin{aligned} |L_{ij}(f; u, v) - f(u, v)| &\leq |L_{ij}(f; u, v) - f(u, v)L_{ij}(e_0; u, v)| + |f(u, v)| |L_{ij}(e_0; u, v) - e_0(u, v)| \\ &\leq L_{ij} \left(\frac{\varepsilon}{4} + \frac{2M}{\delta^2} \{(s - u)^2 + (t - v)^2\}; u, v \right) + M |L_{ij}(e_0; u, v) - e_0(u, v)| \\ &= \frac{\varepsilon}{4} L_{ij}(e_0; u, v) + \frac{2M}{\delta^2} L_{ij}((. - u)^2 + (. - v)^2; u, v) + M |L_{ij}(e_0; u, v) - e_0(u, v)| \\ &\leq \left\{ \frac{\varepsilon}{4} + M \right\} |L_{ij}(e_0; u, v) - e_0(u, v)| + \frac{\varepsilon}{4} + \frac{2M}{\delta^2} L_{ij}((. - u)^2 + (. - v)^2; u, v) \\ &\leq \varepsilon \sigma(u, v) \end{aligned}$$

whenever $(i, j) \in \mathbb{N}^2 \setminus A$ and $(u, v) \in G^2$ with $|u - u_0| \leq \eta$ and $|v - v_0| \leq \eta$. Hence, we get the desired result.

If one replaces the scale function by a non-zero constant, then the next result immediately follows from our main Korovkin type approximation theorem.

Corollary 4.1 Let (L_{ij}) be a double sequence of positive linear operators acting from $C(G^2)$ into itself. Then $(L_{ij}(e_r))$ ($r = 0,1,2,3$) converges statistically uniformly at (u_0, v_0) to e_r iff for each $f \in C(G^2)$, $(L_{ij}(f))$ converges statistically uniformly at (u_0, v_0) to f .

Also, if one replaces the statistical limit with Pringsheim limit and scale function by a non-zero constant, then the next result which was obtained in [21] follows from our main Korovkin type approximation theorem.

Corollary 4.2 [21] Let (L_{ij}) be a double sequence of positive linear operators acting from $C(G^2)$ into itself. Then $(L_{ij}(e_r))$ ($r = 0,1,2,3$) converges uniformly at (u_0, v_0) to e_r iff for each $f \in C(G^2)$, $(L_{ij}(f))$ converges uniformly at (u_0, v_0) to f .

5. An application

In this section, we deal with an example that shows our main Korovkin type approximation theorem is stronger than the corresponding classical ones.

Example 5.1 Let $G^2 = [0,1]^2$. Consider the following Bernstein operators [24] given by

$$B_{ij}(f; u, v) = \sum_{k=0}^i \sum_{l=0}^j f\left(\frac{k}{i}, \frac{l}{j}\right) \binom{i}{k} \binom{j}{l} u^k (1-u)^{i-k} v^l (1-v)^{j-l} \tag{4}$$

where $(u, v) \in G^2, f \in C(G^2)$. Using these polynomials, we introduce the following positive linear operators on $C(G^2)$:

$$L_{ij}(f; u, v) = (1 + h_{ij}(u, v)) B_{ij}(f; u, v) \tag{5}$$

where $h_{ij}(u, v)$ is given by (3.1). Now, observe that

$$L_{ij}(e_0; u, v) = (1 + h_{ij}(u, v)) e_0(u, v), L_{ij}(e_1; u, v) = (1 + h_{ij}(u, v)) e_1(u, v),$$

$$L_{ij}(e_2; u, v) = (1 + h_{ij}(u, v)) e_2(u, v), L_{ij}(e_3; u, v) = (1 + h_{ij}(u, v)) \left[e_3(u, v) + \frac{u-u^2}{i} + \frac{v-v^2}{j} \right].$$

Now we claim that $(L_{ij}(e_r))$ converges statistically uniformly to e_r at $(u_0, v_0) = (0,0)$ to the scale function $\sigma_r := \sigma$ which is given by (3.2) ($r = 0,1,2,3$). Let $\varepsilon > 0$ be given and $A_r := A = \{(i, j): i = k^2 \text{ and } j = l^2, k, l = 1,2, \dots\}$, then $\delta_2(A_r) = 0$ ($r = 0,1,2,3$).

Now, let $(i, j) \in \mathbb{N}^2 \setminus A_0$ and $(u, v) \in [0,1]^2$ with $|u| \leq \eta_0$ and $|v| \leq \eta_0$ where $\eta_0 = \sqrt{\frac{\varepsilon}{2}}$. Then,

$$\left| \frac{L_{ij}(e_0; u, v) - e_0(u, v)}{\sigma_0(u, v)} \right| = \left| \frac{h_{ij}(u, v)}{\sigma(u, v)} \right| \leq 2|u||v| < 2\eta_0^2 = \varepsilon$$

our claim is true for $r = 0$. Also,

$$\left| \frac{L_{ij}(e_1; u, v) - e_1(u, v)}{\sigma_1(u, v)} \right| = \left| \frac{e_1(u, v)h_{ij}(u, v)}{\sigma(u, v)} \right| \leq 2|u|^2|v| < 2\eta_1^3 = \varepsilon$$

whenever $(i, j) \in \mathbb{N}^2 \setminus A_1$ and $|u| \leq \eta_1$ and $|v| \leq \eta_1$ where $\eta_1 = \sqrt[3]{\frac{\varepsilon}{2}}$. Similarly,

$$\left| \frac{L_{ij}(e_2; u, v) - e_2(u, v)}{\sigma_2(u, v)} \right| \leq \left| \frac{e_2(u, v)h_{ij}(u, v)}{\sigma(u, v)} \right| \leq 2|u||v|^2 < 2\eta_2^3 = \varepsilon$$

whenever $(i, j) \in \mathbb{N}^2 \setminus A_2$ and $|u| \leq \eta_2$ and $|v| \leq \eta_2$ where $\eta_2 = \sqrt[3]{\frac{\varepsilon}{2}}$. Hence, we get that our claim is true for $r = 1, 2$. Finally,

$$\begin{aligned} \left| \frac{L_{ij}(e_3; u, v) - e_3(u, v)}{\sigma_3(u, v)} \right| &= \left| \frac{1}{\sigma(u, v)} \left[(1 + h_{ij}(u, v)) \left[e_3(u, v) + \frac{u - u^2}{i} + \frac{v - v^2}{j} \right] - e_3(u, v) \right] \right| \\ &\leq \left| \frac{h_{ij}(u, v)}{\sigma(u, v)} \left[e_3(u, v) + \frac{u - u^2}{i} + \frac{v - v^2}{j} \right] \right| + \left| \frac{u - u^2}{i\sigma(u, v)} \right| + \left| \frac{v - v^2}{j\sigma(u, v)} \right| \\ &\leq 4 \left| \frac{h_{ij}(u, v)}{\sigma(u, v)} \right| + 2|u||v| \\ &\leq 10|u||v| \leq 10\eta_2^2 = \varepsilon \end{aligned}$$

whenever $(i, j) \in \mathbb{N}^2 \setminus A_3$ and $|u| \leq \eta_3$ and $|v| \leq \eta_3$ where $\eta_3 = \sqrt{\frac{\varepsilon}{10}}$ and our claim is true for $r = 3$. Hence from our main Theorem 4.2, we get

$$\left| \frac{L_{ij}(f; u, v) - f(u, v)}{\sigma(u, v)} \right| \leq \varepsilon$$

whenever $(i, j) \in \mathbb{N}^2 \setminus A$, $|u| \leq \eta$ and $|v| \leq \eta$ where $\eta = \min \left\{ \sqrt{\frac{\varepsilon}{2}}, \sqrt[3]{\frac{\varepsilon}{2}}, \sqrt{\frac{\varepsilon}{10}} \right\}$. However, since $|L_{ij}(e_0; u, v) - e_0(u, v)| = h_{ij}(u, v)$, the sequence $(L_{ij}(e_0))$ is not statistically uniformly convergent to e_0 at $(0, 0)$. Hence, we can say that Theorem 4.1 (statistical Korovkin type theorem) and Corollary 4.1 do not work for our operators defined by (5). Also, $(L_{ij}(e_0))$ is not uniformly convergent to e_0 at $(0, 0)$ and Corollary 4.2 does not work for our operators, too.

6. Rate of Convergence

The main aim of this section is to study the rate of convergence with the aid of the modulus of continuity that is defined by

$$\omega_2(f; \delta) := \sup \left\{ |f(s, t) - f(u, v)| : (s, t), (u, v) \in G^2, \sqrt{(s - u)^2 + (t - v)^2} \leq \delta \right\}$$

where $f \in C(G^2)$ and $\delta > 0$. In order to obtain our result, we will make use of the elementary inequality, for all $f \in C(G^2)$ and for $\lambda, \delta > 0$,

$$\omega_2(f; \lambda\delta) \leq (1 + [\lambda])\omega_2(f; \delta)$$

where $[\lambda]$ is defined to be the greatest integer less than or equal to λ (see also [25, 26]).

Theorem 6.1 Let (L_{ij}) be a double sequence of positive linear operators acting from $C(G^2)$ into itself. Assume that the following conditions hold:

- (i) $(L_{ij}(e_0))$ converges statistically uniformly to e_0 at (u_0, v_0) with respect to the scale function σ_0 ,

(ii) $st_2 - \lim_{i,j \rightarrow \infty} \frac{\omega_2(f; \delta_{ij})}{|\sigma_1(u,v)|} = 0$ for each $(u, v) \in G^2$ where $\delta_{ij} := \sqrt{L_{ij}((.-u)^2 + (.-v)^2; u, v)}$.

Then we have, for all $f \in C(G^2)$, $(L_{ij}(f))$ converges statistically uniformly to f at (u_0, v_0) with respect to the scale function σ , where $\sigma(u, v) = \max\{|\sigma_r(u, v)|: r = 0, 1\}$.

Proof Let $(u, v) \in G^2$ and $f \in C(G^2)$ be fixed. Using the linearity and the positivity of the operators L_{ij} , for all $(i, j) \in \mathbb{N}^2$ and any $\delta > 0$, we have

$$\begin{aligned} |L_{ij}(f; u, v) - f(u, v)| &\leq |L_{ij}(f; u, v) - f(u, v)L_{ij}(e_0; u, v)| + |f(u, v)||L_{ij}(e_0; u, v) - e_0(u, v)| \\ &\leq L_{ij}\left(\left(1 + \frac{(-u)^2 + (-v)^2}{\delta^2}\right)\omega_2(f; \delta); u, v\right) + |f(u, v)||L_{ij}(e_0; u, v) - e_0(u, v)| \\ &= \omega_2(f; \delta)L_{ij}(e_0; u, v) + \frac{\omega_2(f; \delta)}{\delta^2}L_{ij}((.-u)^2 + (.-v)^2; u, v) + \\ &\quad |f(u, v)||L_{ij}(e_0; u, v) - e_0(u, v)|. \end{aligned}$$

Put $\delta := \delta_{ij} = \sqrt{L_{ij}((.-u)^2 + (.-v)^2; u, v)}$. Hence, we get

$$\frac{|L_{ij}(f; u, v) - f(u, v)|}{\sigma(u, v)} \leq [\omega_2(f; \delta_{ij}) + |f(u, v)|] \left| \frac{L_{ij}(e_0; u, v) - e_0(u, v)}{\sigma_0(u, v)} \right| + 2 \frac{\omega_2(f; \delta_{ij})}{|\sigma_1(u, v)|}.$$

By using (i) and (ii) the proof is completed.

Acknowledgment

The author received no financial support for the research, authorship, and/or publication of this article.

Conflicts of interest

The author states that she did not have a conflict of interest.

References

[1] Fast H., Sur la Convergence Statistique, *Colloq. Math.*, 2 (1951) 241-244.

[2] Steinhaus H., Sur la Convergence Ordinaire et la Convergence Asymptotique, *Colloq. Math.*, 2 (1951) 73-74.

[3] Gadjiev A. D., Orhan C., Some Approximation Theorems via Statistical Convergence, *Rocky Mountain J. Math.*, 32 (2002) 129-138.

[4] Korovkin P. P., Linear Operators and Approximation Theory. Delhi: Hindustan Publ. Co., (1960).

[5] Belen C., Yıldırım M., Generalized A-Statistical Convergence and a Korovkin Type Approximation Theorem for Double Sequences, *Miskolc Mathematical Notes*, 14 (1) (2013) 31-39.

[6] Demirci K., Dirik F., Four-Dimensional Matrix Transformation and Rate of A-Statistical Convergence of Periodic Functions, *Math. Comput. Modelling*, 52 (9-10) (2010) 1858-1866.

[7] Dirik F., Demirci K., Korovkin Type Approximation Theorem for Functions of Two Variables in Statistical Sense, *Turk J Math*, 34 (2010) 73-83.

- [8] Ünver M., Orhan C., Statistical Convergence with Respect to Power Series Methods and Applications to Approximation Theory, *Numerical Functional Analysis and Optimization*, 40 (5) (2019) 535-547.
- [9] Moore E. H., An Introduction to a Form of General Analysis, The New Haven Mathematical Colloquium, Yale University Press, New Haven, (1910).
- [10] Chittenden E. W., On the Limit Functions of Sequences of Continuous Functions Converging Relatively Uniformly, *Transactions of the AMS*, 20 (1919) 179-184.
- [11] Demirci K., Orhan S., Statistically Relatively Uniform Convergence of Positive Linear Operators, *Results Math.*, 69 (2016) 359-367.
- [12] Demirci K., Kolay B., A-Statistical Relative Modular Convergence of Positive Linear Operators, *Positivity*, 21 (3) (2017) 847-863.
- [13] Demirci K., Orhan S., Kolay B., Relative Hemen Hemen Yakınsaklık ve Yaklaşım Teoremleri, *Sinop Üniversitesi Fen Bilimleri Dergisi*, 1 (2) (2016) 114-122.
- [14] Demirci K., Yıldız S., Statistical Relative Uniform Convergence in Dually Residuated Lattice Totally Ordered Semigroups, *Sarajevo J. Math.*, 15 (2) (2019) 227-237.
- [15] Sahin P. O., Dirik F., Statistical Relative Uniform Convergence of Double Sequences of Positive Linear Operators, *Appl. Math. E-Notes*, 17 (2017) 207-220.
- [16] Sahin P. O., Dirik F., Statistical Relative Equal Convergence of Double Function Sequences and Korovkin-Type Approximation Theorem, *Applied Mathematics E-Notes*, 19 (2019) 101-115.
- [17] Yılmaz B., Demirci K., Orhan S., Relative Modular Convergence of Positive Linear Operators, *Positivity*, 20 (3) (2016) 565-577.
- [18] Klippert J., Williams G., Uniform Convergence of a Sequence of Functions at a Point, *Internat. J. Math. Ed. Sci. Tech.*, 33 (1) (2002) 51-58.
- [19] Demirci K., Boccuto A., Yıldız S., Dirik F., Relative Uniform Convergence of a Sequence of Functions at a Point and Korovkin-Type Approximation Theorems, *Positivity*, 24 (1) (2020) 1-11.
- [20] Boccuto A., Demirci K., Yıldız S., Abstract Korovkin-type theorems in the filter setting with respect to relative uniform convergence, *Turkish Journal of Mathematics*, 44 (4) (2020) 1238-1249.
- [21] Dirik F., Demirci K., Yıldız S., Acu A. M., The Uniform Convergence of a Double Sequence of Functions at a Point and Korovkin-Type Approximation Theorems, *Georgian Mathematical Journal*, 1 (ahead-of-print) (2020)
- [22] Pringsheim A., Zur Theorie der Zweifach Unendlichen Zahlenfolgen, *Math. Ann.*, 53 (1) (1900) 289-321.
- [23] Moricz F., Statistical Convergence of Multiple Sequences, *Arch. Math.*, (Basel) 81 (2004) 82-89.
- [24] Stancu D. D., A Method for Obtaining Polynomials of Bernstein Type of Two Variables, *The American Mathematical Monthly*, 70 (3) (1963) 260-264.
- [25] DeVore R.A., Lorentz G.G., Constructive Approximation (Grund. Math. Wiss. 303). Berlin: Springer Verlag, (1993).
- [26] Altomare F., Campiti M., Korovkin-Type Approximation Theory and its Applications. New York: Walter de Gruyter, (1994).



On the solution of a Sturm-Liouville problem by using Laplace transform on time scales

Emrah YILMAZ^{1,*} , Sertaç GÖKTAŞ² 

¹Firat University, Faculty of Science, Department of Mathematics, Elazığ/TURKEY

²Mersin University, Faculty of Science and Letters, Department of Mathematics, Mersin/TURKEY

Abstract

In this study, we solve a Sturm-Liouville problem on time scales with constant graininess by using Laplace transform which is one of the finest representatives of integral transformation used in applied mathematics. Eigenfunctions on the time scale were obtained in different cases with the Laplace transform. Thus, it was seen that the Laplace transform is an effective method on time scales. The results that will contribute to the spectral theory were obtained on the time scale with the examples discussed. It is very interesting that the results obtained differ as the time scale changes and this transformation can be applied to other types of problems. The problems that were established and solved enabled the subject to be understood on the time scale.

Article info

History:

Received:25.11.2020

Accepted:04.03.2021

Keywords:

Time scales,
Sturm-Liouville
problem,
Laplace transform.

1. Introduction

Laplace transform is a valuable tool to solve linear differential equations which include constant coefficients and integral equations. It plays a crucial role in mathematics and engineering. Laplace transform from time domain to frequency domain converts differential equations into algebraic equations and convolution into product. Detailed information on the general structure of the Laplace transform in the classical situation can be found in Schiff's study [1].

Discrete version of Laplace transform is known as Z-transform. It is convenient for linear recurrence relations and summation equations. Laplace transform on time scale was firstly considered by Hilger [2] to unify continuous Laplace transform and discrete Z-transform in one theory in 1999. For arbitrary time scales, Laplace transform was investigated by Bohner and Peterson [3] in 2002. The various forms of Laplace transform on time scale were studied in detail by many authors in literature [4, 5-9, 10-14].

For a better understanding for readers, we provide some principle notions related to delta calculus on time scales. By the time scale \mathbb{T} , we understand any non-empty, closed, arbitrary subset of \mathbb{R} with ordering inherited from reals. This theory was first put forward

by Hilger [15, 16] in 1988, and in the following years, numerous studies were conducted on this subject in various fields. Since a time scale is not necessarily connected, forward and backward jump operators $\sigma, \rho: \mathbb{T} \rightarrow \mathbb{T}$ are defined as

$$\sigma(t) = \inf\{s \in \mathbb{T} : s > t\} \text{ and } \rho(t) = \sup\{s \in \mathbb{T} : s < t\},$$

respectively for $t \in \mathbb{T}$ such that $a < t < b, t < \sup\mathbb{T}, \inf\emptyset = \sup\mathbb{T}, \sup\emptyset = \inf\mathbb{T}$ where \emptyset is empty set; $a = \inf\mathbb{T}$ and $b = \sup\mathbb{T}$. Corresponding forward-step function μ is defined by

$$\mu: \mathbb{T}^{\kappa} \rightarrow [0, \infty), \mu(t) = \sigma(t) - t.$$

However, $t \in \mathbb{T}$ is left dense, left scattered, right dense, right scattered, isolated and dense iff $\rho(t) = t, \rho(t) < t, \sigma(t) = t, \sigma(t) > t, \rho(t) < t < \sigma(t)$ and $\rho(t) = t = \sigma(t)$, respectively. We also should remind delta differentiability region \mathbb{T}^{κ} along with \mathbb{T} to define delta derivative of any function. $\mathbb{T}^{\kappa} = \mathbb{T} - \{b\}$ if \mathbb{T} is bounded above and b is left-scattered; otherwise $\mathbb{T}^{\kappa} = \mathbb{T}$. $f: \mathbb{T} \rightarrow \mathbb{R}$ is right side continuous at $t \in \mathbb{T}$ if there is some $\delta > 0$ such that $|f(t) - f(s)| < \varepsilon$ for all $s \in [t, t + \delta)$ and $\varepsilon > 0$. $C_{rd}(\mathbb{T})$ indicates the set of all right continuous functions on \mathbb{T} . One can define $f^{\Delta}(t)$ to be the value for $t \in \mathbb{T}^{\kappa}$, if one exists, such that for all $\varepsilon > 0$, there is a neighborhood U of t such that for all $s \in U$

*Corresponding author. email address: emrah231983@firat.edu.tr
<http://dergipark.gov.tr/csj> ©2021 Faculty of Science, Sivas Cumhuriyet University

$$|[f^\sigma(t) - f(s)] - f^\Delta(t)[\sigma(t) - s]| < \varepsilon|\sigma(t) - s|.$$

Here, f is delta differentiable on \mathbb{T}^κ if $f^\Delta(t)$ exists for all $t \in \mathbb{T}^\kappa$. Let $f \in C_{rd}(\mathbb{T})$, then there exists a function F such that $F^\Delta(t) = f(t)$, and delta integral is constructed by $\int_a^b f(t)\Delta t = F(b) - F(a)$. Additionally, if $a \in \mathbb{T}$, $\sup\mathbb{T} = \infty$ and f is rd-continuous on $[0, \infty)$, improper integral is defined by

$$\int_a^\infty f(t)\Delta t = \lim_{b \rightarrow \infty} \int_a^b f(t)\Delta t,$$

when right side limit exists and finite [17, 18].

As far as we concerned, the application of Laplace transform to spectral theory on time scales has not been studied. In this study, the eigenfunction of a Sturm-Liouville problem will be constructed by using Laplace transform on time scale with a constant forward-step function.

When Sturm and Liouville investigated the heat conduction problem by the method of separating them into variables, the problem of searching for the solutions of ordinary differential equations containing eigenvalue parameters that meet some boundary

2. Preliminaries

Here, we remind some principle notions and theorems related to Laplace transform on \mathbb{T} .

Definition 1 [17]. $f: \mathbb{T} \rightarrow \mathbb{R}$ is a regulated function if its right-sided limits exist (finite) at all right-dense points in \mathbb{T} and its left-sided limits exist (finite) at all left-dense points in \mathbb{T} .

Definition 2 [17]. $p: \mathbb{T} \rightarrow \mathbb{R}$ is a regressive function if $1 + \mu(t)p(t) \neq 0$ holds for all $t \in \mathbb{T}^\kappa$. $\mathcal{R} = \mathcal{R}(\mathbb{T}) = \mathcal{R}(\mathbb{T}, \mathbb{R})$ indicates the set of all regressive and rd-continuous functions on \mathbb{T} . \mathcal{R} forms an Abelian group with the addition operation \oplus defined by $(p \oplus q)(t) = p(t) + q(t) + \mu(t)p(t)q(t)$ for all $t \in \mathbb{T}^\kappa$, $p, q \in \mathcal{R}$. In addition, the additive inverse of p for this group is denoted by

$$(\ominus p)(t) = -\frac{p(t)}{1 + \mu(t)p(t)},$$

for all $t \in \mathbb{T}^\kappa$, $p \in \mathcal{R}$.

Definition 3 [17]. Exponential function on \mathbb{T} is defined by

$$e_p(t, s) = \exp\left(\int_s^t \xi_{\mu(\tau)}(p(\tau)) \Delta\tau\right),$$

for $s, t \in \mathbb{T}$, $p \in \mathcal{R}$. Here, $\xi_{\mu(\tau)}(z)$ is cylinder transformation where $\xi_h(z) = \frac{1}{h} \text{Log}(1 + hz)$ where $h > 0$. If $h = 0$, $\xi_0(z) = z$ for all $z \in \mathbb{C}$. For details on exponential function, we refer to the books [17, 18].

Let us consider a 2-nd order linear dynamic homogeneous equation with constant coefficients on \mathbb{T}

$$y^{\Delta\Delta}(t) + \alpha y^{\Delta}(t) + \beta y(t) = 0,$$

where $\alpha, \beta \in \mathbb{R}$. From the last equation, the hyperbolic functions (when $\alpha = 0, \beta < 0$) and the trigonometric functions (when $\alpha = 0, \beta > 0$) are defined as follows:

conditions arose. This new equation is known as the Sturm-Liouville equation in literature. The problems in which this equation is handled with various boundary conditions have been studied by many mathematicians ([19-25]). The spectral properties of the Sturm-Liouville equation are given by Levitan et. al [26] from different angles for usual case.

Because of its importance, the main goal of this study is to solve below Sturm-Liouville problem on \mathbb{T} by using Laplace transform:

$$-y^{\Delta\Delta}(t) + cy^\sigma(t) = \lambda y^\sigma(t), t \in (0, \infty)_{\mathbb{T}}, \quad (1)$$

$$y(0, \lambda) = 0, y^\Delta(0, \lambda) = 1, \quad (2)$$

where $\mu(t) \equiv h \geq 0$, $c \in \mathbb{R}$, λ is a spectral parameter. Here, $y: \mathbb{T} \rightarrow \mathbb{C}$ is the solution (eigenfunction) of (1)-(2) where y is second-order delta differentiable on $(0, \infty)_{\mathbb{T}}$.

Our study will be organized as follows: In section 2, we recall some fundamental notions and theorems related to Laplace transform on \mathbb{T} . We construct a Sturm-Liouville problem on \mathbb{T} to solve it by using Laplace transform in section 3. Proof of the main theorem was made in three cases.

Definition 4 [17]. Let $p \in C_{rd}$. If $-\mu p^2 \in \mathcal{R}$, the hyperbolic functions \cosh_p and \sinh_p are defined by

$$\cosh_p = \frac{e_p + e_{-p}}{2} \text{ and } \sinh_p = \frac{e_p - e_{-p}}{2}.$$

If $\mu p^2 \in \mathcal{R}$, the trigonometric functions \cos_p and \sin_p are defined by

$$\cos_p = \frac{e_{ip} + e_{-ip}}{2} \text{ and } \sin_p = \frac{e_{ip} - e_{-ip}}{2i}.$$

For a constant $\alpha \in \mathbb{R}$, the functions $e_\alpha(t, 0)$, $\sin_\alpha(t, 0)$ and $\sinh_\alpha(t, 0)$ have the below forms for common time scales $\mathbb{T} = \mathbb{R}$, $\mathbb{T} = \mathbb{Z}$ and $\mathbb{T} = h\mathbb{Z}$, ($h > 0$), respectively.

Table 1. Representations of $e_\alpha(t, 0)$, $\sin_\alpha(t, 0)$ and $\sinh_\alpha(t, 0)$ on $\mathbb{T} = \mathbb{R}$, $\mathbb{T} = \mathbb{Z}$ and $\mathbb{T} = h\mathbb{Z}$

\mathbb{T}	$e_\alpha(t, 0)$	$\sin_\alpha(t, 0)$	$\sinh_\alpha(t, 0)$
\mathbb{R}	$e^{\alpha t}$	$\sin(\alpha t)$	$\sinh(\alpha t)$
\mathbb{Z}	$(1 + \alpha)^t$	$\frac{(1 + i\alpha)^t - (1 - i\alpha)^t}{2i}$	$\frac{(1 + \alpha)^t - (1 - \alpha)^t}{2}$
$h\mathbb{Z}$	$(1 + \alpha h)^{\frac{t}{h}}$	$\frac{(1 + i\alpha h)^{\frac{t}{h}} - (1 - i\alpha h)^{\frac{t}{h}}}{2i}$	$\frac{(1 + \alpha h)^{\frac{t}{h}} - (1 - \alpha h)^{\frac{t}{h}}}{2}$

Definition 5 [17]. Suppose that $y: \mathbb{T}_0 \rightarrow \mathbb{R}$ regulated. Then, Laplace transform of y is defined by

$$L\{y\}(z) = \int_0^\infty y(t)e_{\ominus z}^\sigma(t, 0) \Delta t,$$

for $z \in D\{y\}$, where \mathbb{T}_0 is a time scale, $0 \in \mathbb{T}_0$ and $\sup \mathbb{T}_0 = \infty$; $D\{y\}$ consists of all complex numbers $z \in \mathcal{R}$ when the improper integral exists.

It was easily seen from the Definition 5 that L is linear as follows:

Theorem 6 [17]. Let x and y be regulated on \mathbb{T}_0 and α, β be constants. Then,

$$L\{\alpha x + \beta y\}(z) = \alpha L\{x\}(z) + \beta L\{y\}(z),$$

for $z \in D\{x\} \cap D\{y\}$.

Theorem 7 [3]. If $y: \mathbb{T}_0 \rightarrow \mathbb{C}$ is a function whose first order delta derivative is regulated, then

$$L\{y^\Delta\}(z) = zL\{y\}(z) - y(0), \tag{3}$$

for all regressive $z \in \mathbb{C}$ when $\lim_{t \rightarrow \infty} \{y(t)e_{\ominus z}(t, 0)\} = 0$.

One of the consequences of this theorem is as follows:

Corollary 8 [3]. If $y: \mathbb{T}_0 \rightarrow \mathbb{C}$ is a function where $y^{\Delta\Delta}$ is regulated, then

$$L\{y^{\Delta\Delta}\}(z) = z^2L\{y\}(z) - zy(0) - y^\Delta(0), \tag{4}$$

for all regressive $z \in \mathbb{C}$ when $\lim_{t \rightarrow \infty} \{y(t)e_{\ominus z}(t, 0)\} = \lim_{t \rightarrow \infty} \{y^\Delta(t)e_{\ominus z}(t, 0)\} = 0$.

Lemma 9 [17]. If \mathbb{T}_0 has constant forward-step function $\mu(t) \equiv h \geq 0$, then

$$L\{y^\sigma\}(z) = (1 + hz)L\{y\}(z) - hy(0). \tag{5}$$

Proof. Considering $y^\sigma(t) = y(t) + hy^\Delta(t)$ (see [17, Theorem 1.16]), we get

$$L\{y^\sigma\}(z) = \int_0^\infty y^\sigma(t)e_{\ominus z}^\sigma(t, 0) \Delta t = \int_0^\infty y(t)e_{\ominus z}^\sigma(t, 0) \Delta t + h \int_0^\infty y^4(t)e_{\ominus z}^\sigma(t, 0) \Delta t$$

$$= L\{y\}(z) + hL\{y^4\}(z)$$

If the formula (3) is taken into consideration in the last equation, the proof is completed.

Theorem 10 [9]. Suppose that \mathbb{T} has constant forward-step function and $y \in C_{rd}([s, \infty)_{\mathbb{T}}, \mathbb{C})$ is a function of exponential order η . Then,

$$L\{y\}(z \ominus w; s) = L\{ye_w^\sigma(\cdot, s)\}(z; s)$$

for all $z \in \mathbb{C}_h(\eta \oplus |w|)$, where $w \in \mathbb{R}([s, \infty)_{\mathbb{T}}, \mathbb{C})$. This theorem is called "First Translation Theorem" in literature.

The following table gives Laplace transforms of some basic functions for usage in Section 3.

Table 2. Laplace transforms of Some Common Functions on \mathbb{T}

$y(t)$	1	t	$e_\alpha(t, 0)$		$\sin_\alpha(t, 0)$	$\sinh_\alpha(t, 0)$	$e_\alpha(t, 0)\sin_{\frac{\beta}{1+\mu\alpha}}(t, 0)$	$e_\alpha(t, 0)\sinh_{\frac{\beta}{1+\mu\alpha}}(t, 0)$
$L\{y\}(z)$	$\frac{1}{z}$	$\frac{1}{z^2}$	$\frac{1}{z - \alpha}$		$\frac{\alpha}{z^2 + \alpha^2}$	$\frac{\alpha}{z^2 - \alpha^2}$	$\frac{\beta}{(z - \alpha)^2 + \beta^2}$	$\frac{\beta}{(z - \alpha)^2 - \beta^2}$

First, we solve Sturm-Liouville problem for classical situation $\mathbb{T} = \mathbb{R}$ by Laplace transform.

Theorem 11. The eigenfunction of the problem

$$-y''(t) + cy(t) = \lambda y(t), t \in (0, \infty)_{\mathbb{R}}, \tag{6}$$

$$y(0, \lambda) = 0, y'(0, \lambda) = 1, \tag{7}$$

has following form

$$y(t) = \begin{cases} \frac{1}{\sqrt{\lambda-c}} \sin(\sqrt{\lambda-ct}), & \text{if } c < \lambda \\ t, & \text{if } c = \lambda. \\ \frac{1}{\sqrt{c-\lambda}} \sinh(\sqrt{c-\lambda}t), & \text{if } c > \lambda \end{cases} \tag{8}$$

Proof. Let us reorganize the equation (6) as

$$y''(t) + (\lambda - c)y(t) = 0, \tag{9}$$

The "usual" Laplace transform is known as

$$L\{y\}(z) = \int_0^\infty y(t)e^{-zt} dt,$$

whenever the right side integral is convergent. It can be easily shown that,

$$L\{y'\}(z) = zL\{y\}(z) - y(0),$$

holds by integration by parts formula. Moreover,

$$L\{y''\}(z) = z^2L\{y\}(z) - zy(0) - y'(0),$$

is one consequence of the last formula.

Let y be the solution of (6)-(7). Then, applying Laplace transform to both sides of (9) yields

$$(z^2 + \lambda - c)L\{y\}(z) - zy(0) - y'(0) = 0.$$

Considering the initial conditions (7) on the last equation, we get

$$L\{y\}(z) = \frac{1}{z^2 + \lambda - c}. \tag{10}$$

After applying the "usual" inverse Laplace transform on the last equality, considering the known table of the "usual" Laplace transform, the solution (8) is obtained.

3. Main Results

Here, we obtain eigenfunction expansion of a Sturm-Liouville problem on \mathbb{T} by using Laplace transform for different cases.

Theorem 12. The eigenfunction of the problem (1)-(2) has the below forms:

i. If $h \geq 0$ and $c - \lambda = 0$, then

$$y(t) = t.$$

ii. If $h = 0$, then

$$y(t) = \frac{1}{\sqrt{c - \lambda}} \sinh_{\sqrt{c - \lambda}}(t, 0),$$

and

$$y(t) = \frac{1}{\sqrt{\lambda - c}} \sin_{\sqrt{\lambda - c}}(t, 0),$$

for $c - \lambda > 0, c - \lambda < 0$, respectively.

iii. If $h > 0$, then

$$y(t) = e^{\frac{\sigma}{2}}(t, 0)t,$$

$$y(t) = \frac{1}{\sqrt{\frac{(c-\lambda)^2 h^2}{4} + (c-\lambda)}} e^{\frac{(c-\lambda)h}{2}}(t, 0) \sinh_{\frac{\sqrt{\frac{(c-\lambda)^2 h^2}{4} + (c-\lambda)}}{1 + \frac{(c-\lambda)h^2}{2}}}(t, 0),$$

and

$$y(t) = \frac{1}{\sqrt{-\frac{(c-\lambda)^2 h^2}{4} - (c-\lambda)}} e^{\frac{(c-\lambda)h}{2}}(t, 0) \sin_{\frac{\sqrt{-\frac{(c-\lambda)^2 h^2}{4} - (c-\lambda)}}{1 + \frac{(c-\lambda)h^2}{2}}}(t, 0),$$

for $c - \lambda = -\frac{4}{h^2}, c - \lambda \in \mathbb{R} \setminus \left(-\frac{4}{h^2}, 0\right), c - \lambda \in \left(-\frac{4}{h^2}, 0\right)$, respectively.

Proof. Let us again reorganize the equation (1) as

$$y^{4\Delta}(t) + (\lambda - c)y^\sigma(t) = 0. \tag{11}$$

Then, applying the Laplace transform to both sides of (11) gives

$$L\{y^{4\Delta}\}(z) + (\lambda - c)L\{y^\sigma\}(z) = 0.$$

By the formulas (4) and (5) into account on the last equality, we have

$$z^2 L\{y\}(z) - zy(0) - y^A(0) + (\lambda - c)((1 + hz)L\{y\}(z) - hy(0)) = 0.$$

Using the initial conditions (2) yields

$$L\{y\}(z) = \frac{1}{z^2 + (\lambda - c)hz + (\lambda - c)}. \tag{12}$$

i. If $h \geq 0$ and $c - \lambda = 0$, then the formula (12) turns into the form

$$L\{y\}(z) = \frac{1}{z^2}.$$

By the formula given in Table 2, it yields that $y(t) = t$.

Now, we can rewrite the formula (12) as follows:

$$L\{y\}(z) = \frac{1}{z^2 - (c-\lambda)hz - (c-\lambda)} = \frac{1}{\left(z - \frac{(c-\lambda)h}{2}\right)^2 - \left(\frac{(c-\lambda)^2 h^2}{4} + (c-\lambda)\right)}. \tag{13}$$

After that, we will examine the solution of the problem (1)-(2) separately for $h = 0$ and $h > 0$.

ii. If $h = 0$, then the formula (12) is written in the form (10). If this form is rearranged to

$$L\{y\}(z) = \frac{1}{\sqrt{c-\lambda}} \frac{\sqrt{c-\lambda}}{z^2 - (\sqrt{c-\lambda})^2},$$

for $c - \lambda > 0$ and

$$L\{y\}(z) = \frac{1}{\sqrt{\lambda-c}} \frac{\sqrt{\lambda-c}}{z^2 + (\sqrt{\lambda-c})^2},$$

for $c - \lambda < 0$, Theorem 12 is proved using Table 2. Note that, the solution of the problem (1)-(2) coincides with the solution (8) in this case.

iii. If $h > 0$, then there are three cases relative to each other of λ and c .

Case 1: $c - \lambda = -\frac{4}{h^2}$. In this case, the formula (13) can be rewritten as:

$$L\{y\}(z) = \frac{1}{\left(z + \frac{2}{h}\right)^2}.$$

By Theorem 10 and the appropriate formula given in Table 2, we obtain

$$y(t) = e^{\frac{\sigma}{h} t}(t, 0)t,$$

as the solution of the problem (1)-(2) for Case 1.

Case 2: $c - \lambda \in \mathbb{R} \setminus \left(-\frac{4}{h^2}, 0\right)$. In this case, since $\frac{(c-\lambda)^2 h^2}{4} + (c-\lambda) > 0$, the formula (13) can be rewritten as:

$$L\{y\}(z) = \frac{1}{\sqrt{\frac{(c-\lambda)^2 h^2}{4} + (c-\lambda)}} \frac{\sqrt{\frac{(c-\lambda)^2 h^2}{4} + (c-\lambda)}}{\left(z - \frac{(c-\lambda)h}{2}\right)^2 - \left(\sqrt{\frac{(c-\lambda)^2 h^2}{4} + (c-\lambda)}\right)^2}.$$

By the appropriate formula given in Table 2, we obtain

$$y(t) = \frac{1}{\sqrt{\frac{(c-\lambda)^2 h^2}{4} + (c-\lambda)}} e^{\frac{(c-\lambda)h}{2} t} \sinh \frac{\sqrt{\frac{(c-\lambda)^2 h^2}{4} + (c-\lambda)}}{1 + \frac{(c-\lambda)h^2}{2}}(t, 0),$$

as the solution of the problem (1)-(2) for Case 2.

Case 3: $c - \lambda \in \left(-\frac{4}{h^2}, 0\right)$. In this case, since $\frac{(c-\lambda)^2 h^2}{4} + (c-\lambda) < 0$, the formula (13) can be rewritten as:

$$L\{y\}(z) = \frac{1}{\sqrt{-\frac{(c-\lambda)^2 h^2}{4} - (c-\lambda)} \left(z - \frac{(c-\lambda)h}{2} \right)^2 + \left(\sqrt{-\frac{(c-\lambda)^2 h^2}{4} - (c-\lambda)} \right)^2}$$

By the appropriate formula given in Table 2, we obtain

$$y(t) = \frac{1}{\sqrt{-\frac{(c-\lambda)^2 h^2}{4} - (c-\lambda)}} \frac{e^{\frac{(c-\lambda)h}{2}t} \sin \frac{\sqrt{-\frac{(c-\lambda)^2 h^2}{4} - (c-\lambda)}}{1 + \frac{(c-\lambda)h^2}{2}}(t, 0)}{2}$$

as the solution of the problem (1)-(2) for Case 3. It completes the proof.

Corollary 13. If $\mathbb{T} = \mathbb{R}$, then $\mu(t) = 0$ for all $t \in \mathbb{T}$. Therefore, the eigenfunctions of the problem (1) -(2) are the same as in the case (ii) of Theorem 12.

Indeed, the problem (1)-(2) is written in form of the problem (6)-(7) on $\mathbb{T} = \mathbb{R}$. It can be easily seen from Table 1 that this corollary is correct.

Corollary 14. If $\mathbb{T} = h\mathbb{Z} = \{hk : k \in \mathbb{Z}\}$, then $\mu(t) = h, h > 0$ for all $t \in \mathbb{T}$. Therefore, the eigenfunctions of the problem (1)-(2) are as in the cases (i) and (iii) of Theorem 12.

On $\mathbb{T} = h\mathbb{Z}$, it can be easily seen from Table 1 and Theorem 10 that the eigenfunctions of the problem (1)-(2) is in the following forms

If $c - \lambda = 0$,

$$y(t) = t,$$

If $c - \lambda = -\frac{4}{h^2}$,

$$y(t) = (-1)^{\frac{t+h}{h}} t,$$

If $c - \lambda \in \mathbb{R} \setminus \left(-\frac{4}{h^2}, 0\right)$,

$$y(t) = \frac{1}{2\sqrt{\frac{(c-\lambda)^2 h^2}{4} + (c-\lambda)}} \left\{ \left(1 + \frac{(c-\lambda)h^2}{2} + h\sqrt{\frac{(c-\lambda)^2 h^2}{4} + (c-\lambda)} \right)^{\frac{t}{h}} - \left(1 + \frac{(c-\lambda)h^2}{2} - h\sqrt{\frac{(c-\lambda)^2 h^2}{4} + (c-\lambda)} \right)^{\frac{t}{h}} \right\},$$

If $c - \lambda \in \left(-\frac{4}{h^2}, 0\right)$,

$$y(t) = \frac{1}{2i\sqrt{-\frac{(c-\lambda)^2 h^2}{4} - (c-\lambda)}} \left\{ \left(1 + \frac{(c-\lambda)h^2}{2} + ih\sqrt{-\frac{(c-\lambda)^2 h^2}{4} - (c-\lambda)} \right)^{\frac{t}{h}} - \left(1 + \frac{(c-\lambda)h^2}{2} - ih\sqrt{-\frac{(c-\lambda)^2 h^2}{4} - (c-\lambda)} \right)^{\frac{t}{h}} \right\}.$$

4. Conclusion

Models obtained by applying the laws of physics (Newton's law or Kirchoff's law) to systems are in the form of differential equations. However, by applying Laplace transformation to linear ordinary differential equations, the transfer function model of the system (frequency domain) can be obtained. With the transfer function representation, dynamic analysis of the system can be performed without

the need of solving differential equations. Because of this importance of Laplace transform, the Sturm Liouville equation is solved with the help of Laplace transform on time scale when the potential function is constant. Although it is possible to find Laplace transformation of the basic functions in many tables in the classical case, it is more difficult to prepare this table on time scale. The results obtained in this study are

therefore very valuable and will bring a different perspective to spectral theory.

Acknowledgment

We would like to thank the referees and editors who contributed to our article.

Conflicts of interest

The authors state that there is no conflict of interests.

References

- [1] Schiff J. L., The Laplace transform: theory and applications (Undergraduate Texts in Mathematics Springer: New York: Springer, (1999).
- [2] Hilger S., Special functions, Laplace and Fourier transform on measure chains, *Dynamic Systems and Applications*, 8 (3-4) (1999) 471-488.
- [3] Bohner M., Peterson A., Laplace transform and Z-transform: Unification and Extension, *Methods and Applications of Analysis*, 9 (1) (2002) 151-158.
- [4] Ameen R., Kose H., Jarad F., On the discrete Laplace transform, *Results in Nonlinear Analysis*, 2 (2) (2019) 61-70.
- [5] Bohner M., Guseinov G. Sh., The convolution on time scales, *Abstract and Applied Analysis*, (2007) 1-24.
- [6] Bohner M., Guseinov G. Sh., The Laplace transform on isolated time scales, *Computers and Mathematics with Applications*, 60(6) (2010) 1536-1547.
- [7] Bohner M. Guseinov G. Sh., The h -Laplace and q -Laplace transforms, *Journal of Mathematical Analysis and Applications*, 365 (1) (2010) 75-92.
- [8] Bohner M., Guseinov G. Sh., Karpuz B., Properties of the Laplace transform on time scales with arbitrary graininess, *Integral Transforms and Special Functions*, 22 (11) (2011) 785-800.
- [9] Bohner M., Guseinov G. Sh., Peterson A., Further properties of the Laplace transform on time scales with arbitrary graininess, *Integral Transforms and Special Functions*, 24 (4) (2013) 289-301.
- [10] Davis J. M., Gravagne I. A., Jackson B. J. , Marks II, R. J. and Ramos A. A., The Laplace transform on time scales revisited, *Journal of Mathematical Analysis and Applications*, 332 (2) (2007) 1291-1307.
- [11] Davis J. M., Gravagne I. A., Marks II, R. J., Convergence of unilateral Laplace transforms on time scales, *Circuits, Systems and Signal Processing*, 29 (5) (2010) 971-997.
- [12] Davis J. M., Gravagne I. A., Marks II, R. J., Bilateral Laplace Transforms on Time Scales: Convergence, Convolution, and the Characterization of Stationary Stochastic Time Series, *Circuits, Systems and Signal Processing*, 29 (1) (2010) 1141-1165.
- [13] Ortigueira M. D., Torres D. F., Trujillo J. J., Exponentials and Laplace transforms on nonuniform time scales, *Communications in Nonlinear Science and Numerical Simulation*, 39 (2016) 252-270.
- [14] Rahmat M. R. S., The $(q; h)$ -Laplace transform on discrete time scales, *Computers & Mathematics with Applications*, 62 (2011) 272-281.
- [15] Hilger S., Ein Masskettenkalkül mit Anwendung auf Zentrumsmannigfaltigkeiten. Ph. D. thesis Universität Würzburg, (1988).
- [16] Hilger S., Analysis on measure chains-a unified approach to continuous and discrete Calculus, *Results in Mathematics*, 18 (1-2) (1990) 18-56.
- [17] Bohner M., Peterson A., Dynamic equations on time scales, an introduction with applications, Boston (MA):Birkauer, Boston, (2001).
- [18] Bohner M., Peterson A., Advances in dynamic equations on time scales, Boston (MA): Birkauer, Boston, (2003).
- [19] Bairamov E., Aygar Y., Karshioğlu D., Scattering analysis and spectrum of discrete Schrödinger equations with transmission conditions, *Filomat*, 31 (17) (2017) 5391-5399.
- [20] Chatzarakis G. E., Jadlovská I., Difference equations with several non-monotone deviating arguments: Iterative oscillation tests, *Dynamic Systems and Applications*, 27 (2) (2018) 271-298.

- [21] Huseynov A., Bairamov, E., On expansions in eigenfunctions for second order dynamic equations on time scales, *Nonlinear Dynamics and Systems Theory*, 9 (1) (2009) 77-88.
- [22] Keskin B., Ozkan A.S., Inverse Nodal Problems for Impulsive Sturm-Liouville Equation with Boundary Conditions Depending on the Parameter, *Advances in Analysis*, 2 (2017).
- [23] Ozkan A. S., Adalar I., Half-inverse Sturm-Liouville problem on a time scale, *Inverse Problems*, 36 (2020) 1-8.
- [24] Ozkan A. S., Keskin B., Inverse nodal problems for Sturm-Liouville equation with eigenparameter-dependent boundary and jump conditions, *Inverse Problem in Science and Engineering*, 23 (2015) 1306-1312.
- [25] Zettl, A., Sturm-Liouville Theory, American Mathematical Society, (2005).
- [26] Levitan B. M., Sargsyan I. S., Introduction to Spectral Theory, *American Mathematical Society*, Rhode Island, (1975).

On the Euler method of summability and concerning Tauberian theorems

Sefa Anıl SEZER^{1,*} , İbrahim ÇANAK² 

¹Istanbul Medeniyet University, Department of Mathematics, İstanbul/ TURKEY

²Ege University, Department of Mathematics, İzmir/ TURKEY

Abstract

For any two regular summability methods (U) and (V), the condition under which $V - \lim x_n = \lambda$ implies $U - \lim x_n = \lambda$ is called a Tauberian condition and the corresponding theorem is called a Tauberian theorem. Usually in the theory of summability, the case in which the method U is equivalent to the ordinary convergence is taken into consideration. In this paper, we give new Tauberian conditions under which ordinary convergence or Cesàro summability of a sequence follows from its Euler summability by means of the product theorem of Knopp for the Euler and Cesàro summability methods.

Article info

History:

Received:01.12.2020

Accepted:17.03.2021

Keywords:

Euler summability, Cesàro summability, Tauberian theorem, order condition

1. Introduction

We consider throughout complex sequences $x = \{x_n\}$ and discuss the relations of Euler and Cesàro summability methods. We say that a sequence $\{x_n\}$ is summable to λ by the

1. Cesàro method C_1 , briefly $C_1 - \lim x_n = \lambda$, if

$$x_n^{(1)} := \frac{1}{n+1} \sum_{k=0}^n x_k \rightarrow \lambda \quad \text{as } n \rightarrow \infty;$$

2. Euler method E_p of order p , briefly $E_p - \lim x_n = \lambda$, if

$$\sum_{k=0}^n \binom{n}{k} p^k (1-p)^{n-k} x_k \rightarrow \lambda \quad \text{as } n \rightarrow \infty.$$

Cesàro method and Euler method of order $p \in (0,1)$ are regular (see [1]). In other words, they sum a convergent sequence to its limit.

For any sequence $\{u_n\}$, the symbols $u_n = O(n^\alpha)$ and $u_n = o(n^\alpha)$ denote, as usual, that $\limsup |n^{-\alpha} u_n| < \infty$ and $\lim n^{-\alpha} u_n = 0$, respectively. The backward difference of $\{u_n\}$ is defined for all $n \geq 0$ by $\Delta u_0 = u_0$ and $\Delta u_n = u_n - u_{n-1}$.

The difference of a sequence and its arithmetic mean is given with the Kronecker identity (see [2])

$$x_n - x_n^{(1)} = \delta_n \tag{1}$$

where

$$\delta_n := \frac{1}{n+1} \sum_{k=0}^n k \Delta x_k = n \Delta x_n^{(1)}.$$

The r -times iterated arithmetic mean of sequences $\{x_n\}$ and $\{\delta_n\}$ are defined respectively as

$$x_n^{(r)} := \frac{1}{n+1} \sum_{k=0}^n x_k^{(r-1)}$$

and

$$\delta_n^{(r)} := \frac{1}{n+1} \sum_{k=0}^n \delta_k^{(r-1)}$$

where $x_n^{(0)} = x_n$ and $\delta_n^{(0)} = \delta_n$.

A sequence $\{x_n\}$ is called slowly oscillating, if

$$x_m - x_n = o(1)$$

as $n \rightarrow \infty, m > n$ and $m/n \rightarrow 1$.

*Corresponding author. email address: sefaanil.sezer@medeniyet.edu.tr
<http://dergipark.gov.tr/csj> ©2021 Faculty of Science, Sivas Cumhuriyet University

Historically, the concept ‘slow oscillation’ goes back to Schmidt [3].

For any two regular summability methods (U) and (V), the condition under which $V - \lim x_n = \lambda$ implies $U - \lim x_n = \lambda$ is called a Tauberian condition and the corresponding theorem is called a Tauberian theorem. Usually in the theory of summability, the case in which the method U is equivalent to the ordinary convergence is taken into consideration.

Tauberian theorems for various methods of summation have a long history; see the classical books [4,5] and they found new attention recently in (see e.g., [6-8]).

In the present paper, we consider Tauberian conditions on $\{x_n\}$ under which $E_p - \lim x_n = \lambda$ implies $C_1 - \lim x_n = \lambda$ or $\lim x_n = \lambda$.

The major Tauberian results for Euler method of summation were proved by Knopp [9]. We use these theorems as a stepping stone to obtain stronger results.

Theorem 1.1 *If $E_p - \lim x_n = \lambda$ for some $0 < p < 1$ and $\Delta x_n = O(n^{-1/2})$, then $\lim x_n = \lambda$.*

Theorem 1.2 *If $E_p - \lim x_n = \lambda$ for some $0 < p < 1$ and $\Delta x_n = o(n^{-1/2})$, then $\lim x_n = \lambda$.*

2. Auxiliary Results

We shall make use of the following four lemmas.

Lemma 2.1 ([10]) *If $\{x_n\}$ is slowly oscillating, then $\delta_n = O(1)$ and $\{\delta_n\}$ is slowly oscillating.*

Lemma 2.2 ([3]) *If $C_1 - \lim x_n = \lambda$ and $\{x_n\}$ is slowly oscillating, then $\lim x_n = \lambda$.*

Lemma 2.3 ([9]) *Let $0 < p < 1$. Then $E_p \subset E_p C_1$; that is, if $\{x_n\}$ is Euler summable to λ , then so is $\{x_n^{(1)}\}$.*

The next lemma proposes a relation between Euler and Cesàro methods.

Lemma 2.4 ([9]) *If $E_p - \lim x_n = \lambda$ for some $0 < p < 1$ and $\Delta x_n = o(1)$, then $C_1 - \lim x_n = \lambda$.*

3. Main Results

In this section, we establish Tauberian conditions for an Euler summable sequence to be Cesàro summable or convergent.

Our first result is a $E_p \rightarrow C_1$ type theorem.

Theorem 3.1 *Let $0 < p < 1$. Then $E_p - \lim x_n = \lambda$ and*

$$\delta_n = O(n^{1/2}) \tag{2}$$

imply $C_1 - \lim x_n = \lambda$.

Proof. By the assumption and Lemma 2.3, we have

$$E_p - \lim x_n^{(1)} = \lambda. \tag{3}$$

Besides, since

$$\delta_n = n\Delta x_n^{(1)} = O(n^{1/2})$$

by (2), we obtain

$$\Delta x_n^{(1)} = O(n^{-1/2}). \tag{4}$$

Therefore, combining (3) and (4) together with Theorem 1.1 imply our result.

Remark 3.1 Note that condition (2) may be replaced with the weaker condition $\delta_n = O(1)$.

Corollary 3.1 ([9]) *Let $0 < p < 1$. Then $E_p - \lim x_n = \lambda$ and*

$$x_n = O(n^{1/2}) \tag{5}$$

imply $C_1 - \lim x_n = \lambda$.

Proof. It is enough to prove $\delta_n = n\Delta x_n^{(1)} = O(n^{1/2})$ or equivalently

$$\psi_n := n^{1/2}\Delta x_n^{(1)} = O(1).$$

In view of (5), we observe

$$\begin{aligned} \psi_n &= n^{1/2} \left[\frac{1}{n+1} \sum_{k=0}^n x_k - \frac{1}{n} \sum_{k=0}^{n-1} x_k \right] \\ &= n^{1/2} \left[\frac{1}{n+1} x_n - \frac{1}{n+1} \frac{1}{n} \sum_{k=0}^{n-1} x_k \right] \\ &= n^{1/2} \left[\frac{1}{n+1} O(n^{1/2}) - \frac{1}{n+1} O(n^{1/2}) \right] \\ &= O(1), \end{aligned}$$

which completes the proof.

Now, we prove some $E_p \rightarrow c$ type theorems.

Theorem 3.2 *Let $0 < p < 1$. Then $E_p - \lim x_n = \lambda$ and*

$$\Delta \delta_n = O(n^{-1/2}) \tag{6}$$

imply $\lim x_n = \lambda$.

Proof. Plainly, we have $E_p - \lim x_n^{(1)} = \lambda$ from Lemma 2.3. We observe using (1) that

$$E_p - \lim \delta_n = 0. \tag{7}$$

Combining (6) and (7) with Theorem 1.1, we get

$$\delta_n = n\Delta x_n^{(1)} = o(1),$$

that necessitates

$$\Delta x_n^{(1)} = o(n^{-1/2}).$$

Further, applying Theorem 1.2 to $\{x_n^{(1)}\}$, we conclude $\lim x_n^{(1)} = \lambda$.

Therefore, the proof follows from (1).

Theorem 3.3 *Let $0 < p < 1$. Then $E_p - \lim x_n = \lambda$ and*

$$\Delta \delta_n^{(1)} = o(n^{-1}) \tag{8}$$

imply $\lim x_n = \lambda$.

Proof. From the hypothesis, it is clear that $E_p - \lim x_n^{(1)} = \lambda$ and $E_p - \lim x_n^{(2)} = \lambda$. We may write the identity

$$x_n^{(1)} - x_n^{(2)} = \delta_n^{(1)} \tag{9}$$

by taking Cesàro mean of both sides of the Kronecker identity (1). Then, it follows from (9) that

$$E_p - \lim \delta_n^{(1)} = 0. \tag{10}$$

Taking (8) and (10) into account together with Theorem 1.2, we observe

$$\delta_n^{(1)} = n\Delta x_n^{(2)} = o(1), \tag{11}$$

which also implies

$$\Delta x_n^{(2)} = o(n^{-1/2}).$$

Now, applying Theorem 1.2 to $\{x_n^{(2)}\}$, we conclude

$$\lim x_n^{(2)} = \lambda. \tag{12}$$

Using (11) and (12), we get via the identity (9) that

$$\lim x_n^{(1)} = \lambda.$$

Since

$$\delta_n - \delta_n^{(1)} = n\Delta \delta_n^{(1)},$$

we find $\delta_n = o(1)$ from (8) and (11). Consequently, it is easy to obtain $\lim x_n = \lambda$ by using (1).

Corollary 3.2 *Let $0 < p < 1$. Then $E_p - \lim x_n = \lambda$ and*

$$\delta_n = o(1) \tag{13}$$

imply $\lim x_n = \lambda$.

Proof. Assuming (13), we have $\delta_n^{(1)} = o(1)$. Hence, by the identity $\delta_n - \delta_n^{(1)} = n\Delta \delta_n^{(1)}$, it follows $\Delta \delta_n^{(1)} = o(n^{-1})$. Thus, the proof follows from Theorem 3.3.

Remark 3.2 In (8) and (13) o -type condition can not be replaced with O -type condition.

The following theorem is first proved by Tam [11]. Here, we give an alternative proof.

Theorem 3.4 *Let $0 < p < 1$. If $E_p - \lim x_n = \lambda$ and $\{x_n\}$ is slowly oscillating, then $\lim x_n = \lambda$.*

Proof. Taking Lemma 2.1 and the slow oscillation of $\{x_n\}$ into account, we clearly have $\delta_n = O(n^{1/2})$ and the slow oscillation of $\{x_n^{(1)}\}$. Hence, we obtain

$$C_1 - \lim x_n = \lambda$$

from Theorem 3.1. Thus, the proof is completed via Lemma 2.2.

Corollary 3.3 *Let $0 < p < 1$. Then $E_p - \lim x_n = \lambda$ and*

$$\Delta x_n = O(n^{-1}) \tag{14}$$

imply $\lim x_n = \lambda$.

Proof. The proof is completed from the fact that (14) implies the slow oscillation of $\{x_n\}$.

Theorem 3.5 *Let $0 < p < 1$. If $E_p - \lim x_n = \lambda$ and $\{\delta_n\}$ is slowly oscillating, then $\lim x_n = \lambda$.*

Proof. By the definition of slow oscillation, obviously $\Delta \delta_n = o(1)$. Further, since $E_p - \lim x_n = \lambda$ we have $E_p - \lim \delta_n = 0$. Then, from Lemma 2.4, we find $C_1 - \lim \delta_n = 0$. Now, by Lemma 2.2, we obtain $\lim \delta_n = 0$ which leads us to

$$\Delta x_n^{(1)} = o(n^{-1/2}).$$

By applying Theorem 1.2 to $\{x_n^{(1)}\}$, we have $C_1 - \lim x_n = \lambda$. Therefore, using (1) we conclude $\lim x_n = \lambda$.

Acknowledgment

The authors would like to thank the anonymous referees for their careful reading of our manuscript and their constructive comments.

Conflicts of interest

The authors declare that there is no conflict of interest.

References

- [1] Hardy G.H., Divergent series. 1st ed. Oxford: Clarendon Press, (1949).
- [2] Meyer-König W., Zeller K., Kronecker-Ausdruck und Kreisverfahren der Limitierungstheorie, *Math. Z.*, 114 (1970), 300-302.
- [3] Schmidt R., Über Divergente Folgen und Lineare Mittelbildungen, *Math. Z.*, 22 (1925), 89-152.

- [4] Korevaar J., Tauberian theory: A century of developments. 1st ed. Berlin: Springer-Verlag, (2004).
- [5] Peyerimhoff A., Lectures on summability, Lecture notes in mathematics. vol. 107 Berlin: Springer-Verlag, (1969).
- [6] Çanak İ., Braha N.L., Totur Ü., A Tauberian Theorem for the Generalized Nörlund Summability Method, *Georgian Math. J.*, 27 (2020), 31-36.
- [7] Sezer S.A., Çanak İ., Tauberian Conditions of Slowly Decreasing Type for the Logarithmic Power Series Method, *Proc. Natl. Acad. Sci., India, Sect. A Phys. Sci.*, 90 (2020), 135-139.
- [8] Sezer S.A., Çanak İ., Tauberian Conditions under which Convergence follows from Summability by the Discrete Power Series Method, *Turk. J. Math.*, 43 (2019), 2898-2907.
- [9] Knopp K., Über das Eulersche Summierungsverfahren II., *Math. Z.*, 18 (1923), 125-156.
- [10] Dik M., Tauberian Theorems for Sequences with Moderately Oscillatory Control Modulo, *Math. Morav.*, 5 (2001), 57-94.
- [11] Tam L., A Tauberian Theorem for the General Euler-Borel Summability Method, *Can. J. Math.*, 44 (1992) 1100–1120.



Geant4 investigation of the alpha-beta-gamma detector system used in medical imaging, environmental and nuclear site monitoring

Nuray YAVUZKANAT ^{1,*} , David JENKINS ² 

¹Bitlis Eren University, Physics Department, Bitlis/ Turkey

²The University of York, Physics Department, York/ UK

Abstract

No commercially available detector system can measure alpha, beta and gamma-rays at the same time and separately with good efficiency, while being cost-effective, portable and offering real-time monitoring. The main purpose of an alpha-beta-gamma detector would be for safety management and nuclear decommissioning in the nuclear industry. This idea for a detector system became more valuable, after Fukushima in Japan, because nuclear waste can contain fission products and transactinide materials which not only emit gamma-rays but also emit alpha and beta particles and in some cases, neutrons. In this research, we investigated the best available alpha-beta-gamma radiation detector materials and their optimum thickness by using Geant4 based GATE simulation. The work revealed a better efficiency result for each radiation type than in previous work. In the simulation, 0.05 mm ZnS(Ag), 3.2 mm plastic scintillator and 1.75 mm BGO were found to be best for the detection and identification of alpha, beta and gamma-rays respectively. In nuclear medicine, this type of detector system could also modify to become a miniaturized radio-guided surgery beta-gamma probe beside of the modification into the robotic surgery. This research result will influence three different areas in imaging technology, homeland security and nuclear industry.

Article info

History:

Received: 25.06.2020

Accepted: 06.11.2020

Keywords:

Detector development, ionizing radiation, medical imaging, environmental monitoring, Geant4 simulation

1. Introduction

Scintillator-based detector systems are widely used in nuclear, particle and medical physics for radiation detection applications such as spectroscopy, creating cross-sectional images and for quality control of medical radioisotopes [1]. Nowadays research labs, nuclear medicine, and nuclear power plants use standard detector systems such as Geiger-Mueller counter, HPGe, NaI(Tl) scintillation, etc. No commercially available detector system can measure alpha, beta and gamma-rays at the same time separately with good efficiency and performance. For some scintillator-based detector applications, two or more scintillators are optically coupled together to form a “phoswich” a name derived from “phos(phor) (sand)wich”. Phoswich detectors have been shown to function effectively in measuring different classes of radiation separately or simultaneously and can discriminate from high ambient background radiation. The scintillators comprising a phoswich need to have different pulse shape characteristics such as rise time and decay times. In particular, decay-time analysis of

signals from a phoswich detector gives a great opportunity to distinguish incident radiation, which

scan be a mixture of charged particles (alpha, beta) and neutrons or gamma rays. It also allows for the separation and identification of which events occurred in which scintillator such as the PARIS calorimeter [1]. In nuclear power plants, nuclear waste can contain fission products and transactinide materials which not only emit gamma-rays but also emit alpha and beta particles and in some cases, neutrons. Moreover, the environmental monitoring of radionuclides following accidents in nuclear power plants not only needs to detect gamma-rays but also necessary to detect alpha and beta particles [2]. That became more important after Fukushima in Japan. A three-layer phoswich alpha-beta-gamma imaging detector was developed by Yamamoto and Ishibashi for simultaneously monitoring alpha-beta-gamma rays following a nuclear accident or for applications in molecular imaging [2]. These considerations show that it is important to simultaneously and separately monitor alpha-beta-

*Corresponding author. email address: nyavuzkanat@beu.edu.tr

gamma radiation via the one detector system. The main aim of this study is the investigation of the measurement alpha-beta-gamma radiation with a single novel detection system by using Monte Carlo simulation. We have completed the work with the Geant4 based GATE simulation to determine which materials and what thicknesses are the most suitable depending on the radiation type. Our result is comparable and better than that obtained with a similar detector system in Japan [2].

Understanding the behaviour of actinides in the nuclear fuel cycle process is important for process and safety management in nuclear power stations [3]. Boiling water reactors, pressurized water reactors and heavy-water reactors are highly contaminated by the fission products [4]. Therefore, the radiation level of the cleaning and cooling systems and reactors have to be monitored regularly and carefully. It is also necessary to carry out continuous monitoring of the levels of radioactivity in the environment around nuclear power plants to ensure compliance with the basic safety standards. There are two methods to monitor the territory; global (outside the zone) and close monitoring to watch and check on the radiological impact on the environment. The radiological monitoring for artificial and natural radioactivity is conducted using two methods; automatic measuring networks and taking a periodic sample to analyse. Automatic measuring networks can play an important role as a warning before the accident and inform the county's citizens the event of the nuclear accident. There are several major radionuclides present in the liquid released from a nuclear power plant to the environment. Their primary decay modes are only beta-emitting (Tritium, Nickel-63, and Strontium-90) and beta-gamma emission related to some radionuclide such as Cobalt-60, Iodine-129, Cesium-134, and Cesium-137, while some of them are alpha-emitting such as Plutonium-239. Tritium contaminated water in a nuclear power plant is regularly diluted, resulting, normally the radiation level in groundwater must be less than drinking water tritium level [5]. Monitoring tritium level in groundwater helps to detect the leaks of underground piping as reported the more tritium level in one of the wells around the Vermont Yankee nuclear power station, where buried piping leaks were found [5]. Similar problems were reported in the detection of radioactive tritium in the groundwater of the more than 48 commercial US nuclear power stations [5]. Obviously, one of the safety requirements at a nuclear power plant is the close monitoring of the tritium level in underground water. Similar to tritium, the other important disposable radioisotope produced during nuclear fission is the long-lived beta-emitting

Strontium-90, resulting from accidents at nuclear power plants and leaking from nuclear waste storage or nuclear weapon testing. If it is ingested into the body, the risk of damage to bone marrow, leukaemia and other bone cancer increases [6]. Therefore, it is also greatly important to monitor its activity in the environment, particularly, in groundwater around the nuclear facilities [6]. Beta-emitting radioisotopes counting system is currently a long and arduous process. Samples must be collected from groundwater wells, transported to a laboratory, processed with hazardous chemicals before the activity can be measured. This procedure also presents logistical and financial challenges for the nuclear industry. After the disaster at the Fukushima nuclear power plant is highlighted the need for Sr-90 detection be able to move quickly and easily to repeat the procedure many times. The existing methods, such as liquid-liquid extraction and chromatography, for beta monitoring, is mainly the separation of the target radionuclide from the sample to remove interface other sources of radiation because of overlapping of their energies. Traditional methods produce a large volume of secondary waste and use very hazardous concentration. Each year, thousands of samples need to be prepared in the nuclear-decommissioning industry, and it needs a new approach to reduce secondary waste production, which is more rapid and safe as well as cost-effective. After the radionuclide is isolated, the beta-emitting radioisotope from the sample can be measured using counting devices (gas ionization chamber and liquid scintillation counters). The other important beta counting device is the Triple to Double Coincidence Ratio (TDCR) which includes the liquid scintillation detector with three PMTs uniformly around a sample. However, these detector systems are large, immobile and not suitable as an in-situ detection system. Gallium-arsenide (GaAs) photodiode for detection of Strontium is a novel detection method and being a potential for direct, in situ beta detection for nuclear decommissioning application [6]. However, this new sensor technology using solid-state detectors, may not be applicable to detect low energy of the beta particles emitted by tritium [5]. These solid-state detectors have several disadvantages like being expensive and radiation damage results in noise in the detector and can negatively affect the counting statistics [6]. Current techniques are lab-based, time-consuming, and produce secondary waste. The existing novel detectors are expensive, poor for the detection of a low energy beta, and negatively affected by the radiation. Therefore, it is necessary to develop a new detector with potential for in situ, cost-effective, real-time monitoring in groundwater and more mobile detector which have not been well developed [5]. In this

research, an alpha-beta-gamma detector system will be investigated using Monte Carlo simulation to fill the needs of the nuclear industry.

Besides, simultaneous detection of three different radiations by one detector is also crucial for some medical cases such as RGS (radio-guided surgery), medical and molecular imaging [2, 7-8]. The effective operation has to remove as many tumoral tissues as possible while preserves the surrounding healthy tissues. Imaging technologies allow to localize the surgeon in the tumour and give information about its size, shape, and stages [9]. Nowadays, pre-operative imaging tools and intra-operative imagine techniques are getting higher importance because they provide real-time information of the picture of tumour boundaries [9]. Aside from these techniques, radio-guided surgery is a promising field for accurate, sensitive tumour detection, and the most available system based on gamma radiation detection. Beta detection provides higher sensitivity and signal-to-noise ratio for shallow tumours, but beta particles inside the tissues have a short range. It requires development of extremely compact devices that can be directly introduced inside the surgical cavity in contact with the surveyed tissues. In the last decade, semiconductor light sensors such as silicon photomultipliers (SiPMs) have gained a favourable position relative to photomultiplier tubes (PMTs). They offer significant advantages in being compact, low voltage, low power and immune to magnetic fields. New generation photosensors, SiPMs, emerge as the most promising for the development of intra-operative beta probes. The performance of SiPMs is also comparable to standard photomultiplier tubes (PMTs). According to the research called the development and evaluation of an intra-operative beta imaging probe studied by Sara Spadola, the performance of the probe designed with two scintillator detection and gamma subtraction method is better than the single detection system [9]. Besides, the depth of interaction method [10], which is recently the most significant improvement in the new generation of high-resolution PET detectors, may be applied to this kind of detection as a PET module to obtain better spatial resolution. In nuclear medicine, an alpha-beta-gamma detector has the potential to become a miniaturized beta-gamma imaging probe and modified to use in robotic surgery. A study conducted using a radio-guided surgery beta probe combined with a robot by an Italian research group, and they concluded that the robotic surgery performance and time consumption is better than man-hand operation [11]. There is also the opportunity to use the small size of the detector system inside a drone, that will be advantageous after

the nuclear accident. This simulation research can also modify into the development and evaluation of intra-operative miniaturized imaging probes. That will be based on two or three layers' scintillators coupled to compact SiPMs as a real-time alpha-beta-gamma monitoring system in the nuclear industry.

2. Materials and Methods

In this study, we aim to investigate the detector which can carry out alpha-beta-gamma monitoring separately and simultaneously by Monte Carlo simulation. Our scintillation material should have better performance and be much more portable than what has previously made. It will apply to many different applications from environment monitoring to medical imaging. We have carried out an initial simulation of such a device using the Geant4 based GATE simulation program. To benchmark the simulation, we reproduced the performance of the Yamamoto et al. detector using the same detector shapes and dimensions illuminated by the same radioactive sources as shown the detector geometry in Figure 1.

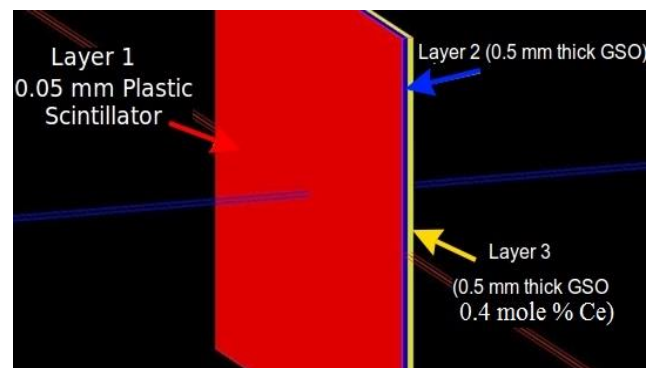


Figure 1. Three different layers described in the simulation; the red layer illustrates to 0.05 mm thick plastic scintillator for detection of the alpha particles. The second layer shows in blue color for beta particles detection and 1.5 mol % Ce doped GSO. The last layer is 0.4 mole % Ce doped GSO as shown in yellow color.

We then explored the effect of increasing each layer's efficiency depending on radiation type, through changing the thickness of layers and component material. Geant4 visualization of the essential detector and three different radioactive sources shown in Figure 2.

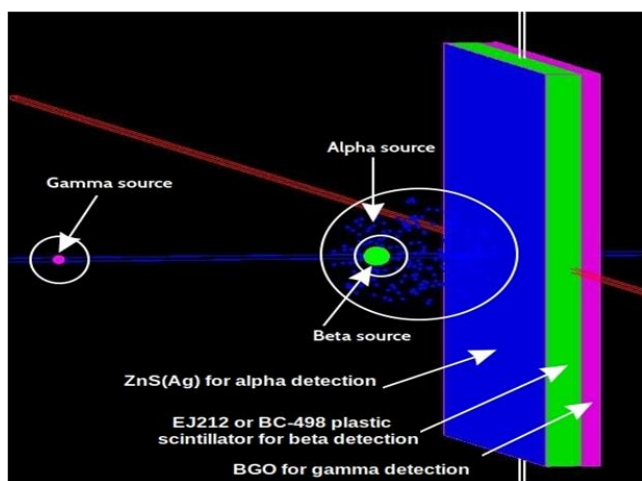


Figure 2. The first layer (blue) defined as Layer 1 is a scintillation material with $50 \times 50 \times 0.05 \text{ mm}^3$ dimension. The blue points represent the alpha source (Am-241) with 15 mm diameter and two kBq activity located in front of the detector. The second layer (green) was Layer 2 scintillation material with $50 \times 50 \times 3.2 \text{ mm}^3$ dimension. Green spherical point showed for beta particle source (Sr, Y-90) with 2 mm diameter and 100 Bq activity positioned 1 cm from the detector surface. The last layer (magenta) determined Layer 3 inorganic scintillation with 1.75 mm thickness. Magenta points also represented the gamma source (Cs-137) with 1 mm diameter and 370 kBq activity located at 4 cm away from the detector surface.

The optimum thickness of the first layer material found to be 0.05 mm and that thickness is enough to absorb almost all alpha particles. The Layer 1 material is ZnS(Ag) powder with medium decay time (200 ns). The second layer, EJ212 or BC-498 plastic scintillator, is 3.2 mm thick with the fast decay time (2.4 ns). The last layer to detect gamma-rays could be various inorganic scintillation materials: LYSO, CsI, LaBr₃, CeBr₃, SrI, GAGG, NaI(Tl), BGO and GSO etc. Some of them are highly hygroscopic materials. Since one of the possible applications for the detector will be to use it in direct contact with water or other liquids, we prefer to use non-hygroscopic materials. Several inorganic scintillations have internal beta or gamma

radiations coming from Lutetium (Lu) such as LYSO, results in the measurement would be deteriorated by the intrinsic activity. Therefore, BGO was found to be the most suitable inorganic scintillator with better efficiency results in the simulation as a Layer 3 material.

If the first layer thickness is increased in the simulation, beta particle absorption went up inside layer 1. Similar behaviour was also observed for the second and third layers. Increasing the second layer thickness seriously affects the gamma-rays count inside the layer 2. In addition, layer 3 is also affected by annihilation photons (511 keV) occurring after positrons annihilate with electrons. The detection of the gamma-ray inside the third layer could be spoiled by the annihilation photons. For this reason, the simulation work completed with annihilation photons to optimize the thickness of each layer. Depending on radiation type, we found out the best three materials and optimum thickness of the layers by using Monte Carlo simulation. In the application, these three different layers have different signal shape characters (different decay time) that will allow applying the pulse shape analysis, resulting in the separation and identification of which events occurred in which layers. Alpha, beta and gamma-rays have different range inside the medium, so these range differences help to show the first layer detects alpha, the second layer detects beta and the last layer detects gamma-rays.

3. Results and Discussion

Geant4 simulation was completed in two parts. The first part reproduced the earlier detector design of S. Yamamoto et al. In the second part, the scintillation material and the thickness were changed step by step to find out the best option and optimum thickness depending on the radiation type. The simulation results listed in Table 1 as a percentage of the detected counts for each layer.

Table1. Comparison between GATE simulation and the work of S. Yamamoto et al. In the simulation, the result obtained after investigating the best materials and thickness for each layer.

Percentage of relative detected counts for alpha particles			
	$\epsilon_{\text{exp.}}(\%)$ (Yamamoto S. et al.)	$\epsilon_{\text{GATE}}(\%)$ (present work)	$\epsilon_{\text{GATE}}(\%)^{\dagger}$ (present work with different material)
First Layer	93.5	93.44	99.87
Secand layer	6.1	5.79	0.13
Third layer	0.4	0.77	0
Percentage of relative detected counts for beta particles			
First Layer	0.4	0.32	1.85
Secand layer	87.7	89.24	90.02
Third layer	11.9	10.44	8.13
Percentage of relative detected counts for gamma-rays			
First Layer	0.6	0.95	1.65
Secand layer	60.0	54.71	19.74
Third layer	39.4	50.33	78.61

[†] Different materials with optimum thickness

The thickness of the first layer material (ZnS(Ag)) was 0.05 mm; that thickness was enough to absorb 99.87% of the alpha particles. The second layer, EJ212 or BC-498 plastic scintillator, was 3.2 mm thick and found to have 90.02% efficiency for beta particles. To detect gamma-rays, a 0.75 mm thick BGO scintillation material was found to be the best option with its 78.61% gamma-rays efficiency value. The detected counts for gamma-rays in the second layer calculated at 19.74 %. In terms of the gamma-ray interaction with the medium, there is no way to remove these counts inside the second layer because of the higher Compton scattering probability of the high energy gamma rays. However, it is highly possible to apply a correction for the gamma detection efficiency of the second and third layers [12]. According to the simulation result, detected counts for alpha, beta particles and gamma rays noticeably increase with these scintillation materials and their optimum thickness found out in the simulation. The experimental result consists of the result obtained by Geant4 simulation in terms of particle detection. Percentage of the relative detected counts for gamma-rays obtained better efficiency in the simulation. That could be related to the experimental conditions. In the literature, there are many determined technical properties for 0.5 mole % Ce doped GSO, but not much more technical information for 0.4 mole % Ce doped GSO. The other difference between

experimental and calculated value in gamma-rays might be about the lack of the material definition for layer3 inside the simulation.

4. Conclusions

No commercially available detector system can measure alpha, beta and gamma-rays at the same time separately with better efficiency and performance. The main aim of this study is the investigation of the measurement alpha-beta-gamma radiation with a single novel detection system by using Monte Carlo simulation. We have completed the work with the Geant4 based GATE simulation to determine which materials and what thicknesses are the most suitable depending on the radiation type. Our result is comparable and better than that obtained with a similar detector system in Japan [2]. In the application, each layer will be optically coupled, then the other side of the last layer will couple with the photosensor (PMTs or SiPMs). For medical imaging, position-sensitive SiPMs or PMTs must be used to define the position of the events. Proper collimators could be employed to obtain a meaningful image from the three layers detector system [13]. The operating principle of this detector will be simple, easily portable and easy to use comprising a combination of novel materials with a state-of-the-art electronic system. This kind of device

can be used for medical or molecular imaging during surgery or other applications in medicine as a beta-gamma probe. In addition, this detector could be modified for different application fields from environmental measurement to monitoring at nuclear power stations. Aside from the detection of the three different radiation types with one detector, the newly designed detector system can also be in direct contact with liquid or water to monitor the radiation inside or

around of the nuclear power plant. We have already succeeded to measure directly beta particles emitted by Ga-68 and F-18, used as a PET radiotracer in Hull PET research centre [14]. This type of detection system is highly suitable to be applied to nuclear-decommissioning applications such as in situ alpha-beta-gamma detection, which will be mobile, and becoming for real-time monitoring in groundwater as shown a possible detector design in Figure 3.

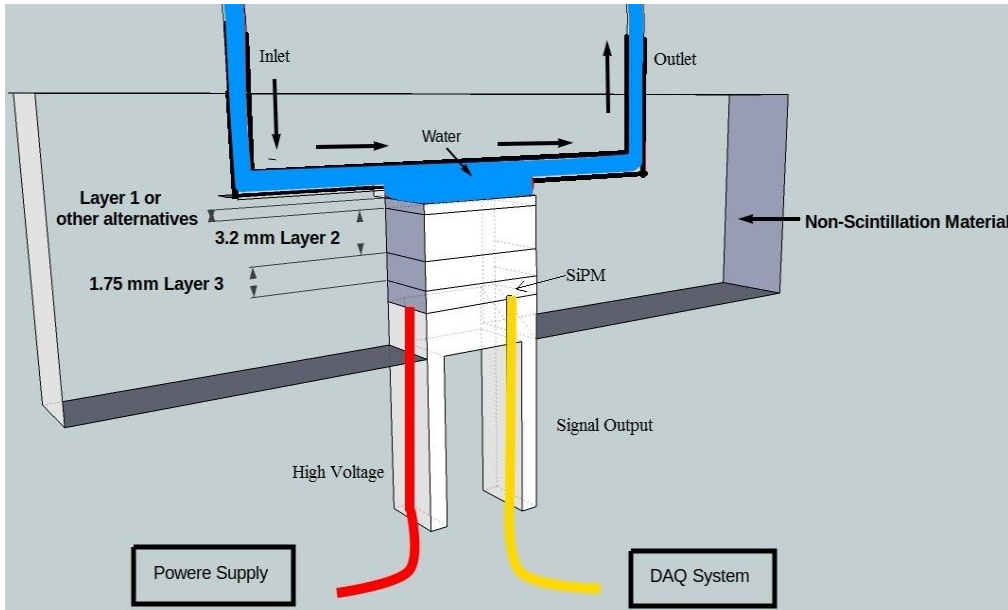


Figure 3. Detector design for monitoring radiation level in water or liquid, which is slightly similar to plastic scintillator-based microfluidic devices developed for measuring positron-emitting radionuclide and successfully patented by the research group of the University of York and University of Hull [1,14]. The first Layer material ZnS(Ag) is a thin powder, and it is commercially available within plastic scintillator. Therefore, it could not damage by liquid or groundwater.

Acknowledgment

This work will be used for the international project program collaboration between Bitlis Eren University and The University of York. We would like to thank Prof. Sefa ERTÜRK, and Dr. Şule KARATEPE.

References

- [1] Yavuzkanat N., Development of Novel Scintillation Detection Techniques for Use in Nuclear Physics and Medical Applications, Doctor of Philosophy thesis, University of York, 2015.
- [2] Seiichi Y., Hiroyuk I., Development of a three-layer phoswich alpha-beta-gamma imaging detector, *Nuclear Instruments and Methods in Physics Research A*, (785) (2015) 129–134.
- [3] Kenichiro Y., Shigekazu U., H. G., Simultaneous Alpha, Beta/Gamma, and Neutron Counting With Phoswich Detectors by Using a Dual-Parameter Technique, *Ieee Transactions On Nuclear Science*, 48(4) (2001) 1162-1167.
- [4] Efremkov V. M., Radioactive waste management at nuclear power plants An overview of the types of low- and intermediate-level wastes and how they are handled, *Iaea Bulletin*, 4 (1989) 37-42.

Conflict of Interest

No conflict of interest was declared by the author.

- [5] Sheen I. S. H., Prokofiev G., Extended In-Situ and Real Time Monitoring Task 4: Detection and Monitoring of Leaks at Nuclear power Plants External to Structures, *Argon National Laboratory*, Accessed April (2020).
- [6] Turkington G., Kelum A. A. G., James G., Beta detection of strontium-90 and the potential for direct in situ beta detection for nuclear decommissioning applications, *Nuclear Instruments and Methods in Physics Research. A: Accelerators, Spectrometers, Detectors, and Associated Equipment*, (911) (2018) 55-65.
- [7] Francesco C., Valerio B., Paolo C., Micol De S., Stefano F., Riccardo F., Alessandro G., Daria M., Carlo M. T., Michela M., Riccardo M., Silvio M., Riccardo S., Teresa S., Giacomo T., Elena S. C., Radioguided surgery with β radiation: a novel application with Ga-68, *Nature/Scientific Reports*, 8 (16171) (2018) 1-9.
- [8] Bipin S., Brendan C. S. J., Samta T., Valeriy G., Twyla B., Val L., Steven C., Gerald E., Vivek N., A Hand-Held Beta Imaging Probe for FDG, *Ann Nucl Med.* 27 (3) (2013) 203–208.
- [9] Spadola S., Development and evaluation of an intraoperative beta imaging probe for radio-guided solid tumor surgery, Doctor of Philosophy thesis, Université Paris Saclay, 2016.
- [10] Mohammad I., Castro I. F. C., Correia P. M. M., Silva A.L.M., Veloso J.F.C.A., Minimization of parallax error in positron emission tomography using depth of interaction capable detectors: methods and apparatus, *IOP Biomed. Phys. Eng. Express*, 5 (062001) (2019).
- [11] Francesco C., Matthias van O., Micol De S., Riccardo F., Marta F., Carlo M. T., Riccardo M., Roberto M., Judith olde H., Elena S.C., Florian van B., Henk van der P., Renato V. O., Pim van L., Fijs van L., Silvio M., Robotic surgery using a DROP-IN beta probe-feasibility study with ^{68}Ga -PSMA in prostate cancer specimens, *Research Square*, (2020).
- [12] Seiichi Y., Jun H., Development of an alpha/beta/gamma detector for radiation monitoring, *Review Of Scientific Instruments*, 82 (2011) 1-6, 113503.
- [13] Yavuzkanat N., Ertürk S., Investigation of the New Generation Detector System Using in Medical Image, *Aksaray University Journal of Science and Engineering*, 3(2) (2019) 99-111.
- [14] Mark D. T. Nuray Y., Mohammad M. N. E., Pankaj J., Nathaniel J. B., Nicole P., David G. J., Stephen J. A., Plastic Scintillator-Based Microfluidic Devices for Miniaturized Detection of Positron Emission Tomography Radiopharmaceuticals, *Chemistry A European Journal*, 24 (2018) 13749-13753.

Determination of order parameter and birefringence depending on temperature of nematic calamitic mesophase formed by TTAB + water binary system using polarized microscopy

Aykut Evren YAVUZ * 

Ege University, Faculty of Science, Department of Physics, Izmir/ TURKEY

Abstract

In the present study, the temperature-dependent optical transmittances of lyotropic nematic calamitic mesophase formed by TTAB-water binary system were measured for certain wavelengths under polarized microscopy to obtain macroscopic order parameter with birefringence. Because birefringence in lyotropics is quite small (order of 10^{-3}), it is very difficult to make sensitive measurements of birefringence and to obtain order parameter. The study easily achieved the order parameter depending on temperature for different wavelengths only using polarized microscopy. Therefore, the parameter could be more easily determined in liquid crystal application and the physical properties of liquid crystals, especially for lyotropics, can be better understood.

Article info

History:

Received:14.09.2020

Accepted:17.11.2020

Keywords:

Lyotropic nematic mesophases,
Polarized microscopy,
Birefringence,
Order parameter

1. Introduction

Liquid crystals are specific mesophases of matter which are between liquid and solid phases and they can simultaneously exhibit anisotropic properties of solids and fluidity ones of liquids [1]. Such mesophases are currently of great importance in terms of technology and they have recently been prominent in optical studies [2,3]. They are generally found in biological systems as lyotropics which are one of their types and thus, lyotropics are taken attention in liquid crystals. These systems are generally formed by the solution of surfactant molecules in water [4]. Basic structural units are micelles, which are spontaneously constituted by the aggregation of surfactant molecules in water. There are different lyotropic mesophases based on micellar structures [5]. Besides, the addition of cosurfactants such as alcohol to the solution enables the formation of a variety of micelles and it can be increased the diversity of lyotropic mesophases [6]. Among the lyotropic mesophases, the most common ones are nematics. There are three different nematic phases as being uniaxial calamitic (N_C), discotic (N_D) and biaxial (N_{BX}) ones. The N_C and N_D phases consist of rod-like and discotic-like micelles, respectively. Because they have anisotropy, it is quite important to study the optical properties of lyotropic nematics in particular [7]. On the other hand, the fact that lyotropics are present in biological materials such as

blood, cellular plasmas and membranes are promising materials in terms of biotechnological studies. Today, they have application fields as in the production of biosensors [8,9]. In order to develop their fields of use, the optical study of their physical properties is necessary. These properties are governed by the order parameter [10]. Thus, the study of the order parameter of lyotropics has accelerated in recent years [11-13]. As the most popular method to measure the parameter, optical anisotropy measurements are preferred due to obtaining better results [14,15]. The optical anisotropy of the nematic phases is given by birefringence (δn). Because the uniaxial nematic phases are described by two refractive indices, the birefringence is found as the difference between these two refractive indices, $\delta n = n_e - n_o$, where n_e and n_o are the refractive indices for extraordinary and ordinary rays, respectively. The polarization direction of n_e (n_o) is parallel (perpendicular) to the nematic phase director, also called optical axis [16,17]. In general, $\delta n < 0$ for N_C and $\delta n > 0$ for N_D mesophases. In the case of the biaxial nematic phase, there exist three principal refractive indices of the medium (n_1 , n_2 and n_3) along three orthogonal laboratory frame axes, and two optical birefringences, $\delta n = n_2 - n_1$ and $\delta n = n_3 - n_2$ [18].

The birefringence of lyotropics is much lower than other liquid crystal mesophases and for this reason, it is quite difficult to determine order parameter in the birefringence measurements. In general, laser

*Corresponding author. email address: aykut.evren.yavuz@ege.edu.tr

conoscopy may be preferred, but this method has a very time-consuming and complex setup in the measurements [19,20]. Berek compensator measurements in a polarizing microscope and refractometry ones are not as sensitive as desired. This study suggests a simpler method to obtain the optical birefringence and order parameter. They were easily calculated from the optical transmittance of given wavelengths in N_C mesophase formed by binary lyotropic system using only polarized microscopy. The optical birefringence and order parameter were found based on wavelength and temperature. In addition, the literature has relatively insufficient for the birefringence and order parameter studies for the lyotropic N_C system at different wavelengths and therefore, the present study aims to eliminate this gap.

2. Materials and Methods

The lyotropic sample was obtained from Tetradecyltrimethylammonium bromide (TTAB) and deionized water. TTAB with purity of not less than 99% was purchased from Sigma (cat. no. T-4762). The concentration of the sample was TTAB: 38.6 and water: 61.4 in weight percent. Per each g of the solution, 1 μ L ferrofluid was used for a better orientation under a magnetic field. Water-based ferrofluid was acquired from Ferrotec Corp. (cat. no. EMG 605). The sample constituents were weighed in a glass tube by an And HR-120 balance with a precision of 10^{-4} g. Then, the sample was kept in Memmert 400 oven at 323 K for two weeks and mixed with a vortex (Nüve NM110) occasionally. The formed sample was placed in sandwich cells of 20 mm in width and 360 μ m in thickness and studied under Olympus BX50 polarizing microscope. The textural properties of the sample were analyzed by the microscope to find out that it was N_C mesophase. Later, the sample was exposed to a 3.7 kG magnetic field parallel to sandwich cell surfaces for 5 hours and it was obtained planar orientation. The temperature of the sample was changed by 0.10 K/min on the Linkam PE120-BX thermoelectric heating table attached to the polarizing microscope. In the process, light intensities of the sandwich cells with and without the sample (I and I_0 , respectively) were measured by Adafruit TSL2561 sensor Arduino system which is sensitive to light transmittance under the polarizing microscope. Optical transmittance (I/I_0) was obtained by a magnification of $\times 100$ by means of optical filters of 440 nm, 550 nm and 694.3 nm placed on the optical way of the microscope.

3. Results and Discussion

The optical transmittances of planar-oriented N_C sample (I/I_0) as a function of temperature were measured for different wavelengths under polarizing microscopy and presented in **Figure 1**. The measurements of the optical transmittance in wavelengths were found to be very different from each other. At 440 nm blue and 550 nm green wavelengths, the transmittances were changed a lot in the N_C mesophase region. However, the differences in the optical transmittance of 694.3 nm red wavelength with temperature were less than the blue and green ones and the wavelength was exhibited a quite high transmittance in the mesophase region.

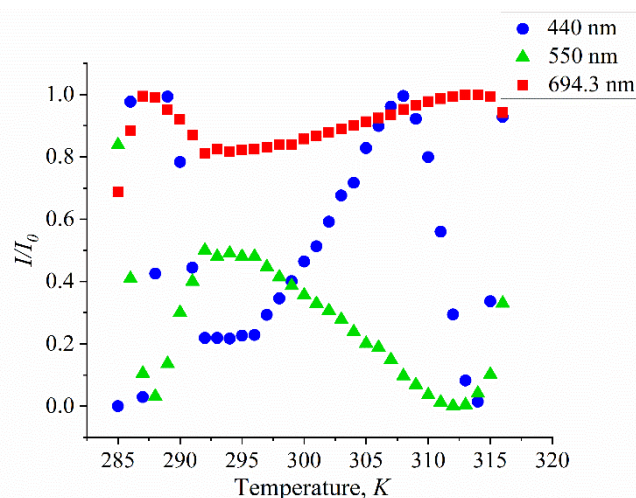


Figure 1. The optical transmittances as a function of temperature for 440 nm, 550 nm and 694.3 nm wavelengths in the lyotropic sample.

The relationship between the optical transmittances and birefringence can be explained by a phase difference. Under the microscope, the polarized light is separated into two rays, which are extraordinary and ordinary ones whose electric field vectors vibrating in parallel and perpendicular to the director, respectively. Therefore, the phase difference ($\Delta\phi$) occurs between the rays after passed passing through the sample. The refractive indices corresponding to these rays are n_e and n_o , and the difference can be explained by the birefringence (δn) as follows:

$$\Delta\phi = \frac{2\pi t}{\lambda} \delta n \quad (1)$$

where λ and t is the wavelength and thickness of the sample, respectively. Thus, the optical transmittance in terms of the phase difference can be as follows [15]:

$$\frac{I}{I_0} = \sin^2 2\theta \sin^2 \frac{\Delta\phi}{2} \quad (2)$$

where \square is the angle between the light polarization direction and director and it was set up as 45° under the microscope. The phase difference in Equation 1 and the optical transmittance in Equation 2 were used to obtain the birefringence of each wavelength (Figure 2). Accordingly, the phase transition from reentrant-isotropic to N_C mesophase occurred at 284 K and N_C mesophase to isotropic phase transition was achieved at 317 K. The birefringence of the 440 nm blue wavelength was highest in value whereas the 694.3 nm red wavelength had the lowest value.

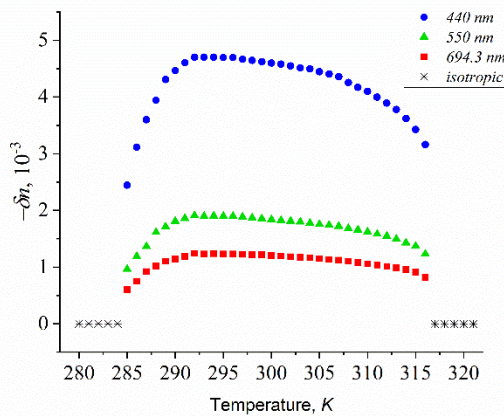


Figure 2. The birefringence as a function of temperature for 440 nm, 550 nm ve 694.3 nm wavelengths.

Macroscopic order parameter (Q) can be obtained from Figure 2 using Haller method [19]. The order parameter can be written in terms of birefringence as follows:

$$Q = \frac{\delta n}{\Delta n} \quad (3)$$

where Dn is birefringence at $T=0$ K which is absolute temperature where liquid crystals are assumed to be completely oriented as in solids and therefore, $Q=1$. The order parameter is very important because it governs all physical properties of liquid crystals. To obtain this parameter, a line was drawn at $\log(dn)$ versus $\log(1-T/T_c)$ in dn -temperature graph. At the point where the line intercepts at $T=0$ K, $\log(Dn)$ is obtained. Dn values for 440 nm, 550 nm and 694.3 nm are 6.851×10^{-3} , 2.794×10^{-3} and 1.777×10^{-3} , respectively. Figure 3 shows the order parameter based on temperature. The parameters were found to be similar for each wavelength and in the sensitivity of 10^{-2} according to each other. However, the maximum order parameter was found as 0.697 at 292 K.

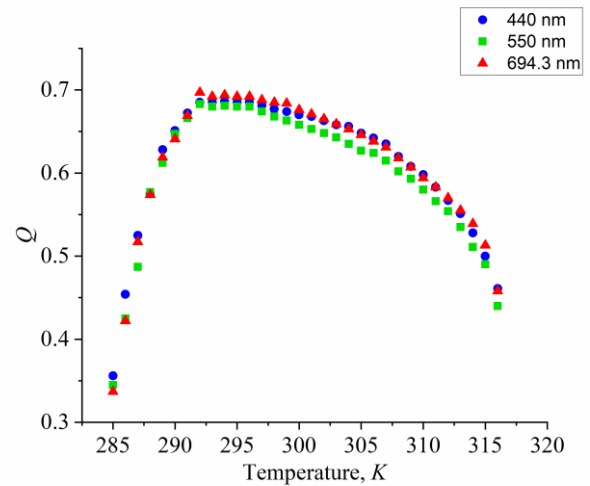


Figure 3. The temperature-dependent order parameter for 440 nm, 550 nm and 694.3 nm wavelengths.

4. Conclusion

In the present study, both the birefringence and order parameter of a lyotropic N_C mesophase were found from the optical transmittances for different wavelengths under the microscope. A variety of methods, especially laser conoscopy, are used to obtain order parameter [19,20]. On the other hand, this study shows obtaining the birefringence and order parameter more sensitively by measuring the optical transmittances only using polarizing microscopy. By evaluating the parameter more easily, the analysis of the physical properties of liquid crystals could be made simpler, especially in applications.

Conflicts of interest

The authors state that did not have conflict of interests.

References

- [1] de Gennes P. G., Prost J., The Physics of Liquid Crystals, Second ed., Oxford: Oxford Science Publications, (1995).
- [2] Nastishin Y. A., Liu H., Schneider T., Nazerenko V., Vasyuta R., Shiyanovskii S. V., Lavrentovich O. D., Optical characterization of the nematic lyotropic chromonic liquid crystals: Light absorption, birefringence, and scalar order parameter, *Phys. Rev. E*, 72 (2005).
- [3] Kanwar A., Measurement of order parameter, birefringence and polarizability of liquid crystals, *J. Opt.*, 42 (2013) 311-315.

- [4] Dierking I., Neto A. M. F., Novel trends in lyotropic liquid crystals, *Crystals*, 10 (2020) 604.
- [5] Neto A. M. F., Salinas S. R. A., Physics of lyotropic liquid crystals, Oxford: Oxford Science Publications, (2005).
- [6] Akpınar E., Canioz C., Turkmen M., Reis D., Neto A. M. F., Effect of the surfactant alkyl chain length on the stabilisation of lyotropic nematic phases, *Liq. Crys.*, 45 (2018) 219.
- [7] Santoro P. A., Sampaio A. R., da Luz H.L.F., Palangana A. J., Temperature dependence of refractive indices near uniaxial–biaxial nematic phase transition, *Physics Letters A*, 353 (2006) 512-515.
- [8] Otón E., Otón J. M., Caño-García M., Escolano J. M., Quintana X., Geday M. A., Rapid detection of pathogens using lyotropic liquid crystals, *Opt. Express*, 27 (2019), 10098-10107.
- [9] Shiyanovskii S. V., Lavrentovich O. D., Schneider T., Ishikawa T., Smalyukh I. I., Woolverton C. J., Niehaus G. D., Doane K. J., Lyotropic chromonic liquid crystals for biological sensing applications, *Mol. Cryst. Liq. Cryst.*, 434 (2005), 259–270.
- [10] Luders D.D., Oliveira D.A., Kimura N.M., Simões M., Palangana A.J., Order parameter in the nematic–isotropic phase transition, *J. Mol. Liq.*, 207 (2015) 195–199.
- [11] Braga W. S., Kimura N. M., Luders D. D., Sampaio A. R., Santoro P. A., Palangana A. J., *Reentrant isotropic-calamitic nematic phase transition in potassium laurate-decanol-D2O mixtures*, *Eur. Phys. J. E*, 24 (2007) 247–250.
- [12] Oliveira D.A., Hioka N., Luders D.D., Kimura N.M., Simões M., Palangana A.J., Absorption coefficient and order parameter in a reentrant isotropic–calamitic nematic phase transition, *J. Mol. Liq.*, 166 (2012) 81-83.
- [13] Singh A.K., Manohar R., Shukla J.P., Biradar A.M., Refractive indices, order parameter and optical transmittance studies of a nematic liquid crystal mixture, *Acta Phys. Pol. A*, 110 (2006) 485-493.
- [14] Kanwar A., Measurement of order parameter, birefringence and polarizability of liquid crystals, *J. Opt.*, 42 (2013) 311-315.
- [15] Kuczyński W., Żywucki B., Małecki J., Determination of orientational order parameter in various liquid-crystalline phases, *Mol. Cryst. Liq. Cryst.*, 381 (2002) 1-19.
- [16] Kimura N. M., Santoro P. A., Fernandes P. R. G., Palangana A. J., Reentrant isotropic–discotic nematic lyotropic phase transition: a refractive index study, *Liq. Crys.*, 31 (2004) 347–350.
- [17] Braga W.S., Santos O.R., Luders D.D., Kimura N.M., Sampaio A.R., Simões M., Palangana A.J., Refractive index measurements in uniaxial and biaxial lyotropic nematic phases, *J. Mol. Liq.*, 213 (2016) 186-190.
- [18] Akpınar E., Turkmen M., Canioz C., Neto A. M. F.; Role of kosmotrope-chaotrope interactions at micelle surfaces on the stabilization of lyotropic nematic phases, *Eur. Phys. J. E*, 39 (2016), 1-16.
- [19] Braga W.S., Santos O.R., Sampaio A.R., Kimura N.M., Simões M., Palangana A.J., An optical conoscopy study of a reentrant discotic nematic–biaxial nematic phase transition, *J. Mol. Liq.*, 170 (2012) 72-75.
- [20] Santos O.R., Braga W.S., Luders D.D., Kimura N.M., Simões M., Palangana A.J., Study of optical conoscopy in uniaxial and biaxial nematic lyotropic phases, *J. Mol. Liq.*, 197 (2014) 120-123.

A study on the activity concentrations of natural radionuclides and annual effective dose values in some tobacco samples

Canel EKE^{1,*} , Mavra ISHFAQ² 

¹Akdeniz University, Faculty of Education, Department of Mathematics and Science Education, Division of Physics Education, Antalya/TURKEY

²The University of Lahore, Faculty of Natural Sciences, Department of Physics, Gujrat Campus, Punjab/PAKISTAN

Abstract

Tobacco samples were collected from different tobacco markets from Antalya in Turkey. To calculate natural radionuclides activity concentration, samples were counted for 86400 seconds by using high purity germanium (HPGe) detector. Activity concentrations of ²²⁶Ra, ²³²Th and ⁴⁰K for tobacco samples found higher than minimum detectable activity (MDA). ¹³⁷Cs was not detected in any sample. Activity concentration of ²²⁶Ra, ²³²Th and ⁴⁰K range from 83±15 Bqkg⁻¹ to 325±45 Bqkg⁻¹, 29±5 Bqkg⁻¹ to 207±37 Bqkg⁻¹ and (2.09±0.28)×10³ Bqkg⁻¹ to (5.07±0.90) ×10³ Bqkg⁻¹, respectively. In addition, annual effective dose value was calculated. The annual effective dose values owing to inhalation for adults change from 2.76 to 9.91 μSvy⁻¹ for ²¹⁴Pb, from 5.69 to 27.69 μSvy⁻¹ for ²¹⁴Bi, from 5.72 to 40.41 μSvy⁻¹ for ²²⁸Ac, from 42.23 to 102.37 μSvy⁻¹ for ⁴⁰K. The total annual effective dose values change from 0.05 to 0.16 mSvy⁻¹.

Article info

History:

Received: 13.12.2019

Accepted: 03.12.2020

Keywords:

Natural radioactivity,
Gamma-ray spectroscopy,
High purity germanium detector,
Annual effective dose,
Tobacco samples.

1. Introduction

Determination of the activity concentrations of the natural radionuclides (²³⁸U, ²³²Th and ⁴⁰K) and artificial radionuclides (¹³⁷Cs, ¹³⁴Cs, ⁹⁰Sr and ¹³¹I) are significant to protection of the radiation. ²³⁸U, ²³²Th and ⁴⁰K are major natural radionuclides which are toxic for health as well as environment. Cosmic rays and naturally occurring radioactive materials being in the earth itself are natural sources of the radiation whereas nuclear accidents, nuclear power plants, medical application of the radionuclides are man-made source of radiation [1].

Uranium has both radionuclide and metallic properties as well as its biological properties outcome from the chemical effects and natural occurring radionuclide. The internal contact with Uranium reveals radiological and chemical consequences which depend partly on chemical form of the intake and the route of intake (mainly ingestion and inhalation). The chemical toxicity effects of uranium species are namely as the renal effects, however others are associated with radiological toxicity of uranium. If we consider of the chemical effects of the uranium species, the kidneys are the easiest and sensitive target organ. Also, it effects central nervous system at higher radiation exposure. Such as, it has been reported that it occurred

abnormal behaviours in animals at higher uranium doses [2].

Exposure to long term radiation causes bone weakening, necrosis of the nasal and mouth tumors, leucopenia and large number of diseases. Such as, ingested or inhaled radium enhance the risk of developing following diseases as bone cancer, lymphoma, and diseases concerning the blood formation, such as aplastic anemia and leukemia etc. The emergences of these diseases are time taking. The hazard effect of the radiation depends upon the exposure time and intensity of radiation [1-3].

With the population growth, smoking becomes fashion of being modern specially in youngsters these days. But there is strong correlation between tobacco, cigarette, its smoke and lungs cancer [4]. Risk of occurring lungs cancer among non-smokers is ten times less than that of smokers [5]. Because tobacco which is main product of cigarette contains radioactive isotopes of ²³⁸U and ²³²Th and their decay series which are carcinogenic in nature [6]. The use of tobacco and its products for smoking increase the coincidental internal intake and radiation dose due to presence of these radioisotopes [7]. It is stated that there is strong

*Corresponding author. email address: ceke@akdeniz.edu.tr

correlation between lung cancer and smoking as well as there is positive correlation between the carcinogenic effect of smoking and radiation [8].

Discussing some serious impacts about radionuclides present in the tobacco samples, lung cancer is very critical and serious issue. Though in recent times cancer gains more attention regarding health agenda all over the world [6]. Therefore, determination of the radioactivity concentration and annual effective dose values of the tobacco samples is significant to protection of the radiation. The aim of this study is to calculate activity concentration of natural radionuclides and dose evaluation in some tobacco samples.

2. Materials and Methods

In Sixteen different types of tobacco samples were collected randomly from different tobacco markets. The samples were numbered randomly from 1 to 16 and kept in plastic containers of 100 ml capacity. Plastic cups were closed firmly to prevent radon emission. Samples waited for 30 days before counting to come into secular equilibrium between radium and radon (uranium and its daughter nuclei) [6].

Samples were counted for 86400 seconds to calculate activity concentration of natural radionuclides using high purity germanium (HPGe) detector (AMATEK-ORTEC GEM40P4 – 83) which has 40% relative efficiency, p type, electrically cooled. The detector is located in department of Physics in Akdeniz University. The energy resolution of the detector is 1.85 keV at 1332 keV for ^{60}Co and 768 eV at 122 keV for ^{57}Co .

Before counting the samples, point sources [^{22}Na (1274 keV), ^{57}Co (122 and 136 keV), ^{54}Mn (834 keV), ^{60}Co (1173 and 1332 keV), ^{133}Ba (80, 276, 302, 356 and 384 keV) and ^{137}Cs (661 keV)] were counted for 1000 seconds to check energy calibration. Multinuclides standard source (IAEA 1364- 43 – 2) was used to determine efficiency calibration from Cekmece Nuclear Research and Training Center in Turkish Atomic Energy Authority (TAEK) [9, 10].

Spectra of tobacco samples were obtained by using MAESTRO-32 computer program [11]. Before analyzing of spectra, background spectrum was subtracted from each spectra of tobacco to reduce background effect. Spectra were analyzed automatically by using Gamma-W computer software [12].

Minimum detectable activity (MDA) was calculated by Currie equation as shown by following relation [13,14];

$$MDA = \frac{2.71 + 4.66\sigma}{t \cdot \epsilon \cdot I_{\gamma} \cdot m} \quad (1)$$

where σ , t , ϵ , I_{γ} and m are standard deviation of count, counting time, efficiency, probability of gamma-ray emission and mass of sample, respectively. Minimum detectable activities of ^{214}Pb (351.93 keV), ^{214}Bi (609.32 keV), ^{228}Ac (911.20 keV), ^{40}K (1460.82 keV) and ^{137}Cs (661.66 keV) radionuclides for 1-kg sample size and 53999 seconds live counting time were calculated using background spectrum.

Activity concentration of radionuclides A (Bqkg^{-1}) were calculated using well-known following formula [15],

$$A = \frac{N}{m \cdot t \cdot \epsilon \cdot I_{\gamma}} \quad (2)$$

where N , m , t , ϵ and I_{γ} shows number of counts of under the peak with background subtraction, mass of the sample, counting time, detector efficiency of gamma-ray energy and probability of gamma-ray emission, respectively.

Uncertainty of activity concentration of radionuclides was calculated by using following relation [16]

$$\Delta A = A \sqrt{\left(\frac{\Delta N}{N}\right)^2 + \left(\frac{\Delta t}{t}\right)^2 + \left(\frac{\Delta \epsilon}{\epsilon}\right)^2 + \left(\frac{\Delta I_{\gamma}}{I_{\gamma}}\right)^2 + \left(\frac{\Delta m}{m}\right)^2} \quad (3)$$

where ΔN , Δt , $\Delta \epsilon$, ΔI and Δm show uncertainties of count of under peak with background, counting time, detector efficiency of gamma-ray energy, probability of gamma-ray emission and mass of sample.

Radium equivalent activity (Ra_{eq}) is calculated using following equation [17]:

$$Ra_{eq} = A_{Ra} + 1.43A_{Th} + 0.077A_K \quad (4)$$

here A_{Ra} , A_{Th} and A_K present activity concentration of ^{226}Ra , ^{232}Th and ^{40}K respectively.

Annual effective dose value (H_E) is calculated as following [18]:

$$H_E = 0.75 \times M_T \times A_i \times F \quad (5)$$

where M_T (kg y^{-1}) is annual consumed quantity of tobacco mass which is estimated as 8.979 kg y^{-1} [4], M_T

(kg^{-1}) is calculated estimating a smoker consumes 30 cigarette per day or 24.6 g of tobacco per day in Ref. [4]. A_i stands the concentration of the i^{th} radionuclide, F (SvBq^{-1}) is dose conversion factor which is $4.8 \times 10^{-9} \text{ SvBq}^{-1}$ for ^{214}Pb , $1.2 \times 10^{-8} \text{ SvBq}^{-1}$ for ^{214}Bi , $2.9 \times 10^{-8} \text{ SvBq}^{-1}$ for ^{228}Ac and $3.0 \times 10^{-9} \text{ SvBq}^{-1}$ for ^{40}K [19].

Excess lifetime cancer risk ($ELCR$) is calculated using following equation [4,20]:

$$ELCR = (\sum H_E) \times DL \times RF \quad (6)$$

where DL is duration of life (~70 years) and RF is the risk factor (0.05 Sv^{-1}) [18,21],

Total annual effective dose $\sum H_E$ value is calculated as following:

$$\sum H_E = \frac{(H_{E(214\text{Pb})} + H_{E(214\text{Bi})})}{2} + H_{E(228\text{Ac})} + H_{E(40\text{K})} \quad (7)$$

Table 1. Activity concentration of ^{226}Ra , ^{232}Th , and ^{40}K in tobacco samples

Sample No	^{226}Ra		Mean Value (Bqkg^{-1}) ($^{214}\text{Pb} + ^{214}\text{Bi}$)/2	^{232}Th	^{40}K ($\times 10^3$)** (Bqkg^{-1})
	^{214}Pb (Bqkg^{-1})	^{214}Bi (Bqkg^{-1})		^{228}Ac (Bqkg^{-1})	
1	307±46	343±46	325±45	183±33	4.22±0.53
2	177±21	202±20	190±21	131±18	4.29±0.39
3	149±19	183±19	166±19	98±13	3.17±0.25
4	122±14	133±21	128±18	38±12	2.44±0.35
5	162±24	188±14	175±19	104±14	4.17±0.34
6	147±15	173±14	160±15	118±15	3.13±0.26
7	85±14	109±13	97±14	111±18	2.25±0.19
8	95±16	70±14	83±15	29±5	2.09±0.28
9	153±18	169±13	161±16	95±14	3.61±0.36
10	147±20	135±17	141±19	109±16	3.03±0.25
11	233±36	229±34	231±35	207±37	5.06±0.90
12	101±15	116±12	108±14	91±12	3.10±0.29
13	110±15	126±12	118±14	99±13	3.03±0.25
14	128±14	164±17	146±16	127±18	4.41±0.36
15	185±23	208±20	197±21	125±19	4.52±0.48
16	133±20	186±16	159±18	122±21	4.08±0.36
Mean Value	152±21	163±19	157±20	112±17	3.54±0.37

**Data can be found in Ref. [22]

3. Results and Discussion

MDA of ^{214}Pb (351.93 keV), ^{214}Bi (609.32 keV), ^{228}Ac (911.20 keV), ^{137}Cs (661.66 keV) and ^{40}K (1460.82 keV) are 4.64 Bqkg^{-1} , 4.37 Bqkg^{-1} , 8.44 Bqkg^{-1} , 1.80 Bqkg^{-1} and 32.71 Bqkg^{-1} , respectively. Activity concentrations of ^{226}Ra , ^{232}Th and ^{40}K for tobacco samples found higher in present studies in compare with MDA. ^{137}Cs was not detected in any sample.

Activity concentration of ^{226}Ra , ^{232}Th and ^{40}K are shown in Table 1. Activity concentration of ^{226}Ra calculated using mean value of ^{214}Pb and ^{214}Bi . Activity concentration of ^{226}Ra ranges from $83 \pm 15 \text{ Bqkg}^{-1}$ to $325 \pm 45 \text{ Bqkg}^{-1}$, the mean value of ^{226}Ra is $157 \pm 20 \text{ Bqkg}^{-1}$. The activity concentration of ^{226}Ra is the highest in sample-1 while the activity concentration of ^{226}Ra is lowest in sample-8.

Activity concentration of ^{232}Th varies from $29 \pm 5 \text{ Bqkg}^{-1}$ to $207 \pm 37 \text{ Bqkg}^{-1}$. The mean value of activity concentration of ^{232}Th is $112 \pm 17 \text{ Bqkg}^{-1}$. The activity concentration of ^{232}Th is highest in sample-11 while the

activity concentration of ^{232}Th is lowest in sample-8. The activity concentration of ^{40}K varies from $(2.09 \pm 0.28) \times 10^3 \text{ Bqkg}^{-1}$ to $(5.06 \pm 0.90) \times 10^3 \text{ Bqkg}^{-1}$. The mean value of activity concentration of ^{40}K is

$(3.54 \pm 0.37) \times 10^3 \text{ Bqkg}^{-1}$. Also, the activity concentrations of ^{40}K can be found previous work in Ref. [22]. Among all the samples the highest value of activity concentration for ^{40}K is found in sample-11 while the lowest value in sample-8.

Activity concentration of ^{40}K is much higher than activity concentration of ^{226}Ra and ^{232}Th . This result is in agreement with Ref. [23]. Activity concentration of ^{40}K and ^{226}Ra are higher than ^{232}Th because tobacco cultivated soil may be including high radioactivity or fertilizer and high activity concentration radionuclides

can be transferred from roots to tobacco plant. General components of fertilizer are potassium, nitrogen, and phosphorus which are commonly used in the agriculture of tobacco plant [4]. The use of fertilizer in soil or cultivated area may bring enhancement in the radionuclide components. The radionuclide (uranium, thorium, radium, and polonium) may be transferred from soil to root and different parts of plants such as leafs, grain and stem [24]. Distribution of activity concentration of ^{226}Ra , ^{232}Th and ^{40}K in tobacco samples are shown in Fig.1, Fig.2 and Fig.3, respectively.

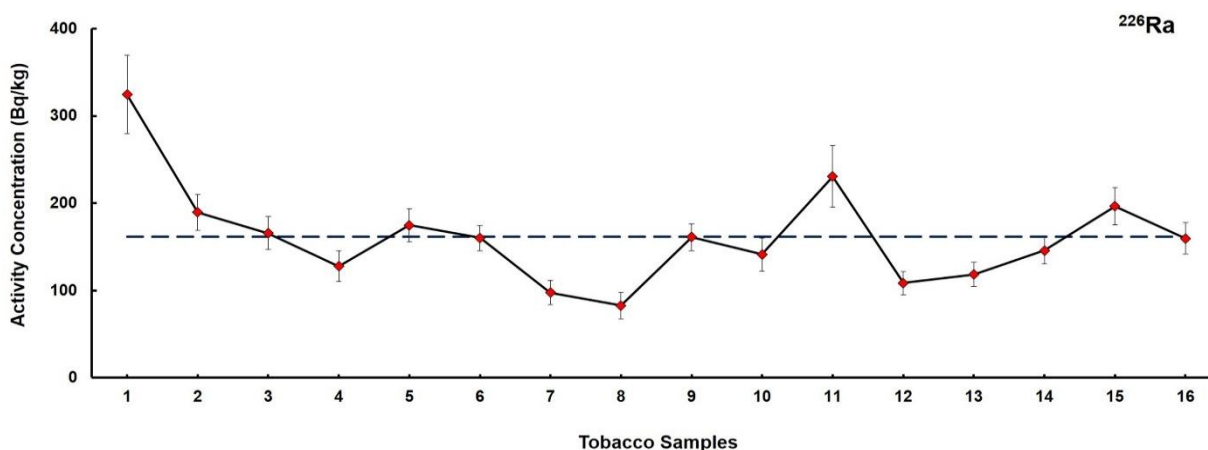


Figure 1. Distribution of radioactivity concentration of ^{226}Ra for tobacco samples and blue-dashed line represents mean value of ^{226}Ra for tobacco samples in this study.

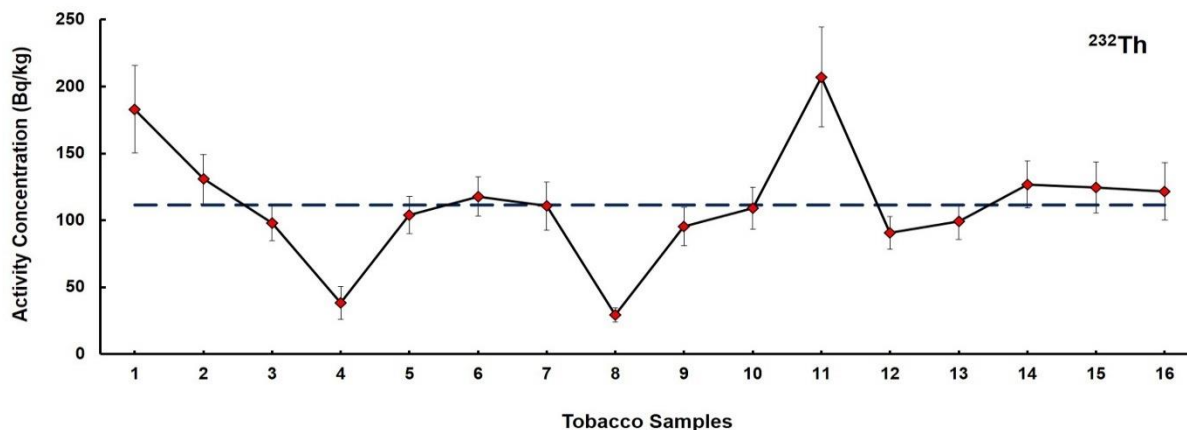


Figure 2. Distribution of radioactivity concentration of ^{232}Th for tobacco samples and blue-dashed line denotes mean value of ^{232}Th for tobacco samples in this study.

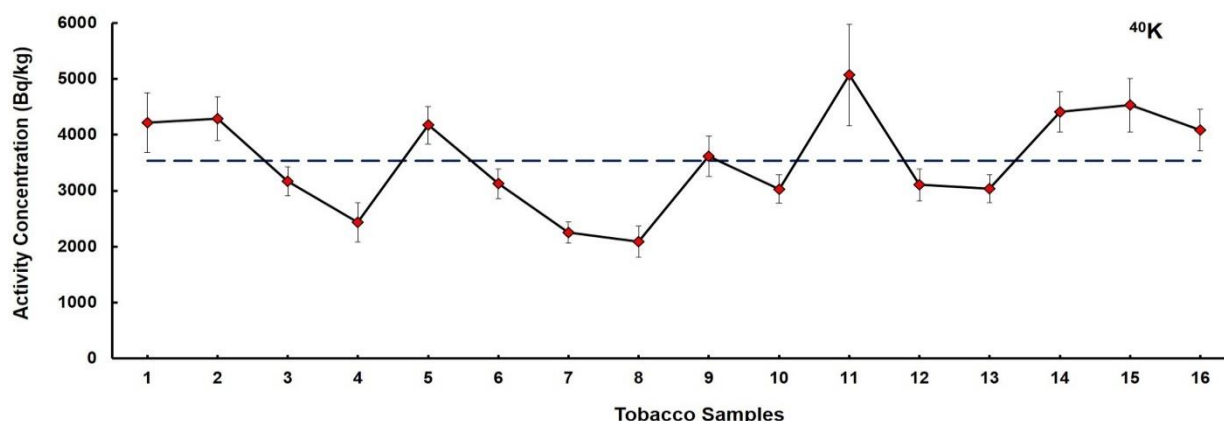


Figure 3. Distribution of radioactivity concentration of ^{40}K for tobacco samples and blue-dashed line denotes mean value of ^{40}K for tobacco samples in this study.

Values of radium equivalent activity (Ra_{eq}), annual effective dose (H_E) for ^{214}Pb , ^{214}Bi , ^{228}Ac and ^{40}K , separately and total value of annual effective dose ($\sum H_E$) and excess lifetime cancer risk ($ELCR$) of tobacco samples were calculated and these values are presented in Table 2.

Table 2. Annual effective dose evaluations for tobacco samples

Sample No	Ra_{eq} ($Bqkg^{-1}$)	H_E (^{214}Pb) ($\mu Sv y^{-1}$)	H_E (^{214}Bi) ($\mu Sv y^{-1}$)	H_E (^{228}Ac) ($\mu Sv y^{-1}$)	H_E (^{40}K) ($\mu Sv y^{-1}$)	$\sum H_E$ ($mSv y^{-1}$)	$ELCR$ ($\times 10^{-3}$)
1	911	9.91	27.69	35.71	85.21	0.14	0.49
2	707	5.71	16.36	25.54	86.70	0.12	0.43
3	550	4.81	14.75	19.12	63.99	0.09	0.33
4	370	3.93	10.79	7.46	49.21	0.06	0.23
5	644	5.23	15.16	20.29	84.28	0.11	0.40
6	569	4.75	14.01	23.01	63.19	0.10	0.33
7	429	2.76	8.84	21.59	45.54	0.07	0.26
8	285	3.06	5.69	5.72	42.23	0.05	0.18
9	509	4.94	13.69	18.61	72.98	0.10	0.35
10	530	4.76	10.91	21.27	61.23	0.10	0.32
11	917	7.52	18.47	40.41	102.37	0.16	0.55
12	477	3.25	9.37	17.71	62.73	0.09	0.30
13	493	3.57	10.17	19.33	61.35	0.09	0.31
14	667	4.13	13.25	24.75	89.19	0.12	0.43
15	723	5.99	16.80	24.33	91.50	0.13	0.45
16	648	4.29	15.05	23.74	82.53	0.12	0.41
Mean Value	594	4.91	13.81	21.79	71.51	0.10	0.36

Total annual effective dose (H_E) varies from 0.05 mSv y^{-1} to 0.16 mSv y^{-1} , the mean value of total annual effective dose is 0.10 mSv y^{-1} . The value of $ELCR$ gives information about possibility of growing cancer excess of lifetime at a certain exposure level and so this value has no units [4]. Value of excess lifetime cancer risk ($ELCR$) varies from 0.18×10^{-3} to 0.55×10^{-3} , the mean value of $ELCR$ is 0.36×10^{-3} which is higher than mean value of 0.29×10^{-3} reported by the UNSCEAR

report [1, 17]. Increasing value of $ELCR$ brings about breast, prostate or even blood cancer [25]. Value of radium equivalent activity, total annual effective dose and excess lifetime cancer risk are the highest in sample-11 and sample-8 is the lowest. Comparison between natural radioactivity concentrations in tobacco samples with previous studies and this study is shown in Table 3.

Table 3. Natural radioactivity concentrations in tobacco samples other studies.

Country (samples collected)	^{238}U (^{226}Ra) (Bqkg ⁻¹)	^{232}Th (Bqkg ⁻¹)	^{40}K (Bqkg ⁻¹)	Ref.
Antalya Market (Turkey)	161.46±19.88	111.56±17.20	3539.82±366.43	Present Study
Iraqi Market	14.86 ±3.76	10.84 ± 3.13	1050.64 ± 47.57	[4]
Greece	2-8		273-2080	[19]
1 Pakistan, 1 Singapore, 1 Egypt, 1 Germany, 1 Switzerland, 11 UK, 8 USA)	7.0	7.8	876	[22]
Baghdad Market	52.543 (^{214}Bi)	1.742 (^{228}Ac) 7.730 (^{212}Pb) 12.122 (^{212}Bi)	75.267	[26]
Serbian Market	9.4±3.2		1160±120	[27]

4. Conclusion and Outlook

Natural radioactivity concentration of ^{226}Ra , ^{232}Th , ^{40}K , radium equivalent activity, annual effective dose, total annual effective dose and excess lifetime cancer risk were calculated using high purity germanium detector (HPGe).

As shown in Table-3, activity concentration of the ^{238}U , ^{232}Th and ^{40}K are the lowest value in Greece region [19] and Baghdad Market [28], respectively. In present study, ^{238}U , ^{232}Th and ^{40}K activity concentration of tobacco samples are higher than other studies. Because the activity concentration of natural radionuclides can be affected by the area where the tobacco is planted and the geological characteristics of the zone [28]. As a result, the activity concentrations of radionuclides may vary depending on the geological characteristics of the soil where tobacco plants are grown and the amount of fertilizer.

Distribution of particulate size, inhalation type, aerodynamic and electrical properties of particle, dissipation and solubility in the lung as well as the rate of the radionuclides in the smoking products are required to determine prediction of dose effect from smoking [22]. This study is first step to prediction of the dose effect from smoking. In the future, all these parameters can be investigated.

Acknowledgment

Mavra Ishfaq wishes to acknowledge the support provided by Scientific and Technological Research Council of Turkey (TUBITAK), Department of Science Fellowships and Grant Programs (BIDEB) 2216 Research Fellowship Program for International Researchers (21514107-115.02-124287).

Conflicts of interest

The authors state that there is no conflict of interests.

References

- [1] UNSCEAR: United Nations Scientific Committee on the Effect of Atomic Radiation. Sources and Effects of Ionizing Radiation. Report to General Assembly, with Scientific Annexes, New York: United Nations, (2000).
- [2] UNSCEAR: United Nations Scientific Committee on the Effect of Atomic Radiation. Sources and Effects of Ionizing Radiation. Report to General Assembly, with Scientific Annexes, New York: United Nations, (2016).
- [3] Taskin H., Karavus M., Ay P., Topuzoglu A., Hidiroglu S., Karahan G., Radionuclide Concentrations in Soil and Lifetime Cancer Risk due to Gamma Radioactivity in Kirklareli, Turkey, *J. Environ. Radioactiv.*, 100 (2009) 49–53.
- [4] Ridha A.A., Hasan A.H., Cancer Risk due to the Natural Radioactivity in Cigarette Tobacco, *Detection*, 4 (2016) 54-65.
- [5] Savidou A., Kehagia K., Eleftheriadis K., Concentration Levels of ^{210}Pb and ^{210}Po in Dry Tobacco Leaves in Greece, *J. Environ. Radioactiv.*, 85 (2006) 94-102.
- [6] Jibiri N.N., Biere P.E., Activity Concentrations of ^{232}Th , ^{226}Ra and ^{40}K and Gamma Radiation Absorbed Dose Rate Levels in Farm Soil for the Production of Different Brands of Cigarette

- Tobacco Smoked in Nigeria. *Iran. J. Radiat. Res*, 8 (4) (2011) 201-206.
- [7] Abd El-Aziz N., Khater A.E.M., Al-Sewaidan H.A., Natural Radioactivity Contents in Tobacco. *International Congress series*, 1276 (2005) 407-408.
- [8] Van Leeuwen F.E., Klokman W.J., Stovall M., Hagenbeek A., Van den Belt-Dusebout A.W., Noyon R., Boice J.D., Burgers J.M.V., Somers R. Roles of Radiotherapy and Smoking in Lung Cancer Following Hodgkin's Disease, *JNCI: Journal of the National Cancer Institute*, 87(20) (1995) 1530–1537.
- [9] Ozmen S.F., Boztosun I., Yavuz M., Tunc M.R. Determination of Gamma Radioactivity Levels and Associated Dose Rates of Soil Samples of the Akkuyu/Mersin Using High-Resolution Gamma-ray Spectrometry. *Radiat. Prot. Dosim.*, 158 (2014) 461– 465.
- [10] Eke C., Boztosun I. Determination of Activity Concentration of Natural and Artificial Radionuclides in Sand Samples from Mediterranean Coast of Antalya in Turkey, *Kerntechnik*, 80 (3) (2015) 3 280– 290.
- [11] Maestro-32: Multi-channel analyser software, A65- B32 model, Ortec (2008). Available at: <https://www.ortec-online.com/media/ametektortec/manuals/a65-mnl.pdf> Retrieved May 30, 2018.
- [12] Gamma-W. 2018. Available at: <http://www.westmeier.com/3gammawfeatures.htm> Retrieved May 30, 2018.
- [13] Currie L., Limits for Qualitative Detection and Quantitative Determination. *J. Anal. Chem.*, 40 (1968) 586-593.
- [14] Knoll G., Radiation detection and measurement. 3rd Edition, United States of America: John Wiley and Sons, Inc., (2000).
- [15] Mohery M., Shadiah B., Kelany A.M., Abdallah A.M., Environmental Radiation Levels in Soil and Sediment Samples Collected from Floating Water from a Land Runway Resulting from Heavy Rains in the Jeddah Region, KSA. *Radiat. Phys. Chem.*, 97 (2014) 16-24.
- [16] ISO-GUM (International Organization for Standardization-Guide to the Expression of Uncertainty in Measurement). Available at: <https://www.bipm.org/en/publications/guides/> Retrieved May 30, 2018.
- [17] Beretka J.J., Mathew P., Natural Radioactivity of Australian Building Materials, Industrial Wastes and by Products, *Health Phys.*, 48 (1985) 87-95.
- [18] Papastefanou C., Radioactivity of Tobacco Leaves and Radiation Dose Induced from Smoking, *Int. J. Environ. Res. Public Health.*, 6 (2009) 558-567.
- [19] ICRP, 2012. Compendium of Dose Coefficients based on ICRP Publication 60. ICRP Publication 119. Ann. ICRP 41(Suppl.)
- [20] Ravisankar R., Sivakumar S., Chandrasekaran A., Jebakumar P.P., J, Vijayalakshmi I., Vijayagopal P., Venkatraman B., Spatial distribution of gamma radioactivity levels and radiological hazard indices in the East Coastal Sediments of Tamilnadu, India with Statistical Approach, *Radiat. Phys. Chem.*, 103 (2014) 89-98.
- [21] NEA-OECD, Exposure to Radiation from Natural Radioactivity in Building Materials. Report by NEA Group of Experts of the Nuclear Energy Agency. OECD, Paris, France, (1979).
- [22] Eke C., Comparison of Radioactivity Concentration of Potassium-40 Radionuclide in Tobacco Samples by using HPGe and NaI(Tl) Detectors, 6th ASM International Congress of Agriculture and Environment, 2018 Proceeding Book, 88-94.
- [23] Abdul-Majid S., Kutbi I.I., Basabrain M., Radioactivity Levels in Jurak and Moasel, Comparison with Cigarette Tobacco, *J. Radioanal. Nucl. Chem.*, 194 (2) (1995) 371– 377.
- [24] Chauhan P., Chauhan R.P., Measurement of Fertilizers Induced Radioactivity in Tobacco Plants and Elemental Analysis using ICAP-AES, *Radiat. Meas.*, 63 (2014): 6-11.
- [25] UNSCEAR: Report of the United Nations Scientific Committee on the Effects of Atomic Radiation. General Assembly, Thirteen session,

Supplement No:17, New York, (1958).

- [26] Farhan N., Studying the Natural Radioactivity in Some Tobacco Cigarettes Imported to Iraq from Unknown Origins, *Jordan Med. J.*, 43 (2) (2009) 83-90.
- [27] Mandic L.J., Dolic M., Markovic D., Todorovic D., Onjia A., Dragovic S., Natural Radionuclides in Cigarette Tobacco from Serbian Market and Effective Dose Estimate from Smoke Inhalation, *Radiat. Prot. Dosim.*, 168(1) (2016) 111–115.
- [28] Papadopoulos A., Altunkaynak S., Koroneos A., Unal A., Kamaci O., Distribution of Natural Radioactivity and Assessment of Radioactive Dose of Western Anatolian Plutons, Turkey, *Turkish J. Earth. Sci.*, 25 (2016) 434-455.



Investigation of the thermoluminescence properties Ti^{4+} doped MgO synthesized solid-state assisted solution combustion synthesis method

Adnan ÖZDEMİR*

Kahramanmaraş İstiklal University, Elbistan Vocational High School of Health Service, Kahramanmaraş/TURKEY

Abstract

In this study, undoped MgO and titanium (Ti^{4+}) doped MgO ceramics were synthesized using the solid state-assisted solution combustion synthesis method. The structural characteristics were investigated using X-ray diffraction (XRD) and scanning electron microscope (SEM). TL curves of the MgO: Ti^{4+} (0.1% wt) ceramic consist of three TL peaks located at 70, 250 and 290 °C with a heating rate of 2 °C/s after 1 Gy beta dose. Radioluminescence (RL) characteristic of the MgO: Ti^{4+} (0.1% wt) ceramic was studied with excitations between 200 - 1000 nm. It was found to be the four emission bands the maximums located at 327 nm (~3.79 eV), 694 nm (~1.78 eV), 715 (~1.73 eV), and 745 (~1.66 eV). Some dosimetric characteristics such as TL curve, reusability, dose-response, of the ceramic were investigated using the thermoluminescence (TL) technique using beta radiation of $^{90}Sr/^{90}Y$. Dose-response characteristics showed the integrated TL signals between 170-350 °C exhibited a linear up to 20 Gy. The experimental results showed that if it is developed of the MgO: Ti^{4+} (0.1% wt) ceramic can be considered as a dosimetric material with suitable properties in personal and medical applications.

Article info

History:

Received:14.05.2020

Accepted:19.01.2021

Keywords:

Thermoluminescence dosimetry, Titanium doped, Magnesium oxide, Radioluminescence, Radiation dosimetry, Beta-dose response

1. Introduction

Thermoluminescence dosimeters (TLDs) are used in many fields such as clinical, radiological as well as environmental. The materials close to tissue equivalent ($Z_{eff}:7.25$) are very important in clinical applications such as radiological examinations and therapeutic treatments. Magnesium oxide (MgO) known as magnesia, a p-type semiconductor with a wide bandgap ($E_g = 7.8$ eV), has been received great attention because of its fundamental and practical applications. As well as chemical stability, it has non-toxicity, tissue-equivalent with 10.7. It has a melting point of ~ 2850 °C. It has a single phase, with rock salt structure (fcc) like oxides of other alkaline earth metals, cubic structure with lattice parameters $a=b=c$ 4.23 Å. MgO ceramic is one of the investigated host materials in radiation dosimetry. But pure MgO does not exhibit high luminescence TL sensitivity to ionizing radiation, so researchers have been synthesized it with various dopants to improve the radiation sensitivity [1-6]. In the literature, there are many synthesis methods such as solution combustion, precipitation sol-gel, solid-state., etc. Wang et al.,

(2009) reported titanium doped MgO synthesized with a chemical coprecipitation method [7]. They studied

the structure analysis of the synthesized nanopowders using XRD, X-ray fluorescence (XRF), differential thermal analysis (DTA) and transmission electron microscope (TEM). Bokhimi et al., (1999) reported the MgO-TiO₂ system produced by sol-gel. They produced a stable phase of the MgO-TiO₂ system such as periclase, anatase, and rutile [8]. Barron et al., 2016 reported that TL dosimetric properties of MgO: Ce^{3+} synthesized by the solution combustion synthesis. They calcined it at 900 °C for 2 h in the air atmosphere. They have been studied its structural characterization with XRD and SEM. They were found to be linear between 0.08 and 5.33 Gy [2]. Rao et al., (1992) reported using various magnesium salts such as Mg(NO₃)₂ and their combination with magnesium oxide in a presence flux. They studied their emission characteristic. Structural characterization produced materials studied with XRD analysis. The emission spectra of Tb doped MgO as six peaks have been recorded [6]. Recently, Mokokeng et al., (2020) reported the thermoluminescence properties of MgO:Al,Li synthesized by microwave-assisted

*Corresponding author. email address: adnan.ozdemir@istiklal.edu.tr
<http://dergipark.gov.tr/csj> ©2021 Faculty of Science, Sivas Cumhuriyet University

solution combustion synthesis. They studied XRD, Energy band gap using Kubelka-Munk relation and some dosimetric properties such as dose-response [4]. Depending on the synthesis methods TL glow curve shape varies significantly in such way that synthesized by many researchers: Barron et al (2016) [2] reported 74 °C for MgO, 103 °C for MgO:Ce and 243 °C for MgO:Ce,Li; Oliviere et al., (2019) [5] reported the main dosimetric TL Peak 80 °C for MgO:Ce,Tm; 180 °C for MgO:Ce,Sm; 180 °C for MgO:Tb,Sm; 180 °C for MgO:Ce,Sm,Li; and 460 °C for MgO:Ce,Yb,Li; Barron reported the main dominant TL peak 80,215,270 °C for MgO:Ce,Li; Barron et al., (2011) [9] reported the temperature TL Peak at 70 °C for undoped MgO, 75 °C for MgO:Tm,Li, (70 and 220) °C for MgO:Tb,Li; and 330 °C for MgO:Eu,Li and Recently Mokofeng et al., (2020) [4] reported the dominant TL Peak TL 105 °C for MgO:Al,Li.

In the literature, there are many synthesis methods for the synthesis of luminescent materials. The material cannot be synthesized in a single step in methods such as sol-gel and solid state, which are problems of energy and time consumption. Unlike this method, solution combustion synthesis (SCS) is a versatile, simple and rapid process, time- and energy saving method which allows the effective synthesis of a variety of nanosized/polycrystal materials. It can be used that chemicals can be dissolved in water such as nitrate in the SCS method. In this study, the SCS method could not be used directly because of the Ti^{4+} ion (TiO_2) cannot be dissolved in water to obtain MgO: Ti^{4+} ceramic. Ti^{4+} activated MgO ceramic was able to synthesis using the solid state assisted solution combustion synthesis method. Solid state assisted solution combustion synthesis method has been effectively used to produce powders in shorter times in comparison with the solid-state synthesis methods. In this study, the structural characterization of the synthesized MgO: Ti^{4+} ceramic was studied with x-ray diffraction (XRD) and scanning electron microscope (SEM). Besides, radioluminescence (RL) was also studied. Some dosimetric properties of the ceramic were investigated using TL techniques.

2. Materials and Methods

Undoped and titanium (Ti^{4+}) doped MgO ceramics were synthesized as follows using solid-state assisted solution combustion method: To produce undoped MgO powder with the solution combustion synthesis method (SCS), magnesium nitrate hexahydrate ($Mg(NO_3)_2 \cdot 6H_2O$, ACS reagent, 99%, Sigma Aldrich) as the source of Mg, glycine ($C_2H_5NO_2$, ReagentPlus, 99%, Sigma Aldrich) as a fuel was dissolved via

magnetic fish in the 200 ml ionized water and placed on the hot plates at 100 °C for 30 minutes. After 30 min, the temperature of the hot plate was increased up to 250 °C until the water of the solution was held up. The powder materials were calcined at 800 °C for 2 hours to remove CO_2 , N_2 , i.e gases. Because Titanium oxide (TiO_2 , powder, 99.8% trace metals basis, Sigma Aldrich) cannot be dissolved in water, the obtained the powders to TiO_2 as a dopant pre-determined weight of Titanium in the range of 0.1 to 1 %wt by using the solid-state method was doped. Mix powders at agate mortar were kindly mixed separately. The pellets with using 30 mg powder were done under 860 kP using Carver Machine. Pellet samples were sintered at 1200 °C for 2 h to obtain the crystal form of MgO: Ti^{4+} (0.1%wt). In the end of this temperature process, ceramics, i.e., undoped MgO, MgO: Ti^{4+} (0.1%), MgO: Ti^{4+} (0.5%) and MgO: Ti^{4+} (1%) ceramics were obtained. Solid state assisted solution combustion synthesis method has been effectively used to produce powders in shorter times in comparison with the solid-state synthesis methods.

The X-ray diffraction (XRD) pattern of the MgO: Ti^{4+} (0.1%wt) ceramic was recorded with a PANalytical EMPYREAN XRD diffractometer equipped with a copper and cobalt X-ray tube using Cu-K α radiation ($\lambda=0.1541$ nm). XRD pattern was recorded in the range from 20° to 80° with the step of 0.0001° in the powder form of the MgO: Ti^{4+} (0.1%wt) ceramic. The structural characterization of the ceramic was performed using a FEI Quanta 650 SEM instrument, field-emission with 30–100 kV accelerating voltage and 100 nA probe current. SEM image of the powder MgO: Ti^{4+} (0.1%wt) ceramic was taken at 5.000X magnification. The radioluminescence (RL) spectra of the undoped MgO and MgO: Ti^{4+} (0.1%wt) pellet ceramics were taken using a homemade RL system that has an attached Ocean Optics model QE Pro (Ocean Optics USB-2000, Inc.,Dunedin, FL, USA) by f/2 collimator in front of fiber optic cable (1mm core diameter, transmission between 200 and 1100 nm) throughout the CCD detector while irradiating by mini x-ray tube operated at from 4 kV up to 40 kV for stimulating the ceramics. RL measurements of ceramic pellets were recorded in the range from 200 to 1000 nm. All TL measurements were carried out by the Riso TL/OSL DA-20 device, equipped with a $^{90}S/^{90}Y$ beta source (40 mCi) in calibrated geometry and delivering a dose rate of 6.689 Gy/min. A Schoot BG 39 filter was used at all TL measurements in the front of Photo Multiple Tube (PMT), which is EMI 923QB. In this study, the dosimetric characteristic of MgO: Ti^{4+} (0.1%wt) pellet ceramics were investigated by taking the integrated TL

signals between 170-350 °C, which is the main dosimetric TL peak of ceramic. In this study, unless otherwise stated, all TL measurements were recorded using pellet ceramic. The same samples ceramics were used all TL experiments and before ceramics were annealed at 400 °C for 20 min. TL curves were recorded with the heating rate of 2 °C/s after preheating 170 °C, following 1 Gy dose.

3. Results and Discussion

3.1. X-ray diffraction (XRD)

X-ray diffraction (XRD) analysis was carried out to determine whether the material has the targeted crystal structure after a series of temperature process to obtain crystal form and also whether the amount of dopant ions concentration changes the main crystal structure. The MgO:Ti⁴⁺(0.1%wt) ceramic synthesized using solid-state assisted SCS after calcination at 800 °C for 2 h and following it sintered at 1200 °C for 2 h was determined using the XRD analysis. Fig. 1 shows the XRD pattern of the MgO:Ti⁴⁺(0.1% wt) ceramic. The diffraction peaks of the MgO:Ti⁴⁺(0.1% wt) ceramic matched to the standard ICDD number of 98-015-7523 in terms of peak position and intensity. The crystal structure was cubic with lattice parameters a=b=c=4.235 Å. The XRD results indicated the crystalline phase of MgO:Ti⁴⁺(0.1% wt) the dominating for these temperature processes. XRD results showed that Ti⁴⁺ introduced to MgO lattice did not significantly change the crystal lattice of MgO. As a result, the material was successfully synthesized using the solid state assisted solution combustion synthesis method.

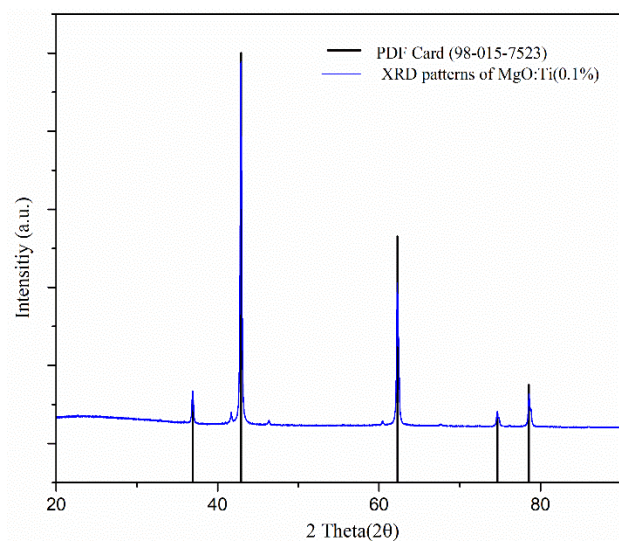


Figure 1. XRD patterns of the MgO:Ti⁴⁺(0.1% wt) ceramic with reference peaks (PDF Card No:98-015-7523).

3.2. Scanning electron microscope (SEM)

The scanning electron microscopy (SEM) was used to examine the surfaces of the MgO:Ti⁴⁺(0.1%wt) ceramic. The surface morphology of the MgO:Ti⁴⁺(0.1%wt) ceramic powder was taken at 5.000X magnification. Fig. 2 shows the SEM image of the ceramic synthesized using solid-state assisted SCS after calcination at 800 °C for 2 h and following it sintered at 1200 °C for 2 h. As seen in Fig. 2, the SEM images show the non-homogeneous and irregular shape structure. These structures were likely attributed to the non-uniform temperature distribution during synthesis.

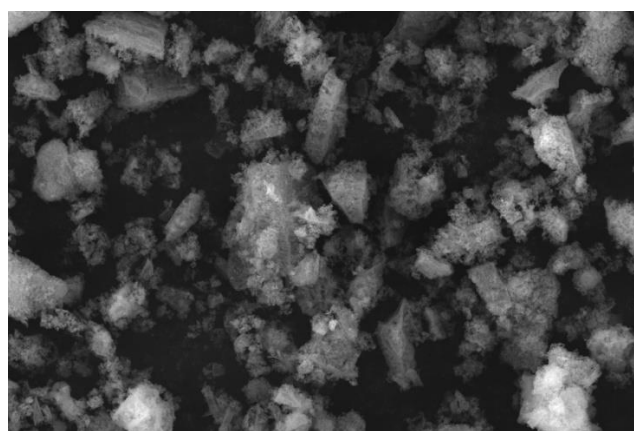


Figure 2. SEM image of the MgO:Ti⁴⁺(0.1% wt) ceramic. Magnification is 5.000X.

3.3. Radioluminescence (RL)

Radioluminescence (RL), known as also X-ray Luminescence (XL), spectra were measured to study the morphology of bulk and surface defects involved in the luminescence processes stimulated by the volume penetrated by ionizing radiation. RL spectra of the undoped MgO and MgO:Ti⁴⁺(0.1% wt) pellet ceramics were recorded in the range from 200 nm to 1000 nm at room temperature. Fig 3. shows the RL spectra of the undoped MgO and MgO:Ti⁴⁺(0.1% wt) ceramics. The three emission peaks for undoped MgO was recorded at near-infrared regions at 694, 715, 745 nm. When Ti⁴⁺ was introduced to MgO lattice crystal, the four emission peaks were located at 327, 694, 715 and 745 nm. As seen in Fig. 3, both undoped MgO and MgO:Ti⁴⁺(0.1% wt) ceramics show similar peak shape and maximum, which indicates that the luminescence most likely originated from the same groups of traps.

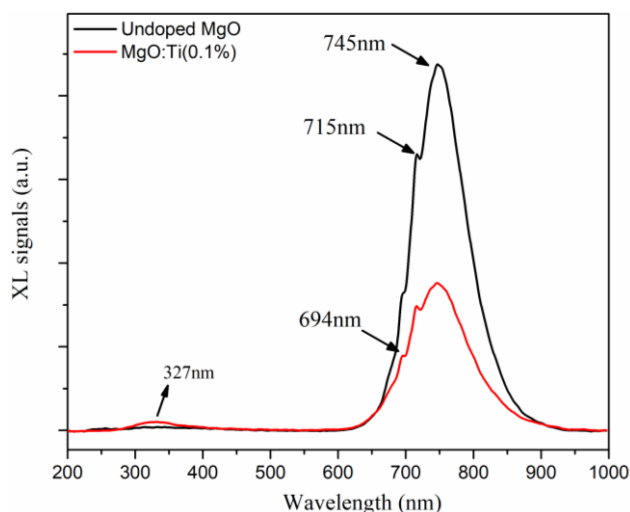


Figure 3. Radioluminescence (RL) spectra of the undoped MgO and MgO:Ti⁴⁺(0.1% wt) ceramics in the range of 200-1000 nm.

3.4. TL glow curve

Fig. 4 shows the comparison TL curves of undoped MgO, MgO:Ti⁴⁺(0.1% wt), MgO:Ti⁴⁺(0.5% wt) and MgO:Ti⁴⁺(1% wt) ceramics after 1 Gy beta dose with a heating rate of 2 °C/s from room temperature to 450 °C. TL curve of the undoped MgO consists of three TL peaks located at 90 °C, 250 °C and 290 °C, respectively. The main dosimetric TL peak characteristic of undoped MgO is 250 °C and 290 °C does not significantly change when the Ti⁴⁺ ions are introduced to the crystal lattice of MgO. TL signals of the main dosimetric TL peak that located between 190 and 350 °C has been increased by ~7.5, 5.6 and 4.2 times for MgO:Ti⁴⁺(0.1% wt), MgO:Ti⁴⁺(0.5% wt) and MgO:Ti⁴⁺(1% wt), respectively while TL signals at 90 °C is decreasing by ~ 0.4, 0.24 and 0.14 times for MgO:Ti⁴⁺(0.1%), MgO:Ti⁴⁺(0.5% wt) and MgO:Ti⁴⁺(1% wt), respectively. The best TL signal was recorded for MgO:Ti⁴⁺(0.1% wt). With the incorporation of Ti⁴⁺ ions into the MgO lattice, Ti⁴⁺ doping can lead to increasing the trap centers (recombination centers) in the forbidden gap of the ceramic. Dosimetric characteristics of the MgO:Ti⁴⁺(0.1% wt) ceramics were investigated among the aforementioned ceramics. The high TL peaks of the MgO:Ti⁴⁺(0.1% wt) located at 250 and 290 °C are suitable for dosimetric investigation.

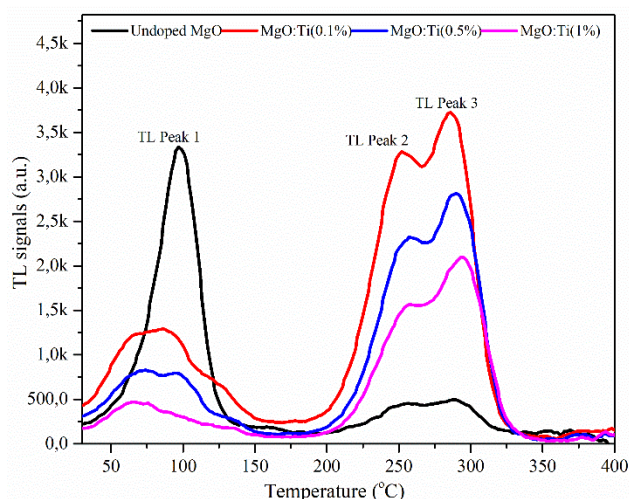


Figure 4. TL curves of the synthesized all ceramics, i.e., undoped MgO, MgO:Ti⁴⁺(0.1% wt), MgO:Ti⁴⁺(0.5% wt) and MgO:Ti⁴⁺(1% wt) after 1 Gy dose.

3.5. Preheat experiment

Preheat experiments are important for the study of thermal stability and in the identification of the nature of the traps responsible for the TL signals. In order to determine the preheat temperature of the MgO:Ti⁴⁺(0.1% wt) ceramic, TL curves were separately recorded after preheating at pre-determined temperatures between 50-300 °C with the step of 10 °C and 20 °C for preheating temperature time of 10 s after 1 Gy dose, following after the ceramic were annealed at 400 °C for 20 min. Then, a TL reading at a heating rate of 2 °C/s up to 450 °C was performed in order to delete residual signals each after TL measurements. The integrated TL signals between 170-350 °C were recorded. The graphic was drawn integrated TL signals vs preheat temperature (Fig 5.). As seen in Fig. 5., temperature about 200 °C has a stable region, if the temperature region >200 °C, the sharp reduce is recorded up to 300 °C. The main reason for this reduction is the decrease of trapped charge population in this range temperature. The preheat temperature of the MgO:Ti⁴⁺(0.1% wt) temperature was selected as a 170 °C. Guckan et al., (2020) [3] reported OSL preheat temperature of MgO:Na,Li ceramic as a 130 °C for 10s.

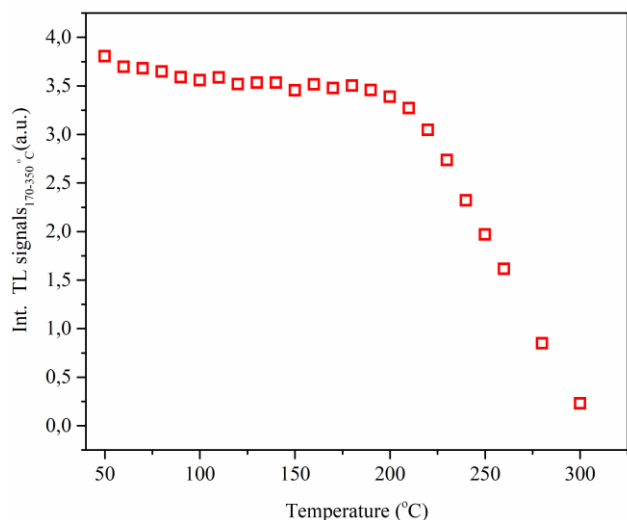


Figure 5. The graphic of preheating for MgO:Ti⁴⁺(0.1% wt) ceramic in the range from 50-300 °C after 1 Gy dose.

3.6. Dose-response experiment

TL sensitivity of thermoluminescent dosimeter (TLD) phosphor to ionizing radiation would ideally be linear over a range of doses. Dose-response of the MgO:Ti⁴⁺(0.1% wt) ceramic was studied in the range of 0.1 Gy–20 Gy. The dose values were taken as 0.1, 0.2, 0.5, 1, 2, 5, 10 and 20 Gy. TL curves were recorded after preheating at 170 °C for 10s with a heating rate of 2 °C/s from room temperature to 450 °C for each dose. Fig. 6 shows a graphic of the integrated TL signals between 170-350 °C data versus absorbed dose. The data points were fitted with a linear function which is given $y=a+bx$, where and its parameters were given as insert table in Fig 6. The slope of the plotted graphic was found to be 1.03. The results indicate the response of ceramics was linear in the 0.1 Gy to 20 Gy.

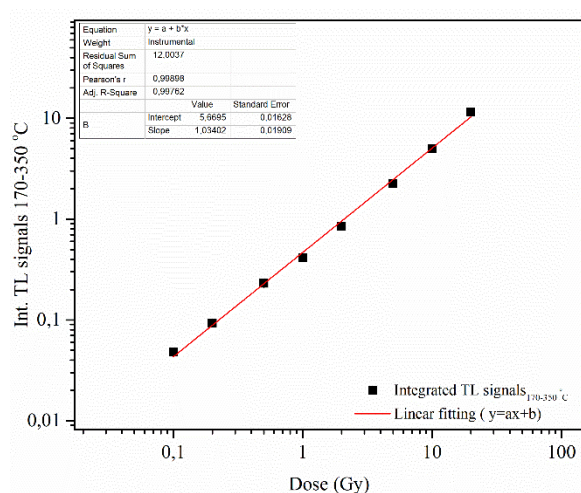


Figure 6. Dose-response of the MgO:Ti⁴⁺(0.1% wt) ceramic.

3.7. Reusability experiment

Reusability is one of the most significant properties that almost every dosimetric material should possess. One of the biggest advantages of thermoluminescence dosimeters (TLDs) is that it can be used repeatedly. The reusability characteristic of the ceramics was studied up to ten experimental cycles under beta radiation. The TL curves were recorded with a heating rate of 2 °C/s after preheating 170 °C for 10 s after 1 Gy beta dose. Then A TL readout was done to delete the remaining signals after reading. Fig. 7 shows (a) the normalized integrated TL signals which are between 170-350 °C versus the number of experimental cycles (b) TL glow curves after reading. As seen in Fig. 7., the reusability showed at 4% standard deviation up to the first readout at the end of ten cycles. This deviation might originate from; (i) variations in the effective number of total traps, (ii) reader system.etc. This deviation was with acceptance limits of 5% [10]. As a result, the ceramic possesses a good reusability under the same experimental conditions.

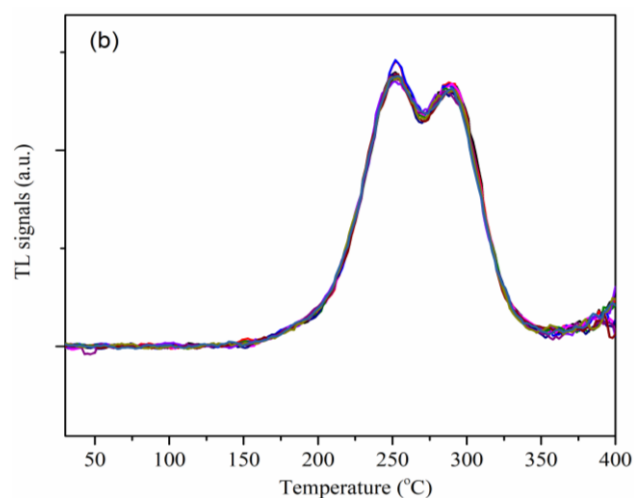
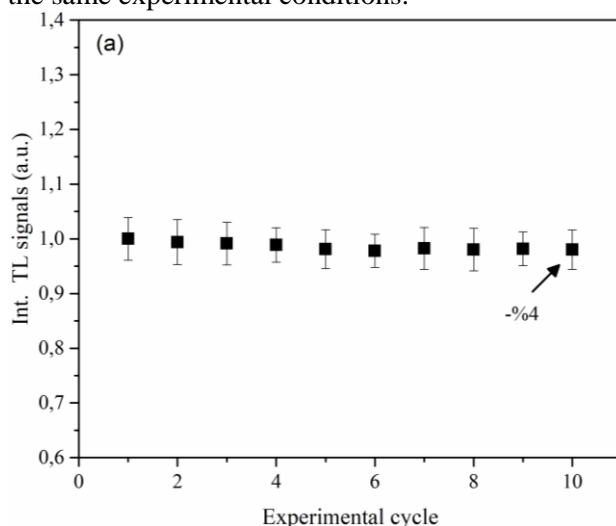


Figure 7. (a) Normalized TL signal (Integrated 170-350 °C) according to the first TL read, (b) TL glow curve after preheating 170 °C up to ten experimental cycles.

4. Conclusions

In this study, the SCS method could not be used directly because of the Ti^{4+} ion (TiO_2) cannot be dissolved in water to obtain the titanium doped MgO ceramics. Ti^{4+} doped MgO ceramic was able to synthesis the using the solid state assisted solution combustion synthesis method. The structural characterization of the synthesized ceramic was studied using the XRD and SEM techniques. XRD results showed that MgO: Ti^{4+} (0.1%wt) ceramic was successfully synthesized by the abovementioned method. RL characteristic of the ceramic showed four emission peaks located at 327, 694, 715 and 745 nm. Some dosimetric properties of the MgO: Ti^{4+} (0.1%wt) ceramic such as dose-response, reusability were reported. The dose-response was studied in the range from 0.1 to 20 Gy, showing a linear response over this range. The ceramic has good reusability up to 10 cycles with the standard deviation of 4% according to the first TL readout under the same experimental condition. The experimental results showed that if it is developed this ceramic can be considered as a dosimetric material with suitable properties in personal and medical applications.

Acknowledgments

The author would like to address a special thank you to Prof. Dr. Zehra Yegingil. Besides, the author wants to address thank research assistant Volkan Altunal and PhD student Veysi Güçkan for their support for TL measurements. This research was supported by the NATO (Science for Peace and Security Programme) under project number SFP MYP G5647.

Conflicts of interest

The author state that did not have conflict of interests.

References

- [1] Alajerami Y., Hashim S., Ghoshal S., Saleh S., Kadni T., Saripan M., Alzimami K., Ibrahim Z., Bradley D., The effect of TiO_2 and MgO on the thermoluminescence properties of a lithium potassium borate glass system, *J. Phys. Chem. Solids.*, 74 (2013) 1816-1822.
- [2] Barrón V.R.O., Ochoa F.M.E., Vázquez C.C., Bernal R., Thermoluminescence of novel MgO–CeO₂ obtained by a glycine-based solution combustion method, *Appl. Radiat. Isotopes.*, 117 (2016) 86-90.
- [3] Guckan V., Altunal V. Ozdemir A., Yegingil. Z., Optically stimulated luminescence of MgO:Na,Li phosphor prepared using solution combustion method, *J. Alloy. Compd.*, 835 (2020) 155253
- [4] Mofokeng S., Noto L., Mlotswa D., Orante-Barrón V., Dhlamini M., Thermoluminescence properties of MgO:Al³⁺-Li⁺ prepared by microwave-assisted solution combustion method, *Physica B.*, (2020) 412008.
- [5] Oliveira L., Yukihiro E., Baffa O., Lanthanide-doped MgO: A case study on how to design new phosphors for dosimetry with tailored luminescent properties, *J. Lumin.*, 209 (2019) 21-30.
- [6] Rao R., Duley W., Preparation and luminescence of MgO:Tb phosphors, *J. Mater. sci.*, 27 (1992) 5883-5886.
- [7] Wang W., Qiao X., Chen J., Tan F., Li H., Influence of titanium doping on the structure and morphology of MgO prepared by coprecipitation method, *Mater. Charac.*, 60 (2009) 858-862.
- [8] Bokhimi X, Boldú J, Munoz E., Novaro O., López T, Hernández J., Gómez R., García-Ruiz A., Structure and composition of the nanocrystalline phases in a MgO–TiO₂ system prepared via Sol–Gel technique, *Chem. Mater.*, 11 (1999) 2716-2721.
- [9] Orante-Barrón V., Oliveira L, Kelly J., Milliken E., Denis G, Jacobssohn L., Puckette J., Yukihiro E., Luminescence properties of MgO produced by solution combustion synthesis and doped with lanthanides and Li, *J. Lumin.*, 131 (2011) 1058-1065
- [10] Furetta C, Handbook of thermoluminescence, Singapore: World Scientific, (2010).



Systematic discrimination of heptane isomers with femtosecond laser linear time of flight mass spectrometry

Yasemin GÜNDOĞDU^{1,2} , Mehmet TAŞER³ , Hamdi Şükür KILIÇ^{2,3,4,*}

¹Selçuk University, Kadınhanı Faik İçil Vocational High School, Department of Computer Technologies, Konya / TURKEY

²Selçuk University, Directorate of Laser Induced Proton Therapy Application and Research Center, Konya / TURKEY

³Selçuk University, Faculty of Science, Department of Physics, Konya / TURKEY

⁴Selçuk University, Directorate of High Technology Research and Application Center, Konya / TURKEY

Abstract

The dissociative ionization processes of heptane molecule with nine isomers have been investigated and presented experimentally in detail by courtesy of femtosecond laser mass spectrometry technique with a fundamental wavelength of 800 nm and 90 fs pulse duration in this study. It has been aimed to show that the classification of heptane isomers using factor analysis as statistical method reducing the dimension of obtained data. The main mass ratio of heptane isomers is known as m/z 100 which is obtained. The dissociation process on the parent molecule was dominant at the laser intensity about 1.42×10^{14} W/cm² used for all isomers. The ions obtained by the breakdown of the main ion peak were primarily determined as factors which were clearly distinguished from each other according to factor 1 and factor 2 axes by applying factor analysis.

Article info

History:

Received: 24.07.2020

Accepted: 18.02.2021

Keywords:

Femtosecond,
Laser,
Mass spectroscopy,
Heptane,
Isomers.

1. Introduction

Alkanes are saturated hydrocarbons with sp^3 hybrid orbitals with some general properties reactive and low biological activity. In addition, the carbon atoms in the alkane group are covalently bonded to each other. Isomers of heptane molecule are known as the aliphatic alkanes (C_nH_{2n+2}) molecules which are called saturated hydrocarbons [1]. Alkanes are formed by bonding hydrogen atoms and carbon atoms to a single carbon-carbon bond. At the same time, another common feature of the molecules in this group is that they are colorless and odorless [2, 3]. The structure forms of heptane isomers (C_7H_{16}) alkane group molecules are in chain structure [4] which are formed by different binding of the methyl (CH_3) group to carbon atoms included in the class of organic molecules [5, 6]. Heptane isomers are all important organic molecules in which their solubilities are well due to low reactivity just as water. The understanding of the character of the heptane molecule will contribute to technology by expanding its areas of use.

Mass spectroscopy (MS) technique and statistical approaches are well known methods to understand structures of chemical, biological or other types materials. MS technique has been used in the process

from the mid-19th century to the present. After the discovery of laser in 1960s, laser ionization mass spectrometry is one of the most widely used techniques in research studies [7]. The most widely used energy source in mass spectrometry in recent years seems to be lasers. Mass spectrometry is also used to determine the molecular characteristics of chemical or biological samples with different laser types. Molecular analysis of high purity metals, alloys, semiconductors, insulators, biological and medical materials, geological samples, nuclear and radioactive materials can be carried out accurately by MS [8-11].

Studies on the determination of thermodynamic, structural and dynamic properties of heptane isomers are presented in literature, but information on the studies on molecular ionization / fragmentation / dissociation processes are limited [5, 6]. In this work, it has been elaborated on dissociative ionization of heptane isomers, and some of their physical and chemical properties of heptane isomers have also been discussed using their mass spectra. Factor analysis (FA) has been applied to focus the distinguish its isomers [12-18]. Femtosecond laser mass spectrometry (FLMS) makes possible to detect and analysis molecules which have been developed by group members as an important analytical tool in MS

*Corresponding author. e-mail address: hamdisukurkili@selcuk.edu.tr

<http://dergipark.gov.tr/csj> ©2021 Faculty of Science, Sivas Cumhuriyet University

technique [8]. Studies on the ionization, dissociation and fragmentation processes of different types of molecules are included by using time of flight mass spectrometry in literature [8-11, 19].

FA has been used commonly in social sciences and in psychology initially, but currently, the method is widely used to distinguish chemicals as well as all areas of science. FA has been defined and situated as a multi-variation analysis method in literature and applied to the obtained spectra and the results compared to those obtained from some other statistical approaches [20-23].

Interpretation of mass spectra take quite a long time and also these data are massive and large dimensional. The main purpose of the application of the FA statistical technique is to achieve the most important information from the data obtained. In general mass spectra are monitored using imaging technique, using statistical approaches give more information such as monitoring, discrimination and also investigation. The most important goal in distinguishing isomers, which are very similar to each other, is to reach a more advanced position in distinguishing cancer and healthy tissues [22, 23].

In this study, FA statistical approach has been used to analyse isomers of heptane organic molecule. The factors mentioned characteristic peaks in the mass spectrum recorded with a computer program and FA statistical approach has been applied to the results to be analysed. The main objective of this study is on to distinguish and classification of nine heptane isomers of heptane molecule by gathering the most important information from the spectral data using factor analysis. In this way, reducing the dimensions of data makes the explanation of spectra is much simpler. The discrimination of the nine-isomer of heptane molecule obtained in this study by factor analysis paves the way for the differentiation of multiple cancerous and healthy tissues [21-22].

2. Materials and Methods

2.1 Femtosecond laser properties

The femtosecond (fs) laser system connected to a home-made linear time of flight mass spectrometer system was used to analyse the liquid form of nine heptane isomers to distinguish them by using FA method.

The experimental apparatus used in this study depicted in Figure 1 consists of a femtosecond laser system, a vacuum chamber and a data acquisition system. The fe laser system consists of three main parts which are

an oscillator, and amplifier and a optical parametric amplifier (OPA) systems. The oscillator (Ti: Light, Quantronix, NY, USA) delivers 90 fs laser pulses at 800 nm wavelength with an 85 MHz repetition rate. The amplifier (Integra-C-3.5, Quantronix, NY, USA) is pumped by Ti-Light oscillator and generates amplified laser pulses at 800 nm wavelength and 90 fs laser pulses at a 1-3 kHz repetition rates. The laser amplifier system produces maximum 3.5 W power per pulse and its output is controlled by using a circular neutral density filter and the energy of the laser beam was measured by using a neutral density filter. Experimental details used in this study have been described in detail in previous studies [9, 20-23]

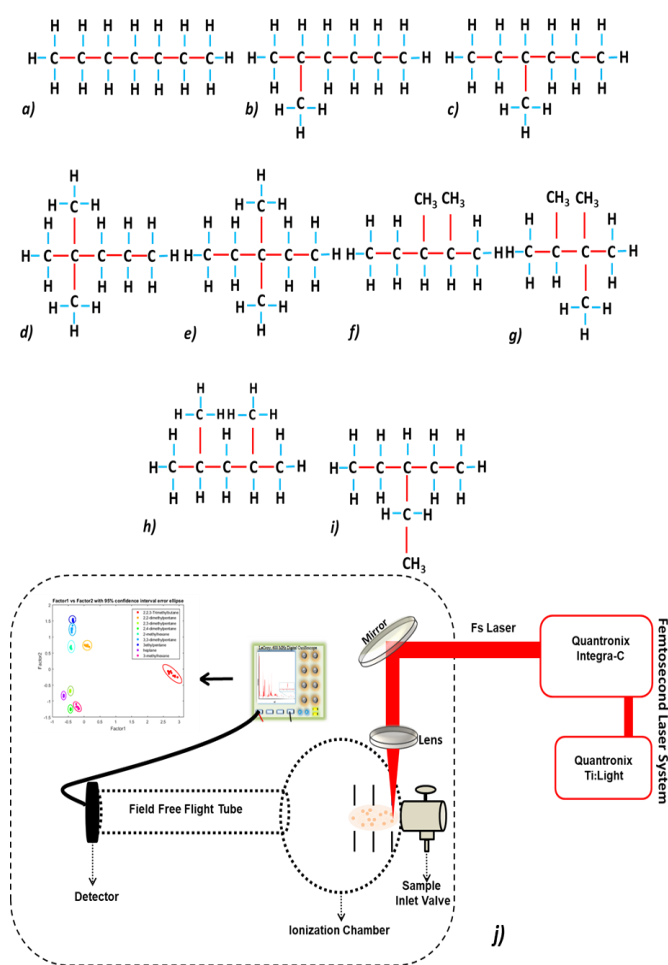


Figure 1. Schematic representation of heptane isomers a) n-heptane, b) 2-methylhexane, c) 3-methylhexane, d) 2,2-dimethylpentane, e) 3,3-dimethylpentane, f) 2,3-dimethylpentane, g) 2,2,3-Trimethylbutane, h) 2,4-dimethylpentane, i) 3-ethylpentane, j) experimental systems consist of a femtosecond laser system, vacuum chamber and data acquisition systems.

2.2 Linear time of flight mass spectrometer properties

The Linear time of Flight (L-TOF) mass spectrometer system was built in local industrial zone in Konya, in the design of Wiley and McLaren [24]. The background pressure in the vacuum chamber can be pumped down to several times 10^{-8} mbar, but during the experiment, sample pressure was kept very stable about 1.6×10^{-6} mbar [21-23, 25].

The mass spectra signal was taken by a MCP detector directly to an oscilloscope and recorded in a four channel fast digital oscilloscope (LeCroy, WaveRunner 64Xi, 600 MHz) connected with a server computer. All recorded mass spectra were taken averaging over 1000 laser shots and recorded as mass spectra in oscilloscope. The spectra of the heptane isomers have been recorded using laser intensities from 7.12×10^{12} W/cm² to 1.42×10^{14} W/cm². The fs laser beam was sent to the laser ionization area in the mass spectrometer where it was focused down to several micrometers (μm) spot area using a lens with a focal length of 25 cm. The purities of used heptane isomers are $\geq 99\%$ in this study.

3. Results and Discussion

FA has been known as one of the dimension reduction methodological approach. Linear combination of used factors is given as:

$$F_i = W_{i1}X_1 + W_{i2}X_2 + W_{i3}X_3 + \dots + W_{ik}X_k$$

$$F_i = i_{\text{th}} \text{ Factors}$$

$$W_i = i_{\text{th}} \text{ Score correlation}$$

$$k = \text{the number of variables}$$

i_{th} set factor score coefficient explains the maximum value of the total variance of the factor [23]. Generally, the formula for factor analysis is given by Equation 1

$$S = V^f R^f V^f + (D_s - H) \quad (1)$$

where S is the correlation matrix of existing variables. V^f is orthogonal and therefore R^f is defined as an identity matrix. After then, the equation 1 is simply rewritten to be

$$S = V^f V^f + (D_s - H) \quad (2)$$

where D_s is a diagonal matrix with diagonal elements S , and H is another diagonal matrix. The diagonal elements of $D_s - H$ are monovalent in equation 2. The factor analysis calculations were carried out by Matlab program considering equation 1 and equation 2 procedure for determined f factors [23, 27, 28].

The m/z 27, 29, 39, 40, 41, 42, 43, 44, 53, 55, 56, 57, 58, 69, 70, 71, 85 and 100 values were used as factors in this study. Main peaks in mass spectra of heptane molecule according to the information for the organic compounds mass/charge (m/z) ratios were obtained by only one electron ionization in NIST database [29].

Algorithm of factor analysis applied in this work is given as in figure 2.

Femtosecond Laser Mass Spectroscopy

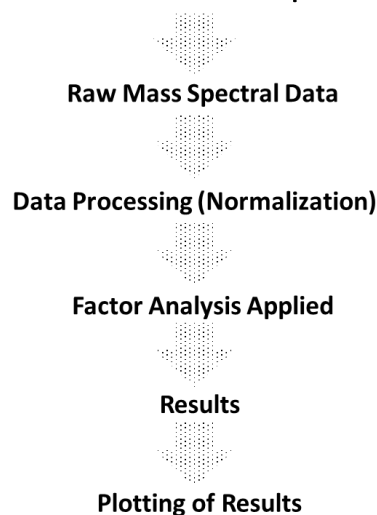


Figure 2. Implemented process of factor analysis to heptane isomers is given.

According to Figure 2, the first of all, the analysis of heptane isomers using FLMS method was recorded by performing experiment using different laser powers with the wavelength of 800 nm. The experimental process was completed by using the parameters given in the experimental part by storing 10 consecutively data savings by courtesy of a four channels digital storage oscilloscope from each spectrum, keeping all parameters constant at the same laser power. Since all recorded spectra were obtained from the oscilloscope depending on the flight time where all flight times were converted to mass units according due to the formula $m = at^2 + b$. One of the important conditions in the experimental process is determination of optimum laser parameters such as laser pulse power, focal point and laser incidence angle. At the same time, it is very important to keep the vacuum conditions stable during the experiment. Keeping all of the determined laser parameters unchanged during the experiment will minimize the experimental error. In the next step, after ensuring the data is recorded carefully, the largest peak in the spectra recorded in m/z was normalized and normalization was applied to all spectra. All these processes were carried out using a MATLAB code produced by our group. The resulting data were plotted and shown in Figure 5.

3.1 Femtosecond laser ionization of heptane isomers

It is well known that in molecules having chain structure, the breakdown of the bond structures occurs either easily or faster than other types of molecules. Detection of parent ion peak at $C_7H_{16}^+$ (m/z 100) without any dissociation taken place is very difficult since the structure of molecules are in chain structures and lifetime in the excited state are very short. Generally, ion peaks with masses smaller than the parent ion are predominant in mass spectra pattern for such ionization processes. In this case, the interpretation of mass spectra makes it difficult to explain for molecules fragmented within a laser pulse duration. Alternative theoretical studies are needed for this to be interpreted clearly.

The spectra of the heptane isomers have been recorded using laser intensities of 7.12×10^{12} W/cm² and 1.42×10^{14} W/cm² and mass spectra are given in Figure 3. When the obtained peak intensities are investigated, it can be seen from Figure 3 that all isomers have similar peak intensities for small m/z range in mass spectra, such as $C_1H_n^+$, $C_2H_n^+$, $C_3H_n^+$.

In Figure 3, noteworthy peak intensities are H^+ , C^+ , CH^+ , CH_2^+ , CH_3^+ , $C_2H_n^+$ ions in the $C_1H_n^+$ ion group, C_2^+ , C_2H^+ , $C_2H_2^+$, $C_2H_3^+$, $C_2H_4^+$, $C_2H_5^+$ ions in $C_2H_n^+$ ion group, C_3^+ , C_3H^+ , $C_3H_2^+$, $C_3H_3^+$, $C_3H_4^+$, $C_3H_5^+$, $C_3H_6^+$, $C_3H_7^+$, $C_3H_n^+$ ion group and $C_4H_8^+$ and $C_4H_9^+$ ions in $C_4H_n^+$ ion group are seen clearly from recorded spectra which were obtained by applying 1.42×10^{14} W/cm² laser intensity.

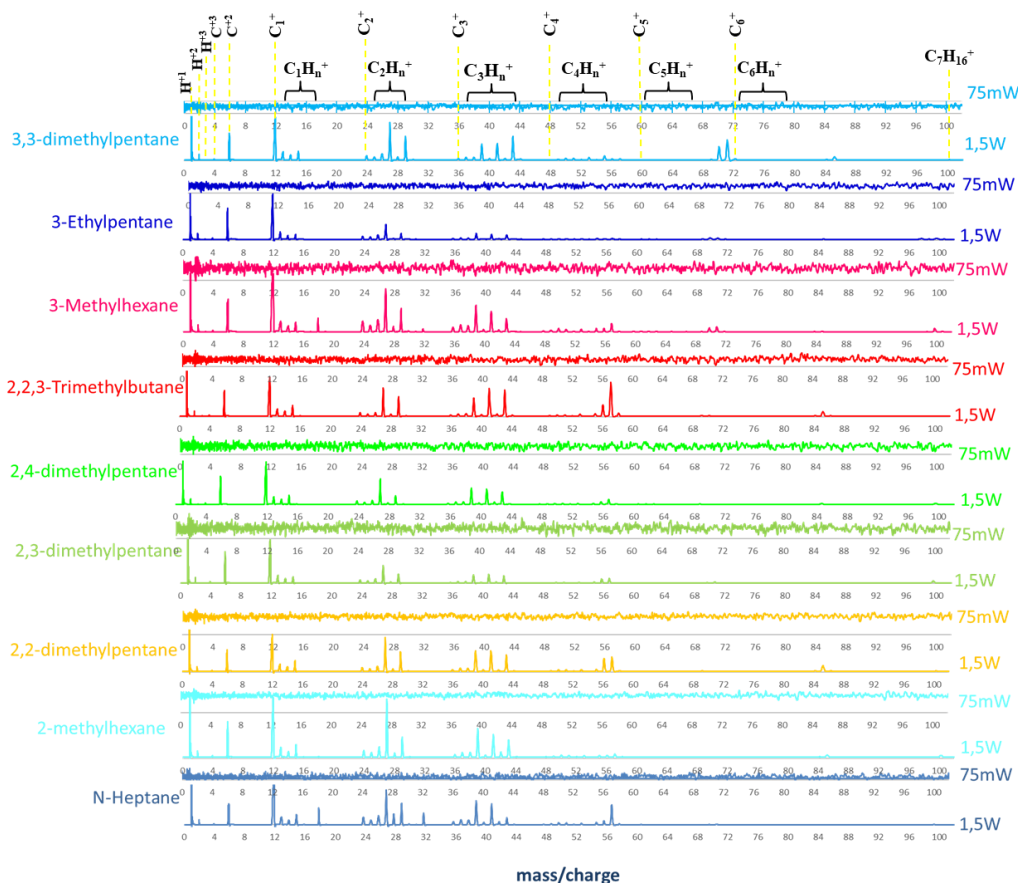


Figure 3. n-heptane, 2-methylhexane, 2,2-dimethylpentane, 2,3-dimethylpentane, 2,4-dimethylpentane, 3-methylhexane, 3-ethylpentane, 3,3-dimethylpentane, 2,2,3-Trimethylbutane were obtained minimum 75 mW laser power and also maximum 1.5 W laser power.

The parent ion peak $C_7H_{16}^+$ (m/z 100) was magnified about a hundred times to show in spectra in Figure 4. All recorded fragment ion peaks at m/z 27, 29, 39, 40, 41, 42, 43, 44, 53, 55, 56, 57, 58, 69, 70, 71 values and also main peak at m/z 100 amu were obtained in spectra shown in Figure 4. The parent ion peak was appeared since the spectrum is magnified. The

multiply charged ions like C_n^+ ($n=2, 3, 6$) are clearly recorded in the spectra for all heptane isomers with the intensity range from 7.12×10^{12} W/cm² to 1.42×10^{14} W/cm².

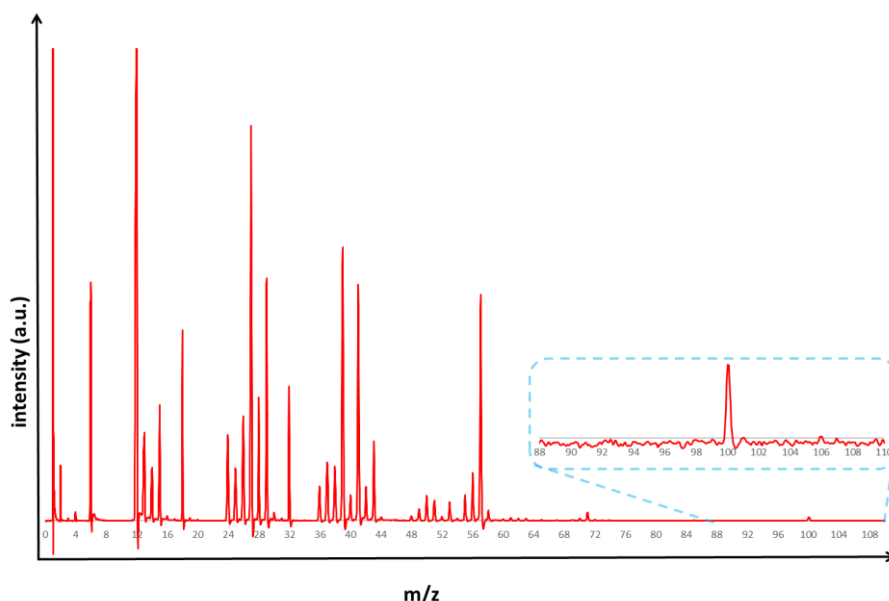


Figure 4. n-heptane was recorded 1.5 W laser power and the parent ion m/z 100 was appeared after the magnification is increased.

The interpretation of data from mass spectrometry takes quite long time and also these data is massive and in very large dimensions. The main purpose of the application of FA statistical technique is to achieve the most important information from the data obtained.

3.2 Factor analysis for Heptane isomers

It is important that the discrimination of the factor components by using FA method which is known as a powerful analysis procedure to distinguish isomers as we have discussed in a number of previous work and give it in literature [20-23]. In laser-based mass spectrometry technique, fragment ions are produced where dissociative ionization process are investigated intensively in mass spectra. The dissociation may become more significant when the interpretation of the data obtained is only meaningful, that is, given the peak intensities specifically appeared in each spectrum. The data obtained in many fields of science, including interdisciplinary fields in the direction of technological developments can reach to very large and high dimensions. The data obtained in mass spectrometric studies can be given as an example [21, 23].

In the process of discrimination of nine isomers using FA, it was shown that the peaks, that are distinct from the spectra, are distinguished from each other by FA. MS data has been recorded as a function of laser power and factors have been determined from the recorded spectra.

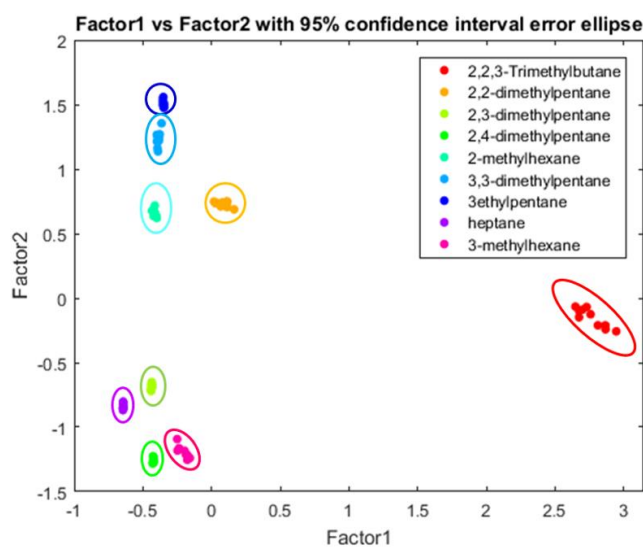


Figure 5. The Factor Analyse result of normalized data from the mass spectra of 9 heptane molecular isomers is given as a result of analysis of isomers that are clearly differentiated each other factor 1 and factor 2 axes

The data used in FA were generated in two dimensions by plotting code in MATLAB program [20, 21]. One of the points in the data of each isomer given in figure 5 was obtained as a result of 10 repetitions of successive recording of spectrum by averaging over 1000 laser shots and this repetition process was obtained using 1.5 W laser power and 800 nm laser wavelength in infrared region. Heptane molecular isomers can be distinguished from each other in factor 1 and factor 2 axes. Data recording and FA application process were performed by running the program codes written in MATLAB programming language by our group [20-23]. With the TCP/IP protocol, the data

were recorded via oscilloscope in accordance with the parameters were determined during the experiment and they were made ready for the next step, FA.

In figure 5, the mass spectra of nine heptane molecular isomers which were normalized as a result of analysis of isomers that were clearly differentiated from each other in factor 1 and factor 2 axes that are symbolized in two dimensions on axes. The process of discrimination is interpreted by looking at these axes.

4. Conclusion

The ionization/fragmentation process of heptane isomers have been demonstrated by using FLMS technique [8]. As a result of interaction between ultrafast laser beam and molecule, since the lifetime of molecules in the excited states are so short, heptane molecular isomers dissociate very fast and therefore it is very difficult to obtain a dominant parent ion in the mass spectra of each isomer. Under these circumstances, even using smaller mass fragment ion peaks, the structure and dissociative ionisation, fragmentation dynamics of molecular isomers have been clearly revealed, and important contributions may be made to literature due to this important data. Fs laser system using 800 nm wavelength, 1 kHz repetition rate, 90fs pulse duration and depending on the varying laser power, ionization and dissociation & fragmentation dynamics for nine isomers of heptane molecule using FLMS technique was clearly analysed and data have been interpreted clearly due to the used statistical analysis.

The m/z ratios of heptane molecular (C_7H_{16}) isomers have the same, all 100, molar mass. While it is possible for some molecular isomers to be distinguished while they have isomers of molecules in the same mass but in different binding forms, it is sometimes difficult to distinguish these in visual spectra. When statistical methods are applied to the spectra obtained for this purpose, the distinguishing these isomers becomes much more meaningful. From this point, it is shown that each isomer can be clearly distinguished from each other by applying FA method. The most important goal in distinguishing isomers, which are very similar to each other, is to reach a more advanced position in distinguishing cancer and healthy tissues.

Therefore, it can be given as a final conclusion that the life time of the molecules in the excited state are very short in comparison with laser pulse duration (90 fs) [8, 9, 19, 29], and within a 90fs laser pulse duration, the access of molecular parent ion is very difficult, and no or very small ion peak at m/z 100 were obtained as seen from Figure 4.

Acknowledgment

Authors kindly would like to thank to,

-Scientific Research Projects Coordination Unit of Selçuk University for financial support via Projects No 17401152 and 20401046.

-Selçuk University, High Technology Research and Application Center (İL-TEK) and SULTAN Center for infrastructures

Conflicts of interest

The authors state that did not have conflict of interests

References

- [1] Ess D.H., Liu S., De Proft F., Density functional steric analysis of linear and branched alkanes, *J. Phys. Chem. A*, 114 (2010) 12952-12957.
- [2] Yagil G., Nadel L., Stein D., On the structural complexity of templated systems, Rehovot, Israel, The Weizmann institute of Science, (1992).
- [3] Arora A., Hydrocarbons (Alkanes, Alkenes and Alkynes), Discovery Publishing House (2006).
- [4] Edgar G., Calingaert G., Marker R., The preparation and properties of the isomeric heptanes. part i. preparation1, *J. Am. Chem. Soc.*, 51 (1929) 1483-1491.
- [5] Lavanchy A., Houriet R., Gäumann T., The mass spectrometric fragmentation of n-heptane, *Org. Mass. Spectrom.*, 13 (1978) 410-416.
- [6] Chen J.-H., Dunbar R.C., Fragmentation of n-heptane ions by photodissociation, *Int. J. Mass Spectrom. Ion Processes*, 72 (1986) 115-123.
- [7] Maiman T.H., Stimulated optical radiation in ruby, *Nature*, 187 (1960) 493-494.
- [8] Kilic H.S., Ledingham K., Kosmidis C., McCanny T., Singhal R., Wang S., Smith D., Langley A., Shaikh W., Multiphoton ionization and dissociation of nitromethane using femtosecond laser pulses at 375 and 750 nm, *The J. of Phys Chem. A*, 101 (1997) 817-823.
- [9] Kilic H.S., Comparison of Nanosecond and Femtosecond Laser Mass Spectrometry (FLMS), University of Glasgow, (1997).
- [10] Kilic H.S., Ledingham K., Smith D., Wang S., Kosmidis C., McCanny T., Singhal R., Langley A., Shaikh W., The Photo-Dissociative Pathways

- of Nitromethane Using Femtosecond Laser Pulses at 375 nm, *AIP Conference Proceedings*, (1997) 395-398.
- [11] Ledingham K., Singhal R., Smith D., McCanny T., Graham P., Kilic H.S., Peng W., Wang S., Langley A., Taday P., Behavior of polyatomic molecules in intense infrared laser beams, *The J. of Phys. Chem. A*, 102 (1998) 3002-3005.
- [12] Shi Y., Lipson R., An overview of organic molecule soft ionization using vacuum ultraviolet laser radiation, *Can. J. Chem*, 83 (2005) 1891-1902.
- [13] Yim Y.H., Kim M.S., Photodissociation breakdown pattern and the internal energy of n-heptane ion generated by charge exchange ionization, *Int. J. Mass Spectrom. Ion Processes*, 123 (1993) 133-137.
- [14] Choe J.C., Kim M.S., Photodissociation of heptane molecular ion: real-time investigation of consecutive reactions, *J. Phys. Chem*, 96 (1992) 726-732.
- [15] Marotta E., Paradisi C., A mass spectrometry study of alkanes in air plasma at atmospheric pressure, *J. Am. Soc. Mass Spectrom*, 20 (2009) 697-707.
- [16] Revel'skii I., Yashin Y.S., Voznesenskii V., Kurochkin V., Kostyanovskii R., Mass spectrometry with photoionization of N-alkanes, alcohols, ketones, esters, and amines at atmospheric pressure, *Russ. Chem. Bull.*, 35 (1986) 1806-1810.
- [17] Song L., Dykstra A.B., Yao H., Bartmess J.E., Ionization mechanism of negative ion-direct analysis in real time: a comparative study with negative ion-atmospheric pressure photoionization, *J. Am. Soc. Mass Spectrom*, 20 (2009) 42-50.
- [18] Silva R., Gichuhi W.K., Doyle M.B., Winney A.H., Suits A.G., Photodissociation of heptane isomers and relative ionization efficiencies of butyl and propyl radicals at 157 nm, *Phys. Chem. Chem. Phys.*, 11 (2009) 4777-4781.
- [19] Kosmidis C., Ledingham K., Kilic H., McCanny T., Singhal R., Langley A., Shaikh W., On the fragmentation of nitrobenzene and nitrotoluenes induced by a femtosecond laser at 375 nm, *J. Phys. Chem. A*, 101 (1997) 2264-2270.
- [20] Kepceoğlu A., Gündoğdu Y., Ledingham K.W.D., Kilic H.S., Identification of the isomers using principal component analysis (PCA) method, *AIP Conference Proceedings*, (2016) 060004.
- [21] Kepceoğlu A., Gündoğdu Y., Ledingham K.W.D., Kilic H.S., Real-Time Distinguishing of the Xylene Isomers Using Photoionization and Dissociation Mass Spectra Obtained by Femtosecond Laser Mass Spectrometry (FLMS), *Anal. Lett.*, 53(2) (2020) 290-307.
- [22] Gündoğdu Y., Alptekin H., Karabağlı P., Şahin M., Kilic H.Ş., Discrimination of cancerous and healthy colon tissues: A new laser-based method, *Laser Surg Med.*, 51 (2019) 363-369.
- [23] Gündoğdu Y., Karabağlı P., Alptekin H., Şahin M., Kılıç H.Ş., Comparison of performances of Principal Component Analysis (PCA) and Factor Analysis (FA) methods on the identification of cancerous and healthy colon tissues, *Int. J. Mass Spectrom.*, 445 (2019) 116204.
- [24] Wiley W., McLaren I.H., Time-of-flight mass spectrometer with improved resolution, *Rev. Sci. Instrum.*, 26 (1955) 1150-1157.
- [25] Gündoğdu Y., Kepceoğlu A., Kılıç H.Ş., Akbaş M., Doğan M., Ledingham K.W., Femtosaniye Laser Pulsları Yardımıyla Cn⁺ (n= 1... 60) Topak İyonlarının Hem C60 Hemde Grafit Hedefler Kullanılarak Ayrı Ayrı Üretimi ve Ölçümü (021101)(1-9), *Afyon Kocatepe University J. Sci. and Engin.*, 14 (2014) 1-9.
- [26] Ritter G.L., Lowry S.R., Isenhour T.L., Wilkins C.L., Factor analysis of the mass spectra of mixtures, *Anal. Chem.*, 48 (1976) 591-595.
- [27] Rozett R.W., Petersen E.M., Methods of factor analysis of mass spectra, *Anal. Chem.*, 47 (1975) 1301-1308.
- [28] National Institute of Standards and Technology-NIST Chemistry WebBook, Available at : <https://webbook.nist.gov/cgi/cbook.cgi?ID=C142825&Mask=200#Mass-Spec>, NIST, (2020).
- [29] Ledingham K.W., Deas R.M., Marshall A., McCanny T., Singhal R.P., Kilic H.S., Kosmidis C., Langley A.J., Shaikh W., A comparison of femtosecond and nanosecond multiphoton ionization and dissociation for some nitro-molecules, *Rapid Commun. Mass Spectrom.*, 9 (1995) 1522-1527.



Description of even-even Ti isotopes within IBM-1 model

Yeşim ŞAHİN^{1,*} Mahmut BÖYÜKATA²

¹ Kırıkkale University, Science Institute, Physics Department, Kırıkkale/Turkey

² Kırıkkale University, Faculty of Science and Arts, Physics Department, Kırıkkale/Turkey

Abstract

In this work, the some collective properties of even-even Ti isotopes in the A~50 mass region were studied by using the interacting boson model-1 (IBM-1). This study includes calculations of the energy levels and the electromagnetic transition rates of ⁴⁴⁻⁴⁸Ti and ⁵²⁻⁶⁰Ti isotopes. The neutron number ⁵⁰Ti isotope is 28, the magic number, and this isotope was excluded from the IBM-1 calculations. First, the energy ratios were analyzed by comparing the typical values of U(5), SU(3), O(6) dynamical symmetries and E(5), X(5) critical point symmetries. Later model Hamiltonian was constructed according to the behavior of given isotopes. The low lying energy levels of each Ti isotopes were calculated by using the fitted parameters of Hamiltonian. B(E2) values were also calculated by using the corresponding electromagnetic transition operator in the IBM-1. The calculation results were compared with experimental data and they are in good agreement with each other. Finally, $R_{4/2} = E(4_1^+)/E(2_1^+)$, $R_{0/2} = E(0_2^+)/E(2_1^+)$ energy ratios and $B(E2: 4_1^+ \rightarrow 2_1^+)/B(E2: 2_1^+ \rightarrow 0_1^+)$, $B(E2: 0_2^+ \rightarrow 2_1^+)/B(E2: 2_1^+ \rightarrow 0_1^+)$ ratios were analyzed to see the behavior of given isotopes. According to obtained results, Ti isotopes show E(5) behavior along the transition path from spherical to deformed γ -unstable region. Overall analysis indicates that these isotopes can be good example for the quantum shape phase studies along the isotopic chain.

Article info

History:

Received: 07.01.2021
Accepted: 10.03.2021

Keywords:

Energy Levels,
B(E2) values,
Dynamical
Symmetries,
Critical Point
Symmetries,
Interacting Boson
Model.

1. Introduction

In nuclear physics studies, nuclear models [1] were developed to understand the complex structure of nucleus consisting of protons and neutrons. One of them is the interacting boson model-1 (IBM-1) [2] introduced to explain the nuclear collective structure of even-even nuclei. The IBM-1 is a group theoretical model and quite successful for the phenomenologically description of the collective properties of nuclei, especially for the medium and heavy ones. This model is still actively used along the isotopic/isotonic chains and different mass regions of the nuclear valley.

During the last decades, the nuclei in A~50 mass region were investigated as reported in Refs. [3-9]. The shape phase transition was studied for the light nuclei with number of proton Z=20–28 including also Ti isotopes [3]. The fully-microscopic shell-model (SM) were used to calculate the first 2⁺ states of Ti isotopes and their B(E2) transition rates along the isotopic chain [4]. Excitation 2⁺, 4⁺ energy states, B(E2) values, and Q(2⁺) of even-even Ca, Ti, Cr isotopes were calculated in the generalized seniority with realistic interactions

and compared with results of full SM calculations performed by using FPD6 and GXPF1 interactions [5]. The shape phase transition was studied for ³⁸⁻⁶⁶Ti isotopes within the Hartree-Fock-Bogoliubov (HFB) approach and ^{46,52,60}Ti isotopes show E(5) behavior [6]. Another SM calculations were performed by using the same interactions for N=Z isotopes [7]. SM was used for the systematic calculations of first 2⁺ levels and B(E2) transitions of the pf-shell nuclei including also even-even Ti isotopes [8]. Excitation energies of J ^{π} =2⁺ states, two-neutron separation energies (S_{2n}), and B(E2) values along the isotopic chains of the fp shell nuclei were analyzed within the SM [9].

More recently, the IBM-1 calculations were applied to neighbours of Ti nuclei, e.g. even-even Cr [10, 11] and Fe nuclei [12] along the isotopic chain. In this study, the structural properties of even-even ⁴⁴⁻⁴⁸Ti and ⁵²⁻⁶⁰Ti isotopes in A~50 mass region were investigated by using the IBM-1 model [2]. Our aim is to calculate their low-lying energy levels by fitting the parameters of the model Hamiltonian and B(E2) transition rate, and also to understand their structural behavior by applying to the analysis of the energy ratios; $R_{4/2} =$

*Corresponding author. email address: yesimsahin1991@gmail.com

$E(4_1^+)/E(2_1^+)$, $R_{0/2} = E(0_2^+)/E(2_1^+)$ and the B(E2) ratios; $B(E2: 4_1^+ \rightarrow 2_1^+)/B(E2: 2_1^+ \rightarrow 0_1^+)$, $B(E2: 0_2^+ \rightarrow 2_1^+)/B(E2: 2_1^+ \rightarrow 0_1^+)$. The results of the model calculations are compared with experimental data [13] and the mentioned ratios are analyzed by comparing typical values of dynamical symmetries and that of the critical point symmetries.

This paper is structured as follows; in first section, the introduction is presented to give brief information about this work and the some recent studies. In the second section, the IBM-1 model is explained with its Hamiltonian and other formulations related the calculations. Later, the obtained results are discussed in third section. Finally, the conclusion are summarized in the last section.

2. Materials and Methods

For the present application, we used the IBM-1 model making no distinguish between neutron and proton, they are taken into account as nucleons. This basic version is also called sd-IBM model since using an interacting system of s and d bosons. In the following subsections, the IBM-1 model is explained with its Hamiltonian used for the calculations of energy levels and other formulations related the calculations of B(E2) values.

2.1. Interacting boson model-1 (IBM-1)

The IBM-1 model was first proposed by Feshbach and Iachello in the 1970s and later developed by Arima and Iachello [2]. This model is still widely used and very successful for the investigation of even-even nuclei, especially in deformed regions. The basic idea of this model tries to describe the low-lying collective states of the given nucleus with a system of s- and d- bosons of angular momenta $J=0$ and $J=2$, respectively. This algebraic model is established on the U(6) unitary group since s and d bosons have six magnetic moments in total, one is $\mu=0$ of the angular momentum $J=0$ and other five magnetic moments are $\mu=0, \pm 1, \pm 2$ of $J=2$. The U(6) group has three possible subgroups U(5), SU(3), O(6) called as dynamical symmetries and these symmetries correspond to the spherical, the axially deformed (prolate/oblate) and deformed γ -unstable nuclei, respectively [2]. The other concept is the critical point symmetries [14] in relation to the structural behavior of nuclei, introduced by Iachello [15, 16]. The X(5) and E(5) symmetries exist in between U(5)-SU(3) and U(5)-O(6) symmetries, respectively. The X(5) critical point symmetry [15] describe the first-order phase transition appearing

along the path from spherical to axially deformed (prolate/oblate) shapes. The E(5) symmetry [16,17] corresponds to a system undergoing a second-order phase transition appear in between the spherical and deformed γ -unstable shapes.

2.2. Model Hamiltonian

To calculate the nuclear collective properties of given nucleus with a system formed by the interaction of N bosons, one can constructs the model Hamiltonian in terms of the boson operators. The general Hamiltonian of the IBM-1 can also be reconstructed as a combination of the linear and quadratic Casimir invariants of corresponding subgroups of U(6) [2]. For the present application, we used another Hamiltonian in multipole expansion form given as following [18];

$$\hat{H} = \varepsilon'' \hat{n}_d + a_0 \hat{P}^\dagger \hat{P} + a_1 \hat{L}^2 + a_2 \hat{Q}^2 + a_3 \hat{T}_3^2 + a_4 \hat{T}_4^2 \quad (1)$$

where constants given by ε'' , a_0 , a_1 , a_2 , a_3 , and a_4 are free parameters fitted from experimental data. The \hat{n}_d , \hat{P} , \hat{L} , \hat{Q} , \hat{T}_3 , and \hat{T}_4 operators are called the boson-number, the pairing, the angular momentum, the quadrupole, the octupole, and the hexadecapole operators, respectively. These operators can be defined in terms of the creation and annihilation operators of the s and d bosons as [18];

$$\hat{T}_l = (d^\dagger \tilde{d})^{(l)} ; (l=0,1,2,3,4), \hat{n}_d = \sqrt{5} \hat{T}_0, \hat{L} = \sqrt{10} \hat{T}_1$$

$$\hat{P} = \frac{1}{2} (\tilde{d}^2 - s^2), \hat{Q} = (d^\dagger s + s^\dagger \tilde{d}) + \chi (d^\dagger \tilde{d})^{(2)} \quad (2)$$

As seen, these operators acts in boson states, not in fermion spaces. The constant χ given in quadrupole operator (\hat{Q}) is another free parameter. This parameter changes in between $-\sqrt{7}/2$ and $+\sqrt{7}/2$ to move from prolate side to oblate side, and $\chi = 0$ corresponds to γ -unstable behavior [18].

2.3. B(E2) transition probabilities

General form of electromagnetic transition operator in the IBM-1 model is written as follows [2],

$$\hat{T}^{(L)} = \gamma_0 \left[\hat{s}^\dagger \times \tilde{\hat{s}} \right]^{(0)} + \alpha_2 \left[\hat{d} \times \tilde{\hat{s}} + \hat{s}^\dagger \times \tilde{\hat{d}} \right]^{(2)} + \beta_L \left[\hat{d}^\dagger \times \tilde{\hat{d}} \right]^{(L)} \quad (3)$$

where γ_0 , α_2 and β_L ($L=0,1,2,3,4$) are parameters specifying various terms in the corresponding operators. In addition to the wave functions of the initial and final states, we need the $\hat{T}^{(E2)}$ operator to calculate B(E2) values. This operator is given as;

$$\hat{T}^{(E2)} = \alpha_2 \left[\hat{d}^\dagger \times \tilde{s} + \tilde{s}^\dagger \times \tilde{d} \right]^{(2)} + \beta_2 \left[\hat{d}^\dagger \times \tilde{d} \right]^{(2)} \quad (4)$$

where, the α_2 and β_2 constants are free parameters for E2 transition polarities. The B(E2) values are defined in terms of reduced matrix elements as [2];

3. Results and Discussion

The energy ratio $R_{4/2}$ of the first 4^+ and 2^+ levels in the ground state (g.s.) band of the given $^{44-60}\text{Ti}$ isotopes in the A~50 mass region were analyzed to have idea about their behavior. Dynamical symmetries of the IBM-1 are U(5), SU(3), and O(6) limits corresponding

$$B(E2; L_i \rightarrow L_f) = \frac{1}{2L_i + 1} \left| \langle L_f || \hat{T}^{(E2)} || L_i \rangle^2 (eb)^2 \right|. \quad (5)$$

to the geometric shapes of nuclei [2] as discussed in subsection 2.1 including also the concept of the X(5) and E(5) critical point symmetries [16,17] appeared in between U(5)–SU(3) and U(5)–O(6) symmetries, respectively. Typical values [14] of the energy ratio ($R_{4/2}$) are listed in Table 1 for dynamical and critical point symmetries.

Table 1. The energy ratios of the dynamical and critical points symmetries, and experimental [13] ones of the Ti isotopes.

$R_{4/2}$	U(5)	O(6)	SU(3)	E(5)	X(5)	^{44}Ti	^{46}Ti	^{48}Ti	^{52}Ti	^{54}Ti	^{56}Ti	^{58}Ti	^{60}Ti
	2.00	2.50	3.33	2.19	2.91	2.27	2.26	2.33	2.21	1.70	2.03	1.95	2.02

The experimental [13] energy ratios of even-even $^{44-48}\text{Ti}$ and $^{52-60}\text{Ti}$ isotopes are given in Table 1 including also typical energy ratios of dynamical symmetries and critical point symmetries. According to the experimental energy ratios, $^{44-52}\text{Ti}$ and ^{52}Ti isotopes are close to E(5) region and other even-even $^{54-60}\text{Ti}$ isotopes are closer to U(5). ^{50}Ti isotope is excluded from the following IBM-1 calculations since its neutron number (N=28) is the magic number.

For the calculations of energy levels, the following model Hamiltonian given equation (1) can be formed as follows;

$$H = (EPS)\hat{n}_d + (PAIR)\hat{P}^\dagger \cdot \hat{P} + (ELL)\hat{L} \cdot \hat{L} + (QQ)\hat{Q} \cdot \hat{Q}, \quad (6)$$

where the constants are free parameters written in the form of the PHINT code [19] used for the IBM-1 calculations. The fitted parameters are listed in Table 2.

Table 2. The PHINT parameters (in units MeV) of Hamiltonian given in equation (6), CHQ is dimensionless parameter.

	^{44}Ti	^{46}Ti	^{48}Ti	^{52}Ti	^{54}Ti	^{56}Ti	^{58}Ti	^{60}Ti
<i>EPS</i>	0.85	0.6	1.1	1.3	1.351	1.0399	0.85	0.858
<i>PAIR</i>	-0.1	-0.17	0.14	0.3	--	--	--	--
<i>QQ</i>	-0.181	-0.46	-0.04	0.03	0.29	0.142	0.115	-0.0006
<i>ELL</i>	--	-0.10	--	--	--	--	--	--
<i>CHQ</i>	-1.5	-0.84	-0.6	-2	-1.3	-1.39	-2.2	-2

The energy levels of $^{44-60}\text{Ti}$ isotopes were the calculated using the parameters given in Table 2. ^{44}Ti , ^{48}Ti and ^{52}Ti isotopes have two bosons, and the IBM-1 model can calculate the energy levels up to $2N$ (N is boson number). Thus, only 2_1^+ , 4_1^+ levels in the g.s. band and also 0_2^+ , 2_2^+ levels were calculated of these two isotopes. ^{46}Ti and ^{54}Ti have three bosons and their energy levels were calculated up to 6_1^+ in the g.s. band. An extra parameter (ELL) was added to the model Hamiltonian (6) to obtain the better results for ^{46}Ti isotope. Another fitted parameter of PHINT is CHQ in related to the parameter χ (CHI) with a relation by

$CHQ \cong 2.24 \cdot CHI$. χ (CHI) is the constant in the \hat{Q} operator given by equation (2). The rest isotopes have more bosons but limited levels are experimentally known. Overall calculated levels are exhibited in Figure 1 and clearly seen that these calculations are very close experimental ones.

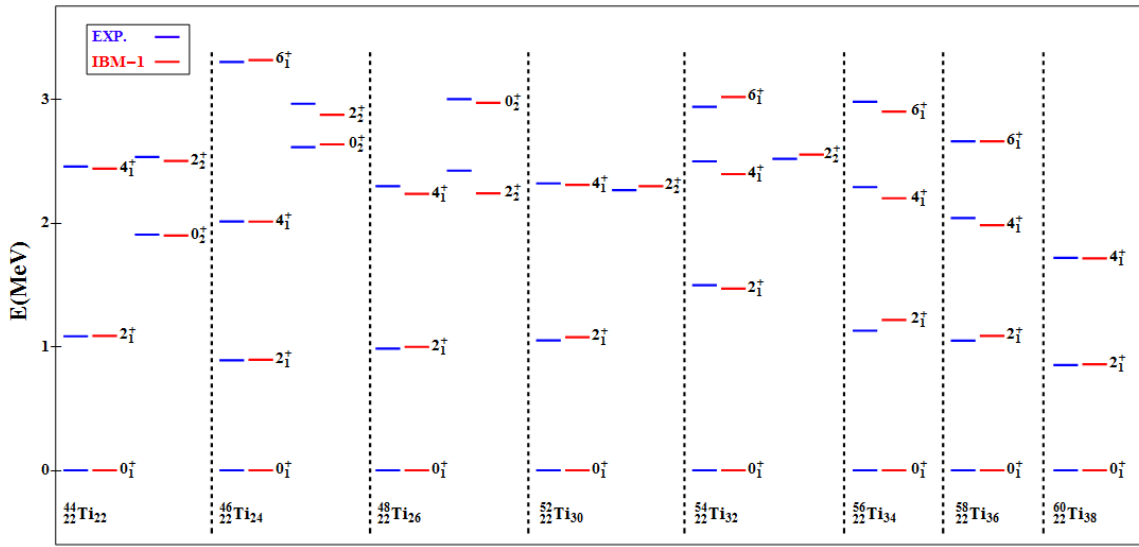


Figure 1. The experimental [13] and calculated energy spectra of given even-even Ti isotopes.

The experimental and calculated $R_{4^+/2^+}$ energy ratios (given in Table 1) are plotted in Figure 2(a) along the isotopic chain. According to the experimental values, ^{44}Ti , ^{46}Ti , ^{52}Ti isotopes are located around E(5) region while other even-even $^{54-60}\text{Ti}$ isotopes are closer to U(5) symmetry. As seen this figure, ^{48}Ti isotope is between E(5)-O(6) symmetries but closer to E(5) point and $^{56-60}\text{Ti}$ isotopes are close to U(5) region. However, the energy ratio of ^{54}Ti is smaller than that of U(5) and it is close to ^{50}Ti isotope having magic neutron number. The calculated $R_{4^+/2^+}$ ratios are mostly same with the experimental ones except for ^{56}Ti and ^{58}Ti isotopes but their calculated ratios are also close U(5). Changing of $R_{0^+/2^+}$ energy ratios are also exhibited in Figure 2(b) along the isotopic chain of Ti nuclei. This figure only includes experimentally known $^{44-48}\text{Ti}$ isotopes. According to the $R_{0^+/2^+}$ ratios, the ^{44}Ti isotope is close to U(5) symmetry, ^{46}Ti and ^{48}Ti isotopes are very close to E(5) point.

In addition to energy levels, the IBM-1 model can also calculate the B(E2) values of given Ti isotopes by fitting the α_2 and β_2 parameters in the the $\hat{T}^{(E2)}$ operator given by equation (3). The parameters α_2 and β_2 are given by E2SD and E2DD in the PBEM code [19]. For the calculation, E2DD = 0 and E2SD is fitted as 0.075, 0.068, 0.083, 0.0714, 0.0657, 0.0412, 0.0416, 0.03 for given ^{44}Ti , ^{46}Ti , ^{48}Ti , ^{52}Ti , ^{54}Ti , ^{56}Ti , ^{58}Ti , ^{60}Ti isotopes, respectively. Overall calculated B(E2: $L_i^\pi \rightarrow L_f^\pi$) transitions values are listed in Table 3.

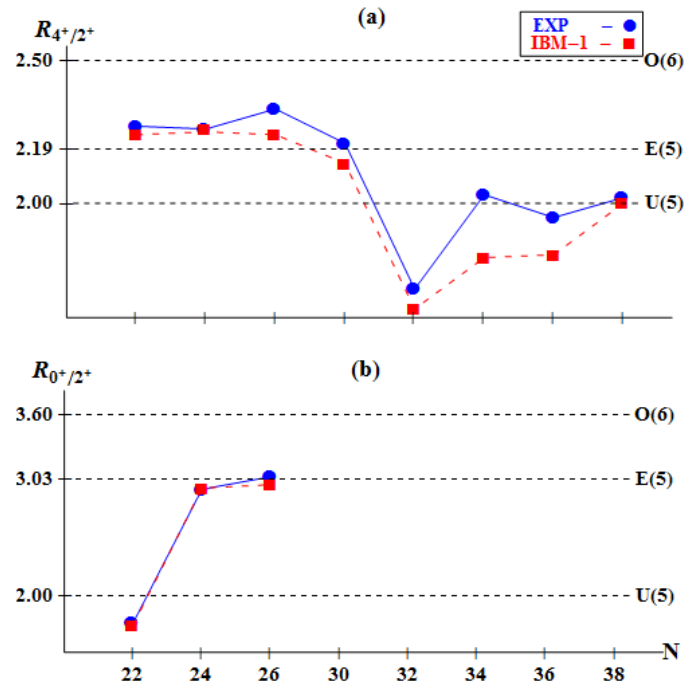


Figure 2. Energy ratios of given Ti nuclei along the isotopic chain. The experimental [13] ratios are denoted by blue and the calculated ones by red. (a) $R_{4^+/2^+}$ ratios (b) $R_{0^+/2^+}$ ratios.

Table 3. Experimental [13] and calculated $B(E2: L_i^\pi \rightarrow L_f^\pi)$ transitions (in units of $10^{-2} e^2b^2$) in given Ti isotopes.

Nucleus	$L_i^\pi \rightarrow L_f^\pi$	Experimental	Calculation
^{44}Ti	$2_1^+ \rightarrow 0_1^+$	1,200 (0,369)	1,195
	$4_1^+ \rightarrow 2_1^+$	2,768 (0,461)	1,108
	$0_2^+ \rightarrow 2_1^+$	<0,313	0,676
^{46}Ti	$2_1^+ \rightarrow 0_1^+$	1,909 (0,59)	1,825
	$4_1^+ \rightarrow 2_1^+$	1,978 (0,127)	2,032
	$6_1^+ \rightarrow 4_1^+$	1,606 (0,147)	1,347
	$0_2^+ \rightarrow 2_1^+$	0,245 (0,069)	0,182
^{48}Ti	$2_1^+ \rightarrow 0_1^+$	1,523 (0,420)	1,556
	$4_1^+ \rightarrow 2_1^+$	1,906 (0,176)	1,377
	$0_2^+ \rightarrow 2_1^+$	0,110 (0,013)	0,481
^{52}Ti	$2_1^+ \rightarrow 0_1^+$	1,141 (0,127)	1,139
	$4_1^+ \rightarrow 2_1^+$	--	1,019
^{54}Ti	$2_1^+ \rightarrow 0_1^+$	0,715 (0,133)	0,724
	$4_1^+ \rightarrow 2_1^+$	--	0,745
^{56}Ti	$2_1^+ \rightarrow 0_1^+$	--	0,432
	$4_1^+ \rightarrow 2_1^+$	--	0,665
	$6_1^+ \rightarrow 4_1^+$	--	0,683
^{58}Ti	$2_1^+ \rightarrow 0_1^+$	--	0,502
	$4_1^+ \rightarrow 2_1^+$	--	0,818
	$6_1^+ \rightarrow 4_1^+$	--	0,909
^{60}Ti	$2_1^+ \rightarrow 0_1^+$	--	0,542
	$4_1^+ \rightarrow 2_1^+$	--	0,903

Table 3 includes experimentally known $B(E2)$ values of $^{44,46,48,52,54}\text{Ti}$ isotopes and their calculations and also some predictions for unknown $B(E2)$ values of $^{52,54,56,58,60}\text{Ti}$ isotopes. As seen this table, the calculated $B(E2: 2_1^+ \rightarrow 0_1^+)$ transition values are in good agreement with the experimental data. Other $B(E2: L_i^+ \rightarrow L_f^+)$ transitions are close to experimental data.

$B(E2: 2_1^+ \rightarrow 0_1^+)$. The different values of $B(E2)$ ratios are taken from Refs. [16, 17] marked by *a* and *b* for $E(5)$ critical point symmetries.

The ratios of $B(E2)$ values are also analyzed along the isotopic chain as shown in Figure 3.

The $B(E2: 4_1^+ \rightarrow 2_1^+)/B(E2: 2_1^+ \rightarrow 0_1^+)$ ratios are plotted as a function of the neutron number for given Ti isotopes in Figure 3 (a) including the typical ratios of $U(5)$, $O(6)$, and $E(5)$ symmetries. There are two different ratios for $E(5)$ point symmetry taken from Refs. [16, 17]. The experimental data of ^{44}Ti isotope is close to $E(5)^a$, while the calculation value is close to $O(6)$. The experimental ratios and the calculated ones of ^{46}Ti and ^{48}Ti isotopes are very close to $O(6)$ symmetry. As seen from Figure 3(a), ^{46}Ti and ^{48}Ti isotopes are close to $O(6)$ symmetry and the ratio of ^{44}Ti isotope is bigger but the error bars of ^{44}Ti and ^{48}Ti isotopes touch to the ratios of $O(6)$ and $E(5)$. The calculated $B(E2)$ ratios of $^{44,46,48}\text{Ti}$ isotopes are close to $O(6)$ symmetry. Figure 3(a) also includes the prediction of $B(E2: 4_1^+ \rightarrow 2_1^+)/B(E2: 2_1^+ \rightarrow 0_1^+)$ ratios for $^{52,54,56,58,60}\text{Ti}$ isotopes, and clearly seen that $^{52,54}\text{Ti}$ isotopes are very close to $O(6)$ symmetry, and $^{56,58,60}\text{Ti}$ isotopes are around the $E(5)$ region. For more detailed analysis, the $B(E2: 0_2^+ \rightarrow 2_1^+)/B(E2: 2_1^+ \rightarrow 0_1^+)$ ratios are plotted in Figure 3(b) along the isotopic chain. This figure includes only experimentally known ratio, and seen that $^{44,46,48}\text{Ti}$ isotopes are close $E(5)$ critical point taken from Refs. [16, 17].

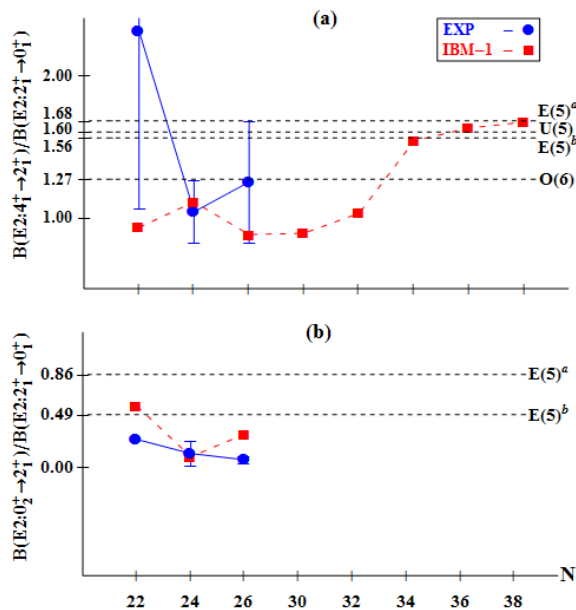


Figure 3. The comparison of the experimental (blue) [13] and the calculated (red) $B(E2)$ ratios of Ti isotopes. (a) $B(E2: 4_1^+ \rightarrow 2_1^+)/B(E2: 2_1^+ \rightarrow 0_1^+)$ (b) $B(E2: 0_2^+ \rightarrow 2_1^+)/B(E2: 2_1^+ \rightarrow 0_1^+)$

4. Conclusion

In this study, the collective properties of even-even Ti isotopes in the A~50 mass region were investigated within the IBM-1 model. First, the parameters of the model Hamiltonian were fitted to calculate their low-lying energy levels and B(E2) values by using these parameters in the PHINT and PBEM codes [19]. The IBM-1 calculations of the energy levels and also B(E2) values are in good agreement with experimental data for given isotopes. Their energy ratios ($R_{4^+/2^+}$, $R_{0^+/2^+}$) and B(E2) ratios were also analyzed along the isotopic chain to understand their structural behavior. According to obtained results, given even-even Ti isotopes show E(5) behavior along the transition path from spherical to deformed γ -unstable region. The $R_{4^+/2^+}$ values along the isotopic chain show that ^{44}Ti , ^{46}Ti , ^{48}Ti , and ^{52}Ti isotopes are close to E(5) critical point while ^{56}Ti , ^{58}Ti , ^{60}Ti isotopes are close to U(5) region, the energy ratio of ^{54}Ti isotope is close to that of ^{50}Ti having magic neutron number. However, the $R_{0^+/2^+}$ ratios show that ^{44}Ti isotope is close to U(5) symmetry and ^{46}Ti , ^{48}Ti isotopes are located around the E(5) point. The B(E2) ratios also suggest that even-even Ti isotopes have signatures for E(5) behavior. Overall analysis indicates that these isotopes can be good example for the quantum shape phase transition from spherical to γ -unstable shapes along the isotopic chain. We again remind that the neutron number ^{50}Ti isotope is the magic number (N=28) and we excluded this isotope from the IBM-1 calculations. For the shape phase transition description of even-even Ti isotopes was performed within HFB approach in Ref. [6] and E(5) behavior was determined for $^{46,52,60}\text{Ti}$ isotopes. Systematic studies can be applied to A~50 mass region to see the behavior of even-even Ti, Cr, and Fe nuclei. For example, it can be interesting to apply the analysis of the energy ratios $R(L) = E(L_1^+)/E(2_1^+)$ in the g.s. band of these nuclei to see the E(5) behavior along the shape phase transition from U(5) to O(6) symmetry.

Acknowledgments

This study was supported by Scientific and Technical Research Council of Turkey (TÜBİTAK), Project Nr. 119F127.

Conflicts of interest

The authors declare no conflict of interest.

References

[1] Heyde K., Basic Ideas and Concepts in Nuclear Physics: An Introductory Approach. Third Edition,

Bristol and Philadelphia: Institute of Physics Publishers; chap. 9 (2004).

- [2] Iachello F., Arima, A., The Interacting Boson Model. Cambridge University Press; chap. 1 (1987).
- [3] Bai H.-B., Li X.-W., Shape phase transition in neutron-rich even-even light nuclei with $Z = 20-28$, *Chin. Phys. C* 35 (2011) 925-929.
- [4] Coraggio L., Covello A., Gargano A., Itaco N., Kuo T.T.S., Fully microscopic shell-model calculations with realistic effective Hamiltonians, *J. Phys.: Conf. Ser.* 312 (2011) 092021.
- [5] Caprio M.A., Luo F.Q., Cai K., Constantinou Ch., Hellemans V., Generalized seniority with realistic interactions in open-shell nuclei, *J. Phys. (London) G* 39 (2012) 105108.
- [6] Bayram T., An investigation on shape evolution of Ti isotopes with Hartree-Fock-Bogoliubov theory, *Mod. Phys. Lett. A* 27, 28 (2012) 1250162.
- [7] Kaneko K., Mizusaki T., Sun Y., Tazaki S., Toward a unified realistic shell-model Hamiltonian with the monopole-based universal force, *Phys. Rev. C* 89 (2014) 011302.
- [8] Robinson S.J.Q., Hoang T., Zamick L., Escuderos A., Sharon Y.Y., Shell model calculations of B(E2) values, static quadrupole moments, and g factors for a number of N=Z nuclei, *Phys. Rev. C* 89 (2014) 014316.
- [9] Ma Y.Z., Coraggio L., De Angelis L., Fukui T., Gargano A., Itaco N., Xu F.R., Contribution of chiral three-body forces to the monopole component of the effective shell-model Hamiltonian, *Phys. Rev. C* 100 (2019) 034324.
- [10] Ullah A., Riaz M., Nabi J.U., Büyükata M., Çakmak N., Effect of deformation on gamowteller strength and electron capture cross-section for isotopes of chromium. *Bitlis Eren Univ. J. Sci. Technol.*, 10 (2020) 25-29.
- [11] Nabi J.-U., Büyükata M., Ullah A., Riaz M., Nuclear structure properties of even-even chromium isotopes and the effect of deformation on calculated electron capture cross sections, *Nucl. Phys. A* 1002 (2020) 121985.

- [12] Çakır Oruç G., Büyükata M., Investigation of nuclear properties of even-even Fe isotopes within the IBM-1 model, *Bitlis Eren Univ. J. Sci.*, 10 (2021) 82-90.
- [13] National Nuclear Data Center (NNDC), <https://nndc.bnl.gov>. Retrieved December 15, 2020.
- [14] Casten R. F., Shape phase transitions and critical-point phenomena in atomic nuclei. *Nature Physics* 2, (2006) 811–820.
- [15] Iachello F., Analytic description of critical point nuclei in a spherical-axially deformed shape phase transition. *Phys. Rev. Lett.* 87 (2001) 052502.
- [16] Iachello F., Dynamic symmetries at the critical point. *Phys. Rev. Lett.* 85 (2000) 3580–3583.
- [17] Arias J.M., E2 transitions and quadrupole moments in the E(5) symmetry, *Phys. Rev. C* 63 (2001) 034308.
- [18] Casten R.F., Warner D.D., The interacting boson approximation, *Rev. Mod. Phys.* 60 (1988) 389-469.
- [19] Scholten O., The program package PHINT and PBEM (1979).



XRD and photoluminescence measurements of GaN grown on dome shaped patterned sapphire with different NH₃ flow rates

İsmail ALTUNTAŞ*

Sivas Cumhuriyet University, Department of Nanotechnology Engineering, Nanophotonics Research and Application Center Cumhuriyet University, Sivas/TURKEY

Abstract

The aim of the study is to understand the effects of NH₃ flow rate in the initial part of high temperature (HT) GaN growth on structural and optical characteristics of the HT-GaN layer grown on dome shaped sapphire substrate by Metal Organic Chemical Vapor Deposition (MOCVD) system. High resolution x-ray diffraction (HRXRD) and photoluminescence (PL) measurements were performed to characterization the growing GaN epilayer. It is observed that the using of different NH₃ flow rate in the initial part of HT-GaN growth has an effect on both full-width at half-maximum (FWHM) values obtained from HRXRD results and intensities of yellow luminescence peaks. It is seen that the FWHM values obtained from the symmetric (00.2) omega scan increased as the NH₃ flow rates in the initial part of HT-GaN growth increased. It is demonstrated that the intensities of yellow luminescence peaks are very sensitive to NH₃ flow rates in the initial part of HT-GaN growth.

Article info

History:

Received:11.01.2021

Accepted:11.03.2021

Keywords:

GaN epilayer,
MOCVD,
NH₃ flow rate,
Epitaxy,
Characterization.

1. Introduction

III-Nitride compound semiconductors (GaN, InN, AlN, and their alloys) have attracted great attention and achieved incredible progress in recent years. The main underlying reason is that GaN and its alloys with AlN and InN have huge application area for optoelectronic device applications (light emitting diode (LEDs), laser diodes and high power and high temperature electronics) [1-6]. MOCVD system is currently the most widely used technology to produce GaN based LEDs. Since the first high-brightness GaN-based blue LED was achieved on the sapphire substrate, researches to obtain LED with high power and high efficiency are still a hot topic area. However, further development in LED is hampered due to two main hindrances. First, GaN has a high crystal defect density because of the large lattice mismatch between GaN and sapphire resulting in impacts the internal quantum efficiency (IQE) of LEDs [7-9]. Second, the light extraction efficiency (LEE) is low due to GaN/sapphire interface [10, 11]. There are plenty of MOCVD growth studies in the literature to investigate the effect of growth parameters on defect density in GaN on flat sapphire substrate. In these studies, the effect of thickness [12], growth temperature [13], reactor pressure [14], annealing [15], total flow [16], V/III ratio [17], and many other growth parameters of LT (low temperature) GaN nucleation layer and HT (high

temperature) GaN layer were deeply investigated. While patterned sapphire substrate (PSS) has proven major advantageous for improving the efficiency of LED, PSS also contributes one step epitaxial growth technology to obtain the lateral growth of GaN which is important to overcome the disadvantages of the two step epitaxial growth [18]. In this regard, using PSS instead of the flat sapphire substrate can improve the epitaxial lateral overgrowth (ELOG) mode and consequently provide to obtain high quality GaN. The crystal defects in the GaN layer can be find as non-radiative recombination centers and therefore decrease some properties such as carrier lifetime and radiative recombination efficiency which are important as regards the efficiency of LEDs [19, 20]. NH₃ flow rate which defines the V/III ratio is also one of the important growth parameters and affects the quality of GaN epilayer. NH₃ flow rate or V/III ratio has important role during transition from 2D to 3D growth. In literature, the effect of V/III ratio or NH₃ flow rate is done for during low temperature GaN (LT-GaN) growth or high temperature GaN (HT-GaN) by using flat sapphire substrate.

In the current study, NH₃ flow rates in the initial part of the HT GaN growth where the transition from 2D to 3D growth mode take place have been changed to improve the quality of the GaN epilayer grown on the dome shaped sapphire substrate. The impact of

*Corresponding author. email address: ialtuntas@cumhuriyet.edu.tr

different NH_3 flow rates in the initial stage of the HT-GaN layer growth on structural and optical properties are studied using HRXRD system, and PL spectroscopy, respectively.

2. Experimental

A series GaN epitaxial layers were grown on dome shaped patterned sapphire substrates by AIXTRON 200/4 RF-S MOCVD system with the horizontal flow. The high purity ammonia (NH_3) and trimethylgallium (TMGa) were used for N and Ga sources, respectively, to grow epitaxial GaN layer. High purity H_2 gas was used as the carrier. All samples were deposited with the same growth conditions except for NH_3 flow rates in the initial stage of HT-GaN growth where the 3D to 2D growth transition take place. Before the growth, the dome shaped patterned sapphire substrates were applied the high temperature desorption (1080°C) for 10 mins at 100 mbar reactor pressure under H_2 ambient to remove any remaining contaminants from the surface of sapphire substrates. GaN grown at low temperature which is called the nucleation layer was grown at 200 mbar and 480°C . After nucleation layer growth, the growth temperature was increased to 1030°C and reactor pressure was fixed to 200 mbar for HT-GaN growth. The GaN layer grown at higher

temperature was included 2 parts with different NH_3 flow rates. While the initial part of HT-GaN was grown for 60 mins with different NH_3 flow rates, remaining part of HT-GaN was grown for 40 mins. NH_3 flow rates in the initial part of HT-GaN were changed as 1250, 1000 and 750 sccm while NH_3 flow rate at second part of HT-GaN growth was kept constant at 1250 sccm. These samples were labeled as S1, S2, and S3. Table I summarizes the NH_3 flow rates in the initial part of HT-GaN growth.

Table 1. The NH_3 flow rates in the initial part of HT-GaN for S1, S2, and S3.

Sample Name	NH_3 flow rates in the initial part of HT-GaN (sccm)
S1	1250
S2	1000
S3	750

Figure 1 demonstrates the schematic representation of growth structure and used dome shaped patterned substrate. NH_3 flow rates in the red layer (initial part of HT-GaN) were adjusted as 1250, 1000, and 750 sccm for S1, S2, and S3, respectively.

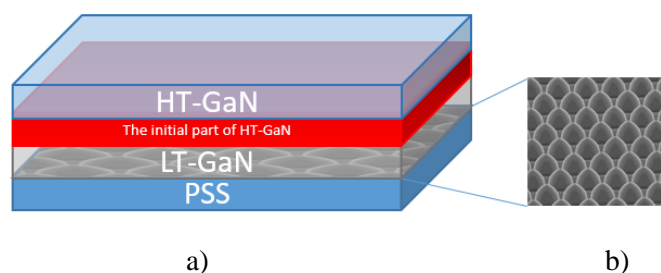


Figure 1. a) the growth structure used to obtain high quality GaN epilayer and b) the dome shaped patterned substrate.

HRXRD and room temperature (RT) photoluminescence measurements were done for structural and optical characterization of these samples, respectively. HRXRD measurements were used to obtain the full-width at half-maximum (FWHM) values to investigate the effect of NH_3 flow rates in the initial part of HT-GaN growth on the structural quality. RT-PL measurements were carried out by the 325 nm HeCd laser which focused on the 10x objective lens for different laser powers. The power of the laser with 100mW was adjusted as 0.1, 1, 5, and 10% by using ND filters. The signal during the photoluminescence measurement was detected by the CCD detector and used 300 gr/mm 500nm blaze grating.

3. Results and Discussion

HRXRD is a commonly utilized method to investigate the structural properties of epitaxial layers for optimization of growth process [21-23]. The rocking curve omega scans for (00.2) and (10.2) planes were done and their FWHM values were used to take information about crystal quality of layer. Figure 2 gives rocking curves omega scans for (00.2) and (10.2) planes and also shows the change of FWHM values obtained from symmetrical and asymmetrical scans with changing NH_3 flow rates in the initial part of HT-GaN growth.

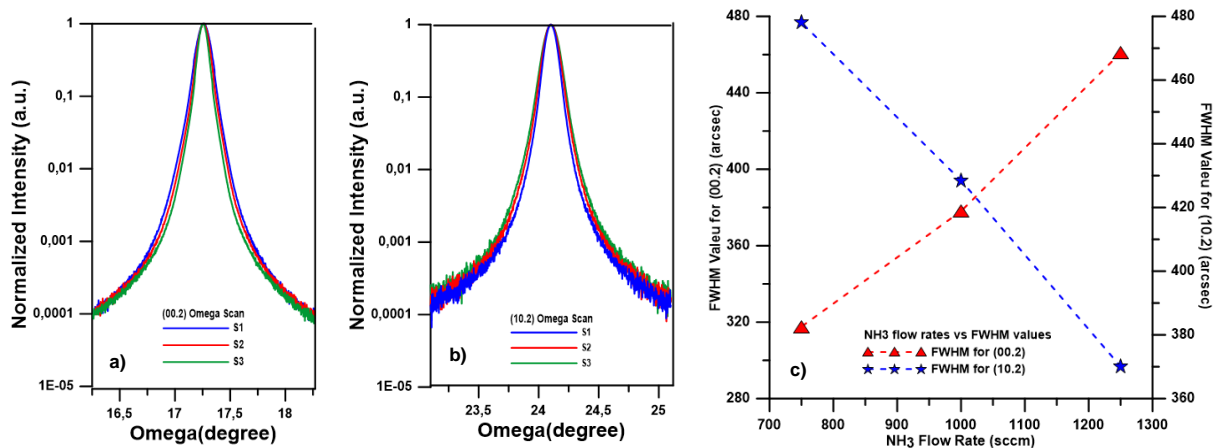


Figure 2. Omega scans for (a) (00.2) and (b) (10.2) planes and (c) the variation of FWHM values with the increase of NH_3 flow rates in the initial part of HT-GaN growth.

The basic aim of using different NH_3 flow rates in the initial part of HT-GaN growth is to optimize the NH_3 flow rates and to minimize the FWHM values obtained from symmetric and asymmetric rocking curve measurement for improving the crystalline quality. It is observed that although there is a linearly increasing dependency between the FWHM values obtained from (00.2) omega measurement and NH_3 flow rates, there is a linearly decreasing dependency between FWHM values obtained from (10.2) omega measurement and NH_3 flow rates. According to the results of HRXRD measurements, the desired growth condition can be determined in terms of the variation of FWHM values in both symmetric and asymmetric rocking curve measurements.

PL measurement is the most common, non-destructive, and fast optical characterization technique to understand the optical properties of structures [24].

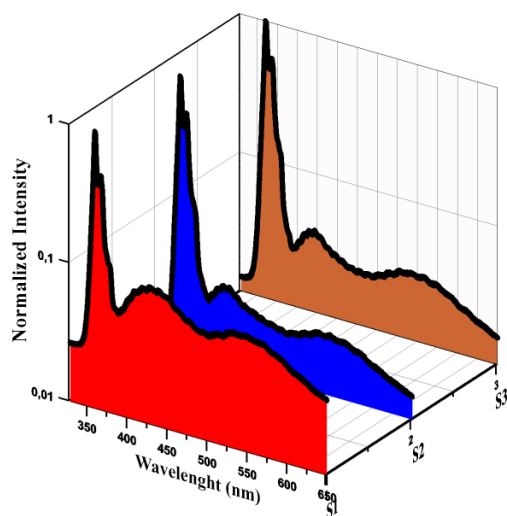


Figure 3. The normalized photoluminescence spectra for S1, S2, and S3 with different NH_3 flow rates in the initial part of HT-GaN growth.

For this reason, photoluminescence measurements were done to understand the effect of different NH_3 flow rates in the initial part of HT-GaN on the quality of the GaN epilayer. Figure 3 shows the normalized PL spectra with 330-650 nm range at RT for S1, S2, and S3 by laser power adjusted 5 %.

Each PL spectra was obtained from the center of the samples and adjusted laser power with 5% (5P). The PL spectra for S1, S2, and S3 have three main peaks; (1) high intensity and narrow PL band called near band edge luminescence at ~ 361 nm and (2) and (3) low intensity and broad PL band called yellow luminescences at ~ 430 and 550 nm. In GaN crystal, the band edge luminescence is caused by the transition from the conduction band to the valance band while yellow luminescences are caused by point defects which are sources of impurity and growth conditions [25]. Point defects have a very important role in the electrical and optical properties of GaN based materials/devices. However, the source of point defects in this semiconductor is still under investigation [25]. Figure 4 demonstrates the comparison of PL peak emissions at ~ 430 and 550 nm for S1, S2, and S3. Fluctuations in the signal are caused by Fabry-Pérot oscillations (FPO) of the sapphire-GaN-air space [26].

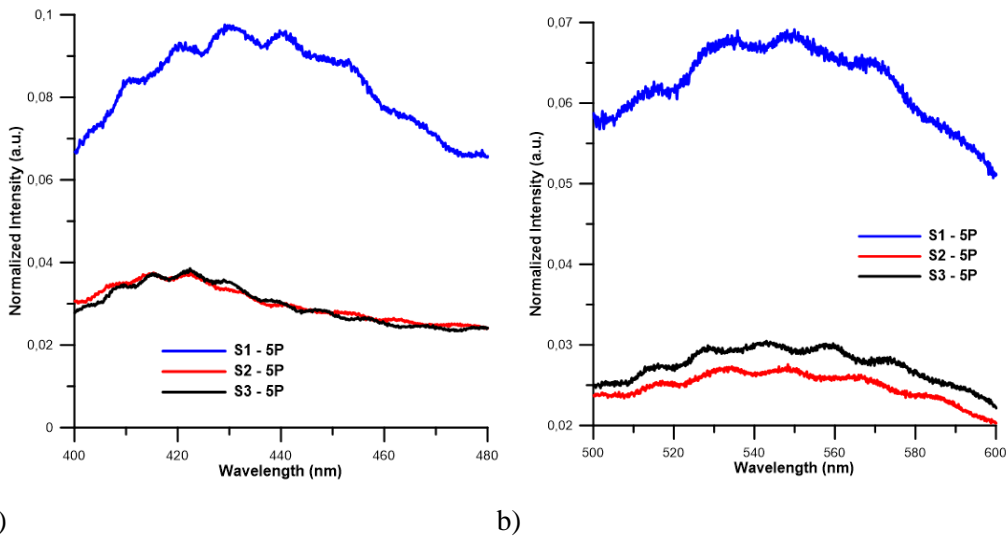


Figure 4. The comparison of PL spectra emissions at ~ 430 (a) and 550 nm (b) for S1, S2, and S3

It was observed that PL peak emission wavelength changed at around 430 nm while PL peak emission wavelength remained constant at around 550 nm for different NH₃ flow rates in the initial part of HT-GaN growth. The reason for this shift at around 430 nm is not completely clear but might be due to more yellow luminescence from deep centers depending on NH₃

flow rates. Generally, a common way to compare the quality of GaN epilayer is that the intensity ratio (I_{NBE}/I_{YL}) between near band edge peak and yellow luminescence peak is found [27]. For this purpose, the I_{NBE}/I_{YL} ratio was plotted against NH₃ flow rates used in the initial part of the HT-GaN growth (Figure 5).

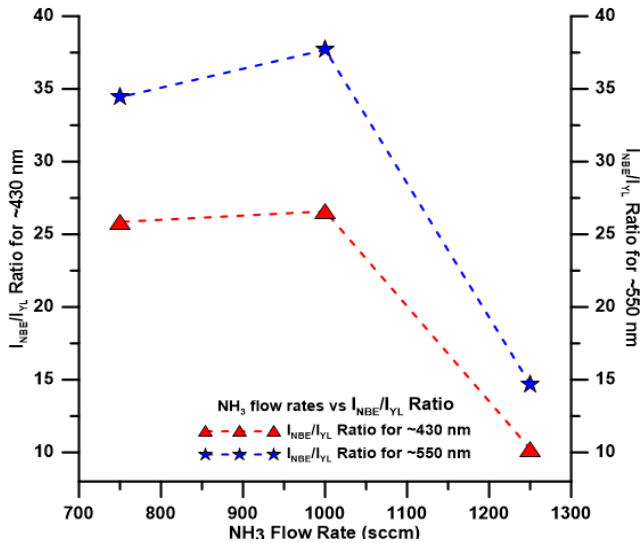


Figure 5. The variation of the I_{NBE}/I_{YL} ratios with NH₃ flow rates for 430 (red) and 550 (blue) nm.

PL measurement result and obtained the I_{NBE}/I_{YL} ratios indicate that the S2 can be chosen to optimize the growth condition. Also the effect of the using different laser powers on intensities of near band edge peak, and yellow luminescence peaks in the PL emission spectra of S2 was investigated. The PL emission spectra with 300-700 nm range were given for different laser powers in Figure 6. With increasing laser power, the NBE band intensity increased, what can be explained by reduction of the depletion region width [28]. It can be said that the intensities of yellow luminescence

peaks become more pronounced with increasing laser power and also the intensity of the band-edge peak gradually increases.

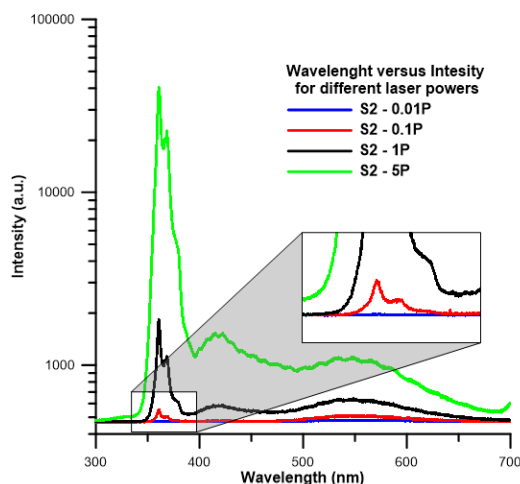


Figure 6. The PL emission spectra with 300-700 nm range obtained from excited by different laser powers for S2.

4. Conclusion

In summary, the impact of NH_3 flow rates in the initial part of HT-GaN growth is investigated on structural and optical properties of GaN epilayer grown on dome shaped sapphire substrate by using HRXRD and PL systems. The symmetric (00.2) and asymmetric (10.2) rocking curve measurements were done to obtain the FWHM values. The change of FWHM values obtained from both symmetric and asymmetric scans was plotted depending on the changing NH_3 flow rates. It is seen that there is a linear relation between the FWHM values obtained from (00.2) omega measurement and NH_3 flow rates in the initial part of HT-GaN growth. PL emission spectra with 300-700 nm range for S1, S2, and S3 were obtained to compare the effect of NH_3 flow rates. The variation of the intensity ratio ($I_{\text{NBE}}/I_{\text{YL}}$) with NH_3 flow rates was plotted to investigate the effect on the quality of the GaN epilayer. It is seen that the S2 has a higher $I_{\text{NBE}}/I_{\text{YL}}$ ratio compared to the other samples.

Acknowledgment

The author acknowledges the usage of Nanophotonics Research and Application Center at Cumhuriyet University (CUNAM) and Sivas Cumhuriyet University Advanced Technology Research and Application Center (CUTAM). This study is supported by the Scientific Research Project Fund of Sivas Cumhuriyet University under the project number M-768.

Conflicts of interest

The authors state that did not have conflict of interests.

References

- [1] Lee J.H., J.H. Lee, Enhanced Performance of Gan-Based Light Emitting Diode With Isoelectronic Al Doping Layer, *Journal of Applied Physics.*, 105 (6) (2009).
- [2] Nakamura S., Senor M., Iwasa N., Nagahama S. I., High-Brightness InGaN Blue, Green And Yellow Light-Emitting Diodes With Quantum Well Structures, *Japanese Journal of Applied Physics.*, 34 (7A) (1995) L797.
- [3] Nakamura S., Sonoh M., Nagahama S.I., Iwasa N., Yamada T., Matsushita T., Sugimoto Y., Kiyoku H., High-Power Long-Lifetime InGaN Multi-Quantum-Well-Structure Laser Diodes, *Japanese Journal of Applied Physics.*, 36 (8B) (1997).
- [4] Youn D.H., Lee J.H., Kumar V., Lee K.S., Lee J.H., Adesida I., The Effects of Isoelectronic Al Doping and Process Optimization for the Fabrication of High-Power AlGaN-GaN HEMTs, *IEEE Transactions on Electron Devices.*, 51 (5) (2004) 785-789.
- [5] Genç M., Sheremet V., Elçi M., Kasapoğlu A. E., Altuntaş İ., Demir İ., Eğin G., İslamoğlu S., Gür E., Muzafferoğlu N., Elagöz S., Gülseren O., Aydınli A., Distributed Contact Flip Chip InGaN/GaN Blue LED; Comparison With Conventional LEDs, *Superlattices and Microstructures.*, 128 (2019) 9-13.
- [6] Robin Y., Ding K., Demir İ., Clintock M., Elagöz S., Razeghi M., High Brightness Ultraviolet Light-Emitting Diodes Grown on Patterned Silicon Substrate, *Materials Science in Semiconductor Processing.*, 90 (2019) 87-91.
- [7] Heying B., Wu X.H., Keller S., Li Y., Kapolnek D., Keller B.P., DenBaars S.P., Speck J.S., Role of Threading Dislocation Structure on the X-Ray Diffraction Peak Widths in Epitaxial GaN Films, *Applied Physics Letters.*, 68 (5) (1996) 643-645.
- [8] Liu L., Edgar J.H., Substrates For Gallium Nitride Epitaxy. *Materials Science and Engineering: R: Reports.*, 37(3) (2002) 61-127.
- [9] Nakamura S., The Roles of Structural Imperfections in InGaN-Based Blue Light-

- Emitting Diodes And Laser Diodes, *Science.*, 281 (5379) (1998) 956-961.
- [10] Benisty H., Neve H.D., Weisbuch C., Impact of Planar Microcavity Effects on Light Extraction-Part I: Basic Concepts and Analytical Trends, *IEEE Journal of Quantum Electronics.*, 34 (9) (1998) 1612-1631.
- [11] Zhmakin A.I., Enhancement of Light Extraction From Light Emitting Diodes, *Physics Reports.*, 498 (4-5) (2011) 189-241.
- [12] Kuznia J.N., Khan M.A., Olson D.T., Influence of Buffer Layers on the Deposition of High Quality Single Crystal GaN Over Sapphire Substrates, *Journal of Applied Physics.*, 73 (9) (1993) 4700-4702.
- [13] Yi M.S., Lee H.H., Kim D.J., Park S.J., Noh D.Y., Effects of Growth Temperature on GaN Nucleation Layers, *Applied Physics Letters.*, 75 (15) (1999) 2187-2189.
- [14] Chen J., Zhang S.M., Zhang B.S., Zhu J.J., Feng G., Shen X.M., Wang, Y.T., Yang, H., Zheng, W.C., Effects of Reactor Pressure on GaN Nucleation Layers and Subsequent GaN Epilayers Grown on Sapphire Substrate, *Journal of Crystal Growth.*, 254 (3-4) (2003) 348-352.
- [15] Ito T., Sumiya M., Takano Y., Ohtsuka K., Fuke S., Influence of Thermal Annealing on GaN Buffer Layers and the Property of Subsequent GaN Layers Grown by Metalorganic Chemical Vapor Deposition, *Japanese Journal of Applied Physics.*, 38 (2R) (1999) 649.
- [16] Demir I., Altuntaş I., Kasapoğlu A.E., Mobtakeri S., Gür E., Elagöz S., Microstructural Evolution of MOVPE Grown GaN by the Carrier Gas, *Semiconductors.*, 52 (16) (2018) 2030-2038.
- [17] Altuntas I., Demir I., Kasapoğlu A.E., Mobtakeri S., Gür E., Elagöz S., The Effects of Two-Stage HT-GaN Growth With Different V/III Ratios During 3D–2D Transition *Journal of Physics D: Applied Physics.*, 51 (3) (2017).
- [18] Ashby C.I.H., Mitchell C.C., Han J., Missert N.A., Provencio P.P., Follstaedt D.W., Peake G.M., Griego L., Low-Dislocation-Density GaN From a Single Growth on a Textured Substrate, *Applied Physics Letters.*, 77 (20) (2000) 3233-3235.
- [19] Dai Q., Schubert M.F., Kim M.H., Kim J.K., Schubert E.F., Koleske D.D., Crawford M.H., Lee S.R., Fischer A.J., Thaler G., Banas M.A., Internal Quantum Efficiency and Nonradiative Recombination Coefficient of GaInN/GaN Multiple Quantum Wells With Different Dislocation Densities, *Applied Physics Letters.*, 94 (11) (2009).
- [20] Lester S.D., Ponce F.A., Craford M.G., Steigerwald D.S., High Dislocation Densities in High Efficiency GaN-Based Light-Emitting Diodes, *Applied Physics Letters.*, 66 (10) (1995) 1249-1251.
- [21] Chierchia R., Böttcher T., Heinke H., Einfeldt S., Figge S., Hommel D., Microstructure of Heteroepitaxial GaN Revealed by X-Ray Diffraction, *Journal of Applied Physics.*, 93 (11) (2003) 8918-8925.
- [22] Korbutowicz R., Kozłowski J., Dumiszewska E., Serafinczuk J., X-Ray Characterization of Thick GaN Layers Grown By HVPE, *Crystal Research and Technology: Journal of Experimental and Industrial Crystallography.*, 40 (4-5) (2005) 503-508.
- [23] Moram M.A., Vickers M.E., X-Ray Diffraction of III-Nitrides, *Reports on Progress in Physics.*, 72 (3) (2009) 036502.
- [24] Pittet P., Lu G.N., Galvan J.M., Bluet J.M., Anas Í., Giraud J.Y., Balosso J., PL Characterization of GaN Scintillator for Radioluminescence-Based Dosimetry, *Optical Materials.*, 31 (10) (2009) 1421-1424.
- [25] Zhang H., Reber A.C., Geng L., Rabayda D., Wu H., Luo Z., Yao J., Khanna S.N., Formation of Al⁺(C₆H₆)₁₃: The Origin of Magic Number in Metal–Benzene Clusters Determined by the Nature of the Core, *CCS Chemistry.*, 1 (5) (2019) 571-581.
- [26] Prall C., Kaspari C., Brunner F., Haberland K., Weyers M., Rueter D., In-Situ Photoluminescence Measurements During MOVPE Growth of GaN and InGaN MQW Structures, *Journal of Crystal Growth.*, 415 (2015) 1-6.

- [27] Robins L.H., Bertness K.A., Barker J.M., Sanford N.A., Sclager J.B., Optical and Structural Study of GaN Nanowires Grown By Catalyst-Free Molecular Beam Epitaxy. II. Sub-Band-Gap Luminescence And Electron Irradiation Effects, *Journal Of Applied Physics.*, 101 (11) (2007).
- [28] Reshchikov M.A., Evaluation of GaN by Photoluminescence Measurement, *Physica Status Solidi c.*, 2011. 8 (7-8) (2011) 2136-2138.



Proposed nonparametric tests for the ordered alternative in a completely randomized and randomized block mixed design

Hasan Hüseyin GÜL¹ * , Hülya BAYRAK² 

¹Giresun University, Department of Statistic, Giresun/ TURKEY

²Gazi University, Department of Statistic, Ankara/ TURKEY

Abstract

Two nonparametric tests are proposed for the mixed design consisting of a randomized complete block and a completely randomized design to test for k nondecreasing treatment effects. The Hollander test and the Page test are used in randomized complete block design and completely randomized design, respectively. We compared the performance of the proposed tests against the Z_{Combl} , Z_{CombII} Page and Hollander tests. A Monte Carlo simulation study was conducted comparing the estimated powers of the tests 3, 4 and 5 treatments under various treatment effects and three different underlying distributions. In conclusion, the two proposed tests have higher powers than the Page, Hollander, Z_{Combl} and Z_{CombII} tests.

Article info

History:

Received: 01.07.2020

Accepted: 12.01.2021

Keywords:

Randomized complete block design, Completely randomized design, Page's test, Hollander test.

1. Introduction

When researchers may wish to compare the effects of treatments, they need to plan an experimental design. Design structures can occur in many ways. Magel and Ndungu [1] gave an example in which a business may have several thousand employees and wants to reduce the annual cost of health care for the employees. For example, a business may have several thousand employees and wants to reduce the annual cost of health care for the employees. For this purpose, the business wants to educate workers to change food habits, as to good nutrition and fitness and make a more appropriate exercise program. The business believes that some factors, including cholesterol level, blood pressure, body mass index, the amount of sleep a person gets, and the amount and types of exercises, are related to the health of workers, represented by a health number. This number is based on the values of the observed factors for the employee with a higher health number indicating better health. A voluntary worker may likely to skip a period time or periods when these factors are measured. For this reason, there could be missing observations within a block; hence, in testing whether this program is efficient, the business may decide to collect some observations using a completely

randomized design in which additional random samples of the employees involved only during a period time. This mixed design consists of a randomized complete block portion and a completely randomized design portion. It is possible to have a mixed design which is a combination of a randomized complete block, paired data, a balanced incomplete block and a completely randomized design.

As can be seen from the above example, in real life problems, researchers may have to change the design structure in order to avoid loss of information. For this reason, these block designs that form the mixed design structure should be analyzed with non-parametric test combinations. However, there are very few studies on mixed designs in the literature. Therefore, in this article, we proposed nonparametric tests which is combined Hollander [2] test statistic (randomized complete block) and Jonckheere-Terpstra (JT) test statistic [3-4] (completely randomized design) for ordered alternatives. We would like to test the following set of hypotheses:

$$H_0: \tau_1 = \tau_2 = \dots = \tau_k$$

$$H_1: \tau_1 \leq \tau_2 \leq \dots \leq \tau_k \quad (1)$$

with τ_i indicating the treatment effect for the i^{th} time period and k indicating the number of treatments.

Several nonparametric tests available to test the differences for more than two treatments in a completely randomized design. Kruskal-Wallis test statistic [5] is a nonparametric test which is an extension of the Mann-Whitney test statistic [6] comparing two treatments in a completely randomized design. The JT test is designed to test the non-decreasing treatment effects for this type of design. Akdur et al. [7] modified generalized Jonckheere test for repeated measures in randomized blocks with circular bootstrap method. To compute the JT test statistic, JT , we calculate the $k(k-1)/2$ Mann-Whitney counts U_{uv} given by

$$U_{uv} = \sum_{i=1}^{n_u} \sum_{j=1}^{n_v} \varphi(X_{iu}, X_{jv}), 1 \leq u < v \leq k,$$

where $\varphi(a, b) = 1$ if $a < b$, 0 otherwise. (Thus, U_{uv} is the number of sample u before sample v precedences). The JT test statistic is the sum of these $k(k-1)/2$ Mann-Whitney counts:

$$JT = \sum_{u=1}^{v-1} \sum_{v=2}^k U_{uv}. \tag{2}$$

The expected value and variance of JT are:

$$E(JT) = \frac{N^2 - \sum_{j=1}^k n_j^2}{4},$$

and

$$Var(JT) = \frac{N^2(2N+3) - \sum_{j=1}^k n_j^2(2n_j+3)}{72}.$$

The standardized version of the test statistic, Z_{JT} , is given as:

$$Z_{JT} = \frac{JT - E(JT)}{\sqrt{Var(JT)}} \tag{3}$$

where n_j is j^{th} treatment sample and N is the total sample size of all treatments. Under H_0 , the test statistic, Z_{JT} , has an asymptotic normal distribution [8]. It is rejected when standardized version is greater than or equal to Z_α at the α level of significance.

There are several nonparametric tests to compare more than two treatments in a randomized complete block design. One of the most important tests is the Page test statistic [9], which compares the treatment effects for non-decreasing alternatives. Gokpınar et al. [10]

compared performances of permutation version of several non parametric tests such as Page, Hollander tests for ordered alternative hypotheses in RCBD. Recently, Akdur et al. [11] proposed a nonparametric test for ordered alternatives in randomized complete block designs (RCBD). Hollander test statistic, H , [2] based on Wilcoxon signed-rank test statistic [12] is used for testing non-decreasing alternatives. For each of pair (u, v) treatment and each of $1 < u < v < t$, T_{uv} is defined as a signed-rank statistic and written as:

$$T_{uv} = \sum_{i=1}^b R_{uv}^i \psi_{uv}^i,$$

where

$$\psi_{uv}^i = \begin{cases} 1 & X_{iu} < X_{iv} \\ \frac{1}{2} & X_{iu} = X_{iv} \\ 0 & X_{iu} > X_{iv} \end{cases}$$

H test statistic depending on the statistic of T_{uv} is

$$H = \sum_{u=1}^{t-1} \sum_{v=u+1}^t T_{uv}. \tag{4}$$

The expected value and variance of the H test statistic are

$$E(H) = \frac{bt(t-1)(b+1)}{8}$$

and

$$Var(H) = \frac{bt(b+1)(2b+1)(t-1)\{3 + 2(t-2)p_U^b\}}{144}$$

where p_U^b , depend on b , is the value of the null correlation between two overlapping signed rank statistics based on n observations. Wilcoxon signed-rank test statistic. The standardized version of the test statistic, Z_H , is given as:

$$Z_H = \frac{H - E(H)}{\sqrt{Var(H)}}. \tag{5}$$

Under H_0 , the test statistic, Z_H , has an asymptotic normal distribution. It is rejected when standardized version is greater than or equal to Z_α at the α level of significance.

Dubnicka et al. [13] proposed a rank-based test for the mixed two-sample design which is a combination of paired data and independent observations. Their proposed test statistic is sum of the Wilcoxon signed rank statistic (paired data) and the Mann-Whitney statistic (independent samples).

Magel et al. [14] proposed tests for testing the equality of k medians when the data are mixture of a randomized complete block, a completely randomized

and incomplete block design. They developed two tests for the umbrella alternatives. The two proposed tests are compared to each other and give suggestions.

Magel and Fu [15] proposed a nonparametric test for a mixed design which is a combination of a paired sample portion and a two-independent-sample portion to test for a difference in treatment effects.

Olet ve Magel [16] proposed six nonparametric tests to test for a difference between the control and any of $k-1$ treatments in a completely randomized and randomized complete block mixed design.

Magel et al. [17] introduced two tests for the non-decreasing alternative for mixed designs consisting of a randomized complete block portion and a completely randomized design portion. Their proposed test statistics are linear combinations of Page's test statistic and the JT test statistic.

The first version of the test can be written as

$$Z_{Combl} = \frac{Z_p + Z_{JT}}{\sqrt{2}}, \quad (6)$$

where Z_p and Z_{JT} are the standardized version of Page's test and standardized version of JT test, respectively. Under H_0 , Z_{Combl} has an asymptotic standard normal distribution since the asymptotic distributions of Z_p and Z_{JT} under H_0 are standard normal. H_0 is rejected if $Z_{Combl} > Z_\alpha$, where Z_α is the $(1 - \alpha)100$ percentile of a standard normal distribution.

The second version of the test can be formulated as

$$Z_{CombII} = \frac{L + JT - E(L + JT)}{\sqrt{Var(L + JT)}}, \quad (7)$$

where

$$E(L + JT) = \frac{bk(k+1)^2}{4} + \frac{(N^2 - \sum_{i=1}^k n_i^2)}{4},$$

$$Var(L + JT) = \frac{b(k^3 - k)^2}{144(k-1)} + \frac{N^2(2N+3) - \sum_{i=1}^k n_i^2(2n_i+3)}{72}.$$

Here, L and JT are Page's test statistic and the JT test statistic, respectively. The test statistic has an asymptotic standard normal distribution when H_0 is true. It is rejected when $Z_{CombII} > Z_\alpha$, where Z_α is the $(1 - \alpha)$ percentile of a standard normal distribution.

We propose two forms of a test statistic for a mixed design consisting of a completely randomized portion and a randomized block portion. We may wish to compare the effects of k treatments. The underlying distributions considered include the normal distribution, exponential distribution and t distribution with 3 degrees of freedom. To use parametric tests, random sample should be drawn from normal

distribution or large enough sample size, and hence, we are considering nonparametric tests.

The paper is organized as follows. Section 2 introduces the proposed nonparametric tests for a mixed design consisting of randomized complete block design and completely randomized design. The simulation results and discussions are provided in Section 3-4. Finally, we give some concluding remarks in Section 5.

2. Proposed Tests

In this article, we propose and compare nonparametric tests for a mixed design consisting of randomized complete block design and completely randomized design based on hypothesis given in Eq. (1). These tests are linear combinations of Hollander test statistic and JT test statistic. The tests we propose are similar to the idea of Magel et al. [17].

The first version of the test statistic considered adds the standardized versions of the Hollander test statistic, denoted by Z_H , and the JT test statistic, denoted by Z_{JT} , and then divided by $\sqrt{2}$. The first proposed test statistic, denoted by Z_I , is given in Eq. (8),

$$Z_I = \frac{Z_H + Z_{JT}}{\sqrt{2}}. \quad (8)$$

Under H_0 , Z_I has an asymptotic standard normal distribution. The null hypothesis is rejected when $Z_I > Z_\alpha$.

The second version of the test statistic considered adds the nonstandardized versions of Hollander test statistic, denoted by H , and the JT test statistic, denoted by JT , together and then restandardized. The second proposed test statistic, denoted by Z_{II} , is given in Eq. (9):

$$Z_{II} = \frac{H + JT - [E(H) + E(JT)]}{\sqrt{[V(H) + V(JT)]}}. \quad (9)$$

Under H_0 , Z_{II} has an asymptotic standard normal distribution. The null hypothesis is rejected when $Z_{II} > Z_\alpha$.

3. Simulation Study

A simulation study was conducted using MATLAB (R2017b) to compare the powers of the proposed test versions with the powers of the tests constructed by [17] and the powers of Page's test and Hollander test discarding the additional observations from the completely randomized design portion. The underlying population distributions considered were the normal, exponential and student's t with 3 degrees of freedom. All powers were estimated based on 5000 iterations for each combination of the distributions, several different equal and unequal arrangements of sample sizes and

different location parameter arrangements. Since the convergence required for the power values and the estimated alpha is at 5000 iterations, so it is taken as the number of iterations. Estimated alpha and power values were found in each case. A relative difference percentage between the two test versions developed by [17] was calculated by:

$$D = \frac{100 * (Power_{Z_I} - Power_{Z_{II}})}{Power_{Z_I}} \quad (10)$$

When this difference is positive, the first test version, Z_I , has a higher estimated power. When this difference is negative, the second version, Z_{II} , has a higher estimated power. In the simulation study, the equal and unequal sample sizes denoted by n (recall, the JT test is used on this portion) were used for the completely randomized design portion. The cases were considered so that the completely randomized portion was 1/8, 1/4 and 1/2 that of the randomized complete block portion (recall, the Page's test and Hollander test were used on the block portion). The following is a list of all of the sample sizes considered where block is randomized block portion and n_i is completely randomized block portion:

1. Block=40, $n_i = 5$.
2. Block=40, $n_i = 10$.
3. Block=40, $n_i = 20$.
4. Block=16, $n_1 = 8, n_2 = n_3 = n_4 = 4$.
5. Block=32, $n_1 = 8, n_2 = n_3 = n_4 = 4$.
6. Block=40, $n_1 = 10, n_2 = n_3 = n_4 = 5$.

In the simulation study, we considered increasing ordered alternatives. Various location parameters were added when estimating the powers of the test statistics. The number of treatments (denoted by k) were taken 3,4 and 5. The u_i value in tables is the location parameter arrangement for i^{th} treatment, $i=1, 2, 3, 4$ and 5. The value n_i is the sample size of i^{th} treatment for the completely randomized portion.

4. Results

Estimated rejection percentages are given for each two proposed test, the two proposed test are given by [17], Page's test and Hollander test (discarding observations from the completely randomized design for the Page's and Hollander test). The percentage rejection difference is defined in Eq. (10). Percentage of rejections for Page's test, Hollander test, the proposed test, denoted by Z_{Combl} and Z_{CombII} , are given by [17], the proposed test version one and proposed test version two are shown in columns Page (%), Hollander (%),

Z_{Combl} (%), Z_{CombII} (%), Z_I (%) and Z_{II} (%). D is the percentage rejection difference between the two proposed tests.

Selected results are given in Tables 1-7. Selected results for the normal distribution and four treatments, $k=4$, are given in Tables 1 and 6. In Tables 1-3, the results are shown for 40 blocks with various equal sample sizes for the completely randomized portion. In Tables 4-6, the results are shown for 16, 32 and 40 blocks with various unequal sample sizes for the completely randomized portion.

5. Conclusion

In this article, we proposed two nonparametric test statistics for a mixed design consisting of randomized complete block design and completely randomized design. These test statistics are weighted versions of the standardized Hollander test statistic and the standardized JT test statistic. When $\sigma_H^2 = \sigma_{JT}^2$, Z_I is a special case of Z_{II} .

$$Z_I = \frac{Z_H + Z_{JT}}{\sqrt{2}} = \frac{1}{\sqrt{2}} \left(\frac{H - U_H}{\sqrt{\sigma_H^2}} + \frac{JT - U_{JT}}{\sqrt{\sigma_{JT}^2}} \right),$$

$$Z_{II} = \frac{H + JT - [E(H) + E(JT)]}{\sqrt{[V(H) + V(JT)]}}$$

$$= \frac{(H + JT) - (u_H + U_{JT})}{\sqrt{\sigma_H^2 + \sigma_{JT}^2}}$$

$$= \frac{\sqrt{\sigma_H^2}}{\sqrt{\sigma_H^2 + \sigma_{JT}^2}} \frac{H - u_H}{\sqrt{\sigma_H^2}} + \frac{\sqrt{\sigma_{JT}^2}}{\sqrt{\sigma_H^2 + \sigma_{JT}^2}} \frac{JT - u_{JT}}{\sqrt{\sigma_{JT}^2}}$$

In the first version of proposed nonparametric tests, denoted by Z_I , the weights of variances of Hollander test and JT test are $1/\sqrt{2}$. In the second version of proposed nonparametric tests, denoted by Z_{II} , if the variance of Hollander test is larger, then Hollander test will get more weight; otherwise, JT test will get more weight.

The results showed that the empirical type I error rate of all tests are close to nominal level within acceptable values ranging between 4.38 and 5.48 over all of the cases considered.

In Tables 1 and 2, one can see that the power of the Z_{II} test statistic is superior to other tests. In Table 3, the Z_I test statistic has higher powers than the Z_{II} test statistic in some cases. We noticed as in comparing Tables 1,2 and 3, when the sample size, n , is equal, the rejection percentage of Z_{II} gradually decreases, which can be

explained by weights. Since the sample size of Hollander test is more than JT test, the weight of the Hollander test will be higher and the power of the Hollander test is higher than the JT test. When the sample size of each treatment in the completely randomized portion starts increasing, the weight of the JT test will increase with the power.

In Tables 4, 5 and 6, unequal sample sizes, n_i , are considered. The proposed two nonparametric test versions, Z_I and Z_{II} , again have higher powers of any of the tests. When Tables 4 and 5 are compared, the rejection percentage of Z_{II} gradually increases because of weights. When the sample size of each treatment in the randomized complete block portion starts increasing, the weight of the Hollander test will increase as the power increases. When Tables 5 and 6 are compared, there is no noticeable difference in terms of the rejection percentage of Z_{II} because both cases are considered, so that the completely randomized portion is 1/8 that of the randomized complete block portion.

The overall recommendation is to use either Z_I or Z_{II} tests. If the completely randomized portion is 1/8 or 1/4 that of the randomized complete block portion, Z_{II} test is recommended. If the completely randomized portion is 1/2 that of the randomized complete block portion, Z_I and Z_{II} tests are recommended together.

Table 7 give the weights of the Hollander's test and JT test for the first and second proposed tests versions, Z_I and Z_{II} . The weights were compared with the rejection percentage results. Moreover, in this table, number of

treatments is considered $k=3$ for exponential distribution and $k=5$ for student's t distribution respectively.

In Table 7, for unequal cases, if the weight of JT test is higher in Z_{II} , the first proposed version is better. For example, the first case: $k=3$, block=16, $n_1 = 8, n_2 = n_3 = n_4 = 4$, the second case: $k=4$, block=16, $n_1 = 8, n_2 = n_3 = n_4 = 4$ and the third case: $k=5$, block=16, $n_1 = 8, n_2 = n_3 = n_4 = n_5 = 4$. Therefore, it is better to use Z_I , in these cases. If the weight of Hollander test is higher in Z_{II} , the second proposed version is better.

For equal cases, the weight of Hollander test is higher in Z_{II} in all situations. Therefore, it is better to use Z_{II} , in these cases.

The range of average D is (-10.94, -0.04). The case for exponential distributions, the number of treatment is 3, block = 16, $n = 4$ has the lowest average D which equals -0.04. The case for t distributions, the number of treatment is 5, block = 16, $n = 8$ has the highest average D which equals -10.94. Since $D < 0$, the second proposed test, Z_{II} , is better.

The range of average D is (0.08, 4.45). The case for exponential distributions, the number of treatment is 3, block = 16, $n_1 = 8, n_2 = n_3 = 4$ has the lowest average D which equals 0.08. The case for t distributions, the number of treatment is 5, block = 16, $n_1 = 8, n_2 = n_3 = n_4 = n_5 = 4$ has the highest average D which equals 4.45. Since $D > 0$, the first proposed test, Z_I , is better.

Table 1. Percentage of rejection for $k=4$; Normal distributions: block = 40 and $n = 5$

u_1	u_2	u_3	u_4	$P(\%)$	$H(\%)$	$Z_{Combl}(\%)$	$Z_{CombII}(\%)$	$Z_I(\%)$	$Z_{II}(\%)$	D
0.000	0.000	0.000	0.000	4.60	4.60	4.48	4.38	4.90	4.74	3.26
0.000	0.100	0.200	0.300	33.22	38.76	32.84	35.30	36.58	39.80	-8.80
0.000	0.000	0.250	0.250	32.96	38.28	32.64	35.12	36.44	39.22	-7.63
0.000	0.125	0.250	0.250	24.42	32.72	27.62	29.10	30.62	33.44	-9.21
0.000	0.000	0.000	0.500	56.34	65.06	55.98	59.06	61.26	66.82	-9.08
0.050	0.100	0.300	0.500	59.08	68.28	59.00	61.68	65.56	69.88	-6.59
0.000	0.000	0.500	0.500	78.30	85.98	77.48	80.38	83.04	87.26	-5.08
0.000	0.250	0.500	0.500	68.78	76.82	67.92	70.88	73.92	78.08	-5.63
0.000	0.500	0.500	1.000	97.40	99.18	97.16	98.18	98.64	99.40	-0.77
0.000	0.250	0.250	0.500	57.10	65.90	57.00	59.96	62.62	67.46	-7.73
0.000	0.250	0.250	0.250	22.34	27.42	22.58	23.86	26.08	28.08	-7.67
0.100	0.200	0.600	1.000	98.18	99.64	98.24	98.80	99.24	99.72	-0.48
0.250	0.250	0.500	0.500	32.96	38.50	32.64	35.12	36.30	39.80	-9.64
0.000	0.100	0.300	0.700	87.18	93.22	86.16	89.12	90.38	94.14	-4.16
0.000	0.050	0.150	0.350	39.88	45.94	39.86	42.56	43.56	47.20	-8.36
0.000	0.150	0.200	0.500	59.26	67.49	59.06	61.90	64.14	69.04	-7.64
0.000	0.000	0.100	0.600	74.20	81.88	73.28	76.40	77.76	83.32	-7.15
0.000	0.000	0.050	0.300	30.94	37.18	30.52	32.86	34.50	38.08	-10.38

Table 2. Percentage of rejection for $k=4$; Normal distributions: block = 40 and $n = 10$

u_1	u_2	u_3	u_4	$P(\%)$	$H(\%)$	$Z_{Combl}(\%)$	$Z_{CombII}(\%)$	$Z_I(\%)$	$Z_{II}(\%)$	D
0.000	0.000	0.000	0.000	4.70	4.60	5.16	5.48	4.78	4.62	3.34
0.000	0.100	0.200	0.300	39.40	38.76	39.52	29.78	43.02	43.10	-0.19
0.000	0.000	0.250	0.250	38.76	38.28	39.02	30.34	41.56	42.50	-2.26
0.000	0.125	0.250	0.250	33.00	32.72	32.54	25.50	34.86	36.44	-4.53
0.000	0.000	0.000	0.500	65.84	65.06	64.96	51.64	68.92	70.39	-2.13
0.050	0.100	0.300	0.500	68.78	68.28	68.00	54.62	73.34	74.22	-1.20
0.000	0.000	0.500	0.500	86.28	85.98	85.80	72.74	87.92	89.86	-2.21
0.000	0.250	0.500	0.500	77.50	76.82	77.38	62.90	81.26	82.06	-0.98
0.000	0.500	0.500	1.000	99.36	99.18	99.12	95.92	99.68	99.72	-0.04
0.000	0.250	0.250	0.500	65.96	65.90	66.16	52.52	70.94	71.30	-0.51
0.000	0.250	0.250	0.250	26.08	27.42	26.58	21.34	28.22	28.32	-0.35
0.100	0.200	0.600	1.000	99.44	99.64	99.28	96.68	99.83	99.90	-0.07
0.250	0.250	0.500	0.500	37.82	38.50	39.02	30.34	40.88	41.52	-1.57
0.000	0.100	0.300	0.700	93.22	93.22	93.08	82.54	94.88	95.67	-0.83
0.000	0.050	0.150	0.350	46.90	45.94	47.28	36.60	50.63	51.42	-1.56
0.000	0.150	0.200	0.500	68.12	67.49	68.38	54.64	71.58	73.08	-2.10
0.000	0.000	0.100	0.600	81.94	81.88	82.34	68.84	85.54	86.76	-1.43
0.000	0.000	0.050	0.300	36.55	37.18	36.42	28.10	39.30	40.33	-2.62

Table 3. Percentage of rejection for $k=4$; Normal distributions: block = 40 and $n = 20$

u_1	u_2	u_3	u_4	$P(\%)$	$H(\%)$	$Z_{Combl}(\%)$	$Z_{CombII}(\%)$	$Z_I(\%)$	$Z_{II}(\%)$	D
0.000	0.000	0.000	0.000	4.80	4.90	5.22	4.96	4.58	4.60	-0.43
0.000	0.100	0.200	0.300	32.90	38.46	48.24	32.40	50.10	50.20	-0.20
0.000	0.000	0.250	0.250	33.32	39.66	47.60	32.40	49.70	50.66	-1.93
0.000	0.125	0.250	0.250	27.20	33.00	40.16	27.32	41.82	42.22	-0.96
0.000	0.000	0.000	0.500	56.24	65.28	75.98	53.88	78.52	79.20	-0.87
0.050	0.100	0.300	0.500	59.58	67.17	78.70	57.34	81.64	81.74	-0.12
0.000	0.000	0.500	0.500	78.78	86.78	92.78	75.74	95.08	95.54	-0.48
0.000	0.250	0.500	0.500	68.38	76.75	86.52	65.60	88.94	89.16	-0.25
0.000	0.500	0.500	1.000	97.50	99.24	99.82	96.22	99.96	99.92	0.04
0.000	0.250	0.250	0.500	56.18	64.75	76.08	54.84	78.42	79.00	-0.74
0.000	0.250	0.250	0.250	22.52	26.97	32.62	22.50	34.68	34.26	1.21
0.100	0.200	0.600	1.000	98.44	99.52	99.88	97.12	99.99	99.96	0.03
0.250	0.250	0.500	0.500	33.32	39.76	47.60	32.40	49.70	50.56	-1.73
0.000	0.100	0.300	0.700	87.14	93.40	97.28	84.92	98.52	98.66	-0.14
0.000	0.050	0.150	0.350	39.76	46.33	57.22	38.32	59.56	60.00	-0.74
0.000	0.150	0.200	0.500	59.52	67.20	78.72	56.94	82.42	81.38	1.26
0.000	0.000	0.100	0.600	73.88	82.36	90.62	71.70	93.12	93.16	-0.04
0.000	0.000	0.050	0.300	30.28	35.90	44.20	29.96	46.58	46.54	0.09

Table 4. Percentage of rejection for $k=4$; Normal distributions: block = 16 and $n_1 = 8$ and $n_2 = n_3 = n_4 = 4$

u_1	u_2	u_3	u_4	$P(\%)$	$H(\%)$	$Z_{Combl}(\%)$	$Z_{CombII}(\%)$	$Z_I(\%)$	$Z_{II}(\%)$	D
0.000	0.000	0.000	0.000	5.10	4.90	5.00	5.20	5.12	5.06	1.17
0.000	0.100	0.200	0.300	20.14	20.84	23.04	22.34	24.18	24.00	0.74
0.000	0.000	0.250	0.250	20.20	21.88	22.24	21.64	22.68	24.09	-6.22
0.000	0.125	0.250	0.250	17.02	18.54	20.54	19.94	20.66	20.18	2.32
0.000	0.000	0.000	0.500	32.22	33.98	33.98	32.64	36.44	38.70	-6.20
0.050	0.100	0.300	0.500	33.76	38.66	37.90	36.64	42.46	43.98	-3.58
0.000	0.000	0.500	0.500	47.20	52.38	53.16	51.14	56.66	58.58	-3.39
0.000	0.250	0.500	0.500	39.98	45.51	48.22	46.92	53.33	52.83	0.94
0.000	0.500	0.500	1.000	76.00	81.76	86.40	84.74	89.34	88.68	0.74
0.000	0.250	0.250	0.500	32.82	34.30	38.40	37.18	41.44	39.94	3.62
0.000	0.250	0.250	0.250	15.04	14.84	18.56	18.42	17.29	16.66	3.64
0.100	0.200	0.600	1.000	79.32	83.78	85.84	83.52	88.62	89.75	-1.28
0.250	0.250	0.500	0.500	20.20	21.54	22.24	21.64	23.20	23.64	-1.90
0.000	0.100	0.300	0.700	56.52	61.46	63.30	60.20	67.02	68.42	-2.09
0.000	0.050	0.150	0.350	23.66	25.20	26.16	25.16	28.32	28.24	0.28
0.000	0.150	0.200	0.500	34.38	36.74	38.62	37.38	42.24	42.62	-0.90
0.000	0.000	0.100	0.600	43.60	48.10	46.70	44.54	51.92	54.32	-4.62
0.000	0.000	0.050	0.300	18.94	20.36	20.60	19.66	21.84	22.48	-2.93

Table 5. Percentage of rejection for $k=4$; Normal distributions: block = 32 and $n_1 = 8$ and and $n_2 = n_3 = n_4 = 4$

u_1	u_2	u_3	u_4	$P(\%)$	$H(\%)$	$Z_{Combl}(\%)$	$Z_{CombII}(\%)$	$Z_I(\%)$	$Z_{II}(\%)$	D
0.000	0.000	0.000	0.000	5.28	4.68	4.78	4.62	4.93	4.68	5.07
0.000	0.100	0.200	0.300	30.24	33.62	31.06	30.84	33.96	35.54	-4.65
0.000	0.000	0.250	0.250	29.66	33.70	29.84	30.06	31.66	34.82	-9.98
0.000	0.125	0.250	0.250	25.22	27.82	26.12	26.20	27.43	28.92	-5.43
0.000	0.000	0.000	0.500	50.86	56.36	48.08	48.78	52.18	58.02	-11.19
0.050	0.100	0.300	0.500	54.04	57.98	52.72	53.62	56.14	60.81	-8.32
0.000	0.000	0.500	0.500	72.50	79.30	71.14	72.02	75.64	81.36	-7.56
0.000	0.250	0.500	0.500	62.48	68.46	64.48	65.12	70.48	71.41	-1.32
0.000	0.500	0.500	1.000	95.22	97.88	95.76	96.18	98.02	98.56	-0.55
0.000	0.250	0.250	0.500	52.08	56.87	52.90	53.34	57.84	59.84	-3.46
0.000	0.250	0.250	0.250	20.56	23.88	22.84	22.56	25.84	25.40	1.70
0.100	0.200	0.600	1.000	96.26	98.32	95.88	96.44	97.70	98.82	-1.15
0.250	0.250	0.500	0.500	29.66	32.66	29.84	30.06	31.18	34.08	-9.30
0.000	0.100	0.300	0.700	82.56	88.24	81.14	82.16	85.86	89.58	-4.33
0.000	0.050	0.150	0.350	36.46	39.24	35.92	36.22	38.36	40.54	-5.68
0.000	0.150	0.200	0.500	54.30	59.68	53.70	54.16	58.32	61.70	-5.80
0.000	0.000	0.100	0.600	67.96	73.66	65.02	65.92	68.89	75.44	-9.51
0.000	0.000	0.050	0.300	27.84	31.50	26.92	27.00	28.99	32.82	-13.21

Table 6. Percentage of rejection for $k=4$; Normal distributions: block = 40 and and $n_1 = 10$ and $n_2 = n_3 = n_4 = 5$

u_1	u_2	u_3	u_4	$P(\%)$	$H(\%)$	$Z_{Combl}(\%)$	$Z_{CombII}(\%)$	$Z_I(\%)$	$Z_{II}(\%)$	D
0.000	0.000	0.000	0.000	5.34	5.28	5.24	5.28	4.88	5.22	-6.96
0.000	0.100	0.200	0.300	33.98	39.42	35.32	34.44	39.26	41.33	-5.27
0.000	0.000	0.250	0.250	33.90	39.28	34.58	33.50	37.12	41.09	-10.70
0.000	0.125	0.250	0.250	28.48	32.26	30.58	29.84	33.18	34.08	-2.71
0.000	0.000	0.000	0.500	56.80	64.24	55.12	53.18	59.78	66.40	-11.07
0.050	0.100	0.300	0.500	59.42	69.48	60.00	58.56	66.44	71.48	-7.59
0.000	0.000	0.500	0.500	78.04	86.32	79.40	77.64	84.44	87.94	-4.14
0.000	0.250	0.500	0.500	67.88	78.44	72.40	70.86	78.92	80.46	-1.95
0.000	0.500	0.500	1.000	97.78	99.36	98.64	98.40	99.32	99.46	-0.14
0.000	0.250	0.250	0.500	56.66	66.62	60.14	58.82	66.14	69.10	-4.48
0.000	0.250	0.250	0.250	23.70	26.91	27.08	26.48	27.86	27.96	-0.36
0.100	0.200	0.600	1.000	98.34	99.56	98.70	98.26	99.16	99.70	-0.54
0.250	0.250	0.500	0.500	33.90	38.58	34.58	33.50	36.96	39.98	-8.17
0.000	0.100	0.300	0.700	87.48	94.14	88.20	86.84	92.00	95.00	-3.26
0.000	0.050	0.150	0.350	40.26	47.74	41.40	39.96	45.83	49.50	-8.01
0.000	0.150	0.200	0.500	59.58	68.58	60.94	59.48	66.38	70.86	-6.75
0.000	0.000	0.100	0.600	74.20	81.66	73.28	71.36	77.40	83.42	-7.78
0.000	0.000	0.050	0.300	31.78	37.12	31.22	30.16	33.56	38.22	-13.89

Table 7. Comparing the Highest Percentages of Rejection with Weights of Hollander’s Test and JT Test (equal cases) for Z_{II}

Block	Case	Z_I	Z_{II}	$\frac{\sigma_H^2}{\sigma_H^2 + \sigma_{JT}^2}$	$\frac{\sigma_{JT}^2}{\sigma_H^2 + \sigma_{JT}^2}$
K=3					
16	$n_1 = 8. n_2 = n_3 = 4$	X		0.3200	0.6800
32	$n_1 = 8. n_2 = n_3 = 4$		X	0.7834	0.2166
40	$n_1 = 10. n_2 = n_3 = 5$		X	0.7830	0.2170
K=4					
16	$n_1 = 8. n_2 = n_3 = n_4 = 4$	X		0.2028	0.7972
32	$n_1 = 8. n_2 = n_3 = n_4 = 4$		X	0.6623	0.3377
40	$n_1 = 10. n_2 = n_3 = n_4 = 5$		X	0.6614	0.3386
K=5					
16	$n_1 = 8. n_2 = n_3 = n_4 = n_5 = 4$	X		0.1311	0.8689
32	$n_1 = 8. n_2 = n_3 = n_4 = n_5 = 4$		X	0.5383	0.4617
40	$n_1 = 10. n_2 = n_3 = n_4 = n_5 = 5$		X	0.8026	0.1974

Conflicts of interest

There is no conflict of interest.

References

[1] Magel R., Ndungu A., Nonparametric Tests for Ordering in Completely Randomized and Randomized Block Mixed Designs, *Journal of Biometrics & Biostatistics*, 4 (2013) 170-4.

[2] Hollander M., Rank Tests for Randomized Blocks When the Alternatives Have a Priori Ordering, *Annals of Mathematical Statistics*, 38 (1967) 867-877.

[3] Jonckheere A.R., A Distribution-Free k-Sample Test Against Ordered Alternatives, *Biometrika*, 41 (1954) 133-145.

[4] Terpstra T.J., The Asymptotic Normality and Consistency of Kendall’s Test against Trend. When Ties Are Present in One Ranking, *Indagationes Mathematicae*, 14 (1952) 327-333.

[5] Kruskal W.H., Wallis W.A., Use of Ranks in One-Criterion Variance Analysis, *Journal of the American Statistical Association*, 47(260) (1952) 583-621.

[6] Mann H.B., Whitney D.R., On a Test of Whether One of Two Random Variables is Stochastically Larger Than The Other, *Annals of Mathematical Statistics*, 18 (1954) 50-60.

[7] Akdur H.T.K., Gokpinar F., Bayrak H., Gokpinar E., A Modified Jonckheere Test Statistic for Ordered Alternatives in Repeated Measures Design, *Suleyman Demirel University Journal of Natural and Applied Sciences*, 20(3) (2016) 391-398.

[8] Hollander M., Wolfe D.A., Nonparametric Statistical Methods., 2nd ed., New York: Wiley, (1999).

[9] Page E.B., Ordered Hypotheses for Multiple Treatments: A Significance Test for Linear Ranks, *Journal of the American Statistical Association*, 58 (1963) 216-230.

[10] Gokpinar E., Gul H.H., Gokpinar F., Bayrak H., Ozonur D., Permutation Test Approach for Ordered Alternatives in Randomized Complete Block Design: A Comparative Study, *Gazi University Journal of Science*, 27(1) (2014) 645-651.

[11] Akdur H.T.K., Ozonur D., Gul H.H., Bayrak H., Comparison of Rank-Based Tests for Ordered Alternative Hypotheses in Randomized Complete Block Designs, *Gazi University Journal of Science*, 32(2) (2019) 705-716.

- [12] Wilcoxon F., Individual Comparisons by Ranking Methods, *Biometrics Bulletin*, 1 (1945) 80-83.
- [13] Dubnicka S.R., Blair R.C., Hettmansperger T.P., Rank-Based Procedures for Mixed Pire and Two Sample Designs, *Journal of Modern Applied Statistical Methods*, 1(1) (2002) 32-41.
- [14] Magel R., Terpstra J., Canonizado K., Park J.I., Nonparametric Tests for Mixed Designs, *Communications in Statistics-Simulation and Computation*, 39 (2010) 1228-1250.
- [15] Magel R., Fu R., Proposed Nonparametric Test for the Mixed Two-Sample Desig., *Journal of Statistical Theory and Practice*, 8(2) (2014) 221-237.
- [16] Olet S., Magel R., A Comparison of Nonparametric Tests in a Mixed Design for the Simple Tree Alternative, *International Journal for Research in Business Management and Accounting*, 3(3) (2017) 1-23.
- [17] Magel R., Terpstra J., Wen J., Proposed Tests for the Nondecreasing Alternative in a Mixed Design, *Journal of Statistics and Management Systems*, 12 (2014) 963-977.



Construction of a bivariate copula by Rüsçendorf's method

Mehmet YILMAZ^{1,*} , Muhammet BEKÇİ² 

¹Ankara University, Faculty of Science, Department of Statistics, Ankara/TURKEY

²Sivas Cumhuriyet University, Faculty of Science, Department of Statistics and Computer Sciences, Sivas/TURKEY

Abstract

In this paper, a new copula model with given unit marginals is proposed, based on Rüsçendorf's Method. A new bivariate copula family is introduced by adding a proper term to independence copula. Thus, we avoid the complexity of the proposed copula model. By choosing a baseline copula from the same marginal, we derive a new copula that can approach from above towards the independence copula. Furthermore, it is established that a bivariate copula constructed by this method allows some flexibility in the dependence measure according to Spearman's correlation coefficient. Additionally, tail dependence measures are investigated. Illustrative examples are given taking into account the specific choices of a baseline copula.

Article info

History:

Received:16.06.2020

Accepted:18.01.2021

Keywords:

Dependence,
Rüsçendorf's method,
Bivariate copula,
Fréchet bounds,
Spearman's rho.

1. Introduction

When creating new bivariate copula models, researchers generally try to obtain models that can express the high correlation. Lai and Xie [1] studied on construction of continuous bivariate positive quadrant dependent distributions. Bairamov et al. [2] provided an extension of the maximal correlation coefficient for the Farlie-Gumbel-Morgenstern (FGM) family. Firstly, we discuss the necessary conditions to construct a new copula. Secondly, we obtain bounds for dependence measure in accordance with Spearman's rank correlation coefficient. At last, the usefulness of this family is discussed by considering illustrative examples.

The genesis of the proposal is based on both works of [1] and [3]. Accordingly, a function $g(u, v)$ can be defined on the unit square as $g(u, v) = uv + k(u, v)$, where $k(u, v) = 0$ at the endpoints of the unit square, with $\frac{-\partial^2 k(u, v)}{\partial u \partial v} \leq 1$.

Let $C(u, v)$ denote the bivariate copula function. Then, according to the eq. (2) and the condition (3) of [1], and Rüsçendorf's method, the function $k(u, v)$ is chosen as $k(u, v) = uv \bar{C}(u, v)$, where \bar{C} denotes survival copula.

The following theorem shows that $g(u, v)$ meets the conditions (3)-(5) given in [1].

Theorem 1. $C_H(u, v) = uv(1 + \bar{C}(u, v))$ is a well-defined copula function.

Proof. According to Definition 2.2.2 of [4], a bivariate copula must satisfy the following properties:

(P1) For every u, v in $[0,1]$, it is obvious that

$$\lim_{u \rightarrow 0} C_H(u, v) = \lim_{u \rightarrow 0} uv(1 + \bar{C}(u, v)) = 0, \quad \lim_{v \rightarrow 0} C_H(u, v) = \lim_{v \rightarrow 0} uv(1 + \bar{C}(u, v)) = 0$$

and

$$\lim_{u \rightarrow 1} C_H(u, v) = \lim_{u \rightarrow 1} uv(1 + \bar{C}(u, v)) = v, \quad \lim_{v \rightarrow 1} C_H(u, v) = \lim_{v \rightarrow 1} uv(1 + \bar{C}(u, v)) = u, \\ \lim_{u \wedge v \rightarrow 1} C_H(u, v) = \lim_{u \wedge v \rightarrow 1} uv(1 + \bar{C}(u, v)) = 1.$$

(P2) We prove the continuous case only.

*Corresponding author. email address: mehmetyilmaz@ankara.edu.tr
<http://dergipark.gov.tr/csj> ©2021 Faculty of Science, Sivas Cumhuriyet University

$$c_H(u, v) = \frac{\partial^2 C_H(u, v)}{\partial u \partial v} = 1 + \bar{C}(u, v) + v \frac{\partial \bar{C}(u, v)}{\partial v} + u \frac{\partial \bar{C}(u, v)}{\partial u} + uv \frac{\partial^2 \bar{C}(u, v)}{\partial u \partial v}. \quad (1)$$

Now, by noting that $\bar{C}(u, v) = 1 - u - v + C(u, v)$, $\frac{\partial \bar{C}(u, v)}{\partial u} = -1 + \frac{\partial C(u, v)}{\partial u}$ and $\frac{\partial^2 \bar{C}(u, v)}{\partial u \partial v} = c(u, v) \geq 0$. Then eq. (1) can be rewritten as

$$c_H(u, v) = 1 - u - v + \bar{C}(u, v) + v \frac{\partial C(u, v)}{\partial v} + u \frac{\partial C(u, v)}{\partial u} + uv c(u, v). \quad (2)$$

Assume that the copula $C(u, v)$ belongs to the class of negative dependent copulas, and then it is easy to conclude that from corollary 5.2.6 of [4], each of the inequalities below holds:

$$u \frac{\partial C(u, v)}{\partial u} \geq C(u, v),$$

and

$$v \frac{\partial C(u, v)}{\partial v} \geq C(u, v).$$

Using both inequalities, a lower bound can be achieved as

$$\begin{aligned} c_H(u, v) &\geq 1 - u - v + C(u, v) + \bar{C}(u, v) + C(u, v) + uv c(u, v) \\ &= 2\bar{C}(u, v) + C(u, v) + uv c(u, v) \\ &\geq 0. \end{aligned}$$

Hence, under the assumption of the negative dependence, it is showed that (P2) holds.

Now, assume that the copula $C(u, v)$ belongs to the class of positive dependent copulas. Thus, the eq. (1) can be rewritten as follows:

$$c_H(u, v) = \left(1 + u \frac{\partial \bar{C}(u, v)}{\partial u}\right) \left(1 + v \frac{\partial \bar{C}(u, v)}{\partial v}\right) - uv \frac{\partial \bar{C}(u, v)}{\partial u} \frac{\partial \bar{C}(u, v)}{\partial v} + \bar{C}(u, v) + uv c(u, v). \quad (3)$$

According to Definition 1.2 of [5], and Theorem 5.2.10 and Theorem 5.2.15 of [4], the positive dependence implies

$$\frac{\partial \bar{C}(u, v)}{\partial u} \frac{\partial \bar{C}(u, v)}{\partial v} \leq c(u, v) \bar{C}(u, v).$$

Then by applying the latter inequality in eq. (3), we have the following lower bound

$$c_H(u, v) \geq \left(1 + u \frac{\partial \bar{C}(u, v)}{\partial u}\right) \left(1 + v \frac{\partial \bar{C}(u, v)}{\partial v}\right) + \bar{C}(u, v) + uv c(u, v)(1 - \bar{C}(u, v)). \quad (4)$$

Note that each summand in eq. (4) is nonnegative thus $c_H(u, v) \geq 0$ is obtained. This completes the proof.

Remark 1. Copula family $C_H(u, v) = uv(1 + \bar{C}(u, v))$ belongs to the class of positive dependent copulas since $uv \leq uv(1 + \bar{C}(u, v))$ for all $(u, v) \in [0, 1]^2$.

2. Lower and Upper Bounds on Spearman’s Rho Measure for C_H

This section is about obtaining the lower and upper bounds of the measure of dependency for the proposed bivariate copula family. According to [6] and [7], for any bivariate copula defined on the unit square contains Fréchet lower and upper bounds, which respectively are defined by

$$C^-(x, y) = \max\{u + v - 1, 0\} \quad (5)$$

$$C^+(x, y) = \min\{u, v\}. \quad (6)$$

For $C(u, v)$, Spearman's rho can be expressed as

$$\rho = 12 \int_0^1 \int_0^1 \{C(u, v) - uv\} dv du \tag{7}$$

(see, [8]). The coefficient of Spearman's rho for the new family can be obtained by

$$\begin{aligned} \rho_{C_H} &= 12 \int_0^1 \int_0^1 uv \bar{C}(u, v) dv du \\ &= 12 \int_0^1 \int_0^1 uv [1 - u - v + C(u, v)] dv du. \end{aligned} \tag{8}$$

Hence, by using eq. (5), the lower bound is as follows

$$\rho_{C_H} \geq -1 + 12 \iint_{u+v-1>0} uv [u + v - 1] dv du = \frac{1}{10}.$$

As we expect from Corollary 1, this lower bound must be positive. We can say that C_H achieves weakly positive dependence from its lower bound. To obtain the upper bound, we use eq. (6) then

$$\rho_{C_H} \leq -1 + 12 \iint_{v>u} u^2 v dv du + \iint_{u>v} uv^2 dv du = \frac{3}{5}.$$

As a result, ρ_{C_H} lies in the interval $[\frac{1}{10}, \frac{3}{5}]$. The proposed copula C_H can only detect positive dependence. Furthermore, C_H can achieve a high correlation through positive dependence.

3. Tail Dependence Measures of C_H

The tail dependence measures can detect how likely both components jointly exceed extreme quantiles. It is useful in determining the common behavior of random variables in the upper and lower quadrants. Upper and lower tail dependence coefficients are defined by

$$\lambda_u = 2 - \lim_{t \rightarrow 1} \frac{1 - C(t, t)}{1 - t}, \lambda_L = \lim_{t \rightarrow 0} \frac{C(t, t)}{t}$$

(see [4], subsection 5.4). Accordingly, after some algebraic calculation, the upper and the lower dependence coefficients for $C_H(u, v)$ are respectively equal to $\lambda_u = \lim_{t \rightarrow 1} \frac{-d\bar{C}(t, t)}{dt}$ and $\lambda_L = 0$.

Next, an example is given to illustrate this family.

4. Illustrative Examples

In this section, we compare in terms of Spearman's rho correlation coefficient the proposed copula with respect to its baseline copula chosen from the most used copulas in modeling real data.

Example 1. (FGM copula) The Farlie-Gumbel-Morgenstern (FGM) family of a bivariate copula is given by $C(u, v) = uv[1 + \theta(1 - u)(1 - v)]$, for $\theta \in [-1, 1]$ (see [9] and [10]). Then, the copula $C_H(u, v)$ is given by

$$C_H(u, v) = uv[1 + (1 - u)(1 - v)(1 + \theta uv)].$$

Hence, $\rho_{C_H} = \frac{1}{12}(\theta + 4)$. Since $\theta \in [-1, 1]$, $\frac{1}{4} \leq \rho_{C_H} \leq \frac{5}{12}$. One can conclude that this family can model weakly positive dependence as FGM does. Furthermore, tail dependence coefficients of $C_H(u, v)$ are equal to zero as FGM has. Hence, $C_H(u, v)$ has no tail dependence in both directions.

Example 2. (Gumbel-Hougaard copula) The bivariate version of the Gumbel-Hougaard family copula is given by

$$C(u, v) = e^{-[(-\log(u))^\theta + (-\log(v))^\theta]^{\frac{1}{\theta}}}$$

where θ lies in the interval $[1, \infty)$ (see, [10-13]). Since the Gumbel-Hougaard copula can detect positive dependence, it is used in modeling bivariate flood frequency, storm, drought, etc. (see, [14]). [15] claimed that no closed-form expression exists for Spearman's rho. [16] obtained an integral form for Spearman's rho as

$$\rho_{GH} = \frac{12}{\theta} \int_0^1 \frac{[t(1-t)]^{\frac{1}{\theta}-1}}{[1 + t^{\frac{1}{\theta}} + (1-t)^{\frac{1}{\theta}}]^2} dt - 3.$$

Calculated values of Spearman's rho for the base model (Gumbel-Hougaard copula) and $C_H(u, v)$ are given in Table 1.

Table 1. Calculated values of Spearman's rho of Gumbel-Hougaard and C_H copulas for some values of θ

θ	1.1	1.3	1.5	1.7	1.9	2.1	3	5	15
ρ_{GH}	0.1353	0.3368	0.4767	0.5773	0.6520	0.7088	0.8488	0.9432	0.9935
ρ_{C_H}	0.3729	0.4300	0.4683	0.4951	0.5147	0.5293	0.5644	0.5870	0.5986

As can be seen from Table 1, when θ is close to 1, C_H seems slightly more dominant than Gumbel-Hougaard in terms of Spearman's rho. However, Gumbel-Hougaard is more dominant in the large values of the θ .

Gumbel-Hougaard copula family has upper tail dependence measured as $\lambda_U = 2 - 2^{\frac{1}{\theta}}$ (see, [4] p.215). After some algebraic calculation, C_H is similarly found to have the same upper tail dependency measure.

Example 3. (Ali-Mikhail-Haq copula) Ali-Mikhail-Haq (AMH) copula is given by

$$C(u, v) = \frac{uv}{1 - \theta(1-u)(1-v)},$$

where $\theta \in [-1, 1]$ (see, [17, 18]). Spearman's rho coefficient for this family is given below:

$$\rho_{AMH} = \frac{12(1 + \theta)dilog(1 - \theta) - 24(1 - \theta)\log(1 - \theta)}{\theta^2} - \frac{3(\theta + 12)}{\theta},$$

where $dilog(\cdot)$ represents the dilogarithm function defined as $dilog(x) = \int_1^x \frac{\log(t)}{1-t} dt$ (see, [4] p. 172 and [19]). They also reported that $\rho_{AMH} \in [-0.2711, 0.4784]$. We use the geometric series representation for $1/(1 - \theta(1-u)(1-v))$ to calculate the correlation coefficient numerically for $C_H(u, v)$. Then, we have

$$\rho_{C_H} = 48 \sum_{j=0}^{\infty} \frac{\theta^j}{((j+3)(j+2)(j+1))^2} - 1.$$

Calculated approximate values of Spearman's rho for the base model AMH copula and $C_H(u, v)$ are tabulated as in Table 2.

Table 2. Calculated values of Spearman's rho of AMH and C_H copulas for some values of θ

θ	-1	-.7	-.4	-0.1	0.1	0.4	0.7	1
ρ_{AMH}	-0.2711	-0.2004	-0.1216	-0.0325	0.0342	0.1490	0.2896	0.4784
ρ_{C_H}	0.2608	0.2806	0.3019	0.32513	0.3418	0.3691	0.3997	0.4353

As can be seen from Table 2, for nonnegative small values of θ , C_H seems more dominant than the AMH copula in terms of Spearman's rho. However, the AMH copula is more dominant in the large positive values of the θ . For negative values of θ , C_H produces a positive correlation, unlike AMH copula does.

AMH copula family has lower tail dependence as $\lambda_L = \frac{1}{2}$ for $\theta = 1$ reported by [19]. After some algebraic calculation, C_H has no tail dependency measure.

Example 4. (Clayton copula) The Clayton copula is first introduced by [20]. The bivariate version of the Clayton copula is given by

$$C_{Clayton}(u, v) = \left(u^{-\frac{1}{\theta}} + v^{-\frac{1}{\theta}} - 1 \right)^{-\theta},$$

where $\theta > 0$. This copula can only model positively associated variables. Spearman's rho coefficient for the Clayton copula is more complex. We calculate numerically to obtain these coefficients for both Clayton and C_H copulas. Table 3 tabulates Spearman's rho coefficients for various values of θ .

Table 3. Calculated values of Spearman's rho of Clayton and C_H copulas for some values of θ

θ	0.1	0.3	0.6	0.9	3	5	8	10
$\rho_{Clayton}$	0.9583	0.8100	0.6300	0.5095	0.2124	0.1356	0.0881	0.0714
ρ_{C_H}	0.5798	0.5254	0.4732	0.4427	0.3763	0.3605	0.3509	0.3475

As can be seen from Table 3, while θ increases, the correlation coefficient of both copula decreases. In terms of Spearman's rho, while Clayton copula is dominant for the small values of θ , the C_H is dominant for the large values.

Clayton copula family has lower tail dependence measured as $\lambda_L = 2^{-\frac{1}{\theta}}$ (see, [4], p.215). After some algebraic calculation, C_H has no tail dependency measure.

Example 5. (Frank copula) The Frank copula is given by

$$C_{Frank}(u, v) = \frac{-1}{\theta} \log \left(1 + \frac{(e^{-\theta u} - 1)(e^{-\theta v} - 1)}{(e^{-\theta} - 1)} \right),$$

where $\theta \in (-\infty, +\infty)$ (see, [21]). This copula can symmetrically model both directions of dependence. Spearman's rho coefficient for the Frank copula is given as

$$\rho_{Frank} = 1 - \frac{12}{\theta} [D_1(\theta) - D_2(\theta)],$$

where $D_k(x)$ is the Debye function which is defined by $\frac{k}{x^k} \int_0^x \frac{z^k}{e^z - 1} dz$ for any positive integer k (see [4], p. 171). To obtain this coefficient for both Frank and C_H copulas, we compute numerically. Table 4 gives tabulated values of Spearman's rho coefficients for various values of θ .

Table 4. Calculated values of Spearman's rho of Frank and C_H copulas for some values of θ

θ	-10	-8	-5	-0.8	-0.3	0.3	0.8	5	8	10
ρ_{Frank}	-.8602	-.8035	-.6435	-.1322	-.0499	.0499	.1322	.6435	.8035	.8602
ρ_{C_H}	.1283	.1407	.1772	.3005	.3209	.3458	.3666	.4990	.5425	.5584

As can be seen from Table 4, while the C_H copula is dominant for the small values of the $\theta \geq 0$, the Frank copula is dominant for the positively large values of θ in terms of Spearman's rho.

Frank copula has no tail dependence measure (see, [4], p.215). After some algebraic calculation, C_H has also no tail dependence measure.

Example 6. (Bivariate Gumbel-Exponential (BGE) copula) The bivariate version of the Gumbel-Exponential (BGE) copula is given by

$$C(u, v) = u + v - 1 + (1 - u)(1 - v)e^{-\theta \log(1-u)\log(1-v)},$$

for $\theta \in [0,1]$. This copula is also known as Gumbel-Barnett copula (see, [10, 22] and [4], p. 23). BGE copula can model only negative dependence. According to [23], the Spearman’s rho coefficient of BGE copula is

$$\rho_{BGE} = 12 \left[-\frac{e^{\frac{4}{\theta}}}{\theta} Ei\left(-\frac{4}{\theta}\right) - \frac{1}{4} \right],$$

where $Ei(\cdot)$ is the exponential integral function. After some algebraic manipulation, ρ_{C_H} can be obtained as

$$\rho_{C_H} = 12 \frac{e^{\frac{4}{\theta}}}{\theta} \left[-Ei\left(-\frac{4}{\theta}\right) + 2e^{\frac{2}{\theta}} Ei\left(-\frac{6}{\theta}\right) - e^{\frac{5}{\theta}} Ei\left(-\frac{9}{\theta}\right) \right].$$

Calculated values of Spearman’s rho for the base model BGE copula and $C_H(u, v)$ are tabulated as in Table 5.

Table 5. Calculated values of Spearman’s rho of BGE and C_H copulas for some values of θ

θ	0.1	0.3	0.5	0.7	0.9	1
ρ_{BGE}	-0.0715	-0.1972	-0.3053	-0.4002	-0.4848	-0.5239
ρ_{C_H}	0.3119	0.2769	0.2494	0.2270	0.2083	0.2000

As can be seen from Table 5, both BGE and C_H decreases in θ in terms of Spearman’s rho. Note that, when θ goes to zero, ρ_{C_H} approaches to 1/3. Note also that both BGE and C_H have no tail dependence. In this case, we can say that both positive and negative associated random variables can be modeled by a mixture of copulas C_H and C_{BGE} . According to Subsection 3.2.4 of [4], for $\delta \in [0,1]$, we can write a convex combination of C_{BGE} and C_H as follows

$$C^*(u, v) = \delta C_H(u, v) + (1 - \delta)C_{BGE}(u, v).$$

Hence, ρ^* lies in interval $[-.52, 0.33]$.

4. Conclusion

In this study, based on Rüschendorf’s Method, we proposed a new bivariate copula distorting independence copula by adding the baseline copula. The baseline copula with a negatively correlated structure certainly transforms into a positively correlated structure in the proposed copula according to the different copula families. However, there may be differences in the direction of change of the correlation coefficients of the proposed copula constructed from baseline copulas with positively correlated structure. This situation is influenced by the presence or absence of lower and upper tail dependencies of the copulas. If we pay attention to the upper and lower bounds of ρ_{C_H} , the values of the Spearman’s rho correlation coefficient for this copula family lie in the interval $[0.1, .60]$. Besides, as a result of illustrative examples, it can be said that except for the extreme value copulas, generated copulas using this method achieve reasonable correlations considering some baseline copulas of which correlation coefficients less than 0.6.

In particular, as illustrated in Example 6, if mixing the proposed copula with a copula that can only model the negative dependence is made, a mixture copula that can model both positive and negative dependencies can be created.

Conflicts of interest

The authors declare that there is no conflict of interest.

References

- [1] Lai C. D., Xie M., A New Family of Positive Quadrant Dependent Bivariate Distributions, *Statistics and Probability Letters*, 46 (4) (2000) 359-364.
- [2] Bairamov I., Kotz S., Bekçi M., New generalized Farlie-Gumbel-Morgenstern distributions and concomitants of order statistics. *Journal of Applied Statistics*, 28 (5) (2001) 521-536.
- [3] Rüschendorf L., Construction of multivariate distributions with given marginals. *Annals of the Institute of Statistical Mathematics*, 37 (1985) 225-233.
- [4] Nelsen R. B., An Introduction to Copulas. Second Edition. Springer, New York (2006).
- [5] Asadian N., Amini M., Bozorgnia A. Some concepts of negative dependence for bivariate distributions with applications. *Journal of Mathematical Extension*, 4 (1) (2009) 43-59.
- [6] Hoeffding W., Masstabinvariante Korrelationstheorie, *Schriften des Mathematischen Instituts und Instituts für Angewandte Mathematik der Universität Berlin*, 5 (1940) 181-233.
- [7] Fréchet M., Sur Les Tableaux de Corrélation Dont Les marges Sont Donnees, *Annales de l'Université de Lyon, Sciences* 4 (1951) 13-84.
- [8] Schweizer B., Wolff E., On Nonparametric Measures of Dependence for Random Variables, *The Annals of Statistics*, 9(4) (1981) 879-885.
- [9] Farlie D., The Performance of Some Correlation Coefficients for a General Bivariate Distribution, *Biometrika*, 47 (3/4) (1960) 307-323.
- [10] Gumbel E. J., Bivariate Exponential Distributions, *Journal of the American Statistical Association*, 55 (292) (1960a) 698-707.
- [11] Gumbel E. J., Bivariate Logistic Distributions, *Journal of the American Statistical Association*, 56 (1961) 335-349.
- [12] Hougaard P., A Class of Multivariate Failure Time Distributions, *Biometrika*, 73 (1986) 671-678.
- [13] Joe H., Multivariate Models and Dependence Concepts. Chapman and Hall, London (1997).
- [14] Singh V.P., Zhang L. Copula–Entropy Theory for Multivariate Stochastic Modeling in Water Engineering, *Geosci. Lett.*, 5(6) (2018).
- [15] Frees E.W., Valdez E.A., Understanding Relationships Using Copulas, *North American Actuarial Journal*, 2 (1) (1998) 1-25.
- [16] Hürlimann W., Properties and Measures of Dependence for the Archimax Copula, *Advances and Applications in Statistics*, 5 (2005) 125-143.
- [17] Ali M.M., Mikhail N.N., Haq M.S., A Class of Bivariate Distributions Including the Bivariate Logistic, *Journal of Multivariate Analysis*, 8 (1978) 405-412.
- [18] Balakrishnan N., Lai C. D., Continuous Bivariate Distributions. Springer Science & Business Media, (2009).
- [19] Kumar P., Probability Distributions and Estimation of Ali-Mikhail-Haq Copula, *Applied Mathematical Sciences*, 4 (14) (2010) 657-666.
- [20] Clayton D., A Model for Association in Bivariate Life Tables and its Application in Epidemiological Studies of Family Tendency in Chronic Disease Incidence, *Biometrika*, 65 (1978) 141-151.
- [21] Frank M.J., On the Simultaneous Associativity of $F(x,y)$ and $x + y - F(x,y)$, *Aequationes Math*, 19 (1979) 194-226.

- [22] Barnett V., Some Bivariate Uniform Distributions, *Communications in Statistics: Theory and Methods*, 9 (1980) 453-461.
- [23] Fredricks G.A., Nelsen R.B., On the Relationship Between Spearman's Rho and Kendall's Tau for Pairs of Continuous Random Variables, *Journal of Statistical Planning and Inference*, 137 (7) (2007) 2143-2150.



The fundamental frequencies of longitudinally vibrating rods carrying tip mass and transversally vibrating beams carrying tip mass by using several methods

Aydın DEMİR^{1,*}

¹Sivas Cumhuriyet University, Engineering Faculty, Department of Mechanical Engineering, TR-58140 Sivas/ TURKEY

Abstract

The present paper is concerned with the determination of the frequency equation and sensitivity of the eigenfrequencies of a fixed-free longitudinally vibrating rod and transversally vibrating beam carrying a tip mass by using several methods. First, the exact frequency equations of the such systems are established, and then approximate formulas are given for the fundamental frequency using several methods which contain the equivalent system, Rayleigh quotient, Dunkerley's formula and continuous system model. The applicability and proximity of these methods versus exact solutions reviewed. The results are compared in a wide range of relevant parameters to give a clear idea about the validity of the proposed formulas. These new derived equations can be very useful for a design engineer who is interested in the eigencharacteristics of similar systems and their sensitivity.

Article info

History:

Received: 02.09.2020

Accepted: 02.03.2021

Keywords:

Transverse vibrations,
Longitudinal vibrations,
Rod,
Beam,
Tip mass.

1. Introduction

Rods and beams especially carrying tip mass systems are often used as approximation models for a variety of structural and machine elements. Hence, we frequently face the task of determining the natural frequencies of such systems. Naturally, the governing equations of longitudinal vibrations are simpler than that for axial vibrations. However, axial vibrations are of greater importance in practice, because the natural frequencies in flexure of a particular beam tend to be considerably lower than those in extension and torsion.

The eigenanalysis problem of rods with tip mass is a common subject of interest, also treated in textbooks [1, 2]. Flexural vibrations of uniform beams for different boundary conditions are studied in textbooks [3, 4]. There are many publications in the literature on vibrations of rods and beams for various boundary conditions in different configurations. The dynamics of longitudinal and transversal vibrations has been a subject of many research reports for many years. Examination of the existing literature shows that the solution of the frequency equations of rods and beams carrying point or heavy masses has attracted the interest of many investigators. Gürgöze [5] investigated the frequency equation and sensitivity of the eigenfrequencies of a fixed-free longitudinally

vibrating rod carrying a tip mass. Turhan [6] studied on the effect of a cross-section discontinuity on the eigencharacteristics of longitudinally vibrating rods. Gürgöze and Erol [7] reviewed the establishment of two methods for computing the eigencharacteristics of a continuous rod, carrying a tip mass, consisting of several parts having different physical parameters and subjected to external viscous damping. Lin and Chang [8] examined the longitudinal free vibrations of a system in which two rods are coupled by multi-spring-mass devices. Gu and Cheng [9] studied the dynamic response of a high-speed spindle subject to a moving mass. There are a number of studies [10-18] dealing with the problem of transverse vibrations of beams carrying a tip mass or point masses or concentrated masses using analytical and various numerical approaches. Chang [10] presented a comprehensive study on the lateral vibration of a simply supported beam carrying a concentrated mass at the center of beam. In the case of selecting the appropriate parameters, Turhan [11] proposed Rayleigh approximations versus exact solutions for finding the fundamental frequency of beams carrying a point mass. Low [12] used a modified Dunkerley formula for eigenfrequencies of Euler-Bernoulli beams carrying concentrated masses. Li [13] proposed a new exact approach for free vibration analysis of a multi-step beam with an arbitrary number of crack and

*Corresponding author. e-mail address: aydindemir@cumhuriyet.edu.tr

<http://dergipark.gov.tr/csj> ©2021 Faculty of Science, Sivas Cumhuriyet University

concentrated masses. Kirk and Wiedemann [14] investigated the natural frequencies and mode shapes of a free-free beam with large end masses. Özkaya [15] studied non-linear transverse vibrations of an Euler-Bernoulli beam carrying concentrated masses. Low [16] presented an eigenanalysis and the Rayleigh's estimation for a frequency analysis of a beam carrying a concentrated mass at an arbitrary locations. Banerjee [17] used the dynamic stiffness approach method for exact free vibration analysis of beams carrying spring-mass systems. Li et al. [18] studied free bending vibration of a Rayleigh cantilever with arbitrary axial loading and tip mass.

In recent years, studies on the longitudinal and transversal vibrations of the beams carrying tip mass have also been encountered. Matt and Frederico [19] proposed a new simulation of the transverse vibrations of a cantilever beam with an eccentric tip mass in the axial direction using integral transforms. Labędzki, Pawlikowski and Radowicz [20] used fractional rheological model for transverse vibration of a cantilever beam under base excitation. Şakar [21] examined the effect of axial force on the free vibration of an Euler-Bernoulli beam carrying a number of various concentrated elements. Transverse vibration of Euler beam for different situations are studied in textbook [22].

In this paper, the validity and applicability of several methods applied to uniform rods and beams carrying point mass has been investigated. The obtained results have been compared to with each other and the literature. The corresponding exact frequency equation is also given for each case and the results are compared in a broad range of the relevant parameters so that a clear idea on the presented methods. It is found that the methods such as Rayleigh quotient, Dunkerley's formula and continuous system model can generally yield good approximation and high accuracy if compared with the results associated to the eigenanalysis. These proposed methods are computationally efficient and give very close to exact results. For this reason, these methods are highly

$$u(x, t) = (A_1 \sin(\omega t) + A_2 \cos(\omega t)) (B_1 \sin(\frac{\omega}{c} x) + B_2 \cos(\frac{\omega}{c} x)) \tag{3}$$

where A_i and B_i $i=1,2$ are arbitrary integration constants to be evaluated from the boundary

conditions, constant $c = \sqrt{\frac{E}{\rho}}$ expression is also

known as the wave propagation velocity and ω eigenfrequency is defined by

recommended for uniform rod and beams carrying point mass. At the same time, these methods can be extended to complex structural systems and the obtained results can be also very useful for the design engineers who are working in the dynamical behaviour of such systems. There is not enough study in the literature about the use of these approximate solution methods in such systems. Therefore, this study also gives an idea about the superiority and reliability of these approximate methods used.

2. Theory and Formulation

2.1. Longitudinal vibrations of rods carrying tip mass

The uniform rod carrying tip mass is shown in Figure 1. It is essentially an longitudinally vibrating fixed-free rod of axial rigidity EA and mass per unit length m carrying a tip mass M . The exact frequency equation of the system described above must derive in order to determine eigenfrequencies. It is well known that the longitudinal vibrations of a uniform elastic rod are governed by the partial differential equation [2]

$$EA u'' = \rho A \ddot{u} \tag{1}$$

where ρ mass density, overdots and primes denote partial derivatives with respect to time t and x , $u(x,t)$ denotes the longitudinal displacement at point x and time t .

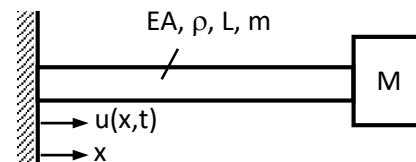


Figure 1. Rod carrying tip mass system.

Assuming harmonic motion of the form

$$u(x, t) = y(x) \cos(\omega t - \varepsilon) \tag{2}$$

and obtains the general solution

$$\omega = \lambda \frac{c}{L} \tag{4}$$

Given the shape of the system shown in the Figure 1, boundary conditions becomes

$$u(0, t) = 0$$

$$EA u' \Big|_{x=L} = -M \ddot{u} \Big|_{x=L} \tag{5}$$

It can be shown after some algebraic manipulations, the eigenequation results in the following simple form

$$\tan \lambda = \frac{1}{\mu \lambda} \tag{6}$$

where the following non-dimensional parameters are introduced:

$$\lambda = \frac{\omega L}{c}, \quad \mu = \frac{M}{m} \tag{7}$$

μ and λ non-dimensional parameters refer to ratio of masses and dimensionless frequency, respectively. The roots of transcendental equation (6) give dimensionless frequency parameter λ and hence by considering equation (4) the eigenfrequencies of the system shown in Figure 1. The approximate solution methods of the frequency equations of uniform rods and beams carrying tip mass will be handled in detail later.

2.2 Transverse vibrations of beams carrying tip mass

Consider an Euler-Bernoulli beam carrying a tip mass M (Figure 2). Transverse vibration of the beam is represented by the partial differential equation given below.

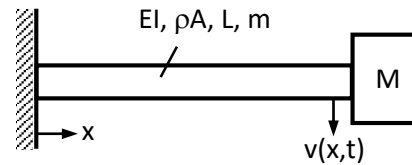


Figure 2. Beam carrying tip mass system.

$$EI v^{IV} + \rho A \ddot{v} = 0 \tag{8}$$

where EI flexural rigidity, ρ mass density, A sectional area, overdots and primes denote partial derivatives with respect to time t and x, $v(x,t)$ denotes the transverse displacement at point x and time t. Assuming harmonic motion of the form

$$v(x, t) = y(x) \cos(\omega t - \varepsilon) \tag{9}$$

one obtains the general solution of the motion

$$v(x, t) = [A \cos(\frac{\lambda}{L} x) + B \sin(\frac{\lambda}{L} x) + C \cosh(\frac{\lambda}{L} x) + D \sinh(\frac{\lambda}{L} x)] \cos(\omega t - \varepsilon) \tag{10}$$

where λ and ξ are defined by

$$\xi = \frac{x}{L}, \quad \lambda^4 = \frac{\rho A L^4}{EI} \omega^2 \tag{11}$$

In this case,

$$y(\xi) = A \cos(\lambda \xi) + B \sin(\lambda \xi) + C \cosh(\lambda \xi) + D \sinh(\lambda \xi) \tag{12}$$

where A, B, C and D are arbitrary integration constants that can be found in the boundary conditions. Boundary conditions for transverse vibration of the beam shown in the Figure 2 becomes

$$\begin{aligned} v(0, t) &= 0 \\ v'(0, t) &= 0 \\ M \ddot{v}(L, t) &= EI v'''(L, t) \\ v''(L, t) &= 0 \end{aligned} \tag{13}$$

By applying boundary conditions, frequency equation is obtained as follows

$$1 + \cos \lambda \cosh \lambda + \mu \lambda (\cos \lambda \sinh \lambda - \sin \lambda \cosh \lambda) = 0 \tag{14}$$

where $\mu = \frac{M}{m}$ non-dimensional parameters refer to ratio of masses and m is mass per unit length ($m = \rho A L$) In the same way, the roots of transandantal equation (14) give dimensionless frequency parameter λ and hence by considering equation (11) the eigenfrequencies of the system.

3. Case study and numerical solutions

In this section, exact frequency equations and approximate frequency equations obtained by several different methods will be derived for rods/beams carrying tip mass systems and their results be compared. The results are presented in accordance with

Rayleigh quotient A : $\lambda = \sqrt{\frac{1}{\mu}}$ (15)

Rayleigh quotient B : $\lambda = \sqrt{\frac{1}{\mu + \frac{1}{3}}}$ (16)

Rayleigh quotient C : $\lambda = \sqrt{5} \sqrt{\frac{3\mu^2 + 3\mu + 1}{15\mu^3 + 20\mu^2 + 10\mu + 2}}$ (17)

Dunkerley’s Formula : $\lambda = \sqrt{\frac{1}{\frac{1}{(\frac{\pi}{2})^2} + \frac{1}{(\frac{3\pi}{2})^2} + \frac{1}{(\frac{5\pi}{2})^2} + \frac{1}{(\frac{7\pi}{2})^2} + \frac{1}{(\frac{9\pi}{2})^2} + \mu}}$ (18)

Continuous system model : $\frac{\beta}{\mu} + (\frac{\beta}{\mu} - 1) \sin \lambda [\cos \lambda \tan((1 + \beta)\lambda) - \sin \lambda_1]$ (19)

In equation (19), $\beta = \frac{L_2}{L}$ (length of mass M / length of the beam). Figure 3 shows dimensionless frequency parameter λ according to ratio of masses by theset methods for longitudinal vibrating of rods carrying tip mass. If Fig. 3 is examined carefully, it is seen that the dimensionless frequency parameter λ decreases with the ratio of masses. However, the dimensionless frequency parameter obtained by the equation (15) don’t give very good results according to the exact solution given by the equation (6). Therefore, other methods except this method are considered in the calculation of the relative error. The relative error is the % error calculated according to the exact solution given by the equation (6).

some appropriate parameters and it is possible to get an idea about the validity of approximate solutions.

3.1. The fundamental frequencies of longitudinal vibrating of rods carrying tip mass

For the system shown in Figure 1, equation (6) yields dimensionless frequency parameter λ . Approximate frequency equations of the same system were obtained by using such as equivalent system, Rayleigh quotient, Dunkerley’s formula and continuous system model. As a result of some corrections and mathematical operations, frequency equations of the longitudinal vibrations of the system given in Figure 1 are obtained by these methods. The results are given by the following equations.

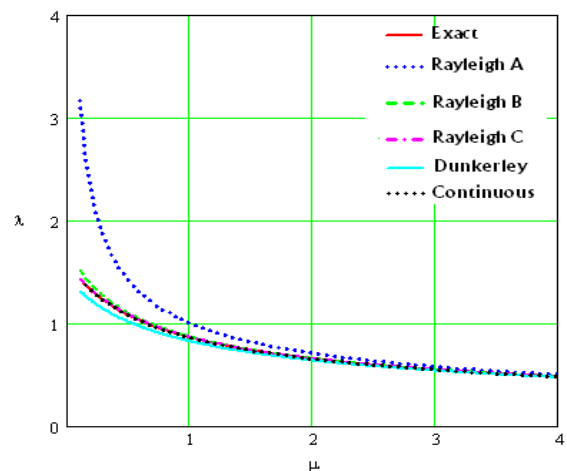


Figure 3. Dimensionless frequency parameter λ according to ratio of masses by different methods for longitudinal vibrating of rods carrying tip mass.

Figure 4 shows relative errors in dimensionless frequency parameter λ according to ratio of masses by different methods for longitudinal vibrating of rods carrying tip mass. When Fig. 4 is examined, it is seen that the relative error in dimensionless frequency parameter of Dunkerley's Formula is slightly high, Rayleigh quotient B is slightly less error and Rayleigh quotient C and continuous system model give very close results to the exact solution. Especially, since continuous system model is quite close to the exact solution, it is seen as the least error method. Therefore, continuous system model is discussed in more detail. Table 1 and Fig. 5 give the results of this model.

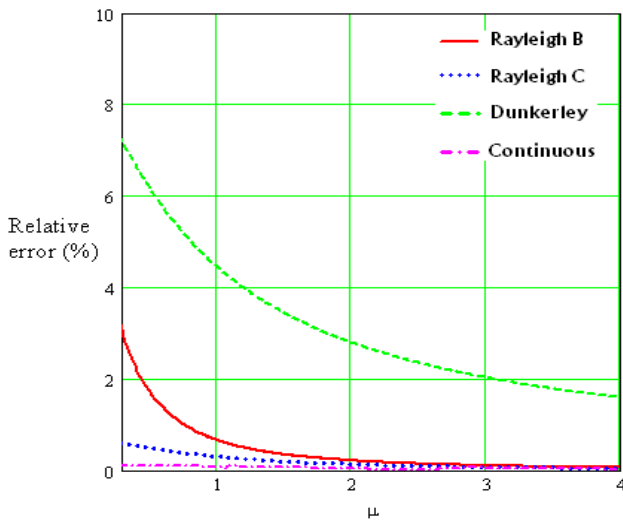


Figure 4. Relative errors in dimensionless frequency parameter λ according to ratio of masses by different methods for longitudinal vibrating of rods carrying tip mass.

In the continuous system model, dimensionless frequency parameter λ by given by the equation (19) varies according to ratio of masses and ratio of lengths. Table 1 shows some values of dimensionless frequency parameter λ by continuous system model for longitudinal vibrating of rods carrying tip mass. Similarly, Fig. 5. displays dimensionless frequency parameter λ according to ratio of masses and ratio of length in continuous system model for longitudinal vibrating of rods carrying tip mass. An inspection of Table 1 and Fig. 5 show that as the ratio of masses and the ratio of lengths increases, the dimensionless frequency parameters decrease. With the increase in the ratio of length, there is less decrease in dimensionless frequency parameters. The higher the ratio of masses, the greater the decrease in dimensionless frequency parameters.

Table 1. Dimensionless frequency parameter λ by continuous system model for longitudinal vibrating of rods carrying tip mass.

$\mu \setminus \beta$	0.05	0.10	0.15	0.20
1.0	0.861	0.860	0.859	0.857
1.5	0.738	0.737	0.735	0.734
2.0	0.659	0.657	0.653	0.653
2.5	0.603	0.593	0.594	0.595
3.0	0.561	0.548	0.549	0.546
3.5	0.512	0.511	0.514	0.510
4.0	0.483	0.482	0.485	0.480

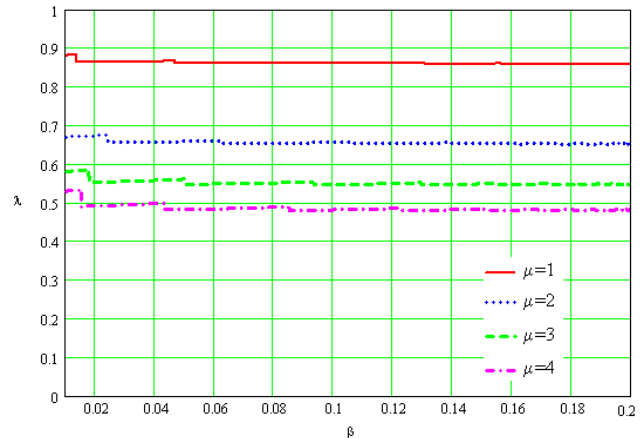


Figure 5. Dimensionless frequency parameter λ according to ratio of masses and ratio of length in continuous system model for longitudinal vibrating of rods carrying tip mass.

3.2. The fundamental frequencies of transversal vibrating of beams carrying tip mass

For the system shown in Figure 2, equation (14) yields the exact solution of dimensionless frequency parameter λ . Approximate frequency equations of these system were obtained by using such as equivalent system, Dunkerley's formula and stepped beam model (continuous system model). The formulas calculated by the equivalent system and Dunkerley formula are given directly below, and the results of the stepped beam model are explained in detail below.

Equivalent System:
$$\lambda = \sqrt[4]{\frac{3}{\frac{33}{140} + \mu}} \tag{20}$$

Dunkerley's Formula:

$$\frac{1}{\lambda^4} = \frac{1}{\lambda_{11}^4} + \frac{1}{\lambda_{22}^4} + \frac{1}{\lambda_{33}^4} + \frac{1}{\lambda_{44}^4} + \frac{\mu}{3} \tag{21}$$

where $\lambda_{11} = 1.8751, \quad \lambda_{22} = 4.6941,$

$\lambda_{33} = 7.8548, \quad \lambda_{44} = 10.9955$

3.2.1 Stepped beam model (continuous system model)

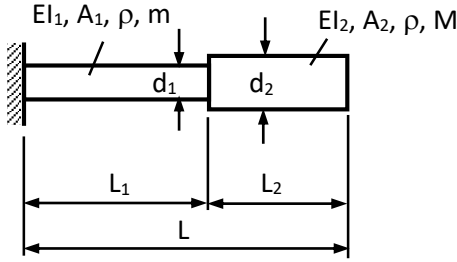


Figure 6. Stepped beam model of the beam carrying tip mass system.

Consider an Euler-Bernoulli beam carrying a tip mass M (Figure 6). Let the transversal motions of the beam points at the left and right of M be represented by $y_1(x,t)$ and $y_2(x,t)$. Both y_1 and y_2 have to obey the partial differential equation (8). Using the

dimensionless parameters given the equation (22) and with the assumption of harmonic motion,

$$\alpha = \frac{L_1}{L}, \quad \beta = \frac{L_2}{L}, \quad \gamma = \frac{A_2}{A_1} = \frac{d_2^2}{d_1^2}$$

$$\lambda_1^4 = \frac{\rho A_1 L_1^4}{E I_1} \omega^2, \quad \lambda_2^4 = \frac{\rho A_2 L_2^4}{E I_2} \omega^2,$$

$$\frac{\lambda_1^4}{\lambda_2^4} = \frac{A_1 L_1^4}{I_1} \cdot \frac{I_2}{A_2 L_2^4} = \gamma \left(\frac{\alpha}{\beta}\right)^4, \tag{22}$$

$$\frac{\lambda_1}{\lambda_2} = \sqrt[4]{\gamma} \frac{\alpha}{1-\alpha} = \eta$$

$$\mu = \frac{M}{m} = \frac{\rho A_2 L_2}{\rho A_1 L_1} = \gamma \frac{\beta}{\alpha}, \quad \frac{I_2}{I_1} = \frac{d_2^4}{d_1^4} = \gamma^2$$

one obtains the general solutions for the space dependence of the motion.

$$y_1(x) = A_1 \cos(\lambda_1 \frac{x}{L}) + B_1 \sin(\lambda_1 \frac{x}{L}) + C_1 \cosh(\lambda_1 \frac{x}{L}) + D_1 \sinh(\lambda_1 \frac{x}{L}) \tag{23}$$

$$y_2(x) = A_2 \cos(\lambda_2 \frac{x}{L}) + B_2 \sin(\lambda_2 \frac{x}{L}) + C_2 \cosh(\lambda_2 \frac{x}{L}) + D_2 \sinh(\lambda_2 \frac{x}{L}) \tag{24}$$

$$y_1(0) = 0$$

$$y_1'(0) = 0$$

$$y_1(L_1) = y_2(L_1)$$

$$y_1'(L_1) = y_2'(L_1) \tag{25}$$

$$I_1 y_1''(L_1) = I_2 y_2''(L_1)$$

$$I_1 y_1'''(L_1) = I_2 y_2'''(L_1)$$

$$y_2''(L) = 0$$

$$y_2'''(L) = 0$$

The following matrix was obtained by applying the boundary conditions given equation (22). The roots of the determinant of this matrix give dimensionless frequency parameter λ of the problem. Because this calculation is very difficult, the solutions have been

found with numerical methods. Table 2 gives dimensionless frequency parameter λ calculated by the four methods for transversal vibrating of beams carrying tip mass according to the ratio of masses.

$$\begin{pmatrix} 1 & 0 & 1 & 0 & 0 & 0 & 0 & 0 \\ 0 & 1 & 0 & 1 & 0 & 0 & 0 & 0 \\ \cos(\lambda 1-\alpha) & \sin(\lambda 1-\alpha) & \cosh(\lambda 1-\alpha) & \sin(\lambda 1-\alpha) & -\cos(\lambda 1-\alpha) & -\sin(\lambda 1-\alpha) & -\cosh(\lambda 1-\alpha) & -\sinh(\lambda 1-\alpha) \\ -\eta \cdot \sin(\lambda 1-\alpha) & \eta \cdot \cos(\lambda 1-\alpha) & \eta \cdot \sinh(\lambda 1-\alpha) & \eta \cdot \cosh(\lambda 1-\alpha) & \sin(\lambda 2-\alpha) & -\cos(\lambda 2-\alpha) & -\sinh(\lambda 2-\alpha) & -\cosh(\lambda 2-\alpha) \\ -\frac{\eta^2}{\gamma^2} \cdot \cos(\lambda 1-\alpha) & -\frac{\eta^2}{\gamma^2} \cdot \sin(\lambda 1-\alpha) & \frac{\eta^2}{\gamma^2} \cdot \cosh(\lambda 1-\alpha) & \frac{\eta^2}{\gamma^2} \cdot \sinh(\lambda 1-\alpha) & \cos(\lambda 2-\alpha) & \sin(\lambda 2-\alpha) & -\cosh(\lambda 2-\alpha) & -\sinh(\lambda 2-\alpha) \\ \frac{\eta^3}{\gamma^2} \cdot \sin(\lambda 1-\alpha) & -\frac{\eta^3}{\gamma^2} \cdot \cos(\lambda 1-\alpha) & \frac{\eta^3}{\gamma^2} \cdot \sinh(\lambda 1-\alpha) & \frac{\eta^3}{\gamma^2} \cdot \cosh(\lambda 1-\alpha) & -\sin(\lambda 2-\alpha) & \cos(\lambda 2-\alpha) & -\sinh(\lambda 2-\alpha) & -\cosh(\lambda 2-\alpha) \\ 0 & 0 & 0 & 0 & -\cos(\lambda 2) & -\sin(\lambda 2) & \cosh(\lambda 2) & \sinh(\lambda 2) \\ 0 & 0 & 0 & 0 & \sin(\lambda 2) & -\cos(\lambda 2) & \sinh(\lambda 2) & \cosh(\lambda 2) \end{pmatrix} \quad (26)$$

Table 2. Dimensionless frequency parameter λ with the various methods for transversal vibrating of beams carrying tip mass according to the ratio of masses.

Methods \ μ	0.5	1.0	1.5	2.0	2.5	3.0	3.5
Exact solution (Eq. (14))	1.420	1.248	1.146	1.076	1.023	0.981	0.947
Equivalent system (Eq. (20))	1.421	1.248	1.147	1.076	1.023	0.981	0.947
Dunkerley formula (Eq. (21))	1.414	1.245	1.144	1.075	1.022	0.980	0.946
Stepped beam model (Eq. (26))	1.418	1.249	1.145	1.079	1.026	0.981	0.948

In order to check the accuracy of recommended approximate solutions, values numerically calculated from these approximate solutions are compared in Table 2 with the exact values found by solving equation (14) for different values of the parameters μ . It is seen from Table 2 that the dimensionless

frequency values obtained by the various methods are very close to each other. In addition, it is also seen from Table 2 that when the ratio of masses (μ) increase, dimensionless frequency parameter values (λ) decrease.

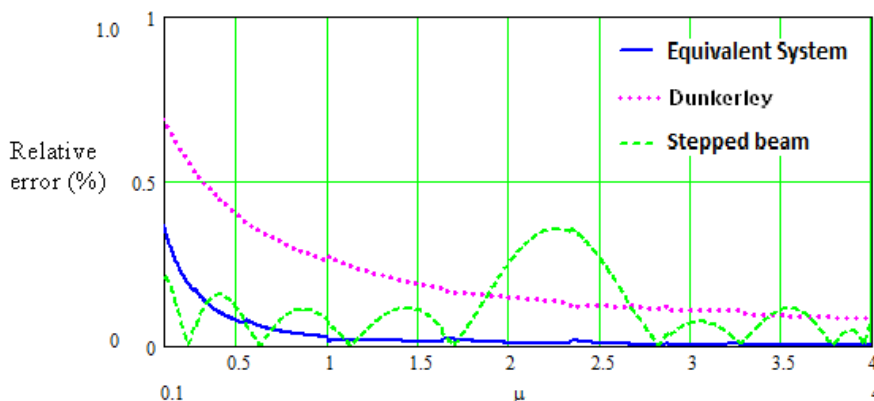


Figure 7. Relative errors in dimensionless frequency parameter λ according to ratio of masses by various methods for transversal vibrating of beams carrying tip mass.

Fig. 7 shows relative errors in dimensionless frequency parameter λ for transversal vibrating of beams carrying tip mass. From carefully review of Fig. 7, it is understood that the relative errors found by all three methods are less than 1%. The relative errors values obtained with the Dunkerley formula appear to be relatively little bit high. It can be said that the relative errors values obtained by the equivalent system are very stable and quite low.

4. Conclusions

In this study, several approximate solution methods have presented on longitudinal vibrations of uniform rods carrying tip mass and transverse vibrations of uniform beams carrying tip mass at the end. First, the exact frequency equations of the systems discussed were established and formulas for the dimensionless frequency parameters of these systems were obtained by methods such as equivalent system, Rayleigh coefficient, Dunkerley formula and continuous system model. In addition to the approximate methods discussed, relative error percentages in case of using these methods are also discussed and presented in tables and graphs depending on the appropriate parameters.

It is shown that the approximate solution methods can reliably predict the fundamental frequencies for longitudinal vibrating of uniform rods carrying tip mass and transversal vibrating of uniform beams carrying tip mass, provided that they are used in proper parameter ranges. The Dunkerley formula and some Rayleigh approximations yielded relatively low errors in both longitudinal vibrating of uniform rods carrying tip mass and transversal vibrating of uniform beams carrying tip mass, however, the continuous system model and equivalent system yielded very close to almost complete solutions.

By using the frequency equations given in this study, the high frequencies of the related systems can be easily calculated if desired. Also, the user has the opportunity to make his own decision about the adequacy of the recommended methods. At the same times, these obtained results can be also very useful for the design engineers who are working in the dynamical behaviour of such systems. It can also be very useful for engineers who want to find the fundamental frequencies of such systems quickly in terms of showing which method will give close results to the exact solution.

Conflicts of interest

The authors state that there is no conflict of interests.

References

- [1] Humar J. L., Dynamics of Structures, 3rd ed. NJ: Prentice-Hall, Englewood Cliffs, (1990).
- [2] Meirovitch L., Analytical Methods in Vibrations 1st ed. London: Collier-Macmillan Limited, (1967).
- [3] Timoshenko S., Young D. H., Weaver W. JR., Vibration Problems in Engineering, 4th ed. New York: Wiley, (1974).
- [4] Tse F. S., Morse I. E., Hinkle R. T., Mechanical Vibrations, Theory and Applications, 2nd ed. Boston MA: Allyn and Bacon, (1978).
- [5] Gürgöze M., On the eigenfrequencies of longitudinally vibrating rods carrying a tip mass and spring-mass in-span, *Journal of Sound and Vibration*, 216(2) (1998) 295-308.
- [6] Turhan Ö., On the eigencharacteristics of longitudinally vibrating rods with a cross-section discontinuity, *Journal of Sound and Vibration*, 248(1) (2001) 167-177.
- [7] Gürgöze M., Erol H., On the eigencharacteristics of multi-step rods carrying a tip mass subjected to non-homogeneous external viscous damping, *Journal of Sound and Vibration*, 267 (2003) 355-365.
- [8] Lin H.P., Chang S.C., Free vibrations of two rods connected by multi-spring-mass systems, *Journal of Sound and Vibration*, 330(11) (2011) 2509-2519.
- [9] Gu U. C., Cheng C. C., Vibration analysis of a high-speed spindle under the action of a moving mass, *Journal of Sound and Vibration*, 278 (2004) 1131-1146.
- [10] Chang C. H., Free vibration of a simply supported beam carrying a rigid mass at the middle, *Journal of Sound and Vibration*, 237(4) (2000) 733-744.
- [11] Turhan Ö., On the fundamental frequency of beams carrying a point mass: Rayleigh approximations versus exact solutions, *Journal of Sound and Vibration*, 230(2) (2000) 449-459.
- [12] Low K. H., A modified Dunkerley formula for eigenfrequencies of beams carrying concentrated masses, *International Journal of Mechanical Sciences*, 42 (2000) 1287-1305.
- [13] Li Q. S., Vibratory characteristics of multi-step beams with an arbitrary number of crack and concentrated masses, *Applied Acoustics*, 62 (2001) 691-706.

- [14] Kirk C. L., Wiedemann S. M., Natural frequencies and mode shapes of a free-free beam with large end masses, *Journal of Sound and Vibration*, 254(5) (2002) 939-949.
- [15] Özkaya E., Non-linear transverse vibrations of a simply supported beam carrying concentrated masses, *Journal of Sound and Vibration*, 257(3) (2002) 413-424.
- [16] Low K. H., Natural frequencies of a beam-mass system in transverse vibration: Rayleigh estimation versus eigenanalysis solutions, *International Journal of Mechanical Sciences*, 45 (6-7) (2003) 981-993.
- [17] Banerjee J. R., Free vibration of beams carrying spring-mass systems -A dynamic stiffness approach, *Computers and Structures*, 104-105 (2012) 21-26.
- [18] Li X. F., Tang A.Y., Xi L.Y., Vibration of a Rayleigh cantilever beam with axial force and tip mass, *Journal of Constructional Steel Research*, 80 (2013) 15-22.
- [19] Matt Carlos Frederico T., Simulation of the transverse vibrations of a cantilever beam with an eccentric tip mass in the axial direction using integral transforms, *Applied Mathematical Modelling*, 37(22) (2013) 9338-9354.
- [20] Labędzki P., Pawlikowski R., Radowicz A., Transverse vibration of a cantilever beam under base excitation using fractional rheological model, AIP Conference, (2018).
- [21] Şakar G., The effect of axial force on the free vibration of an Euler-Bernoulli beam carrying a number of various concentrated elements, *Shock and Vibration*, 20(3) (2013) 357-367.
- [22] Edwards P. , Transverse Vibration of Euler Beam, (2018) 247-266.



Improving sustainable supplier evaluation by an integrated MCDM method under pythagorean fuzzy environment

Fethullah GÖÇER*

Department of Industrial Engineering, Kahramanmaraş Sütçü İmam University, Kahramanmaraş / Turkey

Abstract

Sustainability plays a significant role in promoting competence and collaboration in supply chain management due to increased environmental awareness, tightened regulations, and government policies. The evaluation of sustainable suppliers and selecting the best one is indispensable for companies to promote sustainability. Due to multi-criteria nature of the supplier selection process, it has been considered as a multi-criteria decision making (MCDM) problem in many studies. In this study, a state-of-the-art MCDM method for sustainable supplier selection is developed by integrating AHP and TOPSIS techniques within the Pythagorean Fuzzy Sets (PFSs) linguistic setting. A Group Decision Making (GDM) environment is utilized due to superiority of group consensus over individual decisions. Finally, an apparel industry example is used to illustrate the effectiveness and feasibility of the proposed sustainable supplier selection method. A comparison with existing techniques and sensitivity analysis are done to verify and validate the given outcome.

Article info

History:
Received:16.05.2020
Accepted:02.03.2021

Keywords:
Sustainability
Supplier Selection,
Group Decision
Making (GDM),
Analytic Hierarchy
Process (AHP),
Technique for Order
Preferences by
Similarity to Ideal
Solution (TOPSIS),
Pythagorean Fuzzy
Sets (PFSs).

1. Introduction

The focus on sustainability in the context of supplier evaluation is increasing rapidly. Sustainability is not restricted by the liable practices within an organization's operations but covers the whole value chain. Due to rising energy prices and to respond to the changing needs of consumers and customers, organizations are under immense pressure of regulation changes and sustainability plays a significant role in promoting competence and collaboration in supply chain management. Thus, organizations are encouraged by stakeholders to formulate the objectives of sustainability and to handle the necessary operations to accomplish these objectives. Simply stated, sustainability is a long-term value creating business approach in the light of how a given organization runs under the social, environmental, and economical situations [1]. Sustainability is based upon the assumption that developing solutions strategies to achieve the given objectives foster companies' longevity [2]. Due to increased environmental awareness, tightened regulations, and government policies, the demand for sustainable and transparent suppliers are increasing

worldwide. Sustainable supplier is an industry concern affecting an organization's supply chain management and logistics network in terms of social, environmental, and economical aspects and so supplier selection in the context of developing sustainable supply chain management can be regarded as a decisive operational task. The integration of social, environmental, and economic aspects should be taken into account when evaluating the sustainable suppliers that can enhance the supply chain performance. Nowadays, many of the organizations should have a suitable and accurate assessment of their suppliers to satisfy their needs and achieve sustainability. Besides, social, environmental, and economic factors should be applied to the process of sustainable supplier evaluation. Therefore, several factors considering quantitative and qualitative criteria need to be applied to the evaluation process. However, an exact quantitative value may not be employed due to some data cannot be represented by crisp values. Thus, a proper evaluation method is necessary not only to eliminate these constraints, but also to satisfy the objectives of the study.

Supplier evaluation is one of the significant activities of the sustainable supply chain management. The

*Corresponding author. email address: gocer.fethullah@gmail.com

challenge of determining an effective framework based on sustainability assumptions for supplier selection processes in supply chains is thoroughly examined in this paper. Due to nature of sustainable supplier evaluation process, this analysis entails a suitable multi-criteria analysis and solution methodology. Multi-Criteria Decision-Making (MCDM) process, on the other hand, puts forward a concept in which the most suitable candidate among the predefined ones is selected by assessing them in terms of several criteria. MCDM methods gets to be increasingly popular in supplier evaluations and sustainability assessments. Several significant improvements have been observed on MCDM techniques since the development of modern MCDM theory in the early sixties. Conventional MCDM methods are constantly being applied to evaluate decision problems to select an alternative among many. There exist various types of MCDM techniques and more are introduced day in and day out. Multi-Objective Optimization on the basis of Ratio Analysis (MOORA) [3], AHP (Analytical Hierarchy Process) [4], TOPSIS (Technique for Order Preference by Similarity to Ideal Solutions) [5] are a few of the many. One of the significant problems in these MCDM techniques is how to represent the evaluations of the Decision Makers (DMs) exactly. Subjective representations can benefit from the subjective judgments of DMs, but they are challenging to eliminate bias instigated by the DMs' lack of experience and knowledge. Objective representations, on the other hand, have solid theoretical and mathematical basis, and the assessment does not rely on human judgments, but does not reveal the subjective opinions of DMs, and disregard the DMs' experience and knowledge buildup. In addition, many DMs have a tendency to make use of linguistic expressions in stating their judgments as a result of ambiguous decision environment. The DMs' linguistic evaluations are usually collected by quantitative and qualitative assessments in order to assess the relative significance and performance of the decision criteria to make scientific and accurate decisions. Therefore, Zadeh [6] developed the fuzzy set concept, in which the opinions of DMs are collected as a linguistic evaluations and he introduced a mathematical and scientific foundation to make operations and compute with the given linguistic values. But the conventional fuzzy set theory has some restrictions when it comes to dealing with complex linguistic evaluations due to vagueness and subjectivity associated with the given judgments.

In order to overcome these restrictions on conventional fuzzy set, an extension is proposed by Atanassov [7] and Intuitionistic Fuzzy (IF) sets are developed. Thus, many MCDM problems utilized the notion of IF set

theory to address the decision data. On the other hand, there are some areas in which the IF sets also have some deficiencies. To better address the imprecision and vagueness of the conventional crisp, fuzzy or IF sets, the Pythagorean Fuzzy Set (PFS) concept is developed. Yager extended IF sets into PFSs theory, defining elements having membership degree and non-membership degree, in which the square sum of them is a maximum of 1 [8,9]. Since PFSs can effectively represent the fuzzy characteristics of things, they have been applied to several MCDM problems in earlier studies. Varieties of new solution techniques have been formed to deal with the difficulties aroused during the sustainable supplier evaluation process. One of the latest favored methods to evaluate and analyze these problems is based on MCDM concept. Although MCDM approaches are devised to find faster and efficient solutions to problems, if the methodology is not set straight and structured adequately, MCDM cannot guarantee to find the best solution [10]. On the other hand, if MCDM methods are adequately applied, they can play an indispensable role of finding the solution to the problem. The weights of criteria can be determined most suitably by AHP approach and a fairly accurate ranking can be accomplished by TOPSIS method. The AHP is based on creating a decision hierarchy to better comprehend the sub-problems and analyze them independently by comparing them with one another in a rational and consistent way. TOPSIS technique depends on the concept of shortest distance from positive ideal solution and the farthest distance from negative ideal solution to unravel the complex domains having inconsistent criteria [10]. Besides, the PFSs are used to provide a better viewpoint for a further satisfactory modelling in complex real case situations. Additionally, contribution of multiple DMs in decision making process is crucial for most decision making problems. Wherefore the involvement of more than one DMs benefits the decision quality and thus many MCDM methods are also applied under a group decision making (GDM) environment [12]. Since GDM also benefits in reducing subjectivity and minimizing bias in the decision making process. The contributions of the research are delivered in succeeding sentences:

- to the best of author's knowledge, there is no prior research applying integration of PF-AHP (Pythagorean Fuzzy AHP) and PF-TOPSIS (Pythagorean Fuzzy TOPSIS) approach under GDM setting as a MCDM method in the sustainable supplier selection problem area;

- justification for PFSs environment's impact on decision problems is added distinctive contribution to

the present literature. This is a pioneering research that endorses the effect of PFSs on decision-making in sustainable supplier selection; and

-the contribution to the real-world cases is that developing a ready to use, flexible method modified for sustainable supplier selection. The companies can simply customize the proposed method by varying the criteria, alternatives or decision problem that reflect their own specific environments.

-this new methodology allows to capture the vagueness and hesitation associated with the DMs' judgments with the aid of PFSs' enhanced solution environment.

So, an integrated, state of art, solution method is developed in this research. The developed approach lets dealing the hesitation of the initial information with explicitly by making use of GDM.

The flow of this paper is structured as: Initially, the review of the current literature is introduced. Subsequently, the development of the proposed approach is presented to evaluate and prioritize the sustainable suppliers. After that, a practical case along with the numerical analysis is examined. And a discussion and analysis section are presented before the last section. Finally, summary and conclusion of the research is presented.

2. Literature Review

The evaluation of sustainable suppliers would be best dealt with as a distinctive MCDM problem due to its typical nature of taking multi-criteria into account in a simultaneous matter to rank a finite number of sustainable supplier alternatives. The evaluation process of alternatives is primarily based on the reliable judgment of the industry experts, rather than the given outcome of arithmetic techniques. In the literature, many of the earlier studies have examined and developed suitable sustainable supplier selection criteria. Besides, a lot of research have applied the proposed techniques in different environments. However, there are no study explicitly dealing with the evaluation of sustainable suppliers under GDM setting by the use of integrated AHP and TOPSIS techniques within the PFSs linguistic environment. There are two recent study [13,14] combining the AHP and TOPSIS techniques under PFSs setting. Some parts might indeed seem similar to the presented study as a first look. However, with a detailed comparison, there are distinct differences between the presented methodology and others. First of all, this study develops a novel priority MCDM framework by integrating PFSs objective world environment to capture uncertainty and hesitancy involved in DMs'

judgments. The AHP method is recommended to derive proper criteria weights, and the TOPSIS method is implied as a distance-based closeness to ideal solution approach under GDM setting to get rid of bias in the decision-making process. On the other hand, the mentioned studies utilize only the AHP and TOPSIS methods under the PFSs environment. For instance, the mentioned studies [13,14] applies interval-valued PFSs setting in AHP evaluations, that is rather different solution environment than the presented study in this paper although they also utilizes PFSs environment. If a further comparison is made among the presented paper and cited study, details of the AHP and TOPSIS applications under PFS is also entirely dissimilar. This manuscript uses a 9-point linguistic scale in evaluations, and they apply a 10-point interval-valued scale. The presented study applies normalization and weighting for the given relation matrix, while these steps are excluded in the mentioned studies. They use generalized Pythagorean fuzzy standardized distance operator to determine positive ideal and negative ideal solution. At the same time, we apply another set of distinct equations for their calculations. This list can elongate if the details are further inquired. Therefore, the presented manuscript has its distinctions and superiorities. But we have carefully checked all related studies and take some benefits of them using proper citations of mentioned studies. The subsequent sections present a brief review of current publications that focus on sustainable suppliers, AHP, and TOPSIS techniques under PFSs setting.

2.1. Sustainable supplier selection

Countless studies on various areas of sustainable supplier selection have emerged [1,15,16]. Though these researchers have developed different models for the evaluation of sustainable suppliers, a small number of them assessed the suppliers from the GDM perspective. Xu et al. [17] developed an AHP approach for sustainable supplier selection by applying interval type 2 fuzzy environment. Rabbani et al. [18] introduced an interval valued fuzzy GDM approach to evaluate sustainability performance of suppliers in the sustainable supply chain management. Baset et al. [19] provided a MCDM GDM approach under neutrosophic environment to solve the problem of sustainable supplier selection and illustrate the effectiveness of the proposed approach in importing field. Song and Li [20] developed large scale GDM method to handle sustainable supplier selection problem by considering the incomplete multigranular linguistic sets. Pishchulov et al. [21] proposed voting AHP methodology based on GDM environment to illustrate the application of a real world sustainable supplier

selection problem to their offered method. Foroozesh et al. [22] developed GDM approach to assess the sustainable supplier risks in terms of ecologic, economic, and social aspects. There are several more studies on the subject of sustainable supplier selection. However, as it could be comprehended from above analysis, there are no study using an integrated MCDM approach under PFSs environment for a GDM setting to evaluate sustainable supplier selection.

2.2. PFSs MCDM approaches

The application of PFSs theory in MCDM GDM problem has been stated in literature to a limited extent. Utilization of PFSs in a decision-making environment for sustainable supplier evaluation appears to be relatively new and unexplored research area. The presented research emerges some remarkable managerial insights. There are very few studies exist explicitly dealing with the supplier selection problem in the context of MCDM. As far as the author is aware of, there is no earlier study exist on the subject of

selecting a suitable supplier in the context of sustainability. And the PFSs concept is a relatively new research area. Currently, there are many studies exist in PFSs as either aggregation operator proposals or regular MCDM applications but the number of PF-AHP and PF-TOPSIS MCDM studies are limited as illustrated in Table 1.

This review of literature on the subject inform that many crucial features have been designated rare attention by researchers so far. Limited number of scientific studies exist in the areas of PF-AHP and PF-TOPSIS MCDM approaches but non exist integrating both of them together in GDM environment. To the best knowledge of the author, there are no prior contributions about sustainable supplier evaluations in the context of PFSs linguistic environment. Thus, this is the state of the art methodology to solve sustainable supplier evaluation problem through the proposed method which makes it a more realistic and reliable approach.

Table 1. PF-AHP and PF-TOPSIS MCDM Literature

Reference #	Integrated Method	GDM	Application Area
[13]	Interval Valued PF-AHP and PF-TOPSIS	-	Service Quality
[14]	Interval Valued PF-AHP and PF-TOPSIS	-	Green Supplier
[23]	Interval Valued PF-AHP	-	Regional Development
[24]	Interval Valued PF-AHP	-	Risk Assessment
[25]	Interval Valued PF-AHP	-	Risk Assessment
[26]	Interval Valued PF-AHP	-	Risk Assessment
[27]	Interval Valued PF-AHP	-	Risk Assessment
[28]	PF-TOPSIS	-	Airline Service Quality
[29]	Interval Valued PF-TOPSIS	-	Illustrative
[30]	Choquet Integral PF-TOPSIS	-	Illustrative
[31]	Hesitant PF-TOPSIS	-	Energy Project
[32]	PF-TOPSIS	-	Cloud Service Provider
[33]	PF-TOPSIS	-	Risk Assessment
[34]	Hesitant PF-TOPSIS	-	Illustrative
[35]	PF-TOPSIS	GDM	Illustrative
[36]	Interval Valued PF-TOPSIS	-	Partner Selection

3. Methodology

3.1. Preliminaries

Initial development of PFS concept has been made by Yager and Abbasov [8,9,37]. Initial proposal has been made to extend IF set in order to create a characteristic theory to handle the fuzziness and uncertainty by considering the both membership and nonmembership degrees in pairs $(\mu_P(x): X \rightarrow [0,1], \nu_P(x): X \rightarrow [0,1])$ [8,37].

Let X be a fixed set in a non-empty universe, a PFS P in X is denoted as:

$$P = \{(x, \mu_P(x), \nu_P(x))\}, \tag{1}$$

Subjected to:

$$0 \leq (\mu_P(x))^2 + (\nu_P(x))^2 \leq 1, \tag{2}$$

$$\pi_p(x) = \sqrt{1 - (\mu_p(x))^2 + (v_p(x))^2}, \forall x \in X, \tag{3}$$

The PFSs' arithmetic operations are presented by using two PFS number,

$p_1 = (\mu_{p_1}(x), v_{p_1}(x))$ and $p_2 = (\mu_{p_2}(x), v_{p_2}(x))$ and $\lambda > 0$, as follows [28,38]:

$$p_1 \otimes p_2 = \left(\mu_{p_1}(x) \cdot \mu_{p_2}(x), \sqrt{(v_{p_1}(x))^2 + (v_{p_2}(x))^2 - (v_{p_1}(x))^2 \cdot (v_{p_2}(x))^2} \right), \tag{4}$$

$$p_1 \oplus p_2 = \left(\sqrt{(\mu_{p_1}(x))^2 + (\mu_{p_2}(x))^2 - (\mu_{p_1}(x))^2 \cdot (\mu_{p_2}(x))^2}, v_{p_1}(x) \cdot v_{p_2}(x) \right), \tag{5}$$

if $\mu_{p_1}(x) \leq \min \left\{ \mu_{p_2}(x), \frac{\mu_{p_2}(x) \cdot \pi_{p_1}(x)}{\pi_{p_2}(x)} \right\}$, $v_{p_1}(x) \geq v_{p_2}(x)$,

$$\text{Then, } \frac{p_1}{p_2} = \left(\frac{\mu_{p_1}(x)}{\mu_{p_2}(x)}, \sqrt{\frac{(v_{p_1}(x))^2 - (v_{p_2}(x))^2}{1 - (v_{p_2}(x))^2}} \right), \tag{6}$$

if $\mu_{p_1}(x) \geq \mu_{p_2}(x)$, $v_{p_1}(x) \leq \min \left\{ v_{p_2}(x), \frac{v_{p_2}(x) \cdot \pi_{p_1}(x)}{\pi_{p_2}(x)} \right\}$,

$$\text{Then, } p_1 \ominus p_2 = \left(\sqrt{\frac{(\mu_{p_1}(x))^2 - (\mu_{p_2}(x))^2}{1 - (\mu_{p_2}(x))^2}}, \frac{v_{p_1}(x)}{v_{p_2}(x)} \right), \tag{7}$$

$$p_1^\lambda = (\mu_{p_1}(x)^\lambda, \sqrt{1 - (1 - (v_{p_1}(x))^2)^\lambda}), \tag{8}$$

$$\lambda * p_1 = \left(\sqrt{1 - (1 - (\mu_{p_1}(x))^2)^\lambda}, (v_{p_1}(x))^\lambda \right), \tag{9}$$

$$p_1^c = (v_{p_1}(x), \mu_{p_1}(x)), \tag{10}$$

Pythagorean Fuzzy Weighted Arithmetic (PFWA) Aggregation [8,9] operator is defined as follows:

$$PFWA = P_1^\lambda \otimes P_2^\lambda, \dots, \otimes P_K^\lambda = \left(\sqrt{1 - \prod_{k=1}^K (1 - (\mu_{P_k}(x))^2)^\lambda}, \prod_{k=1}^K v_{P_k}(x)^\lambda \right), \tag{11}$$

3.2. The Developed integrated MCDM method

The step wise representation of the developed approach is delivered through this section. The schematic representation is also given in Figure 2.

Step 1: Describe the criteria and alternatives

The Alternative set (A_i) for m alternative ($i = 1, 2, \dots, m$) is assessed by the use of defined criteria set (C_j) for n criteria ($j = 1, 2, \dots, n$).

Step 2: Estimate the DMs' priority weights

Table 2. Verbal terms to assess DMs and Alternatives [12]

Linguistic Variables	Abbreviations	[$\mu_p(x)$,	$v_p(x)$]
Extremely Important	EI	[0.85,	0.15]
Very Important	VI	[0.75,	0.25]
Important	I	[0.65,	0.35]
Medium Importance	MI	[0.50,	0.45]
Unimportant	U	[0.35,	0.65]
Very Unimportant	VU	[0.25,	0.75]
Extremely Unimportant	EU	[0.15,	0.85]

The level of individual weights ($\lambda_k, \sum_{k=1}^K \lambda_k = 1$) in DMs set ($D_k, k = 1, 2, \dots, K$) can alter due to the different responsibilities, knowledges, and experiences of distinctive DMs. To be able to define the priorities of DMs and their individual weights, the subsequent steps has been applied.

- The verbal terms are expressed to define the priority levels of DMs.
- The linguistic statements for the priority of DMs in Table 2 are applied to calculate the DMs weights.
- The individual DMs priorities are fused together by applying the PFWA aggregation operator.
- The influence level of the k^{th} DM on the judgment is estimated by the Equation (Eq.) (12).

$$\lambda_k = \frac{\sqrt{\frac{\mu_{P_j}(x) - (v_{P_j}(x))^2}{2}}}{\sum_{k=1}^K \sqrt{\frac{\mu_{P_j}(x) - (v_{P_j}(x))^2}{2}}}, \text{ where } \sum_{k=1}^K \lambda_k = 1 \tag{12}$$

Step 3: Gather the evaluations of DMs for each criterion

- The verbal terms are expressed to define the judgments for criteria.
- The pairwise comparison ($\tilde{P}_j^k, j = 1, 2, \dots, n, k = 1, 2, \dots, K$) is established for criteria and sub-criteria by the use of linguistic statements in Table 3.

The preference scale for PFSs AHP is established by applying the consistency conversion [39]. The detailed demonstration of how the PFSs linguistic scale for AHP is constructed is presented in Büyüközkan and Göçer [12].

Step 4: Establish the group consensus for individual assessments

- GDM matrix is established for each DM to evaluate criteria by the use of PFWA aggregation operator in Eq. (11).

Table 3. Linguistic statements for the priority of criteria [12]

Linguistic Statements		PFSs Values	
		[$\mu_p(x)$,	$v_p(x)$]
Equally Important	EI	[0.07,	0.30]
Intermediate	IV	[0.18,	0.49]
Moderately More Important	MI	[0.29,	0.60]
Intermediate	IV2	[0.39,	0.65]
Strongly More Important	SI	[0.50,	0.67]
Intermediate	IV3	[0.61,	0.66]
Very Strong Importance	VSI	[0.71,	0.61]
Intermediate	IV4	[0.82,	0.52]
Extremely More Important	EMI	[1.00,	0.00]

Table 4. RI Values [40]

N	RI	N	RI	n	RI
01	0.000	04	0.900	07	1.320
02	0.000	05	1.120	08	1.410
03	0.580	06	1.240	09	1.450

Step 5: Control the consistency of pairwise comparison matrix

Consistency Ratio (CR) is controlled for all pairwise matrix by the Eq. (13). The Random Index (RI) is adapted from [40]. Table 4 delivers RI table having up to 9 elements;

$$CR = \frac{RI - \frac{\sum \pi_P(x)_{ij}}{n}}{n-1}, \tag{13}$$

Here, n denotes the number of elements in each matrix. $\pi_P(x)_{ij}$ denotes the hesitancy value. When the calculated CR is equal to or less than 0.10, the given matrices is considered as consistent. If the value of CR is above 0.10, then matrix is inconsistent, and the DMs should give their judgments once more.

Step 6: Compute each criterion weight

PFWA operator for aggregation defined in Eq. (11) is applied to fuse the assessment matrices. Each criterion weight (\tilde{w}_j) by applying PFSs AHP method is calculated based on all DMs judgments.

Step 7: Define decision matrix for each DM

The opinions of DMs in the form of linguistic variables are converted by applying the scale in Table 2 and decision matrix $(A_{(k)ij})_{m \times n}$ for each DM is established.

$$A_{(k)ij} = \begin{bmatrix} a_{11} & \dots & a_{1n} \\ \vdots & \ddots & \vdots \\ a_{m1} & \dots & a_{mn} \end{bmatrix}, \tag{14}$$

Step 8: Determine GDM matrix

The evaluations of each DM are fused by the use of Eq. (11) (PFWA aggregation operator) and GDM matrix is established.

$$A_{ij} = \begin{bmatrix} a_{11} & \dots & a_{1n} \\ \vdots & \ddots & \vdots \\ a_{m1} & \dots & a_{mn} \end{bmatrix}, \tag{15}$$

Step 9: Setup weighted and normalized matrix

By the Eq. (10), the decision matrix is normalized. And then, Eq. (16) is used to construct weighted matrix. The criteria weighs are presented in Step 6.

$$\tilde{R}_{ij} = \tilde{w}_j \otimes \tilde{x}_{ij}, \tag{16}$$

where $\tilde{r}_{ij} = (\mu_{\tilde{A}}(x), \nu_{\tilde{A}}(x)), j = 1, 2, \dots, n, i = 1, 2, \dots, m$.

Step 10: Calculate positive and negative ideal solution

Use Eq. (17) and Eq. (18) to find positive (A^+) and negative (A^-) ideal solutions, respectively.

$$A^+ = (\tilde{r}_1^+, \tilde{r}_2^+, \dots, \tilde{r}_n^+), \tilde{r}_j^+ = (\mu_j^+, \nu_j^+, \pi_j^+), \tag{17}$$

$$A^- = (\tilde{r}_1^-, \tilde{r}_2^-, \dots, \tilde{r}_n^-), \tilde{r}_j^- = (\mu_j^-, \nu_j^-, \pi_j^-), \tag{18}$$

Where $j = 1, 2, \dots, n$, suppose J_1 is the benefit type criterion, J_2 is the cost type criterion.

$$\mu_j^+ = \left\{ \left(\max_i \{ \mu_{ij} \} \mid j \in J_1 \right) \right\}, \left\{ \left(\min_i \{ \mu_{ij} \} \mid j \in J_2 \right) \right\}, \tag{19}$$

$$v_j^+ = \left\{ \left(\min_i \{v_{ij}\} \mid j \in J_1 \right) \right\}, \left\{ \left(\max_i \{v_{ij}\} \mid j \in J_2 \right) \right\},$$

$$\mu_j^- = \left\{ \left(\min_i \{\mu_{ij}\} \mid j \in J_1 \right) \right\}, \left\{ \left(\max_i \{\mu_{ij}\} \mid j \in J_2 \right) \right\},$$

$$v_j^- = \left\{ \left(\max_i \{v_{ij}\} \mid j \in J_1 \right) \right\}, \left\{ \left(\min_i \{v_{ij}\} \mid j \in J_2 \right) \right\},$$

Step 11: Calculate separation measures

Use Eq. (20) and Eq. (21) to calculate separation measures of negative and positive ideal solutions.

$$S_i^+ = \sqrt{\frac{1}{2n} \sum_{j=1}^n [|\mu_{ij}^2 - \mu_j^{*2}| + |v_{ij}^2 - v_j^{*2}| + |\pi_{ij}^2 - \pi_j^{*2}|]}, \tag{20}$$

$$S_i^- = \sqrt{\frac{1}{2n} \sum_{j=1}^n [|\mu_{ij}^2 - \mu_j^{-2}| + |v_{ij}^2 - v_j^{-2}| + |\pi_{ij}^2 - \pi_j^{-2}|]}, \tag{21}$$

Step 12: Calculate closeness coefficient

Calculate the closeness coefficient for each alternative using the Eq. (22).

$$C_i^+ = \frac{S_i^-}{S_i^+ + S_i^-}, i = 1, 2, \dots, m \quad 0 \leq C_i^+ \leq 1, \tag{22}$$

Step 13: Rank the alternatives.

The respective candidate is ranked according to the descending order of closeness coefficient (C_i^+).

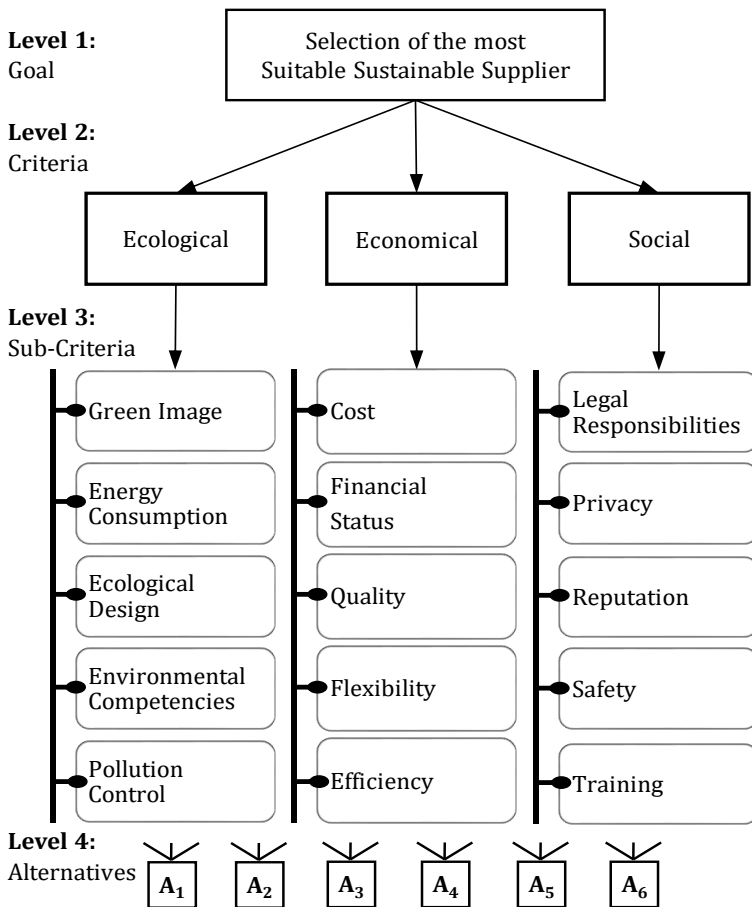


Figure 1. Hierarchical organization of evaluation structure.

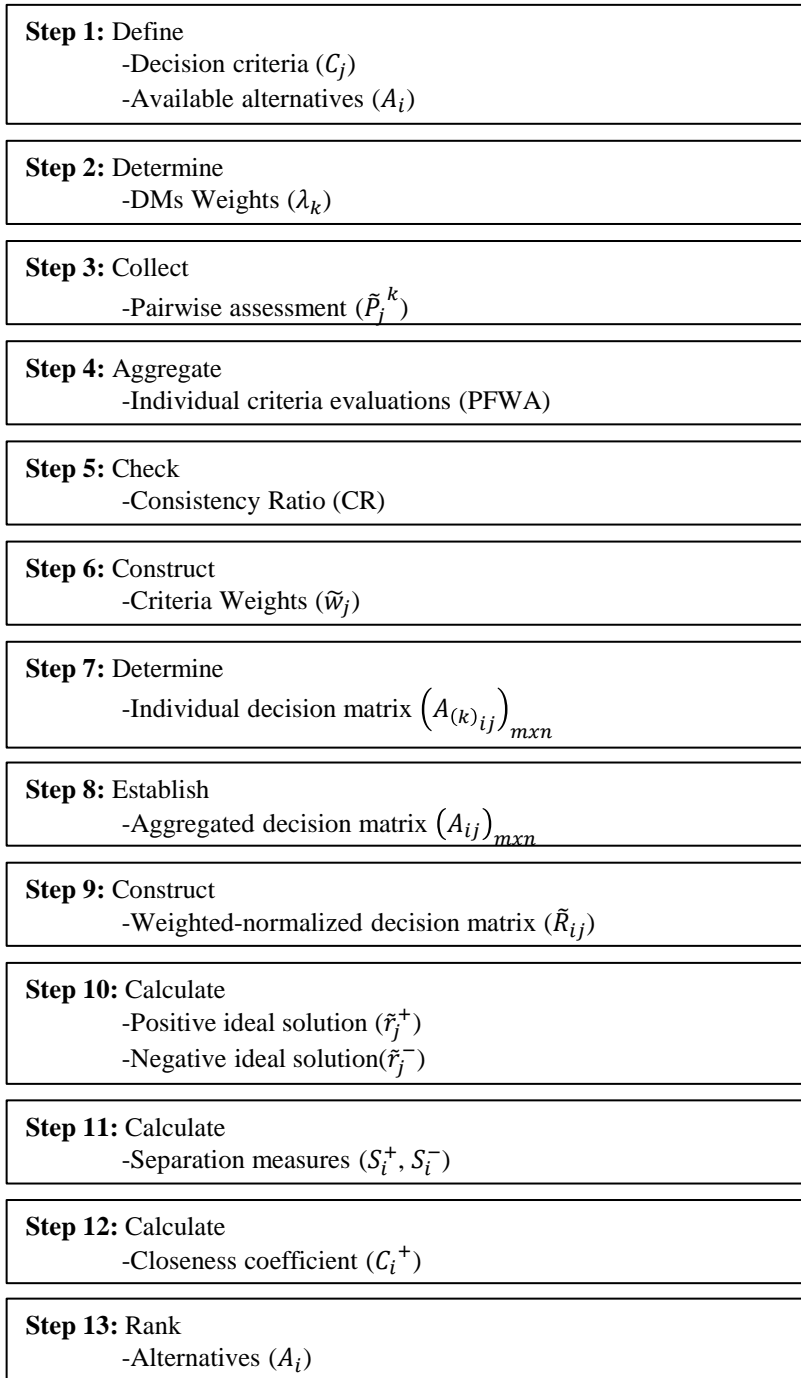


Figure 2. Schematic diagram of the proposed method.

4. Case Study

This section is cascaded into three subsections. Initially, the development of criteria for the evaluation of sustainable suppliers are presented through the review of extant literature and opinions of real experts from the industry. And then, a brief introduction on the background for an apparel industry example is provided using a real case from the city of Kahramanmaraş in Turkey. Numerical results and computational procedure are also included here as the last subsection. The identification of decision criteria to evaluate the given alternatives is the initial step in solving a MCDM problem.

Table 5. The evaluation criteria and their description

Criteria		Description
Ecological	(C ₁)	This pillar stresses the importance of increasing awareness about environmental degradation [16,17].
Green Image	(C ₁₁)	This criterion represents the prioritization of environmental conservation [1,18].
Energy Consumption	(C ₁₂)	This criterion deals with the consumption of energy or power to contribute to more energy efficient processes [16,17].
Ecological Design	(C ₁₃)	This criterion refers how the entire product life cycle at the design stage is impacted environmentally [1,18].
Environmental Competencies	(C ₁₄)	This criterion handles the containment relationships balance capacity between economy and environment [15,19].
Pollution Control	(C ₁₅)	This criterion is a determining factor to work together by considering suppliers' attitude towards pollution [16,17].
Economical	(C ₂)	This pillar expresses the overtime continuation of the wellbeing for the society [1,18].
Cost	(C ₂₁)	This criterion refers to Cost of acquisitioning product, including product, inventory, logistic [41].
Financial Status	(C ₂₃)	This criterion displays the actual ability of performing economic contracts. Good finances is key to improvement [41].
Quality	(C ₂₂)	This criterion is measured in terms of empathy, ease of communication, and blend of services provided [41].
Flexibility	(C ₂₄)	This criterion presents the ability of quick response to product demand variations [15,19].
Efficiency	(C ₂₅)	This criterion present the ability of fulfilling efficient orders within the given period of time [41].
Social	(C ₃)	This pillar defines the security and diversity of supply within public acceptability.
Legal Responsibilities	(C ₃₁)	This criterion stresses the labor relations between workers and employers in the context of legal and human rights [16,17].
Privacy	(C ₃₂)	This criterion refers providing information to stakeholders in respecting the confidentiality [41].
Reputation	(C ₃₃)	This criterion stresses the keeping a good name among competitors in a long-term to gain competitive advantage [41].
Safety	(C ₃₄)	This criterion is concerned with the safety, health, and welfare of labor force [1,18].
Training	(C ₃₅)	This criterion deals with the process of enhancing the skills, capabilities, and knowledge of employees [15,19].

4.1. Sustainable supplier selection criteria

The goal in this sub-section is to determine the best available criteria for sustainable supplier selection through an extensive literature review and expert opinions. As far as the author know, the presented study is the first study to determine the sustainable supplier selection criteria in the context of social, environmental, and economical aspects. In today's competitive businesses, cost and quality are not enough to determine a suitable supplier due to the augmented consumer expectations. Hence, different evaluation criteria such as ecological, economical, and social criteria, have to be taken into account. Three main and 15 sub-criteria are defined based on the extant literature and through the extensive brainstorming of DMs. They are adapted to be used in the proposed methodology. Figure 1 presents the

network structure of evaluation framework. Table 5 delivers the comprehensive description of the evaluation criteria.

4.2. Case background

The developed approach is applied to a textile factory established in Kahramanmaraş, Turkey. The name of the company is undisclosed due to confidentiality and privacy reasons. This factory is addressed as the Textile Company in this paper, hereafter. The factory is specialized in the production and development of innovative fabrics and technical yarns. This Textile Company has been established in 1989 having the first weaving mill of Kahramanmaraş, Turkey. Textile Company value partnerships with sustainable suppliers and apparel manufacturers as a supplier, end-user, and market-oriented factory. The competition in apparel industry is intense and it is a key distress for the Textile

Company to consider during its assessment of suppliers. Thus, the evaluation of the best sustainable supplier is an important decision-making process for the Textile Company.

A group of specialists consisting of three DMs, a chief textile engineer in Textile Company, a top-level manager of the Textile Company, and an academician having a considerable position in a Turkish university, are collaborated to pass judgment on six suppliers. The supplier selection procedure is a remarkable process in sustainability setting, recalling the existence of an obvious distinction between traditional supplier selection and sustainable supplier perspective. With the review of extensive literature and DMs' skills along with the managers of the Textile Company, each decision criterion is composed to evaluate and prioritize the presented candidates. The Textile Company intends to pick the finest alternative according to its expectations and needs. In the given study, six alternatives are assessed which the company

intends to work together. The selected six alternatives are denoted by: A_1, A_2, A_3, A_4, A_5 and A_6 from now on.

4.3. Numerical application

Step 1: The given 6 alternatives are assessed by 3 main criteria and 15 sub-criteria set.

Step 2: A group consisting of 3 DMs are charged to evaluate the defined problem. Their individual weights are calculated by applying the Step 2 of the methodology. Table 6 presents the given individual evaluations of each DM and their respective weights.

Step 3: DMs' individual evaluation on each criterion is gathered in the form of verbal terms. The collected judgments are converted to PFSs values by applying Table 3. Due to space limitation and suitable appearance of the paper, the data is scaled. Thus, individual evaluation on main criteria in Table 7 is presented.

Table 6. The level of individual influence for each DM

DM	Preference			$[\mu_p(x),$	$\nu_p(x)]$	λ_k
D_1	-	VI	MI	0.654	0.335	0.385
D_2	I	-	MI	0.585	0.397	0.336
D_3	MI	MI	-	0.500	0.450	0.279

Table 7. DMs' individual evaluation on main criteria

DM	C_1	C_2	C_3	C_1	C_2	C_3	C_1	C_2	C_3
D_1	EI	1/IV4	IV4	IV4	EI	1/IV4	1/IV4	IV4	EI
D_2	EI	1/VSI	IV4	VSI	EI	VSI	1/IV4	1/VSI	EI
D_3	EI	1/IV4	IV4	IV4	EI	IV3	1/IV4	1/IV3	EI

Step 4: Individual evaluations are fused together with PFWA aggregation operation in Eq. (11). The GDM matrix for the main criteria is presented in Table 8.

Step 5: CR is controlled for the aggregated PFSs matrix. The calculated CR values are smaller than 0.10 and so the judgment matrix is consistent.

Table 8. Aggregated pairwise matrix

Criterion	$[\mu_p(x),$	$\nu_p(x)]$
C_1	0.597	0.507
C_2	0.567	0.514
C_3	0.647	0.474

Table 9. The PFSs criteria weights and crisp criteria weights

Main	\tilde{w}_j		Sub	\tilde{w}_{jj}		$\tilde{w}_j \otimes \tilde{w}_{jj}$		w_j	Rank
	$[\mu_p(x),$	$\nu_p(x)]$		$[\mu_p(x),$	$\nu_p(x)]$	$[\mu_p(x),$	$\nu_p(x)]$		
(C_1)	0.597	0.507	(C_{11})	0.463	0.307	0.276	0.572	0.069	12
			(C_{12})	0.579	0.291	0.346	0.566	0.068	10
			(C_{13})	0.607	0.302	0.362	0.570	0.067	9
			(C_{14})	0.628	0.405	0.375	0.615	0.062	1
			(C_{15})	0.568	0.396	0.339	0.611	0.064	4
(C_2)	0.567	0.514	(C_{21})	0.558	0.393	0.317	0.614	0.064	5
			(C_{22})	0.597	0.395	0.338	0.616	0.063	3
			(C_{23})	0.669	0.273	0.379	0.565	0.067	8
			(C_{24})	0.572	0.327	0.325	0.585	0.067	7
			(C_{25})	0.554	0.266	0.314	0.562	0.070	13
(C_3)	0.647	0.474	(C_{31})	0.525	0.336	0.340	0.559	0.069	11
			(C_{32})	0.543	0.451	0.351	0.618	0.063	2
			(C_{33})	0.650	0.346	0.421	0.563	0.065	6
			(C_{34})	0.577	0.254	0.373	0.524	0.071	15
			(C_{35})	0.630	0.241	0.408	0.519	0.070	14

Table 10. The individual linguistic evaluations of each DM

A_i	D_i	C_{11}	C_{12}	C_{13}	C_{14}	C_{15}	C_{21}	C_{22}	C_{23}	C_{24}	C_{25}	C_{31}	C_{32}	C_{33}	C_{34}	C_{35}
A_1	D_1	I	I	VU	U	VU	EU	EU	VU	VU	EU	VU	VU	I	EI	MI
	D_2	MI	MI	VU	U	VU	I	U	EU	VU	U	I	EI	MI	MI	EI
	D_3	VI	MI	U	VU	U	EU	VU	U	I	VU	EU	VI	I	MI	MI
A_2	D_1	VU	VU	I	EI	EI	VU	EI	EU	VU	EI	I	I	MI	I	EU
	D_2	EU	U	VU	VI	EU	U	EI	VU	EU	VI	I	EI	EI	VI	EI
	D_3	VU	I	EU	MI	EI	I	VI	VU	EU	EI	EU	VI	EI	MI	VU
A_3	D_1	EI	MI	VI	MI	I	EI	I	VU	EU	U	VU	U	EI	EI	EI
	D_2	VI	MI	VU	I	U	MI	EI	VI	MI	VU	EU	I	VI	EI	I
	D_3	VI	I	U	VU	U	I	EI	EU	EI	VU	U	VU	VI	EI	I
A_4	D_1	VU	VI	VU	EU	MI	VU	MI	U	VU	I	EI	VI	EU	VU	VU
	D_2	U	I	U	EI	VU	EU	EI	U	EU	EU	MI	EI	I	MI	EU
	D_3	EI	U	VU	EU	EU	VU	I	VI	I	VU	VU	EI	VI	EI	EU
A_5	D_1	U	U	VU	VU	EU	VU	EU	MI	EI	MI	VU	EU	I	MI	I
	D_2	VU	VU	U	VU	U	I	U	VU	VU	VU	EU	VU	EI	MI	MI
	D_3	EU	I	EU	I	VU	EU	VU	EU	U	MI	EI	I	MI	EI	MI
A_6	D_1	EU	I	EU	VU	U	I	VU	EU	U	EU	EU	MI	VU	EU	VI
	D_2	EU	U	VU	EI	EI	VI	U	I	VU	I	VU	VU	VU	EU	VU
	D_3	VU	EU	U	EU	VU	VU	EI	VI	VI	MI	VI	MI	VU	U	I

Step 6: Each criterion weight (\tilde{w}_j) is calculated using each DMs' judgments. Table 9 presents the PFSs criteria weights. In order to better visualize and grasp the priority of criteria on each other, Crisp AHP criteria weights are also created. Table 9 presents the crisp AHP criteria weights. The criterion C_{14} has the utmost priority while criterion C_{34} has the last.

Step 7: The individual judgments of DMs in the form of linguistic variables are converted by the use of Table 2 to form individual decision matrix. Table 10 presents the individual linguistic evaluations of each DM.

Step 8: The alternatives evaluated individually are fused into group opinion to set GDM matrix by PFWA aggregation operator. Table 11 presents the aggregated alternative evaluation matrix.

Step 9: The normalization of evaluation matrix is utilized by the Eq. (10) for each cost type criterion. The Eq. (17) is used to find weighted matrix. Each weight is given in Table 9. Apply PFSs multiplication operator to obtain the new weighted-normalized decision matrix as presented in Table 11.

Step 10: The positive (A^+) and negative (A^-) ideal solutions are calculated by the use of Eq. (18) and (19), respectively. Table 11 presents the positive and negative ideal solutions.

Step 11: separation measures of negative and positive ideal solutions are estimated by the use of Eq. (20) and (21) to calculate. Table 12 presents the calculated separation measures.

Step 12: The closeness coefficients for all alternatives are calculated by the use of Eq. (22). Table 12 presents the calculated closeness coefficient.

Table 11. The aggregated and weighted-normalized matrix of first alternative and respective positive and negative ideal solutions

	A_{1j}		\tilde{R}_{1j}		A^+		A^-	
	$[\mu_P(x),$	$\nu_P(x)]$	$[\mu_P(x),$	$\nu_P(x)]$	μ_j^+	ν_j^+	μ_j^-	ν_j^-
C_{11}	0.80	0.19	0.22	0.65	0.22	0.65	0.05	0.92
C_{12}	0.55	0.40	0.14	0.81	0.19	0.76	0.12	0.85
C_{13}	0.56	0.46	0.20	0.77	0.20	0.77	0.09	0.89
C_{14}	0.52	0.47	0.19	0.80	0.28	0.70	0.12	0.87
C_{15}	0.50	0.50	0.17	0.81	0.26	0.71	0.09	0.90
C_{21}	0.72	0.26	0.08	0.89	0.24	0.70	0.08	0.89
C_{22}	0.80	0.19	0.27	0.69	0.28	0.68	0.09	0.90
C_{23}	0.52	0.53	0.20	0.80	0.22	0.75	0.08	0.90
C_{24}	0.61	0.38	0.20	0.74	0.21	0.74	0.06	0.92
C_{25}	0.29	0.70	0.09	0.87	0.26	0.63	0.08	0.89
C_{31}	0.26	0.73	0.09	0.88	0.23	0.71	0.09	0.88
C_{32}	0.47	0.54	0.17	0.82	0.29	0.68	0.14	0.85
C_{33}	0.80	0.19	0.34	0.65	0.34	0.65	0.11	0.89
C_{34}	0.85	0.14	0.32	0.59	0.32	0.59	0.09	0.89
C_{35}	0.75	0.24	0.31	0.63	0.31	0.63	0.08	0.91

Step 13: By applying a descending order for the closeness coefficient (C_i^+), the alternatives are ranked. Table 12 presents the ranking of alternatives. The result indicated that the best alternative in ranking is A_2 while the worst is A_6 . The obtained outcome is also validated by the DMs as satisfactory.

$$A_6 < A_1 < A_5 < A_4 < A_3 < A_2$$

Table 12. The separation measure, closeness coefficient and ranking of alternatives

	S_i^+	S_i^-	C_i^*	Rank
A_1	0.715	0.653	0.477	5
A_2	0.548	0.797	0.592	1
A_3	0.569	0.784	0.579	2
A_4	0.633	0.732	0.536	3
A_5	0.703	0.665	0.486	4
A_6	0.742	0.622	0.456	6

5. Discussion and Analysis

Sustainability concept has raised a considerable attention in academic and industrial area, yet its meaning is not always clear. Sustainability may imply

very different policy responses depending on its interpretation. The earliest sustainability studies on supply chain management can be traced back to the 90s, when the sustainability concept mainly discussed as environmental management [42]. Sustainability

draws the line between socially responsible and irresponsible businesses. Sustainability has three goals known as the triple bottom line: people, planet, and profit. As the company can effect these three areas positively, it is considered more sustainable [2].

This study reports a novel MCDM method by combining the AHP technique with the TOPSIS technique under PFSs environment to evaluate the most suitable sustainable supplier. In the proposed method, the AHP technique is utilized to compute the optimal evaluation criteria weights; the TOPSIS technique is used to manage DMs' assessments on the alternative sustainable suppliers' performance and to generate the ranking orders of the sustainable supplier alternatives.

The AHP technique is a MCDM method developed by Thomas Saaty [40] in the 1970s. It is a quantitative method used to order and select alternatives with multiple criteria and multiple DMs under certain or uncertain decision environment. AHP allows modeling the hierarchical structure by representing the relationship among the main target of the problem, criteria, and sub-criteria for the complex problems of DMs. AHP technique reduces the complex decision problem (multiple alternative and multiple criteria) to pairwise comparisons, checks whether the comparisons are consistent, and tries to get an outcome.

The TOPSIS technique is a MCDM method developed by Hwang and Yoon in 1981 [5]. The presented approach has exploited the proposition hypothesizing the ideal candidate as the alternative having position very near position to positive ideal solution and very far from the negative ideal solution. The positive ideal solution considers the minimum of the cost criteria and the maximum of the benefit criteria. The negative ideal solution considers the maximum of the cost criteria and the minimum of the benefit criteria. Succinctly, the positive ideal solution considers the best value of the solution criteria while negative ideal solution considers the worst value of the solution criteria. This approach prioritizes the alternatives by considering distances from positive ideal to negative ideal solutions.

Decision-making is a large part of every-day life. If a decision is taken by only one person, making that

decision is relatively easy since an individual can make a quicker decision than a group can. Individual decision-making, however, could create a prejudice and bias when compared to a group's involvement. Many important decisions are made with GDM, and recent literature demonstrates the systematic differences and strengths of GDM both experimentally and theoretically [10].

Yager recently introduced the PFSs theory [8,37] as an extension of IF set theory. Yager recently has showed that there may be some cases in which the sum of membership and non-membership (supporters + opponents > 1) of the opinion of a DM is greater than one in the real-world environment. This is not allowed in conventional theories because the sum is greater than one. According to PFSs theory, the sum of membership and non-membership can exceed one as long as the sum of squares does not exceed one. This property gives a higher flexibility and ability to express the uncertain and vague information compared to IF sets. Therefore, the PFSs theory have been applied to many MCDM problems. PFSs are more advantageous in imprecise and fuzzy modeling of objective world and can model and solve complex problems more adequately.

5.1 Comparison

The reliability and rationality of the obtained rankings by the proposed method is demonstrated by means of a comparative investigation. The similar supplier ranking evaluation is also completed by applying the following comparable MCDM approaches in PFSs environment: PF-VIKOR, PF-COPRAS, PF-TODIM. The rankings attained by these approaches are charted in Figure 3 for comparison. From this figure, it can be seen that the best ranked supplier and the worst ranked supplier are the same in the PF-VIKOR and PF-COPRAS MCDM methods, and the best ranked supplier of the proposed method is the second best in PF-TODIM. Thus, this demonstrates the strength and justification of the developed method. It is easily observable by looking at the given analysis that the outcome is an excellent match to each other and to the consequence of the obtained ranking order.

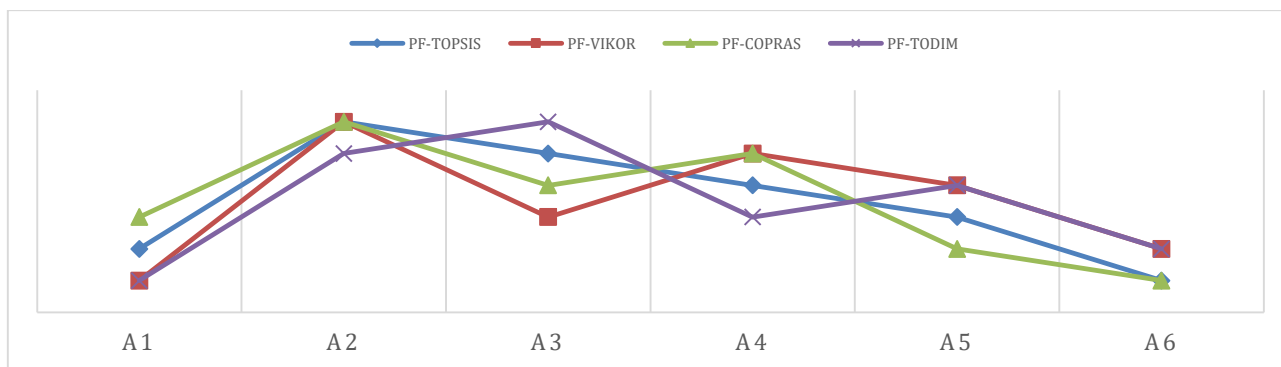


Figure 1. Comparison with existing methods

In order to create a link between the results obtained by the different approaches, Spearman’s correlation coefficient is tested. The Spearman’s correlation coefficient of ranks is a significant and convenient indicator to determine the connection among the obtained results [10]. Besides, the Spearman’s correlation coefficient is suitable to use in case of ordinal or ranked variables, as is the case here. This technique is applied to test the statistical significance of the difference between the ranks. The results of The Spearman’s correlation coefficient for the obtained ranks can be seen in Figure 4, which shows a high correlation among the MCDM approaches for the

obtained ranks. All coefficient values are greater than 0.90 which shows a very high correlation. The result indicate that an extremely high closeness is exist within the proposed method and the existing PFSs methods for the handling of uncertainty. Based on the obtained results of ranking comparison and correlation check, it can be established that the attained rankings of the proposed method are robust and justifiable. In addition to credibility of the ranks, the method proposed can successfully exploits the hesitations that occur in GDM environment. The computations are not incorporated here since the section is only devoted to a comparative analysis of the attained final ranks

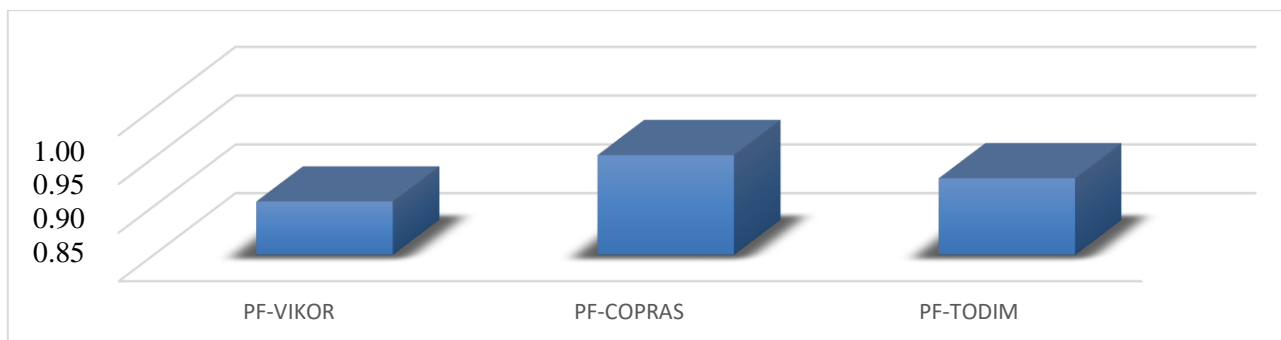


Figure 2. Spearman’s correlation coefficient of ranks

5.2 Sensitivity analysis

The sensitivity analysis is carried out by changing the weight of one criterion at a time while keeping others unchanged. For example, the weight of criterion C_{11} is varied and given the PFSs value corresponding to the EI linguistic term, and subsequently, the weight of other criteria is also exchanged with the weight of EI. A total of 16 experiments are conducted and results are charted in Figure 5. Figure 5 represents variations in the final ranking of different supplier evaluations with

the change of the criteria. Fifteen experiments of sensitivity analysis together with the base scenario of obtained outcome is depicted in Figure 5 shows that alternative A_2 is the best alternative among sustainable supplier alternatives for 10 scenarios and second best one for the rest. The ranking of other alternatives does not change considerably with the criteria’s weight. This shows that the ranking of sustainable supplier alternative is sensitive to the weight of selected criteria.

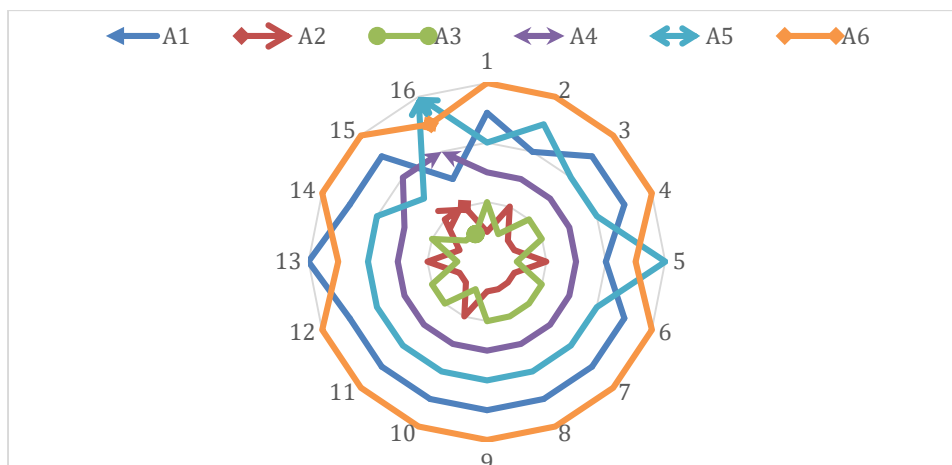


Fig. 3. Sensitivity Analysis

6. Conclusion

Sustainability has gained an increasing consideration among scholars and practitioners in the last several decades. Several different types of initiatives exist which aim to provide methods and tools for the supplier selection process in the context of sustainability assessment. The proposed MCDM methodology is built on the combination of AHP technique and TOPSIS method using PFSs setting for GDM environment. In the given methodology, the AHP method is applied to determine criterion weight and the TOPSIS method is applied to assess the candidates. Thus, the priority ranks are obtained for each alternative. The study provides a systematic decision approach in order to choose the logical candidate for sustainable suppliers. In addition, many DMs have a tendency to make use of linguistic expressions in stating their judgments as a result of ambiguous decision environment. This new methodology allows to capture the vagueness and hesitation associated with the DMs' judgments with the aid of PFSs' enhanced solution environment. Besides, the AHP technique can obtain the near optimal weights of criteria by constructing hierarchical evaluation structure. For the evaluation of supplier alternatives, The TOPSIS as a distance based, intuitive and reliable ranking technique can achieve a better result. Compared with the given approaches applied in the above comparative analysis section, the proposed approach has the distinct gains. The sensitivity analysis verifies the stability of the proposed method, which has benefit of reliability in decision-making process. Consequently, the proposed method is more preferable to the others for a range of GDM problems that deal with vague and subjective data. In order to determine the identification criteria for sustainable supplier selection, the available and relevant literature is examined. The developed main and sub criteria are stated to be the most relevant, which is confirmed by

the DMs and the Textile Company and cover the widest aspects in comparison to the extant literature. Involving PFSs theory with MCDM approaches can conclude in far better reliable result due to DMs' opacity and fuzziness of information. The cohesive PFSs approach integrates the PFSs theory with AHP and TOPSIS, which can reach more consistent results. The obtained outcome justifies that the developed method is more capable to capture uncertainty and ambiguity of DMs' evaluations and it is further effective and efficient to derive the ranking orders of sustainable supplier alternatives.

The proposed method has the advantage of enabling a quick decision for supplier selection process. The limitation of the research can be the dependence to the DMs' experience and the quality of their judgments. The hierarchical inter-dependency and mutual relationships between main and sub criteria has not yet studied. The ANP technique can be used in future studies to enhance solution quality. Furthermore, the approach can also be applied by extending it to interval valued PFSs environments and the rationality could be verified in uncertain MCDM setting.

Acknowledgments

The author would like to thank the DMs for their valuable contribution to this research, which significantly improved the manuscript. The author also gratefully acknowledges valuable comments and suggestions of the editors and anonymous reviewers, which improved the quality of the paper.

Conflicts of interest

The author declare that he has no conflict of interest.

References

- [1] Luthra S., Govindan K., Kannan D., Mangla S.K., Garg C.P., An integrated framework for sustainable supplier selection and evaluation in supply chains, *J. Clean. Prod.*, 140 (2017) 1686–1698.
- [2] Büyüközkan G., Çifçi G., An integrated QFD framework with multiple formatted and incomplete preferences: A sustainable supply chain application, *Appl. Soft Comput. J.*, 13 (2013) 3931–3941.
- [3] Brauers W.K.M., Zavadskas E.K., The MOORA method and its application to privatization in a transition economy, *Control Cybern.*, 35 (2006) 445–469.
- [4] Saaty T.L., The analytic hierarchy process: planning, priority setting, resources allocation, McGraw-Hill. (1980).
- [5] Hwang C.L., Yoon K., Multiple Attribute Decision Making-Methods and Application, New York: Springer, (1981).
- [6] Zadeh L.A., Fuzzy sets, *Inf. Control.*, 8 (1965) 338–353.
- [7] Atanassov K., Intuitionistic fuzzy sets, *Fuzzy Sets Syst.*, 20 (1986) 87–96.
- [8] Yager R.R., Abbasov A.M., Pythagorean Membership Grades, Complex Numbers, and Decision Making, *Int. J. Intell. Syst.*, 28 (2013) 436–452.
- [9] Yager R.R., Pythagorean Membership Grades in Multicriteria Decision Making, *IEEE Trans. Fuzzy Syst.*, 22 (2014) 958–965.
- [10] Büyüközkan G., Göçer F., Smart medical device selection based on intuitionistic fuzzy Choquet integral, *Soft Comput.*, 23 (2019) 10085–10103.
- [11] Büyüközkan G., Göçer F., Karabulut Y., A new group decision making approach with IF AHP and IF VIKOR for selecting hazardous waste carriers, *Measurement.*, 134 (2019) 66–82.
- [12] Büyüközkan G., Göçer F., A Novel Approach Integrating AHP and COPRAS Under Pythagorean Fuzzy Sets for Digital Supply Chain Partner Selection, *IEEE Trans. Eng. Manag.*, (2021) 1–18.
- [13] Yucesan M., Gul M., Hospital service quality evaluation: an integrated model based on Pythagorean fuzzy AHP and fuzzy TOPSIS, *Soft Comput.*, 24 (2020) 3237–3255.
- [14] Çalık A., A novel Pythagorean fuzzy AHP and fuzzy TOPSIS methodology for green supplier selection in the Industry 4.0 era, *Soft Comput.*, 24 (2020) 3237–3255.
- [15] Liu H.-C., Quan M.-Y., Li Z., Wang Z.-L., A new integrated MCDM model for sustainable supplier selection under interval-valued intuitionistic uncertain linguistic environment, *Inf. Sci. (Ny)*. 486 (2019) 254–270.
- [16] Zimmer K., Fröhling M., Schultmann F., Sustainable supplier management – a review of models supporting sustainable supplier selection, monitoring and development, *Int. J. Prod. Res.*, 54 (2016) 1412–1442.
- [17] Xu Z., Qin J., Liu J., Martínez L., Sustainable supplier selection based on AHPSort II in interval type-2 fuzzy environment, *Inf. Sci.*, 483 (2019) 273–293.
- [18] Rabbani M., Foroozesh N., Mousavi S.M., Farrokhi-Asl H., Sustainable supplier selection by a new decision model based on interval-valued fuzzy sets and possibilistic statistical reference point systems under uncertainty, *Int. J. Syst. Sci. Oper. Logist.*, 6 (2019) 162–178.
- [19] Abdel-Baset M., Chang V., Gamal A., Smarandache F., An integrated neutrosophic ANP and VIKOR method for achieving sustainable supplier selection: A case study in importing field, *Comput. Ind.*, 106 (2019) 94–110.
- [20] Song Y., Li G., A large-scale group decision-making with incomplete multi-granular probabilistic linguistic term sets and its application in sustainable supplier selection, *J. Oper. Res. Soc.*, 70 (2019) 827–841.
- [21] Pishchulov G., Trautrimas A., Chesney T., S. Gold, L. Schwab, The Voting Analytic Hierarchy Process revisited: A revised method with application to sustainable supplier selection, *Int. J. Prod. Econ.*, 211 (2019) 166–179.
- [22] Foroozesh N., Tavakkoli-Moghaddam R., Mousavi S.M., An interval-valued fuzzy statistical group decision making approach with new evaluating indices for sustainable supplier selection problem, *J. Intell. Fuzzy Syst.*, 36 (2019) 1855–1866.
- [23] Ozdemir Y., Gul M., Measuring development levels of NUTS-2 regions in Turkey based on capabilities approach and multi-criteria decision-making, *Comput. Ind. Eng.*, 128 (2019) 150–169.

- [24] Tepe S., Kaya İ., A fuzzy-based risk assessment model for evaluations of hazards with a real-case study, *Hum. Ecol. Risk Assess. An Int. J.*, (2019) 1–26.
- [25] Gul M., Ak M.F., A comparative outline for quantifying risk ratings in occupational health and safety risk assessment, *J. Clean. Prod.*, 196 (2018) 653–664.
- [26] Gul M., Application of Pythagorean fuzzy AHP and VIKOR methods in occupational health and safety risk assessment: the case of a gun and rifle barrel external surface oxidation and colouring unit, *Int. J. Occup. Saf. Ergon.*, (2018) 1–14.
- [27] Gul M., Guneri A.F., Nasirli S.M., A fuzzy-based model for risk assessment of routes in oil transportation, *Int. J. Environ. Sci. Technol.*, 16 (2019) 4671–4686.
- [28] Zhang X., Xu Z., Extension of TOPSIS to Multiple Criteria Decision Making with Pythagorean Fuzzy Sets, *Int. J. Intell. Syst.*, 29 (2014) 1061–1078.
- [29] Garg H., A New Improved Score Function of an Interval-Valued Pythagorean Fuzzy Set based TOPSIS Method, *Int. J. Uncertain. Quantif.*, 7 (2017) 463–474.
- [30] Khan A., Abdullah S., Yousaf M.A., Hussain I., Farooq M., Extension of TOPSIS method base on Choquet integral under interval-valued Pythagorean fuzzy environment, *J. Intell. Fuzzy Syst.*, 34 (2018) 267–282.
- [31] Liang D., Xu Z., The new extension of TOPSIS method for multiple criteria decision making with hesitant Pythagorean fuzzy sets, *Appl., Soft Comput.*, 60 (2017) 167–179.
- [32] Onar S.C., Oztaysi B., Kahraman C., Multicriteria Evaluation of Cloud Service Providers Using Pythagorean Fuzzy TOPSIS, *J. Mult. Log. Soft Comput.*, 30 (2018) 263–283.
- [33] Oz N.E., Mete S., Serin F., Gul M., Risk assessment for clearing and grading process of a natural gas pipeline project: An extended TOPSIS model with Pythagorean fuzzy sets for prioritizing hazards, *Hum. Ecol. Risk Assess., An Int. J.*, (2018) 1–18.
- [34] Sajjad Ali Khan M., Ali A., Abdullah S., Amin F., Hussain F., New extension of TOPSIS method based on Pythagorean hesitant fuzzy sets with incomplete weight information, *J. Intell. Fuzzy Syst.*, 35 (2018) 5435–5448.
- [35] Biswas A., Sarkar B., Pythagorean fuzzy TOPSIS for multicriteria group decision-making with unknown weight information through entropy measure, *Int. J. Intell. Syst.*, 34 (2019) 1108–1128.
- [36] Wang L., Wang H., Xu Z., Ren Z., The interval-valued hesitant Pythagorean fuzzy set and its applications with extended TOPSIS and Choquet integral-based method, *Int. J. Intell. Syst.*, 34 (2019) 1063–1085.
- [37] Yager R.R., Pythagorean fuzzy subsets, in: 2013 Jt. IFSA World Congr. NAFIPS Annu., *Meet., IEEE*, 2013: pp. 57–61.
- [38] Peng X., Yang Y., Some Results for Pythagorean Fuzzy Sets, *Int. J. Intell. Syst.*, 30 (2015) 1133–1160.
- [39] Abdullah L., Najib L., A new preference scale of intuitionistic fuzzy analytic hierarchy process in multi-criteria decision making problems., *J. Intell. Fuzzy Syst.*, 26 (2014) 1039–1049.
- [40] Saaty T.L., A scaling method for priorities in hierarchical structures, *J. Math. Psychol.*, 15 (1977) 234–281.
- [41] Feyzioğlu O., Göçer F., Büyüközkan G., Interval-valued intuitionistic fuzzy MULTIMOORA approach for new product development, in: *Data Sci. Knowl. Eng. Sens. Decis. Support*, World Scientific, (2018), 1066–1073.
- [42] Büyüközkan G., Berkol Ç., Designing a sustainable supply chain using an integrated analytic network process and goal programming approach in quality function deployment, *Expert Syst. Appl.* 38 (2011) 13731–13748.

AUTHOR GUIDELINES

Thank you for choosing to submit your paper to Cumhuriyet Science Journal. The following instructions will ensure we have everything required so your paper can move through pre-evaluating, peer review, production and publication smoothly. Please take the time to read and follow them as closely as possible, as doing so will ensure your paper matches the journal's requirements.

Submission

Cumhuriyet Science Journal is an international, peer-reviewed, free of charge journal covering the full scope of both natural and engineering sciences. Manuscripts should be submitted by one of the authors of the manuscript as online submission after registration to the Cumhuriyet Sciences Journal. Microsoft Word (.doc, .docx, .rtf), files can be submitted. There is no page limit. If there is a problem while uploading the files of manuscript, please try to reduce their file size, especially manuscripts including embedded figures. Submissions by anyone other than one of the authors will not be accepted. The submitting author takes responsibility for the paper during submission and peer review. If for some technical reason submission through the online submission system is not possible, the author can contact csj@cumhuriyet.edu.tr for support.

Submission or processing charges

Cumhuriyet Science Journal does not charge any article submission, processing charges, and printing charge from the authors.

Terms of Submission

Papers must be submitted on the understanding that they have not been published elsewhere (except in the form of an abstract or as part of a published lecture, review, or thesis) and are not currently under consideration by another journal. The submitting author is responsible for ensuring that the article's publication has been approved by all the other coauthors. It is also the authors' responsibility to ensure that the articles emanating from a particular institution are submitted with the approval of the necessary institution. Only an acknowledgment from the editorial office officially establishes the date of receipt. Further correspondence and proofs will be sent to the author(s) before publication unless otherwise indicated. It is a condition of submission of a paper that the corresponding author permit editing of the paper for readability. All enquiries concerning the publication of accepted papers should be addressed to csj@cumhuriyet.edu.tr. Please note that Cumhuriyet Science Journal uses iThenticate software to screen papers for unoriginal material. By submitting your paper to Cumhuriyet Science Journal are agreeing to any necessary originality checks your paper may have to undergo during the peer review and production processes. Upon receiving a new manuscript, the Editorial office conducts initial pre-refereeing checks to ensure the article is legible, complete, correctly formatted, original, within the scope of the journal in question, in the style of a scientific article and written in clear English. Any article that has problems with any of the journal criteria may be rejected at this stage.

Peer Review

This journal operates a single blind review process. All contributions will be initially assessed by the editor for suitability for the journal. Papers deemed suitable are then typically sent to a minimum of two independent expert reviewer to assess the scientific quality of the paper. The author is required to upload the revised article to the system within 15 days by making the corrections suggested by the referee. The article will be rejected if there are no fixes in it. The Editor is responsible for the final decision regarding acceptance or rejection of articles. The Editor's decision is final

Title and Authorship Information

The following information should be included

Paper title

Full author names

Full institutional mailing addresses

Corresponding address

Email address

Abstract

The manuscript should contain an abstract. The researchers who are native speakers of Turkish have to add Turkish title and abstract as well. The abstract should be self-contained and citation-free and should be 250-300 words.

Keywords

Keywords of the scientific articles should be selected from the web address of www.bilimadresleri.com

Introduction

This section should be succinct, with no subheadings.

Materials and Methods

This part should contain sufficient detail so that all procedures can be repeated. It can be divided into subsections if required.

Conflicts of interest

Sample sentence if there is no conflict of interest: The authors stated that did not have conflict of interests.

Acknowledgements

Sample sentences for acknowledgements: The work was supported by grants from CUBAP (T-1111). We would like to acknowledge Prof. Mehmet Sözer, MD, for his precious technical and editorial assistance. We would like to thank

References

References to cited literature should be identified by number in the text in square brackets and grouped at the end of the paper in numerical order of appearance. Each reference must be cited in the text. Always give inclusive page numbers for references to journal articles and a page range or chapter number for books. References should be styled and punctuated according to the following examples

- [1] Karaca E., Ulusoy S., Morgül Ü., Ulusoy H.I., Development of Analytical Method for Sensitive Determination of Streptozotocin based on Solid Phase Extraction, Cumhuriyet Sci. J., 41 (4) (2020) 826-831. (sample reference for journals)
- [2] Keskin B., Ozkan A.S., Inverse Spectral Problems for Dirac Operator with Eigenvalue Dependent Boundary and Jump Conditions, Acta Math. Hungar., 130 (2011) 150-159(sample reference for journals)
- [3] Mazur M.T., Kurman R.J., Dysfunctional Uterine Bleeding. In: Mazur M.T., Kurman R.J., (Eds). Diagnosis of endometrial biopsies and curettings, A practical approach. 2nd ed. Berlin: Springer, (2005) 100-120. (sample reference for book chapters)
- [4] Mazur M.T., Kurman R.J.,Diagnosis of endometrial biopsies and curettings, A practical approach. 2nd ed. Berlin, (2005) 100-120. (sample reference for book)
- [5] National Cancer Institute, Surveillance Epidemiology and End Results. Cancer of the Corpus and Uterus, NOS. Available at: http://seer.cancer.gov/statfacts/html/corp.html?statfacts_page=corp. Retrieved March 2, 2008. (sample reference for websites)
- [6] Surname N., Title of thesis, PD or master thesis, Name of university, name of institue, year. (sample reference for thesis)
- [7] Surname N., Title of fulltext conference paper, name of conference, city, year, pages. (sample reference for Abstratcs in conferences are not accepted as a valid reference except full text)

Preparation of Figures

Each figure can be integrated in the paper body or separately uploaded and should be cited in a consecutive order. Figure widths can be 4-6 inch as 300 dpi. The labels of the figures should be clear and informative. The name and the subtitles of the figures must be 9-point font.

Preparation of Tables

Tables should be cited consecutively in the text. Every table must have a descriptive title and if numerical measurements are given, the units should be included in the column heading. Tables should be simple with simple borders and text written as left text. The name and the subtitle of the tables must be 9-point font

Proofs

Corrected proofs must be returned to the publisher within 2 weeks of receipt. The publisher will do everything possible to ensure prompt publication. It will therefore be appreciated if the manuscripts and figures conform from the outset to the style of the journal.

Copyright

Open Access authors retain the copyrights of their papers, and all open access articles are distributed under the terms of the Creative Commons Attribution license, which permits unrestricted use, distribution and reproduction in any medium, provided that the original work is properly cited.

The use of general descriptive names, trade names, trademarks, and so forth in this publication, even if not specifically identified, does not imply that these names are not protected by the relevant laws and regulations.

While the advice and information in this journal are believed to be true and accurate on the date of its going to press, neither the authors, the editors, nor the publisher can accept any legal responsibility for any errors or omissions that may be made. The publisher makes no warranty, express or implied, with respect to the material contained herein.

Ethical Guidelines

New methods and ethically relevant aspects must be described in detail, bearing in mind the following:

Human Experiments. All work must be conducted in accordance with the Declaration of Helsinki (1964). Papers describing experimental work on human subjects who carry a risk of harm must include:

A statement that the experiment was conducted with the understanding and the consent of the human subject.

A statement that the responsible Ethical Committee has approved the experiments.

Animal Experiments. Papers describing experiments on living animals should provide:

A full description of any anaesthetic and surgical procedure used.

Evidence that all possible steps were taken to avoid animal suffering at each stage of the experiment. Papers describing experiments on isolated tissues must indicate precisely how the donor tissues were obtained.

Submission Preparation Checklist

As part of the submission process, authors are required to check off their submission's compliance with all of the following items, and submissions may be rejected that do not adhere to these guidelines.

The submission has not been previously published, nor is it before another journal for consideration (or an explanation has been provided in Comments to the Editor).

The submission file is in Microsoft Word document file (Times New Roman) format.

Where available, URLs for the references have been provided.

The text is single-spaced; uses a 11-point font; employs italics, rather than underlining (except with URL addresses); and all illustrations, figures, and tables are placed within the text at the appropriate points, rather than at the end.

The text adheres to the stylistic and bibliographic requirements outlined in the Author Guidelines, which is found in About the Journal.

If submitting to a peer-reviewed section of the journal, the instructions in Ensuring a Double-Blind Review have been followed.